Technical University of Catalonia
Department of Signal Theory and Communications

Opportunistic Communications in Large Uncoordinated Networks

Ph.D. Dissertation by
Jordi Borràs Pino

Advisor
Prof. Gregori Vázquez Grau

Barcelona, November 2022

Nobody said it was easy.
Coldplay. "The Scientist".

A la Júlia i als meus pares.

Abstract

The increasing growth of wireless devices demanding high data-rate services burdens the coexistence of wireless systems sharing the same resources in a given geographical area due to the constantly increasing inter-system interference. Consequently, interference management plays a fundamental role in easing the coexistence of various heterogeneous communication services. Nevertheless, the classic interference management strategies, such as orthogonal access schemes, precoding, and decoding, require a certain amount of side information to successfully deal with interferences. Acquiring this side information originates the necessity of inter-system coordination and cooperation, which is not practical given the heterogeneity of coexisting communication services.

Opportunistic communications offer a potential solution to the problem of managing inter-system interferences. The basic principle of opportunistic communications is to efficiently and robustly exploit the available resources in a wireless network and to adapt the transmitted signals to the network state occupancy in order to avoid inter-system interferences. Accordingly, opportunistic communications rely on inferring which network resources are available and can be safely exploited without inducing interference on the coexisting neighboring communication nodes. Once the available network resources have been identified, it is possible to tune conventional modulations to avoid interfering with the coexisting nodes. Nevertheless, the most prominent opportunistic communications techniques consist in designing dedicated scenario-aware precoding/decoding strategies to exploit the so-called null space, i.e., the set of available network resources. Despite that, the classic solutions in the literature suffer from two main drawbacks: the lack of robustness to sensing errors and the necessity of intra-system coordination and cooperation.

This thesis deals with the design of a null space-based opportunistic communication scheme facing the drawbacks exhibited by the existing methodologies under the cumbersome assumption that the *opportunistic nodes* do not cooperate. For this purpose, a generalized sensing error model is introduced that allows the design of solutions exhibiting minimum worst-case inter-system interferences. This generalized error model is independent of the considered null-space identification mechanism, being the proposed solutions of general interest. These solutions respond to a maximum transmitting signal-to-interference ratio (SIR) criterion, which is optimal under feedforward (i.e., non-cooperative) conditions. The proposed methodology permits designing a family of orthonormal waveforms that spread the modulated symbols within the sensed null space. This spreading is the key to minimizing the interference per network resource erroneously sensed as available. It is important to highlight that the proposed solutions are invariant (i.e., unique) within the sensed null space, which permits safely removing the until-now considered feedback link and still performing coherent waveform detection.

Nevertheless, when the coordinated feedback link is removed, the waveform design relies only on local sensing information, leading to an end-to-end null-space mismatch, i.e., the opportunistic transmitting and receiving nodes can identify slightly different null spaces. As a consequence, feedforward opportunistic communication suffers from detection energy loss and self-induced inter-symbol interference, which can a priori severely degrade the system performance. Even though the derived null-space opportunistic communication scheme is robust to the null-space mismatch effects, the problem of enhanced opportunistic detection is also studied in this thesis by leveraging the active subspace detection framework.

As the number of total network resources arbitrarily increases, the proposed solutions tend to be linear combinations of complex exponentials, providing a frequency-domain interpretation of the proposed opportunistic communication technique. It is worth noting that frequency-domain spreading typically requires the use of pseudo-random sequences, meaning that coherent opportunistic communication is possible when the employed pseudo-random sequences are shared between the transmitting and receiving nodes. Nevertheless, the technique proposed in this thesis achieves the desired frequency-domain spreading using deterministic signals that can be locally designed thanks to the invariance property. Moreover, this asymptotic behavior permits designing a cyclic prefix-based opportunistic transmission scheme able to deal with the frequency-selectivity of the wireless channel in wideband regimes. In terms of practical implementation, this thesis studies a variant of the time-division multiple-access scheme that employs circulant pulse-shaping waveforms.

Finally, this thesis studies the impact of using multiple antennas in null space-based opportunistic communications. The performed analysis permits concluding that under symmetry conditions, i.e., when the number of transmitting and receiving antennas is equal, the properties studied for the single-antenna case still hold. Despite its importance, this result is not general enough because the communicating nodes will be usually equipped with a different number of antennas. For this purpose, this thesis leverages the array manifold separation theory framework to corroborate that using different array geometries has no impact on opportunistic communication and that the number of sensors translates into a transmitting SIR improvement. In the context of wideband multi-antenna communications, the proposed strategy asymptotically performs an antenna selection policy, prioritizing those antennas detecting a more significant number of available network resources since they exhibit a better signal spreading performance.

Resum

El creixement incremental dels dispositius sense fils que requereixen serveis d'alta velocitat de dades limita la coexistència de sistemes sense fils que comparteixen els mateixos recursos en una àrea geogràfica donada a causa de la interferència entre sistemas, cada vegada més important. En conseqüència, la gestió d'interferència exerceix un paper fonamental per a facilitar la coexistència de diversos serveis de comunicació heterogenis. No obstant això, les estratègies clàssiques de gestió d'interferència, com ara els esquemes d'accés ortogonal, la precodificació i la descodificació, requereixen una certa quantitat d'informació lateral per tractar amb èxit les interferències. Adquirir aquesta informació lateral origina la necessitat de coordinació i cooperació entre sistemes, la qual cosa no és pràctic donada l'heterogeneïtat dels serveis de comunicació coexistents.

Les comunicacions oportunistes ofereixen una solució potencial al problema de la gestió de les interferències entre sistemes. El principi bàsic de les comunicacions oportunistes és explotar de manera eficient i robusta els recursos disponibles en una xarxa sense fils i adaptar els senyals transmesos a l'estat de la xarxa per evitar interferències entre sistemes. Per tant, les comunicacions oportunistes depenen de la inferència de quins recursos de xarxa estan disponibles i poden ser explotats de manera segura sense induir interferència en els nodes de comunicació coexistents. Una vegada que s'han identificat els recursos de xarxa disponibles, és possible sintonitzar les modulacions convencionals per evitar interferir amb els nodes coexistents. No obstant això, les tècniques de comunicació oportunistes més prominents consisteixen en el disseny d'estratègies de precodificació/descodificació adaptades a l'escenari per explotar l'anomenat espai nul, és a dir, el conjunt de recursos de xarxa disponibles. Malgrat això, les solucions clàssiques en la literatura sofreixen dos inconvenients principals: la falta de robustesa als errors de detecció i la necessitat de coordinació i cooperació intra-sistema.

Aquesta tesi tracta el disseny d'un esquema de comunicació oportunista basat en l'espai nul que afronta els inconvenients exposats per les metodologies existents sota la suposició que els nodes oportunistes no cooperen. Per a aquest propòsit, s'introdueix un model generalitzat d'error de detecció que permet el disseny de solucions que exhibeixen interferències mínimes entre sistemes en el cas pitjor. Aquest model generalitzat d'error és independent del mecanisme d'identificació de l'espai nul, sent les solucions proposades d'interès general. Aquestes solucions responen a un criteri de máxima relació de senyal a interferència (SIR), que és òptim en condicions de no cooperació. La metodologia proposada permet dissenyar una família de formes d'ona ortonormals que realitzem un *spreading* dels símbols modulats dins de l'espai nul detectat. Aquest *spreading* és la clau per minimitzar la interferència per recurs de xarxa que erròniament es percep com a disponible. És important destacar que les solucions proposades són invariants (és a dir, úniques) dins de l'espai nul inferit, cosa que permet eliminar de manera

segura l'enllaç de retroalimentació considerat fins ara i, tot i així, realitzar una detecció coherent de forma d'ona.

No obstant això, quan s'elimina l'enllaç de retroalimentació coordinat, el disseny de la forma d'ona es basa únicament en la informació de l'estat de la xarxa detectada localment, el que condueix a un desajustament d'espai nul d'extrem a extrem, és a dir, els nodes transmissor i receptor oportunistes poden identificar espais nuls lleugerament diferents. Com a conseqüència, la comunicació oportunista pateix una pèrdua d'energia en detecció i interferències entre símbols autoinduïdes, que a priori poden degradar severament el rendiment del sistema. Tot i que l'esquema de comunicació oportunista d'espai nul derivat és robust als efectes de desajustament d'espai nul, el problema de la detecció oportunista millorada també s'estudia en aquesta tesi mitjançant fent ús de tècniques de detecció de subespai actiu.

A mesura que el nombre total de recursos de xarxa augmenta arbitràriament, les solucions proposades tendeixen a ser combinacions lineals d'exponencials complexes, proporcionant una interpretació en el domini freqüencial de la tècnica de comunicació oportunista proposada. Val la pena assenyalar que l'*spreading* en el domini freqüencial normalment requereix l'ús de seqüències pseudoaleatòries, el que significa que la comunicació oportunista coherent és possible quan les seqüències pseudoaleatòries emprades es comparteixen entre els nodes transmissor i receptor. No obstant això, la tècnica proposada en aquesta tesi aconsegueix l'*spreading* desitjat en el domini freqüencial mitjançant senyals deterministes que es poden dissenyar localment gràcies a la propietat d'invariància. A més, aquest comportament asimptòtic permet dissenyar un esquema de transmissió oportunista basat en prefix cíclic capaç de tractar la selectivitat freqüencial del canal sense fil en règims de banda ampla. En termes d'implementació pràctica, aquesta tesi estudia una variant de l'esquema d'accés múltiple de la divisió de temps que empra formes d'ona circulant amb forma de pols.

Finalment, aquesta tesi estudia l'impacte de l'ús de múltiples antenes en comunicacions oportunistes basades en l'espai nul. L'anàlisi realitzada permet concloure que sota condicions de simetria, és a dir, quan el nombre d'antenes de transmissió i recepció és igual, les propietats estudiades per al cas d'una sola antena encara es mantenen. Malgrat la seva importància, aquest resultat no és prou general perquè els nodes oportunistes normalment estaran equipats amb un nombre diferent d'antenes. Per a aquest propòsit, aquesta tesi utilitza el marc de la teoria de *manifold separation* per corroborar que l'ús de diferents geometries de les agrupacions d'antenes no té cap impacte en la comunicació oportunista i que el nombre de sensors es tradueix en una millora en termes de SIR. En el context de les comunicacions multiantena de banda ampla, l'estratègia proposada realitza asimptòticament una política de selecció d'antenes, donant prioritat a aquelles antenes que detecten un nombre més significatiu de recursos de xarxa disponibles, ja que presenten un millor rendiment en termes d'*spreading*.

Resumen

El crecimiento incremental de los dispositivos inalámbricos que requieren servicios de alta velocidad de datos limita la coexistencia de sistemas inalámbricos que comparten los mismos recursos en una área geográfica dada a causa de la interferencia entre sistemas, cada vez más importante. En consecuencia, la gestión de interferencia ejerce un papel fundamental para facilitar la coexistencia de varios servicios de comunicación heterogéneos. Sin embargo, las estrategias clásicas de gestión de interferencia, como por ejemplo los esquemas de acceso ortogonal, la precodificación y la descodificación, requieren cierta cantidad de información lateral para tratar con éxito las interferencias. Adquirir esta información lateral origina la necesidad de coordinación y cooperación entre sistemas, lo cual no es práctico dada la heterogeneidad de los servicios de comunicación coexistentes.

Las comunicaciones oportunistas ofrecen una solución potencial al problema de la gestión de las interferencias entre sistemas. El principio básico de las comunicaciones oportunistas es explotar de manera eficiente y robusta los recursos disponibles en una red inalámbrica y adaptar las señales transmitidas al estado de la red para evitar interferencias entre sistemas. Por lo tanto, las comunicaciones oportunistas dependen de la inferencia de qué recursos de red están disponibles y pueden ser explotados de manera segura sin inducir interferencia en los nodos de comunicación coexistentes. Una vez que se han identificado los recursos de red disponibles, es posible sintonizar las modulaciones convencionales para evitar interferir con los nodos coexistentes. Sin embargo, las técnicas de comunicación oportunistas más prominentes consisten en el diseño de estrategias de precodificación/descodificación adaptadas al escenario para explotar el llamado espacio nulo, es decir, el conjunto de recursos de red disponibles. A pesar de esto, las soluciones clásicas en la literatura sufren dos inconvenientes principales: la falta de robustez a los errores de detección y la necesidad de coordinación y cooperación intra-sistema.

Esta tesis trata el diseño de un esquema de comunicación oportunista basado en el espacio nulo que afronta los inconvenientes que sufren las metodologías existentes bajo la suposición que los nodos oportunistas no cooperan. Para este propósito, se introduce un modelo generalizado de error de detección que permite el diseño de soluciones que exhiben interferencias mínimas entre sistemas en el caso peor. Este modelo generalizado de error es independiente del mecanismo de identificación del espacio nulo, siente las soluciones propuestas de interés general. Estas soluciones responden a un criterio de máxima relación de señal a interferencia (SIR), que es óptimo en condiciones de no cooperación. La metodología propuesta permite diseñar una familia de formas de onda ortonormales que realizan un *spreading* de los símbolos modulados dentro del espacio nulo detectado. Este *spreading* es la clave para minimizar la interferencia por recurso de red que erróneamente se percibe como disponible. Es importante destacar que

las soluciones propuestas son invariantes (es decir, únicas) dentro del espacio nulo inferido, cosa que permite eliminar de manera segura el enlace de retroalimentación considerado hasta ahora y, aun así, realizar una detección coherente de forma de onda.

Sin embargo, cuando se elimina el enlace de retroalimentación coordinado, el diseño de la forma de onda se basa únicamente en la información del estado de la red detectada localmente, lo que conduce a un desajuste de espacio nulo de extremo a extremo, es decir, los nodos transmisor y receptor oportunistas pueden identificar espacios nulos ligeramente diferentes. Como consecuencia, la comunicación oportunista sufre una pérdida de energía en detección e interferencias entre símbolos autoinducidas, que a priori pueden degradar severamente el rendimiento del sistema. A pesar de que el esquema de comunicación oportunista de espacio nulo derivado es robusto a los efectos de desajuste de espacio nulo, el problema de la detección oportunista mejorada también se estudia en esta tesis mediante el uso de técnicas de detección de subespacio activo.

A medida que el número total de recursos de red aumenta arbitrariamente, las soluciones propuestas tienden a ser combinaciones lineales de exponenciales complejas, proporcionando una interpretación en el dominio frecuencial de la técnica de comunicación oportunista propuesta. Merece la pena señalar que el *spreading* en el dominio frecuencial normalmente requiere el uso de secuencias pseudoaleatorias, lo que significa que la comunicación oportunista coherente es posible cuando las secuencias pseudoaleatorias utilizadas se comparten entre los nodos transmisor y receptor. Sin embargo, la técnica propuesta en esta tesis consigue el *spreading* deseado en el dominio de frecuencia mediante señales deterministas que se pueden diseñar localmente gracias a la propiedad de invariancia. Además, este comportamiento asintótico permite diseñar un esquema de transmisión oportunista basado en prefijo cíclico capaz de tratar la selectividad frecuencial del canal inalámbrico en regímenes de banda ancha. En términos de implementación práctica, esta tesis estudia una variante del esquema de acceso múltiple de la división de tiempo que emplea formas de ola circulante con forma de polvo.

Finalmente, esta tesis estudia el impacto del uso de múltiples antenas en comunicaciones oportunistas basadas en el espacio nulo. El análisis realizado permite concluir que, bajo condiciones de simetría, es decir, cuando el número de antenas de transmisión y recepción es igual, las propiedades estudiadas para el caso de una sola antena todavía se mantienen. A pesar de su importancia, este resultado no es bastante general porque los nodos oportunistas normalmente estarán equipados con un número diferente de antenas. Para este propósito, esta tesis utiliza el marco de la teoría de *manifold separation* para corroborar que el uso de diferentes geometrías de las agrupaciones de antenas no tiene ningún impacto en la comunicación oportunista y que el número de sensores se traduce en una mejora en términos de SIR. En el contexto de las comunicaciones multiantena de banda ancha, la estrategia propuesta realiza asintóticamente una política de selección de antenas, dando prioridad a aquellas antenas que detecten un número más significativo de recursos de red disponibles, puesto que presentan un mejor rendimiento en términos de *spreading*.

Acknowledgments

Curiosament, aquesta ha estat la darrera pàgina que s'ha escrit d'aquesta tesi. I no precisament perquè no sigui important. Escriure aquestes línies suposen el final d'una etapa. Escriure aquestes línies suposa una confrontació de sentiments. D'una banda, l'alegria per culminar un objectiu molt important. Però també la tristesa pel que deixo enrere. Voldria aprofitar aquestes línies per agrair a tots els que han estat partícips, directament o indirecta, d'aquest camí.

Sense més preàmbuls, gràcies Gregori! Ha esta un immens plaer treballar al teu costat. No sabria com agrair-te tot el que m'has ensenyat, no només tècnicament, sinó en altres aspectes de la vida. Gràcies per la confiança i deixar sempre oberta la porta del teu despatx. Gràcies per trobar sempre la manera d'ajudar-me i motivar-me, sobretot en els moments difícils.

També voldria agrair a tots els membres del grup: Xell, Francesc, Jaume, Josep i Xavi. Moltes gràcies per fer-me sentir un més, per l'ajuda que m'heu ofert, les converses i els dinars.

Un especial agraïment als meus companys de camí: Ferran, Miquel, Fran i Sergi. Gràcies per la complicitat, recolzament i amistat que m'heu ofert. Gràcies pels bons moments, especialment durant els viatges, tot i què encara en tenim algun de pendent.

Aprofito també per recordar totes aquelles persones que m'han acompanyat els darrers anys, per la vostra amistat. Tot i les diverses situacions personals, és gratificant poder retrobar-nos.

Finalment, però no per això menys important, voldria donar les gràcies de tot cor a la meva família, als meus pares, als meus germans i a la meva iaia. Gràcies per estar sempre al meu costat. Voldria també recordar als que ja no hi són, especialment als meus avis i al meu iaio, que també són partícips d'aquesta tesi. Júlia, des de que vas arribar et vas convertir en la peça clau i indispensable. Gràcies per la teva paciència, la teva complicitat, i la teva estima. Gràcies per ser-hi sempre: en els bons moments, però sobretot en els no tan bons. Espero algun dia poder estar a l'alçada que tu has demostrat. Gràcies de tot cor.

Jordi Borràs
Barcelona, Novembre de 2022

This thesis has been supported by:

- The Spanish Ministry of Science and Innovation under the fellowship FPI BES-2017-080071;
- "Agencia Estatal de Investigación" (AEI) and European Regional Development Fund under projects *Wrestling with Interference in Communications and Information Processing* (TEC2016-76409-C2-1-R) and *Robust Methods for Statistical Inference, Data Integrity, and Interference Management* (PID2019-105717RB-C22); and
- Agency for Management of University and Research Grants (AGAUR, Catalan administration) under Grant 2017 SGR 578.

Acronyms

1D One dimensional.

2D Two dimensional.

3D Three dimensional.

AIC Akaike information criterion.

BC Broadcast channel.

BER Bit error rate.

BIA Blind interference alignment.

BIC Bayesian information criterion.

BPDN Basis pursuit denoising.

BSR Binary sparse recovery.

CCDF Complementary cumulative distribution function.

CDF Cumulative distribution function.

CDMA Code-division multiple-access.

CIP Constructive interference precoding.

CML Conditional maximum likelihood.

CP Cyclic prefix.

CS-TDMA Circulant-shaping time-division multiple-access.

CSI Channel state information.

D2D Device-to-device.

DFT Discrete Fourier transform.

DoF Degrees of freedom.

DPC Dirty paper coding.

DSSS Direct-sequence spread-spectrum.

DVB-T Digital video broadcasting-terrestrial.

FBMC Filter-bank multicarrier.

FDMA Frequency-division multiple-access

FHSS Frequency-hopping spread-spectrum.

GFDM Generalized frequency-division multiplexing.

IA Interference alignment.

IC Interference channel.

IDFT Inverse discrete Fourier transform.

IGS Improper Gaussian signaling.

INR Interference-to-noise ratio.

IoT Internet of things

ISAC Integrated sensing and communication.

ISI Inter-symbol interference.

LASSO Least absolute shrinkage and selector operator.

LS Least-squares.

LTE Long-term evolution.

MAC Multiple-access channel.

MC-CDMA Multicarrier code-division multiple-access.

MDL Minimum description length.

MIMO Multiple-input multiple-output.

MISO Multiple-input single-output.

ML Maximum likelihood.

MMSE Minimum mean-square error.

MNTLS Minimum-norm total least-squares.

MOS Model order selection.

MSE Mean-square error.

MST Manifold separation theory.

MUD Multiuser detector.

NDA Non-data-aided.

NOMA Non-orthogonal multiple-access.

NR New radio.

OFDM Orthogonal frequency-division multiplexing.

OFDMA Orthogonal frequency-division multiple-access.

OIA Opportunistic interference alignment.

OMA Orthogonal multiple-access.

OMP Orthogonal matching pursuit.

OTFS Orthogonal time-frequency space.

PAPR Peak-to-average power ratio.

PDF Probability density function.

PSD Power spectral density.

QoS Quality of service.

RIP Restricted isometry property.

ROC Receiver operating characteristics.

RSMA Rate-splitting multiple-access.

SC-FDMA Single-carrier frequency-division multiple-access.

SDMA Space-division multiple-access.

SIC Successive interference cancelation.

SIDR Signal-to-interference density ratio.

SIMO Single-input multiple-output.

SINR Signal-to-interference-plus-noise ratio.

SIR Signal-to-interference ratio.

SISO Single-input single-output.

SISR Self-ISI-to-signal ratio.

SLP Symbol-level precoding.

SMV Single measurement vector.

SND Simultaneous non-unique decoding.

SNR Signal-to-noise ratio.

SVD Singular value decomposition.

TDCS Transformed-domain communication system.

TDD Time-division duplex.

TDL Tapped-delay line.

TDMA Time-division multiple-access.

THP Tomlinson-Harashima precoding

TIM Topological interference management.

TIN Treating interference as noise.

TLS Total least-squares.

ULA Uniform linear array.

URLLC Ultra-reliable low-latency communication.

VFDM Vandermonde-subspace frequency-division multiplexing.

WiFi Wireless fidelity.

WiMAX Worldwide interoperability for microwave access.

ZF Zero forcing.

Notation

a	A scalar.
$x(t)$	A random process.
$X(\omega)$	The Fourier Transform of $x(t)$.
$\boldsymbol{x}$	A column vector.
$\boldsymbol{X}$	A matrix.
$\boldsymbol{I}_m$	The $m \times m$ identity matrix.
$\mathbf{0}_{m\times n}$	All-zeros $m \times n$ matrix.
$\mathbf{1}_{m\times n}$	All-ones $m \times n$ matrix.
$[\boldsymbol{x}]_m$	The m-th element of vector $\boldsymbol{x}$.
$[\boldsymbol{X}]_{m,n}$	The (m, n)-th entry of matrix $\boldsymbol{X}$.
$[\boldsymbol{X}]_m$	The m-th column of matrix $\boldsymbol{X}$.
$(\cdot)^T$	The transpose operator.
$(\cdot)^*$	The complex conjugate operator.
$(\cdot)^H$	The conjugate transpose (Hermitian) operator.
$\boldsymbol{X}^{-1}$	The inverse of matrix $\boldsymbol{X}$.
$\boldsymbol{X}^{+}$	The Moore-Penrose pseudo-inverse of matrix $\boldsymbol{X}$.
$\mathrm{tr}[\boldsymbol{X}]$	The trace of matrix $\boldsymbol{X}$.
$\det[\boldsymbol{X}]$	The determinant of matrix $\boldsymbol{X}$.

$\mathrm{rank}[\boldsymbol{X}]$	The rank of matrix $\boldsymbol{X}$.
$\langle \boldsymbol{X} \rangle$	The span of matrix $\boldsymbol{X}$.
$\|\boldsymbol{X}\|_{\mathrm{F}}$	The Frobenius norm of matrix $\boldsymbol{X}$.
$\|\boldsymbol{x}\|_p$	The L_p-norm of vector $\boldsymbol{x}$.
$\otimes$	The Kronecker tensor product.
$\odot$	The Schur-Hadamard (element-wise) product.
x^+	The function $\max(0, x)$.
$\log_a$	The logarithm in base a.
$\log$	The natural logarithm.
$\mathrm{sign}(a)$	The sign of the scalar a.
$\mathrm{mod}\ K$	The modulo-K operation.
$\lceil \cdot \rceil$	The ceiling operator.
$\mathcal{X}$	A set or a subspace.
$\|\mathcal{X}\|$	The cardinality of the set $\mathcal{X}$ or the dimension of the subspace $\mathcal{X}$.
$\mathcal{X} \cap \mathcal{Y}$	The intersection of $\mathcal{X}$ and $\mathcal{Y}$.
$\mathcal{X} \subset \mathcal{Y}$	$\mathcal{X}$ is a subset of $\mathcal{Y}$.
$\mathcal{X} \subseteq \mathcal{Y}$	$\mathcal{X}$ is a subset of or equal to $\mathcal{Y}$.
$\mathcal{X} \oplus \mathcal{Y}$	The direct sum of $\mathcal{X}$ and $\mathcal{Y}$.
$\mathbb{R}$	The set of real numbers.
$\mathbb{R}^+$	The set of positive real numbers.
$\mathbb{C}$	The set of complex numbers.
$\mathbb{E}$	The mathematical expectation.

$\mathbb{P}(\mathcal{E})$	The probability of the random event $\mathcal{E}$.
$\mathcal{N}(\boldsymbol{m}, \boldsymbol{C})$	Gaussian distribution with mean $\boldsymbol{m}$ and covariance $\boldsymbol{C}$.
$\mathcal{N}_{\mathbb{C}}(\boldsymbol{m}, \boldsymbol{C})$	Complex Gaussian distribution with mean $\boldsymbol{m}$ and covariance $\boldsymbol{C}$.
χ^2_r	Central Chi-square distribution with r degrees of freedom.

Contents

CHAPTER 1

Introduction

1.1 Scope

The unstoppable growth of wireless devices hinders the coexistence of different wireless systems sharing the same network resources. In this context, interference management plays a fundamental role in alleviating inter-system interference and facilitating resource sharing among the coexisting wireless systems. Accordingly, interference management has been one of the leading research topics of the last decades. Although several strategies have been proposed, ranging from orthogonal access schemes to precoding or decoding techniques, most rely on the necessity of cooperation and coordination between the different involved network nodes.

When dealing with intra-system interference, i.e., the interference caused by the network nodes belonging to the same wireless system, assuming that these nodes can share channel/network state information or other sorts of side information, such as their codebooks, to design interference management schemes seems realistic. However, it is not always practical. When two communication nodes want to set up a communication link, they are not initially coordinated and cannot cooperate. One possibility is to deploy *central* nodes acting as schedulers. These schedulers can assist the network nodes in setting up a communication link or help these nodes to coordinate. This solution, however, can become inefficient when the number of communication nodes grows exponentially.

From a more general perspective, dealing with inter-system interference, i.e. the interference caused by nodes belonging to other wireless systems, would ideally require coordination or cooperation between communication nodes belonging to different wireless systems, which is not practical. In the case where the inter-system interference is caused by two subsystems of the same wireless system, e.g., inter-cell interference in cellular communications, coordination or cooperation between the scheduling nodes may suffice. However, this solution is not general enough to deal with more recently studied scenarios, such as the massively connected Internet of Things (IoT). In this sense, *opportunistic communications* is an interference management strategy dealing with the design of transmission/detection schemes adapted to the particular network conditions to avoid inter-system interferences ideally. Accordingly, opportunistic

communication techniques are generally based on a *two-step* procedure. First, network state information from the wireless environment is obtained. Then, this information is exploited to tune the transmission parameters of existing modulations, e.g., multi-carrier modulations, or to design context-aware transmitting and detection strategies.

In spite of the potential advantages of opportunistic communications to facilitate the coexistence of interfering wireless systems, several technical challenges, which are addressed in this dissertation, have been identified.

The design of opportunistic transmission schemes relies on sensing the wireless environment. The sensing process can be cast as a detection problem and, accordingly, suffers from mainly two drawbacks: the estimation of the statistic and detection errors, in particular, miss-detection and false-alarm errors. These drawbacks may lead to inaccurate detection of the available network resources, meaning that some of the network resources occupied by other wireless systems can be wrongly detected as available. Using these erroneous network resources for opportunistic transmission may produce severe inter-system interferences, corrupting the communication between network nodes of other wireless systems. The main challenge is overcoming the difficulty of providing a general enough sensing error model to cast the robust design of opportunistic transmission strategies.

It is conventionally assumed that the network nodes involved in opportunistic communication are coordinated or can cooperate. In this sense, the classical assumption is that the *opportunistic nodes* share the same reference system for the network resources or, more generally, for the signal space. To be valid, this assumption requires that opportunistic nodes have previously agreed on a common reference system, utilizing a handshake procedure or through a centralized scheduling node. In decentralized networks, where the communication does not rely on a scheduler, it is not reasonable to assume that opportunistic nodes share a common reference system. It is worth noting that, in this case, opportunistic communication seems to be inherently non-coherent, yielding a system performance loss. Here, the term coherent refers to the knowledge of the transmitted pulse-shaping waveforms by the opportunistic receiver. An identified research challenge consists in designing waveforms exhibiting self-calibration properties so as to overcome the non-coherent condition in uncoordinated opportunistic communication scenarios.

Regardless of the capacity of opportunistic nodes to agree on a common reference system, if the sensing is locally performed, i.e., each opportunistic node bases the design of its transmission/detection strategy on the local network state information only, opportunistic communication also suffers from a performance loss due to end-to-end signal-space mismatch. Conventionally, this mismatch is overcome through a coordinated feedback link. Nevertheless, the feedback overheads required to agree on a common reference system and in a common signal space may burden the system complexity and potentially increase the latency. In some contexts, low-rate feedback strategies permit achieving performance similar to the full channel state information case. However, in uncoordinated opportunistic communications, the design of low-rate feedback strategies that allow agreeing on a signal space and a common reference system is troublesome.

The abovementioned research challenges are addressed in this dissertation. The involved research has resulted in the publications enumerated in Section 1.2. The contributions of this thesis are briefly described in Section 1.3, altogether with the organization of this document.

1.2 Publications

The research leading to this dissertation resulted in the following journal publications:

[J1] **J. Borras** and G. Vázquez, "Opportunistic transmission based on circulant-shaping TDMA", *IEEE Communications Letters*, 2022, (in preparation).

[J2] **J. Borras** and G. Vázquez, "Array-Geometry invariant iransmission in feedforward opportunistic communications", *IEEE Transactions on Signal Processing*, 2022, (under review).

[J3] **J. Borras** and G. Vázquez, "Interference mitigation in feedforward opportunistic communications", *IEEE Transactions on Communications*, 2022, (under second revision).

as well as the following publications in conference proceedings:

[C1] **J. Borras** and G. Vázquez, "Array-geometry invariant signaling in MISO feedforward opportunistic communications". In: *21st IEEE International Workshop on Signal Processing Advances in Wireless Communications (SPAWC)*, Atlanta, GA, USA (virtual), May 2020.

[C2] **J. Borras** and G. Vázquez, "Interference mitigation in opportunistic transmission under degrees-of-freedom sensing uncertainties ". In: *IEEE Global Communications Conference (GLOBECOM)*, Waikoloa Village, HI, USA, December 2019.

[C3] **J. Borras** and G. Vázquez, "Distributed feedback-aided subspace concurrent opportunistic communications". In: *20th IEEE International Workshop on Signal Processing Advances in Wireless Communications (SPAWC)*, Cannes, France, July 2019.

[C4] **J. Borras** and G. Vázquez, "Decentralized shaping for pilot generation and detection in opportunistic communications". In: *IEEE International Conference on Communications (ICC)*, Shanghai, China, May 2019.

[C5] **J. Borras** and G. Vázquez, "Uncoordinated space-frequency pilot design for multi-antenna wideband opportunistic communications". In: *19th IEEE International Workshop on Signal Processing Advances in Wireless Communications (SPAWC)*, Kalamata, Greece, June 2018.

[C6] **J. Borras**, J. Font-Segura, J. Riba, and G. Vázquez, "Dimension Spreading for Coherent Opportunistic Communications". In: *2017 51st Asilomar Conference on Signals, Systems, and Computers*, Pacific Grove, CA, USA, October 2017.

In addition to these publications, the author has also contributed in the following poster presentations:

[P1] **J. Borras** and G. Vázquez, "MISO Opportunistic Communications in Noncooperative Networks". In: *2021 IEEE Communication Theory Workshop (CTW) – Virtual Event*, Banff, AB, Canada, June 2021.

[P2] **J. Borras** and G. Vázquez: "Distributed Shaping for Opportunistic Communications: Pilot Design and Detection". In: *2019 IEEE Communication Theory Workshop (CTW)*, Selfoss, Iceland, May 2019.

Other Contributions

Beyond the topic of this dissertation, the author has also contributed to the following works:

- **J. Borras**, F. Molina, R. López-Valcarce, J. Sala-Álvarez, and G. Vázquez, "Energy-Efficient Analog Beamforming under Short Packets and Per-Antenna Power Constraints", *Signal Processing (EURASIP)*, (under review).
- **J. Borras**, F. Molina, R. López-Valcarce, and J. Sala-Álvarez, "Energy-Efficient Analog Beamforming with Short Packets in mmWave MIMO Systems". In: *2020 54th Asilomar Conference on Signals, Systems, and Computers – Virtual Event*, Pacific Grove, CA, USA, November 2020.
- F. Molina and **J. Borras**, "Low-Complexity Switching Network Design for Hybrid Precoding in mmWave MIMO Systems". In: *2019 European Signal Processing Conference (EUSIPCO)*, A Coruña, Spain, September 2019.

1.3 Organization and Contributions

This thesis is structured into five chapters, corresponding to Chapters 2–6. From these chapters, the original research contributions correspond to Chapters 3–5, as sketched in Figure 1.1. In the sequel, a brief overview of each chapter is disclosed, altogether with the derived publications and the relationship between each chapter.

Chapter 2 provides an overview of the problem of the coexistence of wireless systems and emphasizes the fundamental role that interference management plays. With the exponential growth of heterogeneous communication nodes coexisting in the same network, sharing the network resources becomes a more cumbersome task. In this context, dealing with inter-system interference is of paramount interest in guaranteeing coexistence and satisfying the quality-of-service requirements. Network sharing can be tackled in the time, frequency, or spatial domain. For the sake of generality, in this thesis, the different network resources are referred to as Degrees of Freedom (DoF). Accordingly, the formal definition of DoF is also provided in Chapter 2. In order to manage inter-system interferences, one possibility consists in resorting to classical interference management techniques conventionally used in multi-user networks. In this regard, techniques such as orthogonal access, Successive Interference Cancelation (SIC), Dirty Paper Coding (DPC), or Interference Alignment (IA) are potential solutions to dealing with inter-system interferences. Nevertheless, these solutions require cooperation or coordination between network nodes of different wireless systems, which is not a realistic assumption. These difficulties motivate studying opportunistic communication strategies as an inter-system interference management strategy. Chapter 2 summarizes the most relevant background literature on opportunistic communication schemes in both single- and multi-antenna scenarios.

The case of single-antenna feedforward opportunistic communications, i.e., when the opportunistic nodes cannot cooperate and are not coordinated, is addressed in Chapter 3. This chapter describes the fundamental drawbacks of the null space-based opportunistic communication strategies reviewed in Chapter 2: lack of robustness and lack of uniqueness. Null-space opportunistic communication schemes rely on detecting the available network resources –or

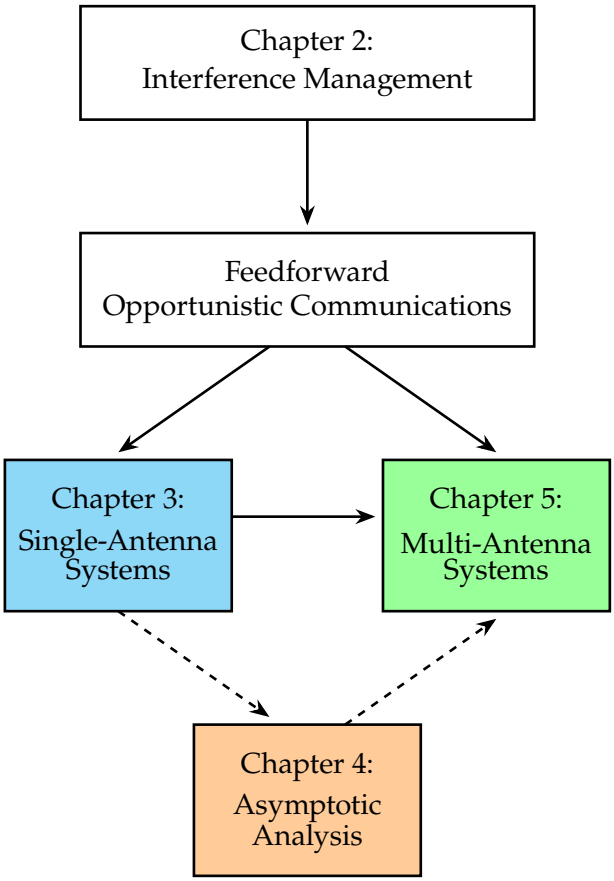

Figure 1.1: Schematic overview of the topics covered in this dissertation.

DoF–. A cumbersome task in these approaches is providing a simple but general enough error model to design robust transmission schemes. The first contribution of this chapter is to provide a generalized model for the null-space sensing errors characterizing the subspace leakage. This effect occurs when some DoF occupied by other wireless systems are erroneously detected as available. Under this error model, we provide the optimum waveform design strategy in the minimum worst-case inter-system interference sense. The robust solution is just the minimum-norm waveform, which is equivalent to the Total Least-Squares (TLS) solution. The robust waveforms are rank-one waveforms able to spread the transmitted symbol within the sensed null space, which is of paramount importance to decrease the inter-system interference density per DoF and minimize the outage probability induced on other neighboring communication nodes. Therefore, the proposed solutions respond to a maximum worst-case Signal-to-Interference Ratio (SIR) criterion. Interestingly, each derived waveform is a specific column, appropriately scaled, of the dimensionally-reduced orthogonal projector onto the sensed null space. Accordingly, the waveforms are unique, thus, invariant, within the sensed null space. This property guarantees the uniqueness of the solutions enabling coherent waveform detection under the lack of cooperation or coordination. The robust transmitting waveforms derived in this chapter, which are referred to as *Minimum-Norm Total Least-Squares (MNTLS) waveforms*, overcome the two major drawbacks of the conventional null-space opportunistic communication strategies. Nevertheless, when a null-space mismatch occurs, i.e., when the opportunistic transmitter and

the opportunistic receiver detect slightly different null spaces, the system performance degrades in the form of energy loss and self-induced inter-symbol interference. These effects are characterized and shown not to have a relevant impact. Either way, opportunistic communication performance can be improved when the opportunistic nodes prune their null spaces to exploit only those commonly detected DoF. In this respect, two active subspace recovery algorithms are proposed. The publications [C2], [C3], [C4], [C6], and [J3], as well as the poster presentation [P2], have been derived from the contributions of this chapter.

The potential interest in exploiting larger bandwidths leads to a higher enough number of total DoF, which naturally induces an asymptotic regime. In this regard, Chapter 4 studies the asymptotic behavior of the MNTLS waveforms. In this scenario, the sensed null-space bases converge to a column subset of the normalized Fourier matrix, admitting a characterization in the frequency domain. This chapter also studies the particular case where the DoF sensed as available are consecutive. In this case, the set of transmitting waveforms behaves as a time-division multiple-access scheme but employs special signaling, bringing to light the *Circulant-Shaping Time-Division Multiple-Access* (CS-TDMA) scheme. Interestingly, the CS-TDMA modulation exhibits a reduced Peak-to-Average Power Ratio (PAPR), which is of great interest for practical implementation due to the increasing energy efficiency requirements. The last part of this chapter studies an adaptation of the MNTLS waveforms to frequency-selective channels. Taking into account the asymptotic behavior of the null-space bases, a cyclic prefix-based strategy is proposed in order to deal with the frequency-selective nature of wideband channels. In contrast to other opportunistic communication strategies focused on frequency-selective channels, such as Vandermonde-Subspace Frequency-Division Multiplexing (VFDM), the proposed strategy does not require estimating the interference-channel matrices to design an appropriate precoding strategy. Even though the complexity of the waveforms design is not increased with the inclusion of the cyclic prefix, the null-space sensing becomes more cumbersome, as it now relies on a non-unitary sensing matrix. Nevertheless, this added difficulty can be relaxed if the opportunistic nodes have additional side information on the signal structure employed by the communication nodes of other wireless systems. In essence, adapting to frequency-selective channels results in a set of non-orthogonal waveforms whose orthogonality is restored at the receiving end when the cyclic prefix is removed. As in Orthogonal Frequency-Division Multiplexing (OFDM), the proposed strategy only requires simple one-tap frequency-domain equalizers to overcome the impact of the opportunistic channel. The contributions of this chapter lead to the publications [J1] and [J3].

Chapter 5 provides the generalization of the proposed null-space opportunistic communication strategy to multi-antenna scenarios. A simple mathematical analysis reveals that the space-time MNTLS waveforms can be designed as in the single-antenna case but now lying in extended signal space. Accordingly, it seems reasonable to believe that the essential properties of DoF spreading and invariance still hold in this general scenario. Regarding the DoF spreading, it is corroborated via numerical simulation. Mathematical analysis of the Signal-to-Interference Density Ratio (SIDR) unveils the potential advantages of employing multiple antennas to further mitigate undesired residual inter-system interferences. Nevertheless, verifying that the invariance property still holds in the multi-antenna case is not straightforward. Note that the use of antenna arrays with probably a different number of sensors prompts the transmitting pulse-shaping waveforms and the receiving matched filters to lie in signal spaces

of different dimensionality. Moreover, the impact of the physical structure of antenna arrays, i.e., their geometry, is unclear. A thorough mathematical analysis based on the *manifold separation theory* reveals that the space-time MNTLS waveforms are invariant to the antenna array geometry. Nevertheless, the number of array sensors impacts opportunistic communication since, as expected from the SIDR analysis, it provides an improved DoF spreading factor and a potential diversity gain improving the detection performance. This result generalizes the invariance property to multi-antenna scenarios. The last part of this chapter deals with extending the asymptotic analysis carried out in Chapter 4 to multi-antenna scenarios. Using the asymptotic eigendecomposition of block-Toeplitz matrices, it is shown that the opportunistic transmitter behaves as a set of mutually-orthogonal single-antenna transmitters. Accordingly, the space-time null-space sensing becomes a per-antenna time-frequency null-space sensing; thus, the waveform design strategy can be adapted to be performed on a per-antenna basis. In this regard, each space-time MNTLS waveform asymptotically performs an antenna selection policy, where the antennas with more time-frequency DoF availability are preferred. The publications [C1], [C5], and [J2], as well as the poster presentation [P1], have been derived from the contributions of this chapter.

Finally, the conclusions of this dissertation are drawn in Chapter 6, together with a summary of potential future research lines.

CHAPTER 2

Interference Management in Wireless Networks

2.1 Introduction

The increasing advents in wireless communication technologies, such as mobile communications, wireless Internet, vehicular communications, or the so-called Internet of Things (IoT), lead to an exponential growth of communications nodes coexisting in the same geographical area and sharing the physical-layer network resources [Pop20; CNY+21]. Each communication technology is characterized by employing different coded-modulation schemes or by different requirements, such as information rate, reliability, or latency. Wireless networks where different communication systems coexist are usually known as *heterogeneous networks*.

As widely discussed in the literature (see, for instance, [EPT07; HEKA16; BPG+16; ZGH17; SBL+18; NLP18; BMA+21]), these scenarios tend to be *interference-limited*. More specifically, the Signal-to-Interference-plus-Noise Ratio (SINR) at the k-th receiving node, defined as

$$\mathrm{SINR}_k \triangleq \frac{S_k}{\sum_{k' \neq k} S_{k'} + N}, \tag{2.1}$$

where S_k is the received power at the k-th receiving node sent by the k-th transmitting node and N is the noise power, arbitrarily decreases as the number of transmitter-receiver pairs coexisting in a heterogeneous network grows.

It is worth noting that, in view of (2.1), dealing with *inter-system interferences* plays a fundamental role to satisfy the stringent Quality-of-Service (QoS) requirements of each transmitter-receiver pair. The simplest and conventional strategy to combat inter-system interferences consists in avoiding interference through *orthogonalizing* the signals sent by each transmitting node, giving birth to the well-known Orthogonal Multiple-Access (OMA) schemes. Accordingly, transmitter-receiver pairs exploit a disjoint fraction of the physical-layer network resources, leading to interference-free transmissions. Even though OMA schemes have been extensively used in cellular communications, they suffer mainly from three drawbacks: (i) the number of transmitter-receiver pairs that can simultaneously coexist in the same wireless network is limited by the number of physical-layer network resources, (ii) OMA schemes require full coop-

eration between the coexisting nodes in order to perfectly avoid inter-system interferences, and (iii) the information-theoretic analysis of multi-user networks reveals that OMA is generally a suboptimal strategy [EK11]. Consequently, the need to mitigate rather than avoid interferences has made *interference management* a major research line in the field of wireless communications for a long time [VEG18].

This chapter aims to provide an extensive review of the interference management problem in the context of single-hop[1] interference networks. In particular, Sections 2.2 and 2.3 are devoted to the (many-user) interference channel problem and the fundamental limits of cooperation, respectively. Accordingly, these two sections can be skipped in the first reading, since the specific context review of the problem addressed in this dissertation is given in Section 2.4. In particular, Section 2.4 describes in a unified manner the state-of-the-art techniques in the context of null space-based opportunistic communications and discusses the current limitations of these techniques, which motivates the study of robust opportunistic communication schemes.

2.2 Interference Management in Communication Networks: Signal Processing Strategies and Fundamental Limitations

Transmitter-receiver pairs sharing the same wireless network can adopt different signal processing techniques to cope with inter-system interferences and satisfy their stringent QoS requirements. These signal processing strategies can involve different dimensions of the *spectrum space*, such as time, frequency, or space. For the sake of generality, we first introduce a generic communication model based on the concept of Degrees of Freedom (DoF), which is extensively used throughout this dissertation. Using this generalized model, we review the most significant interference management techniques and their limitations in terms of channel capacity.

Nevertheless, this study suffers from two major drawbacks. On the one hand, the channel capacity is the ultimate performance metric only when the transmission delay is not accounted for. In the case of delay-sensitive communications, transmitted messages are of short length[2] and the maximum attainable rate is far from the asymptotic capacity result [PPV10; Ers16]. On the other hand, the study of the channel capacity does not reveal the maximum *spatial density* of transmitter-receiver pairs that can simultaneously coexist in a given geographical area. For these reasons, we resort to the concept of *transmission capacity* as an alternative performance metric to assess the size of a communication network given an outage constraint.

2.2.1 A Generic Communication Model

Throughout this thesis, and for the sake of generality, the physical-layer resources of a wireless network are referred to as Degrees of Freedom (DoF). Therefore, this concept deserves a short elaboration before reviewing the different interference management approaches.

[1] Since this thesis is focused on single-hop communications, the literature review on interference management techniques is constrained to single-hop interference networks. An extensive study of the operating regimes and fundamental limits of multi-hop networks can be found in [ÖLT11].

[2] Applications involving short data packets are of significant interest nowadays under the umbrella of Ultra-Reliable Low-Latency Communications (URLLC) [BDP18; SMA+19; PSN+19], which is an enabler of critical massive machine-type communications [PDP+20].

The idea or concept of DoF was introduced by C. E. Shannon [Sha48; Sha49]. In particular, a geometric model for communication systems is provided in [Sha49] where, in essence, the transmitted signals are described as elements of a vector space (referred to as signal space). In this model, the number of DoF represents the dimension of the signal space. It is worth noting that this geometric model permits describing the number of DoF as the number of independent channel uses per second [Pop20].

In the sequel, we resort to the analysis performed in [Gal08] to provide a brief mathematical yet intuitive discussion on which is the dimension of signal space.

Without loss of generality, let us consider a real function (signal) $x(t)$ baseband-limited to W. Through the sampling theorem (see, for instance, [Gal08, Chapter 4]), the signal $x(t)$ can be written in terms of the so-called *sampling function* as

$$x(t) = \sum_{k=-\infty}^{\infty} x(t)|_{t=k/(2W)} \mathrm{sinc}(2Wt-k) = \sum_{k=-\infty}^{\infty} x(kT_\mathrm{s}) \mathrm{sinc}\left(\frac{t}{T_\mathrm{s}} - k\right), \quad \text{with } k \in \mathbb{Z}, \tag{2.2}$$

where $\mathrm{sinc}(t) = \sin(\pi t)/(\pi t)$, meaning that the baseband-limited function $x(t)$ can be specified by its samples at intervals $T_\mathrm{s} = 1/(2W)$. The set of sinc functions $\left\{\mathrm{sinc}\left(\frac{t}{T_\mathrm{s}} - k\right)\right\}_k$ define an orthonormal basis, that is, these functions satisfy the condition

$$\int_{-\infty}^{+\infty} \mathrm{sinc}\left(\frac{t}{T_\mathrm{s}} - k\right) \mathrm{sinc}\left(\frac{t}{T_\mathrm{s}} - k'\right) \mathrm{d}t = \begin{cases} 1 & \text{if } k = k' \\ 0 & \text{otherwise} \end{cases}, \tag{2.3}$$

and, accordingly, we may say that (2.2) describes $x(t)$ in terms of an orthonormal expansion.

A natural question is how many samples are needed to represent $x(t)$ without losing information. As discussed in [Sha49; Gal68; Gal08], a *rule of thumb*[3] is that a function approximately baseband-limited to W and approximately time-limited to $[-T/2, T/2]$ can be specified by about $2TW$ real numbers as coefficients in an orthogonal expansion, if $TW \gg 1$. The rationale behind the number $2TW$ is as follows. If the function is time-limited to $[-T/2, T/2]$, and this function can be specified by its samples taken at *sampling rate* $1/T_\mathrm{s} = 2W$ [samples per second], then the number of samples is $T/T_\mathrm{s} = 2TW$.

Consequently, functions that are approximately baseband-limited to W and approximately time-limited to $[-T/2, T/2]$ have about

$$N \approx 2WT \ \text{ real DoF} \tag{2.4}$$

when the time-bandwidth product is sufficiently large, i.e., $TW \gg 1$. It is worth noting that the provided definition of DoF lacks precision since time-limited signals cannot be baseband-limited, and baseband-limited signals cannot be time-limited. This is the reason why the number of real DoF N in (2.4) is an approximation. A more precise orthogonal expansion yet more challenging to study is composed of *prolate spheroidal functions* [SP61]. This class of functions maximizes the energy concentration in a finite time-frequency region; thus, being the closest approximation to time-limited and frequency-limited functions.

We shall now discuss why (2.4) indicates the number of dimensions of the signal space. Since a function $x(t)$ can be specified by about $2TW$ samples for $TW \gg 1$, these samples can

[3] A formal mathematical proof of this result is provided in [Sle76].

be collected in a vector of $N \approx 2TW$ elements. Such a vector belongs to the N-dimensional real vector space $\mathbb{R}^N$, where there are N orthogonal dimensions. Therefore, since the sampled baseband-limited signals to W and time-limited to $[-T/2, T/2]$ lie in $\mathbb{R}^N$, we can represent up to N non-overlapping (i.e., non-interfering) signals. Therefore, N represents the maximum number of memoryless channel uses available under these conditions.

According to the latter observation, it is worth noting that the number of DoF refers to the *pre-log* factor of the channel capacity as the Signal-to-Noise Ratio (SNR) becomes arbitrarily large. In other words, since the channel capacity (for the Gaussian channel), in nats per second, admits the following expression $C = W\log(1+\mathrm{SNR}) = d \cdot \mathrm{SE}$, with $\mathrm{SE} = \frac{1}{2}\log(1+\mathrm{SNR})$ being the spectral efficiency in nats per channel use and d the number of independent channel uses per second, we have that

$$d = \lim_{\mathrm{SNR}\to\infty} \frac{C}{\log \mathrm{SNR}} = \frac{2WT}{T}, \tag{2.5}$$

meaning that the number of real DoF indicates the number of independent memoryless channel uses. Regarding d, this quantity is sometimes referred to as the DoF of the communication channel or multiplexing gain. Therefore, T is known as the symbol duration, the channel use duration, or the DoF duration [Pop20].

Thus far, the discussion has been focused on a specific orthonormal basis given by a set of orthogonal sinc functions. Nevertheless, the concept of DoF can be further generalized. As per [Gal08], a signal $x(t)$ can be written in terms of a Karhunen-Loève expansion [CF67]. Accordingly, the decomposition in (2.2) admits the following generalization:

$$x(t) = \sum_{k=-\infty}^{\infty} x(t)|_{t=k/\alpha} u(\alpha t - k) = \sum_{k=-\infty}^{\infty} x(k/\alpha) u_k(t), \quad \text{with } k \in \mathbb{Z}, \tag{2.6}$$

where the set of basis functions $\{u_k(t)\}_k$ satisfy the orthonormality condition, i.e.,

$$\int_{-\infty}^{+\infty} u_k(t) u_{k'}(t) \mathrm{d}t = \begin{cases} 1 & \text{if } k = k' \\ 0 & \text{otherwise} \end{cases}. \tag{2.7}$$

This generalization permits writing the sampled signal $\boldsymbol{x} \in \mathbb{R}^N$, being N the number of real DoF, as a linear combination of a signal-space basis, that is

$$\boldsymbol{x} = \sum_{k=0}^{N-1} \boldsymbol{u}_k \lambda_k = \boldsymbol{U}\boldsymbol{\lambda}, \tag{2.8}$$

being $\boldsymbol{u}_k \in \mathbb{R}^N$ the sampled version of the basis functions $u_k(t)$, $\lambda_k = x(k/\alpha)$ the coefficients of the orthogonal expansion describing the sampled signal $\boldsymbol{x}$, $\boldsymbol{U} = [\boldsymbol{u}_0, \ldots, \boldsymbol{u}_{N-1}] \in \mathbb{R}^{N\times N}$ a signal-space basis and $\boldsymbol{\lambda} = [\lambda_0, \ldots, \lambda_{N-1}]^T \in \mathbb{R}^N$ the coefficients vector.

The generic signal model given in (2.8) will be used in the sequel to describe the interference network model and analyze different signal processing strategies for interference management and their associated performance limitations.

2.2.2 Fundamental Limits of Single-Hop Interference Networks

Interference management plays a fundamental role in multi-user networks to guarantee the particular QoS requirement of each involved transmitter-receiver pair. The different interference management strategies developed in the literature can be classified depending on their complexity, the necessity of cooperation between transmitters or receivers, and, of course, their performance in mitigating interferences. This subsection is devoted to summarizing the main signal processing strategies for interference management and discussing their associated performance limitations.

For this purpose, let us consider that K transmitter-receiver pairs coexist in the same wireless network. Using the generic signal model given in (2.8), the signal sent by the k-th transmitter can be written as

$$\boldsymbol{s}_k = \boldsymbol{U}_k \boldsymbol{\lambda}_k a_k = \boldsymbol{\phi}_k a_k \in \mathbb{C}^N, \tag{2.9}$$

where $\boldsymbol{U}_k \in \mathbb{C}^{N \times N}$ is a basis of the N-dimensional signal space, being $N \approx TW$ the number of complex DoF, $\boldsymbol{\lambda}_k$ is a vector with only one non-zero element indicating that the k-th transmitter sends one symbol per dimension (or DoF), and a_k stands for a zero-mean and unit-variance symbol. From this point onwards, we assume that the symbols are independent and identically distributed. Regarding (2.9), note that $\boldsymbol{\phi}_k$ can be seen as the pulse-shaping filter employed by the k-th transmitting node.

Before going deeper, some considerations on the signal-space basis $\boldsymbol{U}_k$ are of order. It is worth noting that in *synchronous* interference networks, all nodes share the same signal-space basis; thus $\boldsymbol{U}_k = \boldsymbol{U}$ for all k. Since matrix $\boldsymbol{U}$ encompasses the sampled basis functions of an orthonormal expansion of the sampled signals, note that $\boldsymbol{U}^H \boldsymbol{U} = \boldsymbol{U}\boldsymbol{U}^H = \boldsymbol{I}_N$. On the other hand, in the case of *asynchronous* interference networks, assuming that each transmitter-receiver pair is end-to-end synchronized, each of these pairs employs a different signal-space basis; hence, $\boldsymbol{U}_k \neq \boldsymbol{U}_{k'}$ for $k \neq k'$. Accordingly, even though the relationship $\boldsymbol{U}_k^H \boldsymbol{U}_k = \boldsymbol{U}_k \boldsymbol{U}_k^H = \boldsymbol{I}_N$ holds, it occurs that $\boldsymbol{U}_k \boldsymbol{U}_{k'}^H \neq \boldsymbol{I}_N$. A more challenging scenario, which will be discussed later, is that where each transmitter-receiver pair is not end-to-end synchronized.

The considerations above justify the generality of the transmitted signal model given in (2.9). In order to keep the discussion as general as possible, the asynchronous interference network case is considered below unless otherwise stated.

Under the assumption that each transmitter-receiver pair is synchronized and coordinated, that is, the receiver knows the pulse-shaping filter employed by the transmitting node, the received signal at the k-th receiving node after matched filtering is given by

$$\boldsymbol{y}_k = g_{kk} \boldsymbol{\phi}_k^H \boldsymbol{s}_k + \sum_{\substack{i=0 \\ i \neq k}}^{K-1} g_{ik} \boldsymbol{\phi}_k^H \boldsymbol{s}_i + \boldsymbol{w}_k, \tag{2.10}$$

where g_{ik} is the channel gain between the i-th transmitting node and the k-th receiver and $\boldsymbol{w}_k \sim \mathcal{N}_{\mathbb{C}}(\boldsymbol{0}; \sigma^2 \boldsymbol{I}_N)$ is a circularly-symmetric additive white Gaussian noise. Regarding the channel gain, note that $g_{ik} = z_{ik} \sqrt{r_{ik}^{-\alpha_i}}$, where $z_{ik} \sim \mathcal{N}_{\mathbb{C}}(0; 1)$ models the small-scale fading, r_{ik} is the distance between the i-th transmitter and the $k - th$ receiver, and α_i is the path-loss exponent modeling the power loss experienced by the signal sent by the i-th transmitter. For the time being, the channel coefficients g_{ik} are assumed to be known, that is, deterministic.

Using (2.9) and the associated discussion, the average SINR at the k-th receiving node reads as

$$\mathrm{SINR}_k = \frac{\|\boldsymbol{\lambda}_k\|^2 r_{kk}^{-\alpha_k}}{N_0 + \sum_{i\neq k} |\boldsymbol{\lambda}_k^H \boldsymbol{U}_k^H \boldsymbol{U}_i \boldsymbol{\lambda}_i|^2 r_{ik}^{-\alpha_i}} = \frac{S_k}{N_0 + \sum_{i\neq k} I_{ik}} = \frac{\mathrm{SNR}_k}{1+\mathrm{INR}_k}, \tag{2.11}$$

being N_0 the power spectral density of the noise and $\mathrm{INR}_k = \sum_{i\neq k} I_{ik}/N_0$ the Interference-to-Noise Ratio (INR) at the k-th receiving node.

It is noteworthy that the relationship provided in (2.10) is the general equation of the K-user Gaussian Interference Channel (IC) [CJ08], whose capacity region remains generally unknown, even for the 2-user case, except for very particular cases. Nevertheless, several signal processing strategies have been studied to combat the impact of the incoming interferences, and associated inner or outer bounds on the capacity region have been established. In order to describe these signal processing schemes and to get insights on the performance limitations, the discussion is first focused on the 2-user case for the sake of simplicity.

For the time being, consider the 2-user Gaussian IC illustrated in Figure 4.1. The capacity region of this channel $\mathcal{C}$, defined as the set of rate pairs (R_1, R_2) satisfying

$$\mathcal{C} = \{(R_1,R_2) \ : \ R_1 < \log_2(1+\mathrm{SNR}_1), R_2 < \log_2(1+\mathrm{SNR}_2)\}, \tag{2.12}$$

remains unknown. Therefore, a wide variety of interference management strategies have been studied to provide achievable (inner) bounds on the capacity region.

A simple strategy to deal with interferences is to orthogonalize the transmissions, i.e., each transmitter employs only a fraction of the signal space. The inner bound achieved by orthogonalization and power control encompasses the set of rate pairs (R_1, R_2) such that [EK11]

$$\begin{aligned} R_1 &\leq \alpha \log_2\left(1+\frac{\mathrm{SNR}_1}{\alpha}\right), \\ R_2 &\leq (1-\alpha)\log_2\left(1+\frac{\mathrm{SNR}_2}{1-\alpha}\right), \end{aligned} \tag{2.13}$$

being $\alpha \in [0,1]$ the fraction of DoF or signal-space dimensions assigned to transmitter $\#1$. This interference management strategy is generally suboptimal. Even though it can be optimum in some particular cases in terms of sum rate when a power control policy is used, it usually leads to an unfair solution if the IC is not symmetric, i.e., $\mathrm{SNR}_1 \neq \mathrm{SNR}_2$. Moreover, note that this scheme requires synchronization and cooperation between the coexisting transmitters.

The most simple interference management technique is known as Treating Interference as Noise (TIN) and consists in ignoring the incoming interference. This scheme does not require cooperation between the two transmitters, whereas the receiving scheme is a matched filter on the intended signal. Nevertheless, the required per-link QoS is compromised as the interference becomes stronger. As discussed in [AV09; EK11], TIN provides an inner bound on the capacity region of the 2-user Gaussian IC encompassing the rate pairs (R_1, R_2) satisfying

$$\begin{aligned} R_1 &\leq \log_2\left(1+\frac{\mathrm{SNR}_1}{1+\mathrm{INR}_1}\right), \\ R_2 &\leq \log_2\left(1+\frac{\mathrm{SNR}_2}{1+\mathrm{INR}_2}\right), \end{aligned} \tag{2.14}$$

which hints at the poor performance of TIN when the interference is relevant. The opposite interference management strategy to TIN consists in letting each receiver recover both the intended signal and the interference signal, similar to the Multiuser Detector (MUD) [Ver98]

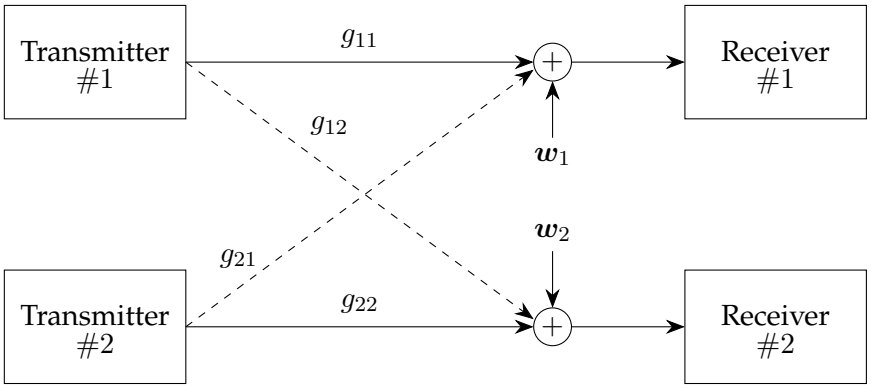

Figure 2.1: The two-user (memoryless) Gaussian interference channel.

scheme developed for the Multiple-Access Channel (MAC). Nevertheless, in the IC case, the recovery of the interference signal is not needed and each receiver has to design a strategy to recover its intended signal that together with some interference signal minimizes the error probability. This strategy is known as Simultaneous Non-Unique Decoding (SND). It is important to highlight that SND requires each receiver to know the codebooks and the transmission strategy employed by the *interfering* transmitter, arising the necessity of cooperation between receivers. The use of SND provides another inner bound on the capacity region of the 2-user Gaussian IC encompassing the rate pairs (R_1, R_2) satisfying

$$\begin{aligned} R_1 &\leq \log_2\left(1+\mathrm{SNR}_1\right), \\ R_2 &\leq \log_2\left(1+\mathrm{SNR}_2\right), \\ R_1+R_2 &\leq \min\left\{\log_2\left(1+\mathrm{SNR}_1+\mathrm{INR}_1\right), \log_2\left(1+\mathrm{SNR}_2+\mathrm{INR}_2\right)\right\}. \end{aligned} \tag{2.15}$$

It is interesting to note that this inner bound can be seen as the intersection of the capacity region of the MAC composed of transmitter $\#1$ and the two receivers and the capacity region of the MAC composed of transmitter $\#2$ and the two receiving nodes.

The complexity of SND can be an implementation drawback. A suboptimal strategy, which is also studied in the context of the MAC, is the well-known Successive Interference Cancellation (SIC) scheme. The SIC is a two-stage receiving scheme that first decodes the interference signal while treating the useful signal as noise, and then the decoded interference is subtracted from the received signal before decoding the useful signal.

Thus far, the basic interference management strategies for the 2-user Gaussian IC have been discussed. As mentioned before, orthogonalizing the transmission is suboptimal in general. Nevertheless, we may wonder whether the non-orthogonal techniques, that is TIN and SND, can be optimal. In order to discuss the performance of these two schemes, we will focus on two extreme cases. On the one hand, when $\mathrm{INR}_2 \geq \mathrm{SNR}_1$ and $\mathrm{INR}_1 \geq \mathrm{SNR}_2$, we say that the interference network operates at the *strong-interference regime*. Under these conditions, the capacity region of the 2-user Gaussian IC is known and achieved through SND [Car75]. When the interference becomes stronger such that the conditions $\mathrm{SNR}_2 \leq \mathrm{INR}_1/(1+\mathrm{SNR}_1)$ and $\mathrm{SNR}_1 \leq \mathrm{INR}_2/(1+\mathrm{SNR}_2)$ hold, the operating regime turns to the so-called *very strong-interference regime*. It is the only case where interference has no impact on the communication performance as each transmitter-receiver pair can achieve the capacity of the point-to-point Gaussian channel [Car75]. In this regime, this performance can be achieved through SIC.

On the other hand, in the *weak-interference regime* defined by the conditions $\mathrm{INR}_2 < \mathrm{SNR}_1$ and $\mathrm{INR}_1 < \mathrm{SNR}_2$, the capacity region remains unknown. However, the sum capacity in the weak-interference regime is known under certain conditions. As pointed out in [AV09], if the following conditions hold

$$\begin{aligned} \sqrt{\frac{\mathrm{INR}_1}{\mathrm{SNR}_2}}(1+\mathrm{INR}_2) &\leq \rho_2\sqrt{1-\rho_1^2}, \\ \sqrt{\frac{\mathrm{INR}_2}{\mathrm{SNR}_1}}(1+\mathrm{INR}_1) &\leq \rho_1\sqrt{1-\rho_2^2}, \end{aligned} \tag{2.16}$$

for some $\rho_1, \rho_2 \in [0,1]$, then the sum-capacity of the Gaussian IC is achieved through TIN and given by

$$C_{\mathrm{sum}} = \log_2\left(1+\frac{\mathrm{SNR}_1}{1+\mathrm{INR}_1}\right) + \log_2\left(1+\frac{\mathrm{SNR}_2}{1+\mathrm{INR}_2}\right). \tag{2.17}$$

Notwithstanding, both TIN and SND can only provide pessimistic inner bounds of the capacity region in the general *mixed-interference regime*, which satisfies $\mathrm{INR}_2 < \mathrm{SNR}_1$ and $\mathrm{INR}_1 \geq \mathrm{SNR}_2$, or $\mathrm{INR}_2 \geq \mathrm{SNR}_1$ and $\mathrm{INR}_1 < \mathrm{SNR}_2$ [ETW08]. Under these conditions, it seems reasonable to think about a strategy that swings between TIN and SND. The latter is exactly the purpose of *rate splitting*. This technique, which was proposed by Carleial in [Car78], consists in splitting the message sent by each transmitter into two messages, known as *private* and *common* messages. Therefore, the received signal at each receiver reads as

$$\boldsymbol{y}_k = \boldsymbol{s}_{c1} + \boldsymbol{s}_{p1} + \boldsymbol{s}_{c2} + \boldsymbol{s}_{p2} + \boldsymbol{w}_k, \quad \text{for } k = 1, 2, \tag{2.18}$$

where $\boldsymbol{s}_{ck}$ and $\boldsymbol{s}_{pk}$, for $k = 1, 2$, refer to the common and private message sent by the k-th transmitting node. The idea is that the k-th receiver first decodes through SIC only the interference induced by the common signal sent by the interfering transmitter while treating all other terms as noise. Then, this interference can be removed from the received signal and the message sent by the intended transmitter, which is given by $\boldsymbol{s}_k = \boldsymbol{s}_{ck} + \boldsymbol{s}_{pk}$, is obtained through TIN. Note that, if the interference cancellation scheme has succeeded, only the interference induced by the private message $\boldsymbol{s}_{pj}$, with $j \neq k$, is treated as noise. In the Gaussian IC with Gaussian inputs, the design of the rate splitting scheme reduces to balancing the power devoted to the common and the private messages.

Even though the rate splitting strategy dates back to 1978, it has recently gained considerable momentum to efficiently exploit the available DoF with imperfect Channel State Information (CSI), under an interference management strategy known as Rate-Splitting Multiple-Access (RSMA) [CJH+16]. The primary motivation behind RSMA comes from noting that using multiple antennas in Non-Orthogonal Multiple-Access (NOMA) leads to inefficient use of the available DoF since the spatial dimension is not fully exploited [MC20; CMS+21]. It is interesting to note that, as per [CMSP20], RSMA provides a unified framework to study OMA, NOMA, and Space-Division Multiple-Access (SDMA). Currently, RSMA is investigated as a potential interference management strategy for next-generation wireless networks [MDC+22].

The rate splitting strategy plays a fundamental role in characterizing the rate region of the IC. In particular, Han and Kobayashi improve the rate splitting strategy in [HK81] to derive the best-known achievable scheme for the (discrete-memoryless) interference channel. This inner bound has been also particularized for the 2-user Gaussian IC. Interestingly, Etkin, Tse, and

Wang use in [ETW08] a simple Han-Kobayashi scheme and a genie-aided[4] receiver to provide an outer bound on the capacity region of the 2-user Gaussian IC that is achievable within *one bit per complex dimension*. The latter means that for any rate pair (R_1, R_2) belonging to the proposed outer bound, the rate pair $(R_1 - 1, R_2 - 1)$ is achievable. A different proof of this important result is also given in [TT07]. Since the outer bound given in [ETW08] is particularized for the weak- and mixed-interference regimes, the general version given in [EK11] is provided for the readers' convenience. Accordingly, all rate pairs (R_1, R_2) satisfying

$$
\begin{aligned}
R_1 &\leq \log_2\left(1+\mathrm{SNR}_1\right), \\
R_2 &\leq \log_2\left(1+\mathrm{SNR}_2\right), \\
R_1+R_2 &\leq \log_2\left(1+\frac{\mathrm{SNR}_1}{1+\mathrm{INR}_2}\right)+\log_2\left(1+\mathrm{SNR}_2+\mathrm{INR}_2\right), \\
R_1+R_2 &\leq \log_2\left(1+\frac{\mathrm{SNR}_2}{1+\mathrm{INR}_1}\right)+\log_2\left(1+\mathrm{SNR}_1+\mathrm{INR}_1\right), \\
R_1+R_2 &\leq \log_2\left(1+\frac{\mathrm{SNR}_1+\mathrm{INR}_1+\mathrm{INR}_1\mathrm{INR}_2}{1+\mathrm{INR}_2}\right) \\
&\quad +\log_2\left(1+\frac{\mathrm{SNR}_2+\mathrm{INR}_2+\mathrm{INR}_1\mathrm{INR}_2}{1+\mathrm{INR}_1}\right), \\
2R_1+R_2 &\leq \log_2\left(1+\frac{\mathrm{SNR}_1}{1+\mathrm{INR}_2}\right)+\log_2\left(1+\mathrm{SNR}_1+\mathrm{INR}_1\right) \\
&\quad +\log_2\left(1+\frac{\mathrm{SNR}_2+\mathrm{INR}_2+\mathrm{INR}_1\mathrm{INR}_2}{1+\mathrm{INR}_1}\right), \\
R_1+2R_2 &\leq \log_2\left(1+\frac{\mathrm{SNR}_2}{1+\mathrm{INR}_1}\right)+\log_2\left(1+\mathrm{SNR}_2+\mathrm{INR}_2\right) \\
&\quad +\log_2\left(1+\frac{\mathrm{SNR}_1+\mathrm{INR}_1+\mathrm{INR}_1\mathrm{INR}_2}{1+\mathrm{INR}_2}\right),
\end{aligned}
\tag{2.19}
$$

are achievable within one bit per complex dimension. Nevertheless, the full characterization of the Han-Kobayashi inner bound for the 2-user Gaussian IC is still an open problem.

In order to provide further insights into these techniques, the inner bounds provided by OMA, TIN, and SND, as well as the outer bound described by (2.19) are depicted in Figure 2.2 for $\mathrm{SNR}_1 = 15$ dB, $\mathrm{SNR}_2 = 10$ dB, and varying INR_1 and INR_2.

Observing Figure 2.2, it is worth noting that cases (a) and (b) correspond to the weak-interference regime, cases (c) and (d) exemplify the strong-interference regime, whereas cases (e) and (f) correspond to the very strong-interference and mixed-interference regimes, respectively. Focusing on the weak-interference regime, only the case depicted in Figure 2.2(a) satisfies the conditions in (2.16); thus, TIN is sum-rate optimal. As the interference increases, orthogonalizing the transmissions provides better performance. Regarding the strong-interference regime, the case depicted in Figure 2.2(c) corresponds to the boundary where $\mathrm{SNR}_1 = \mathrm{INR}_2$ and $\mathrm{SNR}_2 = \mathrm{INR}_1$. We may observe that OMA achieves the sum rate, even though it is not the fairest point given the power imbalance between each link, that is, $\mathrm{SNR}_1 \neq \mathrm{SNR}_2$. As the interference becomes stronger, the gap between the capacity region, achieved by the SND strategy, and the outer vanishes. In the very strong-interference regime, the outer bound described

[4] A *genie* is an entity that provides to each receiver side information about the interference leaked through the *cross* channel.

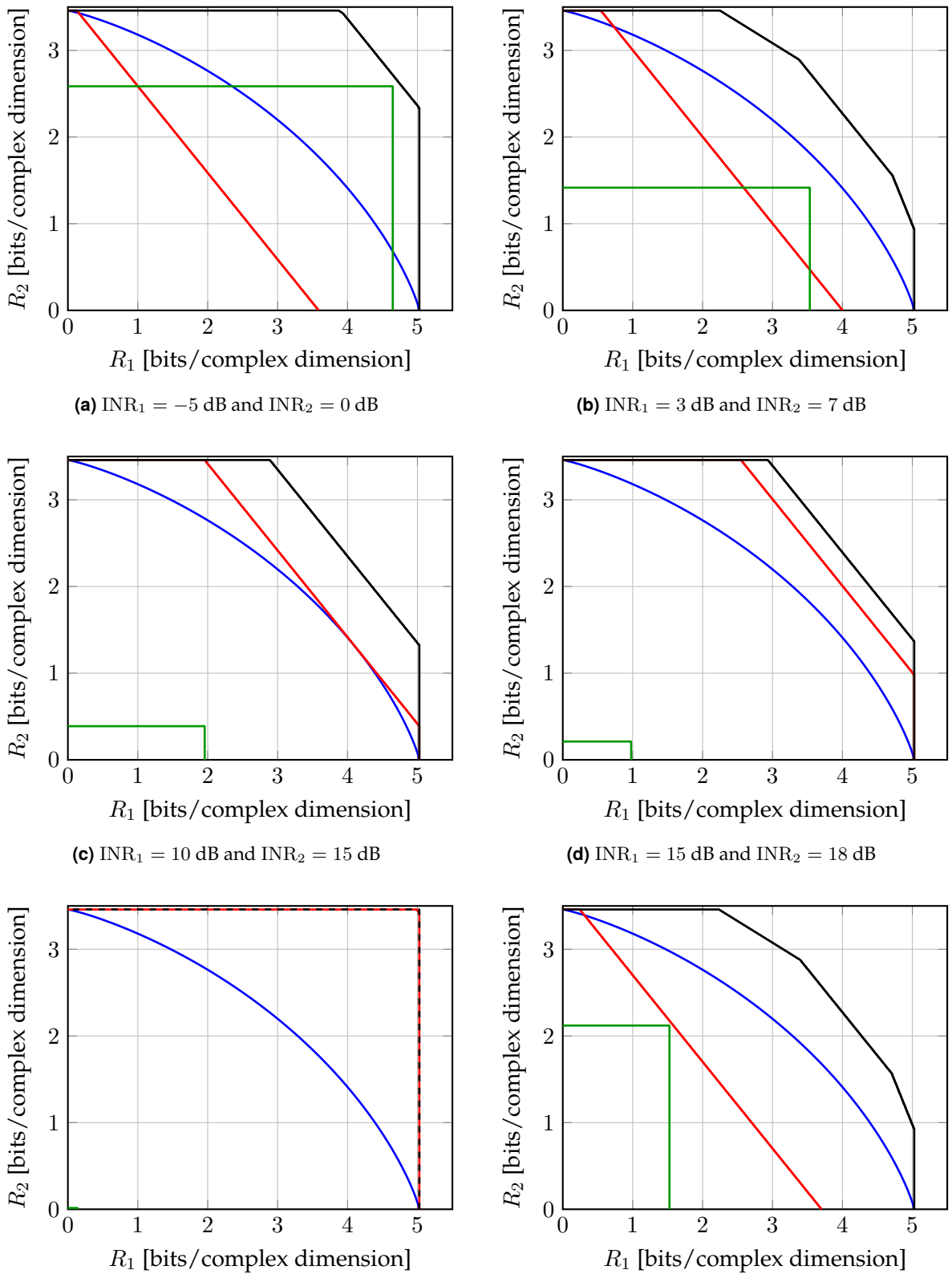

(a) $\mathrm{INR}_1 = -5$ dB and $\mathrm{INR}_2 = 0$ dB

(b) $\mathrm{INR}_1 = 3$ dB and $\mathrm{INR}_2 = 7$ dB

(c) $\mathrm{INR}_1 = 10$ dB and $\mathrm{INR}_2 = 15$ dB

(d) $\mathrm{INR}_1 = 15$ dB and $\mathrm{INR}_2 = 18$ dB

(e) $\mathrm{INR}_1 = 25$ dB and $\mathrm{INR}_2 = 30$ dB

(f) $\mathrm{INR}_1 = 12$ dB and $\mathrm{INR}_2 = 3$ dB

Figure 2.2: Inner bounds achieved with OMA (blue), TIN (green), and SND (red), and outer bound (2.19) in black on the capacity region of the 2-user Gaussian IC.

in (2.19) coincides with the capacity region. Finally, in the mixed-interference regime, both TIN and SND are outperformed by OMA in terms of sum rate. Nevertheless, in the *symmetric* Gaussian IC, that is, when $\mathrm{SNR}_1 = \mathrm{SNR}_2$ and $\mathrm{INR}_1 = \mathrm{INR}_2$, it is known that OMA is only optimal in two particular points: in the boundary of the optimality region of TIN and when $\mathrm{SNR}_1 = \mathrm{SNR}_2 = \mathrm{INR}_1 = \mathrm{INR}_2$.

Thus far, we have reviewed four different interference management strategies for the 2-user Gaussian IC. In contrast to orthogonal access, the other three techniques consider that the signals sent by each transmitting node are superimposed, that is, share the same network resources –or signal-space dimensions–. The two extreme cases, TIN and SND, consist in not decoding and fully decoding inter-system interferences at each receiver, respectively. Rate splitting swings between these two extreme cases and permits finding an outer bound of the capacity region achievable within one bit per complex dimension. Despite the tremendous efforts, the capacity region of this simple case remains unknown, emphasizing the difficulty of finding interference management strategies that achieve the desired optimum performance.

The abovementioned techniques consider that each transmitter is not aware of the message –or signal– sent by the other transmitter. A strategy to improve the system's spectral efficiency consists in letting the transmitters and receivers cooperate. Under this condition, the 2-user Gaussian IC can be seen as a distributed or network Multiple-Input Multiple-Output (MIMO) system [NWSS21]. Accordingly, a significant range of interference management strategies studied for network MIMO systems can be adapted to the 2-user Gaussian IC.

If the transmitters can cooperate, a conventional and simple strategy to mitigate interferences consists in employing a zero-forcing (ZF) precoder [SH07], such that the signal sent by each transmitter is projected onto a low-dimensional subspace. This scheme, however, suffers a performance penalty loss due to the reduction of effective DoF per user. Similar performance can be achieved by using an interference-cancellation combiner at the receiver side. Interestingly, when the transmitters share their messages before sending them, the 2-user Gaussian IC can be seen as a 2×2 MIMO Broadcast Channel (BC). As advocated in [CS03], the Dirty Paper Coding (DPC) scheme proposed by Costa in [Cos83] is capacity-achieving in the MIMO-BC. DPC consists in canceling the interference at the transmitter side beforehand without requiring side information about interferences at the receiver side. A practical low-complexity implementation of DPC is the Tomlinson-Harashima Precoding (THP) [Tom71; HM72].

Interference mitigation when the cooperation takes place at the receivers only has been deeply investigated, from an information-theoretic viewpoint, in order to quantify the performance improvement and determine the appropriate rate of the cooperative link. In this respect, [WT11a] concludes that the per-user information rate does not unboundedly improve as the cooperation rate increases; after a cooperation rate threshold, receiver cooperation only provides a power gain that marginally improves the per-user information rate.

Extension to K-user Interference Networks

Up to this point, the discussion on interference management techniques and their limitations has been focused on the 2-user Gaussian IC. Therefore, the reader may wonder how inter-system interferences can be dealt with in the general K-user Gaussian IC. This general case is not well-understood from an information-theoretic viewpoint. For instance, the definition

of *strong interference* in the K-user case is not clear [EK11]. Nevertheless, several interference management techniques have been proposed for the general case, altogether with the extension of some of the strategies studied for the 2-user case. Regarding the latter case, a Han-Kobayashi scheme for the K-user Gaussian IC is proposed in [BPT10], where each transmitter is able to decode the combined interference.

Among the interference management strategies designed for the general K-user Gaussian IC, Interference Alignment (IA) is optimal in terms of DoF, that is, can achieve the *pre-log* factor of the channel capacity (sum rate) at the high-SNR regime. IA consists of a linear precoding strategy capable of aligning interfering signals in time, space, or frequency into a low-dimensional subspace at the receiver side [Jaf11; ZYJ+16]. IA was initially proposed in [CJ08] to study the DoF region of the K-user symmetric Gaussian IC. The strategy proposed therein dedicates half of the signal space at the receiver to align interferences, whereas the other half is dedicated to interference-free transmissions. This strategy is known to be optimal in terms of the DoF region. It is interesting to remark that, in the K-user Gaussian IC, the use of improper signaling[5] [JASA20] can bring benefits in the rate region achievable by IA even if coded time-sharing is allowed [CJW10]. Nevertheless, at moderate-SNR regimes, IA offers only a suboptimal achievable sum rate. Despite these promising results, one of the main drawbacks of IA is the necessity of tight synchronization to avoid additional interferences introduced by timing, and frequency offsets [EAPH13]. Recently, [LE21] proposes a spatial IA strategy where the approximate alignment of incoming interferences is achieved by tuning the inter-element spacing of the receiving antenna array, assuming that the spacing can be arbitrarily large.

In some cases, finding closed-form solutions that satisfy the IA conditions can be challenging. Therefore, iterative interference management algorithms based on IA [FGSB17; WL19], Minimum Mean-Square Error (MMSE) [RR16], and maximum SINR [AR17] have been studied. Despite providing suboptimal solutions, these iterative schemes enjoy practical implementation and flexibility in being used in arbitrary interference networks.

All the approaches discussed so far are based on exploiting the knowledge about interferences to mitigate or cancel them. Recently, another research perspective consists in using the knowledge about interferences to improve the system performance. This technique is known as constructive interference precoding (CIP) or symbol-level precoding (SLP) [ACO15; LSK+20; LLLS21]. CIP/SLP aims to exploit the known interferences at the transmitting node such that these interferences become constructive interferences to the intended information symbol.

Interference Management without CSI at Transmitters

With the exception of TIN, a common characteristic of the discussed interference management strategies is the necessity of instantaneous CSI at transmitters. While CSI at receivers can be obtained through pilot-assisted channel estimation strategies, a coordinated feedback link is needed to provide CSI to transmitters. Assuming that transmitters know the instantaneous channel conditions is impractical for many reasons. First, if the wireless channel experience fast time variations, the CSI acquired at the receiver may be outdated when communicated to

[5] Improper Gaussian Signaling (IGS) permits improving the achievable rates in some TIN-based MIMO scenarios [ZZGG13; LAV16]. Recently, it has been shown that IGS performs better than conventional proper Gaussian Signaling in the K-user MIMO IC with hardware impairments [SSS20].

the transmitter. Second, communicating CSI to transmitters through a coordinated feedback link may burden the system latency. And third, in heterogeneous networks where different technologies coexist, assuming that all transmitters are aware of the channel conditions may be impractical, especially when the number of coexisting transmitter-receiver pairs K is large.

In this respect, several works explore the interference management problem without CSI at transmitters. Most of these studies are focused on the high-SNR regime. Under this asymptotic condition, the DoF region has been characterized in MIMO networks [HJSV12; VV12], wideband systems [JLT18], and 2-tier networks [MCVA19], to name a few. Recall that in the high-SNR regime with full CSI at transmitters, IA is DoF optimal. Nevertheless, providing CSI to transmitters is one of the main drawbacks of IA since it arises the necessity of large feedback overheads [HLDL11; EALH12]. This drawback can be overcome through Blind Interference Alignment (BIA) [Jaf12; JV20], where the knowledge of channel coherence intervals only at transmitters is needed to align interferences in some cases. A naive interference management strategy under no CSI at transmitters is TIN. Even though we have seen that it is sum-rate optimal only under strictly weak interferences, [GNAJ15] advocates that in K-user fully-connected fully-asymmetric Gaussian IC, the achievable rate region through TIN is, under some conditions, within a constant gap of the entire capacity region. If the interference network is not fully-connected, the relatively new framework known as Topological Interference Management (TIM) [Jaf14; DAA19] permits exploiting the knowledge of the network topology at transmitters without CSI. [MJ13] reveals that, in certain network topologies, orthogonal access is optimal. The TIM framework also permits studying the impact of removing transmitter or receiver cooperation when CSI is not available at transmitters. In this regard, [VEG18] unveils that, under certain conditions, linear cooperation does not improve the per-user DoF.

A recent result on distributed interference management without CSI at transmitters discusses a new strategy, known as the broadcast approach [ZTS21], in the context of the ℓ-state interference channel. This strategy, which consists of a layered rate allocation adapted to each of the possible ℓ channel states, achieves an average rate region whose with respect to the Han-Kobayashi rate region decreases as the number of channel states increases while avoiding the necessity of CSI at transmitters.

Dealing with Interferences in Uncoordinated Networks

We have seen the difficulty of dealing with interferences, especially in moderate-interference regimes and non-asymptotic SNR and INR. Most of the discussed strategies require that non-intended receivers (partially) decode the aggregated interference, meaning that codebooks and modulation schemes employed by interfering transmitters have to be known beforehand. When this information is not available, the general directive of interference management schemes consists in designing a transmission strategy that reduces the impact of interferences.

Recalling (2.11), the instantaneous power of the interference generated by the i-th transmitter on the k-th receiver after matched-filtering is given by

$$I_{ik} = \left| z_{ik} \boldsymbol{\lambda}_k^H \boldsymbol{U}_k^H \boldsymbol{U}_i \boldsymbol{\lambda}_i \right|^2 r_{ik}^{-\alpha_i}. \tag{2.20}$$

When the channel coefficient $g_{ik} = z_{ik}\sqrt{r_{ik}^{-\alpha_i}}$ becomes less significant, the performance of the k-th receiving node tends to be interference-limited. If this receiver cannot decode the

interference, one possibility to reduce its impact consists in orthogonalizing the transmissions. Regarding (2.20), the latter implies that all transmitting nodes agree on a common signal-space basis, that is $\boldsymbol{U}_k = \boldsymbol{U}_i$, and perform an orthogonal DoF allocation, i.e., $\boldsymbol{\lambda}_k^H \boldsymbol{\lambda}_i = 0$. This strategy, however, is not optimal in terms of rate and requires coordination and synchronization at transmitters. Another possibility that does not require synchronization focuses on designing signal-space bases as disjoint as possible. This approach does not require all nodes to share the same signal-space basis but, in turn, it requires the projection $\boldsymbol{U}_k^H \boldsymbol{U}_i$ to be as small as possible. The major drawback of this approach is that transmitter cooperation is still necessary.

In uncoordinated networks, transmitters and receivers do not cooperate and, typically, only the coordination between the nodes of the same transmitter-receiver pair is considered. Under these conditions, interference will limit the network performance since it cannot be, a priori, mitigated. In order to coexist in the same wireless network, it is possible to tune the transmission scheme to control the provided interference. In this sense, the k-th transmitter can decide to use more DoF –or signal-space dimensions– to *spread* the transmitted power and induce a persistent low interference per complex dimension. On the contrary, this transmitter may select one DoF and change its selection according to a pre-defined pseudo-random *hopping* pattern (previously agreed with its intended receiver) to provide a sporadic strong interference.

In general, it is not possible to know a priori which of these two uncoordinated approaches is preferable. Nevertheless, under some conditions, it is possible to quantify the successful transmissions that each of these two schemes admits in a finite geographical area. For this purpose, in the sequel, we introduce a metric known as *transmission capacity*. This metric is derived from the outage probability. Unlike the rate region which focuses on the attainable information rate, transmission capacity focuses on the QoS requirements that can be guaranteed. Moreover, transmission capacity permits measuring the communication density in a finite geographical area since it accounts for the physical dimensions of the wireless network.

2.2.3 Transmission Capacity and Spatial Communication Density

An important result in the context of the K-user Gaussian IC is that, in the high-SNR regime, each transmitter-receiver pair can exploit half of its signal space without interference. This asymptotic performance is achieved through IA. This interference management scheme requires that all transmitting nodes cooperate to appropriately design the precoders that permit aligning interferences. If these conditions hold, note that the achievable per-user DoF are independent of the total number of transmitter-receiver pairs K.

In uncoordinated networks, where transmitters do not cooperate and receivers treat interference as noise, we have previously seen that the per-user information rate decreases as the number of coexisting transmitter-receiver pairs increases. In this context, instead of the information rate, it seems more reasonable to study the number of admissible transmitter-receiver pairs such that each of them can guarantee a certain QoS requirement.

With the purpose of measuring if the QoS requirement of the k-th transmitter-receiver pair is guaranteed, we resort to the outage probability P_{out}. Assume that the k-th transmitting node employs a channel code with encoding rate R_k [bits/complex dimension]. The outage probability is defined as the probability that the per-user channel capacity (per complex dimension)

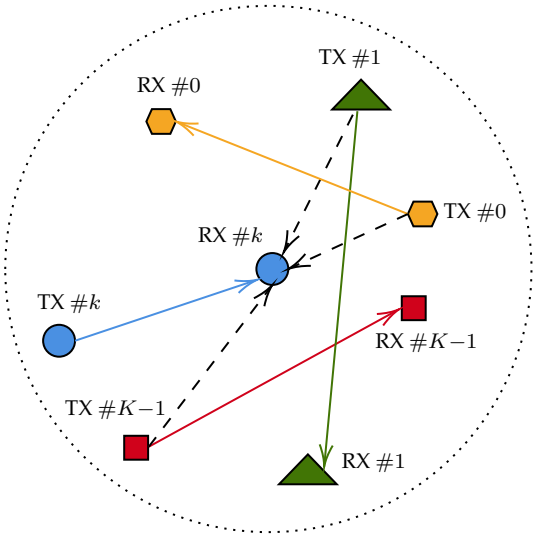

Figure 2.3: Example of an uncoordinated heterogeneous network. The k-th transmitter-receiver pair, represented by blue circles, is the one considered under study. For the sake of clarity, only the interferences (dashed lines) leaked on the k-th receiving node are depicted.

is smaller than the employed encoding rate, that is,

$$P_{\text{out}} \triangleq \mathbb{P}\left\{\log_2(1+\text{SINR}_k) < R_k\right\}, \tag{2.21}$$

where SINR_k is the SINR at the k-th receiver. Note that (2.21) can be re-written as

$$P_{\text{out}}(\beta_k) = \mathbb{P}\left\{\text{SINR}_k < 2^{R_k}-1\right\} = \mathbb{P}\left\{\text{SINR}_k < \beta_k\right\}, \tag{2.22}$$

being β_k the QoS or SINR requirement of the k-th transmitter-receiver pair. Recalling (2.11), SINR_k depends on the number of interfering transmitters coexisting with the k-th transmitter-receiver pair. Accordingly, if SINR_k can be appropriately characterized, it is possible to determine the number of admissible transmissions such that (2.22) is satisfied.

Nevertheless, given the heterogeneity of communication nodes in uncoordinated networks, in which different transmitter-receiver pairs can transmit at different rates and employ different coded-modulation schemes, the analysis of the number of admissible transmissions is very challenging. An alternative is studied in [WA12], where the stochastic geometry framework [HAB+09] is exploited to analyze the *spatial density of successful transmissions given an outage constraint*. This metric is known as transmission capacity.

In order to appropriately define the transmission capacity, and for the reader's convenience, we consider the uncoordinated heterogeneous network depicted in Figure 2.3. Without loss of generality, the analysis is focused on the transmitter-receiver pair represented by blue circles. A conventional assumption is that the locations of the interfering transmitters form a stationary two-dimensional Poisson point process $\mathcal{P}(\lambda)$, which is valid if the transmitting nodes are independently and randomly distributed over the considered geographical area. Note that the latter seems reasonable[6] in uncoordinated networks. The Poisson point process is characterized by the intensity λ, which measures the density of transmitters in the considered geographical area. An example of a stationary Poisson point process is depicted in Figure 2.4.

[6] A generalized formulation can be found in [GAH11].

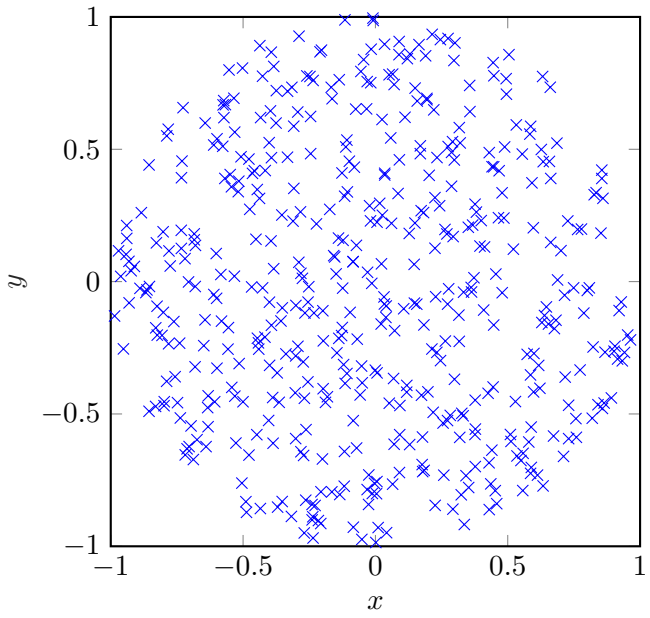

Figure 2.4: Realization of a two-dimensional Poisson point process with intensity $\lambda = 150$ [nodes/units of area] within a circular geographic area of radius 1.

For the sake of simplicity, consider that the receiving node under study is located at the center of the geographical area. Accordingly, the distance between the i-th transmitting node (interferer) and the k-th receiving node (the one under study) r_{ik} is the modulus of the interferer's position P_i, that is, $r_{ik} = |P_i|$. Thus, recalling (2.20), the power of the aggregated instantaneous interference received by the k-th receiving node is given by

$$I_k = \sum_{P_i \in \mathcal{P}(\lambda)} |z_{ik}|^2 \left|\boldsymbol{\lambda}_k^H \boldsymbol{U}_k^H \boldsymbol{U}_i \boldsymbol{\lambda}_i\right|^2 r_{ik}^{-\alpha_i} = \sum_{P_i \in \mathcal{P}(\lambda)} |z_{ik}|^2 J_{ik} r_{ik}^{-\alpha_i}, \tag{2.23}$$

being J_{ik} the power of the interference after matched-filtering without accounting for the channel coefficient. Note that I_k in (2.23) is a random variable since it depends on the random positions of the interferers, the nominal interference powers J_{ik}, and the small-scale fading coefficients. The Probability Density Function (PDF) and the Cumulative Distribution Function (CDF) of I_k are denoted by $f_{I_k}(x)$ and $F_{I_k}(x)$, respectively.

Recalling the definition of the outage probability in (2.22) and assuming $z_{ik} \sim \mathcal{N}_{\mathbb{C}}(0;1)$, P_{out} can be written as a function[7] of the node density λ for a given β_k, that is,

$$P_{\text{out}}(\lambda) = 1 - \mathbb{P}\left\{\text{SINR}_k > \beta_k\right\} = 1 - \mathbb{P}\left\{|z_{kk}|^2 > \frac{\beta_k}{J_{kk}} r_{kk}^{\alpha_k}(I_k + N_0)\right\} \tag{2.24}$$

$$= 1 - \int_0^{+\infty} e^{-\beta_k r_{kk}^{\alpha_k}(x+N_0)/J_{kk}} f_{I_k}(x)\mathrm{d}x \tag{2.25}$$

being $J_{kk} = \left|\boldsymbol{\lambda}_k^H \boldsymbol{U}_k^H \boldsymbol{U}_k \boldsymbol{\lambda}_k\right|^2$. Using the expression of the outage probability as a function of the node density λ we can now define the transmission capacity metric.

[7] A particular case of (2.25) is derived in [WAJ10].

For a fixed outage probability constraint $P_{\text{out}}(\lambda) = \varepsilon$, the transmission capacity $c(\varepsilon)$, as coined in [WYAV05; WAJ10], is given by

$$c(\varepsilon) \triangleq P_{\text{out}}^{-1}(\varepsilon)(1-\varepsilon). \tag{2.26}$$

Note that the first term $P_{\text{out}}^{-1}(\varepsilon)$ corresponds to the spatial density of transmissions (assuming that all transmitters in the network are actively transmitting), whereas the second term $(1-\varepsilon)$ is the success probability. Accordingly, the transmission capacity measures the spatial density of *successful* transmissions in the wireless network.

Unfortunately, the calculation of (2.26) requires knowing the PDF of I_k in (2.23), which generally requires numerical methods. Despite that, the outage probability as a function of the node density λ sometimes admits a closed-form expression. In these scenarios, it is assumed that each interferer produces the same nominal interference, that is, $J_{ik} = I$, and that all interferers suffer the same pathloss conditions, that is $\alpha_{ik} = \alpha$. Even though these cases have been thoroughly analyzed in the tutorials [WYAV05; WA12], we provide two of them as will be used to discuss further insights on the transmission capacity $c(\varepsilon)$.

One of the scenarios is the pathloss-only case, i.e. when the impact of small-scale fading is not considered. This case is usually referred to as the baseline model. The transmission capacity can only be written in a closed-form expression when $\alpha = 4$. Under these conditions, the transmission capacity $c(\varepsilon)$ is given by

$$c(\varepsilon) = \frac{\sqrt{2/\pi}(1-\varepsilon)F_{\mathcal{N}}^{-1}((1+\varepsilon)/2)}{\pi r_{kk}^2}\sqrt{\frac{\text{sir}}{\beta} - \frac{r_{kk}^4}{\text{inr}}}, \tag{2.27}$$

where $\text{sir} = J_k/I$, $\text{inr} = I/N_0$, and $F_{\mathcal{N}}(\cdot)$ is the CDF of a standard Gaussian random variable $\mathcal{N}(0;1)$. Another scenario of interest is the case of Rayleigh fading, where the outage probability is explicitly a particular case of (2.25). In this case, the transmission capacity $c(\varepsilon)$ for any possible value of the pathloss exponent α is given by

$$c(\varepsilon) = (1-\varepsilon)\frac{-\log(1-\varepsilon) - \frac{\beta}{\text{sir}\cdot\text{inr}}r_{kk}^{\alpha}}{\pi r_{kk}^2(\beta/\text{sir})^{2/\alpha}\frac{2\pi}{\alpha}}\sin(2\pi/\alpha). \tag{2.28}$$

These two scenarios are compared in Figure 2.5 for $\alpha = 4$, as it is the only case where the baseline model admits a closed-form expression. Regarding the SINR threshold, the considered values correspond to encoding rates of $1/2$, 1, and $3/2$ bits per complex dimension, respectively. As expected, the transmission decreases when the encoding rate increases since a stringent SINR is required for reliable communication. Another general conclusion that can be drawn from Figure 2.5 is that fading decreases the transmission capacity in low-to-moderate outage probabilities. If appropriately exploited, fading can provide diversity gain leading to an enhanced SINR. Nevertheless, the mathematical rationale behind the transmission capacity formulation assumes uncoordinated nodes that are simultaneously transmitting (similar to the ALOHA mechanism); thus, diversity cannot be exploited under these considerations. Moreover, note that the transmission capacity benefits from (partial) interference cancellation, yielding an increase in the nominal SIR and a decrease in the nominal INR.

As per, e.g., [HAW08; VH12], the transmission capacity performance of a wireless network can be improved when multiple antennas are used through beamforming and interference

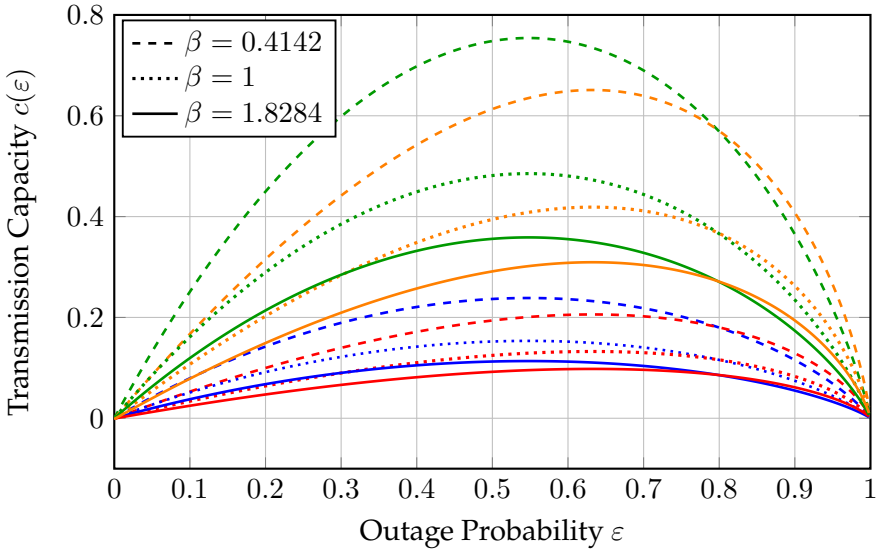

Figure 2.5: Transmission capacity $c(\varepsilon)$ as a function of the outage probability ε for $\alpha = 4$, $r_{kk} = 1$, different SINR requirements β and different $(\mathrm{sir}, \mathrm{inr})$ pairs. Red and blue lines stand for the fading and the pathloss-only model, respectively, with $(\mathrm{sir}, \mathrm{inr}) = (5, 25)$ dB. Orange and green lines stand for the fading and the pathloss-only model, respectively, with $(\mathrm{sir}, \mathrm{inr}) = (15, 15)$ dB.

cancellation. In the context of spectrum sharing, the analysis of the transmission capacity reveals that opportunistic communication (i.e., the interweave[8] paradigm of spectrum sharing) is generally preferred in front of the underlay paradigm, in which all systems use concurrently the same bandwidth subject to interference constraints [LAH11; LAH13].

Interestingly, the transmission capacity framework permits comparing two opposite uncoordinated transmission mechanisms: *hopping* and *spreading*. These two schemes have been used in several practical scenarios to control interferences without transmitter cooperation.

The hopping mechanism is a transmission scheme that selects in a pseudo-random manner the employed network resource, which permits exploiting diversity. An inherent advantage of hopping strategies is their low probability of interception, which is of paramount importance in terms of secrecy. In terms of interference management, hopping schemes exhibit also a low probability of interfering. It is worth noting that, at each channel use, the transmitter changes the selected resource according to a pseudo-random pattern previously agreed with its intended receiver. As the number of *resource slots* M increases, the probability that two uncoordinated transmitters employ the same signal-space dimension decreases. If two transmitters occupy the same dimension, a sporadic strong interference that lasts one channel use is produced. Nevertheless, these events occur with low probability as M is sufficiently large, even in large wireless networks. A representative hopping technique is Frequency-Hopping Spread Spectrum (FHSS), which is used in short-range communication systems such as Bluetooth.

On the other hand, the spreading mechanism permits each user to exploit all the M resource slots allocating to each slot approximately a fraction $1/M$ of the total transmitted power. Un-

[8] In [LAH11], the underlay and interweave paradigms are compared in terms of transmission capacity. Nevertheless, the interweave paradigm is referred to as the overlay paradigm therein. As per [GJMS09], interweave and overlay paradigms are different but sometimes considered as one paradigm in the literature. In this case, the definition of the overlay paradigm provided in [LAH11] corresponds to the case of opportunistic communications.

der these conditions, all coexisting nodes simultaneously exploit the same network resources, meaning that each uncoordinated transmitter produces a persistent weak interference per resource slot. As the hopping mechanism, spreading strategies also exhibit a low probability of interception since the transmitted signal is transmitted within all signal-space dimensions with a power per dimension typically smaller than the noise floor. A classical spreading technique is Direct-Sequence Spread Spectrum (DSSS), where transmitting nodes employ pseudo-random sequences agreed beforehand with the intended receiver to produce noise-like signals.

The comparison of FHSS and DSSS in terms of transmission capacity has been studied in [WYAV05] and surveyed in the sequel in order to get further insights.

Let us consider that the total normalized bandwidth has been divided into M sub-channels of bandwidth $1/M$ each. Accordingly, being N_0 the noise power spectral density, the noise power per sub-channel is N_0/M. Thus, it is straightforward to see that the noise level seen by the receiving node operating under the DSSS scheme is M times larger than the noise level for the FHSS case. The fundamental difference between FHSS and DSSS is in the strategy to mitigate interferences. Since only one resource slot per channel use is used in FHSS, the receiving node only sees interference from the transmitters exploiting the same resource slot at the same time. Recall that the location of transmitting nodes in an uncoordinated network can be modeled through a two-dimensional Poisson point process of density λ. Employing FHSS, the set of possible transmitters is reduced. In fact, if the resource selection is assumed to be equally likely, the interferers' locations under FHSS can be modeled as a Poisson point process with density λ/M. In the DSSS case, the *spreading factor* M reduces the interference per resource slot, which permits reducing the QoS requirement β by a factor of M, meaning that the minimum required QoS parameter is M times smaller in DSSS than in FHSS.

As per [WYAV05], taking into account the discussion above, the transmission capacity $c(\varepsilon)$ exhibited by FHSS and DSSS can be respectively upper-bounded by

$$c_{\text{FH}}(\varepsilon) \leq (1-\varepsilon)\frac{M}{\pi}\varepsilon\left(\frac{r_{kk}^{-\alpha}}{\beta}\text{sir}-\frac{1}{\text{inr}}\right)^{2/\alpha}+\mathcal{O}\left(\varepsilon^2\right) \tag{2.29}$$

$$c_{\text{DS}}(\varepsilon) \leq (1-\varepsilon)\frac{M^{2/\alpha}}{\pi}\varepsilon\left(\frac{r_{kk}^{-\alpha}}{\beta}\text{sir}-\frac{1}{\text{inr}}\right)^{2/\alpha}+\mathcal{O}\left(\varepsilon^2\right) \tag{2.30}$$

where, in both cases, $\mathcal{O}(\varepsilon^2)$ is a second-order term that vanishes as $\varepsilon \to 0$. Taking the quotient of (2.29) and (2.30), that is,

$$\frac{c_{\text{FH}}(\varepsilon)}{c_{\text{DS}}(\varepsilon)} = M^{1-\frac{2}{\alpha}}, \tag{2.31}$$

we note that, for any value of M, the transmission capacity performance exhibited by FHSS is superior to that exhibited by DSSS if $\alpha > 2$. In Figure 2.6, we depict the upper bounds on the transmission capacity of FHSS and DHSS techniques as a function of the pathloss exponent α for different spreading factors M. As already predicted, spreading techniques perform better than hopping when the pathloss exponent α is smaller than 2. Conversely, hopping strategies are preferred in terms of transmission capacity.

The transmission capacity metric reviewed thus far measures the spatial density of successful transmissions in a specific geographical area. The basic communication scheme considered throughout the discussion does not include the use of more sophisticated strategies, such as interference cancellation [HAW08; VH12], scheduling [WAJ07], or power control [WA12].

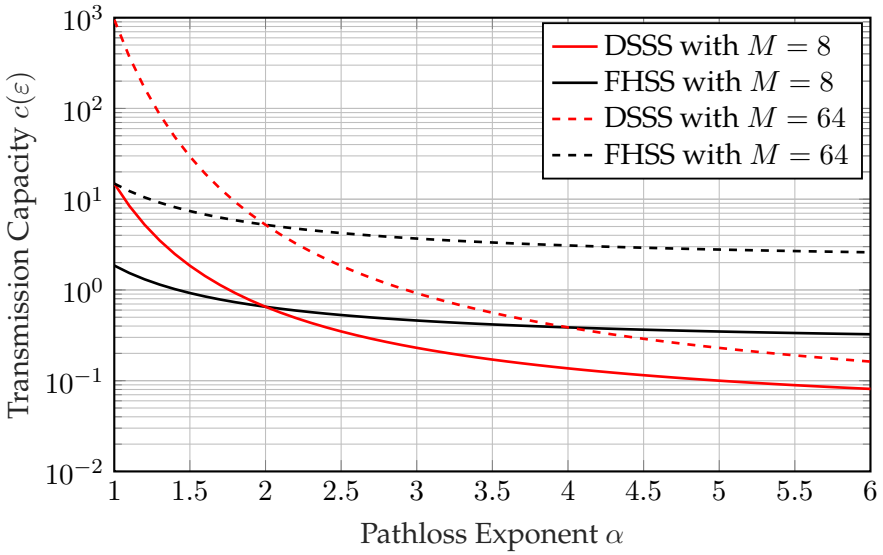

Figure 2.6: Upper bound on the transmission capacity $c(\varepsilon)$ for FHSS and DSSS as a function of the pathloss exponent α with $\mathrm{sir} = 5$ dB, $\mathrm{inr} = 5$ dB, $\beta = 0$ dB, $r_{kk} = 1$, $M = \{8, 64\}$, and $\varepsilon = 10^{-1}$.

These techniques permit improving the density of coexisting communication nodes, yet require additional feedback overhead to fully exploit their potential.

2.3 The Limits of Network Cooperation

The interference management schemes reviewed so far require that the network nodes exchange some sort of information to achieve their optimal operating regime. In this sense, even though it is possible to design interference management strategies without CSI at transmitters, cooperation between them is still needed to fully exploit their capabilities. Furthermore, a transmitting node has to interact with its intended receiver to establish a coherent communication link. From a mathematical perspective, the latter means that transmitters and receivers need to share the signal space and the same signal-space basis. Therefore, cooperation and coordination play a fundamental role in alleviating the interference between coexisting nodes [VEG18].

Coordination and cooperation generally require the existence of feedback links or exchanging information beforehand between transmitters or receivers. In any case, achieving cooperation and coordination consumes some DoF that cannot be used for information transmission. Focusing on feedback, the required overheads to send CSI or other helpful information may drastically affect the overall system performance. For this reason, some works deal with the design of low-rate feedback schemes [LHNL+08], or smart feedback allocation [PLH18]. Even though partial CSI can improve the system performance, in some cases, e.g., in multi-antenna settings, a trade-off exists between system performance and feedback [CE13]. In the search for low-rate feedback schemes, a technique called random beamforming takes advantage of the inherent sparsity of millimeter-wave channels to schedule the transmissions [LSK16; LSS16]; however, its performance degrades when the number of coexisting nodes is low.

It is well known that cooperation can substantially improve system performance since the interference produced by cooperating nodes can be totally suppressed. The latter is especially

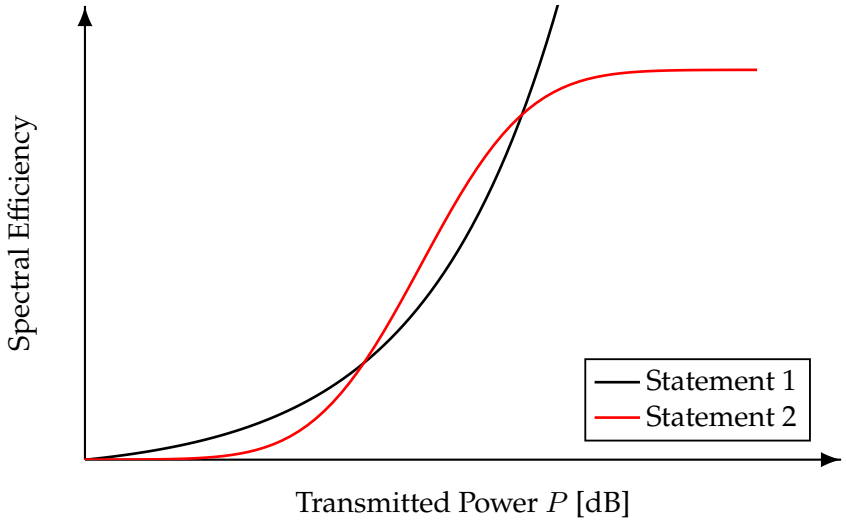

Figure 2.7: Illustration of the spectral efficiency under Statement 1 (2.32) and Statement 2 (2.33) versus the transmitted power P in logarithmic scale. These plots have been adapted from [LHA13].

significant in decentralized communication scenarios, such as device-to-device (D2D) networks [WHC19]. Fully canceling interferences usually involves complex signal processing schemes. Thus, when the interference is not a limiting factor (weak-interference regime) is reasonable to use more simple strategies such as TIN. Nevertheless, as discussed in Section 2.2, TIN is only sum-rate optimal when the interference is very weak and, therefore, the system performance still benefits from cooperation under weak interferences [ZD17].

Despite the important role that network cooperation plays in the interference management framework, the system performance does not unboundedly improve through cooperation. This statement has been pointed out in Section 2.2, where it is mentioned that receiver cooperation only improves the per-user rate up to a known limit [WT11a]. The same conclusion has been found in [WT11b] for the case of transmitter cooperation.

A thorough analysis of the limits of cooperation is carried out in [LHA13]. Therein, two models for the observation at an arbitrary receiver are proposed. On the one hand, if all network nodes can cooperate, the observation at the n-th receiving node is modeled as

$$\text{Statement 1:} \quad Y_n = \sum_{k=1}^{K} \sqrt{P} H_{nk} X_k + Z_n, \tag{2.32}$$

where P is the transmitted power, H_{nk} stands for the channel coefficient between the k-th transmitter and the n-th receiver, X_k refers to the signal sent by the k-th transmitter, and Z_n models the observation noise. If all network nodes cooperate, the interferences can be canceled out, and all the incoming signals can be perfectly decoded. According to this model, it seems that the spectral efficiency should arbitrarily grow with the transmitted power. However, as the number of network nodes increases, the model in (2.32) becomes unrealistic. Hence, it seems more reasonable to consider that only some of the coexisting nodes cooperate. This case requires including an interference term in the received signal model, which can be modeled as

$$\text{Statement 2:} \quad Y_n = \sum_{k=1}^{K} \sqrt{P} H_{nk} X_k + \sum_{k=K+1}^{\tilde{K}} \sqrt{P} H_{nk} X_k + Z_n, \tag{2.33}$$

being K out of $\tilde{K}$ the number of cooperating transmitters. The $\tilde{K} - K$ remaining network nodes do not cooperate; thus, they will induce interferences that cannot be counteracted. Under these conditions, increasing the transmitted power P does not unboundedly increase the spectral efficiency, as illustrated in Figure 2.7. [LHA13] states that even if the number of cooperating transmitters is arbitrarily increased, the spectral efficiency is always bounded due to the selective nature of the wireless channels and the dynamics of wireless networks. Therefore, [LHA13] concludes that an interference-limited network does not become a noise-limited one through cooperation, thus invalidating (2.32) in large wireless networks.

Under certain conditions, it may be acceptable to assume that the communication nodes within the same wireless system can cooperate and share the acquired CSI. Nevertheless, inter-system cooperation between independent systems seems unrealistic and prohibitive in large wireless networks. The fundamental question arising at this point is how to manage inter-system interference if the coexisting systems do not cooperate and are not coordinated. This problem is addressed by the opportunistic communication framework, which is reviewed next.

2.4 Opportunistic Communications

The last section of this chapter describes the concept of *opportunistic communications* and reviews the most relevant state-of-the-art techniques.

In a broad sense, the concept of opportunistic communications refers to a family of transmission and reception techniques that exploit favorable channel or network conditions to transmit and/or decode the signals of interest. Accordingly, opportunistic communications can ideally avoid inter-system interferences even when the coexisting network nodes do not cooperate, which permits drastically reducing the required signaling overhead to manage interferences.

Several examples of opportunistic communications can be found in the literature. For instance, [VTL02] describes a multiuser scheduling technique, known as opportunistic beamforming, which permits reducing the required feedback in point-to-point ergodic fading channels[9]. In these scenarios, the transmitter cannot take advantage of the channel variations, yielding a negligible multiuser diversity gain [Tse97]. The opportunistic beamforming strategy proposed in [VTL02] uses dumb antennas to induce fluctuations in the channel response, creating *artificial* channel variations. Then, all receiving nodes feed back a channel quality indicator (e.g., the measured SINR), and only the node exhibiting the best channel is scheduled. Despite the simplicity of this technique, [SYGM21] corroborates that opportunistic beamforming outperforms space-time coding in terms of sum rate when the channel response exhibits a slow variation. The major drawback of opportunistic beamforming is that the attainable performance degrades when the number of potential receiving nodes is low. However, this drawback can be counteracted by exploiting multiple antennas at each receiving node [SYGM21]. More recently, opportunistic beamforming has been studied in the novel framework of intelligent reflecting surfaces [NCD21].

It is worth noting that opportunistic beamforming is an opportunistic transmission strategy. On the other side, several works have investigated the potential of placing the opportunistic

[9]The ergodic fading channel is the situation where the time scale of communication is much larger than that of the channel fluctuations [TV05].

strategy at the receiver and studying the benefits of dynamically varying the decoding capabilities according to the network state. In this sense, the objective is to achieve a higher data rate when the channel conditions are favorable; otherwise, the data rate is decreased to guarantee the reliable communication. As an example, [KPV09] proposes an opportunistic decoding scheme for the 2-user Gaussian IC problem under bursty interferences. Therein, the message sent by each transmitter is divided into two sub-messages. One of them is always decoded by the intended receiver, whereas the other sub-message is only decoded when there is no interference. This strategy has been also studied in the context of multi-antenna systems [DWSGLA10], multicarrier systems [MWD13], and the K-user IC [NKBJ18]. Another interesting opportunistic decoding strategy is discussed in [YS20] for an interference network with states. Therein, a decoding strategy, denoted as opportunistic TIN, based on SIC and opportunistically treating interference as noise, is shown to be optimal under certain conditions.

The techniques surveyed thus far exploit the channel state to opportunistically transmit or decode the signals of interest. Nevertheless, opportunistic communications can take advantage not only of the channel state but also of the network state. In this sense, another classic example of opportunistic communications is found in the context of cognitive communications under the so-called *interweave* paradigm. It is worth mentioning that opportunistic communications were the initial motivation of *cognitive radio* [MM99; Hay05]. Cognitive radios are wireless communication devices that smartly exploit any sort of available side information, such as the network activity, CSI, and the codebooks or messages employed by the coexisting nodes [GJMS09]. As initially coined, a cognitive radio is able to monitor the *spectral holes*, i.e., those portions of the spectrum that are not being used at a specific time and in a specific geographical area, and exploit these spectral holes for opportunistic communication.

Besides the interweave approach, two more paradigms exist in the context of cognitive radio: the *underlay* and the *overlay* paradigms. In the *underlay* case, the cognitive transmitter is aware of the interference caused to the *non-cognitive* receivers. Accordingly, this paradigm permits the coexistence of different wireless systems using the same frequency resources if the induced interferences are below a known threshold such that the performance of the non-cognitive systems is not significantly degraded. Typically, the objective of underlay cognitive nodes is to maximize the achievable information rate subject to an *interference temperature* constraint (see, e.g., [AAH16; AAH17]). In contrast to the underlay paradigm, the power transmitted by the cognitive transmitter is not limited by an interference constraint in the *overlay* paradigm. However, the cognitive transmitter has to allocate a fraction of its transmitted power to assist the non-cognitive transmission as a relay, while the remaining power is allocated to the cognitive message (see, for instance, [DGV16; DGV17]). For this purpose, the cognitive transmitter needs to know the messages and codebooks employed by the non-cognitive systems and the channel gains. The power allocation at the cognitive transmitter must satisfy a specific QoS requirement at non-cognitive receivers.

More interestingly, the interweave communication paradigm can be generalized not only to exploit the unused spectral holes but to exploit the set of unused physical-layer network resources, signal-space dimensions, or DoF; this set is formally known as *null space*. In this sense, recalling the generic communication model described in Section 2.2.1, an opportunistic transmitting node can exploit only a column subset of the signal-space basis $\boldsymbol{U} \in \mathbb{C}^{N \times N}$. Letting $M < N$ be the number of available DoF, that is, the dimension of the null space, an opportunistic

transmitter can exploit the so-called null-space basis denoted as $\boldsymbol{U}_{\mathcal{N}} \in \mathbb{C}^{N \times M}$ without inducing inter-system interference on the other network nodes. Taking into account that $\boldsymbol{U}_{\mathcal{N}}$ is a column subset of a unitary signal-space basis $\boldsymbol{U}$, the null-space basis is left-unitary, that is, $\boldsymbol{U}_{\mathcal{N}}^H \boldsymbol{U}_{\mathcal{N}} = \boldsymbol{I}_M$. Moreover, note that the external product $\boldsymbol{U}_{\mathcal{N}} \boldsymbol{U}_{\mathcal{N}}^H = \boldsymbol{P}_{\mathcal{N}}$ equals the orthogonal projector onto the null space.

This last property is of paramount importance as the orthogonal projector is a unique representation of the null space. In this respect, let $\boldsymbol{U}_{\mathcal{N},k} \in \mathbb{C}^{N \times M}$ and $\boldsymbol{U}_{\mathcal{N},k'} \in \mathbb{C}^{N \times M}$ be two left-unitary matrices satisfying $\boldsymbol{U}_{\mathcal{N},k}^H \boldsymbol{U}_{\mathcal{N},k'} \neq \boldsymbol{I}_M$. Whenever these two matrices span the same subspace, that is, $\langle \boldsymbol{U}_{\mathcal{N},k} \rangle = \langle \boldsymbol{U}_{\mathcal{N},k'} \rangle$, the orthogonal projector is unique regardless of the considered null-space basis, that is, $\boldsymbol{U}_{\mathcal{N},k} \boldsymbol{U}_{\mathcal{N},k}^H = \boldsymbol{U}_{\mathcal{N},k'} \boldsymbol{U}_{\mathcal{N},k'}^H = \boldsymbol{P}_{\mathcal{N}}$. The non-uniqueness of the null-space basis is not an important issue for the time being, as it is usually considered that the opportunistic transmitter and its intended opportunistic receiver share the same null-space basis. Notwithstanding, as discussed further in Section 2.4.3, this issue is a fundamental assumption of this dissertation.

The family of opportunistic communication strategies exploiting the null space is typically referred to as *null-space opportunistic communications*. Before getting down to the literature review, it is interesting to emphasize that null-space communication strategies have been also used in the context of Integrated Sensing and Communications (ISAC) [MKAC17] to permit the coexistence of communication and radar waveforms, and in URLLC [EP18] to ideally avoid the overlapping between broadband communication systems and latency-constrained transmissions. Beyond the systems' coexistence scenarios, null-space strategies have also been used in RSMA [KS22] to reduce the amount of interference treated as noise and ease the SIC stage, and in the context of secure communications in the millimeter-wave band in the presence of colluding eavesdroppers [DF20].

In the literature, different null-space opportunistic communication schemes can be found in the context of single and multiple antennas, and under narrowband and wideband transmissions. In Section 2.4.1, the most relevant null-space opportunistic communication strategies are surveyed in a unified manner. As we will see, the identification of the null space is a critical task that has been widely studied in the literature. The null-space identification or sensing errors lead to the so-called *subspace leakage* problem, which is the primary source of undesired induced inter-system interferences on the other coexisting network nodes. Accordingly, Section 2.4.2 briefly studies the impact of the subspace leakage problem on the systems' coexistence, which, together with the necessity of opportunistic-node coordination, is a fundamental limitation of state-of-the-art null-space opportunistic communication strategies and the motivation behind this dissertation.

2.4.1 Null Space-based Opportunistic Communications

As already discussed, interweave cognitive radio is a classic example of null-space opportunistic communications. In this context, opportunistic nodes need to infer the spectral holes through a spectrum sensing mechanism (see, for instance, [ALLP12; JLR12; RFSVV14; FSVR14; RVC15; SAVVLV+16; AH17; TJGL18] and references therein). Then, in order to exploit the null space, opportunistic nodes devise a resource allocation strategy or tune the transmission parameters of multi-carrier modulations. Regarding resource allocation schemes, a complete survey can

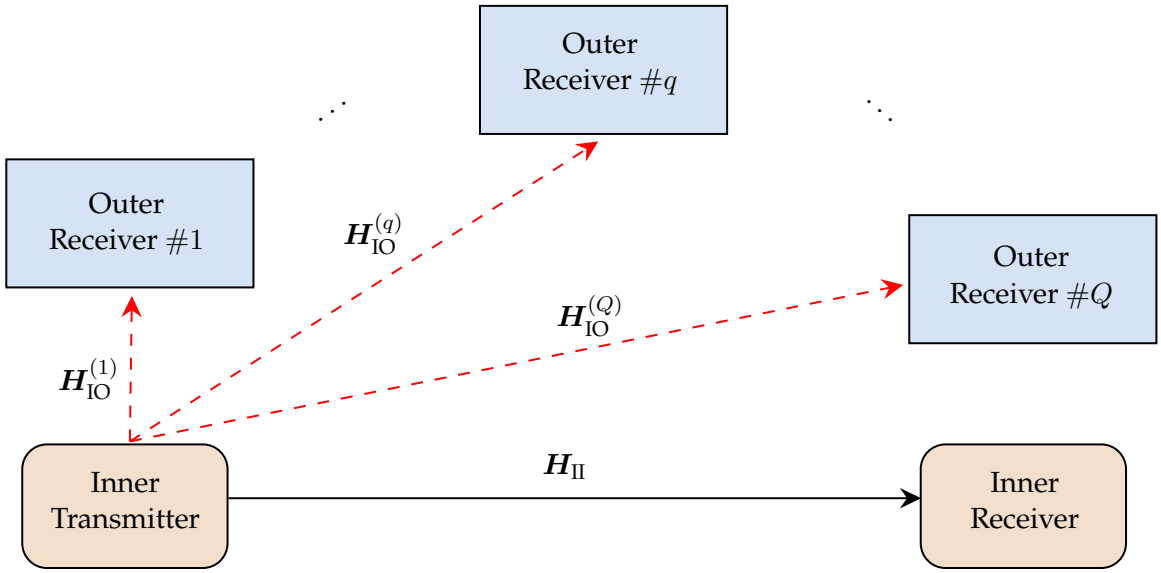

Figure 2.8: General system model for the null-space opportunistic communication problem.

be found in [TDAB16]. The use of multi-carrier modulations for opportunistic communications is proposed in several works. For instance, Orthogonal Frequency-Division Multiple-Access (OFDMA)-based opportunistic communications are studied in [XNHC14], where a game-theoretic scheme is proposed to optimize the spectrum pool. Multi-Carrier Code-Division Multiple-Access (MC-CDMA) is proposed as an opportunistic communication modulation, where the null space is exploited to shape the transmitted signal to minimize inter-system interferences. Similar to MC-CDMA, Transformed-Domain Communication System (TDCS) [CNS+05; HBGL13; JHH+17] consists in designing a fundamental waveform based on the Inverse Discrete Fourier Transform (IDFT) of a pseudo-random phase sequence modulated by a spectral mask, which is obtained from applying hard thresholding on the estimated spectrum of the wireless environment.

In the general sense, the null space-based opportunistic communications problem can be studied through the general system model depicted in Figure 2.8. It is worth noting that this model encompasses both single- and multi-antenna scenarios under both narrowband and wideband transmissions. Therefore, this general system model can be used to study in a unified manner the problem of null space-based opportunistic communications. Regarding Figure 2.8, *inner nodes* refer to the opportunistic nodes, that is, those network nodes exploiting the null space, whereas the other coexisting network nodes are denoted as *outer nodes*. This notation is used throughout this dissertation. Moreover, note that the complex matrices $\boldsymbol{H}_{\mathrm{IO}}^{(q)}$, for $q = 1, \ldots, Q$, are the cross-interference channel matrices between the inner transmitting node and each of the Q outer receiving nodes, whereas $\boldsymbol{H}_{\mathrm{II}}$ is the direct-link opportunistic channel matrix. The sizes of these matrices depend on the particular problem setup and are thus not indicated in this introductory discussion.

It is worth noticing that the cross-interference channels from the outer transmitting nodes, which are not depicted for clarity of illustration, and the inner receiver are not considered in Figure 2.8. The reason why these interference links are omitted is that the primary objective of null-space opportunistic communications is to mitigate (ideally, avoid) the interference induced

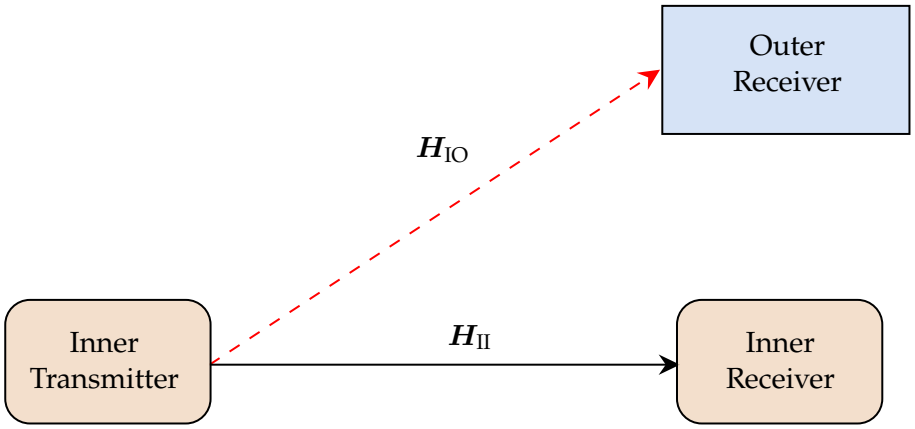

Figure 2.9: Simplified system model considered in the technical discussion.

by the inner transmitter. On the other hand, the interference that outer transmitters can induce on the inner receiver is not typically managed and, sometimes, is assumed to be negligible.

Despite the generality of the model depicted in Figure 2.8, the simplified system model illustrated in Figure 2.9 will be considered in the subsequent technical discussion for ease of exposition. Note that this simplified model admits two interpretations. On the one hand, it corresponds to the particular case where the outer network is composed of only one receiving node ($Q = 1$). From an information-theoretic perspective, this case would correspond to the 2-user cognitive interference channel, as described in [CKCD13]. More interestingly, the simplified model depicted in Figure 2.9 can be also interpreted as the stacking of the general system model given in Figure 2.8, that is, the cross-interference channel matrix $\boldsymbol{H}_{\mathrm{IO}}$ is the stacking of the Q interference channel matrices $\boldsymbol{H}_{\mathrm{IO}}^{(q)}$ from Figure 2.8.

Focusing on Figure 2.9, the primary goal of the inner transmitter is to design a transmission scheme to avoid inducing interference on the outer receiver. Letting $\boldsymbol{\Phi}$ and $\boldsymbol{W}_{\mathrm{out}}$ be the precoding matrix to be designed by the inner transmitter and the combining matrix employed by the outer receiver, respectively, the problem at hand can be mathematically written as

$$\boldsymbol{W}_{\mathrm{out}}^{H}\boldsymbol{H}_{\mathrm{OI}}\boldsymbol{\Phi} = \mathbf{0}. \tag{2.34}$$

This interference-free condition can be satisfied when the inner precoding matrix $\boldsymbol{\Phi}$ lies in the null space of the cross-interference channel matrix $\boldsymbol{H}_{\mathrm{OI}}$, which is the operating principle of null-space precoding. In the context of multiple antennas, null-space precoding has been widely studied. For instance, [ZL08] proposes projecting the inner channel onto the null space of $\boldsymbol{H}_{\mathrm{OI}}$. Other works, such as [ZWO09; ZDG12; WRF+13; AAH16; AAH17], propose different beamforming design strategies under possibly partial CSI on the cross-interference channel matrix. In the case of single-antenna opportunistic nodes, [CKCD13] proposes an IA-like scheme denoted as Vandermonde-Subspace Frequency-Division Multiplexing (VFDM), which exploits the null space induced by the channel memory when the outer-network nodes employ a block transmission with guard intervals[10]. An extension of VFDM in the context of multi-

[10]Even though VFDM has been conventionally studied assuming that outer-network nodes employ Orthogonal Frequency-Division Multiplexing (OFDM), VFDM is still valid when other block-transmission schemes with time redundancy, such as Single-Carrier Frequency-Division Multiple-Access (SC-FDMA), Generalized Frequency-Division Multiplexing (GFDM) [MMG+14], or Filter-Bank Multicarrier (FBMC) [ZLR12]

user opportunistic communications, known as cognitive interference alignment, is studied in [MDV13; MCDV13; YLL+16]. VFDM has also been studied in the context of multiple antennas to permit the joint exploitation of the spatial-domain and frequency-domain DoF [LLM14a; LLM14b; LFP+20]. As a last remark on VFDM, [FPM+20] discusses a variant of VFDM based on the IDFT operation to limit the signal bandwidth, without limiting the interference mitigation capabilities of the basic VFDM scheme, and enforce the coexistence of Long Term Evolution (LTE) and New Radio (NR) transmissions.

Regarding (2.34), a more sophisticated strategy consists in designing the inner precoding matrix $\boldsymbol{\Phi}$ to lie in the null space of the matrix $\widetilde{\boldsymbol{H}}_{\mathrm{OI}} = \boldsymbol{W}_{\mathrm{out}}^{H}\boldsymbol{H}_{\mathrm{OI}}$. The latter is the operating principle of the so-called Opportunistic Interference Alignment (OIA). This technique, which was first in the context of multi-antenna opportunistic communications, is studied in [PFLD10] under the assumption that both inner nodes have perfect CSI of the cross-interference channel matrix and the direct channel matrices of both the inner and the outer channels. These cumbersome constraints are relaxed in [YHR+09; Yi10; TB13], where the null space of the matrix $\widetilde{\boldsymbol{H}}_{\mathrm{OI}}$ is inferred through a Model Order Selection (MOS) on a sample estimate autocorrelation matrix of the observations acquired from the cross-interference channels. Nevertheless, the CSI of the direct-link opportunistic channel matrix is still needed. Even though the inter-system interference induced on the inner receiver is not nulled out in the initial approach, [Yi10; TB13] describe a strategy to mitigate the interference leaked by outer-network transmitters under the assumption that inner nodes can cooperate to agree on a reference system for the signal space, that is, they agree on a common basis. The principle of OIA has been extended to the multi-user opportunistic communication case in [AEKN10], and to space-time opportunistic communications in [ASNS16]. As a final note on OIA, the interference draining technique proposed in [PBS+14] relaxes the interference-free condition in (2.34) and guarantees that the induced interference on the outer receiver does not worsen the demanded QoS.

It is interesting to note that null-space precoding schemes can be seen as a particular case of OIA; nevertheless, the OIA approach tends to exploit a larger null space [PFLD10].

In general, a common assumption considered in both families of null-space opportunistic communication strategies is that the null space can be *perfectly* identified. Under this consideration, and recalling that the direct-link opportunistic channel is also assumed to be known at both inner nodes, the design objective consists in designing a precoding matrix $\widetilde{\boldsymbol{\Phi}} = \boldsymbol{\Phi}\boldsymbol{\Gamma}_{\mathrm{T}}$ and an inner combining matrix $\boldsymbol{\Gamma}_{\mathrm{R}}$ such that

$$\max_{\{\boldsymbol{\Gamma}_{\mathrm{T}},\boldsymbol{\Gamma}_{\mathrm{R}}\}} \quad \log_2\left(\det\left[\boldsymbol{I}_N + \boldsymbol{S}_z^{-1/2}\boldsymbol{\Gamma}_{\mathrm{R}}\boldsymbol{H}_{\mathrm{II}}\boldsymbol{\Phi}\boldsymbol{\Gamma}_{\mathrm{T}}\boldsymbol{S}_a\boldsymbol{\Gamma}_{\mathrm{T}}^{H}\boldsymbol{\Phi}^{H}\boldsymbol{H}_{\mathrm{II}}^{H}\boldsymbol{\Gamma}_{\mathrm{R}}^{H}\boldsymbol{S}_z^{-H/2}\right]\right) \tag{2.35}$$

$$\text{subject to} \qquad \mathrm{tr}\left(\widetilde{\boldsymbol{\Phi}}^{H}\widetilde{\boldsymbol{\Phi}}\boldsymbol{S}_a\right) \leq P \tag{2.36}$$

where $\boldsymbol{S}_z$ is the noise-plus-interference covariance matrix, $\boldsymbol{S}_a$ stands for the transmit symbols covariance matrix, and $\boldsymbol{\Phi}$ is a precoding matrix satisfying the interference-free condition in (2.34). This problem is usually simplified by assuming that the inner receiving node knows in advance the interference-mitigation precoding matrix $\boldsymbol{\Phi}$. Under this assumption, the problem reduces to a subspace-constrained rate maximization, where the equivalent direct-link opportunistic channel matrix is $\widetilde{\boldsymbol{H}}_{\mathrm{II}} = \boldsymbol{H}_{\mathrm{II}}\boldsymbol{\Phi}$, leading to the well-known water-filling power allocation policy. In the particular case of VFDM, since the combining matrix is a normalized Fourier matrix, i.e., $\boldsymbol{\Gamma}_{\mathrm{R}} = \boldsymbol{F}_N$, the problem formulated in (2.36) reduces to the design of the codebook

matrix, that is, the covariance matrix of the transmitted symbols, to maximize the information rate over an equivalent direct-link opportunistic channel given by $\widetilde{\boldsymbol{H}}_{\mathrm{II}} = \boldsymbol{\Gamma}_{\mathrm{R}} \boldsymbol{H}_{\mathrm{II}} \boldsymbol{\Phi} \boldsymbol{\Gamma}_{\mathrm{T}}$. In those cases where the inner receiver mitigates the inter-system interference leaked by outer-network transmitters, the problem described in (2.36) can be adapted by replacing $\boldsymbol{\Gamma}_{\mathrm{R}}$ by $\boldsymbol{\Psi}\boldsymbol{\Gamma}_{\mathrm{R}}$, where the interference-mitigation combining matrix $\boldsymbol{\Psi}$ satisfies the interference-free condition in (2.34).

The discussion above is based on the assumption of perfect knowledge of the null space, which is typically considered in the context of null-space opportunistic communications. Nevertheless, there are some exceptions. For instance, [Yi10] and [WRF+13] consider the existence of null-space inference errors. In [Yi10], the problem is formulated assuming an imperfect knowledge of the null space, yet these errors are not taken into account in the design problem. Instead, the impact of null-space inference errors is analyzed when the design of opportunistic precoding and combining matrices is based on a null-space estimate. In contrast, [WRF+13] uses the expected impact of the cross-interference channel matrix estimation errors to limit the amount of interference that can be induced on the outer receivers, adding an additional constraint to the problem formulated in (2.36). Finally, [AAH16; AAH17] assume partial CSI of the cross-interference channel and design a precoding strategy that maximizes the mismatch between the opportunistic transmitted signal and the partially known covariance matrix of the cross-interference channel.

It is worth noting that, in order to satisfy the design criterion given in (2.36), cooperation between inner nodes is needed; this assumption is not unrealistic and typically considered in general communication problems. Nevertheless, finding an interference-mitigation opportunistic precoding matrix $\boldsymbol{\Phi}$ that satisfies the interference-free condition in (2.34) requires the inner transmitting node to be aware of the cross-interference channel matrix $\boldsymbol{H}_{\mathrm{OI}}$ and/or the outer combining matrix $\boldsymbol{W}_{\mathrm{out}}$. This side information can be conveyed through feedback from the outer receiver to the inner transmitter. In this case, it is possible to perfectly mitigate the undesired inter-system interferences. Under the assumption of channel reciprocity [VT03], a more realistic possibility consists in estimating the matrix $\widetilde{\boldsymbol{H}}_{\mathrm{OI}}$; however, this approach also requires the inner transmitter to be aware of the coded-modulation format employed by the outer-network terminals.

If channel reciprocity holds, there exists another approach to infer the null space of the matrix $\widetilde{\boldsymbol{H}}_{\mathrm{OI}}$ without side information about the outer networks, hence avoiding the necessity of cooperation between the outer receiver and the inner transmitter, and the knowledge of side information on the coded-modulation formats employed by the outer-network terminals. The inner transmitter can collect a set of observations from the cross-interference channel and estimate the autocorrelation matrix. Note that the acquired observations will depend on the outer combining matrix $\boldsymbol{W}_{\mathrm{out}}$ and the cross-interference channel matrix $\boldsymbol{H}_{\mathrm{OI}}$, thus the same null space exploited by OIA can be inferred from the measured autocorrelation matrix. This approach is the operating principle behind the so-called *blind sensing* techniques (see, for instance, [AAT19]). Once a sample estimate of the observations' autocorrelation matrix is obtained, these techniques detect the available DoF through its *eigendecomposition*. Examples of relevant blind detectors include, for instance, the maximum-to-minimum eigenvalue ratio test [BDGH18] or model order selection [SS04] based sensing mechanisms [MGC15; FSRV15]. In essence, these tests split the subspace into the so-called *signal subspace*, which encompasses the occupied sensed DoF, and the null space, which contains the available sensed DoF.

Recalling this last approach to infer the null space of the matrix $\widetilde{\boldsymbol{H}}_{\mathrm{OI}}$, the inner transmitter can obtained a *sensed* null-space basis, denoted as $\widehat{\boldsymbol{U}}_{\mathcal{N}}$. The interference-mitigation opportunistic precoding matrix $\boldsymbol{\Phi}$ is thus designed from the available null-space information encompassed in $\widehat{\boldsymbol{U}}_{\mathcal{N}}$. The classical null-space opportunistic communication schemes surveyed in this section arbitrarily select K out of the M DoF spanned by the sensed null-space basis $\widehat{\boldsymbol{U}}_{\mathcal{N}}$. Thus, in general, the interference-mitigation opportunistic precoding matrix $\boldsymbol{\Phi} = [\boldsymbol{\phi}_0, \ldots, \boldsymbol{\phi}_{K-1}]$ can be written as

$$\boldsymbol{\phi}_k = \widehat{\boldsymbol{U}}_{\mathcal{N}} \boldsymbol{\lambda}_k, \quad \text{for } k = 0, \ldots, K-1, \tag{2.37}$$

with $\boldsymbol{\lambda}_k = [\mathbf{0}^T_{m(k)-1} \; 1 \; \mathbf{0}^T_{M-m(k)}]^T$. It is noteworthy that this blind null-space inference approach can overestimate the null space. In other words, some of the DoF occupied by the outer-network nodes can be erroneously detected as available. This effect is known as *subspace leakage* [SV15]. Thus, regarding (2.37), there exists the possibility that some of the wrongly available sensed DoF are used for opportunistic transmission. If the latter occurs, the inner transmitter can break the interference-free condition in (2.34), and harmfully interfere with the outer-network communication. In the sequel, the impact of the inter-system interference induced by subspace leakage under the classic null-space approach is studied, motivating the necessity of designing robust opportunistic communication schemes.

2.4.2 The Impact of Uncertainty in Network State Information

For the sake of concreteness, the subsequent technical discussion will revolve around the null space inferred from estimating the autocorrelation matrix of the observations acquired from the cross-interference channel. Accordingly, from the eigendecomposition, let $\widehat{\boldsymbol{U}}$ be the eigenvectors' matrix of the sample estimate autocorrelation matrix. Using a subspace thresholding criterion, such as model order selection, the eigenvectors' matrix can be partitioned into

$$\widehat{\boldsymbol{U}} = \left[\begin{array}{c:c} \widehat{\boldsymbol{U}}_{\mathcal{S}} & \widehat{\boldsymbol{U}}_{\mathcal{N}} \end{array} \right], \tag{2.38}$$

where $\widehat{\boldsymbol{U}}_{\mathcal{S}} \in \mathbb{C}^{N \times N-M}$ spans the sensed occupied signal-space dimensions or DoF, and $\widehat{\boldsymbol{U}}_{\mathcal{N}} \in \mathbb{C}^{N \times M}$ spans the considered available DoF, that is, the null space. As discussed above, the partition in (2.38) suffers from the subspace leakage problem, and therefore the sensed null-space basis $\widehat{\boldsymbol{U}}_{\mathcal{N}}$ can be written as

$$\widehat{\boldsymbol{U}}_{\mathcal{N}} = \left[\begin{array}{c:c} \widetilde{\boldsymbol{U}}_{\mathcal{N}} & \boldsymbol{E}_{\mathcal{N}} \end{array} \right], \tag{2.39}$$

where $\widetilde{\boldsymbol{U}}_{\mathcal{N}} \in \mathbb{C}^{N \times M-N_E}$ contains the correctly sensed available DoF, whereas $\boldsymbol{E}_{\mathcal{N}} \in \mathbb{C}^{N \times N_E}$ models the sensing errors containing the critical N_E occupied DoF wrongly sensed as available.

Recalling (2.37) and taking into account the null-space sensing error model given in (2.39), each column of the interference-mitigation opportunistic precoding matrix $\boldsymbol{\phi}_k$ is given by

$$\boldsymbol{\phi}_k = \widehat{\boldsymbol{U}}_{\mathcal{N}} \boldsymbol{\lambda}_k = \left[\begin{array}{c:c} \widetilde{\boldsymbol{U}}_{\mathcal{N}} & \boldsymbol{E}_{\mathcal{N}} \end{array} \right] \boldsymbol{\lambda}_k, \quad \text{for } k = 0, \ldots, K-1, \tag{2.40}$$

where $\boldsymbol{\lambda}_k = [\mathbf{0}^T_{m(k)-1} \; 1 \; \mathbf{0}^T_{M-m(k)}]^T$. In accordance with this model, note that the interference-mitigation opportunistic precoding matrix $\boldsymbol{\Phi}$ is composed of a subset of columns of the sensed null-space basis $\widehat{\boldsymbol{U}}_{\mathcal{N}}$.

In order to evaluate the impact of the imperfect network state information, or the subspace leakage problem, we define the Signal-to-Interference Ratio (SIR) at the inner transmitter output as the quotient between the opportunistic (non-interfering) signal power and the interference level induced by the subspace leakage, that is,

$$\text{SIR} \triangleq \frac{\text{Opportunistic Non-Interfering Transmitted Power}}{\text{Total Induced Inter-System Interference Level}}.$$

More formally, letting S_{T} and I_{T} be the average transmitted power and the average inter-system interference power measured at the inner transmitter output, respectively, the SIR is given by

$$\text{SIR} = \frac{S_{\text{T}} - I_{\text{T}}}{I_{\text{T}}}. \tag{2.41}$$

Regarding (2.40), since each column of the interference-mitigation opportunistic precoding matrix $\mathbf{\Phi}$ corresponds to an eigenvector, the total average transmitted signal power is $S_{\text{T}} = \sum_k \|\boldsymbol{\phi}_k\|^2/N = K/N$. However, the calculation of the average induced inter-interference level has some subtle details. To begin with, we must recall that the column selection can be arbitrary, that is, without responding to any specific criterion. Hence, different choices lead to different interferences. An appropriate manner to remove the column choice uncertainty is to average the time-average inter-system interference level over different column choices. In this respect, the time-average interference level induced by the k-th waveform is given by

$$i_k = \frac{1}{N}\|\boldsymbol{\phi}_k\|^2 \mathbb{1}_k, \tag{2.42}$$

where $\mathbb{1}_k$ is the classical indicator function, defined as

$$\mathbb{1}_k = \begin{cases} 1 & \text{if } \boldsymbol{\phi}_k \in \langle \boldsymbol{E}_{\mathcal{N}} \rangle \\ 0 & \text{otherwise} \end{cases}. \tag{2.43}$$

Note that (2.43) takes one with probability N_E/M. By taking the mathematical expectation of (2.42), we will remove the uncertainty due to the arbitrary column selection criterion. Thus,

$$I_k = \frac{1}{N}\mathbb{E}[i_k] = \frac{N_E}{MN} = \frac{I}{N}, \tag{2.44}$$

leading to an average induced inter-system interference level of $I_{\text{T}} = K \cdot I/N$. Therefore, the SIR as defined in (2.41) is given by

$$\text{SIR} = \frac{K/N - K/N \cdot I}{K/N \cdot I} = \frac{1 - N_E/M}{N_E/M}. \tag{2.45}$$

It is interesting to note that the quantity N_E/M, which corresponds to the ratio between the number of erroneously sensed DoF and the total number of available sensed DoF, measures the *inaccuracy* of the employed subspace thresholding criterion.

We would like to emphasize that (2.45) corresponds to the average SIR, as the instantaneous SIR offered by the classic null-space approach is unpredictable due to the arbitrary column selection criterion. Among the different scenarios, a particular case of interest is the worst case. For this purpose, let us consider that the inner transmitter exploits K out of M null-space DoF. In

this respect, the worst case implies that $N_E \leq K \leq M$, and that all the wrongly available sensed DoF N_E are selected. Under these critical conditions, it is straightforward to see that the average inter-system interference power measured at the inner transmitter output is $I_{\mathrm{T}} = N_E/N$, as the N_E wrongly available sensed DoF are used for opportunistic communication. Accordingly, the worst-case SIR exhibited by classic null-space schemes is given by

$$\mathrm{SIR}_{\mathrm{T}}^{\text{worst-case}} = \frac{K/N - N_E/N}{N_E/N} = \frac{K/M - N_E/M}{N_E/M}, \quad \text{for } N_E \leq K \leq M, \tag{2.46}$$

where the dimension of the sensed null space M has been introduced in the second equality for ease of interpretation. Regarding (2.46), we note that the SIR not only depends on the inaccuracy of the employed subspace thresholding criterion N_E/M but also depends on the fraction of exploited null-space DoF K/M. As expected, under the worst-case condition, the SIR exhibited by classic null-space schemes only approaches their average performance when the null space is saturated, that is, when all M DoF sensed as available are used for opportunistic communication. The average and worst-case SIR performance exhibited by classic null-space schemes are illustrated in Figures 2.10 and 2.11. We can observe that, on average, the fraction of the non-interfering opportunistic signal power is only slightly higher than the induced interference level due to network state information uncertainties. Regarding the worst case, the classic null-space approach exhibits poor performance if only a fraction of the null space is exploited for opportunistic communication.

It is worth noting that saturating the null space can be optimal in terms of information rate; nevertheless, this approach can be devastating for the outer-network nodes as these levels of interference per DoF can induce outage on the outer receiving nodes and severely corrupt outer-network communication. Furthermore, saturating the null space can be devastating in multi-user opportunistic communications, as other potential inner nodes may not be able to exploit the null space. The latter motivates the necessity of strategies robust to the subspace leakage problem.

A straightforward approach to counteract the subspace leakage problem, and hence the induced inter-system interferences, is to let all network nodes cooperate. Under the full cooperation assumption, interference may not be a limiting factor and the optimal communication strategy is then the maximization of the information rate. Nevertheless, as discussed in Section 2.3, an interference-limited scenario cannot turn into a noise-limited one even under full cooperation. In the case of limited or partial cooperation, opportunistic nodes can know a QoS requirement of the outer-network nodes, such as the maximum interference level supported by the outer-network terminals, and then maximize the opportunistic information rate constraining the induced interference level.

The aforementioned approaches require cooperation between outer and inner network nodes, which is not always feasible. A more realistic approach is to let the opportunistic nodes cooperate only between them. In this case, the inner transmitting and receiving nodes can reduce the subspace leakage problem by agreeing on a *common* null space. If the null-space inference is locally done at each opportunistic node, the sensing uncertainties may be independent, meaning that the errors made by the transmitter may be different from the sensing errors made by the receiver. Therefore, agreeing on a common null space can reduce the number of occupied DoF erroneously sensed as available N_E. This approach is the operating principle of the so-called *cooperative sensing* schemes (see, for instance, [CKB16; PRJV18; TJGL18]).

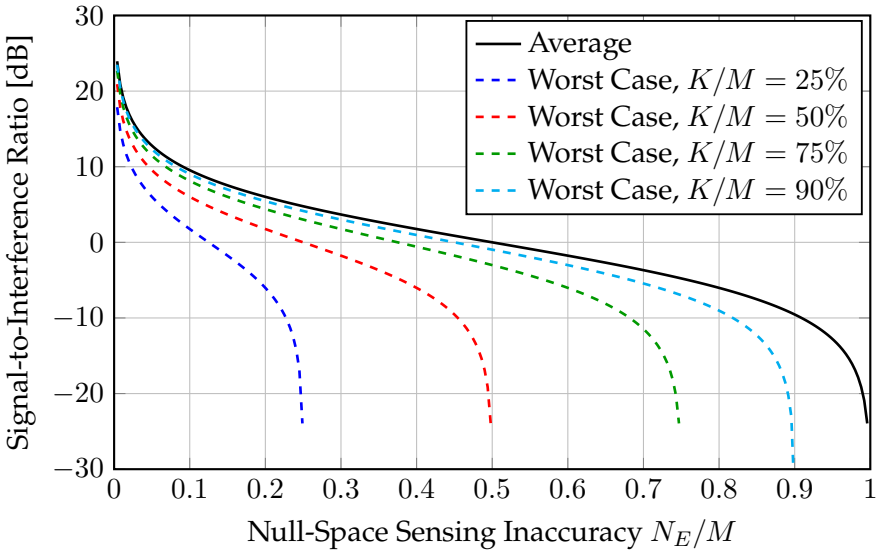

Figure 2.10: $\mathrm{SIR}_{\mathrm{T}}^{\text{worst-case}}$ (2.46) and average $\mathrm{SIR}_{\mathrm{T}}$ (2.45)as a function of the sensing inaccuracy N_E/M of the classic null-space approach for different fractions of exploited null-space DoF.

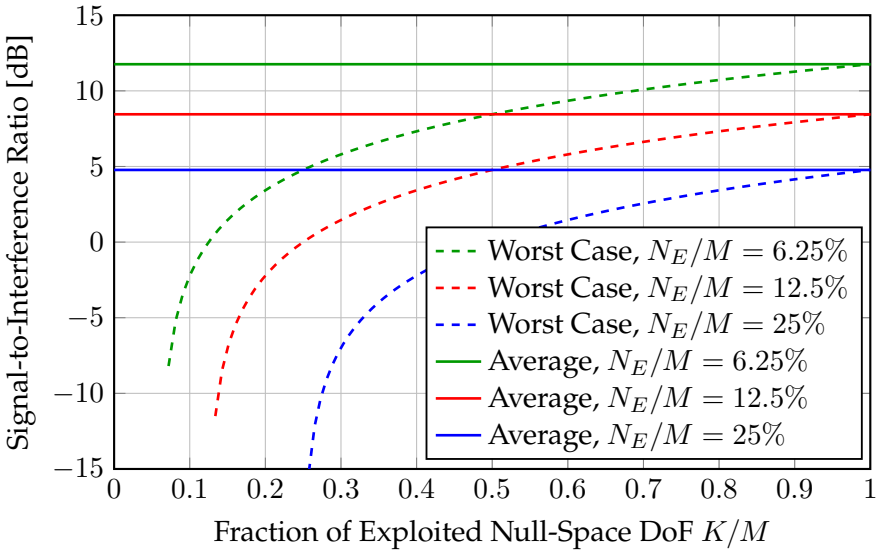

Figure 2.11: $\mathrm{SIR}_{\mathrm{T}}^{\text{worst-case}}$ (2.46) and average $\mathrm{SIR}_{\mathrm{T}}$ (2.45) as a function of the fraction of exploited null-space DoF K/M of the classic null-space approach for null-space sensing inaccuracies.

Nevertheless, dealing with the subspace leakage problem in non-cooperative opportunistic communication scenarios is more cumbersome. Under these conditions, the interference-mitigation precoder design can be only based on the locally sensed null space; thus, making the abovementioned approaches useless. This scenario, which is the one considered in this dissertation, is referred to as *feedforward opportunistic communications* and briefly discussed next.

2.4.3 Feedforward Opportunistic Communications

The abovementioned strategies to deal with the subspace leakage problem require cooperation between the coexisting network nodes. Notwithstanding, assuming that inner and outer nodes can cooperate may be too optimistic regardless of the fundamental limits of full cooperation reviewed in Section 2.3. Furthermore, there are some scenarios where inner nodes do not cooperate between them either. These scenarios are referred to as *feedforward opportunistic communications* throughout this dissertation. An example of these scenarios is during the opportunistic communication setup, also known as, access channels.

Under these cumbersome conditions, two major issues have to be addressed. On the one hand, since the inner transmitter does not cooperate with the other network nodes, including the intended inner receiver, the design of the interference-mitigation precoding matrix relies only on locally sensed network state information. Therefore, without any a priori side information or interaction with the coexisting nodes, the subspace leakage problem can induce severe inter-system interferences, as discussed in Section 2.4.2. In this case, the opportunistic precoding design scheme cannot be based on the information rate maximization, as the inter-system interferences leaked on the outer receivers can corrupt the outer-network communication. In terms of transmission capacity (see Section 2.2.3), a hybrid spreading-hopping technique that can be adapted to different channel conditions would be preferable. Nevertheless, the latter requires CSI to adapt the transmission scheme to the current network state. Since CSI is not available at the inner transmitter in the feedforward case, a more appropriate design strategy relies on the minimization of the induced inter-system interferences. Even though such a strategy may not be optimal in terms of information rate, it guarantees a minimum induced inter-system interference, which is beneficial in terms of systems coexistence.

On the other hand, since the inner transmitter does not interact with the inner receiver, the latter is not aware of the signal space at the inner transmitter. Moreover, the inner nodes may not share a common calibrated reference system for the signal space. In this sense, even if the signal spaces at both inner nodes are the same, the lack of a common calibrated reference system reveals that it is not possible to establish a coherent communication system between the inner nodes, understanding the coherence condition as the a priori knowledge of the transmitted pulse-shaping waveform by the receiving end. Accordingly, it may look like non-coherent communications are inherent to feedforward opportunistic communications, with the associated system performance degradations [GPV05a; GPV05b].

In conclusion, this brief introduction to the feedforward opportunistic communication problem addressed in this dissertation unveils the two major research challenges in this context: the necessity of designing an opportunistic transmission-reception scheme robust to the subspace leakage problem and the lack of interaction between inner nodes.

CHAPTER 3

The Case of Single-Channel Feedforward Opportunistic Communications

3.1 Introduction

This chapter focuses on the waveform design problem in single-antenna feedforward opportunistic communications. In this cumbersome scenario, the opportunistic nodes do not cooperate, and the information about the null space is locally sensed. The motivation of this chapter is to explore the repercussion of removing the cooperation between opportunistic nodes. Nevertheless, as briefly pointed out at the end of the chapter, the provided solutions can also be used in cooperative opportunistic communications to reduce the required feedback rate.[1]

3.1.1 Generalized Null Space-based Opportunistic Communication

The classical approaches in null space-based opportunistic communications discussed in Section 2.4.1 consist in using a set of the null-space basis vectors as a precoding matrix. These approaches achieve interference-free opportunistic communication under ideal operating conditions, i.e., when the opportunistic nodes have perfect network state information. Nevertheless, as discussed in Section 2.4.1, an imperfect knowledge of the network state information leads to *subspace leakage* or partial *subspace swap*. This effect is especially typical in the wideband regime due to its inherent low Signal-to-Noise Ratio (SNR).

Another important aspect is the null-space bases calibration. Imagine that an opportunistic transmitter and an opportunistic receiver locally estimate the interference signals autocorrelation matrix and that these terminals do not cooperate. Then, the null-space eigenvectors can be found using an information-theoretic criterion [WK85], such as the Akaike Information Criterion (AIC) or Minimum Description Length (MDL). Even though they can detect the same null space, the eigenvectors are not unique when the multiplicity of null-space eigenvalues is larger

[1] Some of the results described in this chapter have been submitted for a possible publication to IEEE Transactions on Communications [J3].

than one with high probability. Therefore, the inferred null-space bases can be different at each opportunistic node. This phenomenon may lead to a non-coherent communication scenario, which translates to severe performance degradations at low-SNR regimes [GPV05a; GPV05b]. Under these conditions, the system performance can only improve through a coordinated feedback link.

In this chapter, we consider the existence of subspace leakage errors from the very beginning. Accordingly, we incorporate null-space sensing errors into the waveform design problem through a generalized error model independent of the employed null-space detection scheme. As a result, the opportunistic waveforms derived in this chapter exhibit maximum worst-case Signal-to-Interference Ratio (SIR) at the opportunistic transmitter output. It is shown that the optimum waveforms are unique within the null space, meaning that no feedback overheads are needed to achieve coherent detection. In this sense, the so-called *invariance* property is of paramount importance to guarantee detectability in strict feedforward scenarios.

The opportunistic transmission technique described in this chapter can be seen as a generalization of classic null-space solutions, constituting the major contribution of this dissertation.

Even though the derived solution is suitable in the cumbersome strict feedforward case, the lack of inter-node cooperation brings to light the *subspace mismatch* problem. In other words, the null spaces detected at each opportunistic terminal can be slightly different, leading to detection performance losses. An enhanced detection scheme based on active subspace identification is proposed to counteract the impact of subspace mismatch.

3.1.2 Chapter Organization

This chapter is organized as follows. In Section 3.2, we describe the mathematical formulation of the waveform design problem in the feedforward opportunistic communication case. The solution to this problem is given in Section 3.3, altogether with a technical discussion on the robustness to the induced inter-system interference. Section 3.4 describes the invariance property, which is fundamental for the detectability in non-cooperative scenarios, and the impact of the lack of cooperation in the opportunistic system performance. A technique to improve the opportunistic receiver is described in Section 3.5. Finally, the conclusions are drawn in Section 3.6.

3.2 Problem Statement

Throughout this chapter, we consider the opportunistic communication scenario depicted in Figure 3.1. A set of Q transmitter-receiver pairs exploits the wireless resources in a heterogeneous wireless network, transmitting at different rates and employing probably different modulation and coding schemes. These nodes, which are referred to as *outer nodes* or *terminals*, exploit a fraction of the total system Degrees of Freedom (DoF) N. Recalling Section 2.2.1, the asymptotic total number of complex DoF is given by $N \approx TW$, where T is the signals' duration, and W is the system bandwidth.

A new asynchronous transmitter-receiver pair, referred to as *inner nodes* or *terminals*, wants to access the available DoF opportunistically. We assume that each inner node has to locally identify the available DoF without cooperation between them and the outer-network nodes.

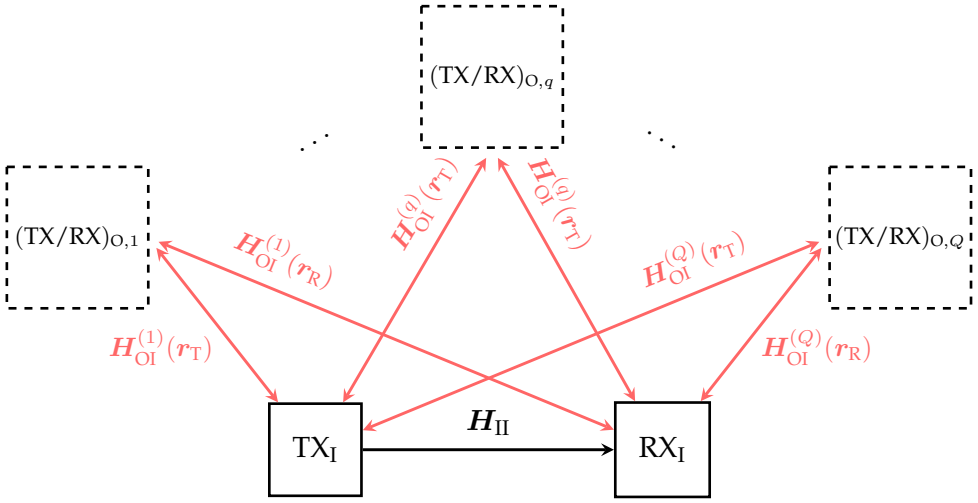

Figure 3.1: The system model considered in this chapter. $(\mathrm{TX/RX})_{\mathrm{O},q}$ stands for the q-th outer transmitter-receiver pair. $\mathrm{TX_I}$ and $\mathrm{RX_I}$ are the inner transmitting and receiving terminals, respectively, transmitting through the inner channel $\boldsymbol{H}_{\mathrm{II}}$. The interference channel between the q-th outer-network pair and the inner node located at position $\boldsymbol{r}$ is denoted by $\boldsymbol{H}_{\mathrm{OI}}^{(q)}(\boldsymbol{r})$. Note that the position of the inner transmitter and receiver is denoted by $\boldsymbol{r} = \boldsymbol{r}_{\mathrm{T}}$ and $\boldsymbol{r} = \boldsymbol{r}_{\mathrm{R}}$, respectively. It is assumed that all channels are unknown by the opportunistic inner transmitter $\mathrm{TX_I}$, whereas the opportunistic inner receiver $\mathrm{RX_I}$ only knows, at most, the inner channel $\boldsymbol{H}_{\mathrm{II}}$.

The objective consists in designing N-sample discrete-time orthogonal waveforms that provide minimum interferences to the outer-network terminals.

For the sake of clarity, we consider the feedforward opportunistic transmission of blocks of K zero-mean and unit-variance independent symbols a_k drawn from a given constellation $\mathcal{C}$. The received signal for an arbitrary block l is given by

$$y_l[n] = \sqrt{\frac{S_{\mathrm{R}}}{K}} \sum_{k=0}^{K-1} a_{k[l]} \phi_k[n - lN] + i[n] + w[n], \quad \text{for } n = 0, \ldots, N-1, \tag{3.1}$$

where $\phi_k[n]$ stands for the n-th sample of the k-th orthonormal waveform to be designed, S_{R} is the average received power, $i[n]$ refers to an unstructured interference term and $w[n] \sim \mathcal{N}_{\mathbb{C}}(0, \sigma_w^2)$ denotes the receiver complex, one-sided, circularly-symmetric Gaussian thermal noise.

It is worth noting that we assume that the channel $\boldsymbol{H}_{\mathrm{II}}$ between the opportunistic nodes is memoryless[2]. The adaptation of this problem to frequency-selective channels is discussed in Chapter 4.

From (3.1), we can now distinguish two potential applications of the transmission scheme derived in this chapter. If the symbols a_k are a priori known by the inner receiving node, this model refers to a training or sounding reference signal. Otherwise, in a general sense, this model describes the problem of a generic linear modulation.

For notational purposes, we define the *shaping transmission matrix* as

$$\boldsymbol{\Phi} = [\boldsymbol{\phi}_0 \ \cdots \ \boldsymbol{\phi}_k \ \cdots \ \boldsymbol{\phi}_{K-1}] \in \mathbb{C}^{N \times K}, \tag{3.2}$$

with $\boldsymbol{\phi}_k = [\phi_k[0], \ldots, \phi_k[N-1]]^T \in \mathbb{C}^N$. Notice that the orthonormal pulses $\{\boldsymbol{\phi}_k\}_{0 \leq k \leq K-1}$ will enjoy interference mitigation capabilities if they lie in the null space of the outer terminals,

[2]That is, the discrete duration of the symbols N is larger than the channel delay spread.

which has to be locally inferred from the interference signals

$$\boldsymbol{x}(\boldsymbol{r}) = \sum_{q=1}^{Q} \boldsymbol{H}_{\mathrm{OI}}^{(q)}(\boldsymbol{r})\boldsymbol{s}_q + \boldsymbol{v}(\boldsymbol{r}), \tag{3.3}$$

where $\boldsymbol{r} = [r_x, r_y, r_z]^T$ denotes the positioning coordinates of an inner node, $\boldsymbol{H}_{\mathrm{OI}}^{(q)}(\boldsymbol{r}) \in \mathbb{C}^{N\times N'}$ stands for the interference channel between the q-th outer-network transmitter and the inner node located at position $\boldsymbol{r}$, with $N \geq N'$; $\boldsymbol{s}_q \in \mathbb{C}^{N'}$ is the transmitted signal by the q-th outer-network transmitting node; and $\boldsymbol{v}(\boldsymbol{r}) \sim \mathcal{N}_{\mathbb{C}}(\boldsymbol{0}_N, \sigma_v^2\boldsymbol{I}_N)$ is the additive observation noise.

It is worth noting that opportunistic communications rely on detecting or learning the null space from the observed interference signals in (3.3). This problem has been widely studied in the literature, and it is out of the scope of this dissertation. Nevertheless, it is briefly sketched next for the reader's convenience.

Detecting or Inferring the Null Space

Traditionally, the null-space identification used to be based on feature detection and sensing schemes (see, for instance, [FSVR14; AH17] and references therein). These approaches imply the knowledge of the modulation formats used by the transmitters and receivers in the wireless environment. When the inner nodes do not have any kind of a priori information about the outer-network composition, the interference channels $\boldsymbol{H}_{\mathrm{OI}}^{(q)}(\boldsymbol{r})$, and the outer-network signals $\boldsymbol{s}_q$, the null space can only be statistically inferred. For this purpose, each inner node needs to obtain a set of observations from the interference channels, denoted as $\mathcal{X}(\boldsymbol{r})$. Then, the *eigendecomposition* of a sample estimate of the aggregate interference signals autocorrelation matrix can be obtained as

$$\widehat{\boldsymbol{R}}_{\boldsymbol{xx}}(\boldsymbol{r}) = \frac{1}{|\mathcal{X}(\boldsymbol{r})|} \sum_{\boldsymbol{x}(\boldsymbol{r})\in\mathcal{X}(\boldsymbol{r})} \boldsymbol{x}(\boldsymbol{r})\boldsymbol{x}^H(\boldsymbol{r}) = \widehat{\boldsymbol{U}}(\boldsymbol{r})\widehat{\boldsymbol{D}}(\boldsymbol{r})\widehat{\boldsymbol{U}}^H(\boldsymbol{r}), \tag{3.4}$$

where the unitary matrix $\widehat{\boldsymbol{U}}(\boldsymbol{r})$ is the autocorrelation's eigenmatrix and the diagonal matrix $\widehat{\boldsymbol{D}}(\boldsymbol{r})$ contains the autocorrelation's eigenvalues in non-increasing order. Given the noisy nature of the interference signals in (3.3), note that $\widehat{\boldsymbol{R}}_{\boldsymbol{xx}}(\boldsymbol{r}) = \widehat{\boldsymbol{R}}_s(\boldsymbol{r}) + \widehat{\boldsymbol{R}}_n(\boldsymbol{r})$, where $\widehat{\boldsymbol{R}}_s(\boldsymbol{r})$ is the autocorrelation of the noise-free interference signal, and $\widehat{\boldsymbol{R}}_n(\boldsymbol{r}) \approx \sigma_v^2\boldsymbol{I}_N$ is the noise autocorrelation matrix. The objective of each inner node is to identify the $M(\boldsymbol{r}) = N - P(\boldsymbol{r})$ eigenvectors from $\widehat{\boldsymbol{U}}(\boldsymbol{r})$ that span the null space, being $P(\boldsymbol{r}) = \mathrm{rank}\left[\widehat{\boldsymbol{R}}_s(\boldsymbol{r})\right]$. In other words, the inner nodes have to determine the order of the data model.

The specific problem of determining the dimension of the parameter vector is known as Model Order Selection (MOS), which is cast as a composite hypothesis testing problem among all the possible dimensions of the parameter vector.

A simple approach to deal with this problem is to identify the $M(\boldsymbol{r})$ eigenvectors whose associated eigenvalues are below a predetermined decision threshold, i.e., detect the signal space dimensions with the lowest energy contribution. Nevertheless, the performance of this energy detection approach is limited by SNR walls [TS08], and it degrades if the noise variance is not accurately known a priori.

As widely studied, a more appropriate alternative to the simple energy detector consists in using information-theoretic criteria. In this sense, the most commonly adopted statistic is

the MDL [Ris78], also known as the Bayesian Information Criterion (BIC) [Sch78]. The MDL is a consistent model order estimator and returns the correct order in the infinite observations regime. Another well-known criterion is the AIC [Aka74], which is inconsistent and typically overestimates the model order. A review of the different MOS statistics can be found in [SS04]. The performance of MOS to determine the dimension of the signal subspace has been evaluated under various criteria and in different frameworks (see, e.g., [ZWYR89; XK95; FGM02; LZ13; FSRV15] and references therein). A more recent reference [MGC15] shows that information-theoretic criteria outperform energy detection in the context of MOS. Since energy detection (and its variants) are the optimal detectors under unknown signal models (see, e.g., [Kay98]), these information-theoretic criteria can be optimal in some scenarios under the lack of side information about the outer networks.

It is worth mentioning that the null-space detection strategies discussed so far are not unique alternatives. Instead, any unitary matrix $\boldsymbol{U}(\boldsymbol{r}) \in \mathbb{C}^{N\times N}$ constructed using any additional a priori information about the outer networks available at the inner nodes is also a valid DoF basis. Moreover, in some situations, using a pseudo-random DoF basis can be interesting to weaken the impact of systematic detection errors and further reduce the residual inter-system interferences.

Either way, as it will be discussed later, the opportunistic transmission scheme designed in this thesis is *transparent* or *independent* to the adopted null-space sensing scheme. Thus, from this point onwards, we assume that using any of the discussed criteria, each inner node has split the signal-space basis $\boldsymbol{U}(\boldsymbol{r})$ into

$$\boldsymbol{U}(\boldsymbol{r}) = \left[\begin{array}{c:c} \widehat{\boldsymbol{U}}_{\mathcal{S}}(\boldsymbol{r}) & \widehat{\boldsymbol{U}}_{\mathcal{N}}(\boldsymbol{r}) \end{array}\right], \tag{3.5}$$

where $\widehat{\boldsymbol{U}}_{\mathcal{S}}(\boldsymbol{r}) \in \mathbb{C}^{N\times P(\boldsymbol{r})}$ spans the sensed *signal subspace*, which contains the sensed occupied dimensions or DoF, and $\widehat{\boldsymbol{U}}_{\mathcal{N}}(\boldsymbol{r}) \in \mathbb{C}^{N\times M(\boldsymbol{r})}$ spans the sensed *null space*, which encompasses the considered available DoF.

Mathematical Problem Formulation

In the sequel, for the sake of clarity, the discussion focuses on the transmitting waveforms design. Therefore, from now on, we consider $\boldsymbol{r} = \boldsymbol{r}_{\mathrm{T}}$, i.e., the inner transmitting node coordinates, and this dependency on $\boldsymbol{r}_{\mathrm{T}}$ is dropped when possible for ease of notation.

In order to avoid inter-system interferences, the opportunistic waveforms to be designed have to be orthogonal to the sensed signal subspace, that is,

$$\widehat{\boldsymbol{U}}_{\mathcal{S}}^{H}\boldsymbol{\Phi} = \mathbf{0}_{P\times K}, \tag{3.6}$$

where $\boldsymbol{\Phi}$ is the shaping transmission matrix defined in (3.2). It is worth noting that the design condition in (3.6) is achieved by aligning the opportunistic waveforms with the sensed outer-network null space $\widehat{\mathcal{N}}_{\mathrm{T}} = \left\langle \widehat{\boldsymbol{U}}_{\mathcal{N}}(\boldsymbol{r}_{\mathrm{T}}) \right\rangle$. Therefore, any waveform satisfying

$$\boldsymbol{\phi}_k = \widehat{\boldsymbol{U}}_{\mathcal{N}}\boldsymbol{\lambda}_k, \quad \text{for } k = 0, \ldots, K-1, \tag{3.7}$$

where $\boldsymbol{\lambda}_k \in \mathbb{C}^M$ contains the linear combination coefficients specifying $\boldsymbol{\phi}_k$, is a candidate to achieve interference-free transmissions in feedforward opportunistic communications. Note

that the waveform model in (3.7) refers to the common model used by all null-space opportunistic communication schemes reviewed in Section 2.4.1.

A first approach to designing opportunistic waveforms with interference mitigation capabilities consists in adopting the classic null-space solution. In this sense, all the classic null-space approaches (see Section 2.4.1) arbitrarily select K columns from the null-space basis $\widehat{\boldsymbol{U}}_{\mathcal{N}}$ as opportunistic transmission waveforms, letting $\boldsymbol{\lambda}_k = [\mathbf{0}^T_{m(k)-1}\ 1\ \mathbf{0}^T_{M-m(k)}]^T$.

It is worth noting that the null-space waveforms satisfying (3.7) rely on the sensed null-space basis. The classic null-space solution provides interference-free opportunistic waveforms if and only if the M signal space dimensions encompassed in the sensed null-space basis $\widehat{\boldsymbol{U}}_{\mathcal{N}}$ are *actually* non-occupied by outer-network nodes, i.e. when the null-space detection scheme provides error-free outcomes. Nevertheless, in practice, the inference of the null-space basis suffers from several *sensing uncertainties*:

(i) *Detection errors*. When the inner terminals do not have a priori side information on the outer networks, the null-space inference relies on the estimation of the statistics, as the observations autocorrelation matrix. Thus, the errors in estimating the statistics and the impact of the subspace thresholding (or MOS) criterion induce false alarms and miss-detection errors.

(ii) *Time variability of the network state*. The occupied DoF and the DoF occupancy may exhibit time variations according to the node activity and the traffic or quality-of-service (QoS) requirements. This thesis deals with the slow time-variant (quasi-static) network state scenario, as the fast time variability of interference channels provides a natural diversity and multiple-access multiplexing mechanism for interference mitigation. In this sense, a quasi-static network state is critical because the sensing uncertainties can last for a considerable time, and the DoF occupied by outer-network nodes may slightly vary within the opportunistic transmission.

(iii) *Local monitoring conditions*. The inference of the null space relies on the set of observations (3.3) acquired at the position of the inner node. In this sense, large-scale fading (shadowing) and small-scale fading may impact the sensed null space. Even though the effects of fading may not be relevant in terms of sensing uncertainties under time division duplex (TDD) transmissions, it is a source of *subspace mismatch* between inner nodes. The problem of subspace mismatch, which is studied further in this chapter, may decrease opportunistic communication performance.

When these sensing uncertainties are jointly taken into account, the problem of subspace leakage, sketched in Figure 3.2, arises. Therefore, the necessity of formulating a null-space error model arises to study robust waveform designs.

Characterizing the subspace leakage problem is challenging and highly depends on the adopted null-space detection scheme. This is the reason why the classic references on null-space precoding, both in single- and multi-antenna scenarios, typically do not incorporate the subspace leakage problem into the waveform design problem[3]. Instead, some works tackle the

[3]To the best of the author's knowledge, only the estimation errors of statistics, as the interference-signal covariance matrix, or the estimation errors of the interference channel matrices are taken into account in some works to set the maximum allowed interference in the context of underlay cognitive radio (see, e.g., [WRF+13]).

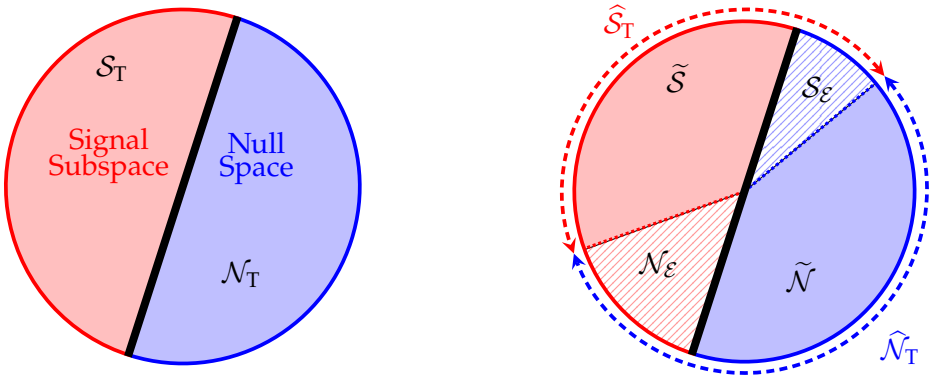

(a) "True" signal and null subspaces

(b) Impact of subspace leakage.

Figure 3.2: Sketch of the "actual" signal subspace and null space at inner transmitting node and the effects of subspace leakage. The sensed signal subspace and the sensed null space are respectively given by $\widehat{\mathcal{S}}_{\mathrm{T}} = \widetilde{\mathcal{S}} \oplus \mathcal{S}_{\mathcal{E}}$ and $\widehat{\mathcal{N}}_{\mathrm{T}} = \widetilde{\mathcal{N}} \oplus \mathcal{N}_{\mathcal{E}}$. $\widetilde{\mathcal{S}}$ and $\widetilde{\mathcal{N}}$ contain the correctly sensed occupied DoF and correctly sensed available DoF, respectively. Note that the null-space DoF encompassed in $\mathcal{S}_{\mathcal{E}}$ only incur a loss of transmit opportunities, whereas the signal-subspace DoF encompassed in $\mathcal{N}_{\mathcal{E}}$ are a source of inter-system interferences.

waveform design problem assuming a *perfect* knowledge of the null space and then study the impact of sensing errors on the system performance.

Contrary, this thesis proposes a generalized null-space error model that can be adopted in robust designs for the null space-based opportunistic transmission schemes, regardless of the null-space detection or sensing method. In Figure 3.2, we note that the sensed null space $\widehat{\mathcal{N}}_{\mathrm{T}}$ is composed of some available DoF correctly sensed as available (represented by $\widetilde{\mathcal{N}}$) and some occupied DoF erroneously detected as available (represented by $\mathcal{N}_{\mathcal{E}}$). Accordingly, the sensed null-space basis $\widehat{\boldsymbol{U}}_{\mathcal{N}}$ admits the following formulation:

$$\widehat{\boldsymbol{U}}_{\mathcal{N}} = \left[\begin{array}{c:c} \widetilde{\boldsymbol{U}}_{\mathcal{N}} & \boldsymbol{E}_{\mathcal{N}} \end{array} \right], \tag{3.8}$$

where $\boldsymbol{E}_{\mathcal{N}} \in \mathbb{C}^{N \times N_E}$ is a basis of the error subspace $\mathcal{N}_{\mathcal{E}}$, whereas $\widetilde{\boldsymbol{U}}_{\mathcal{N}} \in \mathbb{C}^{N \times (M-N_E)}$ spans the available DoF correctly sensed as available and encompassed in $\widetilde{\mathcal{N}}$. It is worth noting that since the null-space inference scheme provides $\widehat{\boldsymbol{U}}_{\mathcal{N}}$, the structure of the sensed null-space basis in (3.8) is transparent to the inner node.

Taking into account the generalized null-space error model in (3.8), the null-space waveforms in (3.7) read as

$$\boldsymbol{\phi}_k = \widehat{\boldsymbol{U}}_{\mathcal{N}} \boldsymbol{\lambda}_k = \left[\begin{array}{c:c} \widetilde{\boldsymbol{U}}_{\mathcal{N}} & \boldsymbol{E}_{\mathcal{N}} \end{array} \right] \boldsymbol{\lambda}_k, \quad \text{for } k = 0, \ldots, K-1. \tag{3.9}$$

Recall that the inner node is not aware of subspace leakage. Therefore, the classic null-space solution, i.e., arbitrarily selecting columns of $\widehat{\boldsymbol{U}}_{\mathcal{N}}$ through $\boldsymbol{\lambda}_k = [\mathbf{0}^T_{m(k)-1} \; 1 \; \mathbf{0}^T_{M-m(k)}]^T$ can severely corrupt the outer-network communication when the dimensions or DoF encompassed in the error matrix $\boldsymbol{E}_{\mathcal{N}}$ are used for opportunistic communication. The latter is a consequence of aligning the opportunistic transmissions with the sensed null-space basis $\widehat{\boldsymbol{U}}_{\mathcal{N}}$.

A naive solution to deal with the undesired inter-system interference consists in *spreading* the opportunistic waveforms within the whole sensed null space. In other words, letting $\boldsymbol{\lambda}_k = \alpha_k \mathbf{1}_{M \times 1}$, where α_k is a scaling factor guaranteeing $\|\boldsymbol{\phi}_k\| = 1$. Although it may seem that just one

waveform saturates the null space, we shall remark that the waveforms satisfying (3.9) are rank-one, meaning that up to M orthogonal waveforms can be designed. Nevertheless, we note that this naive solution is not feasible unless we modify the sensed null-space basis to guarantee the waveform orthogonality. In this sense, we can perform a sequential dimensionality reduction of the null space. For instance, the K opportunistic waveforms can be designed as

$$\boldsymbol{\phi}_k = \alpha_k \widehat{\boldsymbol{U}}_{\mathcal{N}}^{[k]} \mathbf{1}_{M\times 1}, \tag{3.10}$$

where $\widehat{\boldsymbol{U}}_{\mathcal{N}}^{[k]}$ contains the eigenvectors associated with the $M-k$ largest eigenvalues of matrix

$$\boldsymbol{\Omega}[k] = \widehat{\boldsymbol{U}}_{\mathcal{N}} \widehat{\boldsymbol{U}}_{\mathcal{N}}^H \left(\boldsymbol{I}_N - \sum_{i=0}^{k-1} \boldsymbol{\phi}_i \boldsymbol{\phi}_i^H \right). \tag{3.11}$$

Note that the first term $\widehat{\boldsymbol{U}}_{\mathcal{N}} \widehat{\boldsymbol{U}}_{\mathcal{N}}^H$ is the orthogonal projector onto the null space, which guarantees the orthogonality to the sensed signal subspace. In contrast, the second term guarantees the orthogonality between the K designed waveforms.

This naive solution spreads the K symbols sent by the inner transmitter within the sensed null space keeping the orthogonality between them. Spreading the transmitted symbols also means spreading the undesired inter-system interferences, which reduces the provided interference per DoF. Therefore, this approach seems to deal with the severe inter-system interferences that the classic null-space solution may provide. However, is the naive approach optimum? Is this naive approach suitable in feedforward opportunistic communication scenarios?

In order to study the optimality of the signal spreading approach, we need to define a criterion. Taking into account that the K transmitted symbols in (3.1) are statistically independent, the impact of null-space sensing uncertainties or, more specifically, subspace leakage can be measured in terms of the average total inter-system interference power as

$$I_{\mathrm{T}}\left(\boldsymbol{E}_{\mathcal{N}}; \{\boldsymbol{\lambda}_k\}\right) \triangleq \frac{1}{N} \sum_{k=0}^{K-1} \left\| \boldsymbol{E}_{\mathcal{N}}^H \boldsymbol{\phi}_k \right\|_2^2 = \frac{1}{N} \sum_{k=0}^{K-1} \left\| \boldsymbol{E}_{\mathcal{N}}^H \widehat{\boldsymbol{U}}_{\mathcal{N}} \boldsymbol{\lambda}_k \right\|_2^2. \tag{3.12}$$

At this point, some considerations are of order. It is worth noting that the impact of both small-scale and large-scale fadings is not considered in (3.12) since the average total inter-system interference is measured at the inner transmitter output. Although (3.12) is thus a pessimistic metric, it is also general enough to be adopted in a wide variety of scenarios.

Taking into account that the error matrix $\boldsymbol{E}_{\mathcal{N}}$ is unknown, the waveform design problem can be formulated as the following min-max optimization problem:

$$\{\boldsymbol{\lambda}_k\}_{0\le k\le K-1} = \underset{\{\boldsymbol{\lambda}_k\}}{\arg\min} \max_{\boldsymbol{E}_{\mathcal{N}}} \; I_{\mathrm{T}}(\boldsymbol{E}_{\mathcal{N}}; \{\boldsymbol{\lambda}_k\}), \tag{3.13}$$

that is, the set of linear combination vectors $\{\boldsymbol{\lambda}_k\}_{0\le k\le K-1}$ that define the set of orthogonal waveforms $\{\boldsymbol{\phi}_k\}_{0\le k\le K-1}$ have to provide minimum worst-case average total inter-system interference. It is worth noting that the latter is *the best that can be done* without any a priori knowledge about the error matrix $\boldsymbol{E}_{\mathcal{N}}$. The min-max optimization problem in (3.13) is ill-posed and requires certain design constraints that will be introduced in Section 3.3.

In this sense, the solution to the waveform design problem in (3.13) is provided altogether with a consistent technical discussion. We will see that the naive approach in (3.10)–(3.11) is not optimum nor suitable for feedforward opportunistic communications, even though it is more robust than the classic null-space solution.

3.3 Generalized Null-Space Waveforms

This section discusses a general class of linear modulations that satisfy the min-max optimization problem stated in (3.13). The provided result can be seen as a generalization of the classic null-space approach. Moreover, even though the derived solution follows the interference spreading approach as the naive solution in (3.10)–(3.11), the generalized null-space waveforms are unique within the sensed null space. The latter property, which is studied in detail in Section 3.4, is of paramount importance as it permits coherent opportunistic communication in feedforward scenarios.

As claimed before, this optimization problem is ill-posed, and it can only be solved if the degree of uncertainty assumed in the null-space error model (3.8) is constrained. The degree of uncertainty is conventionally defined through the Schatten p-norm (see [AAH16] and references therein). The definition of the Schatten norm can be found, for instance, in [Ber09, Proposition 9.2.3] and given next for the reader's convenience:

Definition 3.1 (Schatten p-norm)**.** *Let $\boldsymbol{A}$ be a (complex) $m \times n$ matrix and σ_i, for $i = 1, \ldots, \min(m, n)$, be its i-th singular value. Then, the Schatten p-norm of matrix $\boldsymbol{A}$ is given by*

$$\|\boldsymbol{A}\|_{\sigma p} \triangleq \begin{cases} \left(\sum_{i=1}^{\min(m,n)} \sigma_i^p(\boldsymbol{A}) \right)^{1/p} & \text{if} \quad 1 \leq p < \infty \\ \sigma_{\max}(\boldsymbol{A}) & \text{if} \quad p = \infty \end{cases}, \tag{3.14}$$

where $\sigma_{\max}(\boldsymbol{A})$ is the maximum singular value of matrix $\boldsymbol{A}$. Several special cases of this family of norms are the following: the Nuclear norm ($p = 1$), i.e., the sum of the singular values; the Frobenius norm ($p = 2$); and the spectral norm ($p = \infty$), i.e., the maximum singular value. As per [Ber09, Proposition 9.2.4], for $p, q \in [1, \infty)$ with $p \leq q$, the following property holds:

$$\|\boldsymbol{A}\|_{\sigma\infty} \leq \|\boldsymbol{A}\|_{\sigma q} \leq \|\boldsymbol{A}\|_{\sigma p} \leq \|\boldsymbol{A}\|_{\sigma 2} \leq \|\boldsymbol{A}\|_{\sigma 1}. \tag{3.15}$$

Recall that, in the problem at hand, we are looking for a constraint for the sensing error matrix $\boldsymbol{E}_{\mathcal{N}}$, which is a unitary basis of an N_E-dimensional subspace of $\mathbb{C}^N$. Thus, the singular values of $\boldsymbol{E}_{\mathcal{N}}$ are equal and normalized to one, implying that there is no dominant dimension. In this case, an informative constraint is to upper-bound the error power through the Frobenius norm (the Schatten 2-norm), i.e., $\|\boldsymbol{E}_{\mathcal{N}}\|_{\mathrm{F}}^2 \leq \xi^2$, with $\xi^2 \in \mathbb{R}^+$. It is worth noting that, since $\boldsymbol{E}_{\mathcal{N}}$ is left-unitary, the following relationship holds

$$\|\boldsymbol{E}_{\mathcal{N}}\|_{\mathrm{F}}^2 = \mathrm{tr}\left[\boldsymbol{E}_{\mathcal{N}}^H \boldsymbol{E}_{\mathcal{N}}\right] = \mathrm{rank}\left[\boldsymbol{E}_{\mathcal{N}}\right] \leq \xi^2, \tag{3.16}$$

meaning that constraining the Frobenius norm of the error matrix $\boldsymbol{E}_{\mathcal{N}}$ is equivalent to constraining its rank, and thus the maximum number of assumed erroneously sensed DoF.

Another essential aspect that must be considered is the orthogonality between the K waveforms in (3.1). In this thesis, the coefficients vector $\boldsymbol{\lambda}_k$ is not constrained to have a predetermined structure as in the classic null-space solution, and the sensed null-space basis is not *ad-hoc* recursively updated as in the naive approach in (3.10)–(3.11).

In this sense, we will further on let $\boldsymbol{\lambda}_k$ be a generic full vector, and thus the orthogonality between waveforms can only be satisfied by a recursive procedure constrained by

$$\boldsymbol{\lambda}_k^H \boldsymbol{\lambda}_{k'} = 0, \quad \text{for } k, k' = 0, \ldots, K-1 \ \text{ with } k \neq k'. \tag{3.17}$$

This constraint is essential to avoid self-induced Inter-Symbol Interference (ISI) between the K transmitted symbols.

The last aspect to discuss is the existence of a trivial solution. Recalling the optimization problem in (3.13), it is clear that, irrespectively of the error matrix $\boldsymbol{E}_{\mathcal{N}}$, the minimum induced inter-system interference is achieved when the inner node does not transmit. Accordingly, a non-trivial design constraint is required. Among other options, the *linear predictor* condition [TK82; TKK82] is adopted, i.e.,

$$\boldsymbol{\lambda}_k^H \widehat{\boldsymbol{U}}_{\mathcal{N}}^H \boldsymbol{e}_k = \alpha_k, \tag{3.18}$$

where $\alpha_k \in \mathbb{R}^+$ is a scaling factor that guarantees that the designed waveforms have unit norm, and

$$\boldsymbol{e}_k \triangleq \left[\mathbf{0}_{n(k)-1}^T \ 1 \ \mathbf{0}_{N-n(k)}^T\right]^T \tag{3.19}$$

is an N-length binary vector with only one non-zero element.

The constraint in (3.19) is commonly adopted in a wide variety of engineering problems, in which the position $n(k)$ of the non-zero element is arbitrarily chosen. Conversely, in the problem at hand, the position $n(k)$ of the non-zero element can be optimized to satisfy a specific criterion that will be discussed later.

At this point, we can formulate the optimization problem addressed in this thesis. Taking into account the three abovementioned constraints in (3.16), (3.17) and (3.18), the min-max problem in (3.13) becomes

$$\{\boldsymbol{\lambda}_k\}_{0\leq k\leq K-1} = \underset{\{\boldsymbol{\lambda}_k\},\{\boldsymbol{e}_k\}}{\arg\min} \left\{ \max_{\boldsymbol{E}_{\mathcal{N}}} \sum_{k=0}^{K-1} \left\| \boldsymbol{E}_{\mathcal{N}}^H \widehat{\boldsymbol{U}}_{\mathcal{N}} \boldsymbol{\lambda}_k \right\|_2^2 \right\} \tag{3.20}$$

$$\text{s.t.} \quad \|\boldsymbol{E}_{\mathcal{N}}\|_{\mathrm{F}}^2 \leq \xi^2 \tag{3.21}$$

$$\boldsymbol{\lambda}_k^H \boldsymbol{\lambda}_{k'} = 0, \ k \neq k' \tag{3.22}$$

$$\boldsymbol{\lambda}_k^H \widehat{\boldsymbol{U}}_{\mathcal{N}}^H \boldsymbol{e}_k = \alpha_k \tag{3.23}$$

As advocated in Appendix 3.A, solving the maximization in (3.20) subject to the constraint in (3.21), the objective function becomes

$$\{\boldsymbol{\lambda}_k\}_{0\leq k\leq K-1} = \underset{\{\boldsymbol{\lambda}_k\},\{\boldsymbol{e}_k\}}{\arg\min} \sum_{k=0}^{K-1} \left\| \widehat{\boldsymbol{U}}_{\mathcal{N}} \boldsymbol{\lambda}_k \right\|_2^2. \tag{3.24}$$

It is worth noting that the design of opportunistic waveforms minimizing the worst-case induced inter-system interference reads as the Tufts-Kumaresan minimum-norm problem [TK82; TKK82]. The minimum-norm solution is based on a linear prediction that provides an accurate estimation of the involved parameters [PF87]. This is the reason why the minimum norm method has been extensively used in the context of robust spectral analysis (see, e.g., [KT82]) and robust direction-of-arrival estimation with both uniform linear arrays [KT83] and arbitrary arrays [LVT89], to name a few.

Therefore, the solution to the waveform design problem stated in (3.20)–(3.23) enjoys the properties of linear prediction filters. In terms robustness to sensing uncertainties, one interesting property is the spectral behavior of the designed waveforms $\{\boldsymbol{\phi}_k\}_{0\leq k\leq K-1}$. As intuitively stated in [Kum83] for the specific case of linear prediction filters and formally studied in [Pak87] for the general case of polynomials orthogonal with respect to a certain positive measure on the unit circle, the zeros of the designed waveforms exhibit an asymptotic uniform distribution on a circle of radius less than or equal to one. The latter suggests that the waveforms $\{\boldsymbol{\phi}_k\}_{0\leq k\leq K-1}$ spread the transmitted energy among all DoF sensed as available; thus, the designed waveforms minimize the induced inter-system interference per erroneous DoF.

Moreover, it is shown in [DD91] that the Tufts-Kumaresan minimum-norm is equivalent to the Total Least-Squares (TLS) method, emphasizing that the designed waveforms are optimum in the TLS sense. The waveform design problem is studied from a TLS perspective in Section 3.3.1, proving that the waveforms minimizing the worst-case inter-system interferences are, in fact, the TLS solutions. For this reason, from this point onwards, the designed waveforms are referred to as Minimum-Norm Total Least-Squares (MNTLS) waveforms.

Recalling the objective function given in (3.24) and the associated constraints (3.22)–(3.23), the vectors $\{\boldsymbol{\lambda}_k\}_{0\leq k\leq K-1}$ defining the MNTLS waveforms $\{\boldsymbol{\phi}_k\}_{0\leq k\leq K-1}$ can be found following the Lagrange multipliers method, as elaborated in Appendix 3.A. In this appendix, it is shown that the MNTLS waveforms rely on the orthogonal projector onto the sensed null space, i.e., $\widehat{\boldsymbol{P}}_0 = \widehat{\boldsymbol{U}}_{\mathcal{N}}\widehat{\boldsymbol{U}}_{\mathcal{N}}^H$. In particular, these waveforms can be sequentially found as

$$\boxed{\boldsymbol{\phi}_k = \gamma_k \widehat{\boldsymbol{P}}_0 \left(\boldsymbol{I}_N - \sum_{i=0}^{k-1} \boldsymbol{\phi}_i \boldsymbol{\phi}_i^H\right) \boldsymbol{e}_k = \gamma_k \widehat{\boldsymbol{P}}_k \boldsymbol{e}_k,} \tag{3.25}$$

where $\widehat{\boldsymbol{P}}_{k+1} = \widehat{\boldsymbol{P}}_k \left(\boldsymbol{I}_N - \boldsymbol{\phi}_k \boldsymbol{\phi}_k^H\right)$ are the projection matrices onto a subspace of the sensed complete null space. Note that a recursive dimensionality reduction is required to satisfy the waveform orthogonality constraint. The term $\gamma_k = \left(\boldsymbol{e}_k^T \widehat{\boldsymbol{P}}_k \boldsymbol{e}_k\right)^{-1/2}$, which is also derived in Appendix 3.A, is a scaling factor such that $\|\boldsymbol{\phi}_k\|_2 = 1$.

In the abovementioned Appendix 3.A in a formal manner and in Appendix 3.B trying to provide a physical interpretation, the optimization of the linear predictor condition in (3.19) is discussed. As thoroughly analyzed in Section 3.3.2, the entries of the main diagonal of $\widehat{\boldsymbol{P}}_k$ are inversely proportional to the level of inter-system interference injected on outer-network nodes. Thus, the linear predictor vector $\boldsymbol{e}_k$ in (3.19) satisfying the minimum-norm condition corresponds to the $n(k)$-th column of $\widehat{\boldsymbol{P}}_k$ that has the largest diagonal element. Then,

$$n(k) = \underset{n\in\{1,\ldots,N\}}{\arg\max}\, \boldsymbol{e}_k^T \widehat{\boldsymbol{P}}_k \boldsymbol{e}_k = \underset{n\in\{1,\ldots,N\}}{\arg\max} \left[\widehat{\boldsymbol{P}}_k\right]_{n(k),n(k)}. \tag{3.26}$$

Despite being the mathematically optimal approach for minimum worst-case inter-system interference, a particular case deserves our attention. When the main diagonal of $\widehat{\boldsymbol{P}}_k$ is constant, all columns exhibit the same performance in terms of worst-case inter-system interference. To avoid complexity, especially at the inner receiver, we adopt a sequential column selection by taking the first non-null element of the main diagonal of $\widehat{\boldsymbol{P}}_k$, that is,

$$n(k) = k + 1. \tag{3.27}$$

This case can be further generalized. When the dynamic margin of the main diagonal of $\widehat{\boldsymbol{P}}_k$,

$$\Delta\left[\mathrm{diag}\left(\widehat{\boldsymbol{P}}_k\right)\right] \triangleq \left|\max\left[\widehat{\boldsymbol{P}}_k\right]_{nn} - \min_{\left[\widehat{\boldsymbol{P}}_k\right]_{nn}\neq 0}\left[\widehat{\boldsymbol{P}}_k\right]_{nn}\right|, \tag{3.28}$$

is sufficiently small, the optimum approach in (3.26) incurs additional implementation complexity, arising the necessity of a non-coherent detection scheme. In feedforward systems, where the involved network nodes do not cooperate, it is preferable to decrease the processing complexity. In this case, a trade-off between complexity and performance is identified. If the dynamic margin in (3.28) is sufficiently small, all columns of the projector $\widehat{\boldsymbol{P}}_k$ approximately impose the same interference level. Thus, the distinction between columns does not significantly improve the performance in terms of worst-case inter-system interferences, meaning that the additional complexity is not justified. Therefore, for sufficiently small $\epsilon \in \mathbb{R}^+$, we adopt the following strategy for the design of the linear predictor vector $\boldsymbol{e}_k$ in (3.19):

$$n(k) = \begin{cases} k+1 & \text{if } \Delta\left[\mathrm{diag}\left(\widehat{\boldsymbol{P}}_k\right)\right] < \epsilon \\ \underset{n\in\{1,\ldots,N\}}{\arg\max}\left[\widehat{\boldsymbol{P}}_k\right]_{n(k),n(k)} & \text{otherwise} \end{cases}. \tag{3.29}$$

The question that may arise at this point is under which conditions the sequential column selection can be employed. The answer to this question is not immediate and depends explicitly on the numerical evaluation of the diagonal elements of $\widehat{\boldsymbol{P}}_k$. For the sake of illustration, two numerical examples are provided next. In Figure 3.3, we illustrate the diagonal elements of $\widehat{\boldsymbol{P}}_k$ when $N = 64$ DoF and the null space has dimension $M = 32$. We may observe that one element predominates over the rest, where the dynamic margin is of $\Delta\left[\mathrm{diag}\left(\widehat{\boldsymbol{P}}_k\right)\right] = 0.3155$. In this case, since there is no numerical ambiguity, the optimum design criterion of the linear predictor vector in (3.29) should be adopted. Nevertheless, note that this choice has to be reviewed at each recursion k, meaning that it may occur that the dynamic margin at recursion $k+1$ significantly diminishes. Then, the more efficient criterion in (3.27) can be adopted. In Figure 3.4, we depict an example of the diagonal elements of $\widehat{\boldsymbol{P}}_k$ when $N = 512$ DoF and the null space has dimension $M = 32$. It is worth noting that, in this case, there are numerical ambiguities, being the dynamic margin $\Delta\left[\mathrm{diag}\left(\widehat{\boldsymbol{P}}_k\right)\right] = 0.0105$. It seems reasonable to adopt the efficient criterion in (3.27). This case is of paramount importance since it occurs when the total number of DoF N is sufficiently large. When the latter holds, the null-space basis is a column subset of the unitary Fourier matrix, as we will see in detail in Chapter 4. In current and future communication scenarios, the total number of DoF N will be large enough such that the efficient criterion (3.27) can be adopted in practice. Aside from reducing the design complexity at the inner transmitter, the efficient criterion in (3.27) reduces the complexity of the receiving scheme drastically, as discussed in Section 3.4.

Before discussing the properties of the MNTLS waveforms, it is interesting to note that the waveform design scheme can be summarized in the following simple sequential algorithm provided in Algorithm 1.

An important virtue of the proposed design scheme is its simplicity. Observing Algorithm 1, it is essential to highlight that the design of the MNTLS waveforms $\{\boldsymbol{\phi}\}_{0\leq k\leq K-1}$ consists of a *sequential* or *recursive* procedure that admits a closed-form solution. Conversely, the conventional strategies in opportunistic communications, both in single- and multi-antenna scenarios

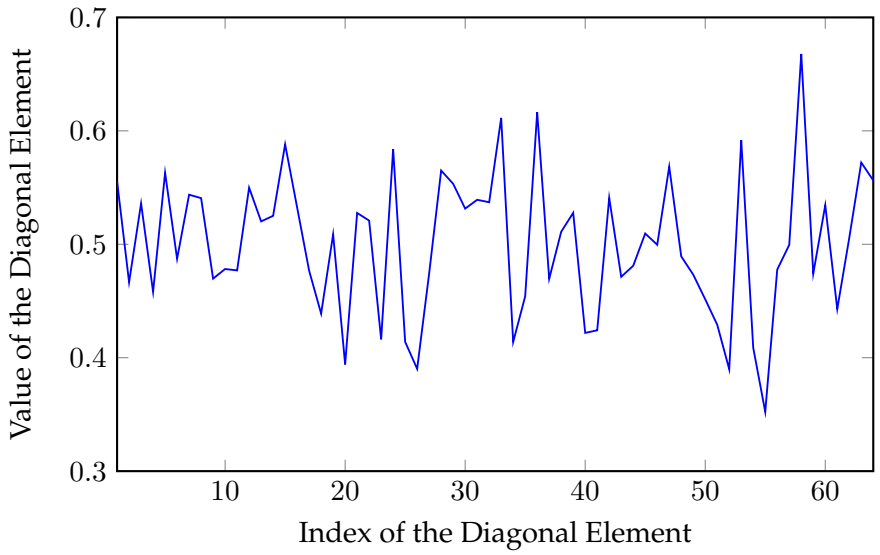

Figure 3.3: Elements of the main diagonal of $\widehat{\boldsymbol{P}}_k$ for $N = 64$ DoF and $M = 32$ DoF.

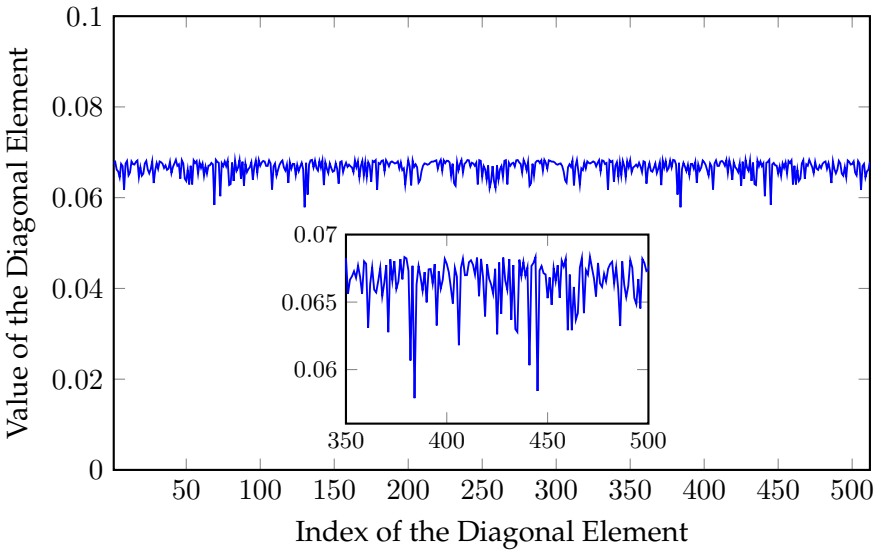

Figure 3.4: Elements of the main diagonal of $\widehat{\boldsymbol{P}}_k$ for $N = 512$ DoF and $M = 32$ DoF.

Algorithm 1 Sequential Design of the Shaping Transmission Matrix $\boldsymbol{\Phi}$

Input: K, $\widehat{\boldsymbol{U}}_{\mathcal{N}}$
Output: $\boldsymbol{\Phi}$
1: $\widehat{\boldsymbol{P}}_0 = \widehat{\boldsymbol{U}}_{\mathcal{N}}\widehat{\boldsymbol{U}}_{\mathcal{N}}^H$
2: **for** $k = 0$ until $K-1$ **do**
3: Find $\boldsymbol{e}_k = \left[\boldsymbol{0}_{n(k)-1}^T \; 1 \; \boldsymbol{0}_{N-n(k)}^T\right]^T$ with $n(k) = \begin{cases} k+1 & \text{if } \Delta\left[\operatorname{diag}\left(\widehat{\boldsymbol{P}}_k\right)\right] < \epsilon \\ \underset{n\in\{1,\ldots,N\}}{\arg\max} \left[\widehat{\boldsymbol{P}}_k\right]_{n(k),n(k)} & \text{otherwise} \end{cases}$
4: $\boldsymbol{\phi}_k = \gamma_k \widehat{\boldsymbol{P}}_k \boldsymbol{e}_k$ with $\gamma_k = (\boldsymbol{e}_k^T \widehat{\boldsymbol{P}}_k \boldsymbol{e}_k)^{-1/2}$
5: $\widehat{\boldsymbol{P}}_{k+1} = \widehat{\boldsymbol{P}}_k \left(\boldsymbol{I}_N - \boldsymbol{\phi}_k \boldsymbol{\phi}_k^H\right)$
6: $\boldsymbol{\Phi} = [\boldsymbol{\Phi} \;\; \boldsymbol{\phi}_k]$
7: **end for**

(see, e.g., [FdG+16; AAH16; LMP17; AAH17] and references therein), are commonly based on iterative optimization procedures that generally do not yield a closed-form solution.

3.3.1 Equivalence of (3.25) with the TLS Solution

Thus far, we have seen that the waveform design problem under the minimum worst-case inter-system interference criterion subject to a sensing uncertainty constraint can be cast as a classic minimum-norm problem. Equivalently, we can leverage the TLS framework to tackle the waveform design problem at hand (3.20)–(3.23).

The TLS [GL80; HV91; MH07] is a generalization of the ordinary Least-Squares (LS) problem. While the LS criterion considers only errors in the so-called measurement model, the TLS criterion considers the existence of errors in both the measurement model and the data model. For the sake of clarity, the mathematical formulation of these criteria is given next.

Let us consider the problem of identifying the input $\boldsymbol{x} \in \mathbb{C}^n$ of a linear system modeled through matrix $\boldsymbol{A} \in \mathbb{C}^{m\times n}$, with $m \geq n$, given the system output $\boldsymbol{y} \in \mathbb{C}^m$. In this example, $\boldsymbol{A}$ corresponds to the *data model*, whereas $\boldsymbol{y}$ is the *measurement model*. Assume that the measurement is corrupted by an observation noise $\boldsymbol{e}$, i.e., $\boldsymbol{y} = \widetilde{\boldsymbol{y}} + \boldsymbol{e}$, being $\widetilde{\boldsymbol{y}} = \boldsymbol{A}\boldsymbol{x}$ the noiseless system output. Under these conditions, if the data model $\boldsymbol{A}$ is perfectly known, the LS framework provides a solution to the following constrained optimization problem [HV91]:

$$\min_{\widehat{\boldsymbol{y}}\in\mathbb{C}^m} \quad \|\boldsymbol{y} - \widehat{\boldsymbol{y}}\|_2 \tag{3.30}$$

$$\text{subject to} \quad \widehat{\boldsymbol{y}} \in \langle \boldsymbol{A} \rangle \tag{3.31}$$

Then, the LS estimate of the system input is any $\widehat{\boldsymbol{x}} \in \mathbb{C}^n$ satisfying $\boldsymbol{A}\widehat{\boldsymbol{x}} = \widehat{\boldsymbol{y}}$, where $\widehat{\boldsymbol{y}}$ is the *best* estimate in the minimum mean-square error (MMSE) sense of the noiseless output $\widetilde{\boldsymbol{y}}$. This simple example illustrates that the LS criterion provides solutions robust to errors in the measurement model. Nevertheless, the LS solution requires the perfect knowledge of the data model $\boldsymbol{A}$, which may not be realistic. In this sense, the TLS framework generalizes the LS criterion admitting errors in the data model, i.e., $\boldsymbol{A} = \widetilde{\boldsymbol{A}} + \boldsymbol{E}$, where $\widetilde{\boldsymbol{A}}$ is the *true* data model and $\boldsymbol{E}$ models the error in the data model. Therefore, the system equation for the TLS problem is given by $\widetilde{\boldsymbol{y}} + \boldsymbol{e} = (\widetilde{\boldsymbol{A}} + \boldsymbol{E})\boldsymbol{x}$. Under these new conditions, the TLS criterion solves

the constrained optimization problem given by [HV91]

$$\min_{\left[\begin{array}{c:c}\widehat{\boldsymbol{A}} & \widehat{\boldsymbol{y}}\end{array}\right]\in\mathbb{C}^{m\times(n+1)}} \left\|\left[\begin{array}{c:c}\boldsymbol{A} & \boldsymbol{y}\end{array}\right]-\left[\begin{array}{c:c}\widehat{\boldsymbol{A}} & \widehat{\boldsymbol{y}}\end{array}\right]\right\|_{\mathrm{F}} \tag{3.32}$$

$$\text{subject to} \qquad \widehat{\boldsymbol{y}}\in\left\langle\widehat{\boldsymbol{A}}\right\rangle \tag{3.33}$$

where the TLS estimate of the system input $\widehat{\boldsymbol{x}}\in\mathbb{C}^n$ satisfies $\widehat{\boldsymbol{A}}\widehat{\boldsymbol{x}}=\widehat{\boldsymbol{y}}$, where $\widehat{\boldsymbol{A}}$ and $\widehat{\boldsymbol{y}}$ are the best approximations in the Frobenius norm sense of the data model and the measurement model, respectively. It is clear that the TLS solution is more general and robust than the LS solution. This is the reason why the TLS framework has been of relevant interest in several engineering disciplines[4], such as system identification [MWVH+05], adaptive filtering [FZCZ04], or spectral analysis [RY87]. The formulation given in (3.32)–(3.33) is known as *basic* TLS formulation. In some cases, the TLS problem lacks a unique solution; thus, the minimum-norm solution is preferable for stability and minimum sensitivity reasons.

In addition to the robustness to modeling errors, the TLS solution exhibits uniqueness in the vector space it lies in. These two properties are of paramount importance in the context of feedforward opportunistic communications. On the one hand, since the modeling errors refer to sensing errors, the MNTLS waveforms in (3.25) are robust to the worst-case induced inter-system interference. On the other hand, since the waveforms (3.25) are unique within the sensed null-space, the MNTLS waveforms are somehow self-calibrated, being independent of the considered sensed null-space basis. As we will discuss in Section 3.4, this property is fundamental to enabling coherent detection[5] under feedforward conditions.

Once the interest in leveraging the TLS framework has been motivated, the waveform design problem in (3.20)–(3.23) is formulated in the sequel using the TLS framework to corroborate that the derived MNTLS waveforms (3.25) are equivalent to the TLS solutions of the problem.

Recalling (3.7), it is worth noting that all null-space waveforms satisfy

$$\widehat{\boldsymbol{U}}_{\mathcal{S}}^{H}\boldsymbol{\phi}_k=\mathbf{0}_{(N-M)\times 1}, \tag{3.34}$$

where $\widehat{\boldsymbol{U}}_{\mathcal{S}}$ is the sensed signal-subspace basis, i.e., span the DoF sensed as occupied, with $\operatorname{rank}\left[\widehat{\boldsymbol{U}}_{\mathcal{S}}\right]=N-M$. Equivalently, we can formulate the following problem:

$$\widehat{\boldsymbol{P}}_{\mathcal{S}}\boldsymbol{\phi}_k=\mathbf{0}_{N\times 1}, \tag{3.35}$$

where $\widehat{\boldsymbol{P}}_{\mathcal{S}}=\widehat{\boldsymbol{U}}_{\mathcal{S}}\widehat{\boldsymbol{U}}_{\mathcal{S}}^{H}$ plays the role of the *assumed* data model in the TLS framework. It is worth noting that, even though it seems that the waveform $\boldsymbol{\phi}_k$ is not inducing interferences, the model is in fact erroneous since

$$\widehat{\boldsymbol{P}}_{\mathcal{S}}=\boldsymbol{P}_{\mathcal{S}}-\widehat{\boldsymbol{P}}_{\mathcal{E}}, \tag{3.36}$$

where $\boldsymbol{P}_{\mathcal{S}}$ is the projector onto the *true* (error-free) signal subspace and $\widehat{\boldsymbol{P}}_{\mathcal{E}}=\boldsymbol{E}_{\mathcal{N}}\boldsymbol{E}_{\mathcal{N}}^{H}$ is the projector onto the subspace spanned by the occupied DoF erroneously sensed as available. In the TLS framework, $\boldsymbol{P}_{\mathcal{S}}$ refers to the *true* data model, whereas $\widehat{\boldsymbol{P}}_{\mathcal{E}}$ corresponds to the error in the data model. Accordingly, the complete signal model for the problem at hand is given by

$$\widehat{\boldsymbol{P}}_{\mathcal{S}}\boldsymbol{\phi}_k=\left(\boldsymbol{P}_{\mathcal{S}}-\widehat{\boldsymbol{P}}_{\mathcal{E}}\right)\boldsymbol{\phi}_k=\boldsymbol{\varepsilon}_k-\boldsymbol{\varepsilon}_k=\mathbf{0}_{N\times 1}, \tag{3.37}$$

[4] A complete bibliographical survey of TLS method and its variants can be found in [Mar10].

[5] Herein, the coherent condition refers to the a priori knowledge of the transmitted shaping waveform by the receiving end.

where $\mathbf{0}_{N\times 1}$ plays the role of the corrupted measurement, $\boldsymbol{\varepsilon}_k$ is the *error-free* measurement, and $-\boldsymbol{\varepsilon}_k$ corresponds to the measurement error. Note that equation (3.37) is naive and purely instrumental to identify the meaningful variables in the TLS framework.

For simplicity, in the sequel, we focus the discussion on the case $k = 0$ since the other $K - 1$ waveforms can be obtained by imposing an orthogonality constraint between waveforms.

Recalling (3.32), the objective is to minimize the impact of all modeling errors, which, in the problem at hand, implies minimizing the induced inter-system interferences. Thus, the waveform design problem can be cast as

$$\min_{\boldsymbol{\phi}_0,\boldsymbol{\varepsilon}_0,\widehat{\boldsymbol{P}}_{\mathcal{E}}} \quad \left\| \left[\begin{array}{c:c} \boldsymbol{\varepsilon}_0 & \widehat{\boldsymbol{P}}_{\mathcal{E}} \end{array} \right] \right\|_{\mathrm{F}}^2 \tag{3.38}$$

$$\text{subject to} \quad \widehat{\boldsymbol{P}}_{\mathcal{S}}\boldsymbol{\phi}_0 = \mathbf{0}_{N\times 1} \tag{3.39}$$

$$\boldsymbol{\phi}_0^H\boldsymbol{\phi}_0 = 1 \tag{3.40}$$

$$\operatorname{rank}\left[\widehat{\boldsymbol{P}}_{\mathcal{E}}\right] = \|\widehat{\boldsymbol{P}}_{\mathcal{E}}\|_{\mathrm{F}}^2 \leq \xi^2,\ \xi^2 > 0 \tag{3.41}$$

i.e., the minimization of the Frobenius norm of the *extended* error matrix or perturbation matrix subject to the data model in (3.37). Two additional constraints have been added. (3.40) is a non-trivial design constraint, whereas (3.41) upper-bounds the maximum degree of assumed uncertainty in the data model error.

Operating the cost function, note that

$$\left\| \left[\begin{array}{c:c} \boldsymbol{\varepsilon}_0 & \widehat{\boldsymbol{P}}_{\mathcal{E}} \end{array} \right] \right\|_{\mathrm{F}}^2 = \|\boldsymbol{\varepsilon}_0\|_2^2 + \left\|\widehat{\boldsymbol{P}}_{\mathcal{E}}\right\|_{\mathrm{F}}^2 \leq \|\boldsymbol{\varepsilon}_0\|_2^2 + \xi^2, \tag{3.42}$$

where the last inequality follows from the constraint (3.41). Therefore, $\forall \xi^2 > 0$ and assuming worst-case sensing uncertainties, we have that the problem at hand reads as

$$\min_{\boldsymbol{\phi}_0,\boldsymbol{\varepsilon}_0,\widehat{\boldsymbol{P}}_{\mathcal{E}}} \quad \|\boldsymbol{\varepsilon}_0\|_2^2 + \xi^2 \tag{3.43}$$

$$\text{subject to} \quad \widehat{\boldsymbol{P}}_{\mathcal{S}}\boldsymbol{\phi}_0 = \mathbf{0}_{N\times 1} \tag{3.44}$$

$$\boldsymbol{\phi}_0^H\boldsymbol{\phi}_0 = 1 \tag{3.45}$$

It is worth noting that this problem leads to a very particular formulation of the classic TLS for the following reasons:

(i) Since the *assumed* data matrix is $\widehat{\boldsymbol{P}}_{\mathcal{S}}$ and the *corrupted* observation vector is $\mathbf{0}_{N\times 1}$, the rank of the *extended* data matrix $\left[\begin{array}{c:c} \widehat{\boldsymbol{P}}_{\mathcal{S}} & \mathbf{0}_{N\times 1} \end{array} \right]$ is equal to the rank of the known data matrix. Therefore, $\widehat{\boldsymbol{P}}_{\mathcal{S}}$ is itself a low-rank approximation of the extended data matrix, meaning that $\widehat{\boldsymbol{P}}_{\mathcal{S}}\boldsymbol{\phi}_0 = \mathbf{0}_{N\times 1}$ is an underdetermined consistent system.

(ii) The data-model measurement noise matrix or perturbation matrix $\widehat{\boldsymbol{P}}_{\mathcal{E}}$ has to be a rank-N_E idempotent matrix corresponding to the orthogonal projector onto $\langle \boldsymbol{E}_{\mathcal{N}} \rangle$. Accordingly, the optimization problem in (3.43)–(3.45) requires an additional constraint on the structure of $\widehat{\boldsymbol{P}}_{\mathcal{E}}$ to ensure that the minimizing $\widehat{\boldsymbol{P}}_{\mathcal{E}}$ is an orthogonal projector; otherwise, the problem may be inconsistent. Nevertheless, constraining the structure of the perturbation matrix may yield an unsolvable optimization problem.

Alternatively, the TLS solution can be understood as an orthogonal L_2 approximation or regression. As per [HV91, Definition 2.5], the TLS problem admits the following interpretation:

$$\min_{\boldsymbol{y}\in\mathbb{C}^{N+1}} \quad \|\boldsymbol{T}\boldsymbol{y}\|_2^2 \tag{3.46}$$

$$\text{subject to} \quad \boldsymbol{y}^H\boldsymbol{y} = 1 \tag{3.47}$$

with $\boldsymbol{T} = \left[\begin{array}{c:c} \widehat{\boldsymbol{P}}_{\mathcal{S}} & \mathbf{0}_{N\times 1} \end{array}\right]$ and $\boldsymbol{y} = \left[\begin{array}{c:c} \boldsymbol{\phi}_0^T & -1 \end{array}\right]^T$. Note that the constraint in (3.47) is needed to avoid the trivial solution. Further analyzing the cost function in (3.46) for our particular case, we see that

$$\|\boldsymbol{T}\boldsymbol{y}\|_2^2 = \boldsymbol{\phi}_0^H\widehat{\boldsymbol{P}}_{\mathcal{S}}\boldsymbol{\phi}_0, \tag{3.48}$$

which follows from recalling that $\widehat{\boldsymbol{P}}_{\mathcal{S}}$ is Hermitian and idempotent. Therefore, by the Lagrange multipliers method and conventional eigenanalysis, it is clear that $\boldsymbol{\phi}_0$ is the eigenvector of $\widehat{\boldsymbol{P}}_{\mathcal{S}}$ associated with the smallest eigenvalue. Since $\widehat{\boldsymbol{P}}_{\mathcal{S}}$ is an orthogonal projector, we have that

$$\widehat{\boldsymbol{P}}_{\mathcal{S}} = \left[\begin{array}{c:c} \widehat{\boldsymbol{U}}_1 & \widehat{\boldsymbol{U}}_2 \end{array}\right] \left[\begin{array}{cc} \boldsymbol{I}_P & \mathbf{0}_{P\times M} \\ \mathbf{0}_{M\times P} & \mathbf{0}_{M\times M} \end{array}\right] \left[\begin{array}{c} \widehat{\boldsymbol{U}}_1^H \\ \hdashline \widehat{\boldsymbol{U}}_2^H \end{array}\right], \tag{3.49}$$

where $P = \operatorname{rank}\left[\widehat{\boldsymbol{P}}_{\mathcal{S}}\right]$ and $M = N - P$. It is worth noting that, back in the problem at hand, $\widehat{\boldsymbol{U}}_1 \in \mathbb{C}^{N\times P}$ is a unitary basis of the sensed signal subspace, and $\widehat{\boldsymbol{U}}_2 \in \mathbb{C}^{N\times M}$ is a unitary basis of the sensed null space. Since the smallest eigenvalue has multiplicity M, this problem admits an infinite number of solutions different from the trivial solution. For reasons of stability and minimum sensitivity, it is convenient to select the solution with minimum norm [HV91; DD91; VHZ93; MH07]. In particular, letting $\boldsymbol{\phi}_0 = \widehat{\boldsymbol{U}}_2\boldsymbol{\lambda}_0$, the waveform design problem can be addressed as follows [HV91, Chapter 3]:

$$\min_{\boldsymbol{\lambda}_0\in\mathbb{C}^N} \quad \left\|\widehat{\boldsymbol{U}}_2\boldsymbol{\lambda}_0\right\|_2^2 \tag{3.50}$$

$$\text{subject to} \quad \boldsymbol{e}_n^T\widehat{\boldsymbol{U}}_2\boldsymbol{\lambda}_0 = 1 \tag{3.51}$$

with $\boldsymbol{e}_n \triangleq \left[\mathbf{0}_{n-1}^T\ 1\ \mathbf{0}_{N-n}^T\right]^T$. Following again the Lagrange multipliers method, the MNTLS waveform $\boldsymbol{\phi}_0^{\text{tls}} = \widehat{\boldsymbol{U}}_2\boldsymbol{\lambda}_0^{\text{tls}}$ leads to

$$\boldsymbol{\phi}_0^{\text{tls}} = \frac{\widehat{\boldsymbol{U}}_2\widehat{\boldsymbol{U}}_2^H\boldsymbol{e}_n}{\boldsymbol{e}_n^T\widehat{\boldsymbol{U}}_2\widehat{\boldsymbol{U}}_2^H\boldsymbol{e}_n}, \tag{3.52}$$

where we shall note that $\widehat{\boldsymbol{U}}_2\widehat{\boldsymbol{U}}_2^H$ is the orthogonal projector onto the sensed null space. For convenience, a norm normalization of $\boldsymbol{\phi}_0^{\text{tls}}$ is preferable. This norm normalization can also be achieved by modifying the constraint in (3.51) such that $\boldsymbol{e}_n^T\widehat{\boldsymbol{U}}_2\boldsymbol{\lambda}_0 = \alpha$, where $\alpha \in \mathbb{R}^+$ guarantees the unit norm. Finally, note that, varying the vector $\boldsymbol{e}_n$, there are N different options for the non-trivial design constraint (3.51). Even though the cases $n = 1$ and $n = N$ are typically considered, the position of the non-zero entry can be modified for convenience. In our problem, as discussed earlier, the position of the non-zero entry of $\boldsymbol{e}_n$ can be optimized to minimize the induced inter-system interference.

Taking into account this discussion, we note that the waveforms given in (3.25) coincide with the solutions of the TLS waveform design problem formulated above. This study justifies that the designed waveforms are referred to as MNTLS waveforms. A fundamental consequence

of this equivalence is that the MNTLS waveforms inherently exhibit the properties of the TLS solution: robustness to modeling mismatch and uniqueness within the sensed null space.

Recalling (3.7), all null-space waveforms (including both the classic solution and the MNTLS solution provided in this dissertation) follow the same general model. The fundamental difference between these two approaches lies in the construction of the coefficients vectors $\boldsymbol{\lambda}_k$. In particular, the vector $\boldsymbol{\lambda}_k$ derived in Appendix 3.A must provide the robustness to modeling mismatch and the solution uniqueness.

From (3.25), note that the coefficients vector $\boldsymbol{\lambda}_k$ admits the following expression:

$$\boldsymbol{\lambda}_k = \boldsymbol{M}_k \boldsymbol{e}_n = \underbrace{\underbrace{\widehat{\boldsymbol{U}}_{\mathcal{N}}^H}_{\text{Rotation}} \underbrace{\left(\boldsymbol{I}_N - \sum_{k'=0}^{k-1} \boldsymbol{\phi}_{k'} \boldsymbol{\phi}_{k'}^H \right)}_{\text{Projection}}}_{\boldsymbol{M}_k} \underbrace{\boldsymbol{e}_k}_{\text{Column Selection}}, \quad \text{for } k = 0, \ldots, K-1, \tag{3.53}$$

where the linear predictor vector $\boldsymbol{e}_k$ can be found as in (3.29). In contrast to the classic null-space solution, where the vector $\boldsymbol{\lambda}_k$ is a column selection on the sensed null-space basis $\widehat{\boldsymbol{U}}_{\mathcal{N}}$, the MNTLS approach given in (3.25) provides linear combination coefficients vectors $\boldsymbol{\lambda}_k$ performing a column selection through the vector $\boldsymbol{e}_k$ on a *transformation* of the sensed null-space basis $\widehat{\boldsymbol{U}}_{\mathcal{N}}$. Note that the role of this transformation, represented through matrix $\boldsymbol{M}_k$ in (3.53), is twofold:

(i) The rotation $\widehat{\boldsymbol{U}}_{\mathcal{N}}^H$ makes the projection matrix $\widehat{\boldsymbol{P}}_0 = \widehat{\boldsymbol{U}}_{\mathcal{N}} \widehat{\boldsymbol{U}}_{\mathcal{N}}^H$ onto the sensed null space $\left\langle \widehat{\boldsymbol{U}}_{\mathcal{N}} \right\rangle$ appear. As will be discussed shortly, this projection matrix plays a fundamental role to guarantee the solution's uniqueness within the sensed null space.

(ii) The projection in (3.53) is sequentially reducing the dimensionality of the sensed null space to guarantee the orthogonality between the K MNTLS waveforms.

Regarding (3.53), we shall note that a fundamental similitude between the classic null-space solution given by $\boldsymbol{\lambda}_k = [\boldsymbol{0}_{m(k)-1}^T \; 1 \; \boldsymbol{0}_{M-m(k)}^T]^T$ and the MNTLS approach given in (3.25) can be established: both strategies are based on a column selection. Nevertheless, the matrix involved in the column selection differs, which is the essential difference between these two null-space strategies. In order to highlight the superiority of the MNTLS waveforms over the classic null-space approaches reviewed in Section 2.4.1, different situations are studied next.

First, we consider the ideal scenario with no sensing uncertainties, i.e., the subspace leakage problem is not present. Mathematically, this case corresponds to $\boldsymbol{E}_{\mathcal{N}} = \boldsymbol{0}_{N \times N_E}$. Under these ideal operating conditions, neither the classic solutions nor the MNTLS approach discussed in this thesis induce inter-system interference on the outer-network nodes. Nevertheless, even under these ideal conditions, the MNTLS approach is preferable due to its uniqueness within the sensed null space. Suppose that the sensed null-space basis is obtained from a MOS on the eigenmatrix of the observations' autocorrelation matrix. This eigenmatrix is not unique, with high probability, since the algebraic multiplicity of the associated eigenvalues equals the dimension of the sensed null space. In fact, if $\widehat{\boldsymbol{U}}_{\mathcal{N}}$ is basis of the null space, then $\widehat{\boldsymbol{V}}_{\mathcal{N}} = \widehat{\boldsymbol{U}}_{\mathcal{N}} \boldsymbol{Q}$ is also a basis of the null space, with $\boldsymbol{Q} \in \mathbb{C}^{M \times M}$ is a right-unitary linear transformation matrix (e.g. a rotation within the null space).

Consequently, classic null-space solutions are not unique since they rely on the sensed null-space basis. Nevertheless, it is of paramount importance to note that the MNTLS approach

given in (3.25) does not depend on the sensed null-space basis; it depends on the projector onto the sensed null space, which is a unique representation of the spanned subspace. Thus, even though the same subspace is exploited by classic solutions and the MNTLS approach, the latter exploits the sensed null space more smartly than the former.

It has already been mentioned that the solution's uniqueness enables coherent detection in non-cooperative, i.e., feedforward, scenarios. We would like to point out that the solution's uniqueness is still of interest when the inner nodes cooperate. In distributed opportunistic communications, the transmitting shaping filters and the receiving matched filters are locally designed, i.e., the inner transmitter and receiver nodes rely on local observations from the wireless environment. Therefore, the null spaces sensed at each inner node may differ slightly. This aspect is studied in detail in Section 3.4. When the inner nodes can cooperate, they can agree on a null space through cooperative feedback. Nevertheless, the solution's uniqueness or invariance permits reducing the required feedback overheads. Suppose the inner nodes find a unique solution within the null space. In that case, subspace agreement can be achieved with low-rate or even null feedback, avoiding agreeing on a common reference system for the signal space. Otherwise, if the necessity of settling on a common reference system arises, the required large feedback overheads may burden implementation complexity and latency.

Thus far, we have seen that even under ideal operating conditions with no sensing uncertainties, the MNTLS waveforms proposed in this thesis outperform classic approaches in terms of detectability. We now consider a more realistic case where subspace leakage occurs, i.e., $\boldsymbol{E}_{\mathcal{N}} \neq \mathbf{0}_{N\times N_E}$. Under these conditions, the classic null-space solution may provide severe inter-system interferences when the DoF encompassed in the unknown sensing error matrix$\boldsymbol{E}_{\mathcal{N}}$ are selected. The MNTLS waveforms given in (3.25) respond to the minimum worst-case inter-system interference criterion described in detail in (3.20). As per (3.53), the optimum solution consists in combining all the dimensions in $\widehat{\boldsymbol{U}}_{\mathcal{N}}$, resorting to the *dimension spreading* principle.

The reader may wonder if the DoF or dimension spreading approach, which is the optimum solution for minimum worst-case interference, exploits the sensed null space efficiently. Since the classic null-space solution performs a column selection on the sensed null-space basis, it exploits one DoF per opportunistic waveform. Conversely, the MNTLS waveforms require an intelligent combination of all columns of the sensed null-space basis. Nevertheless, we shall remark that the waveforms are still rank-one. Each MNTLS waveform exploits one DoF but first performs a change of basis that guarantees the solution's uniqueness.

In conclusion, the superiority of the MNTLS waveforms lies in the fundamental properties inherent in the TLS solution: robustness to modeling mismatch and solution's uniqueness. While the former highlights the optimality in terms of minimum worst-case induced inter-system interference, the latter enables coherent waveform detection in feedforward scenarios. From this point onwards, the waveforms satisfying the uniqueness property are referred to as *invariant* waveforms. The importance of the invariance property in the detectability performance of the MNTLS waveforms is studied in Section 3.4.

3.3.2 Analysis of the Signal-to-Interference Ratio (SIR)

The MNTLS waveforms derived in this thesis and given in (3.25) are optimal in terms of minimum worst-case inter-system interference. Consequently, the waveform design problem

can also be interpreted as maximizing the worst-case Signal-to-Interference Ratio (SIR) at the inner transmitter output, defined as

$$\mathrm{SIR}_{\mathrm{T}} \triangleq \frac{\text{Opportunistic orthogonal component}}{\text{Induced inter-system interferences}}. \tag{3.54}$$

Let S_{T} be the total average transmitted power that accounts for both the opportunistic orthogonal component and the residual induced inter-system interferences and is given by

$$S_{\mathrm{T}} \triangleq \frac{1}{N} \sum_{k=0}^{K-1} \|\boldsymbol{\phi}_k\|^2. \tag{3.55}$$

Then, the $\mathrm{SIR}_{\mathrm{T}}$ defined in (3.54) can be written as

$$\mathrm{SIR}_{\mathrm{T}}\left(\boldsymbol{E}_{\mathcal{N}}; \{\boldsymbol{\lambda}_k\}\right) = \frac{S_{\mathrm{T}} - I_{\mathrm{T}}\left(\boldsymbol{E}_{\mathcal{N}}; \{\boldsymbol{\lambda}_k\}\right)}{I_{\mathrm{T}}\left(\boldsymbol{E}_{\mathcal{N}}; \{\boldsymbol{\lambda}_k\}\right)}, \tag{3.56}$$

where $I_{\mathrm{T}}\left(\boldsymbol{E}_{\mathcal{N}}; \{\boldsymbol{\lambda}_k\}\right)$ is the residual average inter-system interference power defined in (3.12). Since the interference power depends on both the null-space error matrix $\boldsymbol{E}_{\mathcal{N}}$ and the linear combination coefficients that define the opportunistic waveforms $\boldsymbol{\lambda}_k$, it is clear that the $\mathrm{SIR}_{\mathrm{T}}$ also depends on these parameters.

Taking into account the discussion above, the waveform design problem formulated in (3.20)–(3.23) is equivalent to

$$\{\boldsymbol{\lambda}_k\}_{0\leq k\leq K-1} = \arg\max_{\{\boldsymbol{\lambda}_k\}} \min_{\boldsymbol{E}_{\mathcal{N}}} \mathrm{SIR}_{\mathrm{T}}\left(\boldsymbol{E}_{\mathcal{N}}; \{\boldsymbol{\lambda}_k\}\right), \tag{3.57}$$

subject to the constraints (3.21), (3.22), and (3.23). To corroborate this equivalence, we can find first the null-space error matrix $\boldsymbol{E}_{\mathcal{N}}$ providing the worst-case SIR in (3.56). Thus,

$$\boldsymbol{E}_{\mathcal{N}} = \arg\min_{\boldsymbol{E}_{\mathcal{N}}} \frac{\displaystyle\sum_{k=0}^{K-1} \|\boldsymbol{\phi}_k\|_2^2}{\displaystyle\sum_{k=0}^{K-1} \left\|\boldsymbol{E}_{\mathcal{N}}^H \boldsymbol{\phi}_k\right\|_2^2} \tag{3.58}$$

$$\text{s.t.} \quad \|\boldsymbol{E}_{\mathcal{N}}\|_{\mathrm{F}}^2 \leq \xi^2 \tag{3.59}$$

Note that the cost function $\mathrm{SIR}_{\mathrm{T}}\left(\boldsymbol{E}_{\mathcal{N}}; \{\boldsymbol{\lambda}_k\}\right) + 1$ has been considered in (3.58) for the sake of simplicity. Using the Cauchy-Schwarz inequality in the cost function (3.58), we have that

$$\frac{\displaystyle\sum_{k=0}^{K-1} \|\boldsymbol{\phi}_k\|_2^2}{\displaystyle\sum_{k=0}^{K-1} \left\|\boldsymbol{E}_{\mathcal{N}}^H \boldsymbol{\phi}_k\right\|_2^2} = \frac{\|\boldsymbol{\Phi}\|_{\mathrm{F}}^2}{\left\|\boldsymbol{E}_{\mathcal{N}}^H \boldsymbol{\Phi}\right\|_{\mathrm{F}}^2} \geq \frac{1}{\|\boldsymbol{E}_{\mathcal{N}}\|_{\mathrm{F}}^2} \geq \frac{1}{\xi^2}, \tag{3.60}$$

where the last inequality follows from the constraint (3.59). Since we are seeking the null-space error matrix $\boldsymbol{E}_{\mathcal{N}}$ that minimizes the SIR, we can consider the lower bound in (3.60). This lower bound is achieved when the null-space error matrix $\boldsymbol{E}_{\mathcal{N}}$ is proportional to the shaping transmission matrix $\boldsymbol{\Phi}$. This result coincides with the worst-case sensing error matrix obtained

in the derivation of (3.25) in Appendix 3.A. Using the worst-case sensing error matrix in (3.57), the design of the coefficients vectors $\{\boldsymbol{\lambda}_k\}_{0\leq k\leq K-1}$ reads as

$$\{\boldsymbol{\lambda}_k\}_{0\leq k\leq K-1} = \underset{\{\boldsymbol{\lambda}_k\},\{\boldsymbol{e}_k\}}{\arg\max} \left(\sum_{k=0}^{K-1} \left\|\widehat{\boldsymbol{U}}_{\mathcal{N}}\boldsymbol{\lambda}_k\right\|_2^2\right)^{-1} \tag{3.61}$$

$$\text{s.t.} \quad \boldsymbol{\lambda}_k^H\boldsymbol{\lambda}_{k'} = 0,\ k\neq k' \tag{3.62}$$

$$\boldsymbol{\lambda}_k^H\widehat{\boldsymbol{U}}_{\mathcal{N}}^H\boldsymbol{e}_k = \alpha_k \tag{3.63}$$

It is straightforward to see that (3.61)–(3.63) provides the same solution as (3.20)–(3.23), establishing the equivalence between the two different formulations of the problem at hand.

We shall note that the waveform design based on the transmitting SIR is the best that can be done in feedforward opportunistic communications. In terms of opportunistic transmission rate, the optimum receiver approach consists in maximizing the Signal-to-Interference-plus-Noise Ratio (SINR). However, the latter cannot be considered in feedforward scenarios due to the lack of coordination and cooperation between inner nodes.

The formulation of the waveform design problem as in (3.57) can also be deduced from the optimality in the TLS sense of the opportunistic waveforms $\{\boldsymbol{\phi}_k\}_{0\leq k\leq K-1}$ given in (3.25). As per [Gol73; MH07], it is known that the TLS problem is equivalent to the minimization of the Rayleigh quotient. More specifically, the problem formulated in (3.46)–(3.48) is equivalent to

$$\min_{\boldsymbol{\phi}_k} \frac{\boldsymbol{\phi}_k^H\widehat{\boldsymbol{P}}_{\mathcal{S}}\boldsymbol{\phi}_k}{\boldsymbol{\phi}_k^H\boldsymbol{\phi}_k}, \tag{3.64}$$

for the k-th MNTLS waveform. It is clear that, in this particular formulation, the MNTLS waveform $\boldsymbol{\phi}_k$ yields a Rayleigh quotient equal to 0. However, in order to measure the optimality of $\boldsymbol{\phi}_k$ in terms of interference mitigation, we can evaluate the Rayleigh quotient involving the orthogonal projector onto the *true* signal subspace $\boldsymbol{P}_{\mathcal{S}} = \widehat{\boldsymbol{P}}_{\mathcal{S}} + \widehat{\boldsymbol{P}}_{\mathcal{E}}$, which is given by

$$\rho\left(\widehat{\boldsymbol{P}}_{\mathcal{S}} + \widehat{\boldsymbol{P}}_{\mathcal{E}}; \boldsymbol{\phi}_k\right) \triangleq \frac{\left\|\left(\widehat{\boldsymbol{P}}_{\mathcal{S}} + \widehat{\boldsymbol{P}}_{\mathcal{E}}\right)\boldsymbol{\phi}_k\right\|_2^2}{\|\boldsymbol{\phi}_k\|^2}. \tag{3.65}$$

Recalling that $\boldsymbol{\phi}_k = \widehat{\boldsymbol{U}}_{\mathcal{N}}\boldsymbol{\lambda}_k = \left[\begin{array}{c:c} \widetilde{\boldsymbol{U}}_{\mathcal{N}} & \boldsymbol{E}_{\mathcal{N}} \end{array}\right]\boldsymbol{\lambda}_k$, note that $\|\boldsymbol{\phi}_k\|_2^2 = S_k + I_k(\boldsymbol{E}_{\mathcal{N}})$, where S_k refers to the opportunistic orthogonal component and $I_k(\boldsymbol{E}_{\mathcal{N}})$ is the interference leaked on the DoF encompassed in $\boldsymbol{E}_{\mathcal{N}}$. Thus,

$$\rho\left(\widehat{\boldsymbol{P}}_{\mathcal{S}} + \widehat{\boldsymbol{P}}_{\mathcal{E}}; \boldsymbol{\phi}_k\right) = \frac{\left\|\widehat{\boldsymbol{P}}_{\mathcal{E}}\boldsymbol{\phi}_k\right\|_2^2}{S_k + I_k(\boldsymbol{E}_{\mathcal{N}})} = \frac{I_k(\boldsymbol{E}_{\mathcal{N}})}{S_k + I_k(\boldsymbol{E}_{\mathcal{N}})} = \frac{1}{1+\mathrm{SIR}_k\left(\boldsymbol{E}_{\mathcal{N}}\right)}, \tag{3.66}$$

with $\mathrm{SIR}_k\left(\boldsymbol{E}_{\mathcal{N}}\right) = S_k/I_k(\boldsymbol{E}_{\mathcal{N}})$ being the SIR, measured at the transmitter output, induced by the MNTLS waveform $\boldsymbol{\phi}_k$. Since the MNTLS waveforms in (3.25) are optimum in the TLS sense, and the TLS solution minimizes the Rayleigh quotient in (3.66), then, necessarily, these waveforms maximize the attainable worst-case SIR. It is worth noting that (3.66) is just another approach that vindicates the optimality of the MNTLS waveforms in the transmitted SIR sense.

At this point, and knowing that the MNTLS waveforms provide maximum worst-case transmitted SIR, it is natural to wonder what is the operating SIR. We shall remark that the

operating SIR is unknown to the inner transmitter since it depends on the unknown null-space error matrix $\boldsymbol{E}_{\mathcal{N}}$. Nonetheless, the characterization of this parameter is still of interest to assess the performance of the MNTLS waveforms in terms of undesired residual inter-system interferences.

The accurate analysis shown in Appendix 3.B unveils that the operating transmitted SIR admits the following expression:

$$\mathrm{SIR}_{\mathrm{T}}\left(\boldsymbol{E}_{\mathcal{N}};\{\boldsymbol{\lambda}_k\}\right)=\frac{K}{\sum\limits_{k=0}^{K-1}\dfrac{f_k\left(\widehat{\boldsymbol{P}}_{\mathcal{E}}\right)}{\boldsymbol{e}_k^T\widehat{\boldsymbol{P}}_k\boldsymbol{e}_k}}-1, \tag{3.67}$$

where $f_k\left(\widehat{\boldsymbol{P}}_{\mathcal{E}}\right)$ is a positive function of the orthogonal projector onto the subspace spanned by the null-space error matrix, i.e. $\widehat{\boldsymbol{P}}_{\mathcal{E}}=\boldsymbol{E}_{\mathcal{N}}\boldsymbol{E}_{\mathcal{N}}^H$. This function, which is defined in Appendix 3.B, sequentially changes in order to incorporate the dimensionality reduction of the sensed null space implicit in the waveform design scheme described in Algorithm 1.

What it is interesting to note is that the maximum attainable SIR is achieved when the waveform is the column of $\widehat{\boldsymbol{P}}_k$, appropriately scaled, containing its largest diagonal element. This observation reveals that, under worst-case sensing uncertainties, the waveform design procedure detailed in Algorithm 1 is the best solution in terms of interference mitigation. Likewise, as per (3.67), if the dynamic margin of the main diagonal of the projector $\widehat{\boldsymbol{P}}_k$ is sufficiently small, the SIR will not change significantly regardless of the chosen column of $\widehat{\boldsymbol{P}}_k$. Therefore, it could be interesting to reduce the complexity of the waveform design scheme by adopting the criterion in (3.27).

Recalling the definition of the residual inter-system interference power $I_{\mathrm{T}}\left(\boldsymbol{E}_{\mathcal{N}};\{\boldsymbol{\lambda}_k\}\right)$ given in (3.12), it is worth noting that (3.67) is a pessimistic metric since it incorporates the aggregate interference leaked on all DoF encompassed in $\boldsymbol{E}_{\mathcal{N}}$. It would be interesting to propose a metric quantifying the feasibility of the coexistence of the inner and outer networks. In this sense, the performance of the opportunistic transmission can be more appropriately assessed by measuring the ratio between the opportunistic orthogonal signal power and the interference power induced on a single erroneous DoF. The interest of this metric is that it is more appropriate for measuring the compatibility of the outer and inner networks in terms of the coexistence of simultaneous transmissions, similar to the transmission capacity [WYAV05; WAJ10].

Accordingly, we consider a performance metric referred to as Signal-to-Interference Density Ratio (SIDR), measured at the inner transmitter output, and defined as

$$\mathrm{SIDR}_{\mathrm{T}}\left(\boldsymbol{E}_{\mathcal{N}};\{\boldsymbol{\lambda}_k\}\right)\triangleq\frac{S_{\mathrm{T}}-I_{\mathrm{T}}\left(\boldsymbol{E}_{\mathcal{N}};\{\boldsymbol{\lambda}_k\}\right)}{\frac{1}{N_E}I_{\mathrm{T}}\left(\boldsymbol{E}_{\mathcal{N}};\{\boldsymbol{\lambda}_k\}\right)}, \tag{3.68}$$

where S_{T} and $I_{\mathrm{T}}\left(\boldsymbol{E}_{\mathcal{N}};\{\boldsymbol{\lambda}_k\}\right)$ are given in (3.55) and (3.12), respectively, and $N_E=\mathrm{rank}\left[\boldsymbol{E}_{\mathcal{N}}\right]$ is the number of erroneously sensed DoF. Even though it is not possible to analytically characterize the SIDR, it is interesting to highlight that (3.68) admits a simple asymptotic approximation in terms of relevant parameters for the inner system: the total number of system DoF N; the *sensed* network availability $\kappa=M/N$, i.e., the fraction of DoF sensed as available; and the inaccuracy of the null-space sensing scheme $\eta=N_E/M$, i.e., the fraction of erroneously sensed DoF with respect to the dimension of the sensed null space. Appendix 3.C advocates that, for large

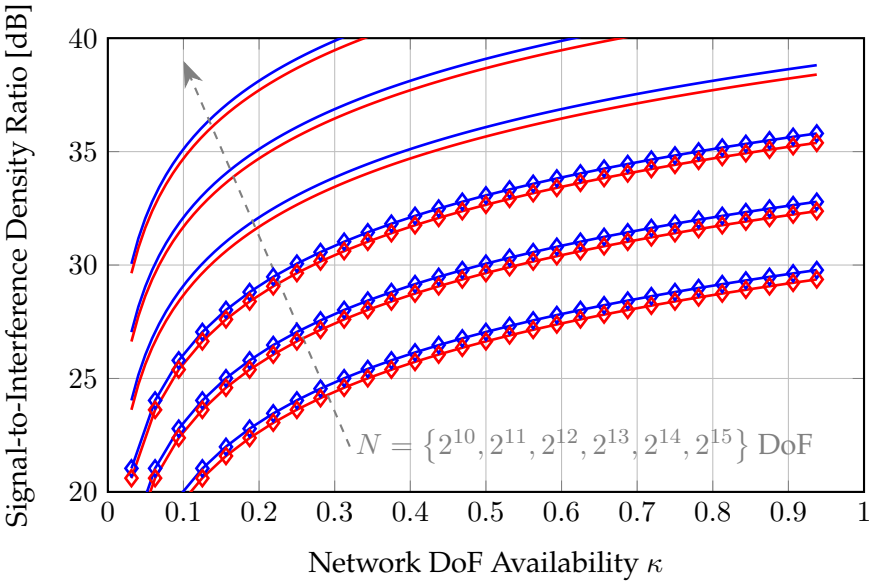

Figure 3.5: Simulated $\mathrm{SIDR}_{\mathrm{T}}$ (3.68) (marks) and the theoretical model in (3.69) (lines) vs. the fraction of DoF sensed as available κ, for different N and with $\eta = 0.01$ (blue) and $\eta = 0.1$ (red).

enough N, (3.68) can be asymptotically approximated by

$$\mathrm{SIDR}_{\mathrm{T}}\left(\boldsymbol{E}_{\mathcal{N}}; \{\boldsymbol{\lambda}_k\}\right) \approx N \cdot \kappa \cdot (1 - \eta)\,. \tag{3.69}$$

This compact and straightforward expression reveals that the opportunistic transmission performance in terms of coexistence compatibility when the MNTLS waveforms are used does not asymptotically depend on the number of transmitted waveforms K. The latter holds whether the opportunistic waveforms are normalized such that $\|\boldsymbol{\phi}_k\| = 1$.

In order to numerically assess the robustness of the MNTLS waveforms to inter-system interferences and validate the tightness of the asymptotic approximation proposed in (3.69), Figures 3.5 and 3.6 are provided. More specifically, we depict in Figure 3.5 the SIDR at the inner transmitter output as a function of the sensed network availability κ, for different numbers of system DoF N and sensing inaccuracies of $\eta = 10^{-2}$ and $\eta = 10^{-1}$. Regarding the number of system DoF, a range of values between 2^{10} and 2^{15} is considered[6]. From Figure 3.5, we shall note that the asymptotic approximation proposed in (3.69) accurately models the attainable SIDR. It is also interesting to observe that the null-space sensing uncertainties are especially critical at low κ. Nevertheless, as the dimension of the sensed null space grows, more dimensions are involved in the opportunistic transmission, and hence the interference density per erroneously sensed DoF diminishes. In any case, the MNTLS waveforms manifest magnificent performance when the system bandwidth –and, therefore, the total system DoF N– is sufficiently large. The impact of the null-space sensing accuracy is depicted in Figure 3.6. In this case, only the theoretical model proposed in (3.69) is illustrated since the tightness of this model has already

[6]Recall that the number DoF is approximately given by WT, where W is the bandwidth, and T is the channel use duration. Because of the demanding user requirements in current and future communication scenarios and the solutions' trend, we can assume a large W. Even though the symbol duration T is permanently reduced to enable low-latency communications, the total number of *system* DoF is large. For instance, assuming a system bandwidth of 100 MHz and a symbol duration of 50 μs, the number of DoF is approximately 5000.

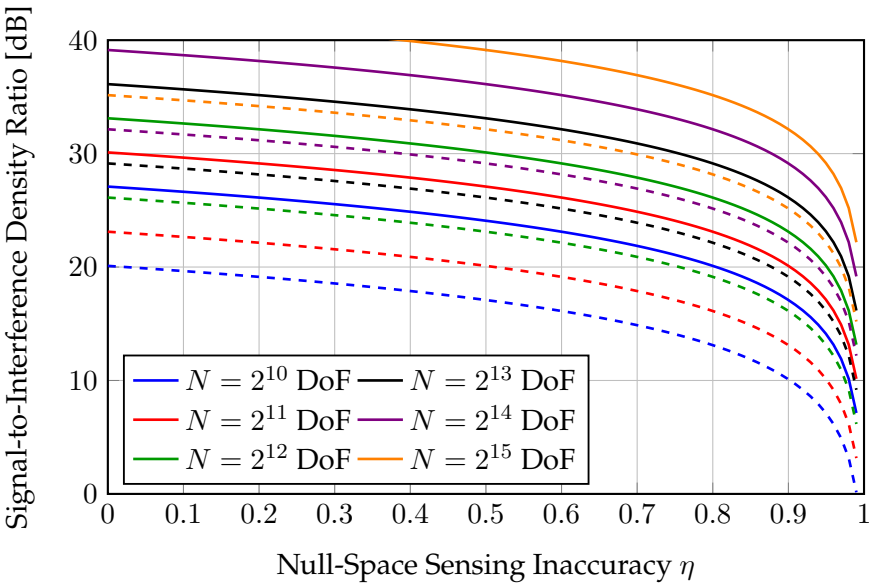

Figure 3.6: Theoretical model for the $\mathrm{SIDR}_{\mathrm{T}}$ (3.69) as a function the inaccuracy of the null-space inference η, for different N and with $\kappa = 0.1$ (dashed) and $\kappa = 0.5$ (solid).

been validated in Figure 3.5. We may notice that the SIDR experiences a slight decrease for increasing η. However, poor performances only occur when the value of the sensing accuracy η becomes unrealistically large. This critical remark reveals the robustness of the derived waveforms in (3.25) to induced inter-system interferences. This aspect will be discussed in detail shortly.

Examining Figures 3.5 and 3.6, we may wonder if the values of the attainable SIDR are pessimistic, especially in congested scenarios, i.e., low κ, and the total number of DoF N is not sufficiently large. Recalling the definition of the inter-system interference given in (3.12), since it does not account for the impact of fading, we note that the SIDR as defined in (3.68) is a pessimistic metric. Therefore, if the path losses are considered, the impact of the undesired inter-system interferences diminishes as the distance between the inner transmitter and the outer-network nodes increases. We may think that the effects of these induced interferences might only be critical at the nearest outer-network nodes. Nevertheless, before drawing premature conclusions, it is essential to think carefully about how null-space sensing works.

Recall that the inner transmitter acquires a set of observations from the wireless environment, given in (3.3). The smaller the distance between the inner transmitter and the outer-network nodes, the higher the SNR of these observations. Consequently, the DoF encompassed in the null-space error matrix $\boldsymbol{E}_{\mathcal{N}}$ correspond, with high probability, to some of the DoF occupied by distant outer-network nodes; it is generally unlikely to erroneously sense as available a DoF occupied by nearby outer-network nodes. In brief, the nearby outer nodes do not typically suffer from induced residual inter-system interferences. In contrast, the interferences caused on distant outer nodes are affected by the path losses that are not considered in the definition of the SIDR. We can now conclude that the SIDR is a demanding and perhaps pessimistic performance metric. Notwithstanding, the SIDR metric in (3.68) does not depend on each particular fading environment; thus, it is general enough to be considered in a wide variety of opportunistic communication scenarios. Moreover, maximizing the worst-case SIR at the inner transmitter

output is the best that can be done under feedforward conditions.

At this point, the robustness of the MNTLS waveforms to the induced inter-system interference remains technically unjustified. It is clear that the derived waveforms in (3.25) exhibit minimum worst-case interference. We have learned from Figure 3.6 that, for fixed and realistic null-space relative sensing errors η, the SIDR significantly improves as the sensed network DoF availability κ increases.

Therefore, we may think that the dimension of the sensed null space M plays an important role in terms of interference mitigation. Recalling the interpretation of $\boldsymbol{\lambda}_k$, for $k = 0, \ldots, K-1$, given in (3.53), we may note that most of the elements of $\boldsymbol{\lambda}_k$ are non-zero. The latter means that $\boldsymbol{\lambda}_k$ combines the M dimensions or DoF sensed as available and encompassed in matrix $\widehat{\boldsymbol{U}}_{\mathcal{N}}$. This linear combination essentially means that the symbol transmitted through the waveform $\boldsymbol{\phi}_k$ is distributed within the sensed null space $\left\langle \widehat{\boldsymbol{U}}_{\mathcal{N}} \right\rangle$. Therefore, the opportunistic transmission scheme based on MNTLS waveforms can be considered as a *dimension spreading* or *DoF spreading* technique, being M the DoF or dimension *spreading factor*. As M increases, the per-DoF energy decreases; thus, the induced residual interference power is maximally spread over the sensed null space minimizing the interference density per DoF.

Regarding the per-DoF energy distribution, the dimension spreading is asymptotically uniform, as advocated in Appendix 3.D. This important property means that, asymptotically, the MNTLS waveforms exhibit a maximally flat spectrum, breaking the structure of the induced inter-system interferences. This property can also be justified as follows. Recalling the adopted non-trivial design constraint in (3.23), we cannot overlook that the MNTLS waveforms in (3.25) are, in fact, linear predictors. Therefore, as already discussed, the zeros of the MNTLS waveforms are asymptotically uniformly distributed in a circle of radius less than or equal to one [Kum83; Pak87].

The DoF or dimension spreading property is of paramount importance to justify the robustness of the MNTLS waveforms (3.25) to the induced inter-system interferences. See next a simple numerical example to illustrate this important property, where the dimension spreading coincides with the spectral distribution for ease of understanding.

Numerical Toy-Example

Let us consider that the unitary inverse Fourier matrix given by

$$\boldsymbol{F}_N^H = \frac{1}{\sqrt{N}} \begin{bmatrix} 1 & 1 & 1 & 1 & \cdots & 1 \\ 1 & \zeta & \zeta^2 & \zeta^3 & \cdots & \zeta^{N-1} \\ 1 & \zeta^2 & \zeta^4 & \zeta^6 & \cdots & \zeta^{2(N-1)} \\ \vdots & \vdots & \vdots & \vdots & \ddots & \vdots \\ 1 & \zeta^{(N-1)} & \zeta^{2(N-1)} & \zeta^{3(N-1)} & \cdots & \zeta^{(N-1)^2} \end{bmatrix}^*, \tag{3.70}$$

where $\zeta = e^{-j2\pi/N}$ is a primitive N-th root of the unity, is an optimum basis for the DoF or signal space dimensions representation. Even though it may seem that this assumption limits the validity of this example, we shall recall that the unitary inverse Fourier matrix is, in fact, the optimum representation in several interesting scenarios. For instance, in those cases where the outer-network nodes operate under Orthogonal Frequency-Division Multiple-Access (OFDMA), which is used in several commercial communication systems, e.g. Wireless Fidelity

(WiFi), Long Term Evolution (LTE), Digital Video Broadcasting-Terrestrial (DVB-T), and New Radio (NR). Nonetheless, the use of unitary Fourier matrices is even more general. When the number of total system DoF $N \approx WT$ is sufficiently large, the autocorrelation's eigenmatrix converges to the N-size unitary Fourier matrix [Gra06]. This case, which is of greatest interest concerning practical implementation, is discussed in detail in Chapter 4.

For this simple example, we assume that the inner transmitter acquires a set of observations from the wireless environment and, using the unitary inverse Fourier matrix in (3.70), decides which frequency bins are available for opportunistic communication. Accordingly, the inner transmitting node finds a basis of the sensed null space as

$$\widehat{\boldsymbol{U}}_{\mathcal{N}} = \boldsymbol{F}_N^H \boldsymbol{S} \in \mathbb{C}^{N \times M}, \tag{3.71}$$

where the $N \times M$ matrix $\boldsymbol{S}$ selects the columns of $\boldsymbol{F}_N^H$ associated with the frequency bins sensed as available, i.e.

$$[\boldsymbol{S}]_{ii} = \begin{cases} 1 & \text{if the } i\text{-th column of } \boldsymbol{F}_N^H \text{ is sensed as available} \\ 0 & \text{otherwise} \end{cases}. \tag{3.72}$$

This descriptive and simple numerical example aims to illustrate the dimension spreading property. Since the sensed null-space basis is a column subset of the unitary inverse Fourier matrix, the DoF can be read as frequency bins or subcarriers. Thus, the dimension spreading property can be studied from the spectral behavior perspective. We assume $N = 32$ DoF, of which 12 are occupied by the active outer-network nodes, corresponding to a DoF occupation of $3/8$. This case is unrealistic, as the total number of system DoF N will be much larger in practice. Nevertheless, as the distribution of the zeros is also numerically analyzed in this example, a small value of N has been chosen to clarify the graphical representation. Moreover, for the sake of simplicity, only the first MNTLS waveform is analyzed in this example.

Two different scenarios are considered, and both are depicted on the next page. On the one hand, Figure 3.7 illustrates the dimension spreading property and zeros distribution in an ideal case without subspace leakage. On the other hand, a simple case with subspace leakage, involving only one occupied DoF erroneously sensed as available, is represented in Figure 3.8.

In both cases, the DoF (in this case, frequency bins) occupied by the outer-network nodes are contained within the spectral mask plotted in dashed lines.

Regarding the ideal case depicted in Figure 3.7, we qualitatively compare the operational difference between the MNTLS waveforms derived in this thesis and the classic null-space solution. For clarity, the total system bandwidth has been normalized between 0 and 1. It is worth noting that, whereas the latter solution fully exploits one DoF of the sensed null-space basis, the former performs a change of basis that combines all DoF represented in the original sensed null-space basis. Apart from keeping the orthogonality between waveforms, this change of basis guarantees the solution's invariance and distributes the transmitted energy among all DoF sensed as available. Since the sensed null-space basis comprises complex exponentials, the dimension spreading is uniform (cf. Appendix 3.D). However, this uniform per-DoF energy distribution can only be guaranteed, in general, when N is sufficiently large.

Observing the Z-plane in Figure 3.7(b), we note that the zeros of the null-space waveform are uniformly distributed on a circle of radius less than one. The latter follows by noting that the

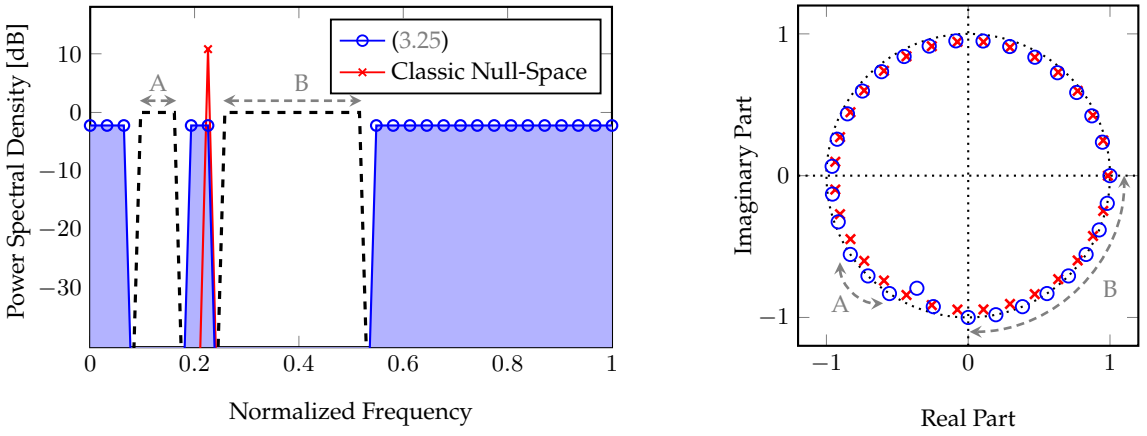

(a) Power Spectral Density (PSD).

(b) Zero distribution.

Figure 3.7: Sketch of the dimension spreading property for the subspace leakage-free case. The PSD of the MNTLS waveforms is represented by the shadowed areas delimited by blue solid lines with circle markers. The zeros corresponding to the classic null-space waveform are depicted with red exes, whereas those corresponding to the MNTLS waveform are illustrated with blue circles.

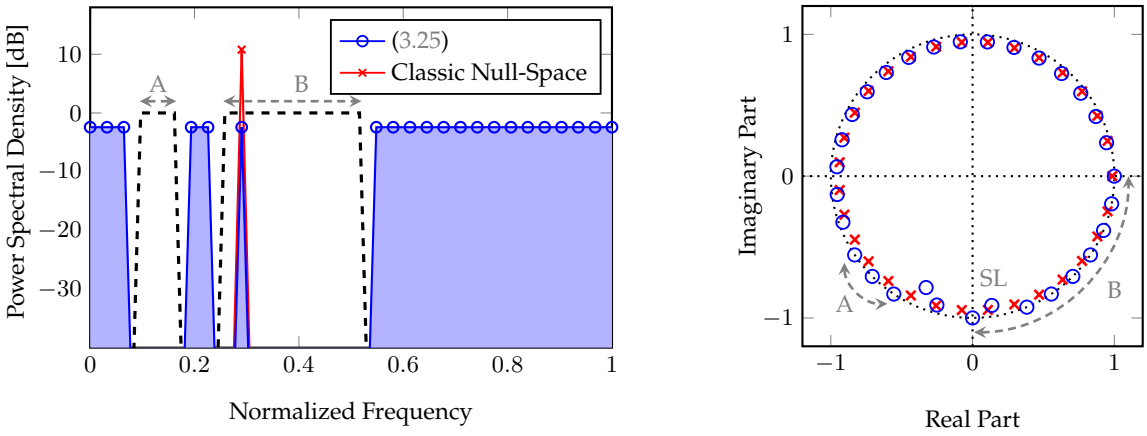

(a) Power Spectral Density (PSD).

(b) Zero distribution.

Figure 3.8: Sketch of the dimension spreading property under the presence of subspace leakage. The outer-system DoF occupation is the same as in Figure 3.7. In this case, however, one occupied frequency bin has been erroneously sensed as available. The zeros corresponding to the classic null-space waveform are depicted with red exes, whereas those corresponding to the MNTLS waveform are illustrated with blue circles. The zero identified with "SL" highlights the impact of subspace leakage on the distribution of the zeros.

classic null-space waveform is, in this case, an orthogonal polynomial with complex-exponential coefficients. Conversely, the MNTLS waveform zeros follow the zeros distribution of a linear predictor filter. The signal-subspace zeros are located on the circle of radius equal to one. In contrast, the so-called *extraneous zeros*, corresponding to the null space, are almost uniformly distributed on a circle of radius less than one. Notwithstanding, this behavior can only be observed when the sensed null-space basis is of the form of (3.70) because then the DoF can be read as frequency bins. In general, when the DoF cannot be interpreted as frequency bins, and taking into account that the MNTLS waveforms are orthogonal polynomials, their zeros will be asymptotically uniformly distributed on a circle of radius less than or equal to one, as discussed in [Pak87].

A simple example of subspace leakage is depicted in Figure 3.8. Note that one DoF occupied by outer-network nodes is sensed as available. For the sake of a fair comparison, we assume that the classic null-space waveform corresponds to the DoF erroneously sensed as available. This illustrative example reveals the interest in dimension spreading to alleviate the impact of induced inter-system interference. The classic null-space solution corrupts the outer-network communication on the DoF erroneously sensed as available, producing a strong interference. Conversely, the MNTLS waveform derived in this thesis *does not put all eggs in one basket* and maximally spreads the transmitted power within the sensed null space; thus, the interference density per erroneously sensed DoF is minimized. The latter is of paramount importance in terms of reducing the outage induced on outer-network nodes.

Carefully looking at the occupied DoF sensed as available, we realize that the power transmitted by the MNTLS waveform is $\mu = 10\log_{10}(M)$ [dB] lower than the spectral peak produced by the classic null-space waveform, where M is the dimension of the sensed null space. In this simple example, since there are 20 actually available DoF, $M = 21$, meaning that the interference produced by the classic null-space is $\mu \approx 13.22$ dB higher. It is worth noting that M plays the role of the *dimension spreading factor* and reflects the superiority of the MNTLS waveform in terms of reducing the undesired inter-system interference.

Finally, the zero distribution depicted in Figure 3.8(b) remains almost unchanged in comparison to Figure 3.7(b), except for the zero involved in the subspace leakage, denoted by "SL", which now becomes an extraneous zero since the associated DoF has been sensed as available.

SIDR Comparison of Classic Null-Space Approach and MNTLS

The previous numerical toy example has unveiled, from a qualitative viewpoint, the importance of the DoF spreading capability that the MNTLS solutions enjoy. A formal comparison in terms of SIDR between the MNTLS waveforms and the classic null-space approach is discussed next.

In Section 2.4.2, the performance of classic null-space strategies have been assessed in terms of SIR. Nevertheless, we must recall that each waveform designed by these classic approaches is directly a column of the sensed null-space basis, meaning that the SIDR exhibited by these classic approaches equals the SIR. Therefore, using the expressions derived in Section 2.4.2, we can compare the performance exhibited by the proposed MNTLS waveforms and the performance exhibited by the classic null-space approaches.

For this purpose, recalling the expression for the average SIR offered by the classic null-space approaches given in (2.45), the average SIDR is proportional to the SIDR of the MNTLS

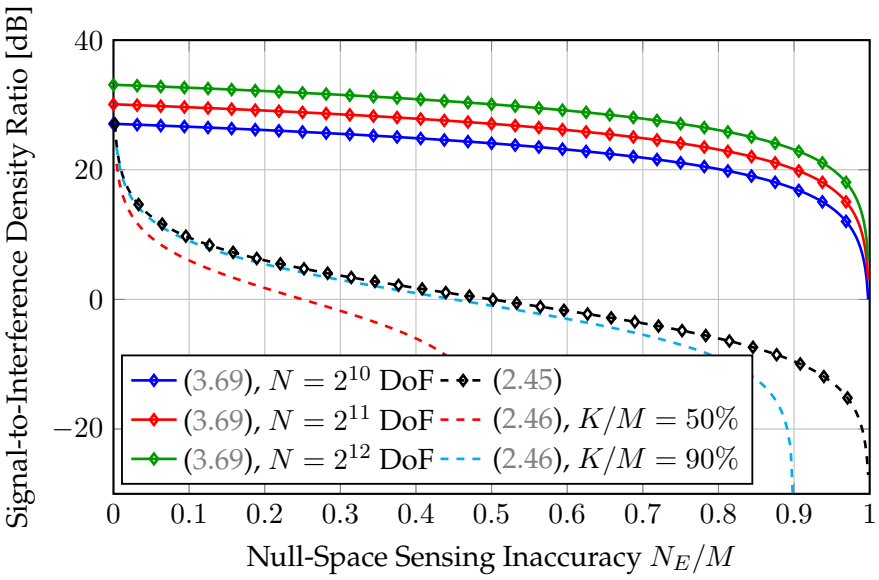

Figure 3.9: $\mathrm{SIDR}_{\mathrm{T,MNTLS}}$ (3.69), $\mathrm{SIDR}_{\mathrm{T,NS}}$ (2.45), and $\mathrm{SIDR}_{\mathrm{T,NS}}^{\text{worst-case}}$ (2.46) as a function of the null-space sensing inaccuracy N_E/M for a network DoF availability of $M/N = 25\%$.

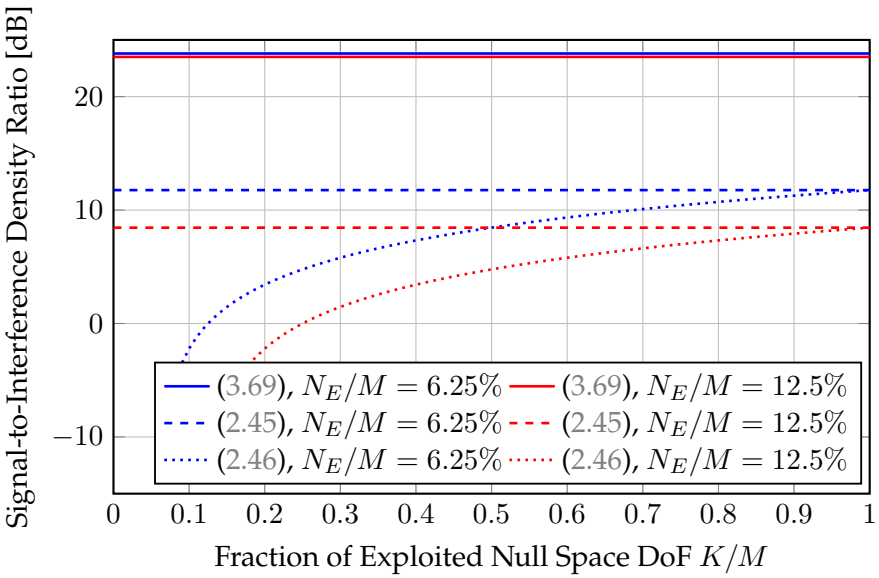

Figure 3.10: $\mathrm{SIDR}_{\mathrm{T,MNTLS}}$ (3.69), $\mathrm{SIDR}_{\mathrm{T,NS}}$ (2.45), and $\mathrm{SIDR}_{\mathrm{T,NS}}^{\text{worst-case}}$ (2.46) for $N = 2^{10}$ total system DoF, network DoF availability of $M/N = 25\%$, and different relative sensing errors N_E/M, as a function of the fraction of exploited null-space DoF K/M.

solutions and satisfies

$$\mathrm{SIDR}_{\mathrm{T,NS}} = \frac{1 - N_E/M}{N_E/M} = \frac{\mathrm{SIDR}_{\mathrm{T,MNTLS}}}{N_E}, \tag{3.73}$$

being $\mathrm{SIDR}_{\mathrm{T,MNTLS}}$ the asymptotic approximation given in (3.69). This relationship reveals that, on average, the SIDR exhibited by the proposed MNTLS is N_E times higher than the classic null-space approaches. This performance gain is due to the DoF spreading property enjoyed by the MNTLS waveforms. In this regard, since the inter-system interference is spread over all the sensed null space, the impact per erroneously sensed as available DoF also decreases. Moreover, comparing (3.69) and (3.73), we note that the SIDR exhibited by the proposed MNTLS grows with the total number of DoF. The latter follows from noting that, under the same network DoF occupancy conditions, increasing the total number of DoF also increases the number of available ones, meaning that the *spreading factor* increases and can improve their interference-mitigation capabilities.

It is interesting to note that the MNTLS waveforms are robust to worst-case null-space sensing errors; thus, the asymptotic approximation of $\mathrm{SIDR}_{\mathrm{T,MNTLS}}$ is a worst case. Accordingly, it can be of interest to include also the worst-case performance of the classic null-space schemes in this comparison. Therefore, recalling (2.46), we note that the SIDR exhibited by the MNTLS solutions and the average SIDR of the classic null-space approaches are related to the worst-case performance of the classic approaches according to

$$0 \leq \mathrm{SIDR}_{\mathrm{T,NS}}^{\text{worst-case}} = \frac{K/M - N_E/M}{N_E/M} \leq \mathrm{SIDR}_{\mathrm{T,NS}} = \frac{1}{N_E}\mathrm{SIDR}_{\mathrm{T,MNTLS}}, \tag{3.74}$$

which is valid for $N_E \leq K \leq M$. In view of (2.46), in contrast to $\mathrm{SIDR}_{\mathrm{MNW}}$, $\mathrm{SIDR}_{\mathrm{NS}}^{\text{worst-case}}$ depends on the fraction of exploited null-space DoF K/M. Again, the factor K/M highlights the lack of robustness to sensing errors exhibited by classic null-space schemes.

In order to illustrate the improvement exhibited by the MNTLS waveforms with respect to the worst-case and average performance offered by classic null-space schemes, a numerical comparison is provided in Figures 3.9 and 3.10. These Figures reveal that, under worst-case conditions, null-space schemes need to saturate the null space to achieve their average SIDR performance and get a little closer to the SIDR performance exhibited by the MNTLS waveforms. Otherwise, the performance gain exhibited by the latter is even more accentuated.

3.4 The Invariance Property and Detectability

Thus far, the discussion on generalized null space-based opportunistic communication has been focused on the shaping transmission matrix $\mathbf{\Phi}$. At this point, it is natural to wonder how the matched-filter receiving matrix can be designed under feedforward conditions. It is noteworthy that, under the lack of coordination and cooperation between inner nodes, it may look like feed-forward opportunistic communications are inherently non-coherent. Nevertheless, accounting for the invariance of the MNTLS waveforms, this section demonstrates that coherent detection is still feasible.

We first assume in Section 3.4.1 that both the inner transmitter and the inner receiver have identified the same null space. Under these ideal operating conditions, the invariance property exhibited by the MNTLS waveforms is self-calibrating the inner nodes, which enables coherent

$\boldsymbol{r}_{\mathrm{T}}$	Positioning coordinates of the inner transmitter
$\boldsymbol{r}_{\mathrm{R}}$	Positioning coordinates of the inner receiver
$\widehat{\boldsymbol{U}}_{\mathcal{N}}(\boldsymbol{r}_{\mathrm{T}}) \in \mathbb{C}^{N \times M_{\mathrm{T}}}$	Null-space basis sensed at the inner transmitter
$\widehat{\boldsymbol{U}}_{\mathcal{N}}(\boldsymbol{r}_{\mathrm{R}}) \in \mathbb{C}^{N \times M_{\mathrm{R}}}$	Null-space basis sensed at the inner receiver
M_{T}	Number of DoF sensed as available at the inner transmitter
M_{R}	Number of DoF sensed as available at the inner receiver
$\widehat{\mathcal{N}}_{\mathrm{T}} = \left\langle \widehat{\boldsymbol{U}}_{\mathcal{N}}(\boldsymbol{r}_{\mathrm{T}}) \right\rangle$	Sensed null space at the inner transmitter
$\widehat{\mathcal{N}}_{\mathrm{R}} = \left\langle \widehat{\boldsymbol{U}}_{\mathcal{N}}(\boldsymbol{r}_{\mathrm{R}}) \right\rangle$	Sensed null space at the inner receiver
$\boldsymbol{\phi}_k \in \mathbb{C}^N$	k-th shaping transmission waveform
$\boldsymbol{\psi}_k \in \mathbb{C}^N$	k-th matched-filter receiving waveform
$\boldsymbol{\Phi} = [\boldsymbol{\phi}_0 \ \cdots \ \boldsymbol{\phi}_{K-1}] \in \mathbb{C}^{N \times K}$	Shaping transmission matrix
$\boldsymbol{\Psi} = [\boldsymbol{\psi}_0 \ \cdots \ \boldsymbol{\psi}_{K-1}] \in \mathbb{C}^{N \times K}$	Matched-filter receiving matrix

Table 3.1: Basic notation used throughout Section 3.4.

waveform detection. Nevertheless, in practice, the inner transmitter may identify as available one or more DoF sensed as occupied by the inner receiver, and vice versa, giving rise to a phenomenon known as *subspace mismatch*. Consequently, opportunistic communication suffers from performance losses that are studied in Section 3.4.2.

Since this section deals with the analysis of the receiving scheme, notation regarding both the inner transmitter and the inner receiver appear. Thus, for the reader's convenience, the basic notation[7] used throughout this section is summarized in Table 3.1.

3.4.1 Generalized Null-Space Matched Filter Detection

Recalling the receiver signal model described in (3.1), note that it can be vectorized as

$$\boldsymbol{y}_l = \sqrt{\frac{S_{\mathrm{R}}}{K}} \sum_{k=0}^{K-1} a_{k[l]} \boldsymbol{\phi}_k^{(l)} + \boldsymbol{i} + \boldsymbol{w} = \sqrt{S_{\mathrm{R}}} \boldsymbol{\Phi}^{(l)} \boldsymbol{a}_l + \boldsymbol{i} + \boldsymbol{w}, \tag{3.75}$$

where l indexes the arbitrary received block, $\boldsymbol{\phi}_k^{(l)} = [\phi_k[0 - lN], \ldots, \phi_k[N - 1 - lN]]^T$ is the vectorization of the shaping transmission waveform at the l-th block; the vectorizations of the interference and the noise is given by $\boldsymbol{i} = [i[0], \ldots, i[N-1]]^T$ and $\boldsymbol{w} = [w[0], \ldots, w[N-1]]^T$, respectively; $\boldsymbol{a}_l = \left[a_{0[l]}, \ldots, a_{(K-1)[l]}\right]^T$ is the transmitted symbol vector; and the shaping trans-

[7] Additional notation will be defined as needed.

mission matrix reads as $\boldsymbol{\Phi}^{(l)} = \left[\boldsymbol{\phi}_0^{(l)} \ \cdots \ \boldsymbol{\phi}_{K-1}^{(l)}\right]$. Without loss of generality, from now on we will drop the block index l, which simplifies the notation.

Accordingly, letting $\boldsymbol{\Psi} = [\boldsymbol{\psi}_0 \ \cdots \ \boldsymbol{\psi}_{K-1}] \, \mathbb{C}^{N\times K}$ be the matched-filter receiving matrix, the sufficient statistic for symbols decoding are given by

$$\boldsymbol{z} = \boldsymbol{\Psi}^H \boldsymbol{y} \in \mathbb{C}^K. \tag{3.76}$$

Therefore, the aim of the inner receiving node consists in locally designing the matched-filter receiving matrix $\boldsymbol{\Psi}$ exhibiting a small Frobenius distance with respect to the shaping transmission matrix $\boldsymbol{\Phi}$, i.e.

$$\|\boldsymbol{\Phi} - \boldsymbol{\Psi}\|_{\mathrm{F}} \tag{3.77}$$

has to be minimum. Note that the condition in (3.77) is a requirement for coherent waveform detection. The problem's difficulty lies in the fact that the inner nodes are not coordinated and do not cooperate. Therefore, the matrix $\boldsymbol{\Psi}$ has to be locally designed using only the sensed null space at the receiver side. It is important to remark that the only information shared between the inner nodes is the number of total system DoF N.

At this point, let us assume that the inner transmitter and the inner receiver have identified the same null space, i.e., $\widehat{\mathcal{N}}_{\mathrm{T}} = \widehat{\mathcal{N}}_{\mathrm{R}}$, implying that $M_{\mathrm{T}} = M_{\mathrm{R}} = M$. Nevertheless, it is worth noting that the sensed null-space bases at each inner node may differ, i.e., $\widehat{\boldsymbol{U}}_{\mathcal{N}}(\boldsymbol{r}_{\mathrm{T}}) \neq \widehat{\boldsymbol{U}}_{\mathcal{N}}(\boldsymbol{r}_{\mathrm{R}})$.

Recalling (3.25), notice that the MNTLS waveforms are obtained by performing a column selection on the projector onto the sensed null space. As previously discussed, this property is of paramount importance since the projectors are unique representations of the spanned subspace. In other words, the projection matrix is always the same irrespective of the considered subspace basis.

Back in the problem at hand, let $\widehat{\boldsymbol{U}}_{\mathcal{N}}(\boldsymbol{r}_{\mathrm{T}}) \in \mathbb{C}^{N\times M}$ and $\widehat{\boldsymbol{U}}_{\mathcal{N}}(\boldsymbol{r}_{\mathrm{R}}) \in \mathbb{C}^{N\times M}$ be the sensed null-space basis at the inner transmitter and receiver. If $\widehat{\mathcal{N}}_{\mathrm{T}} = \widehat{\mathcal{N}}_{\mathrm{R}}$, then there exists a matrix $\boldsymbol{Q} \in \mathbb{C}^{M\times M}$ satisfying $\boldsymbol{Q}\boldsymbol{Q}^H = \boldsymbol{I}_M$ such that $\widehat{\boldsymbol{U}}_{\mathcal{N}}(\boldsymbol{r}_{\mathrm{T}}) = \widehat{\boldsymbol{U}}_{\mathcal{N}}(\boldsymbol{r}_{\mathrm{R}})\boldsymbol{Q}$. Therefore, we shall note that

$$\widehat{\boldsymbol{P}}_0(\boldsymbol{r}_{\mathrm{T}}) = \widehat{\boldsymbol{U}}_{\mathcal{N}}(\boldsymbol{r}_{\mathrm{T}})\widehat{\boldsymbol{U}}_{\mathcal{N}}^H(\boldsymbol{r}_{\mathrm{T}}) = \widehat{\boldsymbol{U}}_{\mathcal{N}}(\boldsymbol{r}_{\mathrm{R}})\boldsymbol{Q}\boldsymbol{Q}^H\widehat{\boldsymbol{U}}_{\mathcal{N}}^H(\boldsymbol{r}_{\mathrm{R}}) = \widehat{\boldsymbol{P}}_0(\boldsymbol{r}_{\mathrm{R}}), \tag{3.78}$$

i.e., even though the sensed null-space basis at the inner transmitter and receiver differ, both nodes share the same orthogonal projector. It is worth noting that, although a sequential dimensionality reduction is performed in Algorithm 1, an orthogonal projector is used at each recursion. Thus, the condition in (3.78) is sequentially satisfied.

A direct consequence of the invariance property described in (3.78) is that the matched filters for the K transmitted waveforms $\{\boldsymbol{\phi}_k\}_{0\leq k\leq K-1}$ satisfy the design condition

$$\boldsymbol{\psi}_k = \widehat{\boldsymbol{U}}_{\mathcal{N}}(\boldsymbol{r}_{\mathrm{R}})\boldsymbol{\lambda}_k(\boldsymbol{r}_{\mathrm{R}}), \ \text{ for } k = 0, \ldots, K-1, \tag{3.79}$$

and can be recursively designed as in Algorithm 1. Therefore, note that $\boldsymbol{\Phi} = \boldsymbol{\Psi}$ under ideal operating conditions, yielding to a Frobenius distance (3.77) equal to zero. The receiving scheme based on MNTLS waveforms is depicted in Figure 3.11, where the "Matched Filter Design" block is implemented using Algorithm 1.

It is noteworthy that the invariance property has two major consequences:

(i) under ideal operating conditions, the opportunistic communication ideally does not suffer from ISI, since $\boldsymbol{\psi}_{k'}^H\boldsymbol{\phi}_k = 0$, for $k \neq k'$, and

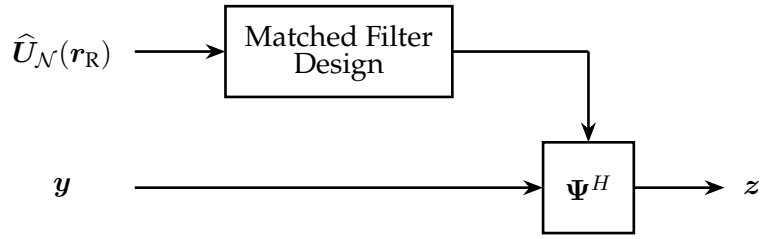

Figure 3.11: *Modus operandi* of the inner receiver in feedforward opportunistic communications.

(ii) the inner receiver obeys a minimum-distance detection criterion, i.e., a minimum squared distance $\|\boldsymbol{\psi}_k - \boldsymbol{\phi}_k\|^2$ is achieved despite the lack of interaction between inner nodes.

These two consequences imply that the inner receiver can reliably detect the transmitted information in feedforward scenarios. As already discussed in Section 3.3.1, the invariance property is a fundamental difference between the MNTLS waveforms given in (3.25) and the classic null-space solution. Recalling that the latter selects columns of the sensed null-space basis as shaping transmission waveforms, it is clear that full end-to-end coordination is necessary to neutralize the effects of the end-to-end sensed null-space bases miscalibration and, thus, guarantee coherent waveform detection. Therefore, the classic null-space scheme is unsuitable for opportunistic communication in feedforward scenarios.

3.4.2 The Problem of Inter-Node Subspace Mismatch

Previously, the design of the matched-filter receiving matrix has been discussed under ideal operating conditions, i.e., when both the inner transmitter and the inner receiver have identified the same null space. In practice, however, the null spaces sensed at each inner node differ, i.e., $\widehat{\mathcal{N}}_{\mathrm{T}} \neq \widehat{\mathcal{N}}_{\mathrm{R}}$. In the sequel, this phenomenon is referred to as *subspace mismatch*.

It is worth noting that the problem of subspace mismatch is inherent in feedforward opportunistic communications since the inner nodes do not cooperate, and the distributed design of pulse-shaping waveforms and matched filters are based only on the locally sensed null space. In this context, the reader may wonder if opportunistic communication is feasible.

In order to provide an accurate answer, let us consider the graphical representation illustrated in Figure 3.12. The blue and red circles represent the sensed null spaces at the inner transmitting and receiving nodes, respectively. As we may observe, the sensed null spaces can be decomposed into two subspaces: the *common* DoF, represented by $\mathcal{N}_0$, and the null-space excess, represented by $\mathcal{D}_{\mathrm{T}}$ at the inner transmitter and by $\mathcal{D}_{\mathrm{R}}$ at the inner receiver. Mathematically, the DoF sensed as available at the same time at the inner transmitter and receiver span the *intersection* of $\widehat{\mathcal{N}}_{\mathrm{T}}$ and $\widehat{\mathcal{N}}_{\mathrm{R}}$, which hereinafter stands for *effective null space*.

Definition 3.2 (Effective Null Space). *Let $\widehat{\mathcal{N}}_T$ and $\widehat{\mathcal{N}}_R$ be the null spaces sensed at the inner transmitting and receiving nodes, being M_T and M_R their dimensions, respectively. The effective null space $\mathcal{N}_0$ is defined as*

$$\mathcal{N}_0 \triangleq \widehat{\mathcal{N}}_T \cap \widehat{\mathcal{N}}_T, \tag{3.80}$$

whose dimension is, in general, $M_0 \leq \min\{M_T, M_R\}$.

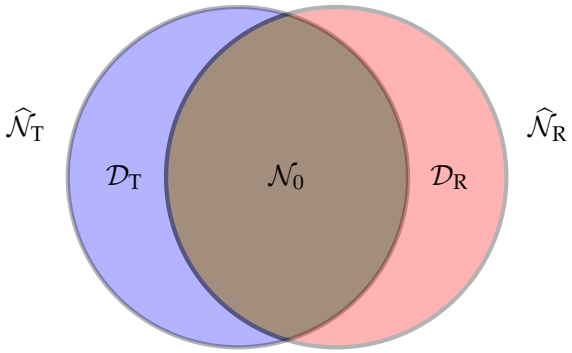

Figure 3.12: Graphical representation of the relation between null spaces sensed at the inner transmitting and receiving nodes. Note that $\widehat{\mathcal{N}}_{\mathrm{T}} = \mathcal{N}_0 \oplus \mathcal{D}_{\mathrm{T}}$ and $\widehat{\mathcal{N}}_{\mathrm{R}} = \mathcal{N}_0 \oplus \mathcal{D}_{\mathrm{R}}$.

Therefore, taking into account Definition 3.2 and Figure 3.12, the sensed null spaces at the inner transmitter and receiver can be decomposed as

$$\widehat{\mathcal{N}}_{\mathrm{T}} = \mathcal{N}_0 \oplus \mathcal{D}_{\mathrm{T}}, \tag{3.81}$$

$$\widehat{\mathcal{N}}_{\mathrm{R}} = \mathcal{N}_0 \oplus \mathcal{D}_{\mathrm{R}}, \tag{3.82}$$

since the null-space excesses $\mathcal{D}_{\mathrm{T}}$ and $\mathcal{D}_{\mathrm{R}}$ satisfy $\mathcal{D}_{\mathrm{T}} \cap \mathcal{D}_{\mathrm{R}} = \emptyset$ and $\mathcal{N}_0 \cap \mathcal{D}_{\mathrm{T}} = \mathcal{N}_0 \cap \mathcal{D}_{\mathrm{R}} = \emptyset$. Therefore, letting $\kappa_{\mathrm{T}} = \dim[\mathcal{D}_{\mathrm{T}}]$ and $\kappa_{\mathrm{R}} = \dim[\mathcal{D}_{\mathrm{R}}]$, note that the number of DoF sensed as available at each inner node is given by

$$M_{\mathrm{T}} = M_0 + \kappa_{\mathrm{T}}, \tag{3.83}$$

$$M_{\mathrm{R}} = M_0 + \kappa_{\mathrm{R}}. \tag{3.84}$$

Taking into account the mathematical model for the subspace mismatch problem discussed above, we can state that (single-hop) feedforward opportunistic communications are feasible if and only if $\mathcal{N}_0 \neq \emptyset$. Otherwise, the inner network suffers from the *hidden node* problem, which can be counteracted through inner relay nodes, which is beyond the scope of this thesis.

A final comment on this mathematical model is of order. Recall Figure 3.1. Assuming that the interference channels are statistically independent, note that the subspace leakage errors at different inner nodes will be highly likely independent. The latter means that the same occupied DoF will not be erroneously sensed as available by the inner transmitter and receiver simultaneously. Therefore, the effective null space $\mathcal{N}_0$ does not contain occupied DoF erroneously sensed as available with high probability. Under these conditions, it seems reasonable to model the inter-node subspace mismatch problem using the same model as for the subspace leakage errors described in (3.8). Nevertheless, for the sake of generality, the subspace mismatch problem is studied through the following model:

$$\widehat{\boldsymbol{U}}_{\mathcal{N}}(\boldsymbol{r}_{\mathrm{T}}) = \left[\begin{array}{c:c} \boldsymbol{U}_{\mathcal{N}_0,\mathrm{T}} & \boldsymbol{\Delta}_{\mathrm{T}} \end{array}\right], \tag{3.85}$$

$$\widehat{\boldsymbol{U}}_{\mathcal{N}}(\boldsymbol{r}_{\mathrm{R}}) = \left[\begin{array}{c:c} \boldsymbol{U}_{\mathcal{N}_0,\mathrm{R}} & \boldsymbol{\Delta}_{\mathrm{R}} \end{array}\right], \tag{3.86}$$

where $\mathcal{N}_0 = \langle \boldsymbol{U}_{\mathcal{N}_0,\mathrm{T}} \rangle = \langle \boldsymbol{U}_{\mathcal{N}_0,\mathrm{R}} \rangle$, $\mathcal{D}_{\mathrm{T}} = \langle \boldsymbol{\Delta}_{\mathrm{T}} \rangle$, and $\mathcal{D}_{\mathrm{R}} = \langle \boldsymbol{\Delta}_{\mathrm{R}} \rangle$. This model will be used to study the impact of subspace mismatch on the detectability performance, whereas the error model described in (3.8) has been used to analyze the impact of sensing uncertainties on the coexistence of the inner and outer networks.

Observing (3.85)–(3.86), it is clear that the orthogonal projectors onto $\widehat{\mathcal{N}}_{\mathrm{T}}$ and onto $\widehat{\mathcal{N}}_{\mathrm{R}}$, i.e. $\widehat{\boldsymbol{P}}_0(\boldsymbol{r}_{\mathrm{T}}) = \widehat{\boldsymbol{U}}_{\mathcal{N}}(\boldsymbol{r}_{\mathrm{T}})\widehat{\boldsymbol{U}}_{\mathcal{N}}^H(\boldsymbol{r}_{\mathrm{T}})$ and $\widehat{\boldsymbol{P}}_0(\boldsymbol{r}_{\mathrm{R}}) = \widehat{\boldsymbol{U}}_{\mathcal{N}}(\boldsymbol{r}_{\mathrm{R}})\widehat{\boldsymbol{U}}_{\mathcal{N}}^H(\boldsymbol{r}_{\mathrm{R}})$, are not longer equal. Accordingly, the shaping transmission matrix $\boldsymbol{\Phi}$ and the matched-filter receiving matrix $\boldsymbol{\Psi}$ also differ. Under these conditions, if $\boldsymbol{\Phi}$ is designed through (3.26), the design of the receiving matrix $\boldsymbol{\Psi}$ may require an iterative non-coherent waveform detection leading to an inefficient computationally complex design scheme. On the contrary, if the design of $\boldsymbol{\Phi}$ and $\boldsymbol{\Psi}$ relies on the sequential column selection policy described in (3.27), the opportunistic communication still benefits from the invariance property within the effective null space $\mathcal{N}_0$. Regarding the optimality of this strategy, as discussed below (3.29), the sequential column selection policy becomes optimal as the dynamic margin of the main diagonal of the orthogonal projectors decreases, which occurs for practical values of N.

Impact of Subspace Mismatch on the Opportunistic Communication Performance

Once the mathematical model for the subspace mismatch has been discussed, we are now in a position to study the impact of the subspace mismatch phenomenon on the detectability.

Recalling Figure 3.12, we can straightforwardly identify a performance loss in terms of SNR degradation. More specifically, the energy transmitted through $\mathcal{D}_{\mathrm{T}}$ is lost since the inner receiver does not perform detection on this subspace.

Moreover, another performance loss in terms of ISI is not as evident as the abovementioned energy loss. Taking into account that the orthogonal projectors $\widehat{\boldsymbol{P}}_0(\boldsymbol{r}_{\mathrm{T}})$ and $\widehat{\boldsymbol{P}}_0(\boldsymbol{r}_{\mathrm{R}})$ slightly differ as a consequence of the subspace mismatch, the recursive design scheme described in Algorithm 1 may break the orthogonality between transmitted waveforms at the matched filter output.

In the sequel, two performance metrics are defined to analyze the impact of subspace mismatch on the detectability performance. From (3.76), note that the sufficient statistic for symbols decoding read as

$$\boldsymbol{z} = \boldsymbol{\Psi}^H\boldsymbol{y} = \sqrt{\frac{S_{\mathrm{R}}}{K}}\boldsymbol{\Psi}^H\boldsymbol{\Phi}\boldsymbol{a} + \boldsymbol{\Psi}^H(\boldsymbol{i}+\boldsymbol{w}) = \underbrace{\boldsymbol{\Psi}^H\boldsymbol{\Phi}}_{\triangleq\,\boldsymbol{\Sigma}}\widetilde{\boldsymbol{a}} + \boldsymbol{\upsilon}, \tag{3.87}$$

where $\widetilde{\boldsymbol{a}} = \sqrt{S_{\mathrm{R}}/K}\boldsymbol{a} \in \mathbb{C}^K$ contains the transmitted symbols scaled by the average received power, and $\boldsymbol{\upsilon} = \boldsymbol{\Psi}^H(\boldsymbol{i}+\boldsymbol{w})$ is the filtered interference-plus-noise term.

The matrix $\boldsymbol{\Sigma} \in \mathbb{C}^{K\times K}$ encompasses the effects of the subspace mismatch phenomenon. Observing (3.87), it is worth noting that $\boldsymbol{\Sigma} = \boldsymbol{I}_K$ under ideal operating conditions, i.e., in the absence of subspace mismatch. Nevertheless, under realistic conditions, $\boldsymbol{\Sigma}$ is a generic non-diagonal matrix with

$$[\boldsymbol{\Sigma}]_{ij} = \boldsymbol{\psi}_i^H\boldsymbol{\phi}_j, \quad \text{for } i,j = 0,\ldots,K-1. \tag{3.88}$$

The main diagonal of $\boldsymbol{\Sigma}$, corresponding to the case $i=j$, measures the received energy after matched filtering. Note that, in the absence of subspace mismatch, the main diagonal of $\boldsymbol{\Sigma}$ is constant and equal to one. In the sequel, the subspace-mismatch energy loss is analyzed

through the *detection relative energy loss ratio* Γ_K, given by

$$\Gamma_K \triangleq \frac{\|\boldsymbol{\Phi}^H\boldsymbol{\Phi}\|_{\mathrm{F}}^2}{\|\left(\boldsymbol{\Psi}^H\boldsymbol{\Phi}\right)\odot\boldsymbol{I}_K\|_{\mathrm{F}}^2} = \frac{\displaystyle\sum_{k=0}^{K-1}\|\boldsymbol{\phi}_k\|^2}{\displaystyle\sum_{k=0}^{K-1}\|\boldsymbol{\psi}_k^H\boldsymbol{\phi}_k\|^2}, \tag{3.89}$$

where the numerator is, by definition, $\|\boldsymbol{\Phi}^H\boldsymbol{\Phi}\|_{\mathrm{F}}^2 = K$, and the denominator corresponds to the squared Frobenius norm of a diagonal matrix containing the main diagonal of matrix $\boldsymbol{\Sigma}$. In contrast, the off-diagonal elements of $\boldsymbol{\Sigma}$, i.e. the case $i \neq j$, measure the inter-waveform interference, translating into ISI. As already discussed, this ISI is the consequence of the loss of orthogonality between transmitted waveforms at the output of the matched filter. The impact of the self-induced ISI is studied through the *ISI-to-signal energy ratio* $\mathrm{ISR}_{\mathrm{sm}}[K]$, defined as

$$\mathrm{ISR}_{\mathrm{sm}}[K] \triangleq \frac{\|\left(\boldsymbol{\Psi}^H\boldsymbol{\Phi}\right)\odot\left(\boldsymbol{1}_{K\times K}-\boldsymbol{I}_K\right)\|_{\mathrm{F}}^2}{\|\left(\boldsymbol{\Psi}^H\boldsymbol{\Phi}\right)\odot\boldsymbol{I}_K\|_{\mathrm{F}}^2} = \frac{\displaystyle\sum_{k=0}^{K-1}\sum_{\substack{k'=0\\k'\neq k}}^{K-1}\|\boldsymbol{\psi}_{k'}^H\boldsymbol{\phi}_k\|^2}{\displaystyle\sum_{k=0}^{K-1}\|\boldsymbol{\psi}_k^H\boldsymbol{\phi}_k\|^2}. \tag{3.90}$$

Note that the matrix in the numerator in (3.90) is a $K\times K$ matrix with zeros in the main diagonal, and the off-diagonal elements correspond to the off-diagonal entries of the matrix $\boldsymbol{\Sigma}$, whereas the denominator measured the *useful* energy after matched filtering. Under ideal operating conditions, the numerator in (3.90) equals zero.

Plugging the expressions for $\{\boldsymbol{\phi}_k\}_{0\leq k\leq K-1}$ and $\{\boldsymbol{\psi}_k\}_{0\leq k\leq K-1}$ provided by Algorithm 1, it is worth noting that both (3.89) and (3.90) depend on diagonal and off-diagonal elements of the projectors $\widehat{\boldsymbol{P}}_{k+1}(\boldsymbol{r}_{\mathrm{T}}) = \widehat{\boldsymbol{P}}_k(\boldsymbol{r}_{\mathrm{T}})\left(\boldsymbol{I}_N-\boldsymbol{\phi}_k\boldsymbol{\phi}_k^H\right)$ and $\widehat{\boldsymbol{P}}_{k+1}(\boldsymbol{r}_{\mathrm{R}}) = \widehat{\boldsymbol{P}}_k(\boldsymbol{r}_{\mathrm{R}})\left(\boldsymbol{I}_N-\boldsymbol{\psi}_k\boldsymbol{\psi}_k^H\right)$, due to the recursive nature of Algorithm 1. Therefore, the analysis of both performance metrics (3.89) and (3.90) lack a closed-form expression, arising the necessity of a simulation-based analysis.

Nevertheless, the detection relative energy loss ratio Γ_k in (3.89) admits an asymptotic closed-form characterization for the particular case $K = 1$. Especially, this particular case is of relevant interest to predict the behavior of the performance metric in (3.89). Recalling Algorithm 1, it is noteworthy that the dimensionality reduction required to guarantee the orthogonality between waveforms only discards one dimension of the sensed null space at each recursion. Accordingly, the performance metric in (3.89) can be fairly approximated by the detection relative energy loss ratio for $K = 1$. Following this rationale, the latter is a tight approximation when the number of transmitted waveforms K is small[8].

The analysis reported in Appendix 3.E reveals that, for large N, (3.89) for $K = 1$ behaves as

$$\Gamma_1 = \frac{\boldsymbol{\phi}_0^H\boldsymbol{\phi}_0}{|\boldsymbol{\psi}_0^H\boldsymbol{\phi}_0|^2} \xrightarrow[N\to\infty]{} 1+\frac{\kappa_{\mathrm{T}}}{M_0}+\frac{\kappa_{\mathrm{R}}}{M_0}+\frac{\kappa_{\mathrm{T}}\kappa_{\mathrm{R}}}{M_0^2} = 1+\rho_{\mathrm{T}}+\rho_{\mathrm{R}}+\rho_{\mathrm{T}}\rho_{\mathrm{R}}, \tag{3.91}$$

where the parameters $\rho_{\mathrm{T}} \triangleq \kappa_{\mathrm{T}}/M_0$ and $\rho_{\mathrm{R}} \triangleq \kappa_{\mathrm{R}}/M_0$ are referred to as normalized uncertainties at the inner transmitter and the inner receiver, respectively.

[8]It is worth noting that small K means that the opportunistic communication is conservative, which seems reasonable in feedforward scenarios, due to the non-cooperative nature.

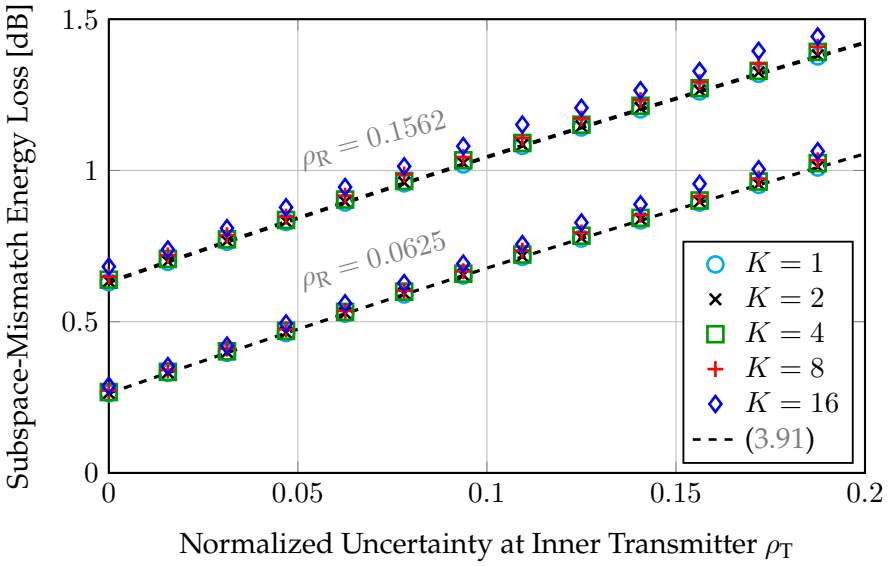

Figure 3.13: Energy Loss induced by inter-node null-space mismatch Γ_K (3.89) in dB as a function of the normalized uncertainty at the inner transmitter ρ_{T}, with $N = 1024$, $M_0 = N/8$ and $\rho_{\mathrm{R}} = \{0.0625,\ 0.1562\}$, for different transmitted waveforms K. The closed-formed expression in (3.91) has been plotted as reference.

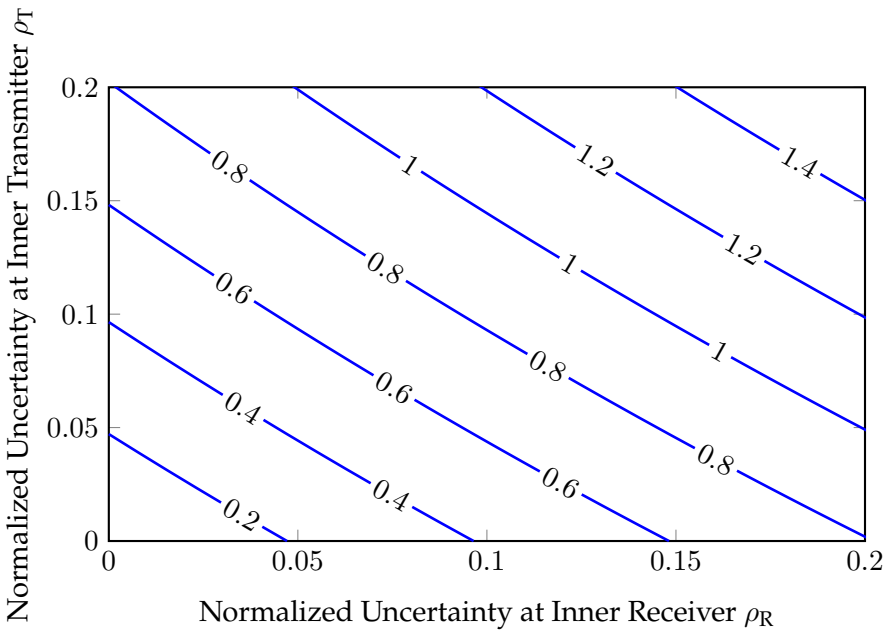

Figure 3.14: Contour plot of the asymptotic subspace-mismatch energy loss given in (3.91), in dB, as a function of normalized uncertainties at inner transmitter and receiver, ρ_{T} and ρ_{R}, respectively.

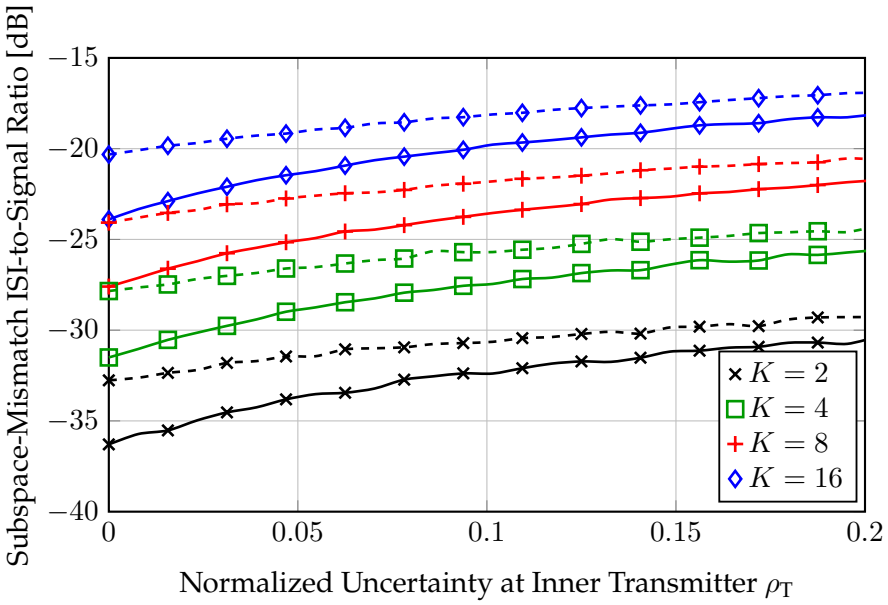

Figure 3.15: ISI-to-Signal Energy Ratio $\mathrm{ISR}_{\mathrm{sm}}[K]$ induced by inter-node null-space mismatch (3.90) in dB as a function of the normalized uncertainty at the inner transmitter ρ_{T}, with $N = 1024$, $M_0 = N/8$, and $\rho_{\mathrm{R}} = \{0.0625,\ 0.1562\}$ (solid and dashed lines, respectively), for different transmitted waveforms K.

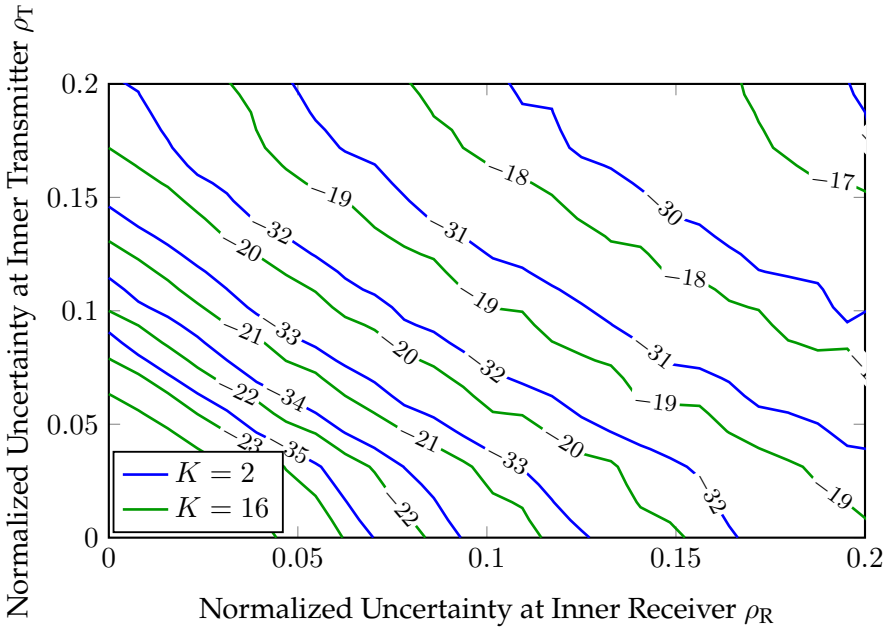

Figure 3.16: Contour plot of the ISI-to-Signal Energy Ratio $\mathrm{ISR}_{\mathrm{sm}}[K]$ (3.90), in dB, as a function of the normalized uncertainties at inner transmitter and receiver, ρ_{T} and ρ_{R}, respectively, and for different transmitted waveforms $K = \{2, 16\}$.

The detection relative energy loss ratio Γ_K (3.89) is numerically evaluated in Figure 3.13, where the asymptotic approximation given in (3.91) is also plotted as reference. First, we shall observe that, as expected, (3.91) is a tight approximation for Γ_K in (3.89), particularly when the number of transmitted waveforms K is small. The latter is of paramount importance to validate the prediction that Γ_K exhibits an almost constant behavior with K and that the dependence on the number of transmitted waveforms is irrelevant for small K. It is interesting to note that Γ_K is lower than 1.5 dB even when the dimension of the excess null space at the inner transmitter $\mathcal{D}_{\mathrm{T}}$ is the 20% of M_0 and the dimension of $\mathcal{D}_{\mathrm{R}}$ is 15.62% of the dimension of $\mathcal{N}_0$. Note that these values of ρ_{T} and ρ_{R} are pessimistic and may signify either that the inner nodes are observing relatively different environments or that the null-space sensing scheme can be improved.

The behavior of the asymptotic approximation in (3.91) for a broader range of ρ_{R} can be observed in the contour plot depicted in Figure 3.14. It is interesting to note that the values of the detection relative energy loss ratio range from 0.2 to 1.4 dB, even in cumbersome scenarios with both ρ_{T} and ρ_{R} being approximately the 20% of M_0.

Apropos of the self-induced ISI, the ISI-to-Signal Energy Ratio $\mathrm{ISR}_{\mathrm{sm}}[K]$ is numerically characterized in Figure 3.15 as a function of the normalized uncertainty at the inner transmitter ρ_{T} for different number of transmitted waveforms K and for $\rho_{\mathrm{R}} = \{0.0625, 0.1562\ \}$. In this case, the impact of the recursive design scheme cannot be bypassed. Note that (3.90) depends explicitly on off-diagonal elements of orthogonal projectors, which cannot be modeled even in the asymptotic case. Therefore, it is not possible to find a theoretical approximated model for the $\mathrm{ISR}_{\mathrm{sm}}[K]$. As for the numerical evaluation of (3.89), the values of ρ_{T} and ρ_{R} leading to higher $\mathrm{ISR}_{\mathrm{sm}}[K]$ are pessimistic. Even under these cumbersome conditions, the proposed opportunistic communication scheme behaves fairly robustly to the ISI induced by the subspace mismatch problem. Specifically, for practical values of K, we may observe from Figure 3.15 that $\mathrm{ISR}_{\mathrm{sm}}[K] \in (-29, -17)$ dB, approximately, when $\rho_{\mathrm{T}} = 20\%$ and $\rho_{\mathrm{R}} = 15.62\%$. The numerical evaluation for a wider range of ρ_{R} is provided in the contour plot illustrated in Figure 3.16, where the $\mathrm{ISR}_{\mathrm{sm}}[K]$ has been evaluated for $K = \{2, 16\}$.

To conclude, under the cumbersome conditions numerically evaluated in Figures 3.13 and 3.15, the MNTLS waveforms derived in this thesis exhibit a robust behavior to the subspace mismatch problem. Nevertheless, as we will discuss in Section 3.5, better performance is possible if the receiver is able to infer $\mathcal{N}_0$ and, thus, counteract the impact of ρ_{R}.

3.5 Enhanced Detection through Active Subspace Inference

The study carried out in the previous section reveals that the opportunistic communication based on the MNTLS waveforms is robust to the impact of end-to-end subspace mismatch in terms of both detection energy loss and self-induced ISI. Nevertheless, the received signal $\boldsymbol{y}$ in (3.75) contains valuable side information on the effective null space $\mathcal{N}_0$ that the inner receiver can exploit to improve the detection performance.

The last section of this chapter is devoted to analyzing an enhanced two-step design scheme of the matched filters $\{\boldsymbol{\psi}_k\}_{0\leq k\leq K-1}$, such that:

(i) *Step 1*: using the sensed null-space basis at the receiver side $\widehat{\boldsymbol{U}}_{\mathcal{N}}(\boldsymbol{r}_{\mathrm{R}})$ and the received signal $\boldsymbol{y}$, the inner receiver *prunes* the sensed null space $\widehat{\mathcal{N}}_{\mathrm{R}}$ trying to discard those DoF

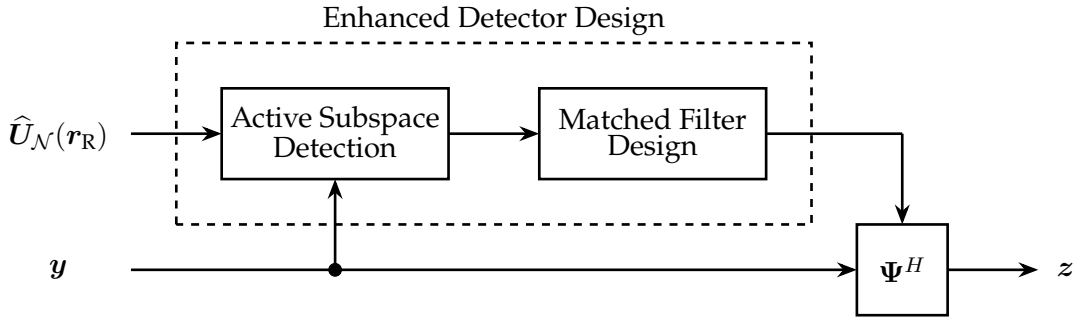

Figure 3.17: Enhanced opportunistic receiving scheme based on MNTLS waveforms. The inner receiver takes advantage of the side information on the effective null space $\mathcal{N}_0$ encompassed in the received signal $\boldsymbol{y}$ to discard those DoF spanned by the excess matrix $\boldsymbol{\Delta}_{\mathrm{R}}$.

not belonging to the effective null space $\mathcal{N}_0$.

(ii) *Step 2*: the inner receiver leverages Algorithm 1 to design the enhanced matched filters making use of a basis of the *pruned* sensed null space.

The enhanced receiving scheme is depicted in Figure 3.17. It is worth noting that the first step consists in identifying which of the DoF encompassed in $\widehat{\boldsymbol{U}}_{\mathcal{N}}(\boldsymbol{r}_{\mathrm{R}})$ are active in the received signal $\boldsymbol{y}$; thus, this step can be seen as an *active subspace detection*[9] problem. Once the inner receiver has identified a basis of the *inferred* or *recovered* effective null space $\mathcal{N}_0$, the sequential waveform design scheme described in Algorithm 1 can be used to design the improved matched filters. It should be noted that using this procedure, we can guarantee that the matched filters maximally counteract the impact of interferences from the wireless environment and that the improved matched filters keep the invariance property.

Mathematically speaking, leveraging the enhanced receiving scheme illustrated in Figure 3.17, the inner receiver can counteract the impact of the subspace mismatch due to $\mathcal{D}_{\mathrm{R}}$, meaning that the normalized uncertainty at the inner receiver ρ_{R} can be reduced. This effect is numerically illustrated in Figure 3.18, where we compare the impact of subspace mismatch when $\rho_{\mathrm{R}} = 0.1562$, which is the worst scenario considered in the previous section, and the ideal case where the inner receiver can maximally reduce the normalized uncertainty, i.e., $\rho_{\mathrm{R}} = 0$. Regarding the detection relative energy loss ratio, observe that the use of the enhanced receiving scheme leads to a decrease of 0.6 dB. Even though it may not seem much, the ISI-to-Signal Energy Ratio depicted in Figure 3.18(b) experiences a decrease of approximately 4 dB when $\rho_{\mathrm{T}} = 0.1$, leading to an increased SINR and a reduced Bit Error Rate (BER).

A natural question that may arise at this point is where the side information on the effective null-space $\mathcal{N}_0$ is. The answer to this question comes straightforwardly from looking at the received signal and the sufficient statistic for symbols decoding given in (3.75) and (3.87),

[9]The problem of active subspace detection has been recently studied in the context of detection theory for the union of subspaces [LB18]. In this scenario, the signal to be detected belongs to a union of low-dimensional subspaces. The objective of the sensor/detector is to identify the subspace to which the received signal belongs. In our case, the received signal $\boldsymbol{y}$ cannot be modeled through the union-of-subspaces signal model. As for the dimension spreading property of the MNTLS waveforms, all dimensions of the sensed null space at the inner transmitter are active in the received signal. Thus, the goal of the receiver consists in identifying which of the DoF spanned by $\widehat{\boldsymbol{U}}_{\mathcal{N}}(\boldsymbol{r}_{\mathrm{R}})$ are active in the received signal. This problem can be seen as a *subspace recovery* problem.

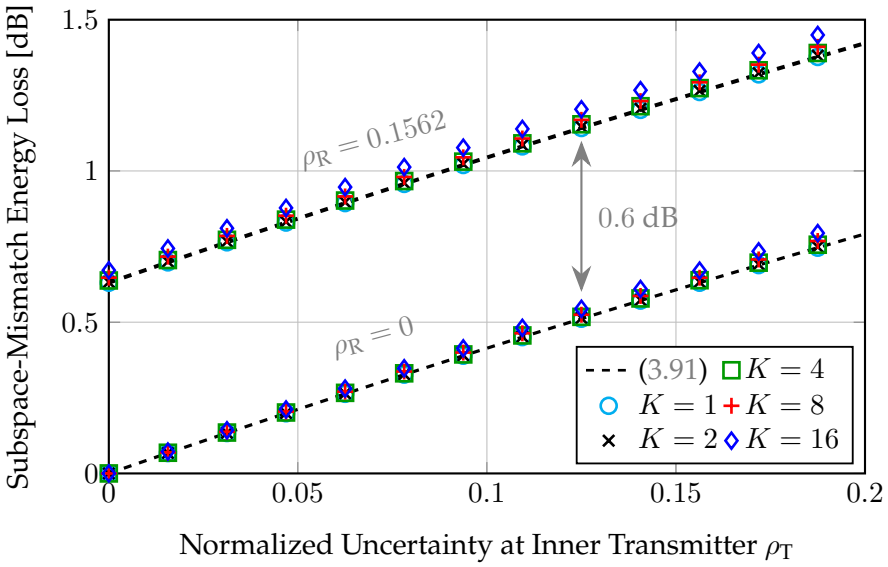

(a) Improvement in terms of detection relative energy loss ratio Γ_K (3.89).

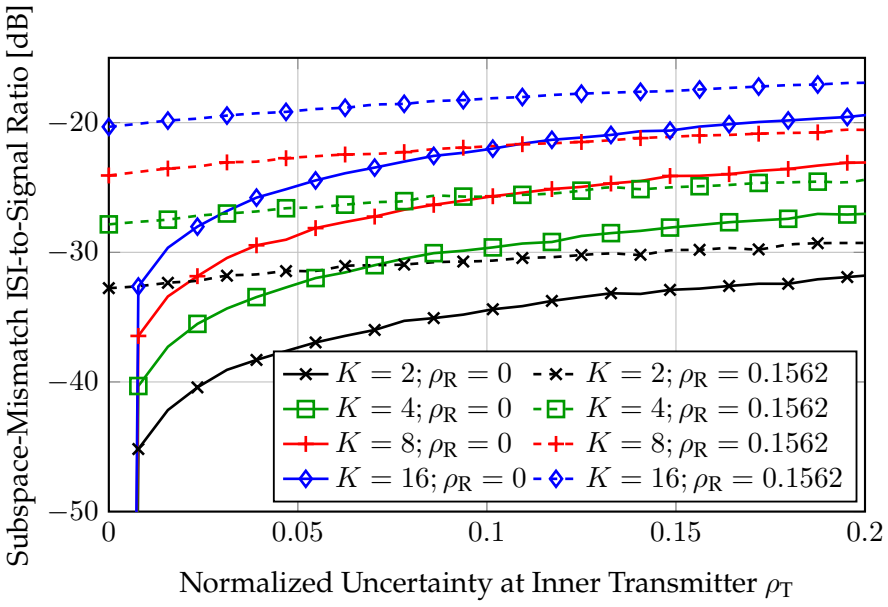

(b) Improvement in terms of ISI-to-Signal Energy Ratio $\mathrm{ISR}_{\mathrm{sm}}[K]$ (3.90).

Figure 3.18: Comparison of the impact of subspace mismatch in both the detection relative energy loss ratio Γ_K (3.89) and the ISI-to-Signal Energy Ratio $\mathrm{ISR}_{\mathrm{sm}}[K]$ (3.90) with $\rho_R = 0.1562$ and $\rho_R = 0$, i.e., the ideal case where the inner receiver is able to perfectly counteract the subspace uncertainty.

respectively. Recalling the subspace mismatch model given in (3.81)–(3.82), we have that

$$\langle \boldsymbol{\Phi} \rangle \subseteq \widehat{\mathcal{N}}_{\mathrm{T}} = \mathcal{N}_0 \oplus \mathcal{D}_{\mathrm{T}}, \tag{3.92}$$

$$\langle \boldsymbol{\Psi} \rangle \subseteq \widehat{\mathcal{N}}_{\mathrm{R}} = \mathcal{N}_0 \oplus \mathcal{D}_{\mathrm{R}}. \tag{3.93}$$

Therefore, since the received signal $\boldsymbol{y}$ lies in $\widehat{\mathcal{N}}_{\mathrm{T}}$, the inner receiver can only detect the information transmitted through $\mathcal{N}_0$. Does it mean that opportunistic communication loses information? Taking into account the dimension spreading behavior of the MNTLS waveforms, all transmitted symbols are spread out within $\widehat{\mathcal{N}}_{\mathrm{T}}$, meaning that a fraction of the per-symbol energy of all transmitted symbols is transmitted through $\mathcal{N}_0$. Accordingly, the subspace mismatch does not incur an information loss. Thus, the signal arrived at the inner receiver is itself the side information necessary to try to infer or recover the effective null space $\mathcal{N}_0$.

Two methods for recovering the effective null space are discussed in the sequel. The first method exploits the fact that the MNTLS waveforms are specific scaled columns of an orthogonal projector. Unfortunately, this methodology is suitable only for the particular case $K = 1$; for a generic $K > 1$, this strategy requires estimating several nuisance parameters. This problem is circumvented by the second proposed method. Moreover, the latter admits a closed-form implementation through a bank of energy detectors, whereas the first method requires an iterative procedure that becomes computationally costly as N increases.

3.5.1 Structure-Aware Active Subspace Inference

Let us consider the vectorized signal model in (3.75). First, the discussion is focused on the particular case $K = 1$. Under this assumption, note that (3.75) becomes

$$\boldsymbol{y} = \sqrt{S_{\mathrm{R}}} a_0 \boldsymbol{\phi}_0 + \boldsymbol{i} + \boldsymbol{w}, \tag{3.94}$$

where, as in Section 3.4, the index of the arbitrary received block l has been dropped. Accordingly, the sufficient statistic for symbol decoding leads to

$$z = \boldsymbol{\psi}_0^H \boldsymbol{y}. \tag{3.95}$$

The objective of the active subspace detection procedure consists in finding which DoF belonging to $\widehat{\mathcal{N}}_{\mathrm{R}}$ are active in the received signal (3.94). For this purpose, and in order to minimize the BER, the maximization of the power of the sufficient statistic (3.95) is considered.

Noting that the matched filter $\boldsymbol{\psi}_0$ is a scaled column, the enhanced matched filter $\widetilde{\boldsymbol{\psi}}_0$ can be constructed as

$$\widetilde{\boldsymbol{\psi}}_0 = \gamma_0 \widehat{\boldsymbol{P}}_{\mathcal{N}_0} \boldsymbol{e}_0, \tag{3.96}$$

where $\boldsymbol{e}_0$ is defined as in (3.19), γ_0 is a scaling factor guaranteeing unit norm, and $\widehat{\boldsymbol{P}}_{\mathcal{N}_0}$ is the orthogonal projector onto the inferred or recovered effective null space. Let $\widehat{\boldsymbol{P}}_m(\boldsymbol{r}_{\mathrm{R}})$ be the rank-one orthogonal projector onto the m-th dimension, for $m = 1, \ldots, M_{\mathrm{R}}$, of the sensed null space at the receiver side. Thus, $\widehat{\boldsymbol{P}}_{\mathcal{N}_0}$ can be written as[10]

$$\widehat{\boldsymbol{P}}_{\mathcal{N}_0} = \sum_{m=1}^{M_{\mathrm{R}}} \widehat{\boldsymbol{P}}_m(\boldsymbol{r}_{\mathrm{R}}) \mu_m, \quad \text{with} \quad \widehat{\boldsymbol{P}}_m(\boldsymbol{r}_{\mathrm{R}}) = \widehat{\boldsymbol{u}}_m(\boldsymbol{r}_{\mathrm{R}}) \widehat{\boldsymbol{u}}_m^H(\boldsymbol{r}_{\mathrm{R}}), \tag{3.97}$$

[10] In general, the sum of projection matrices is not a projector. Nevertheless, in this specific case, since each $\widehat{\boldsymbol{P}}_m(\boldsymbol{r}_{\mathrm{R}})$ projects onto orthogonal dimensions of the sensed null space at the receiver side, the sum of these rank-one projectors is also a projector.

where $\widehat{\boldsymbol{u}}_m(\boldsymbol{r}_{\mathrm{R}})$ is the m-th column of $\widehat{\boldsymbol{U}}_{\mathcal{N}}(\boldsymbol{r}_{\mathrm{R}})$ and $\mu_m \in \{0,1\}$ determines if the m-th dimension of $\widehat{\mathcal{N}}_{\mathrm{R}}$ belongs to the effective null space $\mathcal{N}_0$. Defining $\boldsymbol{\mu} = [\mu_1, \ldots, \mu_m, \ldots, \mu_{M_{\mathrm{R}}}]^T$, and using (3.96) and (3.97), the enhanced matched filter $\widetilde{\boldsymbol{\psi}}_0$ can be compactly written as

$$\widetilde{\boldsymbol{\psi}}_0 = \gamma_0 \boldsymbol{\Pi} \boldsymbol{\beta}, \tag{3.98}$$

with

$$\boldsymbol{\Pi} = \left[\widehat{\boldsymbol{P}}_1(\boldsymbol{r}_{\mathrm{R}}) \ \cdots \ \widehat{\boldsymbol{P}}_m(\boldsymbol{r}_{\mathrm{R}}) \ \cdots \ \widehat{\boldsymbol{P}}_{M_{\mathrm{R}}}(\boldsymbol{r}_{\mathrm{R}})\right] \in \mathbb{C}^{N \times NM_{\mathrm{R}}}, \tag{3.99}$$

$$\boldsymbol{\beta} = \boldsymbol{\mu} \otimes \boldsymbol{e}_0 \in \{0,1\}^{NM_{\mathrm{R}}}. \tag{3.100}$$

In view of (3.98)–(3.100), and recalling (3.95), the design of the enhanced matched filter can be tackled as

$$\boldsymbol{\beta} = \max_{\boldsymbol{\beta} \in \{0,1\}^{NM_{\mathrm{R}}}} \mathbb{E}\left[\widetilde{\boldsymbol{\psi}}_0^H \boldsymbol{y}\boldsymbol{y}^H \widetilde{\boldsymbol{\psi}}_0\right] = \max_{\boldsymbol{\beta} \in \{0,1\}^{NM_{\mathrm{R}}}} \widetilde{\boldsymbol{\psi}}_0^H \boldsymbol{R}_{\boldsymbol{y}\boldsymbol{y}} \widetilde{\boldsymbol{\psi}}_0, \tag{3.101}$$

where $\boldsymbol{R}_{\boldsymbol{y}\boldsymbol{y}} = \mathbb{E}\left[\boldsymbol{y}\boldsymbol{y}^H\right]$ is the autocorrelation matrix of the received signal. From (3.101), the reader may recognize two different *detection* problems, that are jointly solved. On the one hand, the inner receiver has to detect those dimensions of its sensed null space that are active in the received signal $\boldsymbol{y}$. On the other hand, the inner receiver has to decide which column of $\widehat{\boldsymbol{P}}_{\mathcal{N}_0}$ is the best matched filter for the transmitted waveform $\boldsymbol{\phi}_0$. Interestingly, finding the vector $\boldsymbol{\beta}$ solving (3.101) suffices to address both problems.

Taking into account the Boolean nature of $\boldsymbol{\beta}$, it is worth noting that a combinatory problem arises, unfeasible to tackle at large NM_{R}. In the particular case where the dynamic margin of $\widehat{\boldsymbol{P}}_{\mathcal{N}_0}$ is small enough, $\widetilde{\boldsymbol{\psi}}_0$ corresponds to the first column of $\widehat{\boldsymbol{P}}_{\mathcal{N}_0}$, appropriately scaled, additional constraints can be incorporated in (3.101) to decrease the number of unknown parameters to be found. In general, however, the linear model described in (3.98) is underdetermined, and $\boldsymbol{\beta}$ is an s-sparse vector[11], meaning that only s out of NM_{R} components are non-zero. In order to circumvent the underdetermined nature of (3.98) and take advantage of the inherent sparsity of the vector $\boldsymbol{\beta}$, it seems reasonable to tackle the design of $\boldsymbol{\beta}$ as

$$\min_{\boldsymbol{\beta} \in \mathcal{F}_\beta} \quad f(\boldsymbol{\beta}) \tag{3.102}$$

$$\text{subject to} \quad g(\boldsymbol{y}, \boldsymbol{\beta}) \leq \eta \tag{3.103}$$

where $\mathcal{F}_\beta$ is the feasible set of $\boldsymbol{\beta}$, $f(\boldsymbol{\beta})$ has to be a sparsity-promoting function, e.g. the L_0-norm, $g(\boldsymbol{y}, \boldsymbol{\beta})$ should measure the error between the input $\boldsymbol{y}$ and a reconstruction of the received signal $\widehat{\boldsymbol{y}} = \gamma_0 \boldsymbol{\Pi} \boldsymbol{\beta}$ based on the inferred vector $\boldsymbol{\beta}$, and η is the maximum allowed error. Recall the vectorized model in (3.94). In order to improve the reconstruction $\widehat{\boldsymbol{y}}$, the inner receiver can also estimate the data symbol a_0 and the signal amplitude $\sqrt{S_{\mathrm{R}}}$, which are nuisance parameters for the active subspace detection problem, such that $\widehat{\boldsymbol{y}} = \widehat{\Xi} \gamma_0 \boldsymbol{\Pi} \boldsymbol{\beta}$ with $\Xi = a_0 \sqrt{S_{\mathrm{R}}}$. As per [RSV01], these nuisance parameters can be estimated by leveraging the Conditional Maximum Likelihood (CML) framework.

Recalling (3.102)–(3.103), note that in this case the feasible set of $\boldsymbol{\beta}$ is $\mathcal{F}_\beta = \{0,1\}^{NM_{\mathrm{R}}}$, i.e., the set of NM_{R}-length Boolean vectors. Therefore, one possibility is to make use of the Binary Sparse Recovery (BSR) framework. Several approaches to the problem of BSR can be found in

[11] Assuming that the inner receiver can perfectly recover the effective null space, note that $s = M_0$.

the recent literature (see, e.g., [FK18; Fos18; FA19; CFR21; SP21]). From these works, [Fos18; FK18] are outperformed by the polynomial optimization proposed in [FA19], [CFR21] is based on a non-convex optimization problem assuming known the L_0-norm of the solution, and [SP21] is focused on a specific signal model different from the signal model considered herein [cf. (3.94)]. Even though the approach discussed in [FA19] seems the most appropriate for the problem at hand from the BSR framework, the exact recovery of the sparse vector $\boldsymbol{\beta}$ requires a sufficiently small number of non-zero entries; a sufficiently large number of measurements, i.e., the dimension of $\boldsymbol{y}$; and a sufficiently high SNR.

An alternative formulation is proposed to circumvent the binary nature of the vector $\boldsymbol{\beta}$ to be designed. Let the matrix $\boldsymbol{B} \in \mathbb{C}^{N \times M_{\mathrm{R}}}$ be the unvectorization of $\boldsymbol{\beta}$, given by

$$\boldsymbol{B} = [\mu_1 \boldsymbol{e}_0 \ \cdots \ \mu_m \boldsymbol{e}_0 \ \cdots \ \mu_{M_{\mathrm{R}}} \boldsymbol{e}_0] \,. \tag{3.104}$$

From this matrix, we can define the following variables:

$$\boldsymbol{b}_1 \triangleq \boldsymbol{B}^T \mathbf{1}_N = [\mu_1 \ \cdots \ \mu_m \ \cdots \ \mu_{M_{\mathrm{R}}}] \in \mathbb{C}^{M_{\mathrm{R}} \times 1}, \tag{3.105}$$

$$\boldsymbol{b}_2 \triangleq \boldsymbol{B} \mathbf{1}_{M_{\mathrm{R}}} = \left[\mathbf{0}_{n-1} \ \ \widehat{M}_0 \ \ \mathbf{0}_{N-n}\right] \in \mathbb{C}^{N \times 1}, \tag{3.106}$$

with $n = 1, \ldots, N$. Notice that (3.105) is an M_{R}-element vector containing the sum of the N rows of matrix $\boldsymbol{B}$, whereas (3.106) is an N-element vector containing the sum of the M_{R} columns of matrix $\boldsymbol{B}$. The parameter $\widehat{M}_0$ refers to the dimension of the identified effective null space. The rationale behind (3.106) is the following. Since the vector $\boldsymbol{e}_0$ selects one column from the orthogonal projector onto the inferred effective null space $\widehat{\boldsymbol{P}}_{\mathcal{N}_0}$, all entries of (3.106) are zero but the one indicating the selected column. This entry, namely n, is equal to

$$[\boldsymbol{b}_2]_n = \sum_{k=1}^{M_{\mathrm{R}}} \mu_k = \widehat{M}_0, \tag{3.107}$$

which follows from noting that $\lambda_k \in \{0, 1\}$. This discussion is of paramount interest since it reveals that, once the vector $\boldsymbol{\beta}$ satisfying (3.102)–(3.103) is obtained, the active dimensions can be identified from (3.105), whereas the most suitable column to demodulate the received signal $\boldsymbol{y}$ is found from (3.106).

In the sequel, we propose dropping the constraint on the feasible set of $\boldsymbol{\beta}$, letting $\mathcal{F}_\beta = \mathbb{C}^{NM_{\mathrm{R}}}$. This relaxation is of paramount importance because it permits addressing (3.102)–(3.103) through the classic compressed sensing framework [EK12]. More specifically, $\boldsymbol{\beta}$ can be found as

$$\min_{\boldsymbol{\beta} \in \mathbb{C}^{NM_{\mathrm{R}}}} \quad \|\boldsymbol{\beta}\|_0 \tag{3.108}$$

$$\text{subject to} \quad \|\boldsymbol{y} - \widehat{\boldsymbol{y}}\|_2^2 \leq \eta^2 \tag{3.109}$$

where $\widehat{\boldsymbol{y}}$ is the reconstruction of the received signal $\boldsymbol{y}$, as discussed on the previous page. Optimizing the L_0-norm is an NP (non-convex) problem. A conventional approach to circumvent this non-convexity consists in using the L_1-norm in lieu of the L_0-norm; this approach is known as *convex relaxation*. Another possibility is to leverage a *matching pursuit* algorithm. The latter are greedy algorithms that recover the signal iteratively, providing a sparse approximation in polynomial complexity; thus, these greedy algorithms are, in general, more computationally

efficient than the convex relaxation methods, also known as L_1-based optimization. A third approach to deal with the sparse recovery problem consists in using non-convex optimization techniques, which exploit the statistical distribution of the signal. The main drawback of this third approach is the computational inefficiency in high-dimensional problems. A complete review of sparse recovery algorithms can be found in [MMN+18].

Once the $\boldsymbol{\beta}$ solving (3.108)–(3.109) is found, the matrix $\boldsymbol{B}$ in (3.104) can be constructed. From this matrix, we can also find the vector $\boldsymbol{b}_1$ in (3.105), which is the statistic to infer the effective null space. Note that, under the assumption $\boldsymbol{\beta} \in \mathbb{C}^{NM_{\mathrm{R}}}$, $\boldsymbol{b}_1$ is not Boolean, requiring a binarization. Therefore, the problem of identifying the effective null space from $\boldsymbol{b}_1$ hints at a set of M_{R} binary hypothesis testing problems. Accordingly,

$$\left|\left[\widetilde{\boldsymbol{b}}_1\right]_m\right| = \begin{cases} 1, & \text{if } |[\boldsymbol{b}_1]_m| \geq \gamma_{\mathrm{th}} \\ 0, & \text{otherwise} \end{cases}, \tag{3.110}$$

where the decision threshold γ_{th} can be set to keep the false-alarm probability of the active subspace detection problem, i.e., the probability of detecting as active a dimension not belonging to the effective null space as low as possible. In this case, we may say that γ_{th} has to be optimum in the Neyman-Pearson sense [Kay98].

Finally, once the vector $\boldsymbol{b}_1$ has been binarized, the most suitable column of $\widehat{\boldsymbol{P}}_{\mathcal{N}_0}$ can be found leveraging (3.106). Alternatively, we can leverage (3.110) to infer the dimensions of $\widehat{\mathcal{N}}_{\mathrm{R}}$ belonging to the effective null space $\mathcal{N}_0$, and the column selection from $\widehat{\boldsymbol{P}}_{\mathcal{N}_0}$ (3.97) can be done as in (3.29). Note that whenever the sequential column selection policy in (3.27) can be adopted from the very beginning, the first column of $\widehat{\boldsymbol{P}}_{\mathcal{N}_0}$ is selected.

It is interesting to note that the problem formulated in (3.108)–(3.109) is based on the single measurement vector (SMV) compressive signal model, i.e., a single received block $\boldsymbol{y}$ is considered. The performance of the active subspace detection problem may benefit from stacking $l = 1, \ldots, Q$ received blocks. In this sense, let $\widetilde{\boldsymbol{y}} \in \mathbb{C}^{NQ}$ be a collection of Q received blocks, i.e.

$$\widetilde{\boldsymbol{y}} = \left[\boldsymbol{y}_1^T \ \cdots \ \boldsymbol{y}_l^T \ \cdots \ \boldsymbol{y}_Q^T\right]^T, \tag{3.111}$$

and $\widetilde{\boldsymbol{\Pi}} \in \mathbb{C}^{NQ \times NM_{\mathrm{R}}}$ be the vertical stacking of Q matrices Π (3.99), i.e.

$$\widetilde{\boldsymbol{\Pi}} = \begin{bmatrix} \boldsymbol{\Pi} \\ \vdots \\ \boldsymbol{\Pi} \end{bmatrix}. \tag{3.112}$$

Accordingly, the sparse recovery of $\boldsymbol{\beta}$ can be reformulated as

$$\min_{\boldsymbol{\beta} \in \mathbb{C}^{NM_{\mathrm{R}}}} \quad \|\boldsymbol{\beta}\|_0 \tag{3.113}$$

$$\text{subject to} \quad \tfrac{1}{Q}\|\widetilde{\boldsymbol{y}} - \widetilde{\boldsymbol{\Pi}}\boldsymbol{\beta}\|_2^2 \leq \eta^2 \tag{3.114}$$

where the factor $1/Q$ in (3.114) guarantees that the same maximum allowed squared-error η^2 as in (3.109) can be used. Intuitively, including multiple received blocks can improve the performance of the sparse recovery problem at expense of increasing the computational complexity

due to the dimension increase observed in (3.113)–(3.114). Nonetheless, expanding the L_2-norm in the constraint, we note that

$$\frac{1}{Q}\|\widetilde{\boldsymbol{y}} - \widetilde{\boldsymbol{\Pi}}\boldsymbol{\beta}\|_2^2 = \frac{1}{Q}\sum_{l=1}^{Q}\|\boldsymbol{y}_l - \boldsymbol{\Pi}\boldsymbol{\beta}\|_2^2, \tag{3.115}$$

which is more computationally efficient. Note that (3.115) states that the squared-error constraint in (3.114) is equivalent to the cumulative squared-error of each received block.

At this point, we shall discuss the objective of *relaxing* the feasible set of $\boldsymbol{\beta}$, letting $\mathcal{F}_\beta = \mathbb{C}^{NM_{\mathrm{R}}}$. It is worth noting that dropping the constraint on the feasible set, the vector $\boldsymbol{\beta}$ solving (3.102)–(3.103) is a generic sparse complex vector. Therefore, regardless of the algorithm considered to circumvent the non-convexity of the L_0-norm, $\boldsymbol{\beta}$ is adapted to minimize the power of the residual in (3.109), avoiding the necessity of estimating nuisance parameters to obtain a more accurate reconstruction $\widetilde{\boldsymbol{y}}$ of the observed received block.

A fundamental aspect to discuss is whether the recovery of the *exact* vector $\boldsymbol{\beta}$ is guaranteed. In the literature on compressed sensing, several criteria have been proposed to assess if the *sensing* or *measurement* matrix is suitable to recover the sparse vector, such as the *spark* [DE03], the *mutual coherence* [DH01], and the *restricted isometry property* [CT05]. Note that, in the problem at hand, the measurement matrix is $\boldsymbol{\Pi}$, defined in (3.99). The analysis reported in Appendix 3.F reveals that the recovery of $\boldsymbol{\beta}$ cannot be guaranteed in general. This pessimistic conclusion seems to limit the interest in the proposed active subspace detection scheme. Nevertheless, we have to keep in mind that the objective is not the recovery of $\boldsymbol{\beta}$, but the inference of the effective null space $\mathcal{N}_0$. In this sense, the numerical analysis carried out in Section 3.5.3 illustrates that, under specific conditions, the effective null space $\mathcal{N}_0$ can be identified.

Thus far, the discussion is focused on the particular case $K = 1$, i.e., the transmitted block is composed of a single symbol. We have seen that using a thresholding criterion to binarize the inferred vector $\boldsymbol{\beta}$, we can tackle the active subspace detection and the matched filter design jointly. For a generic $K > 1$, however, the latter approach is not possible as the design of the matched-filter receiving matrix involves a sequential procedure. Taking into account this consideration, is it worthwhile to solve the non-convex problem stated in (3.113)–(3.114)?

Exploiting the structure of the MNTLS waveforms is not appropriate for detecting the effective null space $\mathcal{N}_0$; this approach lacks a closed-form expression requiring approximations to circumvent the non-convexity inherent in sparse optimization problems. A more general active subspace detection scheme is proposed in the following subsection. In contrast to the structure-aware approach discussed above, the more general strategy separates the active subspace inference and the design of the matched-filter receiving matrix. Consequently, a closed-form solution for the active subspace detection problem is found, which can be efficiently implemented through a bank of energy detectors.

3.5.2 Energy-based Effective Null Space Inference

Previously, an attempt has been made to jointly detect the effective null space $\mathcal{N}_0$ and select the appropriate column of the projector onto the inferred $\mathcal{N}_0$ to demodulate the received signal. However, the problem faces a cumbersome sparse optimization problem, whose solution involves approximations or greedy algorithms incurring a possible inefficiency in terms of computational complexity, especially for large N. In any case, the solution proposed in the previous

subsection is only valid for $K = 1$, as the proposed problem formulation cannot circumvent the recursive nature of Algorithm 1.

In the sequel, the problems of detecting the effective null space and designing the matched-filter receiving matrix are tackled separately. As already discussed on the previous page, this *divide and conquer* approach is the only possibility to efficiently circumvent the recursive nature of Algorithm 1. It is worth noting that the inner receiver knows how to design the matched filters for a given null-space basis; thus, efforts have to be made to identify a basis of the effective null space to decrease the impact of the subspace mismatch. At the end of this subsection, we will see that, interestingly, the general case admits an efficient closed-form solution.

For notational purposes, let us write the shaping transmission matrix as

$$\boldsymbol{\Phi} = [\boldsymbol{\phi}_0, \ldots, \boldsymbol{\phi}_{K-1}] = \widehat{\boldsymbol{U}}_{\mathcal{N}}(\boldsymbol{r}_{\mathrm{T}}) \left[\boldsymbol{\lambda}_0(\boldsymbol{r}_{\mathrm{T}}), \ldots, \boldsymbol{\lambda}_{K-1}(\boldsymbol{r}_{\mathrm{T}})\right] = \widehat{\boldsymbol{U}}_{\mathcal{N}}(\boldsymbol{r}_{\mathrm{T}})\boldsymbol{\Lambda}_{\mathrm{T}}. \tag{3.116}$$

Accordingly, the matched-filter receiving matrix can be written as

$$\boldsymbol{\Psi} = [\boldsymbol{\psi}_0, \ldots, \boldsymbol{\psi}_{K-1}] = \widehat{\boldsymbol{U}}_{\mathcal{N}}(\boldsymbol{r}_{\mathrm{R}})\boldsymbol{\Lambda}_{\mathrm{R}}. \tag{3.117}$$

Recalling the vectorized signal model described in (3.75), we note that the relevant information at the received side is given by

$$\boldsymbol{\nu}_l = \widehat{\boldsymbol{P}}_0(\boldsymbol{r}_{\mathrm{R}})\boldsymbol{y} = \sqrt{\frac{S_{\mathrm{R}}}{K}} \left[\begin{array}{c:c} \boldsymbol{U}_{\mathcal{N}_0,\mathrm{T}} & \boldsymbol{0} \end{array}\right] \boldsymbol{\Lambda}_{\mathrm{T}}\boldsymbol{a} + \boldsymbol{n}, \tag{3.118}$$

which follows from noting that, since $\widehat{\mathcal{N}}_{\mathrm{T}} \neq \widehat{\mathcal{N}}_{\mathrm{R}}$ under the existence of inter-node subspace mismatch, and that $\boldsymbol{n} = \widehat{\boldsymbol{P}}_0(\boldsymbol{r}_{\mathrm{R}})(\boldsymbol{i} + \boldsymbol{w})$ is the relevant interference-plus-noise term. It should be emphasized that all interferences laying outside the sensed null space at the inner receiver $\widehat{\mathcal{N}}_{\mathrm{R}}$ will be canceled out by the matched-filter receiving matrix relying on the MNTLS waveforms. In (3.118), we have dropped the received block index, as in Section 3.4. As for (3.85), the matrix $\boldsymbol{U}_{\mathcal{N}_0,\mathrm{T}}$ spans the effective null space $\mathcal{N}_0$. The relevant information modeled in (3.118) emphasizes that only the amount of signal energy transmitted through the effective null space is detected by the inner receiver; thus, the energy transmitted through the excess null space at the inner transmitter $\mathcal{D}_{\mathrm{T}}$ is not represented in the relevant information model.

Note that, regardless of the existence of subspace mismatch, the invariance property holds within the effective null space $\mathcal{N}_0$. Therefore, recalling (3.86), the relevant information in (3.118) admits, without loss of generality, the following interpretation:

$$\boldsymbol{\nu}_l = \sqrt{\frac{S_{\mathrm{R}}}{K}} \left[\begin{array}{c:c} \boldsymbol{U}_{\mathcal{N}_0,\mathrm{R}} & \boldsymbol{\Delta}_{\mathrm{R}} \end{array}\right] \left[\begin{array}{c} \boldsymbol{\Lambda}_{\mathcal{N}_0,\mathrm{R}} \\ \hdashline \boldsymbol{0} \end{array}\right] \boldsymbol{a} + \boldsymbol{n} = \widehat{\boldsymbol{U}}_{\mathcal{N}}(\boldsymbol{r}_{\mathrm{R}})\boldsymbol{\theta} + \boldsymbol{n}, \tag{3.119}$$

i.e., if the inner receiver is able to identify which of the dimensions of $\widehat{\mathcal{N}}_{\mathrm{R}}$ do not belong to the effective null space $\mathcal{N}_0$, only the coefficients defining the enhanced matched filters, encompassed in matrix $\boldsymbol{\Lambda}_{\mathcal{N}_0,\mathrm{R}}$, have to be designed. As per (3.119), note that the coefficients vector $\boldsymbol{\theta}$ satisfies

$$|[\boldsymbol{\theta}]_m| = \begin{cases} C_m & \text{if and only if } \widehat{\boldsymbol{u}}_m(\boldsymbol{r}_{\mathrm{R}}) \in \mathcal{N}_0 \\ 0 & \text{otherwise} \end{cases}, \quad \text{for } m = 1, \ldots, M_{\mathrm{R}}, \tag{3.120}$$

where $C_m \in \mathbb{R}^+$ and $\widehat{\boldsymbol{u}}_m(\boldsymbol{r}_{\mathrm{R}})$ refers to the m-th column of $\widehat{\boldsymbol{U}}_{\mathcal{N}}(\boldsymbol{r}_{\mathrm{R}})$. It is interesting to emphasize that the coefficients vector $\boldsymbol{\theta}$ encompasses the information of the linear combinations $\boldsymbol{\Lambda}_{\mathcal{N}_0,\mathrm{R}}$ defining the K matched filters, the data symbols $\boldsymbol{a}$, and the signal amplitude.

Observing the model described in (3.119), it is worth noting that the objective of the inner receiver consists in identifying the coefficients vector $\boldsymbol{\theta}$. This problem can be cast as a subspace recovery problem, i.e., identify which dimensions of $\widehat{\mathcal{N}}_{\mathrm{R}}$ are active in the received signal $\boldsymbol{y}$. As discussed in [YV15b; LYV18] (and references therein), this problem can be formulated as a classical (noisy) sparse recovery problem. In contrast to the problem formulated in (3.108)–(3.109), in this case, we leverage a specific optimization principle known as Basis Pursuit Denoising (BPDN), also known as Least Absolute Shrinkage and Selection Operator (LASSO) in statistics. The use of this methodology will be justified afterward. Therefore, the BPDN/LASSO problem can be formulated as an L_1-regularized least-squares optimization problem, whose Lagrangian form [MMN+18; HTW19] is given by

$$\boldsymbol{\theta} = \underset{\boldsymbol{\theta}}{\arg\min} \left\{ \|\boldsymbol{y} - \widehat{\boldsymbol{U}}_{\mathcal{N}}(\boldsymbol{r}_{\mathrm{R}})\boldsymbol{\theta}\|_2^2 + \gamma\|\boldsymbol{\theta}\|_1 \right\}, \tag{3.121}$$

where γ is the regularization parameter. At this point, some considerations are of order. Note that the measurement matrix in (3.121) is $\widehat{\boldsymbol{U}}_{\mathcal{N}}(\boldsymbol{r}_{\mathrm{R}})$, which is left-unitary. Therefore, the problem formulated in (3.121) has two relevant properties:

(i) The measurement matrix $\widehat{\boldsymbol{U}}_{\mathcal{N}}(\boldsymbol{r}_{\mathrm{R}})$ meets the mutual incoherence condition, i.e.

$$\mu\left(\widehat{\boldsymbol{U}}_{\mathcal{N}}(\boldsymbol{r}_{\mathrm{R}})\right) = \max_{\substack{m\neq n \\ m,n=1,\ldots,M_{\mathrm{R}}}} \frac{\left|\widehat{\boldsymbol{u}}_m^H(\boldsymbol{r}_{\mathrm{R}})\widehat{\boldsymbol{u}}_n(\boldsymbol{r}_{\mathrm{R}})\right|}{\|\widehat{\boldsymbol{u}}_m(\boldsymbol{r}_{\mathrm{R}})\|_2 \, \|\widehat{\boldsymbol{u}}_n(\boldsymbol{r}_{\mathrm{R}})\|_2} = 0, \tag{3.122}$$

providing recovery guarantees of the sparse signal $\boldsymbol{\theta}$. Moreover, as per [YV15a; YV15b], the mutual incoherence is a sufficient condition for the subspace recovery problem.

(ii) As emphasized in [HTW19] solving the LASSO problem involves a cyclic coordinate descent algorithm. Nevertheless, as also reported therein, if the measurement matrix is an orthogonal basis, then the L_1-regularized least-squares problem in (3.121) admits a non-iterative closed-form solution given by

$$[\boldsymbol{\theta}]_m = \mathcal{S}_\gamma\left(\widehat{\boldsymbol{u}}_m^H\boldsymbol{y}\right) = \begin{cases} \widehat{\boldsymbol{u}}_m^H\boldsymbol{y} - \gamma & \text{if } \widehat{\boldsymbol{u}}_m^H\boldsymbol{y} > \gamma \\ 0 & \text{if } |\widehat{\boldsymbol{u}}_m^H\boldsymbol{y}| \leq \gamma \\ \widehat{\boldsymbol{u}}_m^H\boldsymbol{y} + \gamma & \text{if } \widehat{\boldsymbol{u}}_m^H\boldsymbol{y} < -\gamma \end{cases}, \quad \text{for } m = 1, \ldots, M_{\mathrm{R}}, \tag{3.123}$$

where $\mathcal{S}_\gamma(x) = \mathrm{sign}(x)(|x| - \gamma)^+$ is a *soft-thresholding* function [FR13; HTW19].

These two properties justify using the BPDN/LASSO framework to address the aforementioned subspace recovery problem. Conversely, in the previous subsection, since the measurement matrix does not provide any measurement guarantee and the problem does not admit a closed-form solution, choosing the strategy to solve (3.108)–(3.109) depends on the computational capacity of the inner nodes and the desired accuracy level; thus, the discussion has not been focused on any particular methodology.

A direct consequence of the closed-form solution provided in (3.123) is that the active subspace detector is Nondata-Aided (NDA) since side information on the signal amplitude, the

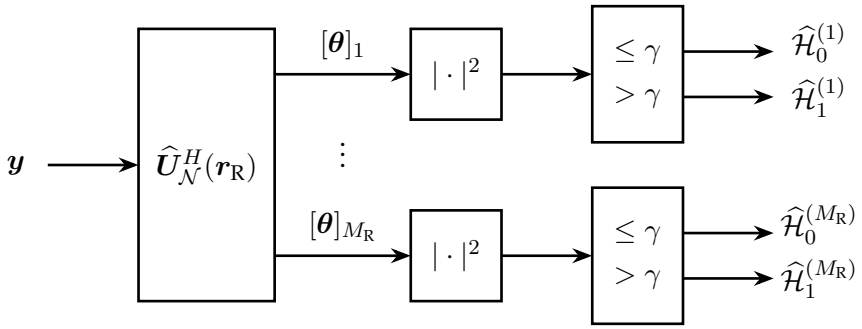

Figure 3.19: Implementation of (3.123) as a bank of energy detectors (3.124)–(3.125).

data symbols, or the linear combination coefficients matrix $\boldsymbol{\Lambda}_{\mathcal{N}_0,\mathrm{R}}$ are not needed. Accordingly, no nuisance parameters have to be estimated.

Carefully observing (3.123), it is noteworthy that this NDA active subspace detector hints at a set of M_{R} binary hypothesis testing problems, where the null and alternative hypotheses are given by

$$\mathcal{H}_0^{(m)} \quad : \quad \left|\widehat{\boldsymbol{u}}_m^H \boldsymbol{y}\right| \leq \gamma \tag{3.124}$$

$$\mathcal{H}_1^{(m)} \quad : \quad \left|\widehat{\boldsymbol{u}}_m^H \boldsymbol{y}\right| > \gamma \tag{3.125}$$

for $m = 1, \ldots, M_{\mathrm{R}}$. Note that these binary hypothesis testing problems can be tackled as a bank of classic energy detectors [Kay98]. This observation is of paramount importance since an NDA active subspace detector enjoying subspace recovery guarantees can be tackled by a simple per-DoF energy detector as illustrated in Figure 3.19, avoiding the implementation of complex greedy algorithms or convex approximations as in (3.108)–(3.109). From (3.123), note that the decision is based on a single sample per DoF; thus, the detection problem may suffer from the randomness introduced by the noise and the unknown information symbols. However, this randomness can be counteracted when the receiver uses $l = 1, \ldots, Q$ received blocks.

As a final note, notice that by implementing an active subspace detector to infer $\mathcal{N}_0$, the inner receiver may counteract the impact of subspace mismatch due to $\mathcal{D}_{\mathrm{R}}$. A natural question that may arise is how to counteract the subspace mismatch at the transmitter side. The inner transmitter may exploit the response message sent by the inner receiver and infer $\mathcal{N}_0$ leveraging the per-DoF energy detection-based active subspace detector illustrated in Figure 3.19 under TDD conditions. This approach does not require additional side information, even though it may improve detection performance. This problem was briefly studied by the author in [BV19] for the particular case $K = 1$ leveraging the strategy discussed in Section 3.5.1. Concluding, we should emphasize that both inner nodes can counteract the impact of subspace mismatch in a single bidirectional round, meaning that once the inner transmitter has identified $\mathcal{N}_0$, the opportunistic communication performance is (near) optimal.

3.5.3 Simulation Analysis

In this subsection, the active subspace detection schemes previously discussed are numerically evaluated. A total of $N = 1024$ system DoF is considered. Under subspace mismatch, the inner transmitter and the inner receiver sense different null spaces. For this evaluation, we

have considered that the effective null space $\mathcal{N}_0$ has dimension $M_0 = 128$ DoF. After sensing the wireless environment, the inner transmitter detects 192 available DoF, whereas the inner receiver senses 256 available DoF. Therefore, the normalized uncertainties at the inner transmitter and the inner receiver are $\rho_{\mathrm{T}} = 0.5$ and $\rho_{\mathrm{R}} = 1$. It is worth noting that these values are very pessimistic and probably unrealistic. They define a challenging scenario to validate the robustness of the active subspace detection schemes discussed in this section. In order to evaluate the performance of these schemes, we define the following metrics:

- Probability of Detection P_{D}:
$$P_{\mathrm{D}} \triangleq \mathbb{P}\left\{ \widehat{\mathcal{H}}_1^{(m)} \,\middle|\, \mathcal{H}_1^{(m)} \right\}, \tag{3.126}$$
i.e., the probability of detecting as *active* a DoF belonging to the effective null space $\mathcal{N}_0$.

- Probability of False-Alarm P_{FA}:
$$P_{\mathrm{FA}} \triangleq \mathbb{P}\left\{ \widehat{\mathcal{H}}_1^{(m)} \,\middle|\, \mathcal{H}_0^{(m)} \right\}, \tag{3.127}$$
i.e., the probability of detecting as *active* a DoF not belonging to $\mathcal{N}_0$.

In the sequel, the transmission of K waveforms carrying 16-QAM symbols through a channel that remains constant during the transmission is considered. Moreover, the performance of both schemes described is analyzed when $Q \geq 1$ data blocks are taken into account.

The Particular Case $K = 1$

First, we consider an opportunistic communication scenario involving only a single waveform. Even though it is the most simple case, it is useful enough to compare the performance of both active subspace detection schemes discussed in this section.

Regarding the structure-aware active subspace inference scheme described in Section 3.5.1, note that there are several options to deal with the non-convexity of the sparse optimization problem described in (3.108)–(3.109) or, equivalently, in (3.113)–(3.114). Among the different alternatives, the use of a greedy algorithm is considered. Greedy algorithms offer a fair complexity-performance trade-off and even outperform convex relaxation-based optimization schemes in some cases [EK12, Chapter 8]. In particular, the well-known Orthogonal Matching Pursuit (OMP) algorithm [Tro04; TG07; CW11] is chosen. Even though the OMP has two main drawbacks when applied to large-scale data –computation and storage costs and the number of required iterations– it can outperform its variations that deal with these two drawbacks [EK12, Chapter 8]. The OMP has basically two stopping criteria. A natural option to limit the number of iterations is the sparsity level of the vector to be recovered. Nevertheless, the sparsity level is usually unknown and has to be estimated. In the problem at hand, the sparsity level is exactly the dimension of the effective null space, which is unknown. Another typical stopping criterion, which is considered herein, is based on upper-bounding the residual error, i.e., (3.109) or, equivalently, (3.114).

Another aspect that has to be discussed is the selection of the threshold for each active subspace detection strategy. In order to set the threshold in (3.110), the output of the OMP algorithm has been analyzed. Since the objective consists in determining if the m-th dimension is active, the thresholding step in (3.110) has been tackled as the detection of an unknown

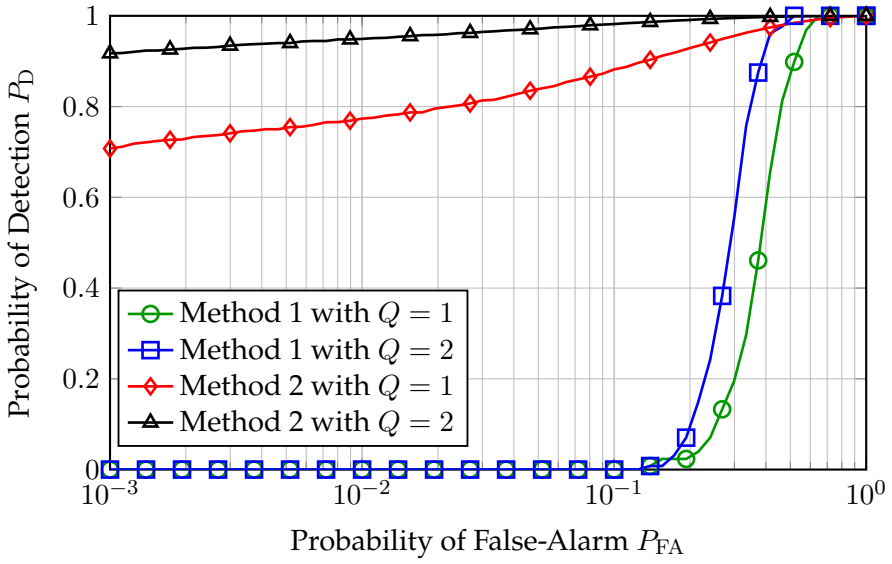

(a) $E_b/N_0 = 0$ dB.

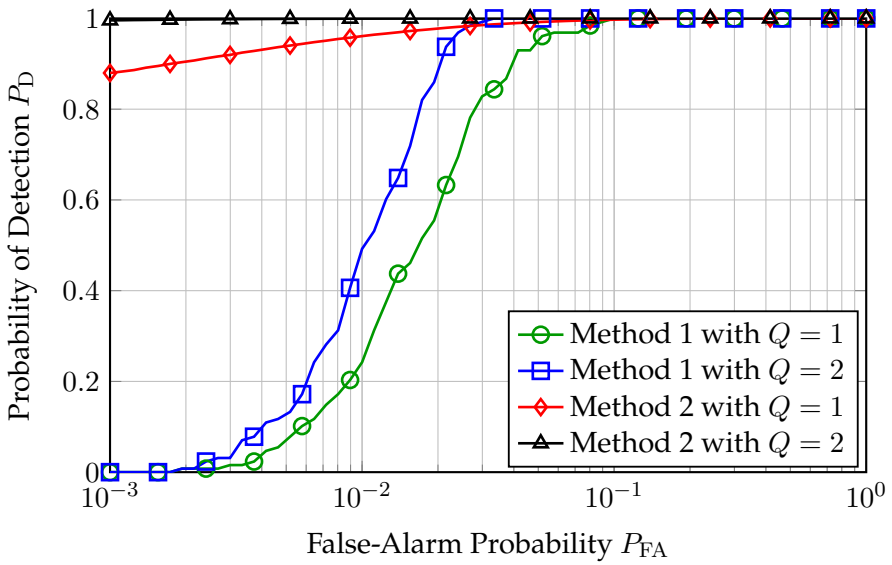

(b) $E_b/N_0 = 5$ dB.

Figure 3.20: Comparison of the Receiver Operating Characteristics of Method 1 and Method 2, corresponding to the active subspace detection schemes described in Sections 3.5.1 and 3.5.2, respectively, for different E_b/N_0.

constant in Gaussian noise [Kay98, Chapter 3]. On the other hand, the active subspace detection strategy in (3.121) has been tackled as a classical energy detection. For the sake of simplicity, the decision threshold in (3.123) or, equivalently, in (3.124)–(3.125), has been set as the square-root of the decision threshold for an energy detection problem under the Gaussian assumption[12] [VV07]. As per [Kay98, Chapter 5], $\gamma = \sqrt{Q^{-1}_{\chi^2_{2L}}(P_{\mathrm{FA}})\sigma_n^2}$, where $Q^{-1}_{\chi^2_{2L}}(\cdot)$ is the tail probability of a central Chi-square distribution with $2L$ degrees of freedom and σ_n^2 is the noise variance.

Figure 3.20 compares the Receiver Operating Characteristics (ROC) of the two active subspace detection schemes discussed in this section for different bit energy-to-noise ratio E_b/N_0. Note that *Method 1* and *Method 2* refer to the active subspace detection schemes described in Sections 3.5.1 and 3.5.2, respectively. It is worth noting that, for a given number of received blocks Q, Method 2 outperforms Method 1 regardless of the operating E_b/N_0. Nevertheless, we can observe that Method 1 exhibits a faster growth in P_{D}. A possible reason behind this observation lies in how each method obtains the test statistic for the active subspace detection problem. While Method 2 requires only a *matched filtering* stage using the sensed null-space basis at the inner receiver, Method 1 requires a greedy algorithm that can be computationally costly and inefficient in terms of storage for large-scale data. The test statistic employed by Method 1 contains inherent information on some nuisance parameters, i.e., since the test statistic is iteratively adapted to the received signal, the test statistic encompasses the scaling introduced by the signal amplitude and the information symbol. On the contrary, Method 2 treats the signal per DoF as a random variable without requiring the estimation of nuisance parameters.

In conclusion, we note that, despite its simplicity, Method 2 exhibits a better performance in terms of subspace recovery. The main reason behind this fact lies in its proven optimality in terms of mutual incoherence, which is a sufficient but not necessary condition to guarantee the recovery of a subspace. Therefore, since Method 1 is more computationally complex and is outperformed by Method 2, it will not be studied for the general case $K > 1$. Moreover, we shall recall that, in the general case, Method 1 requires incorporating the recursive nature of the waveform design scheme in Algorithm 1, becoming more computationally challenging.

The General Case $K > 1$

In the sequel, we numerically analyze the general case where opportunistic communication involves $K > 1$ waveforms, which is more attractive and realistic. Note that, for $K = 1$, Method 2 suffers from the subspace-mismatch energy loss. However, this energy loss can be counteracted thanks to the SNR gain introduced by transmitting $K > 1$ waveforms, which justifies the interest of this general case. The analysis described below aims to corroborate that, under mild operating conditions, the effective null space $\mathcal{N}_0$ can be almost perfectly identified.

For this purpose, we consider the opportunistic transmission of $K = \{1, 2, 4\}$ waveforms (equivalently, information symbols). As for the previous case, the Gaussian assumptions is considered; hence, the decisions threshold is set to $\gamma = \sqrt{Q^{-1}_{\chi^2_{2L}}(P_{\mathrm{FA}})\sigma_n^2}$. In this case, however,

[12] Even though the test statistic will not be Gaussian distributed with high probability for $K = 1$ and $Q = 1$, it will converge to a Gaussian variable as K or Q increase, which occurs with high probability at low-SNR and may occur at high-SNR for relatively small values of K and Q if the *data* has not constant modulus. Accordingly, the Gaussian assumption has been considered in all simulations for ease of discussion.

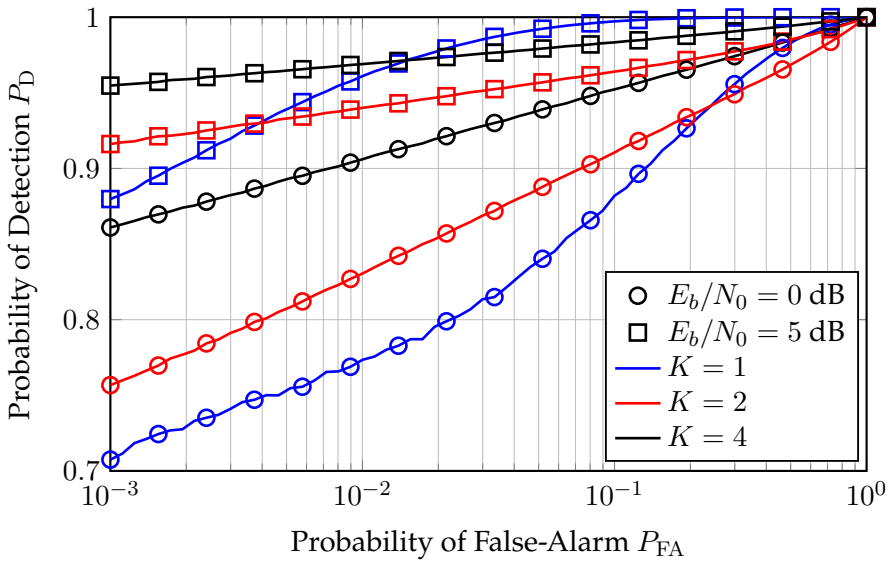

Figure 3.21: Receiver Operating Characteristics for active subspace detection with $\rho_{\mathrm{T}} = 0.5$ and $\rho_{\mathrm{R}} = 1$, for different waveforms K and E_b/N_0.

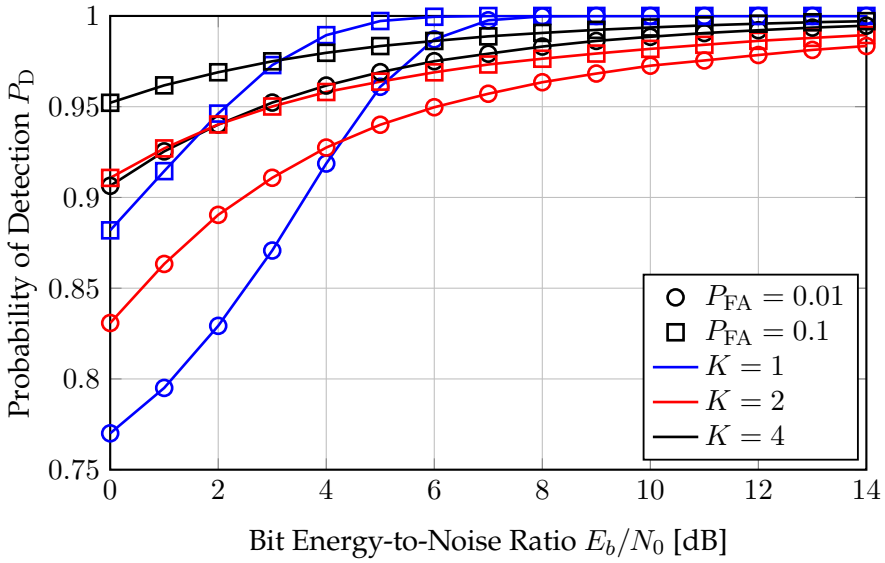

Figure 3.22: Probability of Detection (P_{D}) vs. E_b/N_0 for active subspace detection with $\rho_{\mathrm{T}} = 0.5$ and $\rho_{\mathrm{R}} = 1$, for different waveforms K and false-alarm rates.

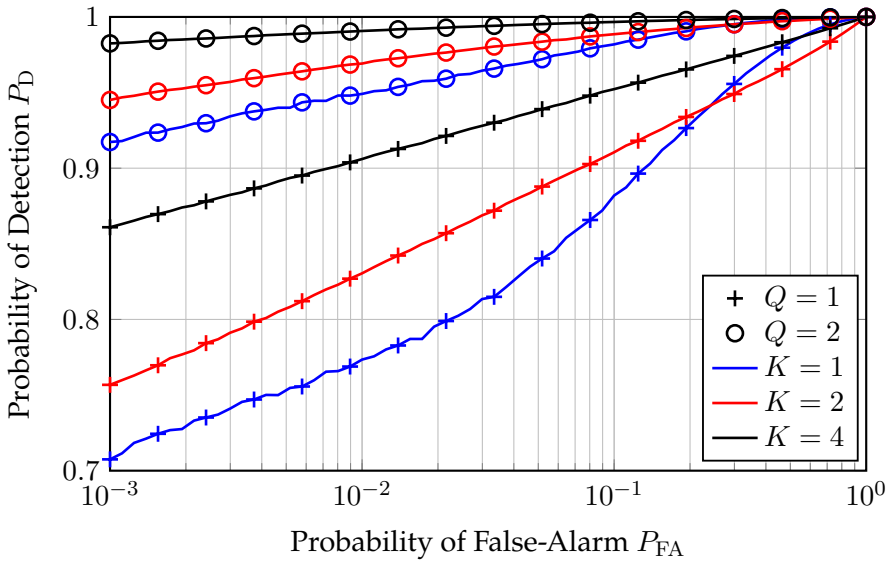

Figure 3.23: ROC for active subspace detection with $\rho_{\mathrm{T}} = 0.5$, $\rho_{\mathrm{R}} = 1$, and $E_b/N_0 = 0$ dB for different waveforms K and received blocks Q.

the Gaussian assumption holds almost surely for $K > 1$ since the information symbols are drawn from a 16-QAM constellation [VV07].

First, we study the case where the inner receiver performs the active subspace detection using only one received block, i.e., $Q = 1$. Note that this case corresponds to the use of *one sample per dimension*. Figures 3.21 and 3.22 evaluate the ROC and the probability of detection P_{D} versus the E_b/N_0, respectively, for Method 2, corresponding to (3.121)–(3.123) or, equivalently, to (3.124)–(3.125). Under challenging conditions, i.e., a low operating false-alarm rate P_{FA} and low operating E_b/N_0, the proposed active subspace detection scheme improves with K, as K introduces an SNR gain. In fact, the expected SNR improvement is $10\log_{10}(K)$ dB. This improvement is more clearly emphasized in Figure 3.22. For instance, with $P_{\mathrm{FA}} = 10^{-1}$, note that a probability of detection of $P_{\mathrm{D}} = 0.95$ is achieved at $E_b/N_0 \approx 3$ dB when $K = 2$ waveforms are transmitted, whereas an $E_b/N_0 = 0$ dB is required if $K = 4$ waveforms are used.

It is worth noting that, for $K = 1$, the model is not accurate since the Gaussian assumption does not hold, which motivates the study for $Q > 1$. Moreover, the randomness introduced by the information symbols and the noise can be averaged out in this more general case.

In Figures 3.23 and 3.24 we compare the detection performance when the inner receiver uses $Q = \{1, 2\}$ to infer the effective null space $\mathcal{N}_0$. Regarding the ROC of the proposed methodology depicted in Figure 3.23, we may observe that, even at low-SNR regimes, it is possible to achieve a probability of detection higher than 0.9 when $K = 1$ waveforms are transmitted, and the receiver accounts for $Q = 2$ received data blocks. However, it is worth noting that this improvement incurs an increased latency since the inner receiving node has to wait for the reception of Q data blocks before solving the hypothesis test.

The impact of considering $Q = \{1, 2\}$ received blocks is also illustrated in Figure 3.24, where the probability of detection is depicted versus the operating E_b/N_0. We can appreciate the peculiar behavior of P_{D} for $K = 1$ and $Q = 1$. Nevertheless, as the number of received blocks Q increases, P_{D} tends to have a more stable behavior as for the cases when $K > 1$.

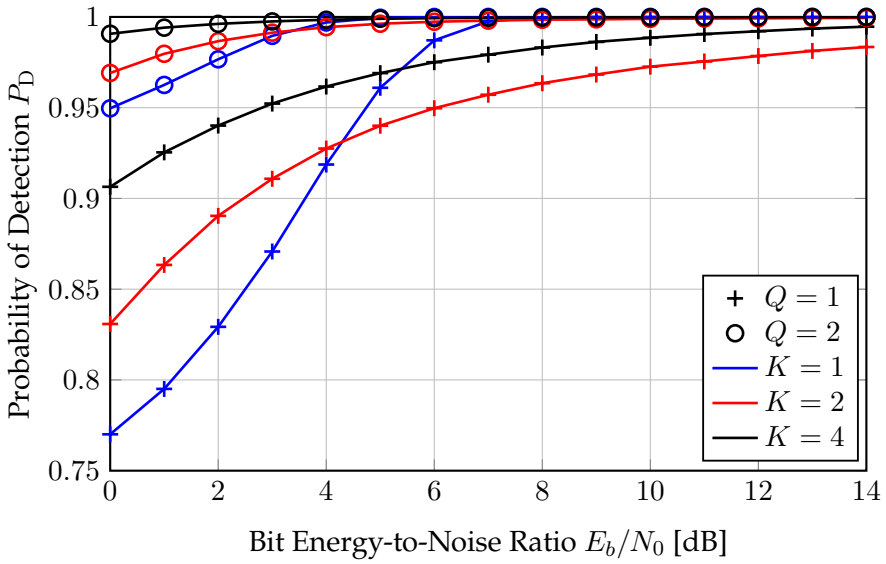

Figure 3.24: P_{D} vs. E_b/N_0 for active subspace detection with $\rho_{\mathrm{T}} = 0.5$, $\rho_{\mathrm{R}} = 1$ and $P_{\mathrm{FA}} = 0.01$ for different waveforms K and received blocks Q.

When more than one waveform is involved in opportunistic communication, the use of multiple received blocks reinforces the Gaussian assumption and provides an additional increase in SNR. The Gaussian assumption is fundamental to decreasing the complexity of the active subspace detection scheme proposed in Section 3.5.2. Suppose the inner receiver had to estimate the underlying statistical distribution of the received data. In that case, the advantages of the closed-form energy detection-based active subspace detector could be shadowed by the complexity inherent to the statistical distribution inference.

This discussion leads to a trade-off between detection performance, complexity, and latency. In most cases, using the energy-based active subspace detector (Method 2) under the Gaussian assumption is practical even if $Q = 1$ for the realistic case $K > 1$. This method admits a closed-form implementation, becoming a simple solution from a computational complexity view, and permits working at a low false-alarm rate[13] P_{FA} even at the low-SNR regime.

3.6 Conclusions

This chapter has dealt with the design of minimum-interference waveforms for feedforward opportunistic communications. In this respect, the solutions to the constrained minimization problem on the worst-case inter-system interference level have a closed-form solution; thus, they can be recursively designed. The solution to this optimization problem has been shown to be an appropriately scaled column of the orthogonal projector onto the sensed null space. Nevertheless, a recursive dimensionality reduction is required to keep the orthogonality between the designed waveforms.

Two main properties of the designed waveforms have been discussed in this chapter. On

[13] Note that false-alarm events can be more critical than miss-detection errors since the impact of the latter can be counteracted by the inner transmitter performs the active subspace identification scheme. Conversely, if the inner receiver discarded some DoF laying in $\mathcal{N}_0$, opportunistic communication would suffer from an energy loss.

the one hand, it has been shown that these waveforms minimize the total residual inter-system interference by spreading the transmitted symbols over the whole sensed null space. Asymptotically, this spreading has been proven to be uniform; thus, the same amount of energy is asymptotically allocated at each dimension of the sensed null space basis. The latter is of paramount importance in reducing the interference density per DoF. On the other hand, it has been demonstrated that the proposed waveforms are invariant to linear transformations of the sense null space basis (e.g., rotations), meaning that the proposed waveforms are unique within the sensed null space. This property permits the inner receiver to design the matched filters without cooperating nor being coordinated with the inner transmitter, which is crucial in feedforward scenarios. These two properties can be seen as improvements with respect to classic null-space waveforms; hence, the waveforms proposed in this chapter are referred to as *MNTLS waveforms*.

Even though the inner nodes can design the pulse-shaping and matched filters without coordination or cooperation, opportunistic communication may suffer from inter-node subspace mismatch. This chapter has also analyzed the impact of this subspace mismatch, highlighting the robustness of the MNTLS waveforms. Nevertheless, an enhanced detection scheme has been proposed to improve opportunistic communication performance. It has been illustrated that the system performance can improve if the inner receiver performs an active subspace detection scheme to counteract the impact of the subspace mismatch on the detectability. In this respect, two different active subspace detection schemes have been studied. Whereas one of them requires solving a non-convex sparsity-based optimization problem, the other one admits a closed-form solution that can be implemented through a bank of classic energy detectors. The performance of both active subspace detection strategies has been assessed through numerical simulations, which reveal that the energy detection-based strategy exhibits a robust performance in challenging low-E_b/N_0 regimes and a better detection performance than the sparsity-based alternative.

Appendix 3.A Proof of (3.25)

The waveform design problem addressed in this work can be tackled as in (3.20), i.e.,

$$\{\boldsymbol{\lambda}_k\}_{0\leq k\leq K-1} = \underset{\{\boldsymbol{\lambda}_k\},\{\boldsymbol{e}_k\}}{\arg\min} \left\{ \max_{\boldsymbol{E}_{\mathcal{N}}} \sum_{k=0}^{K-1} \left\| \boldsymbol{E}_{\mathcal{N}}^H \widehat{\boldsymbol{U}}_{\mathcal{N}} \boldsymbol{\lambda}_k \right\|_2^2 \right\} \tag{3.128}$$

$$\text{s.t.} \quad \|\boldsymbol{E}_{\mathcal{N}}\|_{\mathrm{F}}^2 \leq \xi^2 \tag{3.129}$$

$$\boldsymbol{\lambda}_k^H \boldsymbol{\lambda}_{k'} = 0,\ k \neq k' \tag{3.130}$$

$$\boldsymbol{\lambda}_k^H \widehat{\boldsymbol{U}}_{\mathcal{N}}^H \boldsymbol{e}_k = \alpha_k \tag{3.131}$$

Therefore, we first address the maximization with respect to $\boldsymbol{E}_{\mathcal{N}}$. Since only the constraint (3.129) involves the null-space error matrix, the Lagrangian associated with the maximization step is given by

$$\mathcal{L}\left(\boldsymbol{E}_{\mathcal{N}}, \mu\right) = \sum_{k=0}^{K-1} \left\| \boldsymbol{E}_{\mathcal{N}}^H \boldsymbol{\phi}_k \right\|_2^2 - \mu \left(\|\boldsymbol{E}_{\mathcal{N}}\|_{\mathrm{F}}^2 - \xi^2 \right), \tag{3.132}$$

where μ is the Lagrange multiplier. This quadratic problem is solved by

$$\sum_{k=0}^{K-1} \boldsymbol{\phi}_k \boldsymbol{\phi}_k^H \boldsymbol{E}_{\mathcal{N}} = \mu \boldsymbol{E}_{\mathcal{N}}. \tag{3.133}$$

Thus, the worst-case null-space error matrix $\boldsymbol{E}_{\mathcal{N}}$ is given by

$$\boldsymbol{E}_{\mathcal{N}} = \boldsymbol{\Phi} = \left[\boldsymbol{\phi}_0\ \boldsymbol{\phi}_1 \ldots \boldsymbol{\phi}_{K-1}\right], \tag{3.134}$$

i.e., the worst-case $\boldsymbol{E}_{\mathcal{N}}$ is a rank-K matrix equal to the shaping transmission matrix $\boldsymbol{\Phi}$ defined in (3.2). Note that this is indeed the worst-case scenario in which the uncertainty fully focuses on the DoF exploited by the inner transmitter. Taking into account this pessimistic case, the minimization with respect to $\{\boldsymbol{\lambda}_k\}, \{\boldsymbol{e}_k\}$ yields

$$\{\boldsymbol{\lambda}_k\}_{0\leq k\leq K-1} = \underset{\{\boldsymbol{\lambda}_k\},\{\boldsymbol{e}_k\}}{\arg\min} \sum_{k=0}^{K-1} \left\| \widehat{\boldsymbol{U}}_{\mathcal{N}} \boldsymbol{\lambda}_k \right\|_2^2 \tag{3.135}$$

$$\text{s.t.} \quad \boldsymbol{\lambda}_k^H \boldsymbol{\lambda}_{k'} = 0,\ k \neq k' \tag{3.136}$$

$$\boldsymbol{\lambda}_k^H \widehat{\boldsymbol{U}}_{\mathcal{N}}^H \boldsymbol{e}_k = \alpha_k \tag{3.137}$$

Note that this constrained minimization problem corresponds to the classic minimum-norm optimization problem (see, e.g., [KT82; KT83; DD91]). The constraints (3.136) and (3.137) have been characterized in (3.17) and (3.18)–(3.19), respectively. Letting $\{\eta_{kk'}\}$ and $\{\gamma_k\}$ be the Lagrange multipliers, the Lagrangian associated with (3.135)–(3.137) is given by

$$\mathcal{L}\left(\{\boldsymbol{\lambda}_k\}, \{\gamma_k\}, \{\eta_{kk'}\}\right) = \sum_{k=0}^{K-1} \boldsymbol{\lambda}_k^H \boldsymbol{\lambda}_k - \sum_{k'=0}^{K-1} \sum_{k=k'+1}^{K-1} \eta_{kk'} \boldsymbol{\lambda}_k^H \boldsymbol{\lambda}_{k'} - \sum_{k=0}^{K-1} \gamma_k \left[\boldsymbol{\lambda}_k^H \widehat{\boldsymbol{U}}_{\mathcal{N}}^H \boldsymbol{e}_k - \alpha_k \right]. \tag{3.138}$$

Taking the gradient of (3.138) with respect to $\boldsymbol{\lambda}_k$ and equating to zero, the $\boldsymbol{\lambda}_k$ minimizing the worst-case inter-system interference is given by

$$\boldsymbol{\lambda}_k = \gamma_k \widehat{\boldsymbol{U}}_{\mathcal{N}}^H \boldsymbol{e}_k + \sum_{k'=0}^{k-1} \eta_{kk'} \boldsymbol{\lambda}_{k'}. \tag{3.139}$$

We now have to find the Lagrange multipliers. Substituting (3.139) into (3.136), we get for $k' \leq k$

$$\boldsymbol{\lambda}_k^H \boldsymbol{\lambda}_i = \gamma_k^* \boldsymbol{e}_k^T \widehat{\boldsymbol{U}}_{\mathcal{N}} \boldsymbol{\lambda}_i + \sum_{k'=0}^{k-1} \eta_{ik'}^* \boldsymbol{\lambda}_{k'}^H \boldsymbol{\lambda}_i \overset{\text{(a)}}{=} \gamma_k^* \boldsymbol{e}_k^T \widehat{\boldsymbol{U}}_{\mathcal{N}} \boldsymbol{\lambda}_{k'} + \eta_{kk'}^* = 0, \tag{3.140}$$

where (a) is a consequence of the orthogonality constraint in (3.136), i.e., the k-th waveform has to be orthogonal with the $k-1$ waveforms previously designed. Isolating $\eta_{kk'}^*$, we have that

$$\eta_{kk'}^* = -\gamma_k^* \boldsymbol{e}_k^T \widehat{\boldsymbol{U}}_{\mathcal{N}} \boldsymbol{\lambda}_{k'}. \tag{3.141}$$

Plugging (3.141) into (3.139), we get

$$\boldsymbol{\lambda}_k = \gamma_k \left[\widehat{\boldsymbol{U}}_{\mathcal{N}}^H \boldsymbol{e}_k - \sum_{k'=0}^{k-1} \boldsymbol{\lambda}_{k'} \left(\boldsymbol{e}_k^T \widehat{\boldsymbol{U}}_{\mathcal{N}} \boldsymbol{\lambda}_{k'} \right)^* \right] = \gamma_k \left[\widehat{\boldsymbol{U}}_{\mathcal{N}}^H \boldsymbol{e}_k - \sum_{k'=0}^{k-1} \boldsymbol{\lambda}_{k'} \boldsymbol{\lambda}_{k'}^H \widehat{\boldsymbol{U}}_{\mathcal{N}}^H \boldsymbol{e}_k \right]. \tag{3.142}$$

Note that (3.142) is the $\boldsymbol{\lambda}_k$ defining the MNTLS waveforms. Thus, using (3.142) into the null-space waveform model in (3.7) and recalling that $\widehat{\boldsymbol{P}}_0 = \widehat{\boldsymbol{U}}_{\mathcal{N}} \widehat{\boldsymbol{U}}_{\mathcal{N}}^H$, the MNTLS waveforms are given by

$$\boldsymbol{\phi}_k = \gamma_k \widehat{\boldsymbol{P}}_0 \left[\boldsymbol{I}_N - \sum_{k'=0}^{k-1} \boldsymbol{\phi}_{k'} \boldsymbol{\phi}_{k'}^H \right] \boldsymbol{e}_k = \gamma_k \widehat{\boldsymbol{P}}_k \boldsymbol{e}_k. \tag{3.143}$$

It is worth noting that (3.143) is based on a column selection on the orthogonal projector $\widehat{\boldsymbol{P}}_k$. We have yet to determine the Lagrange multiplier γ_k. Substituting (3.143) into the constraint (3.137), we obtain $\gamma_k = \alpha_k \left(\boldsymbol{e}_k^T \widehat{\boldsymbol{P}}_k \boldsymbol{e}_k \right)^{-1}$. As discussed in Section 3.3, α_k can be any real number. Since we want $\boldsymbol{\phi}_k$ to be unit norm, note that $\alpha_k = \left(\boldsymbol{e}_k^T \widehat{\boldsymbol{P}}_k \boldsymbol{e}_k \right)^{1/2}$. Then,

$$\gamma_k = \left(\boldsymbol{e}_k^T \widehat{\boldsymbol{P}}_k \boldsymbol{e}_k \right)^{-1/2}. \tag{3.144}$$

The final step of this waveform design procedure is to optimize the linear prediction vector to minimize the induced inter-system interference. Plugging (3.144) into (3.143), the column of $\widehat{\boldsymbol{P}}_k$ meeting the minimum-norm condition in (3.135) is the one including the maximum diagonal element of $\widehat{\boldsymbol{P}}_k$, i.e.,

$$n(k) = \underset{n \in \{1,\ldots,N\}}{\arg\max}\ \boldsymbol{e}_k^T \widehat{\boldsymbol{P}}_k \boldsymbol{e}_k = \underset{n \in \{1,\ldots,N\}}{\arg\max} \left[\widehat{\boldsymbol{P}}_k \right]_{n(k),n(k)}. \tag{3.145}$$

Taking into account (3.143), (3.144), and (3.145), the shaping transmission matrix $\boldsymbol{\Phi} = [\boldsymbol{\phi}_0\ \boldsymbol{\phi}_1 \ldots \boldsymbol{\phi}_{K-1}]$ can be sequentially designed as in Algorithm 1.

Appendix 3.B Derivation of the Attainable Worst-Case SIR

It is worth noting that (3.60) lower-bounds the SIR, which is very pessimistic. In order to find the operating SIR, let us consider the cost function in (3.58)

$$\frac{\sum_{k=0}^{K-1}\|\boldsymbol{\phi}_k\|^2}{\sum_{k=0}^{K-1}\|\boldsymbol{E}_{\mathcal{N}}^H\boldsymbol{\phi}_k\|^2}=\mathrm{SIR}_{\mathrm{T}}\left(\boldsymbol{E}_{\mathcal{N}};\{\boldsymbol{\lambda}_k\}\right)+1\overset{\text{(a)}}{=}\frac{K}{\sum_{k=0}^{K-1}\boldsymbol{\phi}_k^H\widehat{\boldsymbol{P}}_{\mathcal{E}}\boldsymbol{\phi}_k}, \tag{3.146}$$

where (a) follows from recalling that $\|\boldsymbol{\phi}_k\|^2=1$, for $k=0,\ldots,K-1$. Using the definition of $\boldsymbol{\phi}_k$ given in (3.25), we have that

$$\left(\mathrm{SIR}_{\mathrm{T}}\left(\boldsymbol{E}_{\mathcal{N}};\{\boldsymbol{\lambda}_k\}\right)+1\right)^{-1}=\frac{1}{K}\sum_{k=0}^{K-1}\frac{\boldsymbol{e}_k^T\widehat{\boldsymbol{P}}_k\widehat{\boldsymbol{P}}_{\mathcal{E}}\widehat{\boldsymbol{P}}_k\boldsymbol{e}_k}{\boldsymbol{e}_k^T\widehat{\boldsymbol{P}}_k\boldsymbol{e}_k}=\frac{1}{K}\sum_{k=0}^{K-1}\left(\mathrm{SIR}_k\left(\boldsymbol{E}_{\mathcal{N}}\right)+1\right)^{-1}, \tag{3.147}$$

which reveals that $\left(\mathrm{SIR}_{\mathrm{T}}\left(\boldsymbol{E}_{\mathcal{N}};\{\boldsymbol{\lambda}_k\}\right)+1\right)^{-1}$ is the harmonic mean of $\{(\mathrm{SIR}_k\left(\boldsymbol{E}_{\mathcal{N}}\right)+1)\}_{0\leq k\leq K-1}$, being $\mathrm{SIR}_k\left(\boldsymbol{E}_{\mathcal{N}}\right)$ the SIR exhibited by the k-th MNTLS waveform. Recalling from Appendix 3.A that

$$\widehat{\boldsymbol{P}}_k=\widehat{\boldsymbol{P}}_0\left(\boldsymbol{I}_N-\sum_{i=0}^{k-1}\boldsymbol{\phi}_i\boldsymbol{\phi}_i^H\right), \tag{3.148}$$

(3.147) becomes

$$\left(\mathrm{SIR}_{\mathrm{T}}\left(\boldsymbol{E}_{\mathcal{N}};\{\boldsymbol{\lambda}_k\}\right)+1\right)^{-1}= \\ \frac{1}{K}\sum_{k=0}^{K-1}\frac{\boldsymbol{e}_k^T\widehat{\boldsymbol{P}}_0\left(\boldsymbol{I}_N-\sum_{i=0}^{k-1}\boldsymbol{\phi}_i\boldsymbol{\phi}_i^H\right)\widehat{\boldsymbol{P}}_{\mathcal{E}}\widehat{\boldsymbol{P}}_0\left(\boldsymbol{I}_N-\sum_{i=0}^{k-1}\boldsymbol{\phi}_i\boldsymbol{\phi}_i^H\right)\boldsymbol{e}_k}{\boldsymbol{e}_k^T\widehat{\boldsymbol{P}}_k\boldsymbol{e}_k}. \tag{3.149}$$

The denominator of (3.149) can be identified as the $n(k)$-th diagonal element of matrix $\widehat{\boldsymbol{P}}_k$. Expanding the numerator, we get

$$\boldsymbol{e}_k^T\widehat{\boldsymbol{P}}_0\widehat{\boldsymbol{P}}_{\mathcal{E}}\widehat{\boldsymbol{P}}_0\boldsymbol{e}_k-2\boldsymbol{e}_k^T\widehat{\boldsymbol{P}}_0\widehat{\boldsymbol{P}}_{\mathcal{E}}\widehat{\boldsymbol{P}}_0\sum_{i=0}^{k-1}\boldsymbol{\phi}_i\boldsymbol{\phi}_i^H\boldsymbol{e}_k+\boldsymbol{e}_k^T\widehat{\boldsymbol{P}}_0\sum_{i=0}^{k-1}\boldsymbol{\phi}_i\boldsymbol{\phi}_i^H\widehat{\boldsymbol{P}}_{\mathcal{E}}\widehat{\boldsymbol{P}}_0\sum_{i=0}^{k-1}\boldsymbol{\phi}_i\boldsymbol{\phi}_i^H\boldsymbol{e}_k. \tag{3.150}$$

Recalling that $\widehat{\boldsymbol{P}}_0=\widehat{\boldsymbol{U}}_{\mathcal{N}}\widehat{\boldsymbol{U}}_{\mathcal{N}}^H$ and $\widehat{\boldsymbol{P}}_{\mathcal{E}}=\boldsymbol{E}_{\mathcal{N}}\boldsymbol{E}_{\mathcal{N}}^H$, and noting that $\boldsymbol{E}_{\mathcal{N}}$ is encompassed in $\widehat{\boldsymbol{U}}_{\mathcal{N}}$, we have that $\widehat{\boldsymbol{P}}_0\widehat{\boldsymbol{P}}_{\mathcal{E}}=\widehat{\boldsymbol{P}}_{\mathcal{E}}$. Thus, (3.150) reads as

$$\underbrace{\left[\widehat{\boldsymbol{P}}_{\mathcal{E}}\right]_{n(k),n(k)}}_{n(k)\text{-th diagonal element of }\widehat{\boldsymbol{P}}_{\mathcal{E}}}\underbrace{-2\boldsymbol{e}_k^T\widehat{\boldsymbol{P}}_{\mathcal{E}}\sum_{i=0}^{k-1}\boldsymbol{\phi}_i\boldsymbol{\phi}_i^H\boldsymbol{e}_k+\boldsymbol{e}_k^T\sum_{i=0}^{k-1}\boldsymbol{\phi}_i\boldsymbol{\phi}_i^H\widehat{\boldsymbol{P}}_{\mathcal{E}}\sum_{i=0}^{k-1}\boldsymbol{\phi}_i\boldsymbol{\phi}_i^H\boldsymbol{e}_k}_{\text{Second-order term}}\triangleq f_k\left(\widehat{\boldsymbol{P}}_{\mathcal{E}}\right), \tag{3.151}$$

which, for simplicity, has been denoted as $f_k\left(\widehat{\boldsymbol{P}}_{\mathcal{E}}\right)$, i.e., a function that depends on the projector $\langle\boldsymbol{E}_{\mathcal{N}}\rangle$ and on the recursion index k. Finally, using (3.151) in (3.149), we have that

$$\mathrm{SIR}_{\mathrm{T}}\left(\boldsymbol{E}_{\mathcal{N}};\{\boldsymbol{\lambda}_k\}\right)=\frac{K}{\sum_{k=0}^{K-1}\frac{f_k\left(\widehat{\boldsymbol{P}}_{\mathcal{E}}\right)}{\boldsymbol{e}_k^T\widehat{\boldsymbol{P}}_k\boldsymbol{e}_k}}-1, \tag{3.152}$$

which concludes the proof.

Appendix 3.C Asymptotics of the Signal-to-Interference Density Ratio (SIDR)

Since all designed waveforms $\boldsymbol{\phi}_k$ have been normalized such that $\|\boldsymbol{\phi}_k\|^2 = 1$, the average transmitted power S_{T} defined in (3.55) is given by

$$S_{\mathrm{T}} = \frac{1}{N}\sum_{k=0}^{K-1}\|\boldsymbol{\phi}_k\|^2 = \frac{K}{N}. \tag{3.153}$$

Taking into account (3.25), and the definition of the projectors $\widehat{\boldsymbol{P}}_k$ and $\widehat{\boldsymbol{P}}_{\mathcal{E}}$, the statistically average interference power is given by

$$I_{\mathrm{T}} = \frac{1}{N}\sum_{k=0}^{K-1}\|\boldsymbol{E}_{\mathcal{N}}^H\boldsymbol{\phi}_k\|^2 = \frac{1}{N}\sum_{k=0}^{K-1}\frac{\boldsymbol{e}_k^T\widehat{\boldsymbol{P}}_k\widehat{\boldsymbol{P}}_{\mathcal{E}}\widehat{\boldsymbol{P}}_k\boldsymbol{e}_k}{\boldsymbol{e}_k^T\widehat{\boldsymbol{P}}_k\boldsymbol{e}_k}. \tag{3.154}$$

Regarding the numerator in (3.154), we have that

$$\begin{aligned}
\boldsymbol{e}_k^T\widehat{\boldsymbol{P}}_k\widehat{\boldsymbol{P}}_{\mathcal{E}}\widehat{\boldsymbol{P}}_k\boldsymbol{e}_k &= \boldsymbol{e}_k^T\widehat{\boldsymbol{P}}_0\left(\boldsymbol{I}_N - \sum_{i=0}^{k-1}\boldsymbol{\phi}_i\boldsymbol{\phi}_i^H\right)\widehat{\boldsymbol{P}}_{\mathcal{E}}\widehat{\boldsymbol{P}}_0\left(\boldsymbol{I}_N - \sum_{i=0}^{k-1}\boldsymbol{\phi}_i\boldsymbol{\phi}_i^H\right)\boldsymbol{e}_k && (3.155)\\
&= \boldsymbol{e}_k^T\widehat{\boldsymbol{P}}_0\widehat{\boldsymbol{P}}_{\mathcal{E}}\widehat{\boldsymbol{P}}_0\boldsymbol{e}_k && (3.156)\\
&- 2\boldsymbol{e}_k^T\widehat{\boldsymbol{P}}_0\widehat{\boldsymbol{P}}_{\mathcal{E}}\widehat{\boldsymbol{P}}_0\sum_{i=0}^{k-1}\boldsymbol{\phi}_i\boldsymbol{\phi}_i^H\boldsymbol{e}_k + \boldsymbol{e}_k^T\widehat{\boldsymbol{P}}_0\sum_{i=0}^{k-1}\boldsymbol{\phi}_i\boldsymbol{\phi}_i^H\widehat{\boldsymbol{P}}_{\mathcal{E}}\widehat{\boldsymbol{P}}_0\sum_{i=0}^{k-1}\boldsymbol{\phi}_i\boldsymbol{\phi}_i^H\boldsymbol{e}_k && (3.157)
\end{aligned}$$

We recognize two important terms. First, (3.156), which leads to $\boldsymbol{e}_k^T\widehat{\boldsymbol{P}}_0\widehat{\boldsymbol{P}}_{\mathcal{E}}\widehat{\boldsymbol{P}}_0\boldsymbol{e}_k = \boldsymbol{e}_k^T\widehat{\boldsymbol{P}}_{\mathcal{E}}\boldsymbol{e}_k$ since $\boldsymbol{E}_{\mathcal{N}}$ is a subset of columns of $\widehat{\boldsymbol{U}}_{\mathcal{N}}$. This term corresponds to a certain diagonal element of $\widehat{\boldsymbol{P}}_{\mathcal{E}}$. Second, (3.157), which is further on denoted as $\delta_k^{(1)}$, is a second-order term that contains combinations of off-diagonal elements of projectors $\widehat{\boldsymbol{P}}_{\mathcal{E}}$ and $\widehat{\boldsymbol{P}}_0$. Regarding to the denominator in (3.154), note that it is a certain diagonal element of projector $\widehat{\boldsymbol{P}}_k$, that reads as

$$\boldsymbol{e}_k^T\widehat{\boldsymbol{P}}_k\boldsymbol{e}_k = \boldsymbol{e}_k^T\widehat{\boldsymbol{P}}_0\boldsymbol{e}_k - \boldsymbol{e}_k^T\sum_{i=0}^{k-1}\boldsymbol{\phi}_i\boldsymbol{\phi}_i^H\boldsymbol{e}_k = \boldsymbol{e}_k^T\widehat{\boldsymbol{P}}_0\boldsymbol{e}_k + \delta_k^{(2)}, \tag{3.158}$$

where $\delta_k^{(2)}$ is also a second-order term containing combinations of off-diagonal elements of projector $\widehat{\boldsymbol{P}}_0$. Substitute (3.156), (3.157) and (3.158) into (3.154). Then, plugging the resulting expression and (3.153) into the definition of SIDR in (3.68), we have that

$$\mathrm{SIDR}_{\mathrm{T}}\left(\boldsymbol{E}_{\mathcal{N}};\{\boldsymbol{\lambda}_k\}\right) = \frac{S_T - I_T}{\frac{1}{N_E}I_T} = \frac{K - \displaystyle\sum_{k=0}^{K-1}\left(\frac{\boldsymbol{e}_k^T\widehat{\boldsymbol{P}}_{\mathcal{E}}\boldsymbol{e}_k + \delta_k^{(1)}}{\boldsymbol{e}_k^T\widehat{\boldsymbol{P}}_0\boldsymbol{e}_k + \delta_k^{(2)}}\right)}{\dfrac{1}{N_E}\displaystyle\sum_{k=0}^{K-1}\left(\frac{\boldsymbol{e}_k^T\widehat{\boldsymbol{P}}_{\mathcal{E}}\boldsymbol{e}_k + \delta_k^{(1)}}{\boldsymbol{e}_k^T\widehat{\boldsymbol{P}}_0\boldsymbol{e}_k + \delta_k^{(2)}}\right)}. \tag{3.159}$$

As per [BS16], off-diagonal elements of spectral projectors become asymptotically irrelevant in comparison with the diagonal elements. A numerical example of this property is depicted in Figure 3.25. Thus, as $N \to \infty$ and $M = \mathrm{rank}\left[\widehat{\boldsymbol{U}}_{\mathcal{N}}\right] \gg 1$, both second-order terms $\delta_k^{(1)}$ and $\delta_k^{(2)}$ can be neglected. Furthermore, taking into account the asymptotic eigendecomposition of an

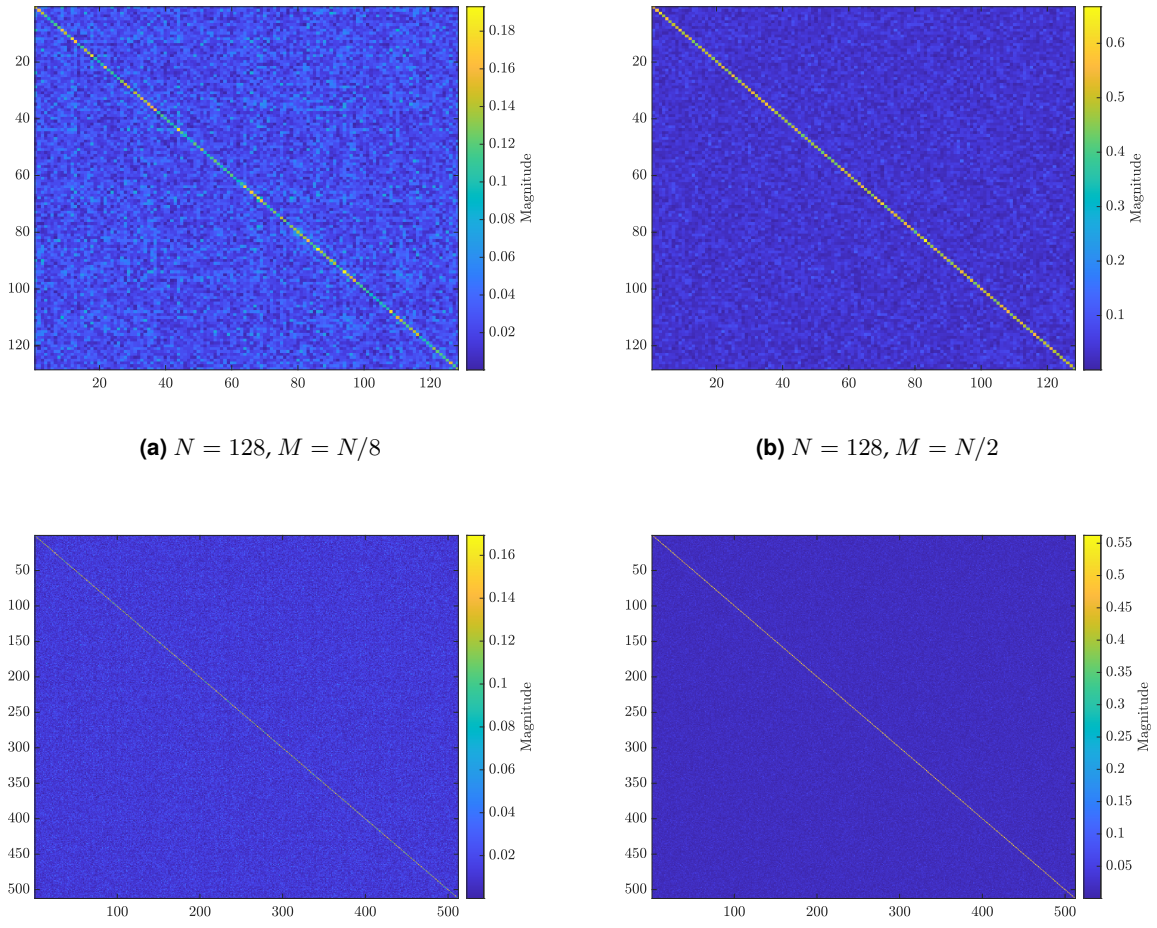

(a) $N = 128$, $M = N/8$

(b) $N = 128$, $M = N/2$

(c) $N = 512$, $M = N/8$

(d) $N = 512$, $M = N/2$

Figure 3.25: Magnitude of the entries of the projector onto an M-dimensional subspace of $\mathbb{C}^N$.

autocorrelation matrix [Gra06], the main diagonal of projectors $\widehat{\boldsymbol{P}}_0$ and $\widehat{\boldsymbol{P}}_{\mathcal{E}}$ are asymptotically constant and equal to M/N and N_E/N, respectively.

Thus, the SIDR in (3.68) can be asymptotically approximated as

$$\mathrm{SIDR}_{\mathrm{T}}\left(\boldsymbol{E}_{\mathcal{N}};\{\boldsymbol{\lambda}_k\}\right) \approx \frac{K - \displaystyle\sum_{k=0}^{K-1} \frac{\boldsymbol{e}_k^T \widehat{\boldsymbol{P}}_{\mathcal{E}} \boldsymbol{e}_k}{\boldsymbol{e}_k^T \widehat{\boldsymbol{P}}_0 \boldsymbol{e}_k}}{\dfrac{1}{N_E} \displaystyle\sum_{k=0}^{K-1} \frac{\boldsymbol{e}_k^T \widehat{\boldsymbol{P}}_{\mathcal{E}} \boldsymbol{e}_k}{\boldsymbol{e}_k^T \widehat{\boldsymbol{P}}_0 \boldsymbol{e}_k}} = \frac{K - K\frac{N_E}{M}}{\frac{1}{N_E} K \frac{N_E}{M}} = M - N_E. \tag{3.160}$$

Finally, (3.160) can be rewritten as

$$\mathrm{SIDR}_{\mathrm{T}}\left(\boldsymbol{E}_{\mathcal{N}};\{\boldsymbol{\lambda}_k\}\right) \approx N \cdot \frac{M}{N} \cdot \left(1 - \frac{N_E}{M}\right) = N \cdot \kappa \cdot (1 - \eta), \tag{3.161}$$

yielding (3.69), which concludes the proof.

Appendix 3.D The Per-DoF Energy Distribution

Each MNTLS waveform is given by $\boldsymbol{\phi}_k = \widehat{\boldsymbol{U}}_{\mathcal{N}}\boldsymbol{\lambda}_k$, where $\boldsymbol{\lambda}_k$ is the linear combination coefficients vector minimizing the worst-case induced inter-system interferences. In order to measure the energy allocated to each DoF spanning the sensed null space $\left\langle \widehat{\boldsymbol{U}}_{\mathcal{N}} \right\rangle$, we can inspect the main diagonal of the matrix

$$\boldsymbol{\Gamma}_k = \widehat{\boldsymbol{U}}_{\mathcal{N}}^H \boldsymbol{\phi}_k \boldsymbol{\phi}_k^H \widehat{\boldsymbol{U}}_{\mathcal{N}} = \boldsymbol{\lambda}_k \boldsymbol{\lambda}_k^H. \tag{3.162}$$

Recall the expression of $\boldsymbol{\lambda}_k$ found in (3.142) (Appendix 3.A). Since it depends on the optimum linear combination coefficients vectors defining the $k-1$ waveforms previously defined, the analysis of the per-DoF energy distribution would benefit from a simplification. Therefore, we can simplify (3.142) by inspection leading to

$$\boldsymbol{\lambda}_k = \gamma_k \left[\widehat{\boldsymbol{U}}_{\mathcal{N}}^H \boldsymbol{e}_k - \sum_{k'=0}^{k-1} \boldsymbol{\lambda}_{k'} \boldsymbol{\lambda}_{k'}^H \widehat{\boldsymbol{U}}_{\mathcal{N}}^H \boldsymbol{e}_k \right] = \gamma_k \widehat{\boldsymbol{U}}_{\mathcal{N}}^H \left[\boldsymbol{e}_k - \sum_{k'=0}^{k-1} \beta_{kk'} \boldsymbol{e}_{k'} \right], \tag{3.163}$$

where $\beta_{kk'}$ is a function of γ_i, for $0 \leq i \leq k'-1$, $\gamma_{k'}$, $\left[\widehat{\boldsymbol{P}}_0\right]_{kk'}$, and $\left[\widehat{\boldsymbol{P}}_0\right]_{ik'}$, for $0 \leq i \leq k'-1$. As an example, we provide next the detailed derivation for $k=2$. Particularizing the left-hand side of (3.163) for $k=2$, we have that

$$\boldsymbol{\lambda}_2 = \gamma_2 \left[\widehat{\boldsymbol{U}}_{\mathcal{N}}^H \boldsymbol{e}_2 - \boldsymbol{\lambda}_0 \boldsymbol{\lambda}_0^H \widehat{\boldsymbol{U}}_{\mathcal{N}}^H \boldsymbol{e}_2 - \boldsymbol{\lambda}_1 \boldsymbol{\lambda}_1^H \widehat{\boldsymbol{U}}_{\mathcal{N}}^H \boldsymbol{e}_2 \right], \tag{3.164}$$

where we can easily find that $\boldsymbol{\lambda}_0 = \gamma_0 \widehat{\boldsymbol{U}}_{\mathcal{N}}^H \boldsymbol{e}_0$ and $\boldsymbol{\lambda}_1 = \gamma_1 \widehat{\boldsymbol{U}}_{\mathcal{N}}^H \left[\boldsymbol{e}_1 - \gamma_0^2 \boldsymbol{e}_0^T \widehat{\boldsymbol{P}}_0 \boldsymbol{e}_1 \boldsymbol{e}_0 \right]$. Note that we can define $\beta_{10} = \gamma_0^2 \boldsymbol{e}_0^T \widehat{\boldsymbol{P}}_0 \boldsymbol{e}_1$. Therefore,

$$\boldsymbol{\lambda}_2 = \gamma_2 \left[\widehat{\boldsymbol{U}}_{\mathcal{N}}^H \boldsymbol{e}_2 - \gamma_0^2 \widehat{\boldsymbol{U}}_{\mathcal{N}}^H \boldsymbol{e}_0 \boldsymbol{e}_0^T \widehat{\boldsymbol{P}}_0 \boldsymbol{e}_2 - \gamma_1^2 \widehat{\boldsymbol{U}}_{\mathcal{N}}^H \left(\boldsymbol{e}_1 - \beta_{10} \boldsymbol{e}_0 \right) \left(\boldsymbol{e}_1^T - \beta_{10}^* \boldsymbol{e}_0^T \right) \widehat{\boldsymbol{P}}_0 \boldsymbol{e}_2 \right]. \tag{3.165}$$

Operating (3.165), let us define $\beta_{20}^{'} = \gamma_0^2 \boldsymbol{e}_0^T \widehat{\boldsymbol{P}}_0 \boldsymbol{e}_2$ and $\beta_{21}^{'} = \left[\boldsymbol{e}_1^T \widehat{\boldsymbol{P}}_0 \boldsymbol{e}_2 - \beta_{10} \boldsymbol{e}_0^T \widehat{\boldsymbol{P}}_0 \boldsymbol{e}_2 \right]$, yielding

$$\begin{aligned} \boldsymbol{\lambda}_2 = \gamma_2 \left[\widehat{\boldsymbol{U}}_{\mathcal{N}}^H \boldsymbol{e}_2 - \widehat{\boldsymbol{U}}_{\mathcal{N}}^H \boldsymbol{e}_0 \beta_{20}^{'} - \gamma_1^2 \widehat{\boldsymbol{U}}_{\mathcal{N}}^H \left(\boldsymbol{e}_1 - \beta_{10} \boldsymbol{e}_0 \right) \beta_{21}^{'} \right] = \\ \gamma_2 \widehat{\boldsymbol{U}}_{\mathcal{N}}^H \left[\boldsymbol{e}_2 - \left(\beta_{20}^{'} + \gamma_1^2 \beta_{10} \beta_{21}^{'} \right) \boldsymbol{e}_0 - \gamma_1^2 \beta_{21}^{'} \boldsymbol{e}_1 \right] \end{aligned} \tag{3.166}$$

with $\beta_{20} = \left(\beta_{20}^{'} + \gamma_1^2 \beta_{10} \beta_{21}^{'} \right)$ and $\beta_{21} = \gamma_1^2 \beta_{21}^{'}$.

This example has been included just to illustrate the difficulty of providing a closed-form expression for the scalar parameters $\beta_{kk'}$ in (3.163). Moreover, this example also justifies the necessity of simplifying the expression of $\boldsymbol{\lambda}_k$ to analyze the per-DoF energy distribution.

Plugging (3.163) in (3.162), the main diagonal of matrix $\boldsymbol{\Gamma}_k$ reads as

$$[\boldsymbol{\Gamma}_k]_{ii} = |\gamma_k|^2 \left[\left[\widehat{\boldsymbol{U}}_{\mathcal{N}}^H \boldsymbol{e}_k \boldsymbol{e}_k^T \widehat{\boldsymbol{U}}_{\mathcal{N}} \right]_{ii} + \sum_{k'=0}^{k-1} \beta_{k'}^2 \left[\widehat{\boldsymbol{U}}_{\mathcal{N}}^H \boldsymbol{e}_{k'} \boldsymbol{e}_{k'}^T \widehat{\boldsymbol{U}}_{\mathcal{N}} \right]_{ii} \right], \tag{3.167}$$

since $\operatorname{diag}\left[\boldsymbol{e}_k \boldsymbol{e}_{k'}^T \right] = \boldsymbol{0}_{N \times 1}$ for $k \neq k'$. Recalling that $\boldsymbol{e}_k$ only has a unique non-zero element and equal to one at position $n(k)$, it is straighforward to verify that $\widehat{\boldsymbol{U}}_{\mathcal{N}}^H \boldsymbol{e}_k$ is the $n(k)$-th column of matrix $\widehat{\boldsymbol{U}}_{\mathcal{N}}^H$, which is referred to as $\boldsymbol{u}_{n(k)}$.

Noting that $\left[\boldsymbol{u}_{n(k)}\boldsymbol{u}_{n(k)}^H\right]_{ii} = \left|\left[\boldsymbol{u}_{n(k)}\right]_i\right|^2$ and $\left[\boldsymbol{u}_{n(k')}\boldsymbol{u}_{n(k')}^H\right]_{ii} = \left|\left[\boldsymbol{u}_{n(k')}\right]_i\right|^2$, (3.167) leads to

$$[\boldsymbol{\Gamma}_k]_{ii} = |\gamma_k|^2 \left[\left|\left[\boldsymbol{u}_{n(k)}\right]_i\right|^2 + \sum_{k'=0}^{k-1} \beta_{k'}^2 \left|\left[\boldsymbol{u}_{n(k')}\right]_i\right|^2\right]. \tag{3.168}$$

Generally, the columns of the matrix $\widehat{\boldsymbol{U}}_{\mathcal{N}}^H$ do not have constant modulus elements, meaning that $\left|\left[\boldsymbol{u}_{n(k)}\right]_i\right| \neq \left|\left[\boldsymbol{u}_{n(k)}\right]_j\right|$ for $i \neq j$. Consequently, the k-th MNTLS waveform does not uniformly distribute the energy within the sensed null space.

Nevertheless, there is a particularly interesting case that deserves our attention. As $N \to \infty$, the eigenmatrix of an autocorrelation matrix behaves as a unitary Fourier matrix [Gra06]. Since a basis of the sensed null space can be asymptotically modeled by a Vandermonde matrix with complex exponential elements, the asymptotic behavior of the eigenvectors unveils that

$$\operatorname{diag}\left[\boldsymbol{\Gamma}_k\right] \xrightarrow[N\to\infty]{} |\gamma_k|^2 \left[1 + \sum_{k'=0}^{k-1} \beta_{k'}^2\right] \mathbf{1}_{N\times 1}, \tag{3.169}$$

meaning that the MNTLS waveforms derived in this thesis asymptotically behave as a *uniform* DoF spreading strategy.

Appendix 3.E Proof of (3.91)

Leveraging Algorithm 1 with the sensed null-space bases at the inner transmitter and the inner receiver given by (3.85) and (3.86), respectively, the shaping transmission waveform and the matched filter are given by

$$\boldsymbol{\phi}_0 = (\boldsymbol{e}_0^T \widehat{\boldsymbol{P}}_{0,\mathrm{T}} \boldsymbol{e}_0)^{-1/2} \widehat{\boldsymbol{P}}_{0,\mathrm{T}} \boldsymbol{e}_0, \tag{3.170}$$

$$\boldsymbol{\psi}_0 = (\boldsymbol{e}_0^T \widehat{\boldsymbol{P}}_{0,\mathrm{R}} \boldsymbol{e}_0)^{-1/2} \widehat{\boldsymbol{P}}_{0,\mathrm{R}} \boldsymbol{e}_0, \tag{3.171}$$

being $\widehat{\boldsymbol{P}}_{0,\mathrm{T}} = \widehat{\boldsymbol{U}}_{\mathcal{N}}(\boldsymbol{r}_{\mathrm{T}})\widehat{\boldsymbol{U}}_{\mathcal{N}}^H(\boldsymbol{r}_{\mathrm{T}})$ and $\widehat{\boldsymbol{P}}_{0,\mathrm{R}} = \widehat{\boldsymbol{U}}_{\mathcal{N}}(\boldsymbol{r}_{\mathrm{R}})\widehat{\boldsymbol{U}}_{\mathcal{N}}^H(\boldsymbol{r}_{\mathrm{R}})$ the orthogonal projectors onto $\widehat{\mathcal{N}}_{\mathrm{T}}$ and $\widehat{\mathcal{N}}_{\mathrm{R}}$, respectively. Therefore, the detection relative energy loss ratio (3.89) for $K = 1$ yields

$$\Gamma_1 = \frac{\boldsymbol{\phi}_0^H \boldsymbol{\phi}_0}{|\boldsymbol{\psi}_0^H \boldsymbol{\phi}_0|^2} = \frac{\boldsymbol{e}_0^T \widehat{\boldsymbol{P}}_{0,\mathrm{R}} \boldsymbol{e}_0 \boldsymbol{e}_0^T \widehat{\boldsymbol{P}}_{0,\mathrm{T}} \boldsymbol{e}_0}{(\boldsymbol{e}_0^T \widehat{\boldsymbol{P}}_{0,\mathrm{R}} \widehat{\boldsymbol{P}}_{0,\mathrm{T}} \boldsymbol{e}_0)^2}. \tag{3.172}$$

It is worth noting that, accounting for the inter-node subspace mismatch model described in (3.81)–(3.82), the orthogonal projectors $\widehat{\boldsymbol{P}}_{0,\mathrm{T}}$ and $\widehat{\boldsymbol{P}}_{0,\mathrm{R}}$ admit the following decomposition:

$$\widehat{\boldsymbol{P}}_{0,\mathrm{T}} = \boldsymbol{P}_{\mathcal{N}_0} + \boldsymbol{P}_{\mathcal{D}_{\mathrm{T}}}, \tag{3.173}$$

$$\widehat{\boldsymbol{P}}_{0,\mathrm{R}} = \boldsymbol{P}_{\mathcal{N}_0} + \boldsymbol{P}_{\mathcal{D}_{\mathrm{R}}}, \tag{3.174}$$

which follows from noting that $\boldsymbol{P}_{\mathcal{N}_0} = \boldsymbol{U}_{\mathcal{N}_0,\mathrm{T}}\boldsymbol{U}_{\mathcal{N}_0,\mathrm{T}}^H = \boldsymbol{U}_{\mathcal{N}_0,\mathrm{R}}\boldsymbol{U}_{\mathcal{N}_0,\mathrm{R}}^H$, since $\boldsymbol{U}_{\mathcal{N}_0,\mathrm{T}}$ and $\boldsymbol{U}_{\mathcal{N}_0,\mathrm{R}}$ are different bases of the effective null space $\mathcal{N}_0$. Note that $\boldsymbol{P}_{\mathcal{D}_{\mathrm{T}}} = \boldsymbol{\Delta}_{\mathrm{T}}\boldsymbol{\Delta}_{\mathrm{T}}^H$ and $\boldsymbol{P}_{\mathcal{D}_{\mathrm{R}}} = \boldsymbol{\Delta}_{\mathrm{R}}\boldsymbol{\Delta}_{\mathrm{R}}^H$. Hence, (3.172) yields

$$\Gamma_1 = \frac{\boldsymbol{e}_0^T(\boldsymbol{P}_{\mathcal{N}_0} + \boldsymbol{P}_{\mathcal{D}_{\mathrm{R}}})\boldsymbol{e}_0 \boldsymbol{e}_0^T(\boldsymbol{P}_{\mathcal{N}_0} + \boldsymbol{P}_{\mathcal{D}_{\mathrm{T}}})\boldsymbol{e}_0}{(\boldsymbol{e}_0^T \boldsymbol{P}_{\mathcal{N}_0} \boldsymbol{e}_0)^2}. \tag{3.175}$$

It is straightforward to see that (3.175) depends on the diagonal elements of $\boldsymbol{P}_{\mathcal{N}_0}$, $\boldsymbol{P}_{\mathcal{D}_{\mathrm{T}}}$, and $\boldsymbol{P}_{\mathcal{D}_{\mathrm{R}}}$, which nothing can be said a priori. Nevertheless, if we take into account that the sensed null-space bases asymptotically converge to a column subset of the normalized Fourier matrix [Gra06], the main diagonal of the orthogonal projectors in (3.173)–(3.174) is asymptotically constant and equal to $[\boldsymbol{P}_{\mathcal{N}_0}]_{nn} = M_0/N$, $[\boldsymbol{P}_{\mathcal{E}_{\mathrm{T}}}]_{nn} = \kappa_{\mathrm{T}}/N$, and $[\boldsymbol{P}_{\mathcal{E}_{\mathrm{R}}}]_{nn} = \kappa_{\mathrm{R}}/N$. Defining the normalized uncertainties at the inner transmitter and at the inner receiver as $\rho_{\mathrm{T}} \triangleq \kappa_{\mathrm{T}}/M_0$ and $\rho_{\mathrm{R}} \triangleq \kappa_{\mathrm{R}}/M_0$, (3.175) leads to

$$\Gamma_1 \xrightarrow[N\to\infty]{} \frac{(M_0 + \kappa_{\mathrm{R}})(M_0 + \kappa_{\mathrm{T}})}{M_0^2} = 1 + \rho_{\mathrm{T}} + \rho_{\mathrm{R}} + \rho_{\mathrm{T}}\rho_{\mathrm{R}}, \tag{3.176}$$

which completes the proof.

Appendix 3.F Analysis of the Sparse Optimization in (3.108)–(3.109)

3.F.1 Conditions to Guarantee the Recovery of Sparse Signals

Let us consider the following signal model

$$\boldsymbol{y} = \boldsymbol{\Omega}\boldsymbol{x} + \boldsymbol{\varepsilon}, \tag{3.177}$$

where $\boldsymbol{y} \in \mathbb{C}^n$ is the observation vector; $\boldsymbol{\Omega} \in \mathbb{C}^{n\times m}$, with usually $n \ll m$, is the measurement or sensing matrix; $\boldsymbol{x} \in \mathbb{C}^m$ is a k-sparse signal, meaning that only k out of m entries are non-zero; and $\boldsymbol{\varepsilon} \in \mathbb{C}^n$ is the measurement noise. The objective in compressed sensing consists in recovering the k-sparse signal $\boldsymbol{x}$ given the observation $\boldsymbol{y}$ and the measurement matrix $\boldsymbol{\Omega}$.

A fundamental problem in compressed sensing consists in assessing the recovery guarantees of the sparse signal $\boldsymbol{x}$. In the literature, several criteria have been studied for this purpose (see, e.g., [EK12; FR13]), which mainly assess the suitability of the designed measurement matrix $\boldsymbol{\Omega}$ for recovering the sparse signal $\boldsymbol{x}$. In the sequel, we review some of these criteria that will be used afterward to assess the recovery guarantees for the sparse problem at hand (3.108)–(3.109).

One of the most important criteria for guaranteeing the recovery of sparse signals is the so-called *null-space property* [CDD09]. The null space of the measurement matrix $\boldsymbol{\Omega}$ is defined as

$$\mathcal{N}(\boldsymbol{\Omega}) \triangleq \{\boldsymbol{x} \,:\, \boldsymbol{\Omega}\boldsymbol{x} = 0\}. \tag{3.178}$$

It is said that the measurement matrix $\boldsymbol{\Omega}$ satisfies the null-space property of order k if there exists a constant $\Xi > 0$ such that, for all $\boldsymbol{x} \in \mathcal{N}(\boldsymbol{\Omega})$,

$$\|\boldsymbol{x}_{\mathcal{I}}\|_2 \leq \Xi \frac{\|\boldsymbol{x}_{\overline{\mathcal{I}}}\|_1}{\sqrt{k}}, \tag{3.179}$$

for any set of indices $\mathcal{I}$ satisfying $|\mathcal{I}| \leq k$. Note that $\boldsymbol{x}_{\mathcal{I}}$ means that only the indices encompassed in $\mathcal{I}$ are non-zero. This property guarantees that any vector belonging to $\mathcal{N}(\boldsymbol{\Omega})$ is not *too compressible in addition to vectors that are sparse* [EK12], meaning that the sparse recovery algorithm do not confuse the sparse vector with a vector laying in $\mathcal{N}(\boldsymbol{\Omega})$. The null-space property (3.179) is a necessary and sufficient condition to guarantee the recovery of sparse signals using convex relaxations. The *spark* [DE03] is one option to characterize the null-space property. The spark of a matrix $\boldsymbol{\Omega}$ is the smallest number of columns from $\boldsymbol{\Omega}$ that are linearly dependent. As per [DE03], the sparse recovery problem has a unique sparsest solution $\boldsymbol{x}$ satisfying

$$\text{spark}[\boldsymbol{\Omega}] > 2\|\boldsymbol{x}\|_0 = 2k, \tag{3.180}$$

where k is the number of non-zero elements of $\boldsymbol{x}$. Unfortunately, the computation of the spark or the null-space property is complex [TP14]. Moreover, even though the null-space property is a necessary and sufficient condition for recovering the sparse vector $\boldsymbol{x}$, it does not account for the presence of noise in the observations.

A more computationally efficient criterion to assess the recovery guarantees of k-sparse signals is the *mutual coherence* [DH01; MZ93], sometimes referred to as *coherence*. The mutual coherence of a matrix $\boldsymbol{\Omega}$ is defined as

$$\mu(\boldsymbol{\Omega}) = \max_{\substack{i\neq j \\ i,j=1,\ldots,m}} \frac{\left|\boldsymbol{\omega}_i^H \boldsymbol{\omega}_j\right|}{\|\boldsymbol{\omega}_i\|_2 \|\boldsymbol{\omega}_j\|_2}, \tag{3.181}$$

i.e., the largest absolute value of the inner products between two distinct columns $\boldsymbol{\omega}_i$ and $\boldsymbol{\omega}_j$ of matrix $\boldsymbol{\Omega}$. Regarding (3.181), a lower bound on the mutual coherence is provided in [Wel74], known as Welch bound. Thus,

$$\mu\left(\boldsymbol{\Omega}\right) \in \left[\sqrt{\frac{m-n}{n(m-1)}}, 1\right], \tag{3.182}$$

where n and m are the numbers of rows and columns of the matrix $\boldsymbol{\Omega}$, respectively. An interesting result concerning the mutual coherence is that a k-sparse signal can be exactly recovered with noisy observations if it meets the mutual incoherent property of the noiseless case [CWX10], i.e.

$$\mu\left(\boldsymbol{\Omega}\right) < \frac{1}{2k-1}; \tag{3.183}$$

however, it is a sharp condition. Moreover, as per [DE03], the mutual coherence and the spark are related as follows:

$$\operatorname{spark}[\boldsymbol{\Omega}] \geq 1 + \mu^{-1}\left(\boldsymbol{\Omega}\right). \tag{3.184}$$

In the context of subspace recovery, the mutual incoherence property is a sufficient condition to guarantee the inference of the subspace.

The last recovery guarantee criterion we are reviewing is the so-called Restricted Isometry Property (RIP). As originally defined in [CT05], matrix $\boldsymbol{\Omega}$ obeys the RIP with a restricted isometry constant $\delta_k \in (0,1)$ if

$$\left(1-\delta_k\right)\left\|\boldsymbol{x}\right\|_2^2 \leq \left\|\boldsymbol{\Omega}\boldsymbol{x}\right\|_2^2 \leq \left(1+\delta_k\right)\left\|\boldsymbol{x}\right\|_2^2, \tag{3.185}$$

for all k-sparse vectors and a sufficiently small δ_k for large enough k. This property (3.185) requires that every column set with cardinality less than or equal to k behaves as an orthonormal system. The RIP has been also used to study the stability of the sparse optimization problem and to verify the null-space property [EK12].

3.F.2 Recovery Guarantees for (3.108)–(3.109)

Once we have reviewed some of the criteria to assess the recovery guarantees of sparse signals, we analyze the sparse recovery guarantees for the sparse optimization problem stated in (3.108)–(3.109).

Taking into account the relationship between the spark and the mutual coherence, we begin studying the mutual coherence of the measurement matrix $\boldsymbol{\Pi}$ defined in (3.99). Recalling the definition of $\boldsymbol{\Pi}$, we note that it is a block matrix where each block is a rank-one orthogonal projector onto one dimension of the sensed null space at the inner receiver. Since the M_{R} dimensions of $\widehat{\mathcal{N}}_{\mathrm{R}}$ are orthogonal, it follows that

$$\widehat{\boldsymbol{P}}_m(\boldsymbol{r}_{\mathrm{R}})\widehat{\boldsymbol{P}}_n(\boldsymbol{r}_{\mathrm{R}}), \text{ for } m \neq n. \tag{3.186}$$

Thus, we have that

$$\mu\left(\boldsymbol{\Pi}\right) = \max_{m=1,\ldots,M_{\mathrm{R}}} \mu\left(\widehat{\boldsymbol{P}}_m(\boldsymbol{r}_{\mathrm{R}})\right). \tag{3.187}$$

A priori, nothing can be said. However, as $N \to \infty$, the sensed null-space basis at the inner receiver converges to a column subset of the normalized Fourier matrix $\boldsymbol{F}_N$ [Gra06]. Therefore,

since all entries of $\widehat{\boldsymbol{P}}_m(\boldsymbol{r}_{\mathrm{R}})$, for $m = 1, \ldots, M_{\mathrm{R}}$, are combinations of complex exponentials, we have that

$$\|\widehat{\boldsymbol{p}}_{m,i}(\boldsymbol{r}_{\mathrm{R}})\|_2 = 1/N \text{ for } i = 1, \ldots, N, \tag{3.188}$$

where $\widehat{\boldsymbol{p}}_{m,i}(\boldsymbol{r}_{\mathrm{R}})$ denotes the i-th column of $\widehat{\boldsymbol{P}}_m(\boldsymbol{r}_{\mathrm{R}})$. Regarding the inner product in the numerator of (3.181), since the orthogonal projector is Hermitian and idempotent, the absolute value of the inner product between two distinct columns i and j, with $i, j = 1, \ldots, N$, equals the absolute value of the ij-th entry of the orthogonal projector. Thus,

$$\left|\widehat{\boldsymbol{p}}_{m,i}^H(\boldsymbol{r}_{\mathrm{R}})\widehat{\boldsymbol{p}}_{m,j}(\boldsymbol{r}_{\mathrm{R}})\right| = 1/N, \tag{3.189}$$

meaning that

$$\mu\left(\boldsymbol{\Pi}\right) = 1. \tag{3.190}$$

Recalling to (3.183), and since the vector $\boldsymbol{\beta}$ is an M_0-sparse vector, note that the measurement matrix $\boldsymbol{\Pi}$ does not satisfy the sharp condition. Taking into account (3.180) and (3.184), nothing can be said on the spark.

Finally, we study the RIP (3.185). Using the measurement vector $\boldsymbol{\Pi}$ and the M_0-sparse vector $\boldsymbol{\beta}$, we have that

$$\left(1 - \delta_{M_0}\right)\|\boldsymbol{\beta}\|_2^2 \leq \|\boldsymbol{\Pi}\boldsymbol{\beta}\|_2^2 \leq \left(1 + \delta_{M_0}\right)\|\boldsymbol{\beta}\|_2^2. \tag{3.191}$$

Recall that vector $\boldsymbol{\beta}$ is structured as in (3.100), but the binary nature of $\boldsymbol{\beta}$ has been relaxed to avoid the binary sparse recovery framework and the necessity of estimating nuisance parameters. Thus, we can write $\boldsymbol{\beta}$ as

$$\boldsymbol{\beta} = \widetilde{\boldsymbol{\mu}} \otimes \boldsymbol{e}_0 \in \mathbb{C}^{NM_{\mathrm{R}}}, \tag{3.192}$$

with $\widetilde{\boldsymbol{\mu}} \in \mathbb{C}^{M_{\mathrm{R}}}$. Therefore, we have that

$$\|\boldsymbol{\beta}\|_2^2 = \boldsymbol{\beta}^H\boldsymbol{\beta} = \left(\widetilde{\boldsymbol{\mu}} \otimes \boldsymbol{e}_0\right)^H\left(\widetilde{\boldsymbol{\mu}} \otimes \boldsymbol{e}_0\right) = \left(\widetilde{\boldsymbol{\mu}}^H\widetilde{\boldsymbol{\mu}}\right) \otimes \left(\boldsymbol{e}_0^T\boldsymbol{e}_0\right) = \|\widetilde{\boldsymbol{\mu}}\|_2^2. \tag{3.193}$$

As nothing can be said about the measurement matrix for finite N, we consider again the asymptotic behavior of the sensed null-space basis. Hence,

$$\|\boldsymbol{\Pi}\boldsymbol{\beta}\|^2 = \boldsymbol{\beta}^H\boldsymbol{\Pi}^H\boldsymbol{\Pi}\boldsymbol{\beta} \tag{3.194}$$

$$= \left[\widetilde{\mu}_1^*\boldsymbol{e}_0^T \cdots \widetilde{\mu}_{M_{\mathrm{R}}}^*\boldsymbol{e}_0^T\right]\begin{bmatrix} \widehat{\boldsymbol{P}}_1(\boldsymbol{r}_{\mathrm{R}}) & & \boldsymbol{0} \\ & \ddots & \\ \boldsymbol{0} & & \widehat{\boldsymbol{P}}_{M_{\mathrm{R}}}(\boldsymbol{r}_{\mathrm{R}}) \end{bmatrix}\begin{bmatrix} \widetilde{\mu}_1\boldsymbol{e}_0 \\ \vdots \\ \widetilde{\mu}_{M_{\mathrm{R}}}\boldsymbol{e}_0 \end{bmatrix} = \frac{1}{N}\|\widetilde{\boldsymbol{\mu}}\|_2^2. \tag{3.195}$$

Plugging (3.193) and (3.195) into (3.191), note that

$$\frac{1}{1 - \delta_{M_0}} \geq N \geq \frac{1}{1 + \delta_{M_0}}. \tag{3.196}$$

While the lower bound always holds, the upper bound is not satisfied for sufficiently small δ_{M_0}. If M_0 decreases, larger values of δ_{M_0} are admissible to guarantee the recovery of $\boldsymbol{\beta}$ under the RIP. However, the required value of δ_{M_0} depends on the considered strategy to solve the sparse optimization problem. For instance, the well-known *orthogonal matching pursuit* (OMP) [Tro04; TG07; CW11] can recover k-sparse vectors with $\delta_{k+1} < (\sqrt{k} - 1)^{-1}$ [WS12]. In the problem at hand, the exact recovery of $\boldsymbol{\beta}$ requires extremely small (impractical) values of M_0.

CHAPTER 4

Asymptotic Study: Frequency Domain and Frequency-Selective Channels

4.1 Introduction

This chapter studies the asymptotic behavior of the MNTLS waveforms, which is of relevant interest for practical implementations. Interestingly, as the number of total DoF N increases [YXXL19; BJA21; WBV21], the MNTLS waveforms converge to linear combinations of column subsets of the normalized N-size Fourier matrix. The similarities with Orthogonal Frequency-Division Multiple-access (OFDMA) implementation open the possibility of adapting the MNTLS waveforms in the cumbersome frequency-selective channels. The solution stands out for its simplicity compared to other null space-based opportunistic transmission schemes specifically developed in frequency-selective environments.

This chapter is organized as follows. A literature review on null-space opportunistic communications in frequency-selective channels is provided in Section 4.2. Section 4.3 studies the asymptotic behavior of the MNTLS waveforms. When the sensed as available DoF are consecutive, a particular case arises giving birth to the Circulant-Shaping Time-Division Multiple-Access (CS-TDMA) scheme, which is discussed in Section 4.4. The problem of opportunistic transmission through frequency-selective channels is analyzed in Section 4.5. Finally, this chapter is concluded in Section 4.6.

4.2 Null Space-based Opportunistic Precoding in Frequency-Selective Channels

In the context of null-space opportunistic communications under frequency-selective channels, Vandermonde-Subspace Frequency-Division Multiplexing (VFDM) is an interference alignment-like strategy that enables ideally interference-free opportunistic communication exploiting the null space induced by the channel memory. VFDM has been well-studied [CKCD13], improved

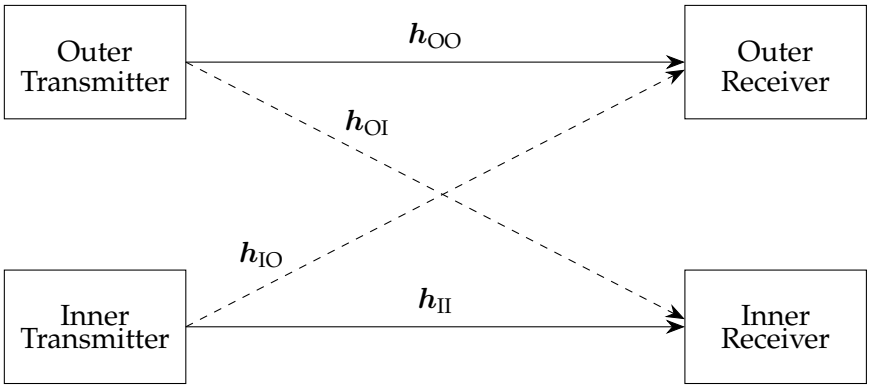

Figure 4.1: The two-user cognitive interference channel model adapted from [CKCD13]. In this context, all involved channels are frequency selective, i.e., $(L_h + 1)$-length vectors, being L_h the channel memory.

[LFP+20], and considered in recent technical works to enable the coexistence of Long Term Evolution (LTE) and New Radio (NR) systems [FPM+20]. Nevertheless, some relevant weaknesses motivate investigating other potential alternatives. Before starting the technical discussion, it is interesting to review the VFDM modulation in detail to outline the main differences concerning what is proposed in this chapter.

For the sake of simplicity, this literature review is based on the simple 2-user cognitive interference channel [CKCD13] depicted in Figure 4.1. The extension to multi-user scenarios can be found in [MDV13] and references therein.

VFDM modulation is a null space-based opportunistic transmission strategy aiming at nulling the inter-system interference caused by the inner transmitter on the outer receiver, provided through channel $\boldsymbol{h}_{\mathrm{IO}}$. Therefore, the outer-system information rate will not be limited by the interference leaked by inner nodes. In contrast, the inner system is subject to inter-system interference imposed by the outer transmitter through channel $\boldsymbol{h}_{\mathrm{OI}}$. For this purpose, the inner system exploits the frequency selectivity and the guard symbols (e.g., the cyclic prefix) employed by the outer system's block-transmission modulation (e.g., OFDM).

More formally, let $\boldsymbol{s}_{\mathrm{I}}$ be the symbol vector sent by the inner transmitter and $\boldsymbol{\Phi}$ the inner precoding matrix to be designed. The signal sent by the inner transmitter is given by

$$\boldsymbol{x}_{\mathrm{I}} = \boldsymbol{\Phi}\boldsymbol{s}_{\mathrm{I}}. \tag{4.1}$$

In order to avoid inducing interferences on the outer-network receiver, the inner precoding matrix must guarantee that $\boldsymbol{x}_{\mathrm{I}}$ lies on the outer-receiver null space. Therefore, in mathematical terms, the objective of the inner transmitter consists in designing a precoding matrix $\boldsymbol{\Phi}$ satisfying

$$\boldsymbol{F}_N \boldsymbol{H}_{\mathrm{IO}} \boldsymbol{\Phi} \boldsymbol{s}_{\mathrm{I}} = \boldsymbol{0}, \tag{4.2}$$

where $\boldsymbol{F}_N$ is the N-size Fourier matrix used by the outer receiver as a combining matrix and $\boldsymbol{H}_{\mathrm{IO}} \in \mathbb{C}^{N \times (N+L_h)}$ is a Toeplitz matrix containing the coefficients of the channel $\boldsymbol{h}_{\mathrm{IO}}$, that is,

$$\boldsymbol{H}_{\mathrm{IO}} = \begin{bmatrix} h_{\mathrm{IO}}[L_h] & \cdots & h_{\mathrm{IO}}[0] & 0 & \cdots & 0 \\ 0 & \ddots & \ddots & \ddots & \ddots & \vdots \\ \vdots & \ddots & \ddots & \ddots & \ddots & 0 \\ 0 & \cdots & 0 & h_{\mathrm{IO}}[L_h] & \cdots & h_{\mathrm{IO}}[0] \end{bmatrix}. \tag{4.3}$$

It is worth noting that (4.2) is satisfied when the precoding matrix lies in the null space of $\boldsymbol{H}_{\mathrm{IO}}$, whose dimensionality is equal to L_h, i.e., the channel memory. Thus, the precoding matrix $\boldsymbol{\Phi}$ is an $(N + L_h) \times L_h$ complex matrix. As per [CKCD13], the precoding matrix $\boldsymbol{\Phi}$ can be found, for instance, through the singular value decomposition of (4.3). Note that the available DoF for opportunistic communication depends on the channel memory.

Regarding the inner receiver, the conventional receiving strategy for OFDM modulation is used, that is, cyclic prefix removal and Discrete Fourier Transform (DFT). Thus, the signal model at the inner receiver reads as

$$\boldsymbol{y}_{\mathrm{I}} = \boldsymbol{F}_N \left(\boldsymbol{H}_{\mathrm{II}} \boldsymbol{\Phi} \boldsymbol{s}_{\mathrm{I}} + \boldsymbol{i} + \boldsymbol{n} \right) = \boldsymbol{F}_N \boldsymbol{H}_{\mathrm{II}} \boldsymbol{\Phi} \boldsymbol{s}_{\mathrm{I}} + \boldsymbol{z}, \tag{4.4}$$

where $\boldsymbol{H}_{\mathrm{II}}$ is the Toeplitz matrix similar to (4.3) but containing the coefficients of the inner channel $\boldsymbol{h}_{\mathrm{II}}$, $\boldsymbol{i}$ is the inter-system interference induced by the outer-network transmitter, and $\boldsymbol{n} \sim \mathcal{N}_{\mathbb{C}}(\boldsymbol{0}_{N\times 1}, \sigma_n^2 \boldsymbol{I}_N)$ is the additive noise.

Regarding (4.4), note that the inner receiver suffers from the inter-system interference caused by the outer transmitter since the employed receiving strategy cannot counteract them. Moreover, the designed precoding matrix $\boldsymbol{\Phi}$ can avoid inducing inter-system interferences on the outer-network receiver, but cannot combat the frequency selectivity of the inner channel $\boldsymbol{h}_{\mathrm{II}}$. Thus, additional transmit processing is required. In particular, for a given precoding matrix $\boldsymbol{\Phi}$ satisfying (4.2), the inner transmitter has to design a codebook matrix $\boldsymbol{S}_{\mathrm{I}} = \mathbb{E}\left[\boldsymbol{s}_{\mathrm{I}} \boldsymbol{s}_{\mathrm{I}}^H\right]$, that is, the covariance of the transmitted information symbols $\boldsymbol{s}_{\mathrm{I}}$, satisfying

$$\max_{\boldsymbol{S}_{\mathrm{I}}} \quad \frac{1}{N + L_h} \log_2 \left(\det \left[\boldsymbol{I}_N + \boldsymbol{S}_z^{-1/2} \boldsymbol{F}_N \boldsymbol{H}_{\mathrm{II}} \boldsymbol{\Phi} \boldsymbol{S}_{\mathrm{I}} \boldsymbol{\Phi}^H \boldsymbol{H}_{\mathrm{II}}^H \boldsymbol{F}_N^H \boldsymbol{S}_z^{-H/2} \right] \right) \tag{4.5}$$

$$\text{subject to} \quad \mathrm{tr}\left(\boldsymbol{\Phi}^H \boldsymbol{\Phi} \boldsymbol{S}_{\mathrm{I}} \right) \leq (N + L_h) P_{\mathrm{I}} \tag{4.6}$$

where $\boldsymbol{S}_z = \mathbb{E}\left[\boldsymbol{z}\boldsymbol{z}^H\right]$ is the interference-plus-noise covariance matrix and P_{I} is a power constraint. The approach considered in [CKCD13] consists in designing a matrix $\boldsymbol{S}_{\mathrm{I}}$ to leverage the water-filling solution, which is known to be capacity-achieving.

It is worth noting that, in addition to the interference channel matrix $\boldsymbol{H}_{\mathrm{IO}}$, the inner transmitter requires knowing the inner channel matrix $\boldsymbol{H}_{\mathrm{II}}$ and the interference-plus-noise covariance matrix $\boldsymbol{S}_z$. In order to acquire this side information, the inner nodes must cooperate. Even though channel estimation has been used in the related literature (see, for instance, [CKCD13; LFP+20]), robust designs for the VFDM precoding matrix have not been proposed in the sense of minimizing the inter-system interference caused by the inner transmitter on the outer receiver. Apart from the required side information at the inner transmitter, we must recall that the inner receiver cannot mitigate the inter-system interference caused by the outer transmitter.

4.3 Asymptotic Analysis of the MNTLS Waveforms

This section discusses the asymptotic behavior of the MNTLS waveforms derived in Chapter 3. Without loss of generality, the whole discussion is focused on the inner transmitting node. Regarding the matched-filtering waveforms, their asymptotic characterization follows the same rationale as for the transmitting pulse-shaping waveforms case.

Let us begin reviewing that these waveforms obey the following model:

$$\boldsymbol{\phi}_k = \gamma_k \widehat{\boldsymbol{P}}_k \boldsymbol{e}_k = \gamma_k \widehat{\boldsymbol{P}}_0 \left(\boldsymbol{I}_N - \sum_{i=0}^{k-1} \boldsymbol{\phi}_i \boldsymbol{\phi}_i^H \right) \boldsymbol{e}_k, \tag{4.7}$$

where $\widehat{\boldsymbol{P}}_0 = \widehat{\boldsymbol{U}}_{\mathcal{N}} \widehat{\boldsymbol{U}}_{\mathcal{N}}^H$ denotes the orthogonal projector onto the sensed null space. As discussed in Chapter 3, the sensed null-space basis $\widehat{\boldsymbol{U}}_{\mathcal{N}}$ is a column subset of the eigenmatrix of a sample estimate observations' autocorrelation matrix. If the estimate is accurate enough, it converges to the exact autocorrelation matrix of the observations, which is a Toeplitz matrix.

A well-known consequence of the Szegö's Limit Theorem is that asymptotically, as $N \to \infty$, Toeplitz matrices behave as circulant matrices [Gra06]. Accordingly, as the number of system DoF N arbitrarily grows, the autocorrelation matrix tends to be circulant. Interestingly, circulant matrices have a very particular eigendecomposition given by

$$\boldsymbol{R}_{\boldsymbol{xx}} \xrightarrow[N \to \infty]{} \boldsymbol{F}_N^H \boldsymbol{\Lambda}_F \boldsymbol{F}_N, \tag{4.8}$$

where $\boldsymbol{\Lambda}_F$ is a diagonal matrix containing the signal power spectral density distribution, and $\boldsymbol{F}_N$ is the N-size unitary Fourier matrix given by

$$\boldsymbol{F}_N = \frac{1}{\sqrt{N}} \begin{bmatrix} 1 & 1 & 1 & 1 & \cdots & 1 \\ 1 & \zeta & \zeta^2 & \zeta^3 & \cdots & \zeta^{N-1} \\ 1 & \zeta^2 & \zeta^4 & \zeta^6 & \cdots & \zeta^{2(N-1)} \\ \vdots & \vdots & \vdots & \vdots & \ddots & \vdots \\ 1 & \zeta^{(N-1)} & \zeta^{2(N-1)} & \zeta^{3(N-1)} & \cdots & \zeta^{(N-1)^2} \end{bmatrix}, \tag{4.9}$$

being $\zeta = e^{-j2\pi/N}$ a primitive N-th root of the unity. A direct consequence of this decomposition is the sensed null-space basis[1] is asymptotically composed of a column subset of $\boldsymbol{F}_N^H$. Therefore, the orthogonal projector $\widehat{\boldsymbol{P}}_0$ can be asymptotically written as

$$\widehat{\boldsymbol{P}}_0 = \sum_{m \in \mathcal{I}_{\mathcal{N}}} \boldsymbol{f}_m \boldsymbol{f}_m^H, \tag{4.10}$$

with $\boldsymbol{f}_m$ the m-th column of $\boldsymbol{F}^H$ and $\mathcal{I}_{\mathcal{N}}$ the set of integers indexing the available frequency bins, which is given by

$$\mathcal{I}_{\mathcal{N}} \triangleq \left\{ m \;\; : \;\; \boldsymbol{f}_m \in \left\langle \widehat{\boldsymbol{U}}_{\mathcal{N}} \right\rangle \right\}. \tag{4.11}$$

It is worth noting that, asymptotically, the projector $\widehat{\boldsymbol{P}}_0$ in (4.10) is a circulant matrix, with constant diagonal elements equal to M/N. Recall that M is the number of DoF sensed as available. Since the projector exhibits this particular structure, it is interesting to observe how the MNTLS waveforms behave. Recalling that the $\boldsymbol{\phi}_0$ is the first column, appropriately scaled, of $\widehat{\boldsymbol{P}}_0$, it is straightforward to see that the n-th element of $\boldsymbol{\phi}_0$ is given by

$$\phi_0[n] = \frac{1}{\sqrt{MN}} \sum_{\forall m \in \mathcal{I}_{\mathcal{N}}} e^{j\frac{2\pi}{N} nm}, \tag{4.12}$$

[1] For the sake of simplicity, the sensed null-space basis is assumed to be a column subset of the autocorrelation's eigenmatrix. Nevertheless, the discussed results in this Chapter apply in general. Note that a basis of the null space can always be written as a rotation of another basis; thus, any basis can be written as a rotation of the null-space eigenmatrix. Therefore, even though the basis can be different, the projector is unique.

for $n = 0, \ldots, N-1$. After simple mathematical manipulations, we note that $\phi_0[n]$ admits the following vectorization

$$\boldsymbol{\phi}_0 = \gamma_0 \left(\boldsymbol{f}_{m_{\min}} \odot \sum_{\forall m \in \mathcal{I}_{\mathcal{N}}} \boldsymbol{f}_{m-m_{\min}} \right), \tag{4.13}$$

with γ_0 a scaling factor such that $\|\boldsymbol{\phi}_0\| = 1$ and $\boldsymbol{f}_{m-m_{\min}} \in \mathbb{C}^N$ a Vandermonde vector whose n-th element is given by

$$[\boldsymbol{f}_{m-m_{\min}}]_n = N^{-1/2} \exp\left(j2\pi(m - m_{\min})n/N\right), \quad \text{for} \quad n = 0, \ldots, N-1. \tag{4.14}$$

Unfortunately, the case $k = 0$ is the single one admitting a simple expression. For $k = 1, \ldots, K-1$, the remaining waveforms have to be derived from Algorithm 1 (Chapter 3).

4.3.1 Comparison with Other Frequency-Domain Spreading Techniques

Regarding (4.12), it is interesting to note that the MNTLS waveforms asymptotically behave as an *in-band* spread spectrum strategy, i.e., the transmitted power is asymptotically uniformly distributed within all DoF (asymptotically, frequency bins) belonging to the sensed null space.

Frequency-domain spreading techniques have been studied in the literature as potential candidates for opportunistic communications-based interference mitigation. It is evident that, when the outer networks admit a certain amount of interference, conventional spread spectrum techniques such as Direct-Sequence Spread-Spectrum (DSSS) or Frequency-Hopping Spread-Spectrum (FHSS) are potential solutions for permitting the coexistence of several uncoordinated systems [WWX+20]. It is worth noting that spread spectrum strategies enable communication exploiting the same frequency band (i.e., the same signal-space dimensions) without coordination. In addition, spread spectrum schemes also offer a low probability of interception, improving the security of communication [ZZY+15]. Nevertheless, additional signal processing is required to attain optimum performance.

In the context of opportunistic communications, spread-spectrum modulations can benefit from spectrum sensing, i.e., instead of spreading the transmitted signal over the whole system bandwidth, nulling beforehand those frequency bins already sensed as occupied. In this sense, two important spread-spectrum schemes in the context of opportunistic communications are Multi-Carrier Code-Division Multiple-Access (MC-CDMA) [HP97] and Transform-Domain Communication Systems (TDCS) [HBGL13]. The fundamental waveforms of these modulations are respectively given by

$$\phi_{\text{mccdma}}[n] = \lambda \frac{1}{\sqrt{N}} \sum_{\forall m \in \mathcal{I}_{\mathcal{N}}} z[m] e^{j\frac{2\pi}{N}nm}, \tag{4.15}$$

$$\phi_{\text{tdcs}}[n] = \mu \frac{1}{\sqrt{N}} \sum_{\forall m \in \mathcal{I}_{\mathcal{N}}} e^{j\theta[m]} e^{j\frac{2\pi}{N}nm}, \tag{4.16}$$

where λ and μ are scaling factors that guarantee unit waveform energy, $\mathcal{I}_{\mathcal{N}}$ represents the set of available frequency bins as defined in (4.11), $z[m]$ is a pseudo-noise sequence, and $\theta[m]$ is a pseudo-random phase sequence. It is worth noting that nulling the frequency bins sensed as occupied is equivalent to limiting the summation in (4.15) and (4.16) to those frequency bins sensed as available.

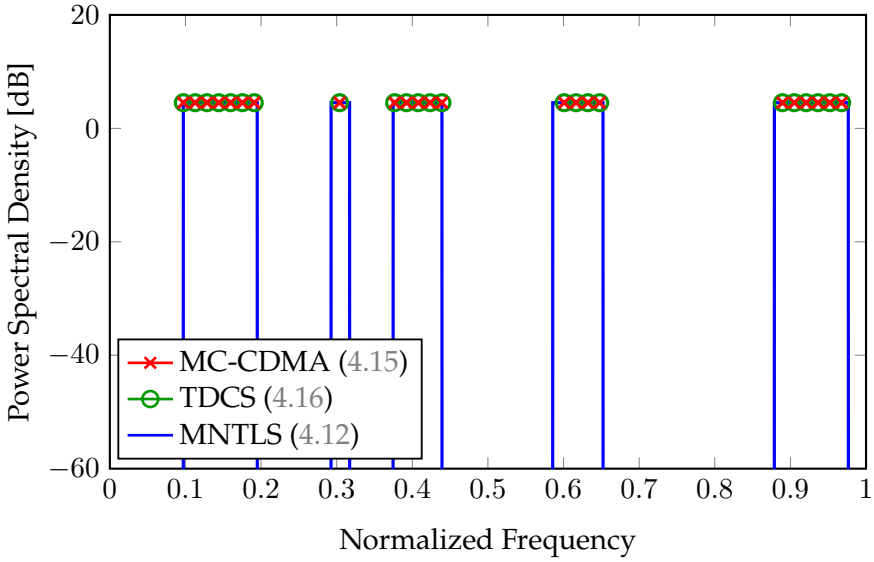

Figure 4.2: Power Spectral Density of the asymptotic MNTLS waveform (4.12) and the fundamental waveforms of MC-CDMA (4.15) and TDCS (4.16).

In order to compare these techniques with the asymptotic MNTLS waveform, the power spectral density of (4.12), MC-CDMA, and TDCS are depicted in Figure 4.2. Assuming the same spectral availability, we note that the three techniques exhibit the same spectral behavior. Regarding the time-domain waveforms, (4.12) is depicted in Figure 4.3, where a realization of each (4.15) and (4.16) is depicted in Figure 4.4.

Before comparing MC-CDMA and TDCS with the asymptotic waveform given in (4.12), emphasizing the differences between MC-CDMA and TDCS can be of interest. Looking at (4.15) and (4.16), we can realize that these two waveforms are extremely similar. In fact, the only difference between these two waveforms is the pseudo-random sequence. MC-CDMA employs a pseudo-noise sequence to perform signal spreading and provide multiple-access capabilities. Conversely, TDCS uses a pseudo-random phase sequence, which does not limit the value of the pseudo-random components to $\{-1, 1\}$. The pseudo-random phase sequence also produces a noise-like signal and maximally spread spectrum within the frequency bins of interest.

Observing Figures 4.2, 4.3, and 4.4, quite a few similarities between the three techniques can be immediately deduced. Regarding the Power Spectral Density (PSD), the three modulations spread the transmitted waveform within all frequency bins of interest. As already stated, the three techniques exhibit exactly the same spectral behavior: a *perfect* dimension spreading. The principal difference between these three modulations can be found in the time domain. Whereas MC-CDMA and TDCS exhibit a noise-like behavior, the MNTLS waveform has a *peaky* time-domain response. Even though the Peak-to-Average Power Ratio (PAPR) can be an issue in all three schemes, PAPR reduction techniques have been widely studied in the context of MC-CDMA, and thus they can be possibly adapted to TDCS. Regarding the MNTLS waveforms, noting the similarities of (4.12) with the OFDMA modulation, a good guess is that the PAPR of (4.12) can be similar to that of OFDMA. Since different PAPR reduction techniques can be found in the literature for the OFDMA scheme, a possibility consists in adapting these techniques to (4.12) or using this framework to design more appropriate PAPR reduction schemes.

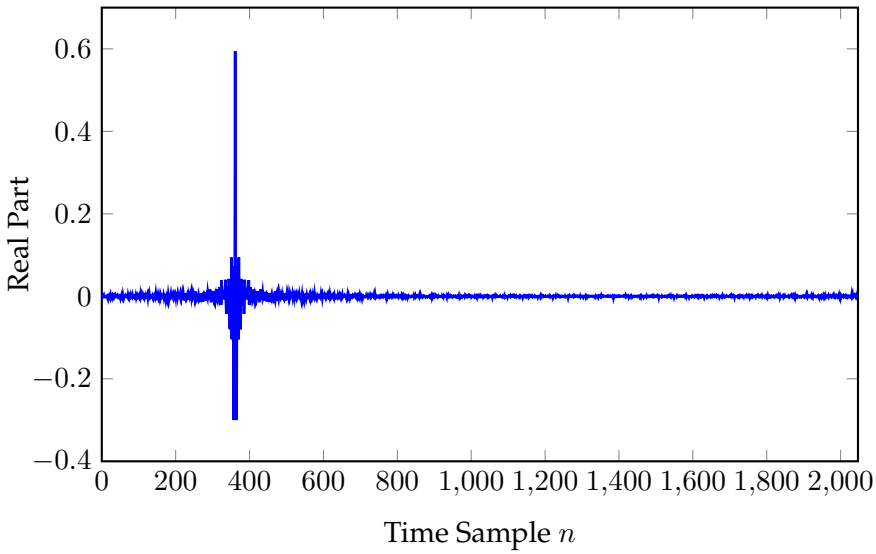

Figure 4.3: Time-domain k-th MNTLS waveform ϕ_k.

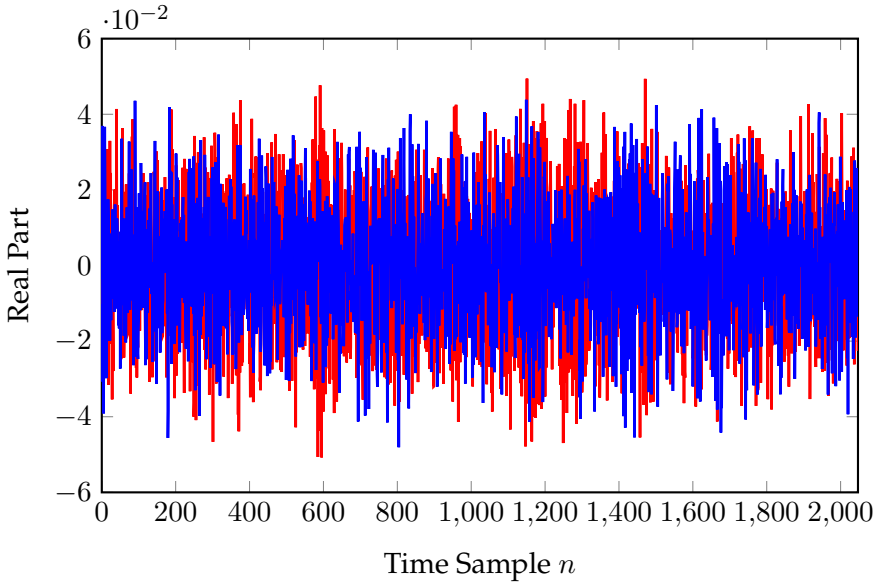

Figure 4.4: One realization of the fundamental waveforms of the MC-CDMA $\phi_{\text{mccdma}}[n]$ (in red) and TDCS $\phi_{\text{tdcs}}[n]$ (in blue) schemes.

From a system coexistence perspective, one is interested in avoiding the use of frequency bins sensed as occupied and minimizing the impact on those occupied frequency bins erroneously sensed as available. The latter is achieved with the dimension spreading behavior exhibited by the three modulations. Suppose they have a similar performance in terms of system coexistence. In that case, a natural question that may arise at this point is which one can be more convenient or more useful for opportunistic communication.

In order to answer this question, let us focus on inner transmission. First, it is interesting to note that the fundamental waveforms of TDCS and MC-CDMA are based on pseudo-random sequences. Therefore, these sequences have to be shared between the inner transmitter and the inner receiver in order to guarantee coherent waveform detection. The latter requires some sort of handshake before opportunistic transmission. In contrast, the asymptotic MNTLS waveform (4.12) is based on the orthogonal projector. Therefore, the possible difference between the sensed null-space bases is absorbed by the projector, giving way to deterministic signaling without the need for coordination or cooperation. The latter is of paramount importance to guarantee coherent waveform detection under challenging feedforward conditions. Nevertheless, the price to pay is its peakiness and a PAPR similar to that of OFDMA.

Another significant difference between (4.12) and MC-CDMA and TDCS is the considered multiplexing domain. The two latter exploit pseudo-random sequences to provide the multi-access capability. Therefore, using different pseudo-noise sequences (in MC-CDMA) and pseudo-random phase sequences (in TDCS), these modulations are able to accommodate simultaneous transmissions without, ideally, inter-waveform interference. However, designing orthogonal sequences is a cumbersome task, and the conventional approach employs pseudo-random sequences that are approximately uncorrelated [Gol05]. In order to perfectly mitigate inter-waveform interference, an additional interference cancellation strategy, such as Successive Interference Cancellation (SIC), is needed at the receiver side. Conversely, a set of K MNTLS waveforms achieve orthogonality in the time domain, forming a time-multiplexing strategy. Under ideal operating conditions, that is, when there is no end-to-end null-space mismatch, a set of K orthogonal waveforms can be locally designed at each inner node without the need for coordination. If the null spaces sensed at each inner node differ, the induced inter-waveform interference has only a little impact and can be efficiently counteracted as per Section 3.5.

4.4 Circulant-Shaping Time-Division Multiple-Access (CS-TDMA)

When the system bandwidth is large enough, the frequency bins sensed as available can be consecutive, as exemplified in Figure 4.5. This may occur, for instance, when opportunistic communication occurs in high-frequency bands (see, for instance, [BJA21; CHW+21]). Under these conditions, the asymptotic MNTLS waveforms exhibit a particular mathematical behavior that can be of relevant interest for efficient implementation.

For the time being, it is assumed that the quotient between the total system DoF N and the number of DoF sensed as available M is an integer. Although this assumption may limit the validity of the result, it may occur when the outer-network communication follows standardized channelization since the total system bandwidth is divided into a certain number of sub-channels. Even though this assumption is necessary to develop the mathematical framework,

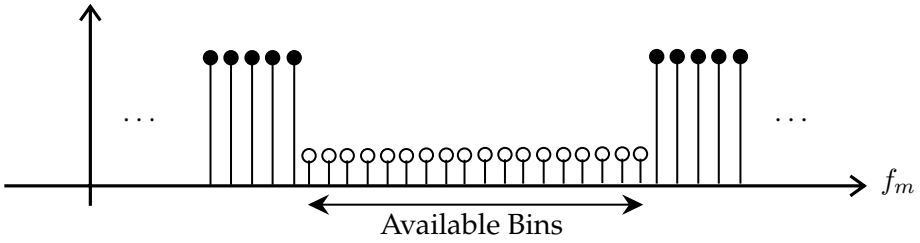

Figure 4.5: Example where the M frequency bins sensed as available are consecutive. Note that filled circles represent the occupied frequency bins.

a practical, reliable approximation for the general case where N/M is not an integer will be provided afterward.

Under the abovementioned assumptions, the set of frequency bins sensed as available $\mathcal{I}_{\mathcal{N}}$ defined in (4.11) becomes

$$\mathcal{I}_{\mathcal{N}} = \{m_0, \ldots, m_0 + M - 1\}, \tag{4.17}$$

and, therefore, the asymptotic MNTLS waveform given in (4.12) can be written in terms of the Dirichlet kernel as

$$\phi_0[n] = \frac{1}{\sqrt{MN}} e^{j\frac{2\pi}{N}nm_0} \sum_{m=0}^{M-1} e^{j\frac{2\pi}{N}nm} = \frac{1}{\sqrt{MN}} \frac{\sin\left(M\frac{\pi n}{N}\right)}{\sin\left(\frac{\pi n}{N}\right)} e^{j\frac{\pi[(M-1)+2m_0]n}{N}}. \tag{4.18}$$

The last equation reveals that the first MNTLS waveform asymptotically behaves as a periodic (discrete) sinc function under the consecutive available bins assumption. In the general asymptotic case discussed in Section 4.3, the remaining $K-1$ waveforms cannot be written as simple as (4.12) since the recursive nature of the design scheme described in Algorithm 1 (Chapter 3) cannot be overcome. Nevertheless, in the particular case studied in this section, the asymptotic behavior of all the K MNTLS waveforms admits a tractable characterization.

Recalling the methodology described in Algorithm 1, the second MNTLS waveform, that is, $k = 1$, corresponds to the column of the orthogonal projector $\widehat{\boldsymbol{P}}_1 = \widehat{\boldsymbol{P}}_0 - \boldsymbol{\phi}_0\boldsymbol{\phi}_0^H$, appropriately scaled, that contains the maximum diagonal element. Since the orthogonal projector $\widehat{\boldsymbol{P}}_0 = \widehat{\boldsymbol{U}}_{\mathcal{N}}\widehat{\boldsymbol{U}}_{\mathcal{N}}^H$ has a constant diagonal equal to M/N, only the matrix $\boldsymbol{\phi}_0\boldsymbol{\phi}_0^H$ deserves our attention. Using (4.18), it is straightforward to see that the diagonal of the matrix $\boldsymbol{\phi}_0\boldsymbol{\phi}_0^H$ can be written in terms of the Féjer kernel as

$$\phi_0[n]\phi_0^*[n] = \frac{1}{MN}\left(\frac{\sin\left(M\frac{\pi n}{N}\right)}{\sin\left(\frac{\pi n}{N}\right)}\right)^2. \tag{4.19}$$

Therefore, the waveform $\boldsymbol{\phi}_1$ is found at the column $n = 0, \ldots, N-1$ of the orthogonal projector $\widehat{\boldsymbol{P}}_1$ where (4.19) is minimum. For the reader's convenience, equation (4.19) is illustrated in Figure 4.6. A simple mathematical analysis reveals that (4.19) is equal to zero at $n = kN/M$, for any integer k, if and only if the quotient N/M is an integer. Interestingly, it is worth noting that the remaining $N-1$ elements of the column $n = kN/M$ os the matrix $\boldsymbol{\phi}_0\boldsymbol{\phi}_0^H$ satisfy the following property:

$$\phi_0[n]\phi_0^*[kN/M] \propto \frac{\sin\left(M\frac{\pi n}{N}\right)}{\sin\left(\frac{\pi n}{N}\right)} \frac{\sin\left(k\pi\right)}{\sin\left(\frac{k\pi}{M}\right)} = 0. \tag{4.20}$$

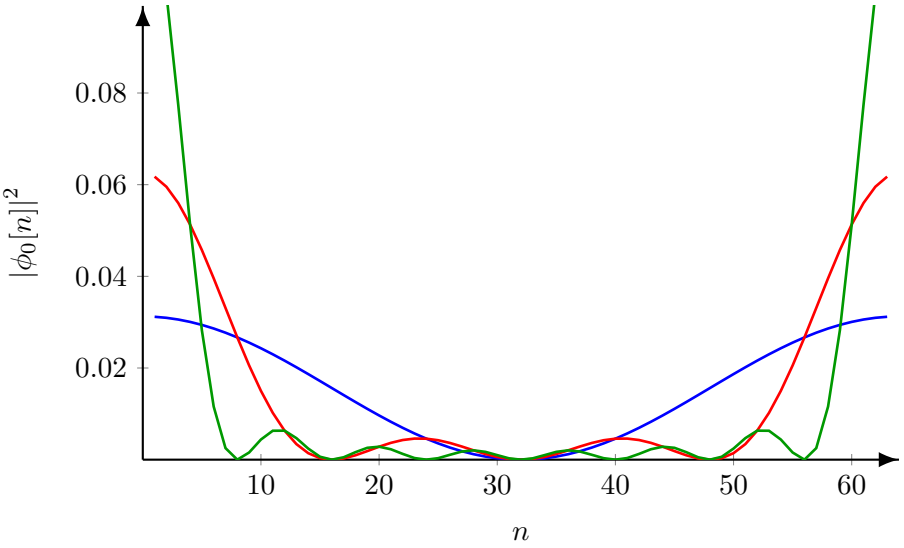

Figure 4.6: Illustration of (4.19) with $N = 64$, and $M = 2$ (blue), $M = 4$ (red), and $M = 8$ (green).

Accordingly, the waveform $\boldsymbol{\phi}_1$ corresponds to the column N/M of the orthogonal projector $\widehat{\boldsymbol{P}}_0$, appropriately scaled. This result can be further generalized and, thus, under the initial assumptions, the k-th waveform $\boldsymbol{\phi}_k$ is just the (kN/M)-th column of the orthogonal projector $\widehat{\boldsymbol{P}}_0$ with a scaling factor equal to $1/\sqrt{MN}$ so as to guarantee unit norm.

More interestingly, it must be recalled that the orthogonal projector $\widehat{\boldsymbol{P}}_0$ is a circulant matrix under asymptotic conditions. Thus, it is worth noting that

$$\phi_k \left[\left(n + k\frac{N}{M} \right) \bmod N \right] = \phi_0[n], \quad \text{for } n = 0, \ldots, N-1, \tag{4.21}$$

meaning that, once the first waveform $\boldsymbol{\phi}_0$ has been identified, the remaining $K-1$ waveforms to be designed can be found as

$$\boldsymbol{\phi}_k = \boldsymbol{\Pi}_{k\frac{N}{M}} \boldsymbol{\phi}_0, \quad \text{for } k = 1, \ldots, K-1, \tag{4.22}$$

being $\boldsymbol{\Pi}_q$ a permutation matrix given by

$$\boldsymbol{\Pi}_q = \left[\; [\boldsymbol{I}_N]_{q+1:N} \; \vdots \; [\boldsymbol{I}_N]_{1:q} \; \right], \tag{4.23}$$

where $[\boldsymbol{I}_N]_{q:r}$ is a column subset of the identity matrix containing the columns from q to r.

In conclusion, (4.22) reveals that the waveforms $\boldsymbol{\phi}_k$, for $k = 1, \ldots, K-1$, are permutations of the first waveform $\boldsymbol{\phi}_0$. Since these permutations introduce a circular time-shift, the linear modulation composed of waveforms $\{\boldsymbol{\phi}_k\}_{0 \leq k \leq K-1}$ exhibits similar behavior to that of the Time-Division Multiple-Access (TDMA). Accordingly, in this particular case, the derived linear modulation is referred to as *Circulant-Shaping* Time-Division Multiple-Access (CS-TDMA). It is noteworthy that, under the assumption of consecutive available frequency bins, it is possible to design the set of orthonormal waveforms $\{\boldsymbol{\phi}_k\}_{0 \leq k \leq K-1}$ avoiding the use of the recursive algorithm described in Chapter 3. Thus, in simple *structured* scenarios, the design complexity of $\{\boldsymbol{\phi}_k\}_{0 \leq k \leq K-1}$ reduces to circular time-shifts. However, in more general and complex scenarios, it is not possible to avoid the recursive nature of Algorithm 1, as discussed in Section 4.3.

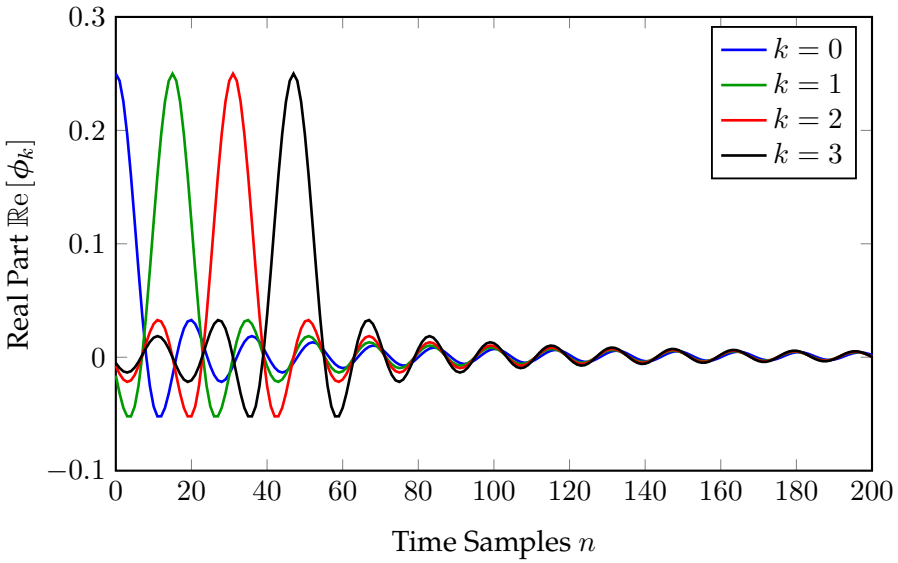

Figure 4.7: Example of a CS-TDMA modulation composed of $K = 4$ waveforms with $N = 2048$ and $M = 128$.

An example of $K = 4$ CS-TDMA waveforms is depicted in Figure 4.7. Observing this figure, it is worth noting that these waveforms concentrate most of their energy in a short time interval, unveiling their short effective duration. This observation characterizes the time-division multiple-access capability of this modulation format. Regarding the frequency-domain behavior, the CS-TDMA waveforms preserve the dimension spreading property illustrated in Section 4.3. Even though it may seem that these waveforms inefficiently use the available resources, it is worth remembering that each waveform spans only one DoF on an invariant null-space basis composed of certain columns of $\widehat{\boldsymbol{P}}_0$, leading to a high-SNR regime. Therefore, the CS-TDMA modulation is optimal in terms of finally exploited DoF.

The main apparent drawback of the CS-TDMA modulation is that end-to-end subspace mismatch errors induce that the parameter m_0 and the number of DoF sensed as available at each inner node may differ. These differences yield frequency synchronization errors and loss of orthogonality between CS-TDMA waveforms. Even though these errors can be counteracted through synchronization schemes, it is possible to neutralize them by leveraging the active subspace detection methodology discussed in Section 3.5.

Observing Figure 4.7, it is worth noting that the involved signals are peaky in the time domain. From an information-theoretic viewpoint, time-domain signals exhibiting a maximally flat frequency response can be capacity-achieving in some multipath channels when the system bandwidth is arbitrarily large [PTN07; Por07], i.e., the so-called wideband regime [Ver02]. Nevertheless, in terms of practical implementation, peaky signals have a large peak-to-average power ratio (PAPR), which worsens the energy efficiency performance of the communication. In order to assess the PAPR performance of the efficient CS-TDMA modulation, Figure 4.8 illustrates the complementary Cumulative Distribution Function (CDF) of the PAPR exhibited by the CS-TDMA modulation and the asymptotic MNTLS waveforms discussed in Section 4.3. As a reference, the PAPR performance of OFDMA has been included. For the sake of a fair comparison, the native version of the three modulation formats is considered without any

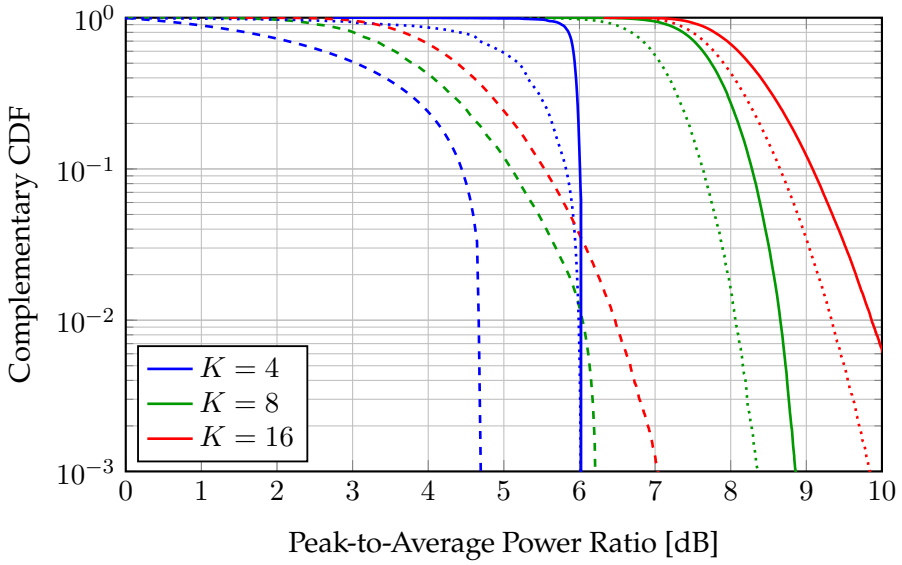

Figure 4.8: Complementary CDF of the minimum PAPR when QPSK symbols are transmitted with a different number of waveforms K. Dashed lines refer to the CS-TDMA modulation format (4.22), dotted lines stand for the asymptotic MNTLS waveform (Section 4.3), and solid lines are for OFDMA.

sort of PAPR reduction technique. Moreover, for the CS-TDMA and the asymptotic MNTLS waveforms case, it is assumed that $K = M$ in order to exploit the same DoF as OFDMA. From Figure 4.8, we can observe that, under the general asymptotic conditions discussed in Section 4.3, the MNTLS waveforms exhibit a better PAPR performance than OFDMA. Nevertheless, it is interesting to note that CS-TDMA has a much smaller PAPR in probability than the other two techniques. The reason is that this modulation is a circulant version of the native TDMA scheme, which exhibits a good PAPR.

In summary, the PAPR exhibited by the MNTLS waveforms (both in the general case and under CS-TDMA conditions) is asymptotically better than the PAPR of the well-known OFDMA scheme. Nevertheless, the numerical simulation depicted in Figure 4.8 does not consider a PAPR reduction technique, which is a common practice in OFDM(A)-based communication systems (see, for instance, [XWG+18]). Therefore, the PAPR of the MNTLS waveforms can be further improved by utilizing a PAPR reduction precoder.

4.4.1 Suboptimal CS-TDMA Approximation

Despite the potential implementation advantages of the CS-TDMA modulation, the entire discussion is based on the assumption that the quotient N/M is an integer. In the sequel, an approximation of the CS-TDMA scheme is discussed for the case where N/M is not an integer but $M \ll N$. It is worth noting that this case corresponds to a complex scenario since $M \ll N$ essentially means that only a small number of DoF are available for opportunistic communication. Conversely, as the DoF availability increases, the scenario becomes favorable since it is possible to sacrifice some DoF sensed as available to guarantee that the quotient N/M is an integer. In this sense, the following methodology reveals that an efficient suboptimal CS-TDMA approximation can be found in congested wireless environments.

Algorithm 2 Suboptimal CS-TDMA Approximation

Input: K, N, M, $\boldsymbol{\phi}_0$
Output: $\{\boldsymbol{\phi}_k\}_{1\leq k\leq K-1}$
1: Find the least common multiple of N and M: $N' = \mathrm{lcm}(N, M)$
2: Interpolate $\boldsymbol{\phi}_0$ to get a sampled waveform with N' samples, namely $\widetilde{\boldsymbol{\phi}}_0$
3: **for** $k = 1$ until $K - 1$ **do**
4: Find the N'-sample waveform $\widetilde{\boldsymbol{\phi}}_k$ as $\widetilde{\boldsymbol{\phi}}_k = \boldsymbol{\Pi}_{k\frac{N'}{M}}\widetilde{\boldsymbol{\phi}}_0$
5: Decimate $\widetilde{\boldsymbol{\phi}}_k$ to obtain the N-sample waveform $\boldsymbol{\phi}_k$
6: **end for**

The efficient implementation of the baseline CS-TDMA modulation comes from noting that, once the first waveform $\boldsymbol{\phi}_0$ has been found, the remaining $K-1$ waveforms can be found as permutations of $\boldsymbol{\phi}_0$, that is,

$$\boldsymbol{\phi}_k = \boldsymbol{\Pi}_{k\frac{N}{M}}\boldsymbol{\phi}_0, \quad \text{for } k = 1, \ldots, K-1. \tag{4.24}$$

Nevertheless, this methodology can only be used when the quotient N/M is an integer. An approximated solution for the general case where N/M is not an integer is as follows. Suppose it is possible to find a high-dimensional complex space of N' dimensions such that the quotient N'/M is an integer. Then, the efficient design strategy described by (4.24) can be applied to find a set of CS-TDMA waveforms laying in an M-dimensional subspace of the N'-dimensional complex space $\mathbb{C}^{N'}$. Finally, the transmit waveforms are found by projecting the obtained solutions in $\mathbb{C}^{N'}$ onto an M-dimensional subspace of $\mathbb{C}^N$, which can be done by decimating the solutions. The proposal is summarized in Algorithm 2.

Even though the solutions provided by Algorithm 2 are not optimal, since the operating conditions do not satisfy the aforementioned CS-TDMA assumptions, it permits avoiding the recursive nature of the waveform design scheme described in Algorithm 1 (Chapter 3) necessary in the general asymptotic case described in Section 4.3. The latter permits efficient implementation of the MNTLS waveforms.

Figure 4.9 depicts the comparison between the waveforms obtained according to the procedure described in Algorithm 2 and the corresponding scaled columns of the orthogonal projector $\widehat{\boldsymbol{P}}_0$. Despite providing a reliable approximation of the columns of $\widehat{\boldsymbol{P}}_0$, observing the zero-crossings, it can be deduced that the suboptimal waveforms are not orthogonal. The latter is better emphasized in Figure 4.10, which illustrates the scalar product between the $K = 4$ designed suboptimal waveforms.

The loss of orthogonality illustrated in Figure 4.10 leads to Inter-Symbol Interference (ISI) that may degrade the performance of opportunistic communication. In order to numerically evaluate the impact of the self-induced ISI, the Self ISI-to-Signal Ratio (SISR), defined as

$$\mathrm{SISR} \triangleq \frac{\| \left(\boldsymbol{\Phi}^H\boldsymbol{\Phi}\right) \odot \left(\mathbf{1}_{K\times K} - \boldsymbol{I}_K\right) \|_{\mathrm{F}}^2}{\| \left(\boldsymbol{\Phi}^H\boldsymbol{\Phi}\right) \odot \boldsymbol{I}_K \|_{\mathrm{F}}^2}, \tag{4.25}$$

where $\boldsymbol{\Phi}$ is the shaping transmission matrix containing the K waveforms designed according to Algorithm 2, is depicted in Figure 4.11. For the sake of generality, the quotient N/M has been rewritten as

$$\frac{N}{M} = Z + \delta, \tag{4.26}$$

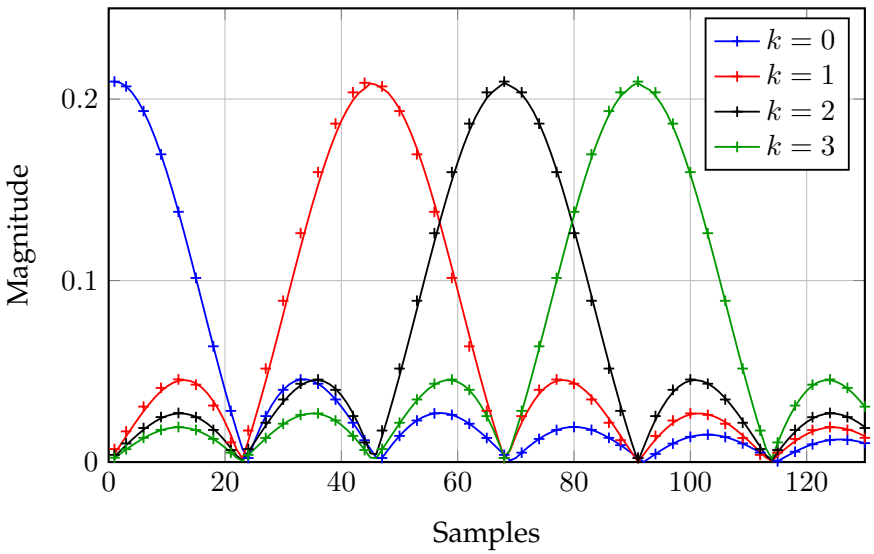

Figure 4.9: Magnitude of the suboptimal CS-TDMA approximation waveforms (lines) and the corresponding appropriately scaled columns of $\widehat{\boldsymbol{P}}_0$ (marks), for $N = 1024$ and $M = 45$.

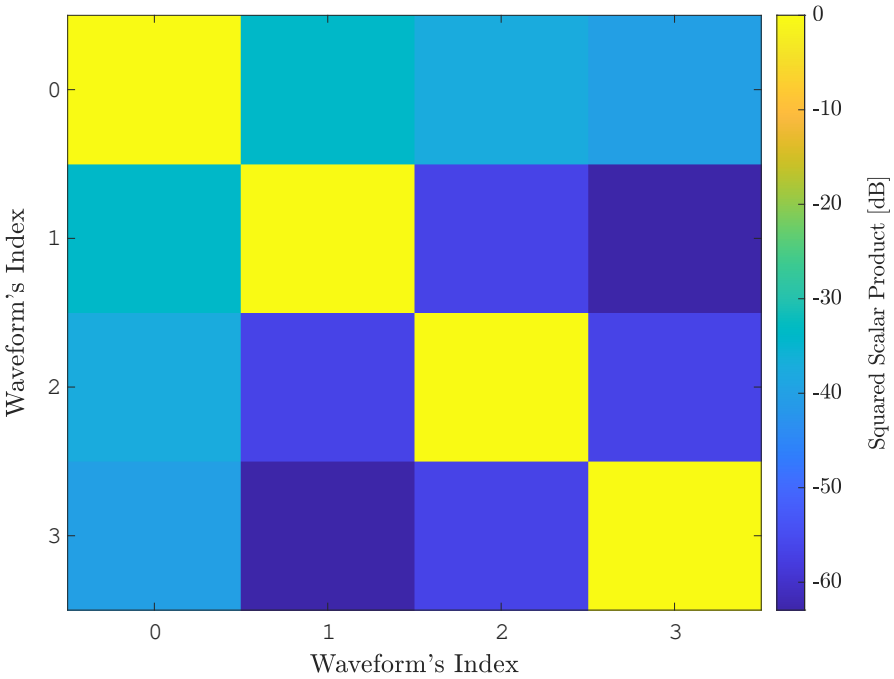

Figure 4.10: Squared scalar product [dB] between the four waveforms designed according to Algorithm 2.

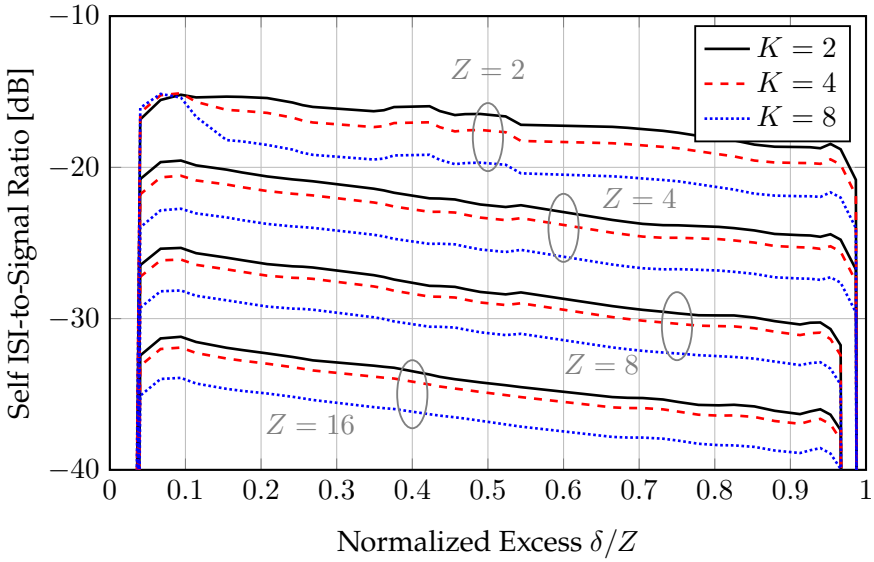

Figure 4.11: SISR [dB] as a function of the relative excess δ/Z with $N = 1024$, for different whole parts Z and transmitted waveforms K.

where Z is an integer referring to the whole part of the quotient, whereas δ refers to the fractional part, and the SISR has been depicted with respect to the ratio δ/Z. It is noteworthy that, as expected, the impact of the self-induced ISI is negligible when the quotient N/M can be well-approximated by an integer, i.e., when $\delta/Z \to 0$ and when $\delta/Z \to 1$. As the whole part Z increases, it becomes more evident that $Z \gg \delta$, validating the approximation $N/M \approx Z$. The latter translates into a severe degradation of the self-induced ISI. Regarding the number of transmitted waveforms K, note that the SISR decreases when more waveforms are transmitted. This observation validates the observation discussed in Chapter 3, stating that the number of waveforms plays the role of an SNR gain. Hence, as K increases, the useful signal becomes more dominant than the induced ISI, which helps to reduce the SISR.

Observing Figure 4.11, it is worth noting that the self-induced ISI becomes negligible as the whole part Z becomes larger. The latter corresponds to the case where N is significantly larger than M, that is, $M \ll N$. Conversely, when the whole part Z becomes smaller, the self-induced ISI degrades the opportunistic communication performance. This situation, however, occurs when the N and M differ by less than a magnitude order. For a fixed N, the latter means that M is sufficiently large that it becomes reasonable to sacrifice a fraction of the DoF sensed as available such that the quotient $N/(\alpha M)$, with $0 < \alpha < 1$, is an integer. Under these conditions, the suboptimal approximation becomes unnecessary, and the inner nodes can resort to the baseline CS-TDMA with $M' = \alpha M$.

4.4.2 Extension of the CS-TDMA Modulation

At the beginning of this section, it is stated that the CS-TDMA modulation requires that the quotient between the number of system DoF N and the number of DoF sensed as available M has to be an integer. In this respect, the baseline CS-TDMA can be extended to the case where, for any integer β, the quotient $N/(\beta M)$ is still an integer. In spite of being of practical interest, this extension is only discussed herein for the sake of completeness, as it requires end-to-end

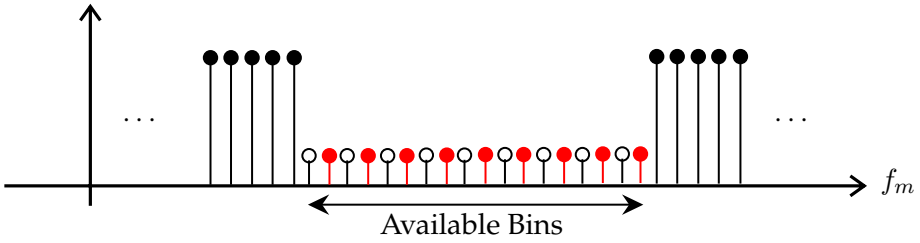

Figure 4.12: Example where among the M' consecutive frequency bins sensed as available, only the $M = M'/\beta$ bins represented by empty circles (separated by $\beta = 2$) are exploited for opportunistic communication.

coordination between inner nodes and, thus, is beyond this dissertation's scope.

Assume that, after setting up the opportunistic communication link, the inner nodes have agreed on an integer β satisfying

$$\frac{N}{\beta M} = Z, \tag{4.27}$$

where Z is an integer. The integer β plays the role of a *DoF hopping factor*, indicating the distance between two DoF sensed as available that will be exploited as exemplified in Figure 4.12.

It is worth noting that the assumption above requires that the number of consecutive frequency bins detected as available be sufficiently large such that the resulting DoF spreading factor guarantee the desired SIDR. The DoF hopping pattern can be, for instance, related to the channel's coherence bandwidth, meaning that the discussed CS-TDMA extension can be seen as a mechanism to combat the frequency-selective nature of the inner channel.

In mathematical terms, the first waveform can be still written in terms of the Dirichlet kernel as in (4.18). Specifically, the exact expression can be found by substituting N/β in (4.18), yielding

$$\phi_0[n] = \sqrt{\frac{\beta}{MN}} \frac{\sin\left(M\beta\frac{\pi n}{N}\right)}{\sin\left(\frac{\beta\pi n}{N}\right)} e^{j\frac{\beta\pi[(M-1)+2m_0]n}{N}}. \tag{4.28}$$

Incorporating the DoF hopping factor β into (4.18) still permits finding the remaining $K-1$ waveforms as permutations of the first waveform $\boldsymbol{\phi}_0$. Nevertheless, in this case, the k-th waveform is given by the column $n = kN/(\beta M)$ of the orthogonal projector onto the sensed null space $\widehat{\boldsymbol{P}}_0$, which accounts for only the M'/β frequency bins that will be exploited for opportunistic communication. Accordingly, note that the k-th extended CS-TDMA waveform is given by

$$\boldsymbol{\phi}_k = \boldsymbol{\Pi}_{k\frac{N}{\beta M}} \boldsymbol{\phi}_0, \quad \text{for } k = 1, \ldots, K-1. \tag{4.29}$$

Notably, the DoF hopping factor can be seen as an undersampling factor of the sensed null space, introducing aliasing in the time domain, as illustrated in Figure 4.13. Nevertheless, this phenomenon does not prevent the inner nodes from finding M'/β orthogonal waveforms obeying the criterion provided in (4.29).

This extension of the CS-TDMA modulation format has additional advantages with respect to the baseline CS-TDMA scheme. For instance, if the DoF hopping factor is set according to the channel coherence bandwidth, the proposed extension can exploit any potential frequency diversity induced by the channel. Moreover, after two channel uses, it is possible to implement a frequency-domain interleaver, breaking any potential correlation between the transmitted

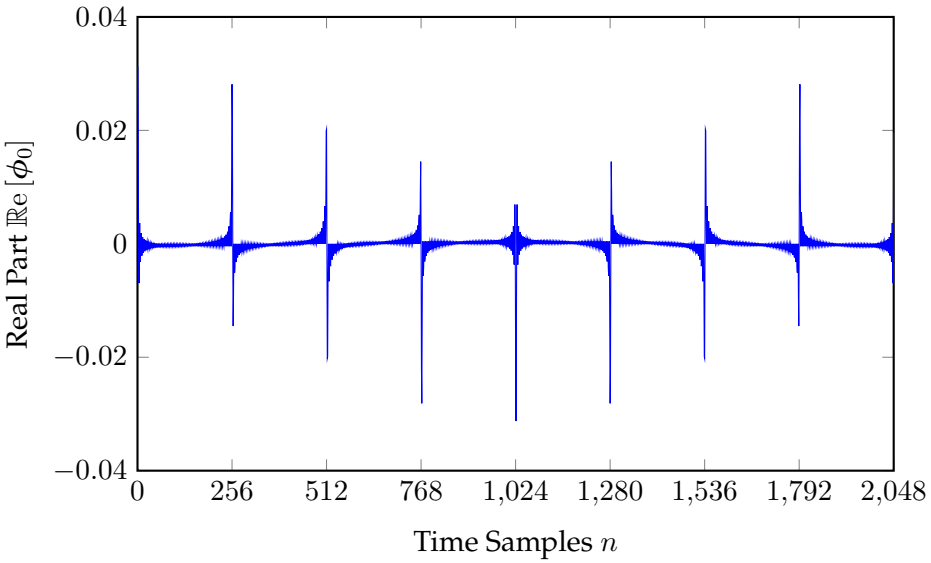

Figure 4.13: The first waveform of the extended CS-TDMA with $N = 2048$, $M = 64$, and $\beta = 8$.

codewords. In the time domain, note that the DoF hopping factor virtually decreases the number of total system DoF, i.e., $N' = N/\beta$, which improves the time-multiplexing capability.

Finally, yet importantly, if the inner nodes not only agree on a DoF hopping factor β but also on a reference starting frequency bin m_0 [cf. (4.17)], it is possible to implement a multi-band frequency hopping scheme. The latter is of paramount importance as this new scheme enjoys the low probability of interception property natively exhibited by spread spectrum systems and, as discussed in Chapter 2.2.3, a better transmission capacity than spreading schemes.

4.5 Opportunistic Transmission in Frequency-Selective Channels

Thus far in this thesis, the inner channel has been assumed to be frequency-flat fading. This assumption has permitted studying the properties of the MNTLS waveforms, derived in Chapter 3, leaving aside the impact of the channel. In practice, however, the wireless channel in wideband scenarios tends to be frequency-selective.

Before going into details, it is interesting to revisit the concept of *available* DoF in the context of frequency-selective channels. When an inner node acquires a set of observations to sense the wireless environment, these observations experience a frequency-selective fading. Under these conditions, a DoF (asymptotically, a frequency bin) occupied by an outer-network node may be *perceived as available* by the inner node due to the frequency-selective nature of the wireless channel. For the sake of clarity, an example of this situation is provided in Figure 4.14. Note that the sensed DoF occupation is illustrated in Figure 4.14(a), where the magnitude of the outer-to-inner channel frequency response is depicted in Figure 4.14(b).

It is worth noting that when the magnitude of the channel frequency response is poor, the inner terminal will perceive, with high probability, the associated frequency bin as available, even if it is occupied by outer-network terminals. This situation is not critical in Time Division

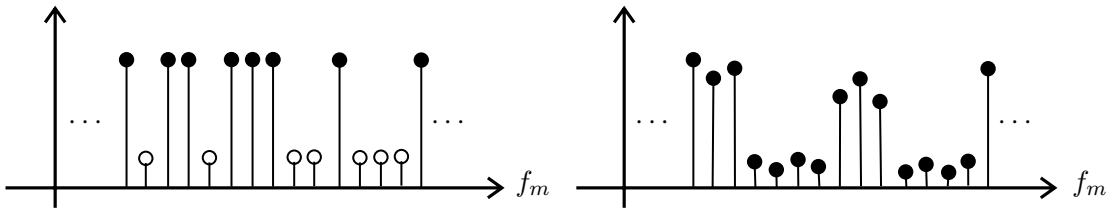

(a) DoF/frequency-bin occupancy pattern. **(b)** Outer-Inner channel frequency response.

Figure 4.14: Example of DoF sensing under frequency-selective fading conditions. Note that the inner node bases the sensing on the observation of the occupancy pattern depicted in (a), modulated by the unknown outer-network signals, through the interference channel whose frequency response (magnitude) is illustrated in (b).

Duplex (TDD)[2] transmissions, where channel reciprocity holds [VT03]. In essence, channel reciprocity means that the *outgoing* channel matrix is the transpose conjugate of the *incoming* channel matrix. Accordingly, the inter-system interference imposed by the inner terminal on that DoF perceived as available due to a poor channel frequency response is mitigated by the channel itself. Thus, the frequency-selective nature is somehow providing more transmit opportunities to the inner nodes, that is, the number of available DoF is virtually larger under frequency-selective fading conditions.

In order to study the adaptation of the MNTLS waveforms to frequency-selective channels, we consider in the sequel the scenario depicted in Figure 4.15, which consists in the opportunistic transmission of a K-symbol vector $\boldsymbol{a} \in \mathbb{C}^K$ through a frequency-selective channel, being $\boldsymbol{H}_{\text{II}}$ the $(N + L_h) \times N$ channel convolution matrix and L_h the channel memory.

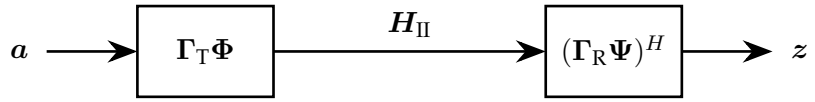

Figure 4.15: Opportunistic communication in frequency-selective channels.

In the cumbersome frequency-selective channel scenario, the design of null-space precoding and combining matrices is not enough to opportunistically transmit the information symbols reliably. In fact, the use of the shaping transmission matrix $\boldsymbol{\Phi} \in \mathbb{C}^{N\times K}$ and the matched-filtering matrix $\boldsymbol{\Psi} \in \mathbb{C}^{N\times K}$ helps in minimizing the inter-system interference imposed on the outer-network nodes. Nevertheless, additional processing at the inner transmitter and the inner receiver is needed to combat the frequency-selective nature of the channel.

A conventional strategy to design precoding and combining matrices for frequency-selective channels relies on Singular Value Decomposition (SVD) processing. In this respect, the channel convolution matrix $\boldsymbol{H}_{\text{II}}$ admits the following SVD decomposition:

$$\boldsymbol{H}_{\text{II}} = \widetilde{\boldsymbol{U}}_{\boldsymbol{H}} \widetilde{\boldsymbol{\Sigma}}_{\boldsymbol{H}} \widetilde{\boldsymbol{V}}_{\boldsymbol{H}}^H \in \mathbb{C}^{(N+L_h)\times N}, \tag{4.30}$$

being L_h the channel memory, $\widetilde{\boldsymbol{U}}_{\boldsymbol{H}} \in \mathbb{C}^{(N+L_h)\times(N+L_h)}$ and $\widetilde{\boldsymbol{V}}_{\boldsymbol{H}} \in \mathbb{C}^{N\times N}$ the left and right singular vectors, respectively, and $\widetilde{\boldsymbol{\Sigma}}_{\boldsymbol{H}} \in \mathbb{C}^{(N+L_h)\times N}$ is a block matrix where the $N \times N$ upper-block $\boldsymbol{\Sigma}_{\boldsymbol{H}}$ is diagonal, containing the singular values, and the $L_h \times N$ lower-block is a zeros

[2]The TDD assumption is conventional in the context of opportunistic communications since most unlicensed and decentralized communication systems operate under this duplexing mode (see, e.g., [ARS16; SKDI16; XGL18]).

matrix. Taking into account the structure of matrix $\widetilde{\boldsymbol{\Sigma}}_{\boldsymbol{H}}$, (4.30) can be compactly written as

$$\boldsymbol{H}_{\mathrm{II}} = \boldsymbol{U}_{\boldsymbol{H}} \boldsymbol{\Sigma}_{\boldsymbol{H}} \boldsymbol{V}_{\boldsymbol{H}}^{H}, \tag{4.31}$$

where $\boldsymbol{U}_{\boldsymbol{H}} \in \mathbb{C}^{(N+L_h)\times N}$ encompasses the left singular vectors associated with the N singular values and $\boldsymbol{V}_{\boldsymbol{H}} = \widetilde{\boldsymbol{V}}_{\boldsymbol{H}}$. Bearing this in mind, the ideal precoding matrix $\boldsymbol{\Gamma}_{\mathrm{T}}$ and combining matrix $\boldsymbol{\Gamma}_{\mathrm{R}}$ can be found from the singular vectors matrices $\boldsymbol{V}_{\boldsymbol{H}}$ and $\boldsymbol{U}_{\boldsymbol{H}}$, respectively, altogether with a power allocation policy (at the transmitter) or with a equalization scheme (at the receiver) to appropriately exploit or counteract the *eigenchannels*.

In opportunistic communications, it is fundamental to recall that the primary objective consists in mitigating the undesired inter-system interference leaked on the outer network. Therefore, the design of the opportunistic transmission strategy in frequency-selective channels has to simultaneously satisfy the following design condition

$$\boldsymbol{\Psi}^{H} \boldsymbol{\Gamma}_{\mathrm{R}}^{H} \boldsymbol{H}_{\mathrm{II}} \boldsymbol{\Gamma}_{\mathrm{T}} \boldsymbol{\Phi} \boldsymbol{a} \propto \boldsymbol{a} \tag{4.32}$$

while guaranteeing a minimum worst-case inter-system interference (3.12), that is,

$$\min_{\boldsymbol{\Phi}} \max_{\boldsymbol{E}_{\mathcal{N}}} \frac{1}{N} \left\| \boldsymbol{E}_{\mathcal{N}}^{H} \boldsymbol{\Gamma}_{\mathrm{T}} \boldsymbol{\Phi} \right\|_{\mathrm{F}}^{2}, \tag{4.33}$$

subject to the design constraints discussed in Section 3.3, for a given $\boldsymbol{\Gamma}_{\mathrm{T}}$. It is worth noting that the additional precoding matrix $\boldsymbol{\Gamma}_{\mathrm{T}}$ has been included, in order to guarantee that the inter-system interference measured at the inner transmitter output is minimum.

Another possibility would consist in designing the covariance matrix (codebook matrix) of the information symbols to maximize the opportunistic transmission rate for given precoding and combining matrices, as in the VFDM scheme described in Section 4.2. Accordingly, letting $\boldsymbol{S}_{\boldsymbol{a}} = \mathbb{E}\left[\boldsymbol{a}\boldsymbol{a}^{H}\right]$, the inner node has to design a codebook matrix $\boldsymbol{S}_{\boldsymbol{a}}$ satisfying

$$\max_{\boldsymbol{S}_{\boldsymbol{a}}} \ \frac{1}{N} \log_2 \left(\det \left[\boldsymbol{I}_K + \boldsymbol{S}_z^{-1/2} \boldsymbol{\Psi}^{H} \boldsymbol{\Gamma}_{\mathrm{R}}^{H} \boldsymbol{H}_{\mathrm{II}} \boldsymbol{\Gamma}_{\mathrm{T}} \boldsymbol{\Phi} \boldsymbol{S}_{\boldsymbol{a}} \boldsymbol{\Phi}^{H} \boldsymbol{\Gamma}_{\mathrm{T}}^{H} \boldsymbol{H}_{\mathrm{II}}^{H} \boldsymbol{\Gamma}_{\mathrm{R}} \boldsymbol{\Psi} \boldsymbol{S}_z^{-H/2} \right] \right), \tag{4.34}$$

subject to a transmit power constraint, being $\boldsymbol{S}_z$ the interference-plus-noise covariance matrix at symbol level. In this approach, the shaping transmission matrix $\boldsymbol{\Phi}$ and the matched-filtering matrix $\boldsymbol{\Psi}$ can be designed as discussed in Chapter 3, whereas the additional precoding and combining matrices $\boldsymbol{\Gamma}_{\mathrm{T}}$ and $\boldsymbol{\Gamma}_{\mathrm{R}}$ can be based on the right and left singular vector matrices of the channel $\boldsymbol{H}_{\mathrm{II}}$. The major difference with respect to the VFDM scheme is that inter-system interferences seen by the inner receiver can be mitigated through $\boldsymbol{\Psi}$.

Both of the discussed strategies satisfy the minimum worst-case inter-system interference condition since the inner transmitter uniquely maps the information symbols onto the sensed null space at its location. Moreover, the use of additional precoding permits dealing with the frequency-selective nature of the channel. Nevertheless, the design of the additional processing matrices $\boldsymbol{\Gamma}_{\mathrm{T}}$ and $\boldsymbol{\Gamma}_{\mathrm{R}}$ requires full Channel State Information (CSI) at both the inner transmitter and the inner receiver, which is impractical under challenging feedforward conditions. Accordingly, a strategy that does not require full CSI at both inner nodes is preferred.

Recalling (4.12), we note that, asymptotically, the MNTLS waveforms behave as a linear combination of sinusoids, similar to OFDMA. This observation brings to light the possibility of

incorporating a Cyclic Prefix (CP) at the transmitter side to deal with the frequency-selective nature of the inner channel.

From this point onwards, we consider that a classic CP is added to the transmitted signal $\widetilde{\boldsymbol{x}} = \boldsymbol{\Phi}\boldsymbol{a}$, such that

$$\boldsymbol{x} = \begin{bmatrix} \widetilde{\boldsymbol{x}}_{\text{CP}} \\ \cdots\cdots \\ \widetilde{\boldsymbol{x}} \end{bmatrix}, \tag{4.35}$$

where $\widetilde{\boldsymbol{x}}_{\text{CP}}$ contains a copy of the last N_{CP} samples of the N-length signal $\widetilde{\boldsymbol{x}}$, satisfying $N_{\text{CP}} \geq L_h$. Nevertheless, extending the transmitted signal with a classic CP can break the orthogonality to those DoF sensed as occupied, providing undesired inter-system interference. In order to avoid these interferences, the null-space sensing has to be modified to account for the use of the CP.

In this sense, when the inner transmitting node employs a classic CP, the minimum worst-case inter-system interference condition can only be guaranteed if all outer-network nodes employ a block transmission with guard symbols (such as CP). Under this assumption, the additional samples will be removed by the outer-network receivers, and then the opportunistic signals satisfy the minimum worst-case inter-system interference condition within the *effective* signal space. Nevertheless, this additional information requires inter-system cooperation, which is not considered in this thesis.

Another possibility is as follows. Under asymptotic conditions, it is known that the eigenmatrix of the observations' autocorrelation matrix is the normalized Fourier matrix. Therefore, a sensing basis under these conditions is $\boldsymbol{U} = \boldsymbol{F}_N^H$. In order to take into account the impact of using a classic CP of length N_{CP}, the inner nodes can design a non-orthogonal sensing basis of size $(N_{\text{CP}} + N) \times N$ given by

$$\boldsymbol{W} = \begin{bmatrix} \boldsymbol{U}_{\text{CP}} \\ \cdots\cdots \\ \boldsymbol{U} \end{bmatrix}, \tag{4.36}$$

where $\boldsymbol{U}_{\text{CP}}$ contains the last N_{CP} rows of $\boldsymbol{U}$. Note that this extension does not increase the rank of the sensing basis. It is interesting to note that sensing the wireless environment with the sensing matrix provided in (4.36) permits finding those DoF that, regardless of the cyclic extension, keep the orthogonality with the outer networks. Even though sensing with a non-orthogonal basis is tougher, the described approach guarantees the orthogonality between those DoF sensed as occupied and the cyclic-extended inner transmitted signal. The described methodology is only needed at the transmitter side, as the inner receiver will remove the CP before.

Therefore, focusing on the inner transmitter, let us now assume that the sensed null-space basis reads as

$$\widehat{\boldsymbol{W}}_{\mathcal{N}} = \begin{bmatrix} \widehat{\boldsymbol{U}}_{\mathcal{N},\text{CP}} \\ \cdots\cdots\cdots \\ \widehat{\boldsymbol{U}}_{\mathcal{N}} \end{bmatrix} \in \mathbb{C}^{(N_{\text{CP}}+N)\times M}, \tag{4.37}$$

being M the number of DoF sensed as available, such that the shaping transmission matrix can be designed following the minimum worst-case inter-system interference criterion leading to

$$\widetilde{\boldsymbol{\Phi}} = \widehat{\boldsymbol{W}}_{\mathcal{N}}\boldsymbol{\Lambda} = \begin{bmatrix} \widehat{\boldsymbol{U}}_{\mathcal{N},\text{CP}} \\ \cdots\cdots\cdots \\ \widehat{\boldsymbol{U}}_{\mathcal{N}} \end{bmatrix} \boldsymbol{\Lambda} = \begin{bmatrix} \boldsymbol{\Phi}_{\text{CP}} \\ \cdots\cdots \\ \boldsymbol{\Phi} \end{bmatrix} \in \mathbb{C}^{(N_{\text{CP}}+N)\times K}, \tag{4.38}$$

where matrix $\boldsymbol{\Lambda}$ contains the linear combination coefficients that define the orthogonal waveforms encompassed in the sub-matrix $\boldsymbol{\Phi} = \widehat{\boldsymbol{U}}_{\mathcal{N}}\boldsymbol{\Lambda}$. These linear combination coefficients are

designed so as to satisfy the minimum worst-case inter-system interference criterion described in Chapter 3. In order to leverage this design criterion, the inner transmitter can remove[3] the first N_{CP} rows of $\widehat{\boldsymbol{W}}_{\mathcal{N}}$ and using Algorithm 1 (Section 3.3).

Analyzing (4.38), it is worth noting that the extended shaping transmission matrix $\widetilde{\boldsymbol{\Phi}}$ is no longer unitary; thus, the opportunistic transmission strategy based on (4.38) produces a self-induced ISI. Nevertheless, removing the cyclic extension, the effective waveforms are orthogonal and the self-induced ISI is canceled out.

Using the shaping transmission matrix defined in (4.38), note that the cyclically extended transmitted signal is given by

$$\boldsymbol{x} = \widetilde{\boldsymbol{\Phi}}\boldsymbol{a}, \tag{4.39}$$

being $\boldsymbol{a}$ the K symbols to be transmitted. The use of a CP at the transmitter and removing it at the receiver side induces a circular convolution, meaning that the signal at the inner receiver input, after removing the CP [TV05, Chapter 3], is given by

$$\widetilde{\boldsymbol{y}} = \boldsymbol{H}_{\text{II,c}}\tilde{\boldsymbol{x}} + \boldsymbol{w} + \boldsymbol{i} = \boldsymbol{H}_{\text{II,c}}\boldsymbol{\Phi}\boldsymbol{a} + \boldsymbol{w} + \boldsymbol{i}, \tag{4.40}$$

where $\boldsymbol{w} \sim \mathcal{N}_{\mathbb{C}}(\boldsymbol{0}_{N\times 1}, \sigma^2\boldsymbol{I}_N)$ is the thermal noise and $\boldsymbol{i}$ stands for the possible interferences, and $\boldsymbol{H}_{\text{II,c}}$ is the circulant channel matrix, given by

$$\boldsymbol{H}_{\text{II,c}} = \begin{bmatrix} h_{\text{II}}[0] & 0 & \cdots & 0 & \cdots & h_{\text{II}}[1] \\ \vdots & h_{\text{II}}[0] & \cdots & \vdots & \cdots & \vdots \\ h_{\text{II}}[L_h] & \vdots & \cdots & 0 & \cdots & h_{\text{II}}[L_h] \\ 0 & h_{\text{II}}[L_h] & \cdots & h_{\text{II}}[0] & \cdots & 0 \\ \vdots & 0 & \cdots & \vdots & \cdots & \vdots \\ 0 & \vdots & \cdots & \vdots & \cdots & 0 \\ 0 & 0 & \cdots & h_{\text{II}}[L_h] & \cdots & h_{\text{II}}[0] \end{bmatrix} \in \mathbb{C}^{N\times N}. \tag{4.41}$$

It is well-known that circulant matrices are factorized by normalized Fourier matrices. Accordingly, (4.41) can be written as

$$\boldsymbol{H}_{\text{II,c}} = \boldsymbol{F}_N^H\boldsymbol{\Sigma}_h\boldsymbol{F}_N. \tag{4.42}$$

Recalling that $\boldsymbol{\Phi} = \widehat{\boldsymbol{U}}_{\mathcal{N}}\boldsymbol{\Lambda}$, note that (4.40) can be written as

$$\widetilde{\boldsymbol{y}} = \boldsymbol{F}_N^H\boldsymbol{\Sigma}_h\boldsymbol{F}_N\widehat{\boldsymbol{U}}_{\mathcal{N}}\boldsymbol{\Lambda}\boldsymbol{a} + \boldsymbol{w} + \boldsymbol{i}. \tag{4.43}$$

Taking into account the discussion above (4.36), we note that the normalized Fourier matrix can indeed be written in terms of the sensing basis $\boldsymbol{U}$ as $\boldsymbol{U}^H = \boldsymbol{F}_N$. Therefore, it is straightforward to see that, without loss of generality, (4.43) can be written as

$$\widetilde{\boldsymbol{y}} = \boldsymbol{U}\begin{bmatrix} \boldsymbol{\Sigma}_{\mathcal{S},h} & \boldsymbol{0} \\ \boldsymbol{0} & \boldsymbol{\Sigma}_{\mathcal{N},h} \end{bmatrix}\left[\begin{array}{c} \boldsymbol{0}_{(N-M)\times M} \\ \hdashline \boldsymbol{I}_M \end{array}\right]\boldsymbol{\Lambda}\boldsymbol{a} + \boldsymbol{w} + \boldsymbol{i} \tag{4.44}$$

$$= \boldsymbol{U}\left[\begin{array}{c} \boldsymbol{0}_{(N-M)\times M} \\ \hdashline \boldsymbol{\Sigma}_{\mathcal{N},h} \end{array}\right]\boldsymbol{\Lambda}\boldsymbol{a} + \boldsymbol{w} + \boldsymbol{i}, \tag{4.45}$$

[3]Note that the use of the non-orthonormal sensing basis $\boldsymbol{W}$ in (4.36) is purely instrumental to determine which of the system DoF are perceived as available when the inner transmitter employs a CP-based signal extension. In practice, once matrix $\widehat{\boldsymbol{W}}_{\mathcal{N}}$ in (4.37) has been determined, only the last N rows are needed to design the MNTLS waveforms.

where M is the dimension of the sensed null space by the inner transmitting node, which is assumed at this point to be equal[4] to the dimension of the sensed null space at the inner receiver. The first reading of (4.45) reveals that the CP-based opportunistic transmission scheme proposed in this section (4.37)–(4.38) steers the information through the *eigenchannels* corresponding to the sensed null space by the inner transmitting node. The latter is of paramount importance since, as expected, minimizes the inter-system interference imposed on the outer-network nodes. As discussed earlier, this transmission scheme is based on a set of non-orthogonal MNTLS waveforms such that they become orthogonal after removing the cyclic extension. However, as per (4.45), the orthogonality between waveforms is preserved at the receiver side if the inner receiving node is able to counteract the impact of the sensed null-space eigenchannels.

Carefully observing (4.45), it is straightforward to see that a simple frequency-domain one-tap null-space channel equalizer suffices to neutralize the null-space eigenchannels. It is worth noting that the latter is similar to the required one-tap equalizer required by the OFDM modulation to deal with the frequency-selective nature of the wireless channel. The latter is due to the transmission scheme proposed in this chapter being also based on the classic CP employed by the OFDM modulation.

At this point, it is important to emphasize that the design of the channel equalization scheme is beyond the scope of this thesis. In this respect, several equalization techniques can be adopted (see, e.g., [PS08]). In the sequel, we adopt for the sake of simplicity the zero-forcing criterion. In spite of not being optimal from a statistical viewpoint, this equalization criterion is simple enough to show that it is possible to adapt the MNTLS waveforms presented in this dissertation to frequency-selective channels. Under this consideration, the frequency-domain one-tap null-space channel equalizer matrix is given by

$$\boldsymbol{G} = \widehat{\boldsymbol{U}}_{\mathcal{N}} \boldsymbol{\Sigma}_{\mathcal{N},h}^{-1} \widehat{\boldsymbol{U}}_{\mathcal{N}}^{H}, \tag{4.46}$$

where $\boldsymbol{\Sigma}_{\mathcal{N},h}^{-1}$ is a diagonal matrix containing the inverse of the non-zero noise-subspace eigenchannels. Thus, the relevant information at the equalizer output reads as

$$\widetilde{\boldsymbol{\nu}} = \boldsymbol{G}\tilde{\boldsymbol{y}} = \widehat{\boldsymbol{U}}_{\mathcal{N}} \boldsymbol{\Lambda} \boldsymbol{a} + \boldsymbol{G}\boldsymbol{w} = \boldsymbol{\Phi}\boldsymbol{a} + \widetilde{\boldsymbol{n}}, \tag{4.47}$$

where $\widetilde{\boldsymbol{n}} \sim \mathcal{N}_{\mathbb{C}}\left(\boldsymbol{0}, \sigma^2 \boldsymbol{U}_{\mathcal{N}} \boldsymbol{\Sigma}_{\mathcal{N},h}^{-1} \boldsymbol{U}_{\mathcal{N}}^{H}\right)$ is the equalized noise. Finally, letting $\boldsymbol{\Psi}$ be the matched-filter matrix designed by the inner receiver according to the minimum worst-case inter-system interference criterion, note that the sufficient statistic for symbol decoding $\boldsymbol{z} \in \mathbb{C}^K$ is given by

$$\boldsymbol{z} = \boldsymbol{\Psi}^{H} \tilde{\boldsymbol{\nu}} = \gamma \boldsymbol{a} + \boldsymbol{\Psi} \tilde{\boldsymbol{n}}, \tag{4.48}$$

being $\gamma < 1$ an energy loss factor due to the CP insertion. Regarding to the noise at symbol level, note that $\boldsymbol{n} = \boldsymbol{\Psi}^{\boldsymbol{H}} \boldsymbol{G}\boldsymbol{w} \sim \mathcal{N}_{\mathbb{C}}(\boldsymbol{0}; \sigma^2 \boldsymbol{\Lambda}^{H} \boldsymbol{S}_{\mathcal{N},h}^{-1} \boldsymbol{\Lambda})$, with $\boldsymbol{S}_{\mathcal{N},h} = \boldsymbol{\Sigma}_{\mathcal{N},h} \boldsymbol{\Sigma}_{\mathcal{N},h}^{H}$ being the power spectral density matrix of the noise-subspace channel. The overall opportunistic receiver strategy is depicted in Figure 4.16.

It is interesting to note that, in contrast to OFDMA, the opportunistic transmission scheme based on the classic CP described in this section performs time multiplexing. Nevertheless, the CP-based MNTLS modulation admits a straightforward extension enabling time-frequency multiplexing. If the null-space basis is not entirely exploited, that is, only a portion of the

[4]Otherwise, it is possible to leverage the enhanced null-space detection scheme described in Section 3.5.

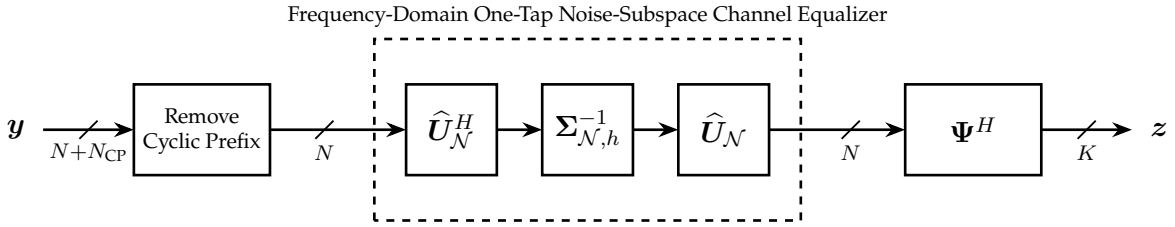

Figure 4.16: Opportunistic receiving scheme in frequency-selective channels.

sensed null space is used, then time multiplexing can be performed within this reduced null space. The remaining null-space DoF (i.e., in the asymptotic case under analysis, frequency bins) form an orthogonal complement of the previously exploited null-space region and also admits time multiplexing. Therefore, it is possible to multiplex the opportunistic signals in both time and frequency domains. The major drawback of performing time-frequency multiplexing is that when the null space is partitioned, the dimension of each portion is smaller than the total DoF sensed as available, which decreases the dimension spreading factor and, accordingly, the capacity of spreading the inter-system interferences.

As a final note on the adaptation of the MNTLS waveforms in frequency-selective channels, it is worth noting that the whole discussion has been based on the use of a sub-optimal equalization criterion. The purpose of adopting this criterion has been to prove that the adaptation to frequency-selective channels exists and can be simply implemented. The latter motivates the adoption of conventional techniques to achieve improved performance. In this sense, when CSI is available at the inner transmitter, it is possible to design a *null-space-constrained* capacity-achieving scheme by adopting a water-filling power allocation policy. In practice, the system inputs (information symbols to be transmitted) are drawn from a finite-size constellation; thus, it can be of interest to adopt a constellation-constrained power allocation policy (see, e.g., [LTV06; LTV08; OG15; HUL21] and references therein).

4.5.1 Comparison with VFDM

Among the opportunistic communication strategies discussed in Section 2.4.1, VFDM has been specifically designed to take advantage of the frequency-selective nature of interference channels and deal with the frequency-selective nature of the inner channel. In order to perfectly mitigate the undesired inter-system interferences, the VFDM transmitting node requires a perfect knowledge of the interference channel matrix to exploit the null space induced by the channel memory. Additionally, this technique also requires that all outer-network nodes employ a block transmission with guard intervals, such as OFDM. These requisites suffice to avoid the inter-system interferences provided by the inner transmitter. Then, to deal with the frequency-selective nature of the inner channel, VFDM is based on designing the codebook exploiting the SVD of the inner channel matrix. It is noteworthy that the latter requires the inner transmitting and receiving nodes to cooperate, bringing to light the necessity of feedback to share the channel coefficients. Another significant drawback of the basic VFDM strategy is that the inner receiver cannot cancel out the interferences from the outer networks.

Conversely, the opportunistic transmission strategy discussed in this section does not require perfect CSI at the inner transmitter nor cooperation between inner nodes to deal with the

frequency-selective nature of the inner channel while avoiding the undesired inter-system interferences to/from the outer networks. In this case, both the inner transmitter and the inner receiver need to locally detect the available DoF by exploiting a set of sampled observations from the wireless environment. The difficulty of the sensing step lies in the fact that the sensing bases are non-unitary. Of course, the sensing simplifies if the inner nodes have additional side information on the transmission format employed by the outer-network nodes. Once the available DoF have been identified at each system end, a CP-based modulation is proposed. As for the OFDM modulation, using a CP induces a circulant channel meaning that the impact of the channel fading can be counteracted by utilizing a simple one-tap equalizer.

In conclusion, the CP-based opportunistic transmission strategy proposed in this section permits dealing with the frequency-selective nature of the opportunistic channel more simply than VFDM, that is, without requiring perfect CSI nor coordination or cooperation between inner nodes. Nevertheless, since VFDM employs a water-filling power allocation policy at the inner transmitter, it can achieve higher spectral efficiencies than the proposed strategy at the expense of additional complexity and feedback overheads. The spectral efficiency of the proposed CP-based modulation can be improved, for instance, once the inner receiver identifies the effective null space, as the DoF with a poorer channel response will be systematically nulled by the active subspace detection strategy discussed in Section 3.5. Another possibility when the null-space eigenchannels are known at the inner transmitter consists in designing a (constrained) capacity-achieving power allocation policy.

4.6 Conclusions

This chapter has dealt with the asymptotic characterization of the MNTLS waveforms derived in Chapter 3. Through the asymptotic eigendecomposition of Toeplitz matrices, it has been found that the proposed waveforms converge to a linear combination of the normalized Fourier matrix. Thus, the MNTLS waveforms asymptotically admit a comparison to other frequency-domain spreading-based modulations classically employed in opportunistic communications, such as MC-CDMA and TDCS. Even though the modulation proposed in this dissertation exhibits similar spectral behavior to that of MC-CDMA and TDCS, the former does not require a beforehand consensus of the employed pseudo-random sequences since the waveforms can be locally and uniquely determined as a consequence of the invariance property.

The particular case where the frequency bins sensed as available are consecutive has been analyzed in detail. This chapter has also shown that it is possible to efficiently design the set of orthogonal waveforms under certain system conditions, overcoming the necessity of the sequential design scheme studied in Chapter 3. When the imposed conditions do not hold, a suboptimal approximation has been provided, exhibiting insignificant performance degradations in congested scenarios. A study of the properties of the CS-TDMA has been reported, emphasizing the TDMA capability based on circulant time shifts and a significantly improved PAPR performance with respect to conventional OFDMA.

Finally, since the MNTLS waveforms asymptotically depend on the normalized Fourier matrix, a straightforward adaptation to frequency-selective channels has been provided using a classic CP. The use of this CP generally hinders the sensing stage since it is based on a structured non-orthogonal sensing basis accounting for the CP insertion. Despite the proposed CP-based

modulation format having a similar implementation to OFDMA, it has been highlighted that the former naturally performs time-multiplexing. The CP-based opportunistic transmission scheme has been compared to VFDM, a null-space opportunistic strategy designed to exploit the null space induced by the channel memory and combat the frequency-selective nature of the inner channel. It has been pointed out that while VFDM maximizes the spectral efficiency of opportunistic communication, full CSI is required at the inner transmitter, suggesting the necessity of end-to-end coordination.

CHAPTER 5

The Case of Multi-Channel Feedforward Opportunistic Communications

5.1 Introduction

The use of multiple antennas may render several advantages in opportunistic communications, as surveyed in Chapter 2. Multi-antenna opportunistic nodes enjoy an increased number of potentially available DoF, which may improve the spectral efficiency of opportunistic communication and have a relevant impact from an interference management viewpoint. In this sense, using multiple antennas can enhance the capability of inner nodes to mitigate undesired inter-system interferences and provide additional signal-space dimensions for enabling multi-user opportunistic communication [SF11; XWGJ16].

Accordingly, this last chapter[1] extends the results of Chapter 3 and Chapter 4 to the case where both the inner transmitter and the inner receiver are equipped with L_{T} and L_{R} antennas, respectively. In this chapter, it is assumed that the antenna arrays have arbitrary and possibly different geometries for the sake of generality. Herein, the term *arbitrary geometry* means that antenna arrays can be either uniform or non-uniform with 1D, 2D, or 3D structures. Note that considering arbitrary arrays differs from the Uniform Linear Array (ULA) assumption, which has been conventionally used in the literature as reported in [LW19]. Moreover, the arbitrary geometry assumption also includes the case of uncalibrated (unstructured) antenna arrays.

5.1.1 Space-Time Degrees of Freedom

Before getting down to the multi-antenna case, we shall revisit the concept of Degrees of Freedom (DoF) involving space-time signals. As discussed in Chapter 2, the number (real) DoF for the single-antenna case can be found through the Interpolation Theorem and refers to the number of coefficients of an orthogonal expansion needed to describe a band-limited signal of

[1] Some of the results described in this chapter have been submitted for possible publication to IEEE Transactions on Signal Processing [J2].

Reference	Involved Parameters	Number of Spatial DoF
[BF89]	Radius R, Wavelength λ	$8\pi^2R^2/\lambda^2$
[PBT05]	Effective Area $\mathcal{A}$, Angular Spread $\lvert\Omega\rvert$	$\mathcal{A}\lvert\Omega\rvert$
[KSAJ07]	Radius R, Wavelength λ	$(\lceil e\pi R/\lambda\rceil + 1)^2$

Table 5.1: Number of spatial DoF for a spherical array of radius R.

finite duration uniquely. Asymptotically, the number of real DoF is given by the well-known time-bandwidth product, i.e.,

$$N \approx 2TW, \tag{5.1}$$

where W and T refer to the system bandwidth and the duration of the signal, respectively. The quantity given in (5.1) is also known as *Nyquist number* [Fra17].

Regarding the multi-antenna case, several works can be found in the literature trying to determine the number of spatial DoF in the case of narrowband transmissions, i.e., letting $W \to 0$. Through a rigorous analysis of the electromagnetic properties of scattered fields in the far-field, [BF89] states that the dimension of a scattered field radiated from a sphere of radius R is proportional to the surface (area) of the sphere and inversely proportional to the squared wavelength. This important finding reveals that the number of spatial DoF does not depend on the volume of the enclosing sphere but on its area. Lately, [PBT05] establishes an analogy between Shannon's result for the time-frequency domain (5.1) and the spatial-angular domain leveraging antenna theory. In essence, the number of spatial DoF found therein for non-polarized antenna arrays is given by the product of the effective area of the aperture and the angular spread (in solid angle). Solving the general wave equation, [KSAJ07] corroborates the quadratic growth rate of the spatial DoF found in [BF89] but with a different slope. A summary of the aforementioned results is provided in Table 5.1 for the reader's convenience.

Regardless of the considered approach, in order to fully exploit the spatial domain, the required number of antennas to be placed coincides with the number of spatial DoF. The latter follows simply from the Sampling Theorem [PBT05]. Given an antenna array of a limited size, the maximum number of spatial DoF is proportional to the effective size of the array. Therefore, using a number of antennas less than the number of spatial DoF leads to spatial aliasing (grating lobes). Otherwise, the spatial domain is oversampled, and there is no need to place more antennas than the number of spatial DoF. Nevertheless, the placed antennas must be uncorrelated to fully exploit the potential diversity or multiplexing offered by the spatial domain. In this sense, the correlation between array elements is considered in [MSA08], which provides the concept of effective spatial DoF, i.e., the multiplexing gain of a Multiple-Input Multiple-Output (MIMO) system when the array elements are correlated. The effective spatial DoF are also studied from an electromagnetic perspective in [YHC+22].

Determining the number of DoF in wideband multi-antenna scenarios is cumbersome since the frequency and spatial dimensions are coupled. A first attempt can be found in [PBT05], where Poon, Brodersen, and Tse stated that the total number of real DoF in wideband multi-antenna channels is given by the product of the spatial DoF and the time-frequency DoF, i.e., $\eta \approx 2TW\mathcal{A}|\Omega|$. A more recent approach can be found in [Fra15] and further analyzed in [Fra17], which extends the approach discussed in [BF89] to the case of wideband transmissions, making use of Landau's eigenvalue theorem [Lan75] and the information cut-sets theory. The main

result discussed in [Fra15] states that the number of space-time DoF is given by the product of the time-frequency DoF and the space-wavenumber DoF. Accordingly, for 2D scenarios, i.e., when the array can be enclosed in a circular domain of radius R, the number of real space-time DoF is asymptotically given by

$$\eta \approx 2TW\frac{2\pi R}{\Lambda}, \tag{5.2}$$

where $\Lambda = c/W$ is the *wavelength bandwidth*, being c the propagation speed. Note that (5.2) relies on (5.1) and the perimeter of the circle normalized by an interval of wavelengths. When the array can be enclosed on a sphere of radius R, i.e., in 3D scenarios, the number of real space-time DoF is given by

$$\eta \approx 2TW \cdot 4\pi R^2\frac{4}{3\Lambda^2}, \tag{5.3}$$

where, as concluded in [BF89], the number of space-wavenumber DoF depends on the surface of the sphere and is inversely proportional to the squared wavelength.

Considering these results, it is possible to design antenna arrays to fully exploit the space-wavenumber DoF given by (5.2) or (5.3). For instance, a simple greedy algorithm is described in [MSA08] to design linear and square arrays so as to maximize the effective spatial DoF. Therein, it is illustrated that optimal configurations in terms of maximum effective DoF are generally non-uniform.

As a final note on the number of space-time DoF, it is worth mentioning that the abovementioned results hold under the far-field assumption, i.e., when the radiated signals are observed beyond the Fraunhofer distance [Han88] and do not account for the polarization of the array. As discussed in [PBT05], polarization can double the spatial DoF. In the near-field, the classic plane wave assumption is no longer valid, i.e., the curvature of the wavefront cannot be approximated as planar over the entire antenna array. Accordingly, the waveform model must be based on spherical waves. As studied in the recent literature (see, for instance, [FMMS15; YHC+22]), the number of spatial DoF increases in the near-field, leading to a large multiplexing capability. For the narrowband case, [KMM17] determines that the number of spatial DoF at the near-field is approximately 1.18 times the number of spatial DoF in the far-field.

5.1.2 Chapter Organization

This chapter is organized as follows. The Minimum-Norm Total Least-Squares (MNTLS) waveforms for multi-antenna opportunistic communications are provided in Section 5.2. This section also studies the properties of the MNTLS waveforms in multi-antenna channels: the Signal-to-Interference Density Ratio (SIDR) and the fundamental invariance property. Regarding the latter, it is shown that it can be straightforwardly extended in the symmetric case, i.e., when $L_{\mathrm{T}} = L_{\mathrm{R}}$. Nevertheless, nothing can be said a priori for general asymmetric MIMO channels. The latter motivates a more thorough general case study, which is provided in Section 5.3. Using the so-called *manifold separation theory*, we prove that the time-domain invariance is preserved in asymmetric MIMO scenarios. The properties of the MNTLS waveforms and the theoretical array-geometry invariance are numerically characterized in Section 5.4. The asymptotic analysis of the MNTLS waveforms provided in Section 5.5 reveals that, in the limit, the transmission strategy performs an antenna selection policy. As well as the adaption of the solution

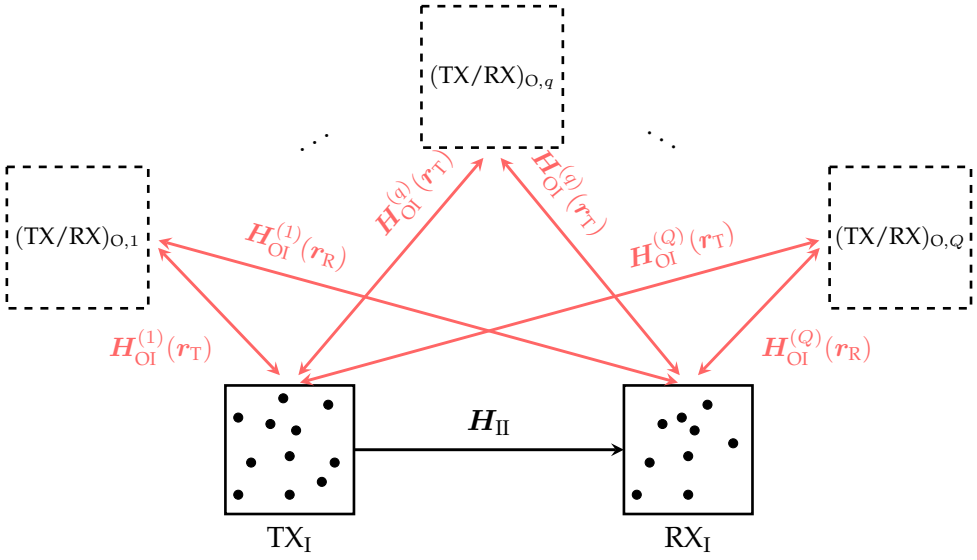

Figure 5.1: The system model for the multi-channel feedforward opportunistic communications problem. An inner transmitter-receiver pair, which are equipped with arbitrary antenna arrays of L_{T} and L_{R} sensors, respectively, tries to coexist with Q outer transmitter-receiver pairs. Unless otherwise stated, it is assumed that $L_{\mathrm{T}} \neq L_{\mathrm{R}}$. For this purpose, the inner nodes exploit the interference channels $\boldsymbol{H}_{\mathrm{OI}}^{(q)}(\boldsymbol{r})$ to infer the space-time null space and ideally avoid interfering the outer transmissions when communicating through the inner channel $\boldsymbol{H}_{\mathrm{II}}$. It is assumed that all channels are unknown by the opportunistic inner transmitter $\mathrm{TX_I}$, whereas the opportunistic inner receiver $\mathrm{RX_I}$ only knows, at most, the inner channel $\boldsymbol{H}_{\mathrm{II}}$.

in multi-antenna frequency-selective channels and the multi-channel version of the CS-TDMA transmission scheme. The conclusions of this chapter are drawn in Section 5.6.

5.2 Multi-Antenna General Null-Space Solution

This section extends the MNTLS waveforms described in Chapter 3 to multi-antenna scenarios. For this purpose, we consider the system model depicted in Figure 5.1, where a pair of inner multi-antenna terminals try to set up a communication link by exploiting the locally available space-time DoF to minimize the impact on the coexisting outer-network terminals. Throughout the whole chapter, we assume that the transmitting and receiving arrays are appropriately configured to exploit all the spatial DoF [cf. (5.2) and (5.3)]. Thus, being L_{T} and L_{R} the number of transmitting and receiving antennas and N the asymptotic number of time-frequency DoF, which is equal at each inner node, the total number of space-time DoF, regardless the existence of antenna correlation, at each inner nodes is given by

$$\eta_t = NL_{\mathrm{T}}, \tag{5.4}$$

$$\eta_r = NL_{\mathrm{R}}. \tag{5.5}$$

The objective of the inner transmitting node consists in designing a set of space-time opportunistic waveforms $\{\boldsymbol{\phi}_{\boldsymbol{k}}\}_{0\leq k\leq K-1}$, with $\boldsymbol{\phi}_{\boldsymbol{k}} \in \mathbb{C}^{NL_{\mathrm{T}}}$, orthogonal to the sensed space-time signal subspace, i.e, orthogonal to the occupied space-time signal-space dimensions or DoF. It is worth

noting that the column-vector stacked space-time waveforms $\boldsymbol{\phi_k}$ can be written as

$$\boldsymbol{\phi}_k = \mathrm{vec}\left([\boldsymbol{\phi}_k[0], \ldots, \boldsymbol{\phi}_k[N-1]]\right), \tag{5.6}$$

with $\boldsymbol{\phi}_k[n] \in \mathbb{C}^{L_\mathrm{T}}$ being the beamvector at the n-th discrete time instant. Accordingly, the multi-antenna opportunistic transmission of a block of K zero-mean and unit variance statistically independent symbols a_k drawn from a known constellation $\mathcal{C}$ is modeled as

$$\boldsymbol{x}_q[n] = \sqrt{\frac{S_\mathrm{T}}{K}} \sum_{k=0}^{K-1} a_{k[q]} \boldsymbol{\phi}_k[n - qN] \in \mathbb{C}^{L_\mathrm{T}}, \tag{5.7}$$

for $n = 0, \ldots, N-1$, where q indexes the transmitted block and S_T is the average transmitted signal power. Therefore, the associated discrete-time received signal for the arbitrary transmitted block $\boldsymbol{x}_q[n]$ is given by

$$\boldsymbol{y}_q[n] = \sqrt{\frac{S_\mathrm{T}}{K}} \sum_{k=0}^{K-1} a_{k[q]} \boldsymbol{H}_\mathrm{II}[n - qN] \boldsymbol{\phi}_k[n - qN] + \boldsymbol{i}[n] + \boldsymbol{v}[n] \in \mathbb{C}^{L_\mathrm{R}}, \tag{5.8}$$

where $\boldsymbol{H}_\mathrm{II}[n] \in \mathbb{C}^{L_\mathrm{R} \times L_\mathrm{T}}$ is the MIMO inner channel matrix, $\boldsymbol{i}[n] \in \mathbb{C}^{L_\mathrm{R}}$ is an unstructured interference term, and $\boldsymbol{v}[n] \in \mathbb{C}^{L_\mathrm{R}}$ is the spatial noise component, distributed according to $\boldsymbol{v}[n] \sim \mathcal{N}_\mathbb{C}(\boldsymbol{0}, \sigma_v^2 \boldsymbol{I}_{L_\mathrm{R}})$. The noise component is also assumed to be uncorrelated in the time domain. For the time being, the frequency selective nature of the MIMO inner channel is omitted, as it will be discussed further in this chapter (Section 5.5). The inner transmitting node has to design the set of orthonormal space-time opportunistic waveforms $\{\boldsymbol{\phi}_k\}_{0 \leq k \leq K-1}$ using the local-only sensing information and without cooperating with the inner receiver or the other outer-network nodes.

On the other side of the problem, the inner receiving node has to design a detection scheme for the MNTLS transmitted waveforms. Letting $\boldsymbol{y}_q \in \mathbb{C}^{NL_\mathrm{R}}$ be the stacking of the received signal (5.8) for $n = 0, \ldots, N-1$, the sufficient statistic for symbol decoding $\boldsymbol{z}_q \in \mathbb{C}^K$ for the arbitrary transmitted block q is given by

$$\boldsymbol{z}_q = \boldsymbol{\Psi}^H \boldsymbol{y}_q, \tag{5.9}$$

where $\boldsymbol{\Psi} \in \mathbb{C}^{NL_\mathrm{R} \times K}$ is the receiver processing matrix defined as

$$\boldsymbol{\Psi} \triangleq [\boldsymbol{\psi}_0 \ \cdots \ \boldsymbol{\psi}_k \ \cdots \ \boldsymbol{\psi}_{K-1}], \tag{5.10}$$

being $\boldsymbol{\psi}_k$ the matched filter for the k-th transmitted waveform $\boldsymbol{\phi}_k$. The inner receiver does not cooperate and is not coordinated with the inner transmitter or the outer-network nodes, meaning that the design of the matrix $\boldsymbol{\Psi}$ relies only on the null-space inference locally performed by the receiving node.

We have learned in Chapter 3 that the MNTLS matched filters $\{\boldsymbol{\psi}_k\}_{0 \leq k \leq K-1}$ can be designed with the same recursive procedure employed by the inner transmitter to design the MNTLS pulse-shaping waveforms, thanks to the fundamental invariance property of the proposed solutions. The robustness of the MNTLS waveforms to inter-node subspace mismatch justifies the generality of the proposed scheme. In multi-antenna feedforward opportunistic communications, two distinct scenarios have to be studied. On the one hand, the particular case where the number of transmitting antennas equals the number of receiving antennas, i.e., $L_\mathrm{T} = L_\mathrm{R}$. In this

case, it is straightforward to see that the same rationale discussed in Chapter 3 is still valid. On the other hand, the most general asymmetric MIMO case where the antenna arrays employed by the inner transmitter and the inner receiver have different compositions, i.e., $L_{\mathrm{T}} \neq L_{\mathrm{R}}$. Even though the MNTLS pulse-shaping waveforms and matched-filter receivers can be locally designed as in Chapter 3, it is unclear whether the fundamental invariance property holds in this general case.

The design of the transmitting waveforms $\{\boldsymbol{\phi}_k\}_{0\leq k\leq K-1}$ and matched filters $\{\boldsymbol{\psi}_k\}_{0\leq k\leq K-1}$ is addressed in the sequel. Section 5.2.1 discusses the local design of the transmitting waveforms based on the MNTLS principle described in Chapter 3. Moreover, the performance in terms of SIDR is characterized, as well. Section 5.2.2 deals with analyzing the fundamental invariance property in multi-antenna opportunistic communications.

5.2.1 Multi-Channel Generalized Null-Space Transmitting Waveforms

In order to ideally avoid providing inter-system interferences, the inner transmitting node has to infer the space-time null space. As per [Fra17], the DoF information can be obtained through spectral factorization of the received wavefield. Accordingly, assuming that the inner transmitter does not have side information about the outer networks, the null space can be sensed from a sample estimate of the autocorrelation matrix. For this purpose, the inner transmitter needs a set of space-time sampled observations $\mathcal{X}$ from the surrounding wireless environment. These observations can be obtained by stacking N per-antenna observations, i.e., an arbitrary observations $\boldsymbol{x} \in \mathbb{C}^{NL_{\mathrm{T}}}$ belonging to $\mathcal{X}$ is given by

$$\boldsymbol{x} = \begin{bmatrix} \boldsymbol{x}[0] \\ \vdots \\ \boldsymbol{x}[N-1] \end{bmatrix}, \tag{5.11}$$

where $\boldsymbol{x}[n] \in \mathbb{C}^{L_{\mathrm{T}}}$ contains the samples obtained at each array element at time instant n. Therefore, a sample estimate of the space-time autocorrelation matrix can be found as

$$\widehat{\boldsymbol{R}}_{\boldsymbol{xx}} = \frac{1}{|\mathcal{X}|} \sum_{\boldsymbol{x}\in\mathcal{X}} \boldsymbol{x}\boldsymbol{x}^H = \boldsymbol{U}\boldsymbol{D}\boldsymbol{U}^H \in \mathbb{C}^{NL_{\mathrm{T}}\times NL_{\mathrm{T}}}. \tag{5.12}$$

It is worth noting that the space-time autocorrelation matrix captures both the time-frequency and the space-wavenumber DoF. Thus, through model order selection, the inner transmitter can find the sensed null-space basis composed of the eigenvectors associated with the least significant eigenmodes. Taking into account the detection errors and the time-varying conditions of the network state, the sensed null-space basis $\widehat{\boldsymbol{U}}_{\mathcal{N}}$ is given by

$$\widehat{\boldsymbol{U}}_{\mathcal{N}} = \left[\begin{array}{c:c} \widetilde{\boldsymbol{U}}_{\mathcal{N}} & \boldsymbol{E}_{\mathcal{N}} \end{array}\right] \in \mathbb{C}^{NL_{\mathrm{T}}\times M_{\mathrm{T}}}, \tag{5.13}$$

being $\widetilde{\boldsymbol{U}}_{\mathcal{N}}$ and $\boldsymbol{E}_{\mathcal{N}}$ the matrices spanning the correctly detected available DoF and the occupied DoF wrongly sensed as available, respectively, and M_{T} the total number of available sensed space-time DoF at the inner transmitting node. Therefore, the space-time generalized null-space transmitting waveforms obeying

$$\boldsymbol{\phi}_k = \widehat{\boldsymbol{U}}_{\mathcal{N}}\boldsymbol{\lambda}_k, \tag{5.14}$$

with $\boldsymbol{\lambda}_k$ the linear combination coefficients defining the k-th waveform, can mitigate (ideally avoid) inter-system interferences imposed on outer-network nodes. As in Chapter 3, these waveforms belong to the family of null-space precoding techniques, and thus the choice of $\boldsymbol{\lambda}_k$ is critical to managing the residual interferences caused by the sensing uncertainties.

In view of the sensing uncertainties reflected on the unknown sensing error matrix $\boldsymbol{E}_{\mathcal{N}}$, it seems reasonable to adopt the minimum worst-case inter-system interference criterion described in Chapter 3 to design the space-time MNTLS transmitting waveforms $\{\boldsymbol{\phi}_k\}_{0\leq k\leq K-1}$. It is worth noting that the waveform design problem in multi-antenna feedforward opportunistic communications is just the extension of the problem posed in Chapter 3 to an environment with higher dimensionality.

Taking into account the discussion above and recalling the definition of the inter-system interference average power (3.12), the design of the linear combination coefficients vectors defining the set of linear modulations $\{\boldsymbol{\phi}_k\}_{0\leq k\leq K-1}$ can be found as

$$\{\boldsymbol{\lambda}_k\}_{0\leq k\leq K-1} = \underset{\{\boldsymbol{\lambda}_k\},\{\boldsymbol{e}_k\}}{\arg\min} \left\{ \max_{\boldsymbol{E}_{\mathcal{N}}} \sum_{k=0}^{K-1} \left\| \boldsymbol{E}_{\mathcal{N}}^H \widehat{\boldsymbol{U}}_{\mathcal{N}} \boldsymbol{\lambda}_k \right\|^2 \right\} \tag{5.15}$$

$$\text{subject to} \quad \text{(a) } \|\boldsymbol{E}_{\mathcal{N}}\|_{\mathrm{F}}^2 \leq \xi^2;\ \text{(b) } \boldsymbol{\lambda}_k^H \boldsymbol{\lambda}_{k'} = 0,\ k \neq k';\ \text{(c) } \boldsymbol{\lambda}_k^H \widehat{\boldsymbol{U}}_{\mathcal{N}}^H \boldsymbol{e}_k = \alpha_k \tag{5.16}$$

where the constraints (5.16) upper-bound the degree of uncertainty assumed in the sensing model in (5.13), guarantee the orthogonality between designed space-time waveforms, and avoid the trivial solution, respectively. Thus, as per Appendix 3.A, the set of space-time MNTLS transmitting waveforms can be found as

$$\boldsymbol{\phi}_k = \left(\boldsymbol{e}_k^T \widehat{\boldsymbol{P}}_k \boldsymbol{e}_k \right)^{-1/2} \widehat{\boldsymbol{P}}_k \boldsymbol{e}_k, \tag{5.17}$$

where $\widehat{\boldsymbol{P}}_{k+1} = \widehat{\boldsymbol{P}}_k \left(\boldsymbol{I}_{NL_{\mathrm{T}}} - \boldsymbol{\phi}_k \boldsymbol{\phi}_k^H \right)$ is the orthogonal projector onto (a subset of) the sensed noise subspace, being $\widehat{\boldsymbol{P}}_0 = \widehat{\boldsymbol{U}}_{\mathcal{N}} \widehat{\boldsymbol{U}}_{\mathcal{N}}^H$ the orthogonal projector onto the whole space-time null space sensed at the inner transmitter, and $\boldsymbol{e}_k \triangleq \left[\boldsymbol{0}_{n(k)-1}^T\ 1\ \boldsymbol{0}_{NL_{\mathrm{T}}-n(k)}^T \right]^T$. As discussed in Chapter 3, the vector $\boldsymbol{e}_k$ can be optimized to minimize the inter-system interference power as

$$n(k) = \underset{n(k)\in\{1,\ldots,NL_{\mathrm{T}}\}}{\arg\max} \left[\widehat{\boldsymbol{P}}_k \right]_{n(k),n(k)}. \tag{5.18}$$

It is worth noting that the design of the space-time MNTLS transmitting waveforms can be tackled sequentially using Algorithm 1 (Chapter 3), revealing its efficient implementation. Since the set of waveforms $\{\boldsymbol{\phi}_k\}_{0\leq k\leq K-1}$ satisfying (5.17) depends on the orthogonal projector $\widehat{\boldsymbol{P}}_k$, it seems reasonable to think that the properties discussed in Chapter 3 still hold in the multi-channel case. Specifically, from the inner transmitter viewpoint, the properties revealing the capability exhibited by the designed space-time waveforms to coexist with outer networks are the spectral behavior and the SIDR. These two properties, which will be numerically illustrated in Section 5.4, characterize the *coexistence capability* of the designed linear modulation scheme. In the sequel, we analyze the impact of using multiple antennas on the SIDR.

Analysis of the Signal-to-Interference Density Ratio (SIDR)

The SIDR metric defined in Chapter 3 permits quantitatively evaluating the capability of managing the residual inter-system interferences exhibited by the space-time MNTLS waveforms.

Recalling (3.68), the SIDR measured at the inner transmitter output reads as

$$\mathrm{SIDR}_{\mathrm{T}}\left(\boldsymbol{E}_{\mathcal{N}};\{\boldsymbol{\lambda}_k\}\right)=\frac{S_{\mathrm{T}}-I_{\mathrm{T}}\left(\boldsymbol{E}_{\mathcal{N}};\{\boldsymbol{\lambda}_k\}\right)}{\frac{1}{N_E}I_{\mathrm{T}}\left(\boldsymbol{E}_{\mathcal{N}};\{\boldsymbol{\lambda}_k\}\right)}, \tag{5.19}$$

where S_{T} and $I_{\mathrm{T}}\left(\boldsymbol{E}_{\mathcal{N}};\{\boldsymbol{\lambda}_k\}\right)$ are the total average transmitted power and the aggregate average inter-system interference power, and N_E is the number of occupied space-time DoF erroneously sensed as available. In order to highlight the potential advantages of using multiple transmit antennas, an asymptotic analysis of (5.19) is provided in Appendix 5.B. Specifically, as $N\to\infty$, the SIDR at the inner transmitter output can be approximated by

$$\mathrm{SIDR}_{\mathrm{T}}\left(\boldsymbol{E}_{\mathcal{N}};\{\boldsymbol{\lambda}_k\}\right)\approx NL_{\mathrm{T}}\cdot\frac{M}{NL_{\mathrm{T}}}\cdot\left(1-\frac{N_E}{M}\right)=NL_{\mathrm{T}}\cdot\kappa\cdot\left(1-\frac{\epsilon}{\kappa}\right), \tag{5.20}$$

where κ refers to the fraction of the space-time DoF sensed as available by the inner transmitting node with respect to the total number of space-time DoF NL_{T}, whereas ϵ stands for the relative sensing errors made by the inner transmitter with respect to NL_{T}. Hence, note that $0\leq\epsilon\leq\kappa$. As discussed in Appendix 5.B, it should be noted that (5.20) is valid whenever the inner transmitter activates all the L_{T} antennas. Nevertheless, several differences with respect to the single-channel case deserve our attention and are discussed next.

In spite of the simplicity of the approximation provided in (5.20), the SIDR heavily depends on each particular scenario. Note that both M and N_E have a non-trivial dependence on the number of independent transmitting antennas L_{T}. Focusing on M, note that equals the sum of the per-antenna available DoF M_ℓ if the L_{T} transmitting antennas are statistically independent. In our case, the antennas should be statistically independent in order to span all the system space-time DoF; however, the L_{T} antennas may be generally correlated. Considering that each antenna can be subject to different sensing conditions, we note that, generally, $M_\ell\neq M_{\ell'}$. Accordingly, it is straightforward to see that M grows with L_{T} slower than the number of total system space-time DoF NL_{T}. This observation unveils that $\kappa\leq M_\ell/N$, with equality when the transmitting antennas are maximally correlated or when $M_\ell=M_{\ell'}$ for all $\ell\neq\ell'$. It is worth noting that the relative sensed space-time DoF is upper-bounded by the single-channel case. Thus, what is the advantage of using multiple antennas? The advantage of employing antenna arrays is only recognized in absolute terms since increasing the number of antennas may lead to a higher DoF spreading coefficient M. Increasing the DoF spreading coefficient implies that the power per DoF diminishes, yielding a lower interference density per DoF. Conversely, the advantage of using multiple antennas on the relative sensing errors ϵ can be appreciated in relative terms since, following the same rationale as for M, the parameter ϵ is also upper-bounded by the single-channel case.

5.2.2 The Invariance Property and Multi-Channel Receiving Scheme

Thus far, the capability of managing inter-system interferences exhibited by the space-time MNTLS waveforms has been discussed. At this point, we have to examine the fundamental invariance property, which guarantees coherent waveform detection without any coordination or cooperation between inner nodes.

Recalling the single-channel case, the invariance property follows from the uniqueness of orthogonal projectors. It is worth noting that this argument is valid whenever the sensed

null spaces at each inner node are subspaces of the same ambient vector space, i.e., $\mathbb{C}^N$ for the single-channel case. Nevertheless, three different scenarios must be considered in multi-channel opportunistic communications. For the sake of simplicity, we assume that the number of time-frequency DoF N is the same at each inner node.

The first scenario to be analyzed is where the transmitting and receiving arrays have the same structure or architecture (e.g., ULA) and have the same number of elements, i.e., $L_{\mathrm{T}} = L_{\mathrm{R}}$. This particular case is just a trivial extension of the single-channel case and, as studied by the author in [BV18], the invariance property can be straightforwardly shown by accounting for the uniqueness of orthogonal projectors. Imagine now that the number of transmitting and receiving antennas is still the same, but the antenna arrays at each system end have different geometry (for instance an L_{T}-element ULA and an L_{R}-element planar array, with $L_{\mathrm{T}} = L_{\mathrm{R}}$). Under ideal operating conditions, i.e., when inter-node subspace mismatch is not present, the number of sensed available space-time DoF is the same at each inner node. Since $L_{\mathrm{T}} = L_{\mathrm{R}} = L$, the null spaces sensed at each inner node are equal $\widehat{\mathcal{N}}_{\mathrm{T}} = \widehat{\mathcal{N}}_{\mathrm{R}}$ despite that the different array geometries naturally induce that the sensed null-space bases at the inner transmitter and receiver differ. Accordingly, there exists a right-unitary linear transformation $\boldsymbol{Q} \in \mathbb{C}^{M\times M}$ such that $\widehat{\boldsymbol{U}}_{\mathcal{N}}(\boldsymbol{r}_{\mathrm{T}}) = \widehat{\boldsymbol{U}}_{\mathcal{N}}(\boldsymbol{r}_{\mathrm{R}})\boldsymbol{Q}$, where $\widehat{\boldsymbol{U}}_{\mathcal{N}}(\boldsymbol{r}_{\mathrm{T}}) \in \mathbb{C}^{NL\times M}$ and $\widehat{\boldsymbol{U}}_{\mathcal{N}}(\boldsymbol{r}_{\mathrm{R}}) \in \mathbb{C}^{NL\times M}$ are the sensed null-space basis at the inner transmitter and receiver, respectively, and M is the dimension of the sensed null space. Under these conditions, we note that

$$\widehat{\boldsymbol{P}}_0(\boldsymbol{r}_{\mathrm{T}}) = \widehat{\boldsymbol{U}}_{\mathcal{N}}(\boldsymbol{r}_{\mathrm{T}})\widehat{\boldsymbol{U}}_{\mathcal{N}}^H(\boldsymbol{r}_{\mathrm{T}}) = \widehat{\boldsymbol{U}}_{\mathcal{N}}(\boldsymbol{r}_{\mathrm{R}})\boldsymbol{Q}\boldsymbol{Q}^H\widehat{\boldsymbol{U}}_{\mathcal{N}}^H(\boldsymbol{r}_{\mathrm{R}}) = \widehat{\boldsymbol{P}}_0(\boldsymbol{r}_{\mathrm{R}}), \tag{5.21}$$

meaning that the uniqueness of orthogonal projectors is still a valid argument to prove the invariance property of the space-time MNTLS waveforms. This statement reveals that the array geometry does not play an important role if the number of antennas at each system end is equal and the sensed null-space sensed at the inner transmitter and receiver are equal.

In the two scenarios discussed above, the invariance property holds in the space-time null space, meaning that the matched filters for the K transmitted waveforms can be designed through the recursive design scheme described in Algorithm 1, as in the single-channel case. Nevertheless, the most general and sophisticated scenario is the completely asymmetric MIMO scenario, i.e., when $L_{\mathrm{T}} \neq L_{\mathrm{R}}$, regardless of the considered array geometries. In this general case, the rotational invariance property of orthogonal projectors does not justify the optimality of (5.15)–(5.16) to design the matched filters $\{\boldsymbol{\psi}_k\}_{0\leq k\leq K-1}$. A sophisticated analysis of this general case is elaborated in the following section, unveiling that, despite the array-geometry asymmetries, (5.15)–(5.16) is still the optimum design strategy for the opportunistic receiving scheme under ideal operating conditions.

5.3 The Impact of the Array Geometry

This section deals with analyzing the asymmetric MIMO scenario in feedforward opportunistic communications. For the purpose of characterizing the impact of different array geometries, we first describe a physical model for the space-time DoF. Then, using the manifold separation theory, which is briefly reviewed in Appendix 5.A, we show that the fundamental invariance property is preserved in asymmetric MIMO opportunistic channels. This theoretical result is

accompanied by a simulation analysis in Section 5.4 corroborating that the space-time MNTLS waveforms are invariant to the antenna array geometry.

5.3.1 Physical Model

In order to mitigate inter-system interferences, the inner nodes need to sense the wireless environment and decide which of the space-time DoF are presumably available for opportunistic communication. This problem can be addressed through conventional eigenanalysis of a sample estimate of the autocorrelation matrix. It is worth noting that the geometry of the antenna array is embedded in the eigenvectors' matrix but does not appear explicitly. Even though the eigenvectors' matrix suffices for designing the space-time MNTLS waveforms, the array geometry must expressly appear on the null-space basis to characterize its impact.

Let us assume that an inner node equipped with an L-element array knows the array geometry, i.e., the array is perfectly calibrated and is aware of the transmission parameters of the outer-network nodes. Under these assumptions, the wideband snapshots observed from the far-field at time instant n by the inner node can be modeled as the sum of monochromatic plane waves [Van02], i.e.,

$$\boldsymbol{z}_n = \sum_{p=1}^{P} \sum_{\omega \in \mathcal{W}_p} \boldsymbol{b}[\omega] \otimes (\boldsymbol{s}_p[\omega] \odot \boldsymbol{\alpha}_{n,p}[\omega]) + \boldsymbol{v} \in \mathbb{C}^{NL} \tag{5.22}$$

where P is the number of propagation direction including the line-of-sight path and the multi-path reflections; $\mathcal{W}_p \subset (-W/2, W/2]$ is the spectral support of the p-th path, being W the system bandwidth; $\boldsymbol{\alpha}_{n,p}[\omega]$ refers to the per-antenna time-domain contribution; $\boldsymbol{v} \in \mathcal{N}_{\mathbb{C}}(\boldsymbol{0}, \sigma_v^2 \boldsymbol{I}_{NL})$ is the observation noise; $\boldsymbol{b}[\omega]$ is the frequency-bin vector given by

$$\boldsymbol{b}[\omega] \triangleq \begin{bmatrix} 1 \\ e^{j\omega} \\ \vdots \\ e^{j\omega(N-1)} \end{bmatrix} \in \mathbb{C}^N, \tag{5.23}$$

where $\omega = 2\pi f$ is the angular frequency; and $\boldsymbol{s}_p[\omega]$ refers to the array steering vector defined as

$$\boldsymbol{s}_p[\omega] \triangleq \begin{bmatrix} 1 \\ e^{j\boldsymbol{k}_{\omega,p}^T \boldsymbol{r}_1} \\ \vdots \\ e^{j\boldsymbol{k}_{\omega,p}^T \boldsymbol{r}_{L-1}} \end{bmatrix} \in \mathbb{C}^L, \tag{5.24}$$

being $\boldsymbol{r}_\ell \triangleq [x_\ell, y_\ell, z_\ell]^T$ the cartesian coordinates of the ℓ-th array sensor with respect to the phase-reference element, and $\boldsymbol{\kappa}_{\omega,p}$ is the wavenumber vector corresponding to the p-th propagation path and to the wavelength λ_ω associated with frequency ω. Letting $\{\theta_p \in [-\pi/2, \pi/2]\}_{1 \leq p \leq P}$ and $\{\varphi_p \in [-\pi, \pi]\}_{1 \leq p \leq P}$ be the elevation and azimuth angles, respectively, $\boldsymbol{\kappa}_{\omega,p}$ is given by

$$\boldsymbol{\kappa}_{\omega,p} \triangleq \frac{2\pi}{\lambda_\omega} \begin{bmatrix} \sin(\theta_p)\cos(\varphi_p) \\ \sin(\theta_p)\sin(\varphi_p) \\ \cos(\theta_p) \end{bmatrix}. \tag{5.25}$$

Under the unrealistic assumption that the inner node has a perfect knowledge of the propagation conditions and the structure of the outer networks, (5.22)–(5.25) can be used to construct a null-space basis where the array geometry appears explicitly through the steering vector in (5.24).

In order to circumvent this unrealistic assumption, the inner node can design an *ad-hoc* DoF sensing basis that spans the whole space-time ambient space and can be further used to sense the wireless environment and determine the null space. For this purpose, let us define the frequency-bin matrix $\boldsymbol{B} \in \mathbb{C}^{N\times N}$ as

$$\boldsymbol{B} \triangleq [\boldsymbol{b}[\omega_0] \cdots \boldsymbol{b}[\omega_n] \cdots \boldsymbol{b}[\omega_{N-1}]] \,, \tag{5.26}$$

being $\boldsymbol{b}[\omega_n]$ the frequency-bin vector defined in (5.23), and the array steering matrix $\boldsymbol{S}[\omega] \in \mathbb{C}^{L\times L}$ at a given frequency ω as

$$\boldsymbol{S}[\omega] \triangleq [\boldsymbol{s}_0[\omega] \cdots \boldsymbol{s}_\ell[\omega] \cdots \boldsymbol{s}_{L-1}[\omega]] \,, \tag{5.27}$$

where $\boldsymbol{s}_\ell[\omega]$ is the steering vector given in (5.24). With the aim of spanning the whole NL-dimensional ambient space-time signal space, the inner node has to find a set of N frequency bins

$$\Omega = \{\omega_n \ : \ |\omega_n| < W/2\}_{0\leq n\leq N-1} \,, \tag{5.28}$$

and a set of L elevation-azimuth angle pairs

$$\Theta = \{(\theta_\ell, \varphi_\ell) \ : \ |\theta_\ell| < \pi/2, \ |\varphi_\ell| < \pi\}_{0\leq \ell\leq L-1} \,, \tag{5.29}$$

such that both the frequency-bin matrix $\boldsymbol{B}$ defined in (5.26) and the array steering matrix $\boldsymbol{S}[\omega]$ given in (5.27) are full-rank matrices. Accordingly, a basis spanning the NL space-time DoF that explicitly depends on the array geometry can be found as

$$\boldsymbol{M}(\Theta, \Omega) = [\boldsymbol{M}[\omega_0] \cdots \boldsymbol{M}[\omega_n] \cdots \boldsymbol{M}[\omega_{N-1}]] \in \mathbb{C}^{NL\times NL}, \tag{5.30}$$

being $\boldsymbol{M}[\omega_n] \triangleq \boldsymbol{b}[\omega_n] \otimes \boldsymbol{S}[\omega_n] \in \mathbb{C}^{NL\times L}$. It is worth noting that the full-rank condition is necessary to span the whole NL-dimensional ambient signal space, and, thus the sets Ω and Θ have to be iterated until the condition is satisfied.

The basis of the whole NL-dimensional ambient signal space provided in (5.30) can be used to sense the wireless environment and design the space-time MNTLS waveforms. Nevertheless, we should remark that (5.30) is not a unitary basis, which may hinder the sensing process since the statistical independence between space-time DoF is not guaranteed.

As per [SM00], any unitary basis of the NL-dimensional ambient signal space is expressed in the canonical coordinate system. Thus, if the L antennas are uncorrelated[2], the canonical coordinate system guarantees statistical independence between DoF under Gaussian conditions. Thus, a unitary basis of the ambient space-time signal space can be found applying a *canonical transformation* [SM00] on (5.30).

[2] As per [MSA08], under certain conditions, the inter-element spacing should be larger than half wavelength so as to guarantee that the antennas are uncorrelated, and, thus, all of the spatial DoF can be exploited. Grating lobes appear in the radiation pattern when all inter-element spacings of an antenna array are larger than a half wavelength. It is interesting to note that, in this dissertation, this scenario is also contemplated through the full-rank constraint imposed on (5.30).

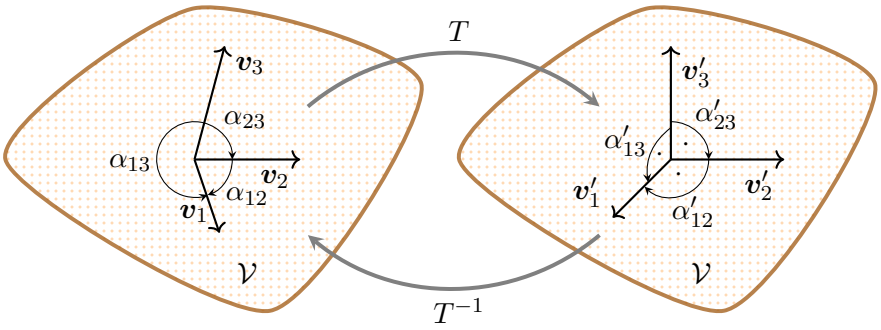

Figure 5.2: Given a non-orthonormal basis $\{\boldsymbol{v}_1, \boldsymbol{v}_2, \boldsymbol{v}_3\}$ of the linear subspace $\mathcal{V}$, with principal angles $\alpha_{12}, \alpha_{13}, \alpha_{23} \neq \pi/2$, the canonical transformation T finds the orthonormal basis $\{\boldsymbol{v}'_1, \boldsymbol{v}'_2, \boldsymbol{v}'_3\}$, with $\alpha'_{12} = \alpha'_{13} = \alpha'_{23} = \pi/2$, of the same subspace $\mathcal{V}$.

Definition 5.1 (Canonical Transformation). *Let us consider a linear application T on a linear subspace $\mathcal{V}$ such that*

$$\begin{aligned} T \ &: \mathcal{V} \to \mathcal{V} \\ &\boldsymbol{V} \mapsto \boldsymbol{V}' = \boldsymbol{T}\boldsymbol{V} \end{aligned} \tag{5.31}$$

with $\boldsymbol{T} = \left(\boldsymbol{V}\boldsymbol{V}^H\right)^{-1/2}$ the matrix of the linear application T. Given a non-orthonormal basis $\boldsymbol{V}$ of a subspace $\mathcal{V}$, the transformation T provides an orthonormal (unitary) basis $\boldsymbol{V}'$ of the same subspace $\mathcal{V}$. This linear application T, sketched in Figure 5.2, is known as canonical transformation.

Through a canonical transformation, it is possible to obtain a unitary basis of the NL-dimensional ambient signal space. In this sense, two different cases are identified. If the frequency-bin matrix is a Fourier matrix, i.e., it is composed of N uniformly separated consecutive frequencies, it is straightforward to see that

$$\boldsymbol{M}(\Theta,\Omega)^H\boldsymbol{M}(\Theta,\Omega) = \begin{bmatrix} \boldsymbol{M}[\omega_0]^H\boldsymbol{M}[\omega_0] & & \boldsymbol{0}_{L\times L} \\ & \ddots & \\ \boldsymbol{0}_{L\times L} & & \boldsymbol{M}[\omega_{N-1}]^H\boldsymbol{M}[\omega_{N-1}] \end{bmatrix}, \tag{5.32}$$

i.e., the inner product of the non-unitary basis $\boldsymbol{M}(\Theta,\Omega)$ is a block-diagonal matrix with $L \times L$ blocks $\boldsymbol{M}[\omega_n]^H\boldsymbol{M}[\omega_n]$. In this particular case, a unitary basis can be obtained by means of a *per-frequency* canonical transformation, i.e., $\boldsymbol{T}[\omega_n] = \left(\boldsymbol{M}[\omega_n]\boldsymbol{M}[\omega_n]^H\right)^{-1/2}$, such that a unitary basis of the NL-dimensional ambient signal space can be found as

$$\begin{aligned} \boldsymbol{U} = [\boldsymbol{T}[\omega_0]\boldsymbol{M}[\omega_0] \cdots \boldsymbol{T}[\omega_n]\boldsymbol{M}[\omega_n] \cdots \boldsymbol{T}[\omega_{N-1}]\boldsymbol{M}[\omega_{N-1}]] = \\ [\boldsymbol{U}[\omega_0] \cdots \boldsymbol{U}[\omega_n] \cdots \boldsymbol{U}[\omega_{N-1}]] \in \mathbb{C}^{NL\times NL}. \end{aligned} \tag{5.33}$$

On the other hand, dropping the constraint on the set of frequency bins Ω defining the frequency-bin matrix $\boldsymbol{B}$, a unitary basis of the NL-dimensional ambient signal space is given by

$$\boldsymbol{U} = \boldsymbol{T}\boldsymbol{M}(\Theta,\Omega) \in \mathbb{C}^{NL\times NL}, \tag{5.34}$$

being $\boldsymbol{T} = \left(\boldsymbol{M}(\Theta,\Omega)\boldsymbol{M}(\Theta,\Omega)^H\right)^{-1/2}$ a *full* canonical transformation.

At this point, some comments are of order. First, note that the unitary basis $\boldsymbol{U}$ is not unique and highly depends on the particular choice of the set of frequencies Ω and the set of elevation-azimuth angle pairs Θ. Despite this non-uniqueness, the design of the space-time MNTLS waveforms relies on the orthogonal projector onto the null space, meaning that the solution is unique regardless of the chosen basis. Second, the discussion on the unitary basis has been included for the sake of completeness, as it can guarantee the statistical independence between space-time DoF, leading to a sensing performance improvement. Nevertheless, the unitary basis obtained as in (5.33) or (5.34) exhibits a non-trivial dependence on the array geometry, which hinders the analysis. Therefore, in the sequel, it is assumed that the basis considered for designing the space-time MNTLS waveforms is non-unitary and composed of a subset of columns of (5.30). Since these waveforms do not rely on a particular null-space basis, the drawn conclusions hold irrespectively of the considered null-space basis.

5.3.2 Problem Statement

The main objective of this section is to prove that the fundamental invariance property is preserved in asymmetric MIMO opportunistic channels, revealing that the space-time MNTLS waveforms (5.17) are invariant to the antenna array geometry.

For this purpose, we consider an inner transmitter-receiver pair where each node is equipped with an arbitrary antenna array of L_{T} and L_{R} antennas, respectively. Without loss of generality, we consider the transmission of a single symbol, and, thus, only one space-time MNTLS waveform and matched filter are involved. It is worth noting that, since all waveforms $\{\boldsymbol{\phi}_k\}_{0\leq k\leq K-1}$ and matched filters $\{\boldsymbol{\psi}_k\}_{0\leq k\leq K-1}$ rely on orthogonal projectors, the conclusions hold for all waveforms and matched filters satisfying (5.15)–(5.16). In order that the waveform $\boldsymbol{\phi}_0$ and the matched filter $\boldsymbol{\psi}_0$ explicitly rely on the transmitting and receiving array geometries, we consider that they have been locally designed using a non-unitary null-space basis composed of a subset of columns of $\boldsymbol{M}(\Theta_{\mathrm{T}},\Omega_{\mathrm{T}})$ and $\boldsymbol{M}(\Theta_{\mathrm{R}},\Omega_{\mathrm{R}})$, respectively. Accordingly, let $\widehat{\boldsymbol{M}}_{\mathcal{N},\mathrm{T}}$ and $\widehat{\boldsymbol{M}}_{\mathcal{N},\mathrm{R}}$ be the sensed null-space bases at the inner transmitter and the inner receiver, respectively. As elaborated in Appendix 5.C, the space-time MNTLS waveform is given by

$$\boldsymbol{\phi}_0 = \widehat{\boldsymbol{M}}_{\mathcal{N},\mathrm{T}}\boldsymbol{\lambda}_{\mathrm{T}} = \gamma\widehat{\boldsymbol{M}}_{\mathcal{N},\mathrm{T}}\widehat{\boldsymbol{M}}^{+}_{\mathcal{N},\mathrm{T}}\boldsymbol{e}_0, \tag{5.35}$$

and, analogously, the space-time MNTLS matched filter is given by

$$\boldsymbol{\psi}_0 = \widehat{\boldsymbol{M}}_{\mathcal{N},\mathrm{R}}\boldsymbol{\lambda}_{\mathrm{R}} = \rho\widehat{\boldsymbol{M}}_{\mathcal{N},\mathrm{R}}\widehat{\boldsymbol{M}}^{+}_{\mathcal{N},\mathrm{R}}\boldsymbol{e}_0, \tag{5.36}$$

where γ and ρ are scaling parameters guaranteeing unit norm, and $\widehat{\boldsymbol{M}}_{\mathcal{N},\mathrm{T}}\widehat{\boldsymbol{M}}^{+}_{\mathcal{N},\mathrm{T}}$ and $\widehat{\boldsymbol{M}}_{\mathcal{N},\mathrm{R}}\widehat{\boldsymbol{M}}^{+}_{\mathcal{N},\mathrm{R}}$ are the orthogonal projectors onto the sensed null space at each system end $\widehat{\mathcal{N}}_{\mathrm{T}} = \left\langle \widehat{\boldsymbol{M}}_{\mathcal{N},\mathrm{T}} \right\rangle$ and $\widehat{\mathcal{N}}_{\mathrm{R}} = \left\langle \widehat{\boldsymbol{M}}_{\mathcal{N},\mathrm{R}} \right\rangle$, respectively.

Regarding the MIMO inner channel $\boldsymbol{H}_{\mathrm{II}}[n]$, the multipath (or multi-ray) model (cf. [TV05, Chapter 7]) is considered. Thus, letting $\vartheta^{(i)}_{\mathrm{T}} = \left(\theta^{(i)}_{\mathrm{T}},\varphi^{(i)}_{\mathrm{T}}\right)$ and $\vartheta^{(i)}_{\mathrm{R}} = \left(\theta^{(i)}_{\mathrm{R}},\varphi^{(i)}_{\mathrm{R}}\right)$ the i-th elevation-azimuth angle pair of departure and the i-th elevation-azimuth angle pair of arrival, and α_i the channel gain associated with the i-th path, the N_{path} MIMO inner channel matrix at frequency ω_ν is given by

$$\boldsymbol{H}_{\mathrm{II}}[\omega_\nu] = \frac{1}{\sqrt{N_{\mathrm{path}}L_{\mathrm{T}}L_{\mathrm{R}}}}\sum_{i=0}^{N_{\mathrm{path}}-1}\alpha_i\boldsymbol{s}_{\mathrm{R}}[\omega_\nu,\vartheta^{(i)}_{\mathrm{R}}]\boldsymbol{s}^{H}_{\mathrm{T}}[\omega_\nu,\vartheta^{(i)}_{\mathrm{T}}] \in \mathbb{C}^{L_{\mathrm{R}}\times L_{\mathrm{T}}}, \tag{5.37}$$

being $\boldsymbol{s}_{\mathrm{R}}[\omega_\nu, \vartheta_{\mathrm{R}}^{(i)}] \in \mathbb{C}^{L_{\mathrm{R}}}$ and $\boldsymbol{s}_{\mathrm{T}}^H[\omega_\nu, \vartheta_{\mathrm{T}}^{(i)}] \in \mathbb{C}^{L_{\mathrm{T}}}$ the steering vectors associated with the receiving and transmitting arrays and pointing to the i-th angle pair of arrival and the i-th angle pair of departure, respectively. Note that, for the sake of clarity, the frequency-selective nature of the channel is omitted, and it will be studied in Section 5.5. Assuming $\alpha_i = 1$, for $i = 0, \ldots, N_{\text{path}}$, the time-domain inner MIMO channel matrix reads as

$$\boldsymbol{H}_{\text{II}}[n] = \frac{1}{N\sqrt{N_{\text{path}} L_{\mathrm{T}} L_{\mathrm{R}}}} \sum_{\nu=0}^{N-1} \sum_{i=0}^{N_{\text{path}}-1} \boldsymbol{s}_{\mathrm{R}}[\omega_\nu, \vartheta_{\mathrm{R}}^{(i)}] \boldsymbol{s}_{\mathrm{T}}^H[\omega_\nu, \vartheta_{\mathrm{T}}^{(i)}] e^{j\frac{2\pi\nu n}{N}}. \tag{5.38}$$

Letting a_0 be the transmitted zero-mean and unit-variance symbol and defining the MIMO response matrix, for $n = 0, \ldots, N-1$, as

$$\widetilde{\boldsymbol{H}}_{\text{II}} \triangleq \begin{bmatrix} \boldsymbol{H}_{\text{II}}[0] & & \boldsymbol{0} \\ & \ddots & \\ \boldsymbol{0} & & \boldsymbol{H}_{\text{II}}[N-1] \end{bmatrix} \in \mathbb{C}^{NL_{\mathrm{R}} \times NL_{\mathrm{T}}}, \tag{5.39}$$

the space-time received signal $\boldsymbol{y} \in \mathbb{C}^{NL_{\mathrm{R}}}$ under the far-field assumption reads as

$$\boldsymbol{y} = a_0 \widetilde{\boldsymbol{H}}_{\text{II}} \boldsymbol{\phi}_0 + \boldsymbol{\upsilon}, \tag{5.40}$$

where $\boldsymbol{\upsilon} \sim \mathcal{N}_{\mathbb{C}}(\boldsymbol{0}, \sigma^2 \boldsymbol{I}_{NL_{\mathrm{R}}})$ is a noise-plus-interference term. Thus, the sufficient statistic for symbol decoding at the inner receiver is given by

$$z = \boldsymbol{\psi}_0^H \boldsymbol{y} = a_0 \boldsymbol{\psi}_0^H \widetilde{\boldsymbol{H}}_{\text{II}} \boldsymbol{\phi}_0 + \boldsymbol{\psi}_0^H \boldsymbol{\upsilon}. \tag{5.41}$$

It is worth noting that (5.41) encompasses in a single equation the transmitting waveform $\boldsymbol{\phi}_0$ and the matched filter $\boldsymbol{\psi}_0$. As per (5.35)–(5.36), both $\boldsymbol{\phi}_0$ and $\boldsymbol{\psi}_0$ depend on the orthogonal projector onto the sensed space-time null-space. Since the orthogonal projector can be written as in (5.35)–(5.36), it is possible to rewrite (5.41) such that the geometries of both the transmitting and receiving arrays appear explicitly. In the following subsection, an expression for the statistic z is proposed such that it directly depends on the steering matrices of the transmitting and receiving array. Then, a thorough analysis based on the manifold separation theory shows that the statistic z depends only on the effective spatial DoF irrespectively of the considered transmitting and receiving array geometries.

5.3.3 Analysis of the Array-Geometry Invariance

In order to evaluate the impact of the array geometry on the opportunistic transmission, we have to analyze if the sufficient statistic for symbol decoding, i.e.,

$$z = a_0 \boldsymbol{\psi}_0^H \widetilde{\boldsymbol{H}}_{\text{II}} \boldsymbol{\phi}_0 + \widetilde{\upsilon}, \tag{5.42}$$

where $\widetilde{\upsilon}$ is the filtered noise, depends on the geometry of the transmitting and receiving arrays. Recalling (5.35)–(5.36), we note that both the transmitted waveform $\boldsymbol{\phi}_0$ and the matched filter $\boldsymbol{\psi}_0$ rely on the orthogonal projector onto the sensed space-time null space. For the analysis' purpose, it would be preferable to be able to study the impact of the spatial DoF alone, i.e., leaving the time-frequency DoF out of the picture.

The study of (5.35)–(5.36) performed in Appendix 5.D reveals that the transmitted waveform $\boldsymbol{\phi}_0$ and the matched filter $\boldsymbol{\psi}_0$ are composed of N blocks of length L_{T} and L_{R}, respectively, i.e.,

$$\boldsymbol{\phi}_0 = \begin{bmatrix} \boldsymbol{\phi}_0[0] \\ \vdots \\ \boldsymbol{\phi}_0[n] \\ \vdots \\ \boldsymbol{\phi}_0[N-1] \end{bmatrix} \quad \text{and} \quad \boldsymbol{\psi}_0 = \begin{bmatrix} \boldsymbol{\psi}_0[0] \\ \vdots \\ \boldsymbol{\psi}_0[n] \\ \vdots \\ \boldsymbol{\psi}_0[N-1] \end{bmatrix}, \tag{5.43}$$

where each block $\boldsymbol{\phi}_0[n] \in \mathbb{C}^{L_{\mathrm{T}}}$ and $\boldsymbol{\psi}_0[n] \in \mathbb{C}^{L_{\mathrm{R}}}$ corresponds to the transmitting and receiving beamvector, respectively, at a given time instant n.

Plugging (5.43) into (5.42) and recalling the definition of the MIMO response matrix $\widetilde{\boldsymbol{H}}_{\mathrm{II}}$ given in (5.39), the statistic z can be written as

$$z = \sum_{n=0}^{N-1} a_0 \boldsymbol{\psi}_0[n]^H \boldsymbol{H}_{\mathrm{II}}[n] \boldsymbol{\phi}_0[n] + \widetilde{v}, \tag{5.44}$$

which emphasizes that the study can be done at a given time instant. The latter is of paramount importance to relegate to the background the time domain. More interestingly, Appendix 5.D also unveils that (5.44) admits a compact expression where the channel steering vectors and the steering matrices of the transmitting and receiving arrays appear explicitly. Accordingly, (5.44) can be written as

$$z = \frac{a_0}{N\sqrt{N_{\mathrm{path}} L_{\mathrm{T}} L_{\mathrm{R}}}} \sum_{n=0}^{N-1} \sum_{\nu=0}^{N-1} \sum_{i=0}^{N_{\mathrm{path}}-1} \boldsymbol{\beta}_{n\nu,\mathrm{R}}^H \boldsymbol{M}_{\mathrm{R}}^H[\omega_\nu] \boldsymbol{s}_{\mathrm{R}}[\omega_\nu, \vartheta_{\mathrm{R}}^{(i)}] \boldsymbol{s}_{\mathrm{T}}^H[\omega_\nu, \vartheta_{\mathrm{T}}^{(i)}] \boldsymbol{M}_{\mathrm{T}}[\omega_\nu] \boldsymbol{\beta}_{n\nu,\mathrm{T}} + \widetilde{v}, \tag{5.45}$$

where $\boldsymbol{M}_{\mathrm{T}}[\omega_\nu] \in \mathbb{C}^{L_{\mathrm{T}} \times L_{\mathrm{T}}}$ and $\boldsymbol{M}_{\mathrm{R}}[\omega_\nu] \in \mathbb{C}^{L_{\mathrm{R}} \times L_{\mathrm{R}}}$ stand for the steering matrices at frequency ω_ν of the transmitting and receiving arrays, respectively, and the vectors $\boldsymbol{\beta}_{n\nu,\mathrm{T}}$ and $\boldsymbol{\beta}_{n\nu,\mathrm{R}}$ read as

$$[\boldsymbol{\beta}_{n\nu,\mathrm{T}}]_\ell \triangleq \begin{cases} 0, & \text{if } ((\theta_\ell, \varphi_\ell); \omega_\nu) \notin \langle \widehat{\boldsymbol{M}}_{\mathcal{N},\mathrm{T}} \rangle \\ \eta_{n\nu} [\boldsymbol{M}_{\mathrm{T}}^+[\omega_\nu] \widetilde{\boldsymbol{e}}_{\mathrm{T},0}]_\ell, & \text{otherwise} \end{cases}, \quad \text{for } \ell = 1, \ldots, L_{\mathrm{T}} \tag{5.46}$$

and

$$[\boldsymbol{\beta}_{n\nu,\mathrm{R}}]_\ell \triangleq \begin{cases} 0, & \text{if } ((\theta_\ell, \varphi_\ell); \omega_\nu) \notin \langle \widehat{\boldsymbol{M}}_{\mathcal{N},\mathrm{R}} \rangle \\ \mu_{n\nu} [\boldsymbol{M}_{\mathrm{R}}^+[\omega_\nu] \widetilde{\boldsymbol{e}}_{\mathrm{R},0}]_\ell, & \text{otherwise} \end{cases}, \quad \text{for } \ell = 1, \ldots, L_{\mathrm{R}}, \tag{5.47}$$

where the boolean vectors $\widetilde{\boldsymbol{e}}_{\mathrm{T},0}$ and $\widetilde{\boldsymbol{e}}_{\mathrm{R},0}$ of length L_{T} and L_{R}, respectively, are appropriately defined in Appendix 5.D.

It is worth noting that (5.45) reveals that the analysis of the impact of the array geometry can be done not only at each time instant individually but also can be done per each propagation path. Therefore, for ease of discussion and without loss of generality, we assume $N_{\mathrm{path}} = 1$, which corresponds to the line-of-sight component. Note that the general case $N_{\mathrm{path}} > 1$ is straightforward, but does not provide any additional insights on the impact of the array geometry. Accordingly, in the sequel, (5.45) is simplified as

$$z = \frac{a_0}{N\sqrt{L_{\mathrm{T}} L_{\mathrm{R}}}} \sum_{n=0}^{N-1} \sum_{\nu=0}^{N-1} \boldsymbol{\beta}_{n\nu,\mathrm{R}}^H \boldsymbol{M}_{\mathrm{R}}^H[\omega_\nu] \boldsymbol{s}_{\mathrm{R}}[\omega_\nu] \boldsymbol{s}_{\mathrm{T}}^H[\omega_\nu] \boldsymbol{M}_{\mathrm{T}}[\omega_\nu] \boldsymbol{\beta}_{n\nu,\mathrm{T}} + \widetilde{v}, \tag{5.48}$$

where $\boldsymbol{s}_{\mathrm{T}}[\omega_\nu]$ and $\boldsymbol{s}_{\mathrm{R}}[\omega_\nu]$ stand for the steering vectors associated with the transmitting and receiving arrays, respectively, corresponding to the line-of-sight component.

Observing the simplified expression for the sufficient statistic given in (5.48), we note that z depends on the inner products of steering vectors. The array steering vector depends simultaneously on the array geometry, including its physical structure and non-idealities (e.g., calibration errors), and on the wavefield or direction $\vartheta = (\theta, \varphi)$. Clearly, the statistic z exhibits a dependence on the latter, as it encompasses the channel or propagation conditions; however, does it mean that z also depends on the array geometry?

To proceed with the analysis, we would ideally need to decompose the array steering vector into two independent terms: a term depending only on the array geometry and a term depending only on the wavefield. This decomposition is provided by the so-called manifold separation theory (MST). According to the MST, the steering vector of an L-element antenna array pointing the direction (θ, φ) at a given frequency ω, i.e,

$$\boldsymbol{a}_\omega(\theta, \varphi) = \left[e^{j\boldsymbol{k}_\omega^T \boldsymbol{r}_0} \ \cdots \ e^{j\boldsymbol{k}_\omega^T \boldsymbol{r}_\ell} \ \cdots \ e^{j\boldsymbol{k}_\omega^T \boldsymbol{r}_{L-1}} \right]^T, \tag{5.49}$$

being $\boldsymbol{r}_\ell$ is the ℓ-th sensor positioning vector with respect to the phase reference point, admits an exact factorization given by

$$\boldsymbol{a}_\omega(\theta, \varphi) = \boldsymbol{G}_\omega \boldsymbol{d}(\theta, \varphi), \tag{5.50}$$

where matrix $\boldsymbol{G}_\omega$ is known as *array sampling matrix* and provides a description of the array geometry only, whereas the so-called *coefficient vector* $\boldsymbol{d}(\theta, \varphi)$ provides a description of the wavefield at direction (θ, φ) and is independent of the physical array. The rationale behind this decomposition follows from the wavefield modeling introduced in [DD94a] and briefly described in Appendix 5.A. In mathematical terms, the coefficient vector is a function defined on a Hilbert space $\mathcal{H}$, i.e., $\boldsymbol{d}(\theta, \varphi) \in \mathcal{H}$, while the array sampling matrix maps the functions defined on $\mathcal{H}$ onto the L-dimensional complex space $\mathbb{C}^L$, i.e., $\boldsymbol{G}_\nu \ : \ \mathcal{H} \to \mathbb{C}^L$. Accordingly, $\boldsymbol{d}(\theta, \varphi)$ has an infinite number of elements, whereas $\boldsymbol{G}_\omega$ is composed of an infinite number of L-element columns, as sketched in Figure 5.3.

As per the related literature, (5.50) provides an orthogonal series expansion of the array steering vector. Specifically, as reported in [DD94a], the expansion is given in terms of Fourier series when the steering vector depends only on the elevation angle θ and, in general, in terms of spherical harmonics. The reader is referred to Appendix 5.A for further details.

Through the decomposition given in (5.50), it is possible to analyze whether the statistic (5.48) depends on the geometry of transmitting and receiving arrays. Accordingly, as elaborated in Appendix 5.E, using the MST in (5.48), we have that

$$z = \frac{a_0}{N\sqrt{L_{\mathrm{T}} L_{\mathrm{R}}}} \sum_{n=0}^{N-1} \sum_{\nu=0}^{N-1} \eta_{n\nu} \mu_{n\nu} \widetilde{\boldsymbol{e}}_{\mathrm{R},0}^T \boldsymbol{G}_{\nu,\mathrm{R}} \boldsymbol{\Pi}_{\boldsymbol{D}_{\mathrm{R}}} \boldsymbol{d}\left(\theta_{\mathrm{R}}, \varphi_{\mathrm{R}}\right) \boldsymbol{d}^H\left(\theta_{\mathrm{T}}, \varphi_{\mathrm{T}}\right) \boldsymbol{\Pi}_{\boldsymbol{D}_{\mathrm{T}}} \boldsymbol{G}_{\nu,\mathrm{T}}^H \widetilde{\boldsymbol{e}}_{\mathrm{T},0} + \widetilde{\upsilon}, \tag{5.51}$$

where $\eta_{n\nu}$, $\mu_{n\nu}$, $\widetilde{\boldsymbol{e}}_{\mathrm{R},0}$, and $\widetilde{\boldsymbol{e}}_{\mathrm{T},0}$ are given in (5.46)–(5.47); $\boldsymbol{G}_{\nu,\mathrm{T}}$ and $\boldsymbol{G}_{\nu,\mathrm{R}}$ are the sampling matrices of the transmitting and receiving arrays, respectively; $\boldsymbol{d}\left(\theta_{\mathrm{T}}, \varphi_{\mathrm{T}}\right)$ and $\boldsymbol{d}\left(\theta_{\mathrm{R}}, \varphi_{\mathrm{R}}\right)$ refer to the coefficient vectors of the channel steering vectors $\boldsymbol{s}_{\mathrm{T}}[\omega_\nu]$ and $\boldsymbol{s}_{\mathrm{R}}[\omega_\nu]$, respectively; and $\boldsymbol{\Pi}_{\boldsymbol{D}_{\mathrm{T}}}$ and

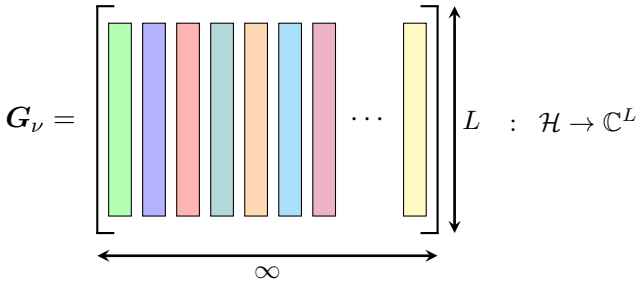

Figure 5.3: Sketch of the array sampling matrix $\boldsymbol{G}_\nu$ at frequency ω_ν. Since it represents the mapping of functions defined on a Hilbert space $\mathcal{H}$ onto the L-dimensional complex space $\mathbb{C}^L$, it has an infinite number of L-element columns. However, only a finite number of columns (or modes) are relevant.

$\boldsymbol{\Pi}_{\boldsymbol{D}_\mathrm{R}}$ are the following projection matrices

$$\boldsymbol{\Pi}_{\boldsymbol{D}_\mathrm{T}} = \boldsymbol{D}_\mathrm{T} \left(\boldsymbol{D}_\mathrm{T}^H \boldsymbol{D}_\mathrm{T}\right)^{-1} \boldsymbol{D}_\mathrm{T}^H, \tag{5.52}$$

$$\boldsymbol{\Pi}_{\boldsymbol{D}_\mathrm{R}} = \boldsymbol{D}_\mathrm{R} \left(\boldsymbol{D}_\mathrm{R}^H \boldsymbol{D}_\mathrm{R}\right)^{-1} \boldsymbol{D}_\mathrm{R}^H, \tag{5.53}$$

being $\boldsymbol{D}_\mathrm{T}$ and $\boldsymbol{D}_\mathrm{R}$ the matrices containing the L_T and L_R coefficient vectors of the steering matrices $\boldsymbol{M}_\mathrm{T}[\omega_\nu]$ and $\boldsymbol{M}_\mathrm{R}[\omega_\nu]$, and given by

$$\boldsymbol{D}_\mathrm{T} \triangleq \left[\boldsymbol{d}\left(\theta_{0,\mathrm{T}}, \varphi_{0,\mathrm{T}}\right) \ \cdots \ \boldsymbol{d}\left(\theta_{L_\mathrm{T}-1,\mathrm{T}}, \varphi_{L_\mathrm{T}-1,\mathrm{T}}\right)\right], \tag{5.54}$$

$$\boldsymbol{D}_\mathrm{R} \triangleq \left[\boldsymbol{d}\left(\theta_{0,\mathrm{R}}, \varphi_{0,\mathrm{R}}\right) \ \cdots \ \boldsymbol{d}\left(\theta_{L_\mathrm{R}-1,\mathrm{R}}, \varphi_{L_\mathrm{R}-1,\mathrm{R}}\right)\right]. \tag{5.55}$$

It is worth noting that, as per (5.46)–(5.47), the inner transmitted signal is not present when $((\theta_\ell, \varphi_\ell); \omega_\nu) \notin \langle \widehat{\boldsymbol{M}}_{\mathcal{N},\mathrm{T}} \rangle$, and the inner receiver does not detect whenever $((\theta_\ell, \varphi_\ell); \omega_\nu) \notin \langle \widehat{\boldsymbol{M}}_{\mathcal{N},\mathrm{R}} \rangle$. Accordingly, without loss of generality, we may consider that the scaling coefficients $\eta_{n\nu}$ and $\mu_{n\nu}$ are zero if these situations occur.

As discussed in Appendix 5.E, we shall observe that all terms involved in (5.51) except $\widetilde{\boldsymbol{e}}_{\mathrm{R},0}^T \boldsymbol{G}_{\nu,\mathrm{R}}$ and $\boldsymbol{G}_{\nu,\mathrm{T}}^H \widetilde{\boldsymbol{e}}_{\mathrm{T},0}$ are clearly independent of the geometry of transmitting and receiving arrays. Regarding the doubtful terms, further analysis is of order.

Let us begin with the term $\boldsymbol{G}_{\nu,\mathrm{T}}^H \widetilde{\boldsymbol{e}}_{\mathrm{T},0}$. As detailed in Appendix 5.D, $\widetilde{\boldsymbol{e}}_{\mathrm{T},0}$ is an L_T-length binary vector with a single non-zero element at position $n(0) \bmod L_\mathrm{T}$, where $n(0) = 1, \ldots, NL_\mathrm{T}$ indicates the column of the projector $\widehat{\boldsymbol{M}}_{\mathcal{N},\mathrm{T}} \widehat{\boldsymbol{M}}_{\mathcal{N},\mathrm{T}}^+$ corresponding to the transmitted waveform $\boldsymbol{\phi}_0$. Accordingly, the term $\boldsymbol{G}_{\nu,\mathrm{T}}^H \widetilde{\boldsymbol{e}}_{\mathrm{T},0}$ corresponds to the transpose conjugate of the row $n(0) \bmod L_\mathrm{T}$ of the transmitting array sampling matrix $\boldsymbol{G}_{\nu,\mathrm{T}}$.

Analyzing the structure of the sampling matrix $\boldsymbol{G}_{\nu,\mathrm{T}}$ (see Figure 5.3), we realize that each column describes the behavior of a particular excitation mode on the array sensors, i.e., the columns provide the characterization of the array geometry, accounting for the physical structure and the possible non-idealities. Conversely, it is worth noting that each row describes the excitation modes at a particular array element. As discussed in Appendix 5.A, even though the matrix $\boldsymbol{G}_{\nu,\mathrm{T}}$ has an infinite number of columns, only a finite number of columns (modes) are significant, given that the number of spatial DoF is limited by the minimum sphere enclosing the antenna array. Accordingly, we may say that the term $\boldsymbol{G}_{\nu,\mathrm{T}}^H \widetilde{\boldsymbol{e}}_{\mathrm{T},0}$ is independent of the transmitting array geometry, and only depends on the effective spatial DoF.

Following the same rationale as for $\boldsymbol{G}_{\nu,\mathrm{T}}^{H}\widetilde{\boldsymbol{e}}_{\mathrm{T},0}$, we note that the term $\widetilde{\boldsymbol{e}}_{\mathrm{R},0}^{T}\boldsymbol{G}_{\nu,\mathrm{R}}$ corresponds to the $n(0) \bmod L_{\mathrm{R}}$ row of the receiving array sampling matrix $\boldsymbol{G}_{\nu,\mathrm{R}}$, and, thus, this term depends only on the effective spatial DoF that can be resolved by the receiving array. Therefore, under the far-field assumption, the sufficient statistic for symbol decoding (5.51) benefits from the additional spatial DoF introduced by the transmitting and receiving antenna arrays in terms of a potential *diversity* gain regardless of the geometry of the transmitting and receiving arrays. The additional DoF due to the spatial dimension at each system end increases the dimension spreading factor, decreasing the per-DoF interference. Concluding, it can be said the time-domain invariance property studied in Chapter 3 is preserved, and the result derived in this section implies a generalization of the fundamental invariance property.

5.3.4 Technical Discussion on the Array-Geometry Invariance

At this point, a brief discussion of the array-geometry invariance property is afforded. On the one hand, a physical interpretation of the abstract result derived so far is provided. On the other hand, since a far-field scenario has been considered throughout this section, the validity of this result in near-field scenarios is discussed.

Physical Interpretation

The array-geometry invariance is the major result of this chapter. Despite the proof being based on the MST framework, the array-geometry invariance admits an intuitive physical interpretation. For the sake of simplicity, let us consider ideal operating conditions, i.e., subspace mismatch is not present. The MIMO response matrix can be understood as concatenating a Multiple-Input Single-Output channel (MISO) and a Single-Input Multiple-Output channel (SIMO). Accordingly, the MIMO response matrix defined in (5.39) can be seen as a double mapping from a mathematical viewpoint.

First, the transmitted signal lying in a subspace of the NL_{T}-dimensional complex space $\mathbb{C}^{NL_{\mathrm{T}}}$ is mapped into the N-dimensional complex space $\mathbb{C}^{N}$, i.e., the channel itself absorbs the spatial DoF mapping a space-time signal into a time-domain signal. Since the channel absorbs the spatial domain, it seems reasonable to think that the structure of the transmitting array has no impact on communication performance. Nevertheless, the channel is also mapping this time-domain signal into a space-time signal lying in a subspace of the NL_{R}-dimensional complex space $\mathbb{C}^{NL_{\mathrm{R}}}$. In this case, the channel introduces the spatial domain again.

At the receiving node, the matched filter $\boldsymbol{\psi}_0$ is responsible for mapping this space-time signal into a time-domain signal. Therefore, after all these mappings, the impact of the transmitting and receiving arrays has been absorbed. The contribution of the spatial domain is reflected in the fact that the transmit and receive dimensions have been virtually increased, resulting in a higher DoF spreading factor. In opportunistic communications, this spreading factor plays a fundamental role in decreasing the interference density imposed on outer-network nodes.

In conclusion, the number of spatial DoF impacts opportunistic communication performance, but how these spatial DoF are physically structured does not. It is worth noting that this conclusion can also be understood by recalling that in multi-antenna communication systems if the appropriate transmission/detection strategy is employed, it is possible to obtain a diversity or multiplexing gain related to the number of antennas, irrespective of the array geometry.

On the Generality of the Analysis

Throughout this section, it is considered that opportunistic communication occurs in the far field. Despite being conventionally assumed in multi-antenna scenarios, it can be of relevant interest to analyze the problem in the near field. A current research trend in the digital communications community consists in exploiting higher frequency bands, e.g., millimeter-wave bands [WKK+18], or terahertz bands [CHW+21]. As the carrier frequency increases, the Fraunhofer distance [Bal15] diminishes, translating the communication into the near field. In spite of being a disadvantage, as discussed in Section 5.1.1, the near field offers additional space-time DoF that can also be exploited to increase the transmit opportunities. However, does the array-geometry invariance property hold in the near field?

The MST theory has been used in this section to show the array-geometry invariance property. The decomposition provided by the MST exists only in the far-field. Nevertheless, when operating in the near field, the array steering vectors, also known as array manifold vectors, can be written as an orthogonal expansion leading to a basis known as *spherical near-field antenna measurements* [Han88; CH17]. This expansion results in a decomposition similar to that of the MST; hence, a similar analysis can be carried out. Another approach to studying the array-geometry invariance property consists in letting the number of array sensors be arbitrarily large but confined into a finite sphere, corresponding to a holographic array [Dar20]. However, the number of spatial DoF does not scale linearly with the number of sensors, as the number of spatial DoF is constrained by the minimum sphere enclosing the antenna array [PMS20a]. As studied in [PMS20b; PSM22], the propagating wavefield can always be written in plane waves, even in the near-field, which follows from noting that a spherical wave can be written as the summation of an infinite number of plane waves. This approach is known as Fourier plane-wave series expansion. Thus, the decomposition provided by the MST framework can be applied to each of the involved plane waves.

In conclusion, although the plane-wave model has been considered, two approaches have been identified for studying this problem under the more general spherical wave assumption. On the one hand, the spherical near-field antenna measurements approach can be used to decompose the steering vector similarly to the decomposition provided by the MST framework. On the other hand, we can let the number of array sensors be arbitrarily large and use the Fourier plane-wave series expansion in the context of holographic MIMO communications.

5.4 Simulation Analysis

This Section is intended to illustrate the interference mitigation properties of the space-time MNTLS waveforms described in Section 5.2 and numerically corroborate the theoretical array-geometry invariance property derived in Section 5.3.

5.4.1 Interference Mitigation Capabilities: Spectral Behavior and SIDR

In Section 5.2, we have seen that the MNTLS waveforms are linear combinations of all elements encompassed in the null-space basis sensed by the inner transmitting node. As discussed for the single-channel case in Chapter 3, the residual inter-system interference imposed on outer-network nodes is spread over the whole sensed null space. Therefore, spectral behavior

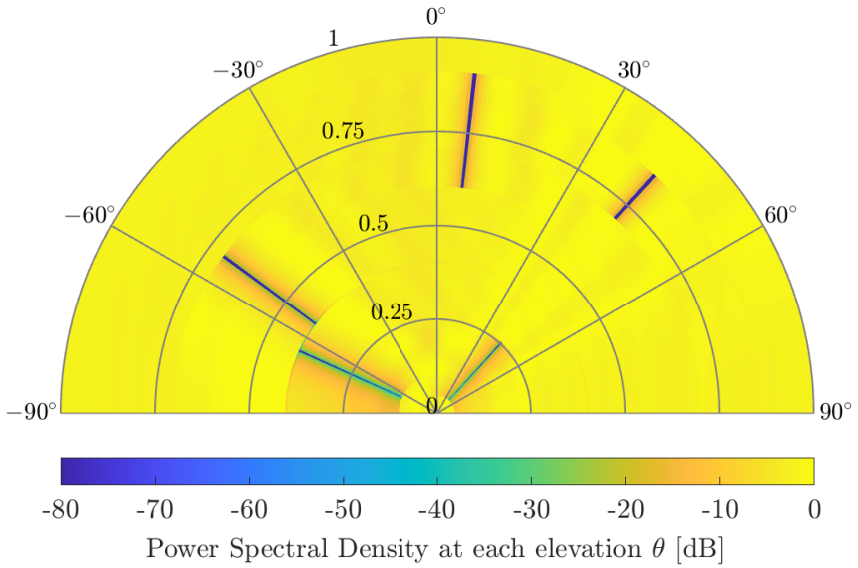

Figure 5.4: Normalized PSD at each elevation angle θ of the designed space-time MNTLS waveform with a 16-element ULA and $N = 256$ time-frequency DoF.

provides a qualitative justification of the robustness of the space-time MNTLS transmitting waveforms to undesired inter-system interferences. In order to illustrate the spectral behavior, some numerical examples are discussed in the sequel.

First, we consider a wideband 16-element ULA with elements spaced $\lambda_u/2$, being λ_u the wavelength at the highest frequency considered. The wideband array is modeled according to the Tapped-Delay Line (TDL) model [Van02], i.e., each array element is attached to a TDL of N coefficients, meaning that the wideband array can resolve N frequency bins. For the sake of clarity, the observed bandwidth has been normalized between 0 and 1. Figure 5.4 illustrates the Power Spectral Density (PSD) for the simple example described in Table 5.2.

	$\theta = -66°$	$\theta = -54°$	$\theta = 6°$	$\theta = 42°$
Occupied Bandwidth	$[0.1, 0.4]$	$[0.4, 0.7]$	$[0.6, 0.9]$	$[0.05, 0.25] \cup [0.7, 0.85]$

Table 5.2: Occupied bandwidth at each elevation angle θ for the numerical example with a 16-element ULA attached to a TDL of $N = 256$ coefficients.

The generality of the spectral behavior property can be further corroborated when a more complex array is considered. In particular, the non-uniform planar array with 16 isotropic elements depicted in Figure 5.7(b) is considered, where each element is attached to a TDL of $N = 256$ coefficients. The scenario parameters are summarized in Table 5.3. In Figure 5.5, the PSD at each azimuthal direction φ is depicted for two cuts at different elevation direction θ.

Azimuth φ / Elevation θ	$-78°$	$-18°$	$6°$	$66°$
$90°$	-	-	$[0.4, 0.7]$	$[0.05, 0.25] \cup [0.7, 0.85]$
$30°$	$[0.1, 0.4]$	$[0.6, 0.9]$	-	-

Table 5.3: Occupied bandwidth at each azimuth-elevation angle pair for the numerical example with a 16-element non-uniform planar array attached to a TDL of $N = 256$ coefficients.

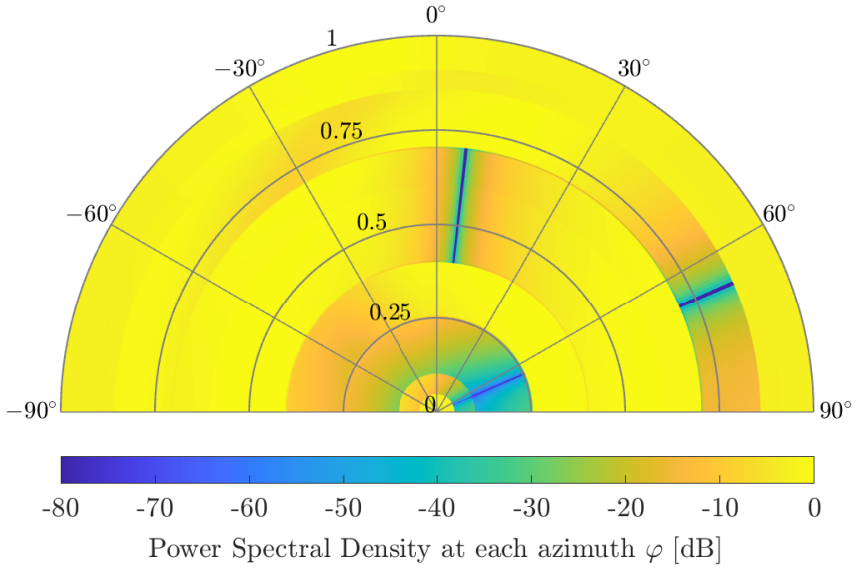

(a) Cut at $\theta = 90°$

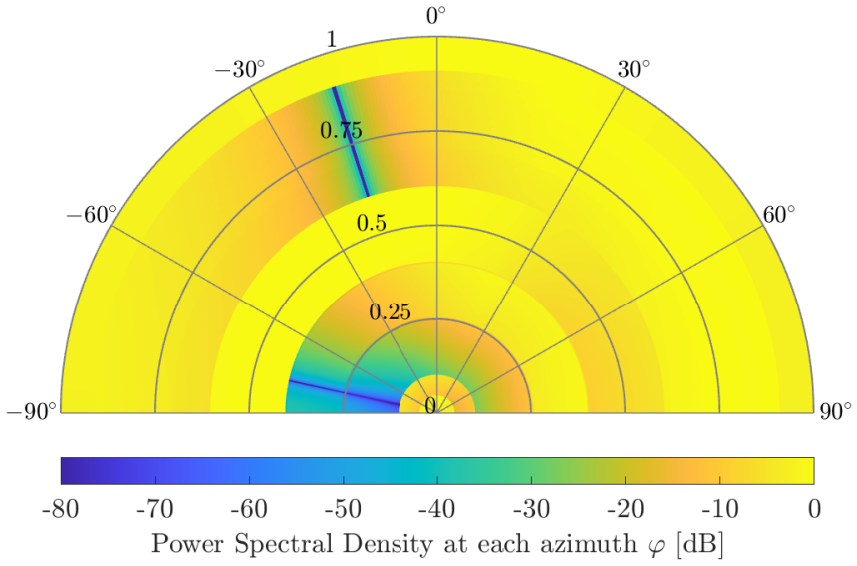

(b) Cut at $\theta = 30°$

Figure 5.5: Different cuts in the elevation direction θ of the normalized PSD at each azimuthal direction φ of the space-time MNTLS waveform with a non-uniform planar array and $N = 256$ time-frequency DoF.

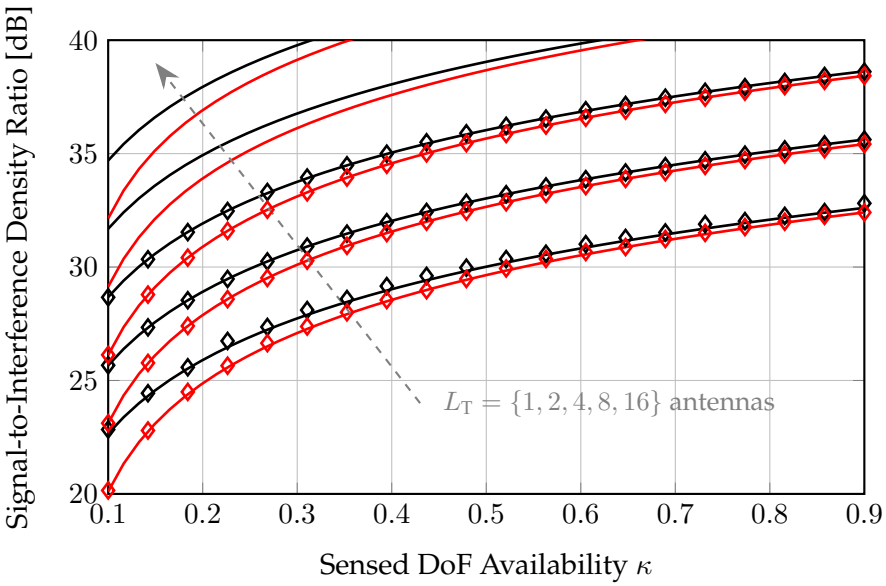

Figure 5.6: Simulated $\mathrm{SIDR}_{\mathrm{T}}$ (markers) and the asymptotic approximation (5.20) (lines) with $N = 2048$ time-frequency DoF, and for $\epsilon = \{1\%, 5\%\}$ (black, red), and for different independent antennas L_{T}.

Observing the examples depicted in Figures 5.4 and 5.5, note that the space-time MNTLS waveforms cancel their contributions to those frequency-angle pairs sensed as occupied while trying to exploit the sensed as available frequency-angle pairs uniformly. It is worth pointing out that the power distribution is almost uniform along the frequency axis. However, regarding the angle domain, we note that providing a uniform distribution is more challenging due to the finite size of the considered arrays. The angular power distribution is expected to become more uniform as the array size increases.

As already concluded in Chapter 3 for the single-channel case, this DoF spreading does not translate into a null-space exploitation inefficiency. Since each waveform in $\{\boldsymbol{\phi}_k\}_{0\leq k\leq K-1}$ is rank-one, only one effective space-time DoF is exploited. The point is that the space-time MNTLS waveforms perform a change of basis so as to spread the unwanted residual inter-system interferences over the whole sensed space-time null space, minimizing the interference density per erroneous space-time DoF.

In terms of uncoordinated access, space-time DoF spreading is the best that can be done when the inner transmitter is not aware of the position of the inner receiver. The latter is exactly the same rationale behind the random beamforming scheme[3] [LSK16; LSS16]. Interestingly, in Time Division Duplex (TDD) scenarios, the enhanced detection strategies described in Section 3.5 (Chapter 3) can be exploited by the inner transmitting node to prune the space-time sensed null space and steer the opportunistic transmission towards the effective space-time null space.

The basic examples discussed thus far permit illustrating the interference mitigation capability of the space-time MNTLS waveforms in a qualitative manner. In order to evaluate this

[3]Random beamforming is a technique aiming at reducing the required feedback to schedule the best receiving node. Specifically, the transmitting node blindly (randomly) sends a set of orthogonal beams. Then, the receiving nodes feed back the measured SINR, and the transmitter allocates the user exhibiting the highest SINR to each orthogonal beam.

capability from a quantitative viewpoint, the advantage of using multiple transmitting antennas on the SIDR is numerically illustrated in Figure 5.6, where the SIDR is depicted as a function of the sensed DoF availability κ for different sensing sensitivities ϵ and for different independent (active) antennas L_{T}. The conclusions from Figure 5.6 are twofold. First, this numerical simulation reveals the tightness of the proposed asymptotic approximation in (5.20). Even though several numbers of transmitted waveforms K have been considered, the plot only accounts for the case $K = 1$ since, as foreseen by (5.20), the SIDR is independent of K. Second, this figure also unveils the advantage of using multiple antennas to improve the coexistence compatibility of the inner system with the other outer systems. In particular, even though the advantage of using antenna arrays cannot be appreciated on the sensed DoF availability κ, it can be noted that doubling L_{T} introduces a 3 dB-gain on the SIDR.

5.4.2 Array-Geometry Invariance

Section 5.3 discusses the impact of the antenna array geometry from a theoretical perspective. In the sequel, this property is numerically illustrated. It is worth noting that the interest of this property is that the time-domain invariance discussed in Chapter 3 is preserved regardless of the use of antenna arrays. For the sake of illustration, a MISO opportunistic transmission is considered. Even though this is the most simple asymmetric MIMO case, it is of relevant interest to appropriately illustrate the array-geometry invariance property.

Before discussing the numerical results, it can be helpful to provide the expression of the time-domain signal observed by the inner receiving node. Particularizing (5.40) for $L_{\mathrm{R}} = 1$ and taking into account the discussion elaborated in Appendix 5.E, the time-domain received signal is given by

$$y[n]=\frac{a_0}{N\sqrt{L_{\mathrm{T}}}}\sum_{\nu=0}^{N-1}\boldsymbol{d}^H\left(\theta_{\mathrm{R}},\varphi_{\mathrm{R}}\right)\boldsymbol{\Pi}_{\boldsymbol{D}_{\mathrm{T}}}\boldsymbol{G}_{\nu,\mathrm{T}}^H\widetilde{\boldsymbol{e}}_{\mathrm{T},0}+\upsilon[n], \tag{5.56}$$

where $\boldsymbol{d}\left(\theta_{\mathrm{R}},\varphi_{\mathrm{R}}\right)$ stands for the steering vector pointing the inner receiving node. This simulation analysis aims at illustrating that (5.56) is invariant to the considered transmitting array geometry. For the sake of simplicity, only the line-of-sight path is analyzed. If multipath propagation is considered, the inner receiver will observe the superposition of signals similar to (5.56).

In order to provide a complete simulation analysis, this array-geometry invariance property is evaluated in 1D, 2D, and 3D antenna arrays. In particular, let us consider the antenna arrays depicted in Figure 5.7, being λ_u the wavelength at the highest frequency considered. In the sequel, we consider that the transmitting array is composed of $L_{\mathrm{T}} = 4$ sensors, each of them attached to a tapped-delay line of $N = 32$ taps, which corresponds to the number of time-frequency DoF. The procedure performed to evaluate the array-geometry invariance property is the same regardless of the considered scenario (1D, 2D, or 3D arrays), and it is described next.

For the purpose of testing the array-geometry invariance, four space-time MNTLS transmitting waveforms are designed in each scenario, where the $L_{\mathrm{T}} = 4$ sensors are randomly chosen from the arrays modeled in Figure 5.7. Then, a non-unitary basis of the whole space-time NL_{T}-dimensional ambient signal space is constructed according to (5.30). Regarding (5.56), it is worth noting that the received signal depends on the projections of $\boldsymbol{d}\left(\theta_{\mathrm{R}},\varphi_{\mathrm{R}}\right)$ onto the set of coefficient vectors of the transmitting array, i.e., $\boldsymbol{d}^H\left(\theta_{\mathrm{R}},\varphi_{\mathrm{R}}\right)\boldsymbol{\Pi}_{\boldsymbol{D}_{\mathrm{T}}}$. Since these vectors are independent of the array geometry, its impact on the received signal (5.56) is not of interest.

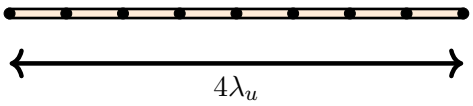

(a) 9-element uniform linear array.

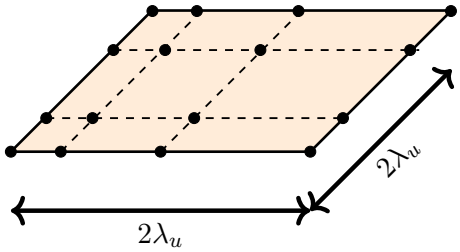

(b) 4×4 non-uniform planar array.

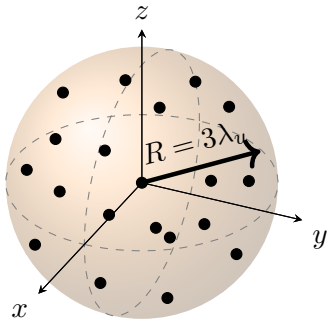

(c) 20-element arbitrary volumetric array.

Figure 5.7: Arrays employed for the evaluation of the array-geometry invariance property.

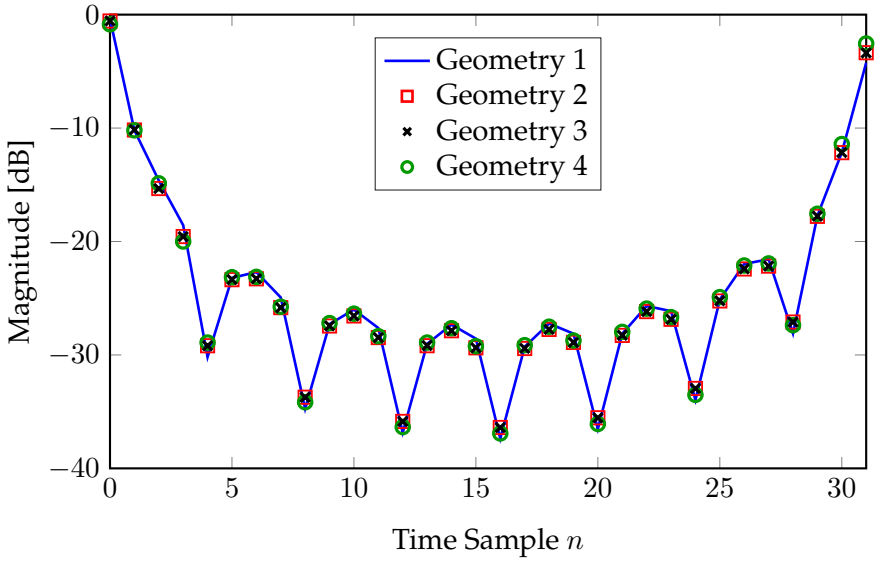

Figure 5.8: Magnitude of the noiseless opportunistic received signal $y[n]$ (5.56) when different transmitting array geometries are used in the 1D scenario depicted in Figure 5.7(a).

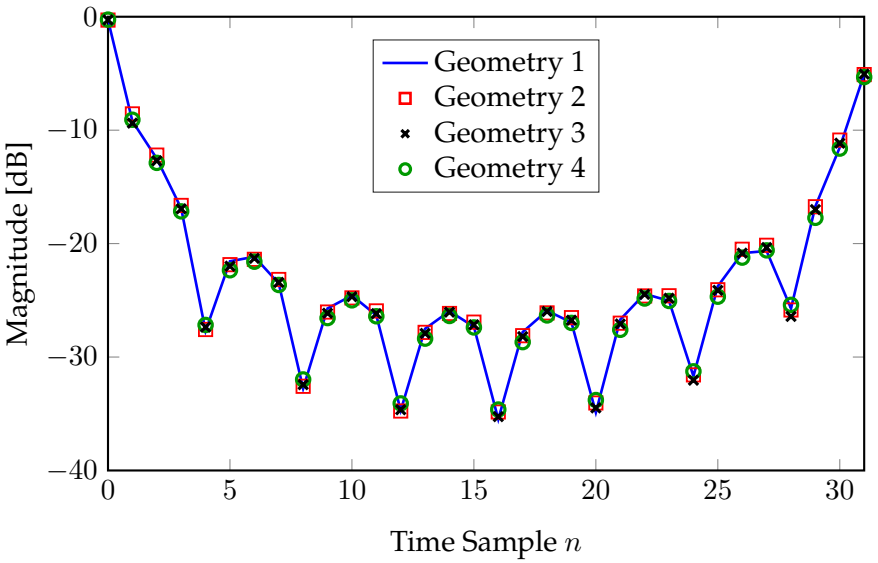

Figure 5.9: Magnitude of the noiseless opportunistic received signal $y[n]$ (5.56) when different transmitting array geometries are used in the 2D scenario depicted in Figure 5.7(b).

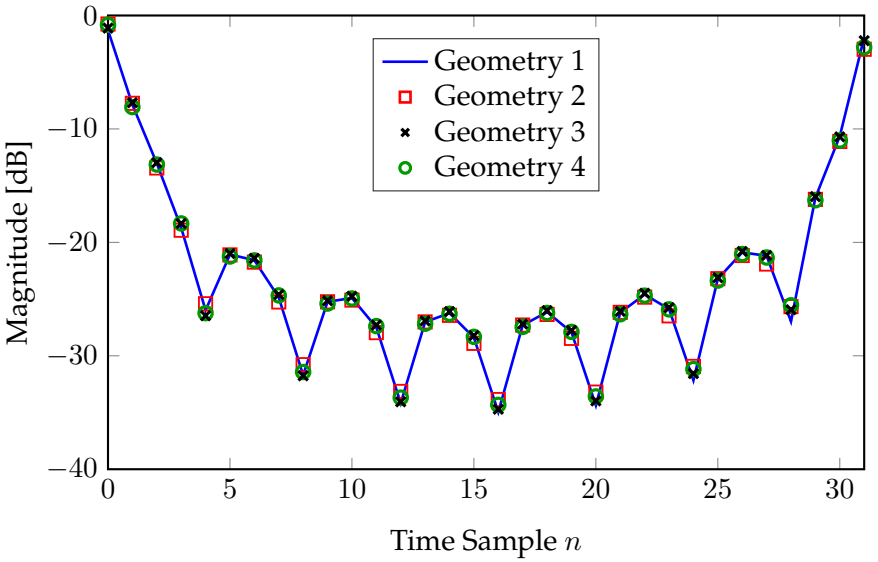

Figure 5.10: Magnitude of the noiseless opportunistic received signal $y[n]$ (5.56) when different transmitting array geometries are used in the 3D scenario depicted in Figure 5.7(c).

Accordingly, in order not to visualize this effect, the same set of L_{T} elevation-azimuth angle pairs Θ is considered in each realization.

In each of the four experiments, the same simulation conditions are considered. In particular, a space-time DoF availability of $M/(NL_{\mathrm{T}}) = 3/4$ is assumed, and it is of paramount importance to guarantee that the same span is considered in each realization. After this sensing part, four waveforms satisfying (5.35) are designed and transmitted through a MISO channel. In all simulations, we assume that the inner receiving node is located at $\theta_{\mathrm{R}} = 30^{\circ}$ with respect to the transmitting array broadside for the linear array case, whereas for the planar and volumetric arrays the location of the receiving node is assumed to be $\theta_{\mathrm{R}} = 30^{\circ}$ and $\varphi_{\mathrm{R}} = 60^{\circ}$.

The noiseless time-domain received signal is depicted in Figures 5.8, 5.9, and 5.10 for the 1D, 2D, and 3D scenarios, respectively. Observing these figures, we immediately notice that the four plots in each scenario are extremely similar, irrespective of the chosen sensors, i.e., the array geometry. Nevertheless, we may observe that some points differ slightly. One reason for these small differences is the unavoidable numerical stability issues. On the other hand, grating lobes will appear in some cases where the minimum inter-element spacing is larger than $d/\lambda_u > 1/2$. These effects are the primary source of the differences observed between different plots in each scenario. Despite these little differences, we may observe that the shape of the noiseless received signal's magnitude is kept, highlighting the array-geometry invariance property exhibited by the space-time MNTLS waveforms.

5.5 Asymptotic Analysis

The last section of this chapter studies the asymptotic behavior of the space-time MNTLS waveforms, extending the analysis performed in Chapter 4.

First of all, the asymptotic behavior of the space-time observations' autocorrelation matrix is provided. Under wide sense stationary conditions, the exact autocorrelation matrix of the space-time observations described in (5.11) has a block-Toeplitz structure, i.e.

$$\boldsymbol{R}_{\boldsymbol{xx}} = \mathbb{E}\left[\boldsymbol{x}\boldsymbol{x}^{H}\right] = \begin{bmatrix} \boldsymbol{R}[0] & \boldsymbol{R}[-1] & \cdots & \boldsymbol{R}[-N+1] \\ \boldsymbol{R}[1] & \boldsymbol{R}[0] & \cdots & \boldsymbol{R}[-N+2] \\ \vdots & \vdots & \ddots & \vdots \\ \boldsymbol{R}[N-1] & \boldsymbol{R}[N-2] & \cdots & \boldsymbol{R}[0] \end{bmatrix} \in \mathbb{C}^{NL \times NL}. \tag{5.57}$$

Each block $\boldsymbol{R}[m] \in \mathbb{C}^{L \times L}$ is the matrix-valued spatial autocorrelation function given by

$$\boldsymbol{R}[m] = \mathbb{E}\left[\boldsymbol{x}[n]\boldsymbol{x}^{H}[n-m]\right], \tag{5.58}$$

where $\boldsymbol{x}[n] \in \mathbb{C}^{L}$ is the observed snapshot at time instant n. It is well-known that, as $N \to \infty$, an $NL \times NL$ block-Toeplitz matrix composed of $N \times N$ blocks of size $L \times L$ is asymptotically equivalent to a block-circulant matrix composed of $N \times N$ blocks of size $L \times L$ [Tee07; RVVLV+11; GGC12; RSV+15], i.e.,

$$\lim_{N \to \infty} \frac{\|\boldsymbol{R}_{\boldsymbol{xx}} - \boldsymbol{C}_{NL \times NL}\|_{\mathrm{F}}}{\sqrt{N}} = 0, \tag{5.59}$$

where $\boldsymbol{C}_{NL \times NL}$ is a block-circulant matrix with the same block structure as $\boldsymbol{R}_{\boldsymbol{xx}}$. Accordingly, under these asymptotic conditions, the eigenmatrix $\boldsymbol{Q}$ of $\boldsymbol{R}_{\boldsymbol{xx}}$ asymptotically converge to the

eigenmatrix of an $NL \times NL$ block-circulant matrix, i.e.,

$$\boldsymbol{Q} \xrightarrow[N\to\infty]{} \boldsymbol{F}_N^H \otimes \boldsymbol{I}_L, \tag{5.60}$$

being $\boldsymbol{F}_N$ the normalized N-size Fourier matrix. For the reader's convenience, a simple example with $N = 5$ and $L = 3$ of the block-Fourier matrix $\boldsymbol{F}_N^H \otimes \boldsymbol{I}_L$ is illustrated in Figure 5.11.

The particular structure introduced by the Kronecker product in (5.60) can be further exploited. Note that permuting the columns of the eigenmatrix $\boldsymbol{Q}$ does not modify its span. Therefore, if $\boldsymbol{Q}$ is a basis of the whole space-time NL-dimensional ambient signal space, any matrix constructed as a column permutation of $\boldsymbol{Q}$ is also a valid basis.

Accordingly, the multi-antenna inner node can design an asymptotic space-time sensing basis given by the horizontal stacking of L matrices of size $NL \times N$. Each of these matrices corresponds to the *sensing basis* at each sensor. Mathematically, the space-time sensing basis reads as

$$\boldsymbol{U} = [\boldsymbol{U}_0 \, \boldsymbol{U}_1 \, \cdots \, \boldsymbol{U}_{L-1}], \tag{5.61}$$

where each block $\boldsymbol{U}_\ell \in \mathbb{C}^{NL\times N}$, for $\ell = 0, \dots L-1$, is given by

$$\boldsymbol{U}_\ell = \boldsymbol{F}_N^H \otimes [\boldsymbol{I}_L]_\ell, \tag{5.62}$$

with $[\boldsymbol{I}_L]_\ell$ standing for the ℓ-th column of $\boldsymbol{I}_L$. An example of the space-time sensing basis described in (5.61) is depicted in Figure 5.12, for the case $N = 5$ and $L = 3$.

A direct consequence of (5.61)–(5.62) is that the wireless environment can be individually sensed at each sensor of the array using the matrix $\boldsymbol{F}_N^H$ as a sensing basis, i.e., the same asymptotic sensing basis as in the single-channel case. Then, the space-time null-space basis can be constructed using (5.62), leading to

$$\widehat{\boldsymbol{U}}_{\mathcal{N}} = \left[\widehat{\boldsymbol{U}}_{\mathcal{N},0} \, \widehat{\boldsymbol{U}}_{\mathcal{N},1} \, \cdots \, \widehat{\boldsymbol{U}}_{\mathcal{N},L-1}\right], \tag{5.63}$$

being $\widehat{\boldsymbol{U}}_{\mathcal{N},\ell}$, for $\ell = 0, \dots, L-1$, the per-antenna sensed null-space bases. It is worth noting that the dimensions of the sensed null space at each sensor can differ, as each sensor may be subject to different sensing conditions. The block structure observed in both (5.61) and (5.63) is also preserved in the orthogonal projector onto $\left\langle \widehat{\boldsymbol{U}}_{\mathcal{N}} \right\rangle$, which is given by

$$\widehat{\boldsymbol{P}}_0 = \widehat{\boldsymbol{U}}_{\mathcal{N}} \widehat{\boldsymbol{U}}_{\mathcal{N}}^H = \sum_{\ell=0}^{L-1} \widehat{\boldsymbol{U}}_{\mathcal{N},\ell} \widehat{\boldsymbol{U}}_{\mathcal{N},\ell}^H. \tag{5.64}$$

Interestingly, the positions of the zeros imposed by the Kronecker product in (5.62) is kept in the sensed space-time null-space basis (5.63) and in the orthogonal projector $\widehat{\boldsymbol{P}}_0$. It is straightforward to verify that this structure is maintained in the asymptotic space-time MNTLS waveforms, regardless of the recursive nature of the design algorithm.

The latter is of paramount importance since it reveals that, asymptotically, the space-time MNTLS waveforms describe a space-time multiplexing scheme, such that each waveform performs an antenna selection policy. Accordingly, the K_ℓ waveforms designed using the M_ℓ time-frequency DoF sensed as available at the ℓ-th antenna only activate this specific antenna. Therefore, asymptotically, the space-time waveforms can be designed on a per-antenna basis, meaning that each antenna can design its associated time-domain waveforms, and these

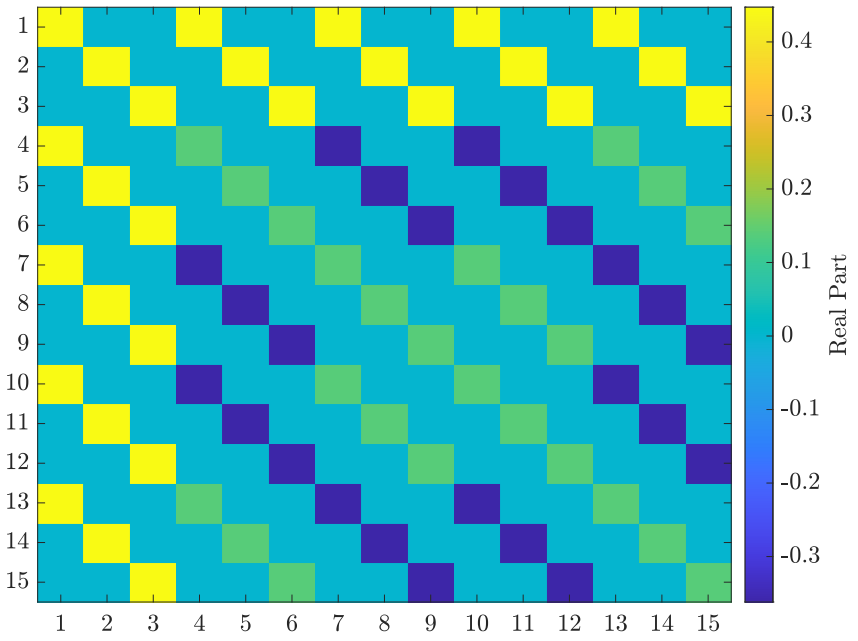

Figure 5.11: Example of a normalized block-Fourier matrix $\boldsymbol{F}_N^H \otimes \boldsymbol{I}_L$ with $N = 5$ and $L = 3$.

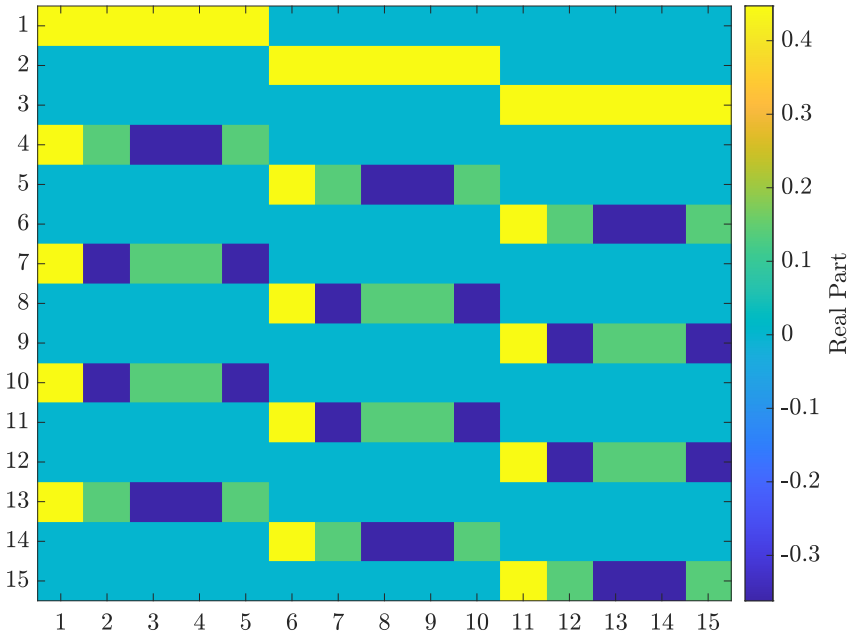

Figure 5.12: Example the structured space-time sensing basis (5.61) with $N = 5$ and $L = 3$.

waveforms can be converted to space-time signals using the Kronecker product as in (5.62). Furthermore, recalling that the space-time waveforms are structured in N blocks of size L, in the asymptotic case, each block only has a single non-zero element corresponding to the coefficient associated with one antenna. This particular structure is exemplified on the next page, where the asymptotic behavior of the space-time shaping transmission matrix $\boldsymbol{\Phi}$ is illustrated in Figure 5.13, and the transmit beamvectors at each time instant are depicted in 5.14, with $N = 5$ and $L = 3$. Note that the values of N and L are kept small for the sake of illustration. In particular, a shaping transmission matrix with $K = 3$ waveforms is depicted in Figure 5.13. Each of these waveforms corresponds to the first waveform designed at each of the three antennas. In order to better illustrate the antenna selection property, the transmit beamvector at each time instant derived from each waveform in $\boldsymbol{\Phi}$ is drawn in Figure 5.14.

The antenna selection property asymptotically exhibited by the space-time MNTLS waveforms opens up the opportunity to incorporate more properties into the designed waveforms. Specifically, deciding which antennas are active for each transmission permits tuning not only the number of transmit antennas but also the geometry of the array. Even though the antenna array geometry has no impact on the opportunistic communication performance, tuning the geometry can be of paramount interest to improve the opportunistic communication performance. For instance, array tuning enables the design of space-time codes [PNG03] or adjusting the diversity-multiplexing trade-off [TVZ04] to satisfy the traffic or quality-of-service requirements of the inner receiving node.

From an opportunistic communication perspective, the particular structure exhibited by the asymptotic space-time MNTLS waveforms permits a straightforward adaptation of the CS-TDMA scheme. If the conditions described in Section 4.4 hold only at some antennas, a per-antenna CS-TDMA scheme can be implemented in the corresponding antennas. However, if all antennas satisfy the conditions, the extension leads to a full multi-antenna CS-TDMA scheme, defining an efficient space-time waveform multiplexing strategy.

Regarding the extension of the opportunistic transmission scheme in frequency-selective channels, it is discussed next for the sake of completeness.

5.5.1 Adaptation to Multi-Antenna Frequency-Selective Channels

Throughout this chapter, the frequency-selective nature of wideband multi-antenna channels has been omitted. As the system bandwidth increases, it becomes reasonable to adopt the asymptotic behavior of the space-time MNTLS waveforms studied in this section. Accordingly, the adaption of these waveforms to frequency-selective channels is discussed next.

As previously considered in Chapter 4, a CP-based multi-antenna opportunistic transmission scheme is adopted. The latter requires defining a structured non-orthogonal sensing basis for each array sensor. Letting $\boldsymbol{V} = \boldsymbol{F}_N^H$, where $\boldsymbol{F}_N$ is the normalized N-size Fourier matrix, the structured non-orthogonal sensing basis at the ℓ-th antenna is given by

$$\boldsymbol{W}_\ell = \left[\begin{array}{c} \boldsymbol{V}_{\text{CP}} \\ \hdashline \boldsymbol{V} \end{array}\right] \otimes [\boldsymbol{I}_L]_\ell \,, \tag{5.65}$$

where $\boldsymbol{V}_{\text{CP}}$ is a wide matrix containing the last $N_{\text{CP}} \geq L_h$ rows of $\boldsymbol{V}$, being L_h the channel memory, and $[\boldsymbol{I}_L]_\ell$ stands for the ℓ-th column of the identity matrix. After the per-antenna

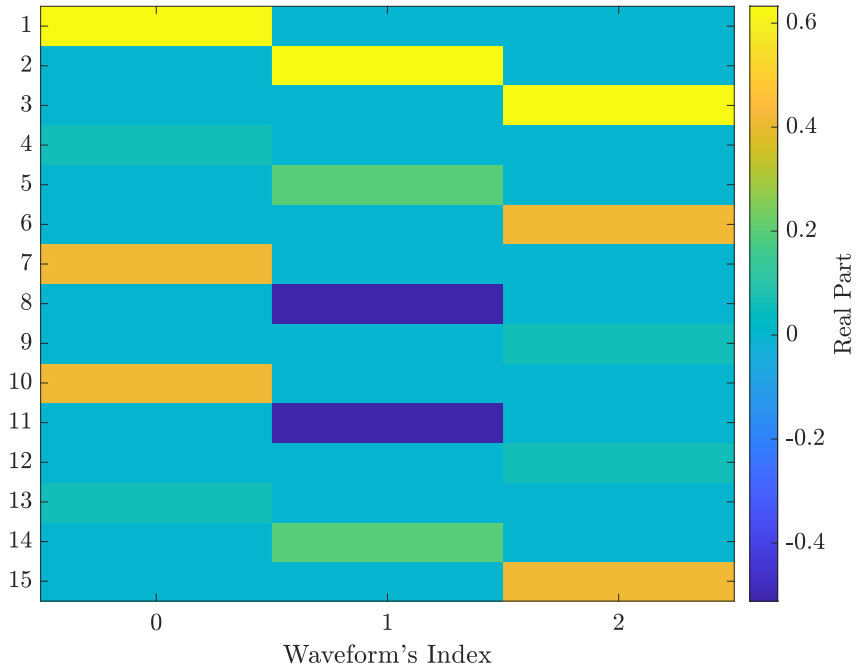

Figure 5.13: Shaping transmission matrix composed of $K = 3$ waveforms corresponding to the first waveform at each of the three antennas.

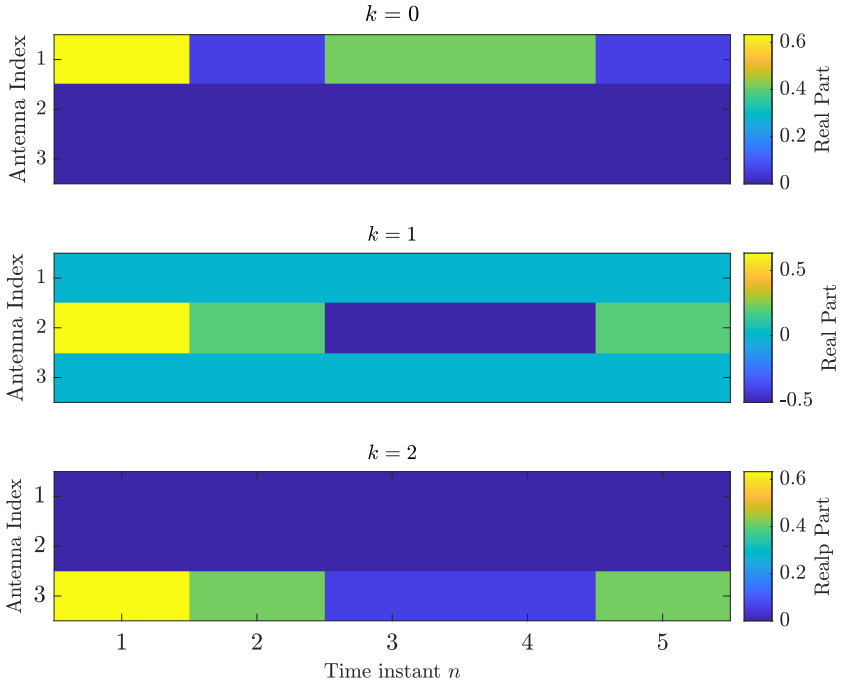

Figure 5.14: Transmit beamvector from each waveform in the shaping transmission matrix depicted in Figure 5.13.

sensing, the inner transmitter obtains a set of L null-space bases of the form

$$\widetilde{\boldsymbol{W}}_{\mathcal{N},\ell} = \left[\begin{array}{c} \boldsymbol{V}_{\mathcal{N},\mathrm{CP}}^{(\ell)} \\ \hdashline \boldsymbol{V}_{\mathcal{N},\ell} \end{array}\right] \otimes [\boldsymbol{I}_L]_\ell \in \mathbb{C}^{(N+N_{\mathrm{CP}})L \times M_\ell}, \tag{5.66}$$

being M_ℓ the number of DoF sensed as available at the ℓ-th sensor, such that the shaping transmission matrix at each antenna is given by

$$\widetilde{\boldsymbol{\Phi}}_\ell = \widetilde{\boldsymbol{W}}_{\mathcal{N},\ell}\boldsymbol{\Lambda}_\ell = \left[\begin{array}{c} \boldsymbol{\Phi}_{\mathrm{CP},\ell} \\ \hdashline \boldsymbol{\Phi}_\ell \end{array}\right] = \left(\left[\begin{array}{c} \boldsymbol{V}_{\mathcal{N},\mathrm{CP}}^{(\ell)} \\ \hdashline \boldsymbol{V}_{\mathcal{N},\ell} \end{array}\right] \otimes [\boldsymbol{I}_L]_\ell\right) \boldsymbol{\Lambda}_\ell \in \mathbb{C}^{(N_{\mathrm{CP}}+N)L \times K_\ell}, \tag{5.67}$$

where K_ℓ is the number of waveforms designed at the ℓ-th antenna, satisfying $K_\ell \leq M_\ell$ and $K_\ell \leq K$. Note that the case $K_\ell = K$ reduces to the single-channel case analyzed in Chapter 4. As per (5.67), note that the cyclically extended waveforms $\widetilde{\boldsymbol{\phi}}_k^{(\ell)} = \widetilde{\boldsymbol{W}}_{\mathcal{N},\ell}\boldsymbol{\lambda}_k^{(\ell)}$ are not orthogonal due to the insertion of the CP. Nevertheless, by removing the cyclic extensions the orthogonality between waveforms is restored.

A direct consequence of the study carried on in this section is that the multi-antenna opportunistic transmission can be tackled as a set of L orthogonal single-channel transmissions. Therefore, the signal received by the inner receiving node, after removing the CP, reads as

$$\boldsymbol{y} = \sqrt{\frac{S_{\mathrm{T}}}{K}} \sum_{k=0}^{K-1} a_k \sum_{\ell=0}^{L-1} \boldsymbol{H}_{\mathrm{II},c}^{(\ell)} \boldsymbol{\phi}_k^{(\ell)} + \boldsymbol{w}, \tag{5.68}$$

where $\boldsymbol{H}_{\mathrm{II},c}^{(\ell)} \in \mathbb{C}^{N \times N}$ is the circulant inner channel matrix between the ℓ-th antenna and the inner receiver, which can be decomposed as $\boldsymbol{H}_{\mathrm{II},c}^{(\ell)} = \boldsymbol{F}_N^H \boldsymbol{\Sigma}_{h,\ell} \boldsymbol{F}_N$, being $\boldsymbol{\Sigma}_{h,\ell}$ a diagonal matrix containing the channel frequency response at the ℓ-th antenna; $\boldsymbol{\phi}_k^{(\ell)} \in \mathbb{C}^N$ is the time-domain opportunistic waveform at the ℓ-th antenna; a_k is the k-th transmitted symbol; and $\boldsymbol{w} \sim \mathcal{N}_{\mathbb{C}}(\boldsymbol{0}, \sigma^2 \boldsymbol{I}_N)$ is the interference-plus-noise term.

Recalling that the structure induced by the Kronecker product in (5.62) translates into an antenna selection policy, each transmitted waveform only activates one antenna. Accordingly, the summation for ℓ in (5.68) has a single non-null element. Therefore, (5.68) can be further simplified as

$$\boldsymbol{y} = \sqrt{\frac{S_{\mathrm{T}}}{K}} \sum_{k=0}^{K-1} a_k \boldsymbol{H}_{\mathrm{II},c}^{(\ell[k])} \boldsymbol{\phi}_k^{(\ell)} + \boldsymbol{w} = \sqrt{\frac{S_{\mathrm{T}}}{K}} \sum_{k=0}^{K-1} a_k \boldsymbol{F}_N^H \boldsymbol{\Sigma}_{h,\ell[k]} \boldsymbol{F}_N \boldsymbol{\phi}_k^{(\ell)} + \boldsymbol{w} \tag{5.69}$$

where $\ell[k]$ indexes the antenna activated by the k-th waveform. From (5.67), it is straightforward to see that $\boldsymbol{\phi}_k^{(\ell)}$ is given by

$$\boldsymbol{\phi}_k^{(\ell)} = \boldsymbol{V}_{\mathcal{N},\ell} \boldsymbol{\lambda}_k^{(\ell)}, \tag{5.70}$$

being $\boldsymbol{\lambda}_k^{(\ell)}$ the k-th column of $\boldsymbol{\Lambda}_\ell$. Therefore, (5.69) can be written as

$$\boldsymbol{y} = \sqrt{\frac{S_{\mathrm{T}}}{K}} \sum_{k=0}^{K-1} a_k \boldsymbol{F}_N^H \left[\begin{array}{c} \boldsymbol{0}_{(N-M_{\ell[k]}) \times M_{\ell[k]}} \\ \hdashline \boldsymbol{\Sigma}_{\mathcal{N},h,\ell[k]} \end{array}\right] \boldsymbol{\lambda}_k^{(\ell[k])} + \boldsymbol{w}, \tag{5.71}$$

denoting $M_{\ell[k]}$ the dimension of the null space at the antenna selected by the k-th waveform. At this point, we can see that with a few notational differences, (5.71) has a similar structure to the received signal in the single-channel case discussed in Chapter 4. Thus, the same receiving structure can be implemented on a per antenna basis. In this sense, considering the sub-optimal zero-forcing criterion, the frequency-domain one-tap equalizer at the ℓ-th antenna is given by

$$\boldsymbol{G}_{\ell} = \widehat{\boldsymbol{V}}_{\mathcal{N},\ell} \boldsymbol{\Sigma}_{\mathcal{N},h,\ell}^{-1} \widehat{\boldsymbol{V}}_{\mathcal{N},\ell}^{H}. \tag{5.72}$$

In conclusion, the frequency-selective nature of the channel can be counteracted in the multi-antenna case with an extension of the CP-based opportunistic transmission scheme described in Chapter 4. However, the proposed strategy defines a space-time multiplexing scheme in this multi-channel case. Nevertheless, as previously discussed in Chapter 4, space-time-frequency multiplexing is possible by appropriately dividing the per-antenna null space into smaller regions at the expense of decreasing the attainable SIDR.

5.6 Conclusions

This chapter has studied the problem of multi-channel feedforward opportunistic communications. From the inner transmitting node perspective, the space-time MNTLS waveforms keep the dimensions spreading property, which is fundamental to guarantee a minimum inter-system interference level per erroneous space-time DoF. In this respect, the analysis of the SIDR metric in multi-antenna scenarios has unveiled the impact of using multiple antennas to increase the dimension further spreading factor.

From an end-to-end opportunistic communication, the fundamental invariance property, which guarantees coherent waveform detection under cumbersome feedforward conditions, has been studied. In particular, the impact of the geometries of transmitting and receiving arrays has been analyzed. When the number of sensors at each system end is equal, the rationale provided in Chapter 3 for the single-antenna case has been straightforwardly extended to multi-channel scenarios. Nevertheless, a more involved discussion has been provided in the more general case where the number of sensors at each system end differs. Specifically, the array manifold separation theory has been used to demonstrate that the opportunistic communication performance is independent of the transmitting and receiving array geometries and only depends on the number of space-time DoF in terms of a potential diversity gain and a larger dimension spreading factor.

Finally, the asymptotic behavior of the space-time MNTLS waveforms has been analyzed. Using the asymptotic eigenanalysis of block-Toeplitz matrices, it has been proven that the proposed opportunistic transmission scheme tends to asymptotically perform an antenna selection policy, behaving similarly to a set of orthogonal single-antenna transmitters. This result has been of paramount importance to extrapolate the CS-TDMA modulation studied in Chapter 4 to multi-antenna opportunistic scenarios and to define a CP-based modulation to operate in multi-antenna frequency-selective channels.

Appendix 5.A On Wavefield Modeling and Manifold Separation

The most significant result of this chapter is based on the manifold separation theory (MST). MST is described through a formalism of array processing called wavefield modeling [DD94a; DD94b; DD94c]. In essence, this formalism states that the signal-only part of the array output can be written in terms of a sampling operator on the received wavefield, leading to an orthonormal expansion of the array steering vector. Accordingly, the steering vector can be decomposed into an array-only dependent matrix and a wavefield-only dependent vector. This Appendix provides a brief review based on [DD94a; DD94b; DD94c] of the rationale behind this theory.

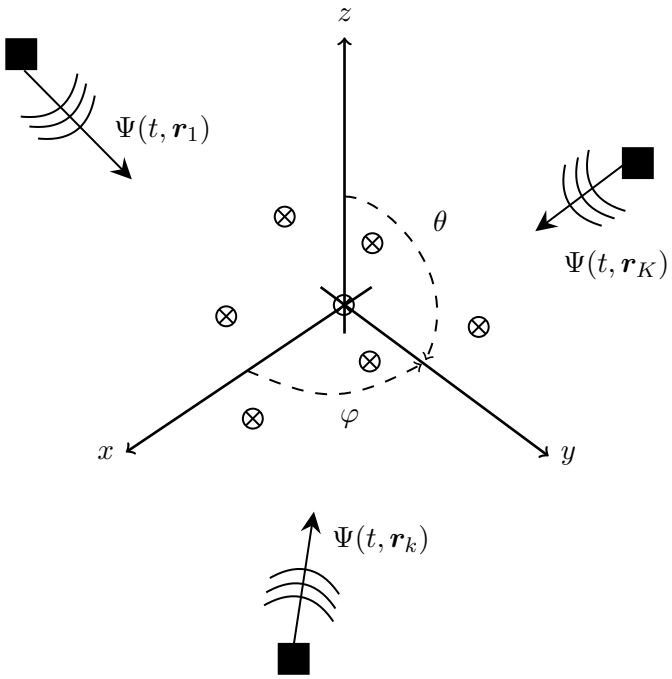

Figure 5.15: K far-field non-polarized narrowband sources (black squares) impinge a volumetric array with an arbitrary geometry composed of L isotropic and uncoupled sensors (circled exes). The phase-reference element is placed at the origin. The vector $\boldsymbol{r}_k$ refers to the spherical coordinates of the sources, i.e., $\boldsymbol{r}_k = (R_k, \theta_k, \varphi_k)^T$, being R_k, θ_k, and φ_k the distance with respect to the phase-reference element, the elevation, and the azimuth, respectively.

Without loss of generality, let us consider the scenario depicted in Figure 5.15, where K far-field non-polarized[4] narrowband sources impinge a volumetric array composed of L isotropic[5] and uncoupled sensors. Each propagating wavefield[6] $\Psi_k(t, \boldsymbol{r})$ has a Fourier integral representation given by

$$\Psi_k(t, \boldsymbol{r}) = \int \Phi_k(\omega, \boldsymbol{r}) e^{j\omega t} \mathrm{d}\omega, \tag{5.73}$$

where $\Phi_k(\omega, \boldsymbol{r})$ are the Fourier components. Taking into account the far-field assumption, the

[4]The manifold separation expansion can be generalized to the case of polarized antenna arrays at the expense of notational complexity [CRK12; CK14; Fri18]. For ease of discussion, the case of non-polarized arrays is considered in this Appendix.

[5]The directivity pattern of the sensors can be straightforwardly incorporated in the array model [DD94a].

[6]As per [DD94a], each $\Psi_k(t, \boldsymbol{r})$ propagates according to the wave equations. Thus, each Fourier component $\Phi_k(\omega, \boldsymbol{r})$ meets the source-free Helmholtz equation.

Fourier components of the propagating wavefield admit the following expression:

$$\Phi_k(\omega, \boldsymbol{r}) = \int_{\mathcal{M}} \rho(\omega, \mu) e^{j\kappa \boldsymbol{r}_k^T \hat{\boldsymbol{\mu}}} \mathrm{d}\mu, \tag{5.74}$$

where $\mathcal{M}$ describes the manifold of possible angles of arrival, i.e.,

$$\mathcal{M} = \begin{cases} \{\varphi \ : \ \varphi \in [0, 2\pi)\} & \text{in 2D scenarios} \\ \{(\theta, \varphi) \ : \ \theta \in [0, \pi], \varphi \in [0, 2\pi)\} & \text{in 3D scenarios} \end{cases}. \tag{5.75}$$

Note that a 2D scenario refers to the case of linear arrays or when the sources impinging the array are located on the xy-plane according to the coordinates depicted in Figure 5.15. Otherwise, the problem is contextualized in a 3D scenario. Regarding (5.74), μ is a point on the manifold $\mathcal{M}$, $\rho(\omega, \mu)$ is an angular distribution of the Fourier component denoted as the radiation density in the direction μ, $\kappa = \omega/c$ is the wavenumber, being c the propagation speed, and $\hat{\boldsymbol{\mu}}$ is a unit vector pointing the direction μ. The exponent in (5.74), i.e., $j\kappa \boldsymbol{r}_k^T \hat{\boldsymbol{\mu}}$ is given by

$$j\kappa \boldsymbol{r}_k^T \hat{\boldsymbol{\mu}} = \boldsymbol{\kappa}_{\omega,k}^T \widetilde{\boldsymbol{r}}_k = \frac{2\pi}{\lambda_\omega} \left[\sin(\theta_k)\cos(\varphi_k), \sin(\theta_k)\sin(\varphi_k), \cos(\theta_k)\right]^T \begin{bmatrix} x_k \\ y_k \\ z_k \end{bmatrix}, \tag{5.76}$$

i.e., the scalar product of the wavenumber vector $\boldsymbol{\kappa}_{\omega,k}$ and the cartesian coordinates vector of the k-th source $\widetilde{\boldsymbol{r}}_k$. Note that λ_ω is the wavelength at frequency ω. As per [DD94a], the Fourier component of the propagating wavefield in (5.74) admits an orthogonal decomposition in the Hilbert space $\mathcal{H}$ given by

$$\Phi_k(\omega, \boldsymbol{r}) = \sum_{n=-\infty}^{\infty} d_{n,k}(\omega) h_n(\boldsymbol{r}_k), \tag{5.77}$$

being $\{h_n(\boldsymbol{r}_k)\}$ the elements of an orthogonal basis in $\mathcal{H}$. The plane waves $e^{j\kappa \boldsymbol{r}_k^T \hat{\boldsymbol{\mu}}}$ solve the Helmholtz equation, the radiation density $\rho(\omega, \mu)$ can be a complex function defined on the space of functions that are absolute-square Lebesgue integrable over the manifold $\mathcal{M}$, i.e., $\mathcal{L}^2(\mathcal{M})$. Accordingly, the radiation density $\rho(\omega, \mu)$ can also be written in terms of an orthogonal expansion in the space $\mathcal{L}^2(\mathcal{M})$ given by

$$\rho(\omega, \mu) = \sum_{n=-\infty}^{\infty} d_{n,k}(\omega) f_n(\mu), \tag{5.78}$$

where $\{f_n(\mu)\}$ are the elements of an orthogonal basis in $\mathcal{L}^2(\mathcal{M})$. Note that $f_n(\mu)$ and $h_n(\boldsymbol{r}_k)$ are related as

$$h_n(\boldsymbol{r}_k) = \int_{\mathcal{M}} f_n(\mu) e^{j\kappa \boldsymbol{r}_k^T \hat{\boldsymbol{\mu}}} \mathrm{d}\mu, \tag{5.79}$$

and the coefficients of the orthogonal expansions in (5.77) and (5.78) are given by

$$d_{n,k}(\omega) = \int_{\mathcal{M}} \rho(\omega, \mu) f_n^*(\mu) \mathrm{d}\mu = \int_{\mathbb{R}^m} \Phi_k(\omega, \boldsymbol{r}) h_n^*(\boldsymbol{r}_k) \mathrm{d}\boldsymbol{r}, \tag{5.80}$$

where $m = 2$ in 2D scenarios and $m = 3$ in 3D scenarios. Thus far, the discussion has not been focused on any particular choice for the bases of the orthogonal expansions. As discussed in [DD94a], noting that the manifold $\mathcal{M}$ represents a unit circle in 2D and a unit sphere in 3D, an

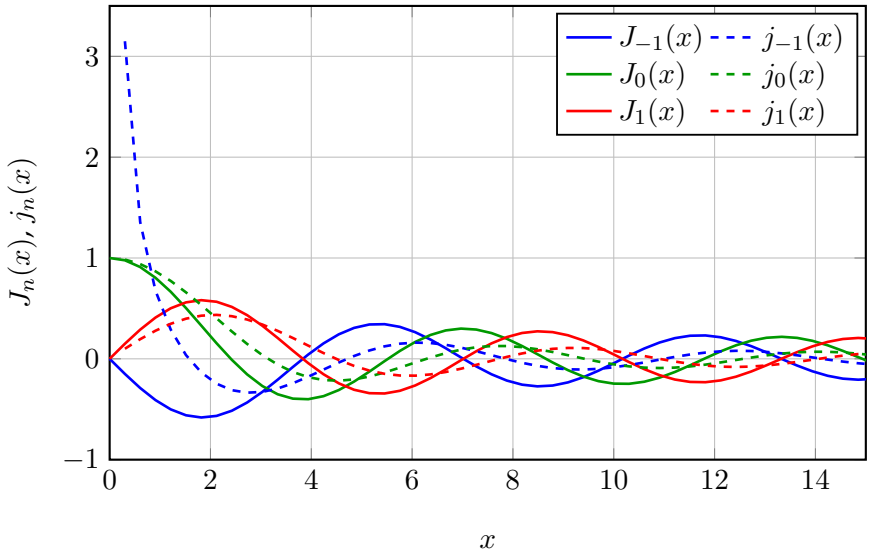

Figure 5.16: Examples of the Bessel function and the spherical Bessel function of the first kind, $J_n(x)$ and $j_n(x)$, respectively, for orders $n = -1, 0, 1$.

adequate orthogonal expansion for the radiation density is given in terms of the Fourier basis in 2D and in terms of the spherical harmonics in 3D, i.e.,

$$f_n(\mu) = \begin{cases} (2\pi)^{-1/2} e^{-jn\varphi} & \text{in 2D scenarios} \\ Y_{lp}(\theta, \varphi) & \text{in 3D scenarios} \end{cases}, \tag{5.81}$$

being $Y_{ln}(\theta, \varphi)$, for $l = 0, 1, \ldots, \infty$ and $p = -l, \ldots, l$, the spherical harmonic functions [Mül06], which can be written as a single index $n = l(l+1) + p$. Accordingly, using the relation (5.79), the corresponding orthogonal basis set $\{h_n(\boldsymbol{r}_k)\}$ in $\mathcal{H}$ is given by

$$h_n(\boldsymbol{r}_k) = \begin{cases} \sqrt{2\pi}(j)^n J_n(\kappa r) e^{-jn\varphi} & \text{in 2D scenarios} \\ 4\pi(j)^l j_l(\kappa r) Y_{lp}(\theta, \varphi) & \text{in 3D scenarios} \end{cases}, \tag{5.82}$$

where $J_n(x)$ and $j_l(x)$, with $n = -\infty, \ldots, -1, 0, 1, \ldots, \infty$ and $l = 0, 1, \ldots, \infty$, are the Bessel functions of the first kind and the spherical Bessel functions of the first kind, respectively. In view of (5.78) and (5.81), it is worth noting that the coefficients $a_n(\omega)$ of the orthonormal expansion are Fourier coefficients in 2D and spherical harmonic coefficients in 3D. Both the Bessel and the spherical Bessel functions of the first kind are illustrated in Figure 5.16.

Thus far, an orthonormal expansion of the propagating wavefield has been provided. Let us now focus on the array response vector, i.e., the array steering vector. An antenna array or a sensor array can be interpreted as a sampler of the spatial domain; the input is the impinging wavefield, and the output is the steering vector. Let $\boldsymbol{y}_k \in \mathbb{C}^L$ be the array output for the k-th impinging wavefield. Neglecting the noise, the array output is given by [DD94a]

$$\boldsymbol{y} = G\left[\Phi_k(\omega, \boldsymbol{r})\right] = G\left[\sum_{n=-\infty}^{\infty} d_{n,k}(\omega) h_n(\boldsymbol{r}_k)\right] = \boldsymbol{G}\boldsymbol{d}_k \tag{5.83}$$

where $G[\cdot]$ denotes the sampling operation, and $\boldsymbol{G}$ and $\boldsymbol{d}$ are the so-called *sampling matrix* and *coefficient vector*, respectively. In view of the previous discussion on the orthogonal expansion

of the propagating wavefield, it is worth noting that the array output can be written in terms of an orthonormal expansion. The sampling matrix is a property of the antenna array, which physically describes the array, accounting for the array architecture and its non-idealities (e.g., calibration errors). On the contrary, the coefficient vector exclusively describes the impinging wavefield, being independent of the antenna array. Note that the dependence on the frequency ω has been dropped in (5.83) for simplicity of notation. Accordingly, from a mathematical viewpoint, the coefficient vector can be seen as a function defined on a Hilbert space, whereas the sampling matrix is just a mapping of the functions defined on a Hilbert space onto vectors belonging to the L-dimensional complex space $\mathbb{C}^L$. That is,

$$\boldsymbol{G} \ : \ \mathcal{H} \to \mathbb{C}^L, \tag{5.84}$$

meaning that matrix $\boldsymbol{G}$ has an infinite number of columns and L rows. It is interesting to note that (5.83) reveals that the output of the antenna array can be written as the product of an array-only dependent matrix and a wavefield-only dependent vector. Likewise, since the steering vector $\boldsymbol{s}(\mu) \in \mathbb{C}^L$ of the corresponding array is the array response to a unit-magnitude plane wave arriving from direction μ, the steering vector $\boldsymbol{s}(\mu)$ can be decomposed as

$$\boldsymbol{s}(\mu) = \boldsymbol{G}\boldsymbol{d}_\mu, \tag{5.85}$$

where $\boldsymbol{a}_\mu$ is the coefficient vector corresponding to a unit-magnitude plane wave arriving from direction μ.

5.A.1 Beyond the Theoretical Foundations of Wavefield Modeling

Even though it was not formally justified, the separability of the array manifold first appeared in [DDW93] as a coherent wideband array processing technique for arrays with arbitrary geometry. The principal motivation of the wavefield model is to ease the use of efficient array processing methods developed for the case of uniform linear arrays (ULA) in more general cases where the array may have an arbitrary geometry. For instance, root-MUSIC (see, e.g., [RH89]) is an efficient direction-finding technique developed for ULA. The last condition implies that the steering matrix, i.e., the matrix encompassing the array steering vectors, is a Vandermonde matrix with complex exponential entries. The steering matrix has only a Vandermonde structure in the ULA case. However, the Vandermonde structure is broken if the array suffers from calibration issues, malfunctioning sensors, or when the array has another topology. An attempt to adapt root-MUSIC consists in mapping the *real* array was mapped into a linear *virtual* array [Fri93]. However, this mapping (and other mapping techniques) produces mapping errors. For this reason, the wavefield model formally derived in [DD94a] has been used for coherent wideband array processing [DD94b], direction-finding [BRK07; RG09; Fri18; PLL+19], polarization estimation [CRK12], or beamforming [CK14].

In the abovementioned applications, a fundamental problem is to find the orthogonal decomposition of the array steering vectors described in (5.85). Since the Hilbert space $\mathcal{H}$ is an infinite-dimensional space, the coefficient vector has an infinite number of elements and the sampling matrix has infinite columns. Both the coefficient vector and the sampling matrix have to be estimated from measurements when the array geometry is unknown. Moreover, in practical applications, using the *true* sampling matrix and coefficient vector is not realistic. Altogether, the truncation and the estimation lead to modeling errors [DD94a; BRK07]. Focusing

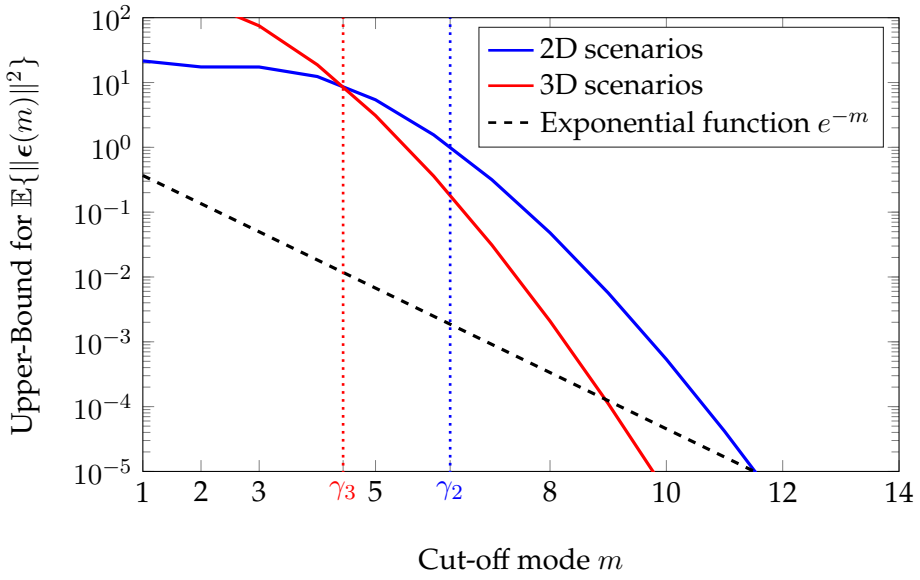

Figure 5.17: Superexponential decay of the upper-bound for the mean-square errors in 2D and 3D scenarios. Beyond a known threshold, $\mathbb{E}\{\|\boldsymbol{\epsilon}(m)\|^2\}$ decays faster than the exponential function.

only on the truncation, it is of relevant interest in practical applications to define the *truncated* sampling matrix and the coefficient vector such that the array steering vector pointing direction $\mu \in \mathcal{M}$ can be written as

$$\boldsymbol{s}(\mu) = \widetilde{\boldsymbol{G}}\widetilde{\boldsymbol{d}}_{\mu} + \boldsymbol{\epsilon}(m), \tag{5.86}$$

where $\boldsymbol{\epsilon}(m)$ is the modeling error due to truncating the sampling matrix and the coefficient vector. Recalling (5.83), the truncation can be defined as

$$\boldsymbol{\epsilon}(m) = \boldsymbol{s}(\mu) - G\left[\sum_{n=-\frac{m-1}{2}}^{\frac{m-1}{2}} d_{n,\mu}(\omega)h_n(\boldsymbol{r})\right] \tag{5.87}$$

The thorough study conducted in [DD94a] reveals that the mean-square truncation error (5.87) in 2D scenarios is upper-bounded by

$$\mathbb{E}\{\|\boldsymbol{\epsilon}(m)\|^2\} \leq 2L^2 \sum_{n=m+1}^{\infty} J_n^2(\kappa R_{\min}), \tag{5.88}$$

where L is the number of array elements, m is the cut-off mode, $\kappa = 2\pi/\lambda$ is the wavenumber, and $R_{\min}$ is the radius of the smallest circle enclosing the array. In the case, of 3D scenarios, $\mathbb{E}\{\|\boldsymbol{\epsilon}(m)\|^2\}$ reads as

$$\mathbb{E}\{\|\boldsymbol{\epsilon}(m)\|^2\} \leq L^2 \sum_{l=m+1}^{\infty} (2l+1) j_l^2(\kappa R_{\min}), \tag{5.89}$$

where $R_{\min}$ is now the radius of the smallest sphere enclosing the array. These two upper-bounds (5.88) and (5.89) are illustrated in Figure 5.17. For 2D scenarios, a 5-element ULA with half-wavelength element separation is considered, whereas we have used a 16-element planar array with sensors distributed within a square of dimensions $2\lambda \times 2\lambda$ for the 3D case. As per [DD94a], it is noted that beyond a threshold given by $\kappa R_{\min}$, the upper-bounds in (5.88) and

(5.89) exhibit a *superexponential* decay, i.e., a decay faster than the exponential function, for $n \to \infty$. As widely studied in the literature (see, e.g., [DD94a; BRK07; CRK10]), the cut-off mode means that the sampling matrix can be safely approximated by around $2\lceil\gamma_2\rceil + 1$ columns in 2D scenarios and by around $2\lceil\gamma_3\rceil^2 + 4\lceil\gamma_3\rceil$ columns in 3D scenarios, where γ_2 and γ_3 refer to the threshold beyond which the error exhibits the superexponential decay.

The abovementioned quantities are of relevant interest from an information-theoretic viewpoint. As per [Han88], the maximum number of independent modes in 2D scenarios is $2\eta + 1$, whereas in 3D scenarios only $2\eta(\eta+2)$ spherical modes are independent. Here, η is the number of relevant modes of the radiated field and is given by $\eta = \lceil \kappa R_{\min} \rceil + \varepsilon$, where ε depends on the considered truncation accuracy. In principle, the radiated field may have an infinite number of propagating modes. Nevertheless, under the assumption that all modes have amplitudes of the same magnitude order at the limit, i.e., at a distance equal to $R_{\min}$, only $\kappa R_{\min}$ modes strongly contribute to the radiated field. Therefore, the quantities $2\eta + 1$ and $2\eta(\eta + 2)$ represent the sufficient number of samples to accurately represent the wavefield in the near-field region with a given accuracy ε.

Appendix 5.B Asymptotic Analysis of the Multi-Channel SIDR

The SIDR, as defined in (5.19), reads as

$$\mathrm{SIDR}_{\mathrm{T}}\left(\boldsymbol{E}_{\mathcal{N}};\{\boldsymbol{\lambda}_k\}\right)=\frac{S_{\mathrm{T}}-I_{\mathrm{T}}\left(\boldsymbol{E}_{\mathcal{N}};\{\boldsymbol{\lambda}_k\}\right)}{\frac{1}{N_E}I_{\mathrm{T}}\left(\boldsymbol{E}_{\mathcal{N}};\{\boldsymbol{\lambda}_k\}\right)}. \tag{5.90}$$

Recalling that $\{\boldsymbol{\phi}_k\}_{0\leq k\leq K-1}$ constitutes a class of orthonormal modulations, we have that the total average transmitted power is given by

$$S_{\mathrm{T}}=\frac{1}{N}\sum_{k=0}^{K-1}\|\boldsymbol{\phi}_k\|^2=\frac{K}{N}. \tag{5.91}$$

Regarding the inter-system interference term $I_{\mathrm{T}}\left(\boldsymbol{E}_{\mathcal{N}};\{\boldsymbol{\lambda}_k\}\right)$, the calculation is more involved. To begin with, recall that the average inter-system interference power, given in (5.15), is defined as

$$I_{\mathrm{T}}\left(\boldsymbol{E}_{\mathcal{N}};\{\boldsymbol{\lambda}_k\}\right)=\frac{1}{N}\sum_{k=0}^{K-1}\left\|\boldsymbol{E}_{\mathcal{N}}^H\widehat{\boldsymbol{U}}_{\mathcal{N}}\boldsymbol{\lambda}_k\right\|^2=\frac{1}{N}\sum_{k=0}^{K-1}\frac{\boldsymbol{e}_k^T\widehat{\boldsymbol{P}}_k\boldsymbol{P}_{\mathcal{E}}\widehat{\boldsymbol{P}}_k\boldsymbol{e}_k}{\boldsymbol{e}_k^T\widehat{\boldsymbol{P}}_k\boldsymbol{e}_k}, \tag{5.92}$$

being $\boldsymbol{P}_{\mathcal{E}}=\boldsymbol{E}_{\mathcal{N}}\boldsymbol{E}_{\mathcal{N}}^H$ the projector onto the subspace spanned by the occupied space-time DoF erroneously sensed as available. Following the same rationale as in Appendix 3.C, (5.92) can be written as

$$I_{\mathrm{T}}\left(\boldsymbol{E}_{\mathcal{N}};\{\boldsymbol{\lambda}_k\}\right)=\frac{1}{N}\sum_{k=0}^{K-1}\frac{\boldsymbol{e}_k^T\boldsymbol{P}_{\mathcal{E}}\boldsymbol{e}_k+\delta_k^{(1)}}{\boldsymbol{e}_k^T\widehat{\boldsymbol{P}}_0\boldsymbol{e}_k+\delta_k^{(2)}}, \tag{5.93}$$

where $\delta_k^{(1)}$ and $\delta_k^{(2)}$ are second-order terms involving off-diagonal elements of projectors $\boldsymbol{P}_{\mathcal{E}}$ and $\widehat{\boldsymbol{P}}_0$ and, thus, are asymptotically irrelevant as in Appendix 3.C (cf. [BS16]). Under these conditions, we only need to characterize the diagonal elements of the projection matrices $\boldsymbol{P}_{\mathcal{E}}$ and $\widehat{\boldsymbol{P}}_0$ in the multi-channel case.

For the latter purpose, it can be helpful to study the asymptotic behavior of the eigenvectors' matrix of the space-time autocorrelation matrix given in (5.12). As discussed in detail in Section 5.5, the eigenmatrix $\boldsymbol{U}$ of the space-time autocorrelation matrix asymptotically converges to [Tee07; RVVLV+11; GGC12; RSV+15]

$$\boldsymbol{U}\xrightarrow[N\to\infty]{}\frac{1}{\sqrt{N}}\boldsymbol{F}_N^H\otimes\boldsymbol{I}_{L_{\mathrm{T}}}, \tag{5.94}$$

with $\boldsymbol{F}_N$ being the N-size Fourier matrix. Equivalently, (5.94) can be written as

$$\boldsymbol{U}=\left[\boldsymbol{U}_0\;\boldsymbol{U}_1\;\cdots\;\boldsymbol{U}_{L_{\mathrm{T}}-1}\right], \tag{5.95}$$

where each block $\boldsymbol{U}_\ell\in\mathbb{C}^{NL_{\mathrm{T}}\times N}$, for $\ell=0,\ldots L_{\mathrm{T}}-1$, is given by

$$\boldsymbol{U}_\ell=\boldsymbol{F}_N^H\otimes[\boldsymbol{I}_{L_{\mathrm{T}}}]_\ell, \tag{5.96}$$

with $[\boldsymbol{I}_{L_{\mathrm{T}}}]_\ell$ is the ℓ-th column of $\boldsymbol{I}_{L_{\mathrm{T}}}$. Taking into account these observations, note that sensing can be done in a per-antenna fashion. Thus, a sensed basis of the space-time null space admits the following expression:

$$\widehat{\boldsymbol{U}}_{\mathcal{N}}=\left[\widehat{\boldsymbol{U}}_{\mathcal{N},0}\;\widehat{\boldsymbol{U}}_{\mathcal{N},1}\;\cdots\;\widehat{\boldsymbol{U}}_{\mathcal{N},L_{\mathrm{T}}-1}\right], \tag{5.97}$$

where $\widehat{\boldsymbol{U}}_{\mathcal{N},\ell}$, for $\ell = 0, \ldots, L_{\mathrm{T}} - 1$, is the sensed null-space at the ℓ-th sensor.

From (5.97), it is worth noting that the projector $\widehat{\boldsymbol{P}}_0$ can be written as

$$\widehat{\boldsymbol{P}}_0 = \widehat{\boldsymbol{U}}_{\mathcal{N}}\widehat{\boldsymbol{U}}_{\mathcal{N}}^H = \sum_{\ell=0}^{L_{\mathrm{T}}-1} \widehat{\boldsymbol{U}}_{\mathcal{N},\ell}\widehat{\boldsymbol{U}}_{\mathcal{N},\ell}^H = \sum_{\ell=0}^{L_{\mathrm{T}}-1} \widetilde{\boldsymbol{P}}_{0,\ell} \otimes \boldsymbol{\Xi}_\ell, \tag{5.98}$$

where $\widetilde{\boldsymbol{P}}_{0,\ell} \in \mathbb{C}^{N\times N}$ is the projection matrix onto the M_ℓ-dimensional null space sensed at the ℓ-th sensor and $\boldsymbol{\Xi}_\ell$ is a square $L_{\mathrm{T}} \times L_{\mathrm{T}}$ matrix with all zeros except the ℓ-th diagonal element, which is equal to one. Note that $\widetilde{\boldsymbol{P}}_{0,\ell}$ is the outer product of a subset of columns of the matrix $\boldsymbol{F}_N^H/\sqrt{N}$. Analogously, the projector $\boldsymbol{P}_{\mathcal{E}}$ reads as

$$\boldsymbol{P}_{\mathcal{E}} = \boldsymbol{E}_{\mathcal{N}}\boldsymbol{E}_{\mathcal{N}}^H = \sum_{\ell=0}^{L_{\mathrm{T}}-1} \boldsymbol{E}_{\mathcal{N},\ell}\boldsymbol{E}_{\mathcal{N},\ell}^H = \sum_{\ell=0}^{L_{\mathrm{T}}-1} \widetilde{\boldsymbol{P}}_{\mathcal{E},\ell} \otimes \boldsymbol{\Xi}_\ell, \tag{5.99}$$

being $\boldsymbol{E}_{\mathcal{N},\ell}$, for $\ell = 0, \ldots, L_{\mathrm{T}} - 1$, the per-antenna sensing error matrix and $\widetilde{\boldsymbol{P}}_{\mathcal{E},\ell} \in \mathbb{C}^{N\times N}$ is the projection matrix onto the $N_E[\ell]$-dimensional subspace encompassing the per-antenna erroneously available sensed frequency bins.

Taking into consideration (5.98) and (5.99), we note that: (i) the main diagonal of $\widetilde{\boldsymbol{P}}_{0,\ell} \in \mathbb{C}^{N\times N}$ is constant and equal to M_ℓ/N, (ii) the main diagonal of $\widetilde{\boldsymbol{P}}_{\mathcal{E},\ell} \in \mathbb{C}^{N\times N}$ is constant and equal to $N_E[\ell]/N$, and (iii) both $\widehat{\boldsymbol{P}}_0$ and $\boldsymbol{P}_{\mathcal{E}}$ do not have a constant diagonal since, in general, $M_\ell \neq M_{\ell'}$ nor $N_E[\ell] \neq N_E[\ell']$, for $\ell \neq \ell'$. These last observations make the analysis of the inter-system interference term non-trivial.

At this point of the analysis, we consider that, despite $M_\ell \neq M_{\ell'}$ for $\ell \neq \ell'$, $\widetilde{L}_{\mathrm{T}}$ out of L_{T} diagonal entries of $\widehat{\boldsymbol{P}}_0$ are *similar*, that is,

$$\frac{M_0}{N} \approx \frac{M_1}{N} \approx \cdots \approx \frac{M_{\widetilde{L}_{\mathrm{T}}-1}}{N} > \frac{M_{\widetilde{L}_{\mathrm{T}}}}{N} \geq \cdots \geq \frac{M_{L_{\mathrm{T}}-1}}{N}, \tag{5.100}$$

where we have assumed, without loss of generality, that $M_0 \geq \cdots \geq M_{L_{\mathrm{T}}}$. Under (5.100), the selected columns of the orthogonal projectors can be chosen to be consecutive in each block of $\widetilde{L}_{\mathrm{T}}$, as discussed in Chapter 3 for the single-antenna case.

For the sake of simplicity, let us assume that the number of transmitted MNTLS space-time waveforms K is proportional to $\widetilde{L}_{\mathrm{T}}$, i.e., $K = \mu\widetilde{L}_{\mathrm{T}}$ with μ a non-zero integer. The generality of this assumption will be discussed afterward. Under this assumption, and recalling the sequential waveform design strategy discussed in Chapter 3, the SIDR for the multi-channel case given in (5.19) can be asymptotically approximated by

$$\mathrm{SIDR}_{\mathrm{T}}\left(\boldsymbol{E}_{\mathcal{N}}; \{\boldsymbol{\lambda}_k\}\right) \approx \frac{K - \dfrac{K}{\widetilde{L}_{\mathrm{T}}} \displaystyle\sum_{\ell=0}^{\widetilde{L}_{\mathrm{T}}-1} \frac{N_E[\ell]}{M_\ell}}{\dfrac{1}{\widetilde{N}_E}\dfrac{K}{\widetilde{L}_{\mathrm{T}}} \displaystyle\sum_{\ell=0}^{\widetilde{L}_{\mathrm{T}}-1} \frac{N_E[\ell]}{M_\ell}}. \tag{5.101}$$

At this point, some comments are of order. On the one hand, since (5.101) follows from (5.100), note that the inner transmitting node only activates $\widetilde{L}_{\mathrm{T}}$; thus N_E in (5.19) has been replaced by $\widetilde{N}_E$ in (5.101), which can be written as

$$\widetilde{N}_E = \sum_{\ell=0}^{\widetilde{L}_{\mathrm{T}}-1} N_E[\ell]. \tag{5.102}$$

On the other hand, recalling (5.100), since $N_E[\ell]$ and M_ℓ are related we may say that

$$\frac{N_E[0]}{N} \approx \cdots \approx \frac{N_E[\widetilde{L}_{\mathrm{T}}-1]}{N} > \frac{N_E[\widetilde{L}_{\mathrm{T}}]}{N} \geq \cdots \geq \frac{N_E[L_{\mathrm{T}}-1]}{N}. \tag{5.103}$$

Therefore, taking into account (5.103), (5.101) leads to

$$\mathrm{SIDR}_{\mathrm{T}}\left(\boldsymbol{E}_{\mathcal{N}};\{\boldsymbol{\lambda}_k\}\right) \approx \frac{K - K\dfrac{N_E[\ell]}{M_\ell}}{\dfrac{1}{N_E}K\dfrac{N_E[\ell]}{M_\ell}} = \widetilde{N}_E\frac{M_\ell - N_E[\ell]}{N_E[\ell]}, \tag{5.104}$$

where $\widetilde{N}_E$ is given in (5.102). Let $\widetilde{M}$ be the total number of space-time DoF sensed as available across the $\widetilde{L}_{\mathrm{T}}$ active antennas at the inner transmitter, i.e.,

$$\widetilde{M} \triangleq \sum_{\ell=0}^{\widetilde{L}_{\mathrm{T}}-1} M_\ell. \tag{5.105}$$

Thus, (5.104) reads as

$$\mathrm{SIDR}_{\mathrm{T}}\left(\boldsymbol{E}_{\mathcal{N}};\{\boldsymbol{\lambda}_k\}\right) \approx \widetilde{N}_E\frac{M_\ell - N_E[\ell]}{N_E[\ell]} = N\widetilde{L}_{\mathrm{T}}\cdot\frac{\widetilde{M}}{N\widetilde{L}_{\mathrm{T}}}\cdot\frac{\widetilde{N}_E}{\widetilde{M}}\cdot\left(\frac{\kappa_\ell}{\epsilon_\ell}-1\right), \tag{5.106}$$

being $\kappa_\ell = M_\ell/N$ and $\epsilon_\ell = N_E[\ell]/N$. Noting that

$$\frac{\widetilde{N}_E}{\widetilde{M}}\frac{\kappa_\ell}{\epsilon_\ell} \approx \frac{\widetilde{L}_{\mathrm{T}}N_E[\ell]/N}{\widetilde{L}_{\mathrm{T}}M_\ell/N} = 1, \tag{5.107}$$

and defining $\kappa \triangleq \widetilde{M}/(N\widetilde{L}_{\mathrm{T}})$ and $\epsilon \triangleq \widetilde{N}_E/(N\widetilde{L}_{\mathrm{T}})$, we finally have that

$$\mathrm{SIDR}_{\mathrm{T}}\left(\boldsymbol{E}_{\mathcal{N}};\{\boldsymbol{\lambda}_k\}\right) \approx N\widetilde{L}_{\mathrm{T}}\cdot\frac{\widetilde{M}}{N\widetilde{L}_{\mathrm{T}}}\cdot\left(1-\frac{\widetilde{N}_E}{\widetilde{M}}\right) = N\widetilde{L}_{\mathrm{T}}\cdot\kappa\cdot\left(1-\frac{\epsilon}{\kappa}\right), \tag{5.108}$$

which completes the proof. For ease of discussion, the case $\widetilde{L}_{\mathrm{T}} = L_{\mathrm{T}}$ is studied in Section 5.2, which corresponds to the case where the inner transmitter activates all antennas.

A final comment is of order. It is worth noting that the whole proof has been based on the assumption that $K \propto \widetilde{L}_{\mathrm{T}}$. However, it is straightforward to see that the proof is still valid when $K < \widetilde{L}_{\mathrm{T}}$, but replacing $\widetilde{L}_{\mathrm{T}}$ by $\widetilde{L}'_{\mathrm{T}} < \widetilde{L}_{\mathrm{T}}$ indicating the number of *active* antennas. Moreover, if $K > \widetilde{L}_{\mathrm{T}}$ but these quantities are not proportional, the proof is still valid assuming that K is the virtual number of active antennas. The latter includes the single-antennas case, that is, $\widetilde{L}_{\mathrm{T}} = 1$.

Appendix 5.C Proof of (5.35)

This Appendix provides the derivation of the space-time MNTLS waveforms when non-unitary sensing basis are considered. Without loss of generality, this proof is focused on the transmitted waveform since the proof for the matched filter is analogous.

Let us consider that the inner transmitting node uses the non-unitary sensing basis $\boldsymbol{M}_{\mathrm{T}}(\Theta,\Omega)$ defined in (5.30). After performing the space-time null-space sensing, the inner transmitter detects as available a set of angle-frequency tuples $((\theta_\ell,\varphi_\ell);\omega_\nu)$, and encompassed in matrix

$$\widehat{\boldsymbol{M}}_{\mathcal{N},\mathrm{T}} = \left[\begin{array}{c:c} \widetilde{\boldsymbol{M}}_{\mathcal{N},\mathrm{T}} & \boldsymbol{E}_{\mathcal{N},\mathrm{T}} \end{array}\right], \tag{5.109}$$

where $\widetilde{\boldsymbol{M}}_{\mathcal{N},\mathrm{T}}$ encompassed those available space-time DoF correctly identified and $\boldsymbol{E}_{\mathcal{N},\mathrm{T}}$ contains those occupied space-time DoF erroneously sensed as available. For the sake of simplicity, only the design for the first null-space waveform is detailed. The remaining $K-1$ waveforms can be recursively found as discussed in Appendix 3.A. Therefore, particularizing the min-max problem (5.15) for $k=0$, we get

$$\boldsymbol{\lambda}_{0,\mathrm{T}} = \underset{\boldsymbol{\lambda}_{0,\mathrm{T}},\boldsymbol{e}_{0,\mathrm{T}}}{\arg\min}\left\{\max_{\boldsymbol{E}_{\mathcal{N},\mathrm{T}}} \left\|\boldsymbol{E}_{\mathcal{N},\mathrm{T}}^H\widehat{\boldsymbol{M}}_{\mathcal{N}}\boldsymbol{\lambda}_0\right\|^2\right\} \tag{5.110}$$

$$\text{subject to} \qquad \text{(a)}\ \left\|\boldsymbol{E}_{\mathcal{N},\mathrm{T}}\right\|_{\mathrm{F}}^2 \le \xi^2;\ \text{(b)}\ \boldsymbol{\lambda}_0^H\widehat{\boldsymbol{M}}_{\mathcal{N},\mathrm{T}}^H\boldsymbol{e}_0 = \alpha_0 \tag{5.111}$$

Solving the maximization problem in (5.110) through the Lagrange multipliers method, the worst-case null-space sensing error matrix is given by

$$\boldsymbol{E}_{\mathcal{N},\mathrm{T}} = \xi^2\boldsymbol{\phi}_0\boldsymbol{\phi}_0^H. \tag{5.112}$$

Plugging (5.112) into (5.110), the linear combination vector $\boldsymbol{\lambda}_0$ can be found through the following minimization problem

$$\boldsymbol{\lambda}_{0,\mathrm{T}} = \underset{\boldsymbol{\lambda}_{0,\mathrm{T}}}{\arg\min}\ \|\widehat{\boldsymbol{M}}_{\mathcal{N},\mathrm{T}}\boldsymbol{\lambda}_{0,\mathrm{T}}\|^2\ \text{ s.t. }\ \boldsymbol{\lambda}_{0,\mathrm{T}}^H\widehat{\boldsymbol{M}}_{\mathcal{N},\mathrm{T}}^H\boldsymbol{e}_{0,\mathrm{T}} = \alpha_0, \tag{5.113}$$

which, through the Lagrange multipliers method, leads to

$$\boldsymbol{\lambda}_{0,\mathrm{T}} = \mu\left(\widehat{\boldsymbol{M}}_{\mathcal{N},\mathrm{T}}^H\widehat{\boldsymbol{M}}_{\mathcal{N},\mathrm{T}}\right)^{-1}\widehat{\boldsymbol{M}}_{\mathcal{N},\mathrm{T}}^H\boldsymbol{e}_0 = \mu\widehat{\boldsymbol{M}}_{\mathcal{N},\mathrm{T}}^{+}\boldsymbol{e}_{0,\mathrm{T}}, \tag{5.114}$$

being μ the Lagrange multiplier. Using the constraint (c) in (5.111), the unit-norm space-time MNTLS waveform reads as

$$\boldsymbol{\phi}_0 = \frac{\widehat{\boldsymbol{M}}_{\mathcal{N},\mathrm{T}}\widehat{\boldsymbol{M}}_{\mathcal{N},\mathrm{T}}^{+}\boldsymbol{e}_{0,\mathrm{T}}}{\sqrt{\boldsymbol{e}_{0,\mathrm{T}}^T\widehat{\boldsymbol{M}}_{\mathcal{N},\mathrm{T}}\widehat{\boldsymbol{M}}_{\mathcal{N},\mathrm{T}}^{+}\boldsymbol{e}_{0,\mathrm{T}}}} = \gamma\widehat{\boldsymbol{M}}_{\mathcal{N},\mathrm{T}}\widehat{\boldsymbol{M}}_{\mathcal{N},\mathrm{T}}^{+}\boldsymbol{e}_{0,\mathrm{T}}. \tag{5.115}$$

Finally, the linear predictor vector can be optimized to satisfy the minimum-norm condition as

$$\boldsymbol{e}_{0,\mathrm{T}} = \underset{n\in\{0,\ldots,NL-1\}}{\arg\max}\left[\widehat{\boldsymbol{M}}_{\mathcal{N},\mathrm{T}}\widehat{\boldsymbol{M}}_{\mathcal{N},\mathrm{T}}^{+}\right]_{nn}, \tag{5.116}$$

which completes the proof.

Appendix 5.D Proof of (5.45)

In order to show that the sufficient statistic for symbol decoding z (5.42) can be written as in (5.45), the proof is split into two parts. First, it is shown that the transmitting waveform $\boldsymbol{\phi}_0$ and the matched filter $\boldsymbol{\psi}_0$ admit the block-structured given in (5.43). Then, using this result, we prove (5.45).

5.D.1 Analysis of the Structure of $\boldsymbol{\phi}_0$ and $\boldsymbol{\psi}_0$

For simplicity of notation, the proof is focused on showing that the term $\widehat{\boldsymbol{P}}_0\boldsymbol{e}_0$, where $\widehat{\boldsymbol{P}}_0$ is the orthogonal projector onto the space-time null space and $\boldsymbol{e}_0$ is an NL-length binary vector with a single non-zero entry, is structured in N blocks of length L. Then, this general result is particularized at the inner transmitter and the inner receiver to provide the block structure given in (5.43).

Recalling (5.30), the non-unitary basis of the whole space-time NL-dimensional ambient space is reads as

$$\boldsymbol{M}(\Theta,\Omega) = \left[\boldsymbol{M}[\omega_0]\cdots\boldsymbol{M}[\omega_n]\cdots\boldsymbol{M}[\omega_{N-1}]\right], \tag{5.117}$$

where $\boldsymbol{M}[\omega_n] \triangleq \boldsymbol{b}[\omega_n]\otimes\boldsymbol{S}[\omega_n]$. By inspection, it is worth noting that (5.117) can be written as

$$\boldsymbol{M}(\Theta,\Omega) = \\ \begin{bmatrix} \boldsymbol{M}[\omega_0] & \cdots & \boldsymbol{M}[\omega_{N-1}] \\ \boldsymbol{M}[\omega_0] & \cdots & \boldsymbol{M}[\omega_{N-1}] \\ \vdots & \cdots & \vdots \\ \boldsymbol{M}[\omega_0] & \cdots & \boldsymbol{M}[\omega_{N-1}] \end{bmatrix} \odot \begin{bmatrix} \mathbf{1}_{L\times L}\left[\boldsymbol{b}[\omega_0]\right]_0 & \cdots & \mathbf{1}_{L\times L}\left[\boldsymbol{b}[\omega_{N-1}]\right]_0 \\ \mathbf{1}_{L\times L}\left[\boldsymbol{b}[\omega_0]\right]_1 & \cdots & \mathbf{1}_{L\times L}\left[\boldsymbol{b}[\omega_{N-1}]\right]_1 \\ \vdots & \cdots & \vdots \\ \mathbf{1}_{L\times L}\left[\boldsymbol{b}[\omega_0]\right]_{N-1} & \cdots & \mathbf{1}_{L\times L}\left[\boldsymbol{b}[\omega_{N-1}]\right]_{N-1} \end{bmatrix}. \tag{5.118}$$

Note that the Θ and Ω can be arbitrary angle pairs and frequencies set as far as $\boldsymbol{M}(\Theta,\Omega)$ is a full-rank matrix. For the sake of simplicity, it is subsequently assumed that the frequencies in Ω are consecutive and uniformly spaced.

After the space-time null-space sensing, the non-unitary basis of the sensed null space is composed of a column subset of (5.118). Accordingly,

$$\widehat{\boldsymbol{M}}_{\mathcal{N}} = \begin{bmatrix} \widehat{\boldsymbol{M}}_{\mathcal{N}}[\omega_0]\left[\boldsymbol{b}[\omega_0]\right]_0 & \widehat{\boldsymbol{M}}_{\mathcal{N}}[\omega_1]\left[\boldsymbol{b}[\omega_1]\right]_0 & \cdots & \widehat{\boldsymbol{M}}_{\mathcal{N}}[\omega_{N-1}]\left[\boldsymbol{b}[\omega_{N-1}]\right]_0 \\ \widehat{\boldsymbol{M}}_{\mathcal{N}}[\omega_0]\left[\boldsymbol{b}[\omega_0]\right]_1 & \widehat{\boldsymbol{M}}_{\mathcal{N}}[\omega_1]\left[\boldsymbol{b}[\omega_1]\right]_1 & \cdots & \widehat{\boldsymbol{M}}_{\mathcal{N}}[\omega_{N-1}]\left[\boldsymbol{b}[\omega_{N-1}]\right]_1 \\ \vdots & \vdots & \cdots & \vdots \\ \widehat{\boldsymbol{M}}_{\mathcal{N}}[\omega_0]\left[\boldsymbol{b}[\omega_0]\right]_{N-1} & \widehat{\boldsymbol{M}}_{\mathcal{N}}[\omega_1]\left[\boldsymbol{b}[\omega_1]\right]_{N-1} & \cdots & \widehat{\boldsymbol{M}}_{\mathcal{N}}[\omega_{N-1}]\left[\boldsymbol{b}[\omega_{N-1}]\right]_{N-1} \end{bmatrix}, \tag{5.119}$$

where $\widehat{\boldsymbol{M}}_{\mathcal{N}}[\omega]\in\mathbb{C}^{L\times M(\omega)}$ is a non-unitary sensed basis of the spatial null space at frequency ω. The orthogonal projector onto the sensed null space is given by $\widehat{\boldsymbol{P}}_0 = \widehat{\boldsymbol{M}}_{\mathcal{N}}\widehat{\boldsymbol{M}}_{\mathcal{N}}^{+}$. Thus far, we have seen that $\widehat{\boldsymbol{M}}_{\mathcal{N}}$ is block-structured. Now, the Moore-Penrose pseudo-inverse $\widehat{\boldsymbol{M}}_{\mathcal{N}}^{+}$ has to be studied. Since $\widehat{\boldsymbol{M}}_{\mathcal{N}}^{+} = \left(\widehat{\boldsymbol{M}}_{\mathcal{N}}^{H}\widehat{\boldsymbol{M}}_{\mathcal{N}}\right)^{-1}\widehat{\boldsymbol{M}}_{\mathcal{N}}^{H}$, we need to analyze the inner product. From (5.119), and recalling that the frequencies in Ω are consecutive and uniformly spaced, it is straightforward to see that

$$\widehat{\boldsymbol{M}}_{\mathcal{N}}^{H}\widehat{\boldsymbol{M}}_{\mathcal{N}} = \begin{bmatrix} \widehat{\boldsymbol{M}}_{\mathcal{N}}^{H}[\omega_0]\widehat{\boldsymbol{M}}_{\mathcal{N}}[\omega_0]\left\|\boldsymbol{b}[\omega_0]\right\|^2 & & \mathbf{0} \\ & \ddots & \\ \mathbf{0} & & \widehat{\boldsymbol{M}}_{\mathcal{N}}^{H}[\omega_{N-1}]\widehat{\boldsymbol{M}}_{\mathcal{N}}[\omega_{N-1}]\left\|\boldsymbol{b}[\omega_{N-1}]\right\|^2 \end{bmatrix}. \tag{5.120}$$

At this point, we shall remark that if all directions are sensed as occupied at a given frequency, the associated block $\widehat{\boldsymbol{M}}_{\mathcal{N}}^{H}[\omega_n]\widehat{\boldsymbol{M}}_{\mathcal{N}}[\omega_n]\left\|\boldsymbol{b}[\omega_n]\right\|^2$ will be removed from (5.120). The latter applies to all the following discussion. Using (5.119)–(5.120), $\widehat{\boldsymbol{M}}_{\mathcal{N}}^{+}$ yields

$$\widehat{\boldsymbol{M}}_{\mathcal{N}}^{+}=\begin{bmatrix}\widehat{\boldsymbol{M}}_{\mathcal{N}}^{+}[\omega_0]\frac{[\boldsymbol{b}[\omega_0]]_0^*}{\|\boldsymbol{b}[\omega_0]\|^2} & \cdots & \widehat{\boldsymbol{M}}_{\mathcal{N}}^{+}[\omega_0]\frac{[\boldsymbol{b}[\omega_0]]_{N-1}^*}{\|\boldsymbol{b}[\omega_0]\|^2}\\ \vdots & \ddots & \vdots\\ \widehat{\boldsymbol{M}}_{\mathcal{N}}^{+}[\omega_{N-1}]\frac{[\boldsymbol{b}[\omega_{N-1}]]_0^*}{\|\boldsymbol{b}[\omega_{N-1}]\|^2} & \cdots & \widehat{\boldsymbol{M}}_{\mathcal{N}}^{+}[\omega_{N-1}]\frac{[\boldsymbol{b}[\omega_{N-1}]]_{N-1}^*}{\|\boldsymbol{b}[\omega_{N-1}]\|^2}\end{bmatrix}, \tag{5.121}$$

being

$$\widehat{\boldsymbol{M}}_{\mathcal{N}}^{+}[\omega_\nu]=\left(\widehat{\boldsymbol{M}}_{\mathcal{N}}^{H}[\omega_\nu]\widehat{\boldsymbol{M}}_{\mathcal{N}}[\omega_\nu]\right)^{-1}\widehat{\boldsymbol{M}}_{\mathcal{N}}^{H}[\omega_\nu]. \tag{5.122}$$

Recalling that $\widehat{\boldsymbol{P}}_0=\widehat{\boldsymbol{M}}_{\mathcal{N}}\widehat{\boldsymbol{M}}_{\mathcal{N}}^{+}$, using (5.119) and (5.121), the orthogonal projector $\widehat{\boldsymbol{P}}_0$ reads as

$$\widehat{\boldsymbol{P}}_0=\begin{bmatrix}\widehat{\boldsymbol{P}}_0[0,0] & \cdots & \widehat{\boldsymbol{P}}_0[0,N-1]\\ \vdots & \cdots & \vdots\\ \widehat{\boldsymbol{P}}_0[N-1,0] & \cdots & \widehat{\boldsymbol{P}}_0[N-1,N-1]\end{bmatrix}. \tag{5.123}$$

Note that (5.123) is an $NL\times NL$ block-structured matrix with $L\times L$ blocks given by

$$\widehat{\boldsymbol{P}}_0[m,n]=\sum_{\nu=0}^{N-1}\widehat{\boldsymbol{M}}_{\mathcal{N}}[\omega_\nu]\widehat{\boldsymbol{M}}_{\mathcal{N}}^{+}[\omega_\nu]\beta_{mn}[\omega_\nu], \tag{5.124}$$

where $\widehat{\boldsymbol{M}}_{\mathcal{N}}^{+}[\omega_\nu]$ is provided in (5.122) and β_{mn} is defined as

$$\beta_{mn}[\omega_\nu]\triangleq\frac{[\boldsymbol{b}[\omega_\nu]_m[\boldsymbol{b}[\omega_\nu]_n^*}{\left\|\boldsymbol{b}[\omega_\nu]\right\|^2}. \tag{5.125}$$

Thus far, the block structure of the projector $\widehat{\boldsymbol{P}}_0$ has been proven. Now, we deal with the block structure of the term $\widehat{\boldsymbol{P}}_0\boldsymbol{e}_0$. As per Appendix 5.C, the NL-length binary vector $\boldsymbol{e}_0$ selects the column of the orthogonal projector $\widehat{\boldsymbol{P}}_0$ containing the maximum diagonal element. Recalling (5.123), we realize that the role of the binary vector $\boldsymbol{e}_0$ is twofold. First, this vector has to select in which of the diagonal blocks $\widehat{\boldsymbol{P}}_0[n,n]$, for $n=0,\ldots,N-1$ contains the maximum value of the main diagonal of $\widehat{\boldsymbol{P}}_0$. Then, once the corresponding block has been identified, the vector $\boldsymbol{e}_0$ points to the position within the block of the main diagonal element. Accordingly, without loss of generality, the binary vector $\boldsymbol{e}_0$ admits the following expression:

$$\boldsymbol{e}_0=\boldsymbol{\zeta}_0\otimes\widetilde{\boldsymbol{e}}_0, \tag{5.126}$$

i.e., $\boldsymbol{e}_0$ can be written as the Kronecker product of two binary vectors $\boldsymbol{\zeta}_0$ and $\widetilde{\boldsymbol{e}}_0$. The N-length binary vector $\boldsymbol{\zeta}_0$ selects the block index $n=0,\ldots,N-1$ encompassing the maximum diagonal element of $\widehat{\boldsymbol{P}}_0$. The L-length binary vector $\widetilde{\boldsymbol{e}}_0$ selects which of the L diagonal entries of the selected block is the maximum. In the sequel, it is considered that the single non-zero element of the N-length binary vector $\boldsymbol{\zeta}_0$ is at position $n_\star$. Letting $n(0)\in\{0,\ldots,NL-1\}$ be the single non-zero entry of the NL-length binary vector $\boldsymbol{e}_0$ in (5.126), it is straightforward to see that the unique non-null element of the L-length binary vector $\widetilde{\boldsymbol{e}}_0$ is found at position $n(0)\bmod L$.

At this point, we can use the discussion above to provide the block structure of the transmitting waveform $\boldsymbol{\phi}_0$ and the matched filter $\boldsymbol{\psi}_0$. Let $\widehat{\boldsymbol{P}}_{0,\mathrm{T}} \in \mathbb{C}^{NL_\mathrm{T} \times NL_\mathrm{T}}$ and $\widehat{\boldsymbol{P}}_{0,\mathrm{R}} \in \mathbb{C}^{NL_\mathrm{R} \times NL_\mathrm{R}}$ be the orthogonal projectors onto the null space sensed by the inner transmitter and the inner receiver. Noting that both projectors have the block structure described in (5.123), $\boldsymbol{\phi}_0$ and $\boldsymbol{\psi}_0$ read as

$$\boldsymbol{\phi}_0 = \gamma \widehat{\boldsymbol{P}}_{0,\mathrm{T}} \boldsymbol{e}_{0,\mathrm{T}} = \gamma \begin{bmatrix} \widehat{\boldsymbol{P}}_{0,\mathrm{T}}[0, n_\star] \widetilde{\boldsymbol{e}}_{0,\mathrm{T}} \\ \vdots \\ \widehat{\boldsymbol{P}}_{0,\mathrm{T}}[N-1, n_\star] \widetilde{\boldsymbol{e}}_{0\mathrm{T}} \end{bmatrix} = \begin{bmatrix} \boldsymbol{\phi}_0[0] \\ \vdots \\ \boldsymbol{\phi}_0[N-1] \end{bmatrix}, \tag{5.127}$$

$$\boldsymbol{\psi}_0 = \rho \widehat{\boldsymbol{P}}_{0,\mathrm{R}} \boldsymbol{e}_{0,\mathrm{R}} = \rho \begin{bmatrix} \widehat{\boldsymbol{P}}_{0,\mathrm{R}}[0, n_\star] \widetilde{\boldsymbol{e}}_{0,\mathrm{R}} \\ \vdots \\ \widehat{\boldsymbol{P}}_{0,\mathrm{R}}[N-1, n_\star] \widetilde{\boldsymbol{e}}_{0\mathrm{R}} \end{bmatrix} = \begin{bmatrix} \boldsymbol{\psi}_0[0] \\ \vdots \\ \boldsymbol{\psi}_0[N-1] \end{bmatrix}, \tag{5.128}$$

where $\widehat{\boldsymbol{P}}_{0,\mathrm{T}}[n, n_\star] \in \mathbb{C}^{L_\mathrm{T} \times L_\mathrm{T}}$, $\widehat{\boldsymbol{P}}_{0,\mathrm{T}}[n, n_\star] \in \mathbb{C}^{L_\mathrm{R} \times L_\mathrm{R}}$, the L_T-length binary vector $\widetilde{\boldsymbol{e}}_{0,\mathrm{T}}$ has its single non-zero entry at position $n(0) \bmod L_\mathrm{T}$, and the L_R-length binary vector $\widetilde{\boldsymbol{e}}_{0,\mathrm{R}}$ has its single non-zero entry at position $n(0) \bmod L_\mathrm{R}$.

5.D.2 Analysis of (5.45)

Recalling (5.39), the MIMO response matrix is given by

$$\widetilde{\boldsymbol{H}}_{\mathrm{II}} \triangleq \begin{bmatrix} \boldsymbol{H}_{\mathrm{II}}[0] & & \boldsymbol{0} \\ & \ddots & \\ \boldsymbol{0} & & \boldsymbol{H}_{\mathrm{II}}[N-1] \end{bmatrix} \in \mathbb{C}^{NL_\mathrm{R} \times NL_\mathrm{T}}. \tag{5.129}$$

Thus, using (5.127)–(5.128), the sufficient statistic for symbol decoding z can be written as

$$z = a_0 \boldsymbol{\psi}_0^H \widetilde{\boldsymbol{H}}_{\mathrm{II}} \boldsymbol{\phi}_0 + \widetilde{v} = \sum_{n=0}^{N-1} a_0 \boldsymbol{\psi}_0^H[n] \boldsymbol{H}_{\mathrm{II}}[n] \boldsymbol{\phi}_0[n] + \widetilde{v}, \tag{5.130}$$

where $\widetilde{v}$ is the filtered noise. Plugging

$$\boldsymbol{H}_{\mathrm{II}}[n] = \frac{1}{N\sqrt{N_{\mathrm{path}} L_\mathrm{T} L_\mathrm{R}}} \sum_{\nu=0}^{N-1} \sum_{i=0}^{N_{\mathrm{path}}-1} \boldsymbol{s}_\mathrm{R}[\omega_\nu, \vartheta_\mathrm{R}^{(i)}] \boldsymbol{s}_\mathrm{T}^H[\omega_\nu, \vartheta_\mathrm{T}^{(i)}] e^{j\frac{2\pi\nu n}{N}}. \tag{5.131}$$

into (5.130), we get

$$z = \frac{a_0}{N\sqrt{N_{\mathrm{path}} L_\mathrm{T} L_\mathrm{R}}} \sum_{n=0}^{N-1} \sum_{\nu=0}^{N-1} \sum_{i=0}^{N_{\mathrm{path}}-1} \boldsymbol{\psi}_0^H[n] \boldsymbol{s}_\mathrm{R}[\omega_\nu, \vartheta_\mathrm{R}^{(i)}] \boldsymbol{s}_\mathrm{T}^H[\omega_\nu, \vartheta_\mathrm{T}^{(i)}] \boldsymbol{\phi}_0[n] e^{j\frac{2\pi\nu n}{N}} + \widetilde{v}. \tag{5.132}$$

Now, recalling (5.124), (5.127), and (5.128), note that $\boldsymbol{\phi}_0[n]$ and $\boldsymbol{\psi}_0[n]$ are given by

$$\boldsymbol{\phi}_0[n] = \gamma \sum_{\nu=0}^{N-1} \widehat{\boldsymbol{M}}_{\mathcal{N},\mathrm{T}}[\omega_\nu] \widehat{\boldsymbol{M}}_{\mathcal{N},\mathrm{T}}^{+}[\omega_\nu] \beta_{nn_\star,\mathrm{T}}[\omega_\nu] \widetilde{\boldsymbol{e}}_\mathrm{T}, \tag{5.133}$$

$$\boldsymbol{\psi}_0[n] = \rho \sum_{\nu=0}^{N-1} \widehat{\boldsymbol{M}}_{\mathcal{N},\mathrm{R}}[\omega_\nu] \widehat{\boldsymbol{M}}_{\mathcal{N},\mathrm{R}}^{+}[\omega_\nu] \beta_{nn_\star,\mathrm{R}}[\omega_\nu] \widetilde{\boldsymbol{e}}_\mathrm{R}. \tag{5.134}$$

It is worth noting that both (5.133) and (5.134) rely on the sensed null-space steering matrices $\widehat{\boldsymbol{M}}_{\mathcal{N},\mathrm{T}}[\omega_\nu]$ and $\widehat{\boldsymbol{M}}_{\mathcal{N},\mathrm{R}}[\omega_\nu]$. For convenience, it is preferable that the *full* steering matrices $\widehat{\boldsymbol{M}}_{\mathrm{T}}[\omega_\nu]$ and $\widehat{\boldsymbol{M}}_{\mathrm{R}}[\omega_\nu]$ appear in the expression for sufficient statistic for symbol decoding. Defining the vectors $\boldsymbol{\beta}_{n\nu,\mathrm{T}} \in \mathbb{C}^{L_\mathrm{T}}$ and $\boldsymbol{\beta}_{n\nu,\mathrm{R}} \in \mathbb{C}^{L_\mathrm{R}}$, satisfying

$$[\boldsymbol{\beta}_{n\nu,\mathrm{T}}]_\ell \triangleq \begin{cases} 0, & \text{if } ((\theta_\ell,\varphi_\ell);\omega_\nu) \notin \langle \widehat{\boldsymbol{M}}_{\mathcal{N},\mathrm{T}} \rangle \\ \eta_{n\nu}[\boldsymbol{M}_\mathrm{T}^{+}[\omega_\nu]\widetilde{\boldsymbol{e}}_{\mathrm{T},0}]_\ell, & \text{otherwise} \end{cases}, \quad \text{for } \ell = 1,\ldots,L_\mathrm{T} \tag{5.135}$$

and

$$[\boldsymbol{\beta}_{n\nu,\mathrm{R}}]_\ell \triangleq \begin{cases} 0, & \text{if } ((\theta_\ell,\varphi_\ell);\omega_\nu) \notin \langle \widehat{\boldsymbol{M}}_{\mathcal{N},\mathrm{R}} \rangle \\ \mu_{n\nu}[\boldsymbol{M}_\mathrm{R}^{+}[\omega_\nu]\widetilde{\boldsymbol{e}}_{\mathrm{R},0}]_\ell, & \text{otherwise} \end{cases}, \quad \text{for } \ell = 1,\ldots,L_\mathrm{R}, \tag{5.136}$$

i.e., selecting only those angles-frequency tuples belonging to the sensed null spaces at each inner node, (5.133)–(5.134) can be generalized as

$$\boldsymbol{\phi}_0[n] = \sum_{\nu=0}^{N-1} \widehat{\boldsymbol{M}}_\mathrm{T}[\omega_\nu]\boldsymbol{\beta}_{n\nu,\mathrm{T}}, \tag{5.137}$$

$$\boldsymbol{\psi}_0[n] = \sum_{\nu=0}^{N-1} \widehat{\boldsymbol{M}}_\mathrm{R}[\omega_\nu]\boldsymbol{\beta}_{n\nu,\mathrm{R}}, \tag{5.138}$$

with

$$\eta_{n\nu} \triangleq \gamma\beta_{nn_\star,\mathrm{T}}[\omega_\nu]e^{j\frac{\pi\nu n}{N}}, \tag{5.139}$$

and

$$\mu_{n\nu} \triangleq \rho\beta_{nn_\star,\mathrm{R}}[\omega_\nu]e^{j\frac{-\pi\nu n}{N}}, \tag{5.140}$$

where now the full per-frequency steering matrices $\widehat{\boldsymbol{M}}_\mathrm{T}[\omega_\nu]$ and $\widehat{\boldsymbol{M}}_\mathrm{R}[\omega_\nu]$ appear explicitly in the expressions for the transmitting waveform and the matched filter. Finally, substituting (5.137)–(5.138) into (5.132), we get (5.45), i.e.,

$$z = \frac{a_0}{N\sqrt{N_\mathrm{path}L_\mathrm{T}L_\mathrm{R}}} \sum_{n=0}^{N-1}\sum_{\nu=0}^{N-1}\sum_{i=0}^{N_\mathrm{path}-1} \boldsymbol{\beta}_{n\nu,\mathrm{R}}^H \boldsymbol{M}_\mathrm{R}^H[\omega_\nu]\boldsymbol{s}_\mathrm{R}[\omega_\nu,\vartheta_\mathrm{R}^{(i)}]\boldsymbol{s}_\mathrm{T}^H[\omega_\nu,\vartheta_\mathrm{T}^{(i)}]\boldsymbol{M}_\mathrm{T}[\omega_\nu]\boldsymbol{\beta}_{n\nu,\mathrm{T}} + \widetilde{\upsilon}, \tag{5.141}$$

which completes the proof.

Appendix 5.E Proof of (5.51)

Recalling (5.48), the sufficient statistic for symbol decoding reads as

$$z = \frac{a_0}{N\sqrt{L_{\mathrm{T}}L_{\mathrm{R}}}} \sum_{n=0}^{N-1}\sum_{\nu=0}^{N-1} \boldsymbol{\beta}_{n\nu,\mathrm{R}}^{H}\boldsymbol{M}_{\mathrm{R}}^{H}[\omega_\nu]\boldsymbol{s}_{\mathrm{R}}[\omega_\nu]\boldsymbol{s}_{\mathrm{T}}^{H}[\omega_\nu]\boldsymbol{M}_{\mathrm{T}}[\omega_\nu]\boldsymbol{\beta}_{n\nu,\mathrm{T}} + \widetilde{v}. \tag{5.142}$$

Note that each summand in (5.142) is just the product of two scalars: $\boldsymbol{\beta}_{n\nu,\mathrm{R}}^{H}\boldsymbol{M}_{\mathrm{R}}^{H}[\omega_\nu]\boldsymbol{s}_{\mathrm{R}}[\omega_\nu]$ and $\boldsymbol{s}_{\mathrm{T}}^{H}[\omega_\nu]\boldsymbol{M}_{\mathrm{T}}[\omega_\nu]\boldsymbol{\beta}_{n\nu,\mathrm{T}}$, which depend on steering vectors, and, thus on the array geometry.

Let us begin with the transmitting array geometry, i.e., the scalar $\boldsymbol{s}_{\mathrm{T}}^{H}[\omega_\nu]\boldsymbol{M}_{\mathrm{T}}[\omega_\nu]\boldsymbol{\beta}_{n\nu,\mathrm{T}}$. Using the orthogonal expansion given by the MST (5.50), $\boldsymbol{s}_{\mathrm{T}}[\omega_\nu]$ and $\boldsymbol{M}_{\mathrm{T}}[\omega_\nu]$ can be written as

$$\boldsymbol{s}_{\mathrm{T}}[\omega_\nu] = \boldsymbol{G}_{\nu,\mathrm{T}}\boldsymbol{d}\left(\theta_{\mathrm{T}},\varphi_{\mathrm{T}}\right), \tag{5.143}$$

$$\boldsymbol{M}_{\mathrm{T}}[\omega_\nu] = \boldsymbol{G}_{\nu,\mathrm{T}}\boldsymbol{D}_{\mathrm{T}}, \tag{5.144}$$

with $\boldsymbol{G}_{\nu,\mathrm{T}}$ the sampling matrix of the transmitting array, $\boldsymbol{d}\left(\theta_{\mathrm{T}},\varphi_{\mathrm{T}}\right)$ the coefficient vector of the channel steering vector associated with the transmitting array, and $\boldsymbol{D}_{\mathrm{T}}$ a matrix containing the L_{T} coefficient vectors of the steering matrix $\boldsymbol{M}_{\mathrm{T}}[\omega_\nu]$, which is defined as

$$\boldsymbol{D}_{\mathrm{T}} \triangleq \left[\boldsymbol{d}\left(\theta_{0,\mathrm{T}},\varphi_{0,\mathrm{T}}\right)\ \cdots\ \boldsymbol{d}\left(\theta_{L_{\mathrm{T}}-1,\mathrm{T}},\varphi_{L_{\mathrm{T}}-1,\mathrm{T}}\right)\right]. \tag{5.145}$$

Taking into account that $\boldsymbol{G}_{\nu,\mathrm{T}}$ is an orthonormal expansion basis in the Hilbert space $\mathcal{H}$, note that

$$\boldsymbol{d}^{H}\left(\theta_{\mathrm{T}},\varphi_{\mathrm{T}}\right)\boldsymbol{G}_{\nu,\mathrm{T}}^{H}\boldsymbol{G}_{\nu,\mathrm{T}}\boldsymbol{D}_{\mathrm{T}} = \boldsymbol{d}^{H}\left(\theta_{\mathrm{T}},\varphi_{\mathrm{T}}\right)\boldsymbol{D}_{\mathrm{T}} \tag{5.146}$$

does not depend on the transmitting array geometry. Regarding the vector $\boldsymbol{\beta}_{n\nu,\mathrm{T}}$, we must recall that this vector depends on the Moore-Penrose pseudo-inverse of $\boldsymbol{M}_{\mathrm{T}}[\omega_\nu]$. Thus, plugging (5.144) into

$$\boldsymbol{M}_{\mathrm{T}}^{+}[\omega_\nu] = \left(\boldsymbol{M}_{\mathrm{T}}^{H}[\omega_\nu]\boldsymbol{M}_{\mathrm{T}}[\omega_\nu]\right)^{-1}\boldsymbol{M}_{\mathrm{T}}^{H}[\omega_\nu], \tag{5.147}$$

we have that

$$\boldsymbol{M}_{\mathrm{T}}^{+}[\omega_\nu] = \left(\boldsymbol{D}_{\mathrm{T}}^{H}\boldsymbol{G}_{\nu,\mathrm{T}}^{H}\boldsymbol{G}_{\nu,\mathrm{T}}\boldsymbol{D}_{\mathrm{T}}\right)^{-1}\boldsymbol{D}_{\mathrm{T}}^{H}\boldsymbol{G}_{\nu,\mathrm{T}}^{H} = \left(\boldsymbol{D}_{\mathrm{T}}^{H}\boldsymbol{D}_{\mathrm{T}}\right)^{-1}\boldsymbol{D}_{\mathrm{T}}^{H}\boldsymbol{G}_{\nu,\mathrm{T}}^{H}. \tag{5.148}$$

Hence, the scalar $\boldsymbol{s}_{\mathrm{T}}^{H}[\omega_\nu]\boldsymbol{M}_{\mathrm{T}}[\omega_\nu]\boldsymbol{\beta}_{n\nu,\mathrm{T}}$ reads as

$$\boldsymbol{s}_{\mathrm{T}}^{H}[\omega_\nu]\boldsymbol{M}_{\mathrm{T}}[\omega_\nu]\boldsymbol{\beta}_{n\nu,\mathrm{T}} = \eta_{n\nu}\boldsymbol{d}^{H}\left(\theta_{\mathrm{T}},\varphi_{\mathrm{T}}\right)\boldsymbol{D}_{\mathrm{T}}\left(\boldsymbol{D}_{\mathrm{T}}^{H}\boldsymbol{D}_{\mathrm{T}}\right)^{-1}\boldsymbol{D}_{\mathrm{T}}^{H}\boldsymbol{G}_{\nu,\mathrm{T}}^{H}\widetilde{\boldsymbol{e}}_{\mathrm{T},0} \tag{5.149}$$

$$= \eta_{n\nu}\boldsymbol{d}^{H}\left(\theta_{\mathrm{T}},\varphi_{\mathrm{T}}\right)\boldsymbol{\Pi}_{\boldsymbol{D}_{\mathrm{T}}}\boldsymbol{G}_{\nu,\mathrm{T}}^{H}\widetilde{\boldsymbol{e}}_{\mathrm{T},0}, \tag{5.150}$$

with

$$\boldsymbol{\Pi}_{\boldsymbol{D}_{\mathrm{T}}} = \boldsymbol{D}_{\mathrm{T}}\left(\boldsymbol{D}_{\mathrm{T}}^{H}\boldsymbol{D}_{\mathrm{T}}\right)^{-1}\boldsymbol{D}_{\mathrm{T}}^{H}. \tag{5.151}$$

Focusing now on the scalar $\boldsymbol{\beta}_{n\nu,\mathrm{R}}^{H}\boldsymbol{M}_{\mathrm{R}}^{H}[\omega_\nu]\boldsymbol{s}_{\mathrm{R}}[\omega_\nu]$ and leveraging the orthogonal expansion in (5.50), note that

$$\boldsymbol{s}_{\mathrm{R}}[\omega_\nu] = \boldsymbol{G}_{\nu,\mathrm{R}}\boldsymbol{d}\left(\theta_{\mathrm{R}},\varphi_{\mathrm{R}}\right), \tag{5.152}$$

$$\boldsymbol{M}_{\mathrm{R}}[\omega_\nu] = \boldsymbol{G}_{\nu,\mathrm{R}}\boldsymbol{D}_{\mathrm{R}}, \tag{5.153}$$

where $\boldsymbol{G}_{\nu,\mathrm{R}}$ the sampling matrix of the receiving array, $\boldsymbol{d}\left(\theta_{\mathrm{R}},\varphi_{\mathrm{R}}\right)$ the coefficient vector of the channel steering vector associated with the receiving array, and $\boldsymbol{D}_{\mathrm{R}}$ a matrix containing the L_{R} coefficient vectors of the steering matrix $\boldsymbol{M}_{\mathrm{R}}[\omega_\nu]$, given by

$$\boldsymbol{D}_{\mathrm{R}} \triangleq \left[\boldsymbol{d}\left(\theta_{0,\mathrm{R}},\varphi_{0,\mathrm{R}}\right) \ \cdots \ \boldsymbol{d}\left(\theta_{L_{\mathrm{R}}-1,\mathrm{R}},\varphi_{L_{\mathrm{R}}-1,\mathrm{R}}\right)\right]. \tag{5.154}$$

Recalling that the vector $\boldsymbol{\beta}_{n\nu,\mathrm{R}}$ relies on the Moore-Penrose pseudo-inverse of $\boldsymbol{M}_{\mathrm{R}}[\omega_\nu]$, we can use (5.153) to write

$$\boldsymbol{M}_{\mathrm{R}}^{+}[\omega_\nu] = \left(\boldsymbol{D}_{\mathrm{R}}^{H}\boldsymbol{G}_{\nu,\mathrm{R}}^{H}\boldsymbol{G}_{\nu,\mathrm{R}}\boldsymbol{D}_{\mathrm{R}}\right)^{-1}\boldsymbol{D}_{\mathrm{R}}^{H}\boldsymbol{G}_{\nu,\mathrm{R}}^{H} = \left(\boldsymbol{D}_{\mathrm{R}}^{H}\boldsymbol{D}_{\mathrm{R}}\right)^{-1}\boldsymbol{D}_{\mathrm{R}}^{H}\boldsymbol{G}_{\nu,\mathrm{R}}^{H}. \tag{5.155}$$

Substituting (5.152), (5.153), and (5.155) into $\boldsymbol{\beta}_{n\nu,\mathrm{R}}^{H}\boldsymbol{M}_{\mathrm{R}}^{H}[\omega_\nu]\boldsymbol{s}_{\mathrm{R}}[\omega_\nu]$ and following the same rationale as for the scalar $\boldsymbol{s}_{\mathrm{T}}^{H}[\omega_\nu]\boldsymbol{M}_{\mathrm{T}}[\omega_\nu]\boldsymbol{\beta}_{n\nu,\mathrm{T}}$, we have that

$$\begin{aligned}\boldsymbol{\beta}_{n\nu,\mathrm{R}}^{H}\boldsymbol{M}_{\mathrm{R}}^{H}[\omega_\nu]\boldsymbol{s}_{\mathrm{R}}[\omega_\nu] &= \mu_{n\nu}\widetilde{\boldsymbol{e}}_{\mathrm{R},0}^{T}\boldsymbol{G}_{\nu,\mathrm{R}}\boldsymbol{D}_{\mathrm{R}}\left(\boldsymbol{D}_{\mathrm{R}}^{H}\boldsymbol{D}_{\mathrm{R}}\right)^{-1}\boldsymbol{D}_{\mathrm{T}}^{H}\boldsymbol{d}\left(\theta_{\mathrm{T}},\varphi_{\mathrm{T}}\right) &(5.156)\\ &= \mu_{n\nu}\widetilde{\boldsymbol{e}}_{\mathrm{R},0}^{T}\boldsymbol{G}_{\nu,\mathrm{R}}\boldsymbol{\Pi}_{\boldsymbol{D}_{\mathrm{R}}}\boldsymbol{d}\left(\theta_{\mathrm{R}},\varphi_{\mathrm{R}}\right), &(5.157)\end{aligned}$$

with

$$\boldsymbol{\Pi}_{\boldsymbol{D}_{\mathrm{R}}} = \boldsymbol{D}_{\mathrm{R}}\left(\boldsymbol{D}_{\mathrm{R}}^{H}\boldsymbol{D}_{\mathrm{R}}\right)^{-1}\boldsymbol{D}_{\mathrm{R}}^{H}. \tag{5.158}$$

Finally, plugging (5.150) and (5.157) into (5.142), we obtain

$$z = \frac{a_0}{N\sqrt{L_{\mathrm{T}}L_{\mathrm{R}}}}\sum_{n=0}^{N-1}\sum_{\nu=0}^{N-1}\eta_{n\nu}\mu_{n\nu}\widetilde{\boldsymbol{e}}_{\mathrm{R},0}^{T}\boldsymbol{G}_{\nu,\mathrm{R}}\boldsymbol{\Pi}_{\boldsymbol{D}_{\mathrm{R}}}\boldsymbol{d}\left(\theta_{\mathrm{R}},\varphi_{\mathrm{R}}\right)\boldsymbol{d}^{H}\left(\theta_{\mathrm{T}},\varphi_{\mathrm{T}}\right)\boldsymbol{\Pi}_{\boldsymbol{D}_{\mathrm{T}}}\boldsymbol{G}_{\nu,\mathrm{T}}^{H}\widetilde{\boldsymbol{e}}_{\mathrm{T},0} + \widetilde{\upsilon}, \tag{5.159}$$

which completes the proof.

CHAPTER 6

Conclusions and Future Work

6.1 Conclusions

This thesis has dealt with the design of transmission strategies in both single- and multi-antenna feedforward opportunistic communication scenarios. In order to mitigate the so-called inter-system interferences, which is the primary objective of opportunistic communications, the null space of the surrounding wireless environment has been exploited. The null space contains those network resources –or DoF– left unused by the other coexisting communication nodes.

The problem of null space-based opportunistic communications is not new, and, as surveyed in Chapter 2, several null-space transmission strategies can be found in the literature. In summary, all the classic null-space schemes use the columns of a basis of the sensed null-space as precoding vectors. Despite avoiding inter-system interferences under ideal operating conditions, these schemes suffer mainly from two drawbacks. On the one hand, it should be noted that the opportunistic nodes identify the null space through a sensing scheme, which can be cast as a detection problem. Accordingly, the sensing step may suffer from classic detection errors, i.e., missed detection, false alarm, and poor monitoring conditions. When these uncertainties are taken into account, some DoF occupied by other neighboring nodes may be erroneously sensed as available. Since the classic null-space strategies do not account for the existence of these uncertainties, severe inter-system interferences can be provided to those occupied DoF erroneously sensed as available, which may corrupt the communication of the neighboring network nodes. On the other hand, the sensed null-space basis is typically obtained from the noise eigenvectors of the measured observations' autocorrelation matrix. The noise eigenvectors are associated with eigenvalues having multiplicity larger than ones, meaning that the eigenvectors are not unique. Therefore, the classic null-space precoding solutions are not unique. This ambiguity requires coordination and cooperation between inner nodes in order to guarantee coherent waveform detection, which may burden the implementation complexity due to large feedback overheads. In summary, the main disadvantages of classic null-space precoding strategies are the lack of robustness to sensing errors and the lack of

solution uniqueness.

The case of single-antenna opportunistic communication under feedforward conditions has been studied in Chapter 3. In order to deal with the abovementioned sensing uncertainties, a generalized sensing error model has been introduced, which is independent of the considered sensing mechanism and captures the critical subspace leakage problem. Leveraging this model, the per-local waveform design strategy has been tackled to satisfy a minimum worst-case inter-system interference criterion. Accordingly, the provided waveforms maximize the SIR at the transmitter output. In this sense, it has been unveiled that the proposed waveforms practice a dimension spreading, i.e., the derived solutions spread the transmitted signal within the sensed null space. The latter is of paramount interest to maximally reduce the provided inter-system interference level per DoF. Interestingly, the derived waveforms are proportional to certain columns of orthogonal projectors onto a subset of the sensed null space. This is a fundamental observation since the orthogonal projector is an invariant (i.e., unique) representation of the subspace. Therefore, the proposed solutions exhibit the fundamental invariance property, which is preferable in feedforward opportunistic communications. Since the opportunistic nodes do not cooperate, invariant solutions enable coherent waveform detection since the waveforms locally designed at each system end are ideally the same regardless of the considered sensed null-space basis. This property guarantees that the opportunistic nodes are self-calibrated, avoiding feedback overheads. Unfortunately, the locality of the sensing may lead to an end-to-end null-space mismatch. It has been argued that subspace mismatch incurs a performance loss in terms of energy loss and self-induced ISI. Even though the robustness of the proposed waveforms to the subspace mismatch has been illustrated, two enhanced detection schemes based on active subspace detection have been presented to counteract the impact of subspace mismatch. Interestingly, one of them admits a closed-form solution that can be efficiently implemented using a bank of per-DoF classic energy detectors.

In Chapter 4, we have studied the asymptotic behavior of the solutions derived in Chapter 3, which can be of practical interest in view of the expected large bandwidths in the forthcoming communication trends. It has been shown that, as the number of system DoF arbitrarily increases, the opportunistic waveforms become linear combinations of Vandermonde vectors. Accordingly, the proposed waveforms can be asymptotically seen as a frequency-domain spreading mechanism. In this respect, the asymptotic waveforms exhibit similar spectral behavior as TDCS and MC-CDMA, which leverage pseudo-random sequences to spread the transmitted signal within the sensed null space. Conversely, the asymptotic waveforms constitute a deterministic spreading mechanism since they rely on columns of the orthogonal projector. The interesting particular case where the available DoF are consecutive has been studied. It has been shown that, under certain operating conditions, the asymptotic opportunistic waveforms derived in Chapter 3 behave as a TDMA-like scheme employing circulant pulse-shaping, thus named Circulant-Shaping TDMA (CS-TDMA). Despite the tight assumptions behind this modulation format, a suboptimal approximation has been proposed for the general case, which avoids the sequential waveform design scheme described in Chapter 3 and enjoys implementation efficiency. At the end of the chapter, an extension of the proposed opportunistic transmission scheme to the frequency-selective channel case has been explored. Taking into account the similarity of the asymptotic waveforms with the OFDMA modulation, a CP-based strategy has been proposed to combat the frequency-selective nature of the opportunistic channel, characteristic

of wideband scenarios. In contrast to other null-space opportunistic techniques focused on frequency-selective channels, such as VFDM, the proposed CP-based strategy does not require CSI at the opportunistic transmitter, avoiding any sort of feedback overheads. Nevertheless, the price to pay is a suboptimal spectral efficiency compared to VFDM and a cumbersome sensing stage using non-unitary sensing bases.

The last technical chapter of this thesis has studied the generalization of the results derived from Chapters 3 and 4 in the case of multi-antenna feedforward opportunistic communications. A straightforward mathematical analysis of the problem at hand has revealed that the important dimension spreading property holds regardless of the use of antenna arrays. In this sense, the impact of using multiple antennas has been emphasized from the SIDR perspective, as increasing the number of antennas permits enlarging the DoF spreading factor and, thus, further minimizing the inter-system interference density. Nevertheless, the critical invariance property has only been easily proven in symmetric multi-antenna scenarios, i.e., when the opportunistic transmitter and receiver have the same number of antennas. In a more general sense, when the multi-antenna opportunistic communication is asymmetric, a more involved mathematical analysis is required. In Chapter 5, leveraging the manifold separation theory framework, it has been shown that opportunistic communication is independent of the geometry of transmitting and receiving arrays, and only depends on the number of sensors, as previously advocated by the SIDR analysis. This result has been shown to be of paramount importance, as it reveals that the space-time opportunistic waveforms are self-calibrated, irrespective of the possible array calibration errors. Even though the array-geometry invariance has been proven under far-field conditions, it has been argued that the result can be extrapolated to the near-field case through different orthogonal expansions of the array manifold. Finally, the asymptotic analysis of the space-time opportunistic waveforms has disclosed that an antenna selection policy is performed by each waveform, meaning that the opportunistic multi-antenna transmitter asymptotically behaves as a set of orthogonal single-antenna transmitters. This observation has been used to extend the CP-based opportunistic transmission discussed in Chapter 4 to multi-antenna frequency-selective channels.

6.2 Future Work

Upon completing this thesis, the following topics have been identified as potential future research lines.

6.2.1 Multi-user Opportunistic Communication

This thesis has focused on the case of single-user (point-to-point) opportunistic communications. In multi-user environments, an access protocol or mechanism is generally required. In this sense, the straightforward TDD/TDMA approach permits using the opportunistic transmission scheme proposed in this thesis to guarantee the coexistence of multiple inner transmitter-receiver pairs. Under these conditions, intra-system interference, i.e., the interference between inner transmitter-receiver pairs, can be practically avoided using a conventional multiple-access scheme. Nevertheless, this approach requires a certain degree of inter-node cooperation.

Suppose one inner transmitter-receiver pair exploits only a number of $K < M$ waveforms that satisfy its traffic requirements and achieve the specified SIDR. Therefore, there are still $M - K$ DoF left unused, being M the total number of null-space DoF. Consequently, a potential research line involves studying multi-user strategies to exploit the remaining unused DoF efficiently. These strategies may require the use of more advanced signal processing techniques at the inner receivers, and the fact that the waveforms ϕ_k are orthogonal can play an essential role in decreasing the receiver complexity. Of course, suppose low-rate feedback cooperation is allowed between inner transmitters or receivers. In that case, it is possible to design non-orthogonal multi-user opportunistic communication schemes, giving birth to a complexity-performance trade-off.

6.2.2 Outage Analysis and Transmission Capacity

In order to study the impact of sensing uncertainties, the SIDR has been defined in this thesis. As discussed earlier, the SIDR is a pessimistic metric as it measures the interference per DoF at the inner transmitter output without accounting for the propagation conditions.

The transmission capacity [WAJ10] is a performance metric that measures the spatial density of successful transmissions given an outage probability constraint. This framework has been extensively used to assess the performance of distributed networks [VH12; LAH11; LAH13], as it accounts for the spatial distribution of the communication nodes and the propagation conditions. In this sense, another potential research line would be characterizing the statistics of the interference imposed by the inner transmitter on the outer-network nodes. This characterization permits studying the outage probability induced by the sensing uncertainties. Specifically, letting κ and η be the sensed DoF availability and the sensing inaccuracy of the sensing mechanism employed by the inner transmitting node, respectively, this research line would pursue the characterization of the outage probability as

$$P_{\text{out}} = f(\kappa, \eta, \alpha, \gamma_{\text{outer}}), \tag{6.1}$$

where α is the path-loss exponent and γ_{outer} is the QoS requirement of the outer-network node. Therefore, characterizing the transmission capacity using the proposed outage probability expression can be of relevant interest to define the possible operating regimes of the opportunistic transmission scheme derived in this thesis and to dimension the coexistence capability in the multi-user opportunistic communication scenario.

6.2.3 Orthogonal Time-Frequency Space Modulation

Orthogonal Time-Frequency Space (OTFS) is a novel modulation format that deals with both the time-selectivity and the frequency-selectivity of the wireless channel. For this purpose, OTFS modulates the information symbols in the Doppler-delay grid rather than in the time-frequency grid as conventional modulations such as OFDM. One of the main problems in the OTFS framework is the design of appropriate pulse-shaping filters to exploit the Doppler-delay characteristics of the channel. It is known that pulses that simultaneously practice frequency-domain and time-domain spreading are suitable for this modulation format.

A novel waveform design strategy has been proposed in this thesis able to spread the signal in the frequency domain so as to minimize the inter-system interference density per erroneous

DoF. A potential research line would consist in adapting the waveform design scheme to exploit the two-dimensional Doppler-delay domain rather than the time-frequency DoF. The use of orthogonal projectors can be of relevant interest to provide a finite response in the Doppler-delay domain while spreading the signals in a two-dimensional time-frequency domain. It can be seen as a generalization of the waveform design scheme to the case where the domain of interest is two-dimensional instead of one-dimensional. A more cumbersome case would involve the use of multiple antennas in an OTFS-like system.

6.2.4 Holographic Multiple-Input Multiple-Output

The appearance of massive MIMO was a turning point in multi-antenna systems since this technique can provide a substantial increase in spectral efficiency and the number of communication nodes served simultaneously. The main problem with simultaneously increasing the number of array elements and moving the communications to higher frequency bands is that the far-field assumption of the antennas becomes no longer valid.

Recently, the case of having an arbitrarily large number of antennas in a confined (finite) region of space has been gaining considerable momentum. This case is known as Holographic MIMO. The potential of this technique lies in the fact that an array of antennas can be approximated by a radiating surface, which allows exploiting the increased spatial DoF offered by near-field communications. Holographic MIMO enables expressing the spherical waves as an infinite sum of plane waves, characteristic of the far field. It thus permits the use of the already developed array processing techniques in the near-field.

In this sense, a potential research topic would be the adaptation of the space-time opportunistic waveforms studied in Chapter 5 in the near-field context through the use of holographic surfaces. In principle, the array-geometry invariance property would be maintained since the decomposition of a spherical wave into a sum of plane waves allows reproducing the mathematical analysis developed in Chapter 5. However, it would be interesting to study how to exploit the DoF gain provided by the near-field and improve spatial multiplexing to allow the coexistence of simultaneous opportunistic links.

References

[AAH16] M. H. Al-Ali and K. C. Ho. "Transmit precoding in underlay MIMO cognitive radio with unavailable or imperfect knowledge of primary interference channel". *IEEE Transactions on Wireless Communications*, vol. 15, no. 8 (2016), pp. 5143–5155.

[AAH17] M. H. Al-Ali and D. K. C. Ho. "Precoding for MIMO channels in cognitive radio networks with CSI uncertainties and for MIMO compound capacity". *IEEE Transactions on Signal Processing*, vol. 65, no. 15 (2017), pp. 3976–3989.

[AAT19] F. Awin, E. Abdel-Raheem, and K. Tepe. "Blind Spectrum Sensing Approaches for Interweaved Cognitive Radio System: A Tutorial and Short Course". *IEEE Communications Surveys & Tutorials*, vol. 21, no. 1 (2019), pp. 238–259.

[ACO15] M. Alodeh, S. Chatzinotas, and B. Ottersten. "Constructive Multiuser Interference in Symbol Level Precoding for the MISO Downlink Channel". *IEEE Transactions on Signal Processing*, vol. 63, no. 9 (2015), pp. 2239–2252.

[AEKN10] M. Amir, A. El-Keyi, and M. Nafie. "Opportunistic interference alignment for multiuser cognitive radio". In: *2010 IEEE Information Theory Workshop on Information Theory (ITW 2010, Cairo)*. 2010, pp. 1–5.

[AH17] A. Ali and W. Hamouda. "Advances on Spectrum Sensing for Cognitive Radio Networks: Theory and Applications". *IEEE Communications Surveys & Tutorials*, vol. 19, no. 2 (2017), pp. 1277–1304.

[Aka74] H. Akaike. "A new look at the statistical model identification". *IEEE Transactions on Automatic Control*, vol. 19, no. 6 (1974), pp. 716–723.

[ALLP12] E. Axell, G. Leus, E. G. Larsson, and H. V. Poor. "Spectrum sensing for cognitive radio : state-of-the-art and recent advances". *IEEE Signal Processing Magazine*, vol. 29, no. 3 (2012), pp. 101–116.

[AR17] P. Aquilina and T. Ratnarajah. "Linear Interference Alignment in Full-Duplex MIMO Networks With Imperfect CSI". *IEEE Transactions on Communications*, vol. 65, no. 12 (2017), pp. 5226–5243.

[ARS16] M. Agiwal, A. Roy, and N. Saxena. "Next Generation 5G Wireless Networks: A Comprehensive Survey". *IEEE Communications Surveys & Tutorials*, vol. 18, no. 3 (2016), pp. 1617–1655.

[ASNS16] Y. Abdulkadir, O. Simpson, N. Nwanekezie, and Y. Sun. "Space-time opportunistic interference alignment in cognitive radio networks". In: *2016 IEEE Wireless Communications and Networking Conference*. 2016, pp. 1–6.

[AV09] V. S. Annapureddy and V. V. Veeravalli. "Gaussian Interference Networks: Sum Capacity in the Low-Interference Regime and New Outer Bounds on the Capacity Region". *IEEE Transactions on Information Theory*, vol. 55, no. 7 (2009), pp. 3032–3050.

[Bal15] C. A. Balanis. *Antenna Theory: Analysis and Design*. John Wiley & Sons, 2015.

[BDGH18] K. Bouallegue, I. Dayoub, M. Gharbi, and K. Hassan. "Blind Spectrum Sensing Using Extreme Eigenvalues for Cognitive Radio Networks". *IEEE Communications Letters*, vol. 22, no. 7 (2018), pp. 1386–1389.

[BDP18] M. Bennis, M. Debbah, and H. V. Poor. "Ultrareliable and Low-Latency Wireless Communication: Tail, Risk, and Scale". *Proceedings of the IEEE*, vol. 106, no. 10 (2018), pp. 1834–1853.

[Ber09] D. S. Berstein. *Matrix Mathematics: Theory, Facts, and Formulas*. Princeton Univ. Press, Princeton, NJ, 2009.

[BF89] O.M. Bucci and G. Franceschetti. "On the degrees of freedom of scattered fields". *IEEE Transactions on Antennas and Propagation*, vol. 37, no. 7 (1989), pp. 918–926.

[BJA21] A.-A. A. Boulogeorgos, J. M. Jornet, and A. Alexiou. "Directional Terahertz Communication Systems for 6G: Fact Check". *IEEE Vehicular Technology Magazine*, vol. 16, no. 4 (2021), pp. 68–77.

[BMA+21] A. K. Bairagi, Md. S. Munir, M. Alsenwi, N. H. Tran, S. S. Alshamrani, M. Masud, Z. Han, and C. S. Hong. "Coexistence Mechanism Between eMBB and uRLLC in 5G Wireless Networks". *IEEE Transactions on Communications*, vol. 69, no. 3 (2021), pp. 1736–1749.

[BPG+16] S. Bhattarai, J. J. Park, B. Gao, K. Bian, and W. Lehr. "An Overview of Dynamic Spectrum Sharing: Ongoing Initiatives, Challenges, and a Roadmap for Future Research". *IEEE Transactions on Cognitive Communications and Networking*, vol. 2, no. 2 (2016), pp. 110–128.

[BPT10] G. Bresler, A. Parekh, and D. N. C. Tse. "The Approximate Capacity of the Many-to-One and One-to-Many Gaussian Interference Channels". *IEEE Transactions on Information Theory*, vol. 56, no. 9 (2010), pp. 4566–4592.

[BRK07] F. Belloni, A. Richter, and V. Koivunen. "DoA Estimation Via Manifold Separation for Arbitrary Array Structures". *IEEE Transactions on Signal Processing*, vol. 55, no. 10 (2007), pp. 4800–4810.

[BS16] M. Benzi and V. Simoncini (eds.) *Exploiting hidden structure in matrix computations: Algorithms and applications*. Springer, 2016.

[BV18] J. Borras and G. Vazquez. "Uncoordinated space-frequency Pilot Design for Multi-Antenna Wideband Opportunistic Communications". In: *2018 IEEE 19th International Workshop on Signal Processing Advances in Wireless Communications (SPAWC)*. 2018, pp. 1–5.

[BV19] J. Borras and G. Vazquez. "Distributed feedback-aided subspace concurrent opportunistic communications". In: *2019 IEEE 20th International Workshop on Signal Processing Advances in Wireless Communications (SPAWC)*. 2019, pp. 1–5.

[Car75] A. Carleial. "A case where interference does not reduce capacity (Corresp.)" *IEEE Transactions on Information Theory*, vol. 21, no. 5 (1975), pp. 569–570.

[Car78] A. Carleial. "Interference channels". *IEEE Transactions on Information Theory*, vol. 24, no. 1 (1978), pp. 60–70.

[CDD09] A. Cohen, W. Dahmen, and R. DeVore. "Compressed sensing and best k-term approximation". *Journal of the American Mathematical Society*, vol. 22, no. 1 (2009), pp. 211–231.

[CE13] J. Chen and P. Elia. "Toward the Performance Versus Feedback Tradeoff for the Two-User MISO Broadcast Channel". *IEEE Transactions on Information Theory*, vol. 59, no. 12 (2013), pp. 8336–8356.

[CF67] Y. Chien and K.-S. Fu. "On the generalized Karhunen-Loève expansion (Corresp.)" *IEEE Transactions on Information Theory*, vol. 13, no. 3 (1967), pp. 518–520.

[CFR21] V. Cerone, S. M. Fosson, and D. Regruto. "A non-convex adaptive regularization approach to binary optimization". In: *2021 60th IEEE Conference on Decision and Control (CDC)*. 2021, pp. 3844–3849.

[CH17] R. Cornelius and D. Heberling. "Spherical Wave Expansion With Arbitrary Origin for Near-Field Antenna Measurements". *IEEE Transactions on Antennas and Propagation*, vol. 65, no. 8 (2017), pp. 4385–4388.

[CHW+21] Z. Chen, C. Han, Y. Wu, L. Li, C. Huang, Z. Zhang, G. Wang, and W. Tong. "Terahertz Wireless Communications for 2030 and Beyond: A Cutting-Edge Frontier". *IEEE Communications Magazine*, vol. 59, no. 11 (2021), pp. 66–72.

[CJ08] V. R. Cadambe and S. A. Jafar. "Interference Alignment and Degrees of Freedom of the K-User Interference Channel". *IEEE Transactions on Information Theory*, vol. 54, no. 8 (2008), pp. 3425–3441.

[CJH+16] B. Clerckx, H. Joudeh, C. Hao, M. Dai, and B. Rassouli. "Rate splitting for MIMO wireless networks: a promising PHY-layer strategy for LTE evolution". *IEEE Communications Magazine*, vol. 54, no. 5 (2016), pp. 98–105.

[CJW10] V. R. Cadambe, S. A. Jafar, and C. Wang. "Interference Alignment With Asymmetric Complex Signaling-Settling the Høst-Madsen-Nosratinia Conjecture". *IEEE Transactions on Information Theory*, vol. 56, no. 9 (2010), pp. 4552–4565.

[CK14] M. Costa and V. Koivunen. "Application of Manifold Separation to Polarimetric Capon Beamformer and Source Tracking". *IEEE Transactions on Signal Processing*, vol. 62, no. 4 (2014), pp. 813–827.

[CKB16] K. Cichon, A. Kliks, and H. Bogucka. "Energy-Efficient Cooperative Spectrum Sensing: A Survey". *IEEE Communications Surveys & Tutorials*, vol. 18, no. 3 (2016), pp. 1861–1886.

[CKCD13] L. S. Cardoso, M. Kobayashi, F. R. P. Cavalcanti, and M. Debbah. "Vandermonde-subspace frequency division multiplexing for two-tiered cognitive radio networks". *IEEE Transactions on Communications*, vol. 61, no. 6 (2013), pp. 2212–2220.

[CMSP20] B. Clerckx, Y. Mao, R. Schober, and H. V. Poor. "Rate-Splitting Unifying SDMA, OMA, NOMA, and Multicasting in MISO Broadcast Channel: A Simple Two-User Rate Analysis". *IEEE Wireless Communications Letters*, vol. 9, no. 3 (2020), pp. 349–353.

[CMS+21] B. Clerckx, Y. Mao, R. Schober, E. A. Jorswieck, D. J. Love, J. Yuan, L. Hanzo, G. Y. Li, E. G. Larsson, and G. Caire. "Is NOMA Efficient in Multi-Antenna Networks? A Critical Look at Next Generation Multiple Access Techniques". *IEEE Open Journal of the Communications Society*, vol. 2 (2021), pp. 1310–1343.

[CNS+05] V. Chakravarthy, A.S. Nunez, J.P. Stephens, A.K. Shaw, and M.A. Temple. "TDCS, OFDM, and MC-CDMA: a brief tutorial". *IEEE Communications Magazine*, vol. 43, no. 9 (2005), S11–S16.

[CNY+21] X. Chen, D. W. K. Ng, W. Yu, E. G. Larsson, N. Al-Dhahir, and R. Schober. "Massive access for 5G and beyond". *IEEE Journal on Selected Areas in Communications*, vol. 39, no. 3 (2021), pp. 615–637.

[Cos83] M. Costa. "Writing on dirty paper (Corresp.)" *IEEE Transactions on Information Theory*, vol. 29, no. 3 (1983), pp. 439–441.

[CRK10] M. Costa, A. Richter, and V. Koivunen. "Unified Array Manifold Decomposition Based on Spherical Harmonics and 2-D Fourier Basis". *IEEE Transactions on Signal Processing*, vol. 58, no. 9 (2010), pp. 4634–4645.

[CRK12] M. Costa, A. Richter, and V. Koivunen. "DoA and Polarization Estimation for Arbitrary Array Configurations". *IEEE Transactions on Signal Processing*, vol. 60, no. 5 (2012), pp. 2330–2343.

[CS03] G. Caire and S. Shamai. "On the achievable throughput of a multiantenna Gaussian broadcast channel". *IEEE Transactions on Information Theory*, vol. 49, no. 7 (2003), pp. 1691–1706.

[CT05] E.J. Candes and T. Tao. "Decoding by linear programming". *IEEE Transactions on Information Theory*, vol. 51, no. 12 (2005), pp. 4203–4215.

[CW11] T. T. Cai and L. Wang. "Orthogonal Matching Pursuit for Sparse Signal Recovery With Noise". *IEEE Transactions on Information Theory*, vol. 57, no. 7 (2011), pp. 4680–4688.

[CWX10] T. T. Cai, L. Wang, and G. Xu. "Stable Recovery of Sparse Signals and an Oracle Inequality". *IEEE Transactions on Information Theory*, vol. 56, no. 7 (2010), pp. 3516–3522.

[DAA19] S. Doumiati, M. Assaad, and H. A. Artail. "A Framework of Topological Interference Management and Clustering for D2D Networks". *IEEE Transactions on Communications*, vol. 67, no. 11 (2019), pp. 7856–7871.

[Dar20] D. Dardari. "Communicating With Large Intelligent Surfaces: Fundamental Limits and Models". *IEEE Journal on Selected Areas in Communications*, vol. 38, no. 11 (2020), pp. 2526–2537.

[DD91] E. M. Dowling and R. D. DeGroat. "The equivalence of the total least squares and minimum norm methods". *IEEE Transactions on Signal Processing*, vol. 39, no. 8 (1991), pp. 1891–1892.

[DD94a] M. A. Doron and E. Doron. "Wavefield modeling and array processing .I. Spatial sampling". *IEEE Transactions on Signal Processing*, vol. 42, no. 10 (1994), pp. 2549–2559.

[DD94b] M.A. Doron and E. Doron. "Wavefield modeling and array processing .II. Algorithms". *IEEE Transactions on Signal Processing*, vol. 42, no. 10 (1994), pp. 2560–2570.

[DD94c] M.A. Doron and E. Doron. "Wavefield modeling and array processing. III. Resolution capacity". *IEEE Transactions on Signal Processing*, vol. 42, no. 10 (1994), pp. 2571–2580.

[DDW93] M. A. Doron, E. Doron, and A. J. Weiss. "Coherent wide-band processing for arbitrary array geometry". *IEEE Transactions on Signal Processing*, vol. 41, no. 1 (1993), pp. 414–.

[DE03] D. L. Donoho and M. Elad. "Optimally sparse representation in general (nonorthogonal) dictionaries via ℓ_1 minimization". *Proceedings of the National Academy of Sciences*, vol. 100, no. 5 (2003), pp. 2197–2202.

[DF20] A. F. Darwesh and A. O. Fapojuwo. "Secrecy rate analysis of mmWave MISO ad hoc networks with null space precoding". In: *2020 IEEE Wireless Communications and Networking Conference (WCNC)*. 2020, pp. 1–6.

[DGV16] D. Darsena, G. Gelli, and F. Verde. "Convolutive Superposition for Multicarrier Cognitive Radio Systems". *IEEE Journal on Selected Areas in Communications*, vol. 34, no. 11 (2016), pp. 2951–2967.

[DGV17] D. Darsena, G. Gelli, and F. Verde. "An Opportunistic Spectrum Access Scheme for Multicarrier Cognitive Sensor Networks". *IEEE Sensors Journal*, vol. 17, no. 8 (2017), pp. 2596–2606.

[DH01] D.L. Donoho and X. Huo. "Uncertainty principles and ideal atomic decomposition". *IEEE Transactions on Information Theory*, vol. 47, no. 7 (2001), pp. 2845–2862.

[DWSGLA10] L. Dritsoula, Z. Wang, H. R. Sadjadpour, and J.J. Garcia-Luna-Aceves. "Antenna selection for opportunistic interference management in MIMO broadcast channels". In: *2010 IEEE 11th International Workshop on Signal Processing Advances in Wireless Communications (SPAWC)*. 2010, pp. 1–5.

[EALH12] O. El Ayach, A. Lozano, and R. W. Heath. "On the Overhead of Interference Alignment: Training, Feedback, and Cooperation". *IEEE Transactions on Wireless Communications*, vol. 11, no. 11 (2012), pp. 4192–4203.

[EAPH13] O. El Ayach, S. W. Peters, and R. W. Heath. "The practical challenges of interference alignment". *IEEE Wireless Communications*, vol. 20, no. 1 (2013), pp. 35–42.

[EK11] A. El Gamal and Y.-H. Kim. *Network Information Theory*. Cambridge University Press, 2011.

[EK12] Y. C. Eldar and G. Kutyniok. *Compressed sensing: theory and applications*. Cambridge University Press, 2012.

[EP18] A. A. Esswie and K. I. Pedersen. "Null space based preemptive scheduling for joint URLLC and eMBB traffic in 5G networks". In: *2018 IEEE Globecom Workshops (GC Wkshps)*. 2018, pp. 1–6.

[EPT07] R. Etkin, A. Parekh, and D. Tse. "Spectrum sharing for unlicensed bands". *IEEE Journal on Selected Areas in Communications*, vol. 25, no. 3 (2007), pp. 517–528.

[Ers16] T. Erseghe. "Coding in the Finite-Blocklength Regime: Bounds Based on Laplace Integrals and Their Asymptotic Approximations". *IEEE Transactions on Information Theory*, vol. 62, no. 12 (2016), pp. 6854–6883.

[ETW08] R. H. Etkin, D. N. C. Tse, and H. Wang. "Gaussian Interference Channel Capacity to Within One Bit". *IEEE Transactions on Information Theory*, vol. 54, no. 12 (2008), pp. 5534–5562.

[FA19] S. M. Fosson and M. Abuabiah. "Recovery of Binary Sparse Signals From Compressed Linear Measurements via Polynomial Optimization". *IEEE Signal Processing Letters*, vol. 26, no. 7 (2019), pp. 1070–1074.

[FdG+16] M. C. Filippou, P. de Kerret, D. Gesbert, T. Ratnarajah, A. Pastore, and G. A. Ropokis. "Coordinated Shared Spectrum Precoding With Distributed CSIT". *IEEE Transactions on Wireless Communications*, vol. 15, no. 8 (2016), pp. 5182–5192.

[FGM02] E. Fishler, M. Grosmann, and H. Messer. "Detection of signals by information theoretic criteria: general asymptotic performance analysis". *IEEE Transactions on Signal Processing*, vol. 50, no. 5 (2002), pp. 1027–1036.

[FGSB17] J. Fanjul, Ó. González, I. Santamaria, and C. Beltrán. "Homotopy Continuation for Spatial Interference Alignment in Arbitrary MIMO X Networks". *IEEE Transactions on Signal Processing*, vol. 65, no. 7 (2017), pp. 1752–1764.

[FK18] A. Flinth and G. Kutyniok. "PROMP: A sparse recovery approach to lattice-valued signals". *Applied and Computational Harmonic Analysis*, vol. 45, no. 3 (2018), pp. 668–708.

[FMMS15] M. Franceschetti, M. D. Migliore, P. Minero, and F. Schettino. "The Information Carried by Scattered Waves: Near-Field and Nonasymptotic Regimes". *IEEE Transactions on Antennas and Propagation*, vol. 63, no. 7 (2015), pp. 3144–3157.

[Fos18] S. M. Fosson. "Non-convex approach to binary compressed sensing". In: *2018 52nd Asilomar Conference on Signals, Systems, and Computers*. 2018, pp. 1959–1963.

[FPM+20] Q. Feng, J. Pang, M. Maso, M. Debbah, and W. Tong. "IDFT-VFDM for supplementary uplink and LTE-NR co-existence". *IEEE Transactions on Wireless Communications*, vol. 19, no. 5 (2020), pp. 3435–3448.

[FR13] S. Foucart and H. Rauhut. *A Mathematical Introduction to Compressive Sensing*. Birkhäuser Basel, 2013.

[Fra15] M. Franceschetti. "On Landau's eigenvalue theorem and information cut-sets". *IEEE Transactions on Information Theory*, vol. 61, no. 9 (2015), pp. 5042–5051.

[Fra17] M. Franceschetti. *Wave theory of information*. Cambridge University Press, 2017.

[Fri18] B. Friedlander. "Antenna Array Manifolds for High-Resolution Direction Finding". *IEEE Transactions on Signal Processing*, vol. 66, no. 4 (2018), pp. 923–932.

[Fri93] B. Friedlander. "The root-MUSIC algorithm for direction finding with interpolated arrays". *Signal Processing*, vol. 30, no. 1 (1993), pp. 15–29.

[FSRV15] J. Font-Segura, J. Riba, and G. Vázquez. "Sphericity minimum description length: Asymptotic performance under unknown noise variance". In: *2015 IEEE International Symposium on Information Theory (ISIT)*. 2015, pp. 1615–1619.

[FSVR14] J. Font-Segura, G. Vazquez, and J. Riba. "Single and multi-frequency wideband spectrum sensing with side-information". *IET Signal Processing*, vol. 8, no. 8 (2014), pp. 831–843.

[FZCZ04] D.-Z. Feng, X.-D. Zhang, D.-X. Chang, and W. X. Zheng. "A fast recursive total least squares algorithm for adaptive FIR filtering". *IEEE Transactions on Signal Processing*, vol. 52, no. 10 (2004), pp. 2729–2737.

[GAH11] R. K. Ganti, J. G. Andrews, and M. Haenggi. "High-SIR Transmission Capacity of Wireless Networks With General Fading and Node Distribution". *IEEE Transactions on Information Theory*, vol. 57, no. 5 (2011), pp. 3100–3116.

[Gal08] R. G. Gallager. *Principles of digital communication*. Vol. 1. Cambridge University Press Cambridge, 2008.

[Gal68] R. G. Gallager. *Information Theory and Reliable Communications*. John Wiley & Sons, 1968.

[GGC12] J. Gutiérrez-Gutiérrez and P. M. Crespo. *Block Toeplitz Matrices: Asymptotic Results and Applications*. Now Publishers, 2012.

[GJMS09] A. Goldsmith, S. A. Jafar, I. Maric, and S. Srinivasa. "Breaking spectrum gridlock with cognitive radios: an information theoretic perspective". *Proceedings of the IEEE*, vol. 97, no. 5 (2009), pp. 894–914.

[GL80] G. H. Golub and C. F. Van Loan. "An analysis of the total least squares problem". *SIAM Journal on Numerical Analysis*, vol. 17, no. 6 (1980), pp. 883–893.

[GNAJ15] C. Geng, N. Naderializadeh, A. S. Avestimehr, and S. A. Jafar. "On the Optimality of Treating Interference as Noise". *IEEE Transactions on Information Theory*, vol. 61, no. 4 (2015), pp. 1753–1767.

[Gol05] A. Goldsmith. *Wireless Communications*. Cambridge University Press, 2005.

[Gol73] G. H. Golub. "Some modified matrix eigenvalue problems". *SIAM review*, vol. 15, no. 2 (1973), pp. 318–334.

[GPV05a] M. C. Gursoy, H. V. Poor, and S. Verdu. "Noncoherent Rician fading channel-part II: spectral efficiency in the low-power regime". *IEEE Transactions on Wireless Communications*, vol. 4, no. 5 (2005), pp. 2207–2221.

[GPV05b] M. C. Gursoy, H. V. Poor, and S. Verdu. "The noncoherent Rician fading channel-part I: structure of the capacity-achieving input". *IEEE Transactions on Wireless Communications*, vol. 4, no. 5 (2005), pp. 2193–2206.

[Gra06] R. M. Gray. *Toeplitz and circulant matrices: A review*. Now Publishers, 2006.

[HAB+09] M. Haenggi, J. G. Andrews, F. Baccelli, O. Dousse, and M. Franceschetti. "Stochastic geometry and random graphs for the analysis and design of wireless networks". *IEEE Journal on Selected Areas in Communications*, vol. 27, no. 7 (2009), pp. 1029–1046.

[Han88] J. E. Hansen, ed. *Spherical Near-field Antenna Measurements*. Electromagnetic Waves. Institution of Engineering and Technology, 1988.

[HAW08] A. M. Hunter, J. G. Andrews, and S. Weber. "Transmission capacity of ad hoc networks with spatial diversity". *IEEE Transactions on Wireless Communications*, vol. 7, no. 12 (2008), pp. 5058–5071.

[Hay05] S. Haykin. "Cognitive radio: brain-empowered wireless communications". *IEEE Journal on Selected Areas in Communications*, vol. 23, no. 2 (2005), pp. 201–220.

[HBGL13] S. Hu, G. Bi, Y. L. Guan, and S. Li. "TDCS-Based Cognitive Radio Networks with Multiuser Interference Avoidance". *IEEE Transactions on Communications*, vol. 61, no. 12 (2013), pp. 4828–4835.

[HEKA16] Y. Han, E. Ekici, H. Kremo, and O. Altintas. "Spectrum sharing methods for the coexistence of multiple RF systems: A survey". *Ad Hoc Networks*, vol. 53 (2016), pp. 53 –78.

[HJSV12] C. Huang, S. A. Jafar, S. Shamai, and S. Vishwanath. "On Degrees of Freedom Region of MIMO Networks Without Channel State Information at Transmitters". *IEEE Transactions on Information Theory*, vol. 58, no. 2 (2012), pp. 849–857.

[HK81] T. Han and K. Kobayashi. "A new achievable rate region for the interference channel". *IEEE Transactions on Information Theory*, vol. 27, no. 1 (1981), pp. 49–60.

[HLDL11] H. Huang, V. K. N. Lau, Y. Du, and S. Liu. "Robust Lattice Alignment for K-User MIMO Interference Channels With Imperfect Channel Knowledge". *IEEE Transactions on Signal Processing*, vol. 59, no. 7 (2011), pp. 3315–3325.

[HM72] H. Harashima and H. Miyakawa. "Matched-Transmission Technique for Channels With Intersymbol Interference". *IEEE Transactions on Communications*, vol. 20, no. 4 (1972), pp. 774–780.

[HP97] S. Hara and R. Prasad. "Overview of multicarrier CDMA". *IEEE Communications Magazine*, vol. 35, no. 12 (1997), pp. 126–133.

[HTW19] T. Hastie, R. Tibshirani, and M. Wainwright. *Statistical learning with sparsity: the lasso and generalizations*. Chapman and Hall/CRC, 2019.

[HUL21] Y. Han, M. Urlea, and S. Loyka. "On Optimal Power Allocation for Modulation-Constrained Gaussian Channels". In: *2021 IEEE International Symposium on Information Theory (ISIT)*. 2021, pp. 3109–3114.

[HV91] S. Van Huffel and J. Vandewalle. *The Total Least Squares Problem*. Society for Industrial and Applied Mathematics, 1991.

[Jaf11] S. A. Jafar. *Interference Alignment: A New Look at Signal Dimensions in a Communication Network*. Now Publishers, 2011.

[Jaf12] S. A. Jafar. "Blind Interference Alignment". *IEEE Journal of Selected Topics in Signal Processing*, vol. 6, no. 3 (2012), pp. 216–227.

[Jaf14] S. A. Jafar. "Topological Interference Management Through Index Coding". *IEEE Transactions on Information Theory*, vol. 60, no. 1 (2014), pp. 529–568.

[JASA20] S. Javed, O. Amin, B. Shihada, and M.-S. Alouini. "A Journey From Improper Gaussian Signaling to Asymmetric Signaling". *IEEE Communications Surveys Tutorials*, vol. 22, no. 3 (2020), pp. 1539–1591.

[JHH+17] C. Jin, S. Hu, Y. Huang, Q. Luo, D. Huang, Y. Li, Y. Gao, and S. Cheng. "On Transform Domain Communication Systems under Spectrum Sensing Mismatch: A Deterministic Analysis". *Sensors*, vol. 17, no. 7 (2017), p. 1594.

[JLR12] M. Jin, Y. Li, and H. Ryu. "On the Performance of Covariance Based Spectrum Sensing for Cognitive Radio". *IEEE Transactions on Signal Processing*, vol. 60, no. 7 (2012), pp. 3670–3682.

[JLT18] Y.-S. Jeon, N. Lee, and R. Tandon. "Degrees of Freedom and Achievable Rate of Wide-Band Multi-Cell Multiple Access Channels With No CSIT". *IEEE Transactions on Communications*, vol. 66, no. 4 (2018), pp. 1772–1786.

[JV20] M. Johnny and A. Vahid. "Exploiting Coherence Time Variations for Opportunistic Blind Interference Alignment". *IEEE Transactions on Communications*, vol. 68, no. 10 (2020), pp. 6054–6069.

[Kay98] S. M. Kay. *Fundamentals of Statistical Signal Processing: Detection Theory, Volume II*. Prentice Hall PTR, 1998.

[KMM17] P.-S. Kildal, E. Martini, and S. Maci. "Degrees of Freedom and Maximum Directivity of Antennas: A bound on maximum directivity of nonsuperreactive antennas". *IEEE Antennas and Propagation Magazine*, vol. 59, no. 4 (2017), pp. 16–25.

[KPV09] N. Khude, V. Prabhakaran, and P. Viswanath. "Opportunistic interference management". In: *2009 IEEE International Symposium on Information Theory*. 2009, pp. 2076–2080.

[KS22] A. Krishnamoorthy and R. Schober. "Downlink MIMO-RSMA with Successive Null-Space Precoding". In: 2022, pp. 1–1.

[KSAJ07] R. A. Kennedy, P. Sadeghi, T. D. Abhayapala, and H. M. Jones. "Intrinsic Limits of Dimensionality and Richness in Random Multipath Fields". *IEEE Transactions on Signal Processing*, vol. 55, no. 6 (2007), pp. 2542–2556.

[KT82] R. Kumaresan and D. Tufts. "Estimating the parameters of exponentially damped sinusoids and pole-zero modeling in noise". *IEEE Transactions on Acoustics, Speech, and Signal Processing*, vol. 30, no. 6 (1982), pp. 833–840.

[KT83] R. Kumaresan and D. W. Tufts. "Estimating the Angles of Arrival of Multiple Plane Waves". *IEEE Transactions on Aerospace and Electronic Systems*, vol. AES-19, no. 1 (1983), pp. 134–139.

[Kum83] R. Kumaresan. "On the zeros of the linear prediction-error filter for deterministic signals". *IEEE Transactions on Acoustics, Speech, and Signal Processing*, vol. 31, no. 1 (1983), pp. 217–220.

[LAH11] J. Lee, J. G. Andrews, and D. Hong. "Spectrum-Sharing Transmission Capacity". *IEEE Transactions on Wireless Communications*, vol. 10, no. 9 (2011), pp. 3053–3063.

[LAH13] J. Lee, J. G. Andrews, and D. Hong. "Spectrum-Sharing Transmission Capacity with Interference Cancellation". *IEEE Transactions on Communications*, vol. 61, no. 1 (2013), pp. 76–86.

[Lan75] H.J. Landau. "On Szegö's eingenvalue distribution theorem and non-Hermitian kernels". *Journal d'Analyse Mathématique*, vol. 28, no. 1 (1975), pp. 335–357.

[LAV16] S. Lagen, A. Agustin, and J. Vidal. "On the Superiority of Improper Gaussian Signaling in Wireless Interference MIMO Scenarios". *IEEE Transactions on Communications*, vol. 64, no. 8 (2016), pp. 3350–3368.

[LB18] M. A. Lodhi and W. U. Bajwa. "Detection Theory for Union of Subspaces". *IEEE Transactions on Signal Processing*, vol. 66, no. 24 (2018), pp. 6347–6362.

[LE21] A. Leshem and U. Erez. "The Interference Channel Revisited: Aligning Interference by Adjusting Antenna Separation". *IEEE Transactions on Signal Processing*, vol. 69 (2021), pp. 1874–1884.

[LFP+20] W. Liu, Q. Feng, J. Pang, Q. Hu, R. Yin, and G. Yu. "Robust Rate-Maximization Precoder Design for VFDM System". *IEEE Transactions on Vehicular Technology*, vol. 69, no. 3 (2020), pp. 2747–2757.

[LHA13] A. Lozano, R. W. Heath, and J. G. Andrews. "Fundamental Limits of Cooperation". *IEEE Transactions on Information Theory*, vol. 59, no. 9 (2013), pp. 5213–5226.

[LHNL+08] D. J. Love, R. W. Heath, V. K. N. Lau, D. Gesbert, B. D. Rao, and M. Andrews. "An overview of limited feedback in wireless communication systems". *IEEE Journal on Selected Areas in Communications*, vol. 26, no. 8 (2008), pp. 1341–1365.

[LLLS21] R. Liu, M. Li, Q. Liu, and A. L. Swindlehurst. "Dual-Functional Radar-Communication Waveform Design: A Symbol-Level Precoding Approach". *IEEE Journal of Selected Topics in Signal Processing*, vol. 15, no. 6 (2021), pp. 1316–1331.

[LLM14a] L. Lu, G. Y. Li, and A. Maaref. "Nullspace releasing for spatial-frequency opportunistic transmission". *IEEE Communications Letters*, vol. 18, no. 10 (2014), pp. 1843–1846.

[LLM14b] L. Lu, G. Y. Li, and A. Maaref. "Spatial-frequency signal alignment for opportunistic transmission". *IEEE Transactions on Signal Processing*, vol. 62, no. 6 (2014), pp. 1561–1575.

[LMP17] K. L. Law, C. Masouros, and M. Pesavento. "Transmit Precoding for Interference Exploitation in the Underlay Cognitive Radio Z-channel". *IEEE Transactions on Signal Processing*, vol. 65, no. 14 (2017), pp. 3617–3631.

[LSK16] G. Lee, Y. Sung, and M. Kountouris. "On the Performance of Random Beamforming in Sparse Millimeter Wave Channels". *IEEE Journal of Selected Topics in Signal Processing*, vol. 10, no. 3 (2016), pp. 560–575.

[LSK+20] A. Li, D. Spano, J. Krivochiza, S. Domouchtsidis, C. G. Tsinos, C. Masouros, S. Chatzinotas, Y. Li, B. Vucetic, and B. Ottersten. "A Tutorial on Interference Exploitation via Symbol-Level Precoding: Overview, State-of-the-Art and Future Directions". *IEEE Communications Surveys Tutorials*, vol. 22, no. 2 (2020), pp. 796–839.

[LSS16] G. Lee, Y. Sung, and J. Seo. "Randomly-Directional Beamforming in Millimeter-Wave Multiuser MISO Downlink". *IEEE Transactions on Wireless Communications*, vol. 15, no. 2 (2016), pp. 1086–1100.

[LTV06] A. Lozano, A.M. Tulino, and S. Verdu. "Optimum power allocation for parallel Gaussian channels with arbitrary input distributions". *IEEE Transactions on Information Theory*, vol. 52, no. 7 (2006), pp. 3033–3051.

[LTV08] A. Lozano, A. M. Tulino, and S. Verdu. "Optimum Power Allocation for Multiuser OFDM with Arbitrary Signal Constellations". *IEEE Transactions on Communications*, vol. 56, no. 5 (2008), pp. 828–837.

[LVT89] F. Li, R.J. Vaccaro, and D.W. Tufts. "Min-norm linear prediction for arbitrary sensor arrays". In: *International Conference on Acoustics, Speech, and Signal Processing*, 1989, 2613–2616 vol.4.

[LW19] W. Liu and Z. Wang. "Non-Uniform Full-Dimension MIMO: New Topologies and Opportunities". *IEEE Wireless Communications*, vol. 26, no. 2 (2019), pp. 124–132.

[LYV18] C. Li, C. You, and R. Vidal. "On geometric analysis of affine sparse subspace clustering". *IEEE Journal of Selected Topics in Signal Processing*, vol. 12, no. 6 (2018), pp. 1520–1533.

[LZ13] Z. Lu and A. M. Zoubir. "Generalized Bayesian information criterion for source enumeration in array processing". *IEEE Transactions on Signal Processing*, vol. 61, no. 6 (2013), pp. 1470–1480.

[Mar10] I. Markovsky. "Bibliography on total least squares and related methods". *Statistics and its interface*, vol. 3, no. 3 (2010), pp. 329–334.

[MC20] Y. Mao and B. Clerckx. "Beyond Dirty Paper Coding for Multi-Antenna Broadcast Channel With Partial CSIT: A Rate-Splitting Approach". *IEEE Transactions on Communications*, vol. 68, no. 11 (2020), pp. 6775–6791.

[MCDV13] M. Maso, L. S. Cardoso, M. Debbah, and L. Vangelista. "Cognitive Orthogonal Precoder for Two-Tiered Networks Deployment". *IEEE Journal on Selected Areas in Communications*, vol. 31, no. 11 (2013), pp. 2338–2348.

[MCVA19] M. Morales-Céspedes, L. Vandendorpe, and A. G. Armada. "Degrees of Freedom of 2-Tier Networks Without Channel State Information at the Transmitter". *IEEE Signal Processing Letters*, vol. 26, no. 2 (2019), pp. 382–386.

[MDC+22] Y. Mao, O. Dizdar, B. Clerckx, R. Schober, P. Popovski, and H. V. Poor. "Rate-Splitting Multiple Access: Fundamentals, Survey, and Future Research Trends". *preprint arXiv:2201.03192* (2022).

[MDV13] M. Maso, M. Debbah, and L. Vangelista. "A distributed approach to interference alignment in OFDM-based two-tiered networks". *IEEE Transactions on Vehicular Technology*, vol. 62, no. 5 (2013), pp. 1935–1949.

[MGC15] A. Mariani, A. Giorgetti, and M. Chiani. "Wideband spectrum sensing by model order selection". *IEEE Transactions on Wireless Communications*, vol. 14, no. 12 (2015), pp. 6710–6721.

[MH07] I. Markovsky and S. Van Huffel. "Overview of total least-squares methods". *Signal Processing*, vol. 87, no. 10 (2007), pp. 2283–2302.

[MJ13] H. Maleki and S. A. Jafar. "Optimality of Orthogonal Access for One-Dimensional Convex Cellular Networks". *IEEE Communications Letters*, vol. 17, no. 9 (2013), pp. 1770–1773.

[MKAC17] J. A. Mahal, A. Khawar, A. Abdelhadi, and T. C. Clancy. "Spectral coexistence of MIMO radar and MIMO cellular system". *IEEE Transactions on Aerospace and Electronic Systems*, vol. 53, no. 2 (2017), pp. 655–668.

[MM99] J. Mitola and G.Q. Maguire. "Cognitive radio: making software radios more personal". *IEEE Personal Communications*, vol. 6, no. 4 (1999), pp. 13–18.

[MMG+14] N. Michailow, M. Matthé, I. S. Gaspar, A. N. Caldevilla, L. L. Mendes, A. Festag, and G. Fettweis. "Generalized Frequency Division Multiplexing for 5th Generation Cellular Networks". *IEEE Transactions on Communications*, vol. 62, no. 9 (2014), pp. 3045–3061.

[MMN+18] E. C. Marques, N. Maciel, L. Naviner, H. Cai, and J. Yang. "A review of sparse recovery algorithms". *IEEE Access*, vol. 7 (2018), pp. 1300–1322.

[MSA08] T. Muharemovic, A. Sabharwal, and B. Aazhang. "Antenna Packing in Low-Power Systems: communication Limits and Array Design". *IEEE Transactions on Information Theory*, vol. 54, no. 1 (2008), pp. 429–440.

[Mül06] C. Müller. *Spherical harmonics*. Vol. 17. Springer, 2006.

[MWD13] S. Mishra, I-H. Wang, and S. Diggavi. "Opportunistic interference management for multicarrier systems". In: *2013 IEEE International Symposium on Information Theory*. 2013, pp. 389–393.

[MWVH+05] I. Markovsky, J.C. Willems, S. Van Huffel, Bart De Moor, and R. Pintelon. "Application of structured total least squares for system identification and model reduction". *IEEE Transactions on Automatic Control*, vol. 50, no. 10 (2005), pp. 1490–1500.

[MZ93] S.G. Mallat and Z. Zhang. "Matching pursuits with time-frequency dictionaries". *IEEE Transactions on Signal Processing*, vol. 41, no. 12 (1993), pp. 3397–3415.

[NCD21] Q.-U.-A. Nadeem, A. Chaaban, and M. Debbah. "Opportunistic Beamforming Using an Intelligent Reflecting Surface Without Instantaneous CSI". *IEEE Wireless Communications Letters*, vol. 10, no. 1 (2021), pp. 146–150.

[NKBJ18] H. Nam, K. S. Ko, I. Bang, and B. C. Jung. "Achievable Rate Analysis of Opportunistic Transmission in Bursty Interference Networks". *IEEE Communications Letters*, vol. 22, no. 3 (2018), pp. 654–657.

[NLP18] G. Naik, J. Liu, and J.-M. J. Park. "Coexistence of Wireless Technologies in the 5 GHz Bands: A Survey of Existing Solutions and a Roadmap for Future Research". *IEEE Communications Surveys & Tutorials*, vol. 20, no. 3 (2018), pp. 1777–1798.

[NWSS21] H. Nikbakht, M. Wigger, and S. Shamai Shitz. "Coordinated Multi-Point Transmission and Reception for Mixed-Delay Traffic". *IEEE Transactions on Communications*, vol. 69, no. 12 (2021), pp. 8116–8131.

[OG15] G. Ozcan and M. C. Gursoy. "Optimal Power Control for Underlay Cognitive Radio Systems With Arbitrary Input Distributions". *IEEE Transactions on Wireless Communications*, vol. 14, no. 8 (2015), pp. 4219–4233.

[ÖLT11] A. Özgür, O. Lévêque, and D. Tse. "Operating regimes of large wireless networks". *Foundations and Trends® in Networking*, vol. 5, no. 1 (2011), pp. 1–107.

[Pak87] L. Pakula. "Asymptotic zero distribution of orthogonal polynomials in sinusoidal frequency estimation". *IEEE Transactions on Information Theory*, vol. 33, no. 4 (1987), pp. 569–576.

[PBS+14] F. Pantisano, M. Bennis, W. Saad, M. Debbah, and M. Latva-aho. "Improving Macrocell-Small Cell Coexistence Through Adaptive Interference Draining". *IEEE Transactions on Wireless Communications*, vol. 13, no. 2 (2014), pp. 942–955.

[PBT05] A. S. Y. Poon, R. W. Brodersen, and D. N. C. Tse. "Degrees of freedom in multiple-antenna channels: a signal space approach". *IEEE Transactions on Information Theory*, vol. 51, no. 2 (2005), pp. 523–536.

[PDP+20] S. R. Pokhrel, J. Ding, J. Park, O.-S. Park, and J. Choi. "Towards Enabling Critical mMTC: A Review of URLLC Within mMTC". *IEEE Access*, vol. 8 (2020), pp. 131796–131813.

[PF87] B. Porat and B. Friedlander. "On the accuracy of the Kumaresan-Tufts method for estimating complex damped exponentials". *IEEE Transactions on Acoustics, Speech, and Signal Processing*, vol. 35, no. 2 (1987), pp. 231–235.

[PFLD10] S. M. Perlaza, N. Fawaz, S. Lasaulce, and M. Debbah. "From spectrum pooling to space pooling: opportunistic interference alignment in MIMO cognitive networks". *IEEE Transactions on Signal Processing*, vol. 58, no. 7 (2010), pp. 3728–3741.

[PLH18] J. Park, N. Lee, and R. W. Heath. "Feedback Design for Multi-Antenna K-Tier Heterogeneous Downlink Cellular Networks". *IEEE Transactions on Wireless Communications*, vol. 17, no. 6 (2018), pp. 3861–3876.

[PLL+19] Y. Pan, G. Q. Luo, Z. Liao, B. Cai, and M. Yao. "Wideband Direction-of-Arrival Estimation With Arbitrary Array via Coherent Annihilating". *IEEE Access*, vol. 7 (2019), pp. 51058–51068.

[PMS20a] A. Pizzo, T. L. Marzetta, and L. Sanguinetti. "Degrees of Freedom of Holographic MIMO Channels". In: *2020 IEEE 21st International Workshop on Signal Processing Advances in Wireless Communications (SPAWC)*. 2020, pp. 1–5.

[PMS20b] A. Pizzo, T. L. Marzetta, and L. Sanguinetti. "Spatially-stationary model for holographic MIMO small-scale fading". *IEEE Journal on Selected Areas in Communications*, vol. 38, no. 9 (2020), pp. 1964–1979.

[PNG03] A. Paulraj, R. Nabar, and D. Gore. *Introduction to space-time wireless communications*. Cambridge University Press, 2003.

[Pop20] P. Popovski. *Wireless Connectivity: An Intuitive and Fundamental Guide*. John Wiley & Sons, 2020.

[Por07] D. Porrat. "Information theory of wideband communications". *IEEE Communications Surveys & Tutorials*, vol. 9, no. 2 (2007), pp. 2–16.

[PPV10] Y. Polyanskiy, H. V. Poor, and S. Verdú. "Channel Coding Rate in the Finite Blocklength Regime". *IEEE Transactions on Information Theory*, vol. 56, no. 5 (2010), pp. 2307–2359.

[PRJV18] A. Patel, H. Ram, A. K. Jagannatham, and P. K. Varshney. "Robust Cooperative Spectrum Sensing for MIMO Cognitive Radio Networks Under CSI Uncertainty". *IEEE Transactions on Signal Processing*, vol. 66, no. 1 (2018), pp. 18–33.

[PS08] J. G. Proakis and M. Salehi. *Digital Communications*. McGraw-Hill, 2008.

[PSM22] A. Pizzo, L. Sanguinetti, and T. L. Marzetta. "Fourier Plane-Wave Series Expansion for Holographic MIMO Communications". *IEEE Transactions on Wireless Communications* (2022), pp. 1–1.

[PSN+19] P. Popovski, Č. Stefanović, J. J. Nielsen, E. de Carvalho, M. Angjelichinoski, K. F. Trillingsgaard, and A.-S. Bana. "Wireless Access in Ultra-Reliable Low-Latency Communication (URLLC)". *IEEE Transactions on Communications*, vol. 67, no. 8 (2019), pp. 5783–5801.

[PTN07] D. Porrat, D. N. C. Tse, and S. Nacu. "Channel uncertainty in ultra-wideband communication systems". *IEEE Transactions on Information Theory*, vol. 53, no. 1 (2007), pp. 194–208.

[RFSVV14] J. Riba, J. Font-Segura, J. Villares, and G. Vázquez. "Frequency-Domain GLR Detection of a Second-Order Cyclostationary Signal Over Fading Channels". *IEEE Transactions on Signal Processing*, vol. 62, no. 8 (2014), pp. 1899–1912.

[RG09] M. Rubsamen and A. B. Gershman. "Direction-of-Arrival Estimation for Nonuniform Sensor Arrays: from Manifold Separation to Fourier Domain MUSIC Methods". *IEEE Transactions on Signal Processing*, vol. 57, no. 2 (2009), pp. 588–599.

[RH89] B.D. Rao and K.V.S. Hari. "Performance analysis of Root-Music". *IEEE Transactions on Acoustics, Speech, and Signal Processing*, vol. 37, no. 12 (1989), pp. 1939–1949.

[Ris78] J. Rissanen. "Modeling by shortest data description". *Automatica*, vol. 14, no. 5 (1978), pp. 465–471.

[RR16] S. M. Razavi and T. Ratnarajah. "Adaptive LS- and MMSE-Based Beamformer Design for Multiuser MIMO Interference Channels". *IEEE Transactions on Vehicular Technology*, vol. 65, no. 1 (2016), pp. 132–144.

[RSV01] J. Riba, J. Sala, and G. Vazquez. "Conditional maximum likelihood timing recovery: estimators and bounds". *IEEE Transactions on Signal Processing*, vol. 49, no. 4 (2001), pp. 835–850.

[RSV+15] D. Ramírez, P. J. Schreier, J. Vía, I. Santamaría, and L. L. Scharf. "Detection of Multivariate Cyclostationarity". *IEEE Transactions on Signal Processing*, vol. 63, no. 20 (2015), pp. 5395–5408.

[RVC15] S. A. Razavi, M. Valkama, and D. Cabric. "Covariance-based OFDM spectrum sensing with sub-Nyquist samples". *Signal Processing*, vol. 109 (2015), pp. 261 –268.

[RVVLV+11] D. Ramirez, G. Vazquez-Vilar, R. Lopez-Valcarce, J. Via, and I. Santamaria. "Detection of Rank-P Signals in Cognitive Radio Networks With Uncalibrated Multiple Antennas". *IEEE Transactions on Signal Processing*, vol. 59, no. 8 (2011), pp. 3764–3774.

[RY87] M.D. Rahman and K.-B. Yu. "Total least squares approach for frequency estimation using linear prediction". *IEEE Transactions on Acoustics, Speech, and Signal Processing*, vol. 35, no. 10 (1987), pp. 1440–1454.

[SAVVLV+16] J. Sala-Alvarez, G. Vázquez-Vilar, R. López-Valcarce, S. Sedighi, and A. Taherpour. "Multiantenna GLR Detection of Rank-One Signals With Known Power Spectral Shape Under Spatially Uncorrelated Noise". *IEEE Transactions on Signal Processing*, vol. 64, no. 23 (2016), pp. 6269–6283.

[SBL+18] S. K. Sharma, T. E. Bogale, L. B. Le, S. Chatzinotas, X. Wang, and B. Ottersten. "Dynamic Spectrum Sharing in 5G Wireless Networks With Full-Duplex Technology: Recent Advances and Research Challenges". *IEEE Communications Surveys & Tutorials*, vol. 20, no. 1 (2018), pp. 674–707.

[Sch78] G. Schwarz. "Estimating the Dimension of a Model". *The Annals of Statistics*, vol. 6, no. 2 (1978), pp. 461–464.

[SF11] C. Shen and M. P. Fitz. "Opportunistic Spatial Orthogonalization and Its Application in Fading Cognitive Radio Networks". *IEEE Journal of Selected Topics in Signal Processing*, vol. 5, no. 1 (2011), pp. 182–189.

[SH07] M. Sharif and B. Hassibi. "A Comparison of Time-Sharing, DPC, and Beamforming for MIMO Broadcast Channels With Many Users". *IEEE Transactions on Communications*, vol. 55, no. 1 (2007), pp. 11–15.

[Sha48] C. E. Shannon. "A mathematical theory of communication". *The Bell System Technical Journal*, vol. 27, no. 3 (1948), pp. 379–423.

[Sha49] C. E. Shannon. "Communication in the Presence of Noise". *Proceedings of the IRE*, vol. 37, no. 1 (1949), pp. 10–21.

[SKDI16] A. Saeed, E. Katranaras, M. Dianati, and M. A. Imran. "Dynamic femtocell resource allocation for managing inter-tier interference in downlink of heterogeneous networks". *IET Communications*, vol. 10, no. 6 (2016), pp. 641–650.

[Sle76] D. Slepian. "On bandwidth". *Proceedings of the IEEE*, vol. 64, no. 3 (1976), pp. 292–300.

[SM00] L. L. Scharf and C. T. Mullis. "Canonical coordinates and the geometry of inference, rate, and capacity". *IEEE Transactions on Signal Processing*, vol. 48, no. 3 (2000), pp. 824–831.

[SMA+19] M. Shirvanimoghaddam, M. S. Mohammadi, R. Abbas, A. Minja, C. Yue, B. Matuz, G. Han, Z. Lin, W. Liu, Y. Li, S. Johnson, and B. Vucetic. "Short Block-Length Codes for Ultra-Reliable Low Latency Communications". *IEEE Communications Magazine*, vol. 57, no. 2 (2019), pp. 130–137.

[SP21] P. Sarangi and P. Pal. "No Relaxation: Guaranteed Recovery of Finite-Valued Signals from Undersampled Measurements". In: *ICASSP 2021 - 2021 IEEE International Conference on Acoustics, Speech and Signal Processing (ICASSP)*. 2021, pp. 5440–5444.

[SP61] D. Slepian and H. O. Pollak. "Prolate spheroidal wave functions, Fourier analysis and uncertainty - I". *The Bell System Technical Journal*, vol. 40, no. 1 (1961), pp. 43–63.

[SS04] P. Stoica and Y. Selen. "Model-order selection: a review of information criterion rules". *IEEE Signal Processing Magazine*, vol. 21, no. 4 (2004), pp. 36–47.

[SSS20] M. Soleymani, I. Santamaria, and P. J. Schreier. "Improper Gaussian Signaling for the K-User MIMO Interference Channels With Hardware Impairments". *IEEE Transactions on Vehicular Technology*, vol. 69, no. 10 (2020), pp. 11632–11645.

[SV15] M. Shaghaghi and S. A. Vorobyov. "Subspace Leakage Analysis and Improved DOA Estimation With Small Sample Size". *IEEE Transactions on Signal Processing*, vol. 63, no. 12 (2015), pp. 3251–3265.

[SYGM21] W.-B. Sun, Q.-Y. Yu, J.-C. Guo, and W.-X. Meng. "Multiuser Opportunistic Beamforming Systems With Multiple Receive Antennas in Nakagami-m Fading Channels". *IEEE Systems Journal* (2021), pp. 1–12.

[TB13] C. G. Tsinos and K. Berberidis. "Blind opportunistic interference alignment in MIMO cognitive radio systems". *IEEE Journal on Emerging and Selected Topics in Circuits and Systems*, vol. 3, no. 4 (2013), pp. 626–639.

[TDAB16] G. I. Tsiropoulos, O. A. Dobre, M. H. Ahmed, and K. E. Baddour. "Radio Resource Allocation Techniques for Efficient Spectrum Access in Cognitive Radio Networks". *IEEE Communications Surveys & Tutorials*, vol. 18, no. 1 (2016), pp. 824–847.

[Tee07] G. J. Tee. "Eigenvectors of block circulant and alternating circulant matrices". *New Zealand Journal of Mathematics*, vol. 36, no. 8 (2007), pp. 195–211.

[TG07] J. A. Tropp and A. C. Gilbert. "Signal Recovery From Random Measurements Via Orthogonal Matching Pursuit". *IEEE Transactions on Information Theory*, vol. 53, no. 12 (2007), pp. 4655–4666.

[TJGL18] J. Tong, M. Jin, Q. Guo, and Y. Li. "Cooperative Spectrum Sensing: A Blind and Soft Fusion Detector". *IEEE Transactions on Wireless Communications*, vol. 17, no. 4 (2018), pp. 2726–2737.

[TK82] D. Tufts and R. Kumaresan. "Singular value decomposition and improved frequency estimation using linear prediction". *IEEE Transactions on Acoustics, Speech, and Signal Processing*, vol. 30, no. 4 (1982), pp. 671–675.

[TKK82] D.W. Tufts, R. Kumaresan, and I. Kirsteins. "Data adaptive signal estimation by singular value decomposition of a data matrix". *Proceedings of the IEEE*, vol. 70, no. 6 (1982), pp. 684–685.

[Tom71] M. Tomlinson. "New automatic equaliser employing modulo arithmetic". *Electronics letters*, vol. 7, no. 5 (1971), pp. 138–139.

[TP14] A. M. Tillmann and M. E. Pfetsch. "The Computational Complexity of the Restricted Isometry Property, the Nullspace Property, and Related Concepts in Compressed Sensing". *IEEE Transactions on Information Theory*, vol. 60, no. 2 (2014), pp. 1248–1259.

[Tro04] J.A. Tropp. "Greed is good: algorithmic results for sparse approximation". *IEEE Transactions on Information Theory*, vol. 50, no. 10 (2004), pp. 2231–2242.

[TS08] R. Tandra and A. Sahai. "SNR Walls for Signal Detection". *IEEE Journal of Selected Topics in Signal Processing*, vol. 2, no. 1 (2008), pp. 4–17.

[Tse97] D. N. Tse. "Optimal power allocation over parallel Gaussian broadcast channels". In: *Proceedings of IEEE International Symposium on Information Theory*. 1997, pp. 27–.

[TT07] E. Telatar and D. Tse. "Bounds on the capacity region of a class of interference channels". In: *2007 IEEE International Symposium on Information Theory*. 2007, pp. 2871–2874.

[TV05] D. Tse and P. Viswanath. *Fundamentals of Wireless Communication*. Cambridge University Press, 2005.

[TVZ04] D.N.C. Tse, P. Viswanath, and L. Zheng. "Diversity-multiplexing tradeoff in multiple-access channels". *IEEE Transactions on Information Theory*, vol. 50, no. 9 (2004), pp. 1859–1874.

[Van02] H. L. Van Trees. *Optimum Array Processing: Part IV of detection, estimation, and modulation theory*. John Wiley & Sons, 2002.

[VEG18] V. V. Veeravalli and A. El Gamal. *Interference management in wireless networks: Fundamental bounds and the role of cooperation*. Cambridge University Press, 2018.

[Ver02] S. Verdu. "Spectral efficiency in the wideband regime". *IEEE Transactions on Information Theory*, vol. 48, no. 6 (2002), pp. 1319–1343.

[Ver98] S. Verdú. *Multiuser detection*. Cambridge University Press, 1998.

[VH12] R. Vaze and R. W. Heath. "Transmission Capacity of Ad-hoc Networks With Multiple Antennas Using Transmit Stream Adaptation and Interference Cancellation". *IEEE Transactions on Information Theory*, vol. 58, no. 2 (2012), pp. 780–792.

[VHZ93] S. Van Huffel and H. Zha. "The total least squares problem". In: *Computational Statistics*. Vol. 9. Handbook of Statistics. Elsevier, 1993, pp. 377–408.

[VT03] P. Viswanath and D.N.C. Tse. "Sum capacity of the vector Gaussian broadcast channel and uplink-downlink duality". *IEEE Transactions on Information Theory*, vol. 49, no. 8 (2003), pp. 1912–1921.

[VTL02] P. Viswanath, D. N. C. Tse, and R. Laroia. "Opportunistic beamforming using dumb antennas". *IEEE Transactions on Information Theory*, vol. 48, no. 6 (2002), pp. 1277–1294.

[VV07] J. Villares and G. Vazquez. "The Gaussian assumption in second-order estimation problems in digital communications". *IEEE Transactions on Signal Processing*, vol. 55, no. 10 (2007), pp. 4994–5002.

[VV12] C. S. Vaze and M. K. Varanasi. "The Degree-of-Freedom Regions of MIMO Broadcast, Interference, and Cognitive Radio Channels With No CSIT". *IEEE Transactions on Information Theory*, vol. 58, no. 8 (2012), pp. 5354–5374.

[WA12] S. Weber and J. G. Andrews. "Transmission Capacity of Wireless Networks". *Foundations and Trends® in Networking*, vol. 5, no. 2–3 (2012), pp. 109–281.

[WAJ07] S. Weber, J. G. Andrews, and N. Jindal. "The Effect of Fading, Channel Inversion, and Threshold Scheduling on Ad Hoc Networks". *IEEE Transactions on Information Theory*, vol. 53, no. 11 (2007), pp. 4127–4149.

[WAJ10] S. Weber, J. G. Andrews, and N. Jindal. "An overview of the transmission capacity of wireless networks". *IEEE Transactions on Communications*, vol. 58, no. 12 (2010), pp. 3593–3604.

[WBV21] T. Wild, V. Braun, and H. Viswanathan. "Joint Design of Communication and Sensing for Beyond 5G and 6G Systems". *IEEE Access*, vol. 9 (2021), pp. 30845–30857.

[Wel74] L. Welch. "Lower bounds on the maximum cross correlation of signals (Corresp.)" *IEEE Transactions on Information Theory*, vol. 20, no. 3 (1974), pp. 397–399.

[WHC19] Y.-S. Wang, Y.-W. P. Hong, and W.-T. Chen. "Dynamic transmission policy for multi-pair cooperative device-to-device communication with block-diagonal-ĂŞization precoding". *IEEE Transactions on Wireless Communications*, vol. 18, no. 6 (2019), pp. 3034–3048.

[WK85] M. Wax and T. Kailath. "Detection of signals by information theoretic criteria". *IEEE Transactions on Acoustics, Speech, and Signal Processing*, vol. 33, no. 2 (1985), pp. 387–392.

[WKK+18] X. Wang, L. Kong, F. Kong, F. Qiu, M. Xia, S. Arnon, and G. Chen. "Millimeter wave communication: A comprehensive survey". *IEEE Communications Surveys & Tutorials*, vol. 20, no. 3 (2018), pp. 1616–1653.

[WL19] Y. Wei and T.-M. Lok. "An Iterative Interference Alignment Algorithm for the General MIMO X Channel". *IEEE Transactions on Wireless Communications*, vol. 18, no. 3 (2019), pp. 1847–1859.

[WRF+13] W. Fu, R. Yao, F. Gao, J. C. F. Li, and M. Lei. "Robust null-space based interference avoiding scheme for D2D communication underlaying cellular networks". In: *2013 IEEE Wireless Communications and Networking Conference (WCNC)*. 2013, pp. 4158–4162.

[WS12] J. Wang and B. Shim. "On the Recovery Limit of Sparse Signals Using Orthogonal Matching Pursuit". *IEEE Transactions on Signal Processing*, vol. 60, no. 9 (2012), pp. 4973–4976.

[WT11a] I-H. Wang and D. N. C. Tse. "Interference Mitigation Through Limited Receiver Cooperation". *IEEE Transactions on Information Theory*, vol. 57, no. 5 (2011), pp. 2913–2940.

[WT11b] I-H. Wang and D. N. C. Tse. "Interference Mitigation Through Limited Transmitter Cooperation". *IEEE Transactions on Information Theory*, vol. 57, no. 5 (2011), pp. 2941–2965.

[WWX+20] X. Wang, J. Wang, Y. Xu, J. Chen, L. Jia, X. Liu, and Y. Yang. "Dynamic Spectrum Anti-Jamming Communications: Challenges and Opportunities". *IEEE Communications Magazine*, vol. 58, no. 2 (2020), pp. 79–85.

[WYAV05] S. P. Weber, X. Yang, J. G. Andrews, and G. de Veciana. "Transmission capacity of wireless ad hoc networks with outage constraints". *IEEE Transactions on Information Theory*, vol. 51, no. 12 (2005), pp. 4091–4102.

[XGL18] Q. Xin, H. Gao, and T. Lv. "Opportunistic Interference Mitigation for D-TDD in Ultra-Dense Networks". In: *2018 IEEE International Conference on Communications Workshops (ICC Workshops)*. 2018, pp. 1–6.

[XK95] W. Xu and M. Kaveh. "Analysis of the performance and sensitivity of eigendecomposition based detectors". *IEEE Transactions on Signal Processing*, vol. 43, no. 6 (1995), pp. 1413–1426.

[XNHC14] Y. Xiao, D. Niyato, Z. Han, and K.-C. Chen. "Secondary Users Entering the Pool: A Joint Optimization Framework for Spectrum Pooling". *IEEE Journal on Selected Areas in Communications*, vol. 32, no. 3 (2014), pp. 572–588.

[XWGJ16] H. Xie, B. Wang, F. Gao, and S. Jin. "A Full-Space Spectrum-Sharing Strategy for Massive MIMO Cognitive Radio Systems". *IEEE Journal on Selected Areas in Communications*, vol. 34, no. 10 (2016), pp. 2537–2549.

[XWG+18] R. Xu, L. Wang, Z. Geng, H. Deng, L. Peng, and L. Zhang. "A Unitary Precoder for Optimizing Spectrum and PAPR Characteristic of OFDMA Signal". *IEEE Transactions on Broadcasting*, vol. 64, no. 2 (2018), pp. 293–306.

[YHC+22] S. S. A. Yuan, Z. He, X. Chen, C. Huang, and W. E. I. Sha. "Electromagnetic Effective Degree of Freedom of an MIMO System in Free Space". *IEEE Antennas and Wireless Propagation Letters*, vol. 21, no. 3 (2022), pp. 446–450.

[YHR+09] H. Yi, H. Hu, Y. Rui, K. Guo, and J. Zhang. "Null space-based precoding scheme for secondary transmission in a cognitive radio MIMO system using second-order statistics". In: *2009 IEEE International Conference on Communications*. 2009, pp. 1–5.

[Yi10] H. Yi. "Nullspace-based secondary joint transceiver scheme for cognitive radio MIMO networks using second-order statistics". In: *2010 IEEE International Conference on Communications*. 2010, pp. 1–5.

[YLL+16] R. Yao, Y. Liu, L. Lu, G. Y. Li, and A. Maaref. "Cooperative precoding for cognitive transmission in two-tier networks". *IEEE Transactions on Communications*, vol. 64, no. 4 (2016), pp. 1423–1436.

[YS20] X. Yi and H. Sun. "Opportunistic Treating Interference as Noise". *IEEE Transactions on Information Theory*, vol. 66, no. 1 (2020), pp. 520–533.

[YV15a] C. You and R. Vidal. "Geometric conditions for subspace-sparse recovery". In: *Proceedings of the 32nd International Conference on International Conference on Machine Learning*. 2015, pp. 1585–1593.

[YV15b] C. You and R. Vidal. "Subspace-sparse representation". *preprint arXiv:1507.01307* (2015).

[YXXL19] P. Yang, Y. Xiao, M. Xiao, and S. Li. "6G Wireless Communications: Vision and Potential Techniques". *IEEE Network*, vol. 33, no. 4 (2019), pp. 70–75.

[ZD17] D. Zahavi and R. Dabora. "On Cooperation and Interference in the Weak Interference Regime". *IEEE Transactions on Information Theory*, vol. 63, no. 6 (2017), pp. 3894–3922.

[ZDG12] Y. Zhang, E. Dall'Anese, and G. B. Giannakis. "Distributed optimal beamformers for cognitive radios robust to channel uncertainties". *IEEE Transactions on Signal Processing*, vol. 60, no. 12 (2012), pp. 6495–6508.

[ZGH17] Z. Zhou, D. Guo, and M. L. Honig. "Licensed and Unlicensed Spectrum Allocation in Heterogeneous Networks". *IEEE Transactions on Communications*, vol. 65, no. 4 (2017), pp. 1815–1827.

[ZL08] R. Zhang and Y. C. Liang. "Exploiting multi-antennas for opportunistic spectrum sharing in cognitive radio networks". *IEEE Journal of Selected Topics in Signal Processing*, vol. 2, no. 1 (2008), pp. 88–102.

[ZLR12] R. Zakaria and D. Le Ruyet. "A Novel Filter-Bank Multicarrier Scheme to Mitigate the Intrinsic Interference: Application to MIMO Systems". *IEEE Transactions on Wireless Communications*, vol. 11, no. 3 (2012), pp. 1112–1123.

[ZTS21] M. Zohdy, A. Tajer, and S. Shamai. "Distributed Interference Management: A Broadcast Approach". *IEEE Transactions on Communications*, vol. 69, no. 1 (2021), pp. 149–163.

[ZWO09] G. Zheng, K. K. Wong, and B. Ottersten. "Robust cognitive beamforming with bounded channel uncertainties". *IEEE Transactions on Signal Processing*, vol. 57, no. 12 (2009), pp. 4871–4881.

[ZWYR89] Q.-T. Zhang, K.M. Wong, P.C. Yip, and J.P. Reilly. "Statistical analysis of the performance of information theoretic criteria in the detection of the number of signals in array processing". *IEEE Transactions on Acoustics, Speech, and Signal Processing*, vol. 37, no. 10 (1989), pp. 1557–1567.

[ZYJ+16] N. Zhao, F. R. Yu, M. Jin, Q. Yan, and V. C. M. Leung. "Interference alignment and its applications: a survey, research issues, and challenges". *IEEE Communications Surveys & Tutorials*, vol. 18, no. 3 (2016), pp. 1779–1803.

[ZZGG13] Y. Zeng, R. Zhang, E. Gunawan, and Y. L. Guan. "Optimized Transmission with Improper Gaussian Signaling in the K-User MISO Interference Channel". *IEEE Transactions on Wireless Communications*, vol. 12, no. 12 (2013), pp. 6303–6313.

[ZZY+15] Y. Zou, J. Zhu, L. Yang, Y.-c. Liang, and Y.-. Yao. "Securing physical-layer communications for cognitive radio networks". *IEEE Communications Magazine*, vol. 53, no. 9 (2015), pp. 48–54.